PFC/RR-86-6, v.1 of 2

DOE/ET-51013-175, v.1 of 2
UC20F

Poloidal Asymmetries in the Limiter Shadow Plasma of the Alcator C Tokamak

LaBombard, Brian

May 1986

Plasma Fusion Center
Massachusetts Institute of Technology
Cambridge, MA 02139

This work was supported by the U.S. Department of Energy Contract No. DE-AC02-78ET51013. Reproduction, translation, publication, use and disposal, in whole or in part by or for the United States government is permitted.

Due to the poor quality of the original document, there is some spotting or background shading in this document.

POLOIDAL ASYMMETRIES IN THE LIMITER SHADOW PLASMA OF THE ALCATOR C TOKAMAK

Brian Louis LaBombard

B.S., The University of Lowell
(1978)

VOLUME I of II

Submitted to the
Department of Nuclear Engineering
in Partial Fulfillment of the Requirements
for the Degree of

DOCTOR OF SCIENCE

at the

MASSACHUSETTS INSTITUTE OF TECHNOLOGY

April 1986

Signature of Author _____

Department of Nuclear Engineering
April 1986

Certified by _____

Dr. Bruce Lipschultz, Principal Staff Scientist
Thesis Supervisor

Certified by _____

Professor Ian H. Hutchinson
Thesis Reader

Accepted by _____

Professor Allan F. Henry
Chairman, Department Committee of Graduate Students

POLOIDAL ASYMMETRIES IN THE LIMITER SHADOW PLASMA OF THE ALCATOR C TOKAMAK

by

Brian Louis LaBombard

Submitted to the Department of Nuclear Engineering
on April 30, 1986 in partial fulfillment of the
requirements for the Degree of Doctor of Science
in Nuclear Engineering

ABSTRACT

A diagnostic system consisting of an array of 80 closely spaced Langmuir probes (DENSEPACK) is developed and used to sample plasma that exists between the limiter radius and the wall of the Alcator C tokamak. Fast numerical computer algorithms are written to reliably fit many Langmuir probe characteristics and infer plasma density and electron temperature via both a simple plane probe model and a more complicated magnetized probe model. Unexpectedly large poloidal asymmetries in density, electron temperature, and radial density e-folding length are detected. Factors of $\sim$ 4–20 variation in density and $\sim$ 5–10 variation in density e-folding lengths are typically recorded in discharges which are bounded by poloidally symmetric ring limiters. These poloidal asymmetries further imply that pressure is not constant on a flux surface. The magnitude of the poloidal asymmetry and its functional dependence on poloidal angle persists independent of machine parameters (toroidal field, plasma current, central density). Simple edge plasma fluid models which include poloidally asymmetric diffusion and $\underline{E} \times \underline{B}$ convection are developed and used to examine mechanisms which might support the observed asymmetry. Also unexpectedly, MARFE phenomena appear as only a slight restructuring and reduction of this poloidal asymmetry. The diagnosis of spatially oscillating MARFE activity supports the hypothesis of a MARFE being the manifestation of a radiation thermal instability.

A database of edge plasma and central plasma parameters is compiled. Regression analysis of edge density data identifies two distinct central plasma parameter scaling laws associated with MARFE and non-MARFE discharges. A critical value of the ratio of central line-averaged density to plasma current ($\bar{n}_e/I_p$) is found to determine the transition between these two edge density scaling laws. Edge plasma parameters, including global particle confinement time (τ_p), is catalogued for a large number of ohmic, gas fueled discharges. Lower Hybrid Radio Frequency (LHRF) heated discharges show a degradation in τ_p (up to $\sim$ 50%), proportional to RF power. Pellet fueling can result in up to $\sim$ 100% increase in τ_p when the pellet size is comparable to the target plasma density ($\Delta\bar{n}_e/\bar{n}_e \gtrsim 1$).

Thesis Supervisor:

Bruce Lipschultz, Principal Staff Scientist, Plasma Fusion Center, M.I.T.

Thesis Reader:

Ian H. Hutchinson, Professor of Nuclear Engineering, M.I.T.

In Memory of Holly R. Ham

"Do not deceive yourselves.... For the wisdom of this world is foolishness in God's sight."

1 Corinth 3:18,19

ACKNOWLEDGEMENTS

This thesis would not have been possible without the support of many people. I am greatly indebted to the Alcator C research group and M.I.T. Plasma Fusion Center for this opportunity of a unique learning experience in experimental plasma physics. At the risk of neglecting many friends and associates who made countless contributions both professionally and personally during my stay at M.I.T., I wish to mention a few people in particular.

The memory of Professor Louis Scaturro lives in my heart. He introduced me to the world of experimental plasma physics and had faith in my determination to succeed in this new field. I thank Dave Overskei for guiding me through some difficult personal times and showing me great optimism and enthusiasm.

I am especially indebted to Bruce Lipschultz who advised me throughout the DENSEPACK project. He was always available for consultation and contributed to nearly every phase of this thesis – from stripping stainless steel clad copper wires during the assembly of DENSEPACK to arguing through some crazy idea that I might have about the Alcator C edge plasma.

Although Professor Ian Hutchinson joined the DENSEPACK project relatively late in its progress, he often provided the most constructive criticism. I sought his objective perspective and experience for the more difficult problems.

I thank Steve Wolfe for his genuine interest and stimulating discussions on the interpretation of DENSEPACK's data. Thanks are extended to Martin Greenwald for his helpful discussions and encouragement. He had the knack of momentarily placing my seemingly critical problems into a refreshing light of absurdity and irrelevance which was often needed. I also thank Reich Watterson for his advice and support.

I thank Professor Ron Parker for his style of leadership and guidance of the Alcator C project. His willingness to integrate graduate student projects into overall program goals provides great opportunity for learning and stimulates the creativity and success of the entire Alcator C project.

Frank Silva, Dave Gwinn, Charles Park and the operations group were responsible for the smooth, reliable operation of the Alcator C tokamak. Without

their efforts, the DENSEPACK experiment would have no plasma to diagnose. Bruce Lipschultz, Dave Gwinn, Brian Lloyd, Ron Parker, and Frank Silva set up the plasma discharges which were investigated by DENSEPACK. I thank them for this sometimes tedious task which is essential for the collection of unambiguous data.

The DENSEPACK data acquisition electronics system would not have been possible without the handiwork and expertise of Bruce Oliver, Marty Hughes, Eric Woodworth, Joe Bosco, and Tom Fredian. Bob Childs, Matt Besen, and Norton Pierce provided helpful suggestions on the design and contruction of the DENSEPACK vacuum hardware. 'Woody' Woodworth and the skilled craftsmen in his shop where responsible for machining the intricate pattern in the stainless steel backbone of DENSEPACK.

Thanks are extended to my more immediate colleagues and friends, the Alcator C graduate students. Mark Foord, Herb Manning, Pat Pribyl, and Alan Wan in particular were responsible for much of my learning experience. Often a difficult problem would arise among us which led to enlightening discussions. I especially thank Pat Pribyl for the measurement and analysis of poloidal flux data and also Alan Wan for the collaboration on his JANUS probe experiments.

I thank John O'Rourke for his encouragement, particularly early in the development of this thesis. Both our friendship and professional association has been invaluable to the completion of this work.

Special thanks are extended again to Bruce Lipschultz and Professor Ron Parker who saw me through a frightening experience during the NATO edge plasma course in Val-Morin, Québec.

I am indebted to Eileen McGettigan for her careful editing of this long manuscript and constructive criticism of my often sloppy English usage. Her encouragement, patience, and understanding, particularly during the final preparation stage of this thesis, is greatly appreciated.

Finally, my most sincere thanks are reserved for my parents and family. They believed in my choice to forgo many material comforts in pursuit of this career in experimental plasma physics and showed undying emotional support and patience over my many years of study.

VOLUME I

TABLE OF CONTENTS

II EXPERIMENTAL APPARATUS & DATA REDUCTION

III EXPERIMENTAL RESULTS

LIST OF FIGURES

CHAPTER 2

CHAPTER 3

CHAPTER 4

CHAPTER 5

CHAPTER 6

CHAPTER 7

CHAPTER 8

CHAPTER 9

CHAPTER 10

CHAPTER 11

APPENDICES

LIST OF TABLES

I INTRODUCTION & BACKGROUND

CHAPTER 1

INTRODUCTION

This thesis investigates conditions which exist in the limiter shadow plasma of the Alcator C tokamak. The understanding of this edge plasma region is approached from both experimental and theoretical points of view. First, a general overview of edge plasma physical processes is presented. Simple edge plasma models and conditions which can theoretically result in a poloidally asymmetric edge plasma are discussed. A review of data obtained from previous diagnostics in the Alcator C edge plasma is then used to motivate the development of a new edge plasma diagnostic system (DENSEPACK) to experimentally investigate poloidal asymmetries in this region. The bulk of this thesis focuses on the marked poloidal asymmetries detected by this poloidal probe array and possible mechanisms which might support such asymmetries on a magnetic flux surface. In processing the probe data, some important considerations on fitting Langmuir probe characteristics are identified. The remainder of this thesis catalogues edge versus central plasma parameter dependences. Regression analysis techniques are applied to characterize edge density for various central plasma parameters. Edge plasma conditions during lower hybrid radio frequency heating and pellet injection are also documented.

First, to introduce and motivate the study of this plasma region in Alcator C, some general remarks on the role of the edge plasma in thermonuclear fusion research are made.

1.1 Introduction to Edge Plasma

The term 'edge plasma' refers in a magnetically confined plasma to a peripheral plasma region in which the effects of a wall surface or divertor chamber are felt. The edge plasma region can include plasma just inside a separatrix or limiter shadow boundary as well as plasma in direct contact with divertor neutralizer plates, limiters, or wall surfaces. Plasma-wall interactions differentiate the edge plasma from the central plasma by adding the physics of recycling, impurity release mechanisms, parallel transport to wall surfaces, and hydrogenic and light impurity radiation. Discharges in which the effect of this 'edge physics' appears in the center of the device is sometimes said to consist entirely of an 'edge plasma', extending the definition to mean a plasma state rather than a location.

The edge plasma is strongly coupled to the central plasma. All plasma lost from the center must pass through the edge, and reciprocally, all non-pellet fueling processes must sweep particles through the edge into the center. In addition, impurity release mechanisms such as sputtering, evaporation, and arcing depend critically on edge conditions.[1] Impurities transported to the center can dominate the central power balance and cause disruptions.[2]

The study of edge plasma can therefore provide some answers to key questions about transport of particles and energy in the edge and the dominant impurity generation mechanisms. Ultimately, a more complete understanding of the edge plasma may lead to new techniques to maintain more desirable central plasma conditions.

1.2 Motivation for Studying Edge Plasma in Tokamaks

There is increased interest in the edge plasma region of tokamaks particularly with the observation of low temperature, high density plasma regions in the edge in limited discharges[3-6] and low or high recycling regimes associated with

the H and L mode regimes of diverted discharges.[7–9] It has been suggested that the transition from low to high energy confinement time of the central plasma in ASDEX depends on the edge temperature and the associated degree of recycling in the divertor.[7] H-mode is suppressed in ASDEX when the plasma is allowed to lean on a limiter. PDX obtained a similar H regime by closing the divertor chamber and isolating neutrals from the main plasma region.[9] The important common ingredient in all these results is the physical processes which are occuring in the edge plasma region and how the edge plasma couples to the central plasma region. Thus, the focus of controlled thermonuclear fusion research has expanded more to encompass the understanding and controlling of edge plasmas.

In an engineering sense, the edge plasma poses one of the most severe material problems in a reliable fusion reactor system. First generation tokamak experiments used limiter systems exclusively to unload plasma energy near the vacuum wall. Even in these relatively short pulse length plasmas, the limiter structure could melt or fracture and become not only a major source of impurities but a mechanical failure mode for these machines. Data from surface temperature measurements of the limiter system in the Alcator A tokamak[10] routinely detected transient power fluxes exceeding 20 kW/cm^2. Clearly, in a near steady state reactor system which must function reliably over long periods of time, power fluxes to wall surfaces must be greatly reduced through the use of a more elaborate geometry limiter and divertor systems. Even with the most exotic materials, a typical design power flux[11] is more on the order of 100–400 W/cm^2 for actively cooled surfaces.

Current generation tokamak experiments such as ASDEX and JT-60 use such divertor systems; however, the problems associated with wall erosion and impurity release remain. It is recognized that it would be beneficial to minimize the edge plasma temperature via such processes as radiative cooling through controlled impurity injection or enhanced radial transport through ergodic field line topologies.[12,13] Thus, the reliable operation of a fusion reactor system may

be contingent upon understanding and exploiting edge plasma processes.

The necessity of sustaining a steady state tokamak discharge for fusion power production requires the development of auxilliary techniques to maintain a plasma current and deposit heat in the central plasma region. Radio frequency (RF) current drive and heating has shown significant progress in this area but requires detailed knowledge of edge plasma conditions to allow optimization of RF power coupling to the central plasma. RF itself can affect the edge plasma. High energy electron tails and large perpendicular energy ions generated by RF injection can interact with wall surfaces and release impurities. Edge densities and temperatures can change due to increased impurity levels, RF ionization, and energy deposition, thereby changing the original coupling conditions. A general characterization of edge plasma parameters with and without RF is useful in itself for addressing these problems.

The edge plasma is an interesting phenomenon in itself. Gradients in density and temperature which can drive instabilities are largest in the edge plasma. Neutral densities are relatively high and parallel electrical conductivity significantly low there. The edge plasma is always measured to be strongly turbulent. Much effort has been devoted to the study of plasma turbulence in the edge as well as in the center of tokamaks.[14] Drift wave turbulence is a widely accepted mechanism that explains the Bohm-like magnitude of the edge diffusion rates and the fluctuation spectra measured in the edge. On a longer time scale, sharp gradients can drive bulk plasma convection which may contribute to increased transport in a way similar to that in which convection cells operate in classical fluid mechanics. The edge plasma then becomes a highly dynamic system in which turbulence and bulk plasma flows can support local variations in density and temperature. The observation of the MARFE phenomena in Alcator C is a manifestation of such a local variation in edge parameters.[5]

1.3 Motivation for Studying Alcator C Edge Plasma

Alcator C provides a unique opportunity for studying edge plasma. The Alcator C tokamak with its Bitter plate magnet construction[15] operates at the highest magnetic field of any tokamak in the world (B $\sim$ 6–13 Tesla). Central current densities from ohmic current drive exceed 2 kA/cm^2 in the highest density plasmas ever achieved in a tokamak ($n_{center} > 10^{15}$/cm^3). With the assistance of pellet injection, Alcator C currently holds the world record for Lawson parameter[16], $n\tau \sim 0.6 - 0.9 \times 10^{14}$ sec/cm^3, in reactor-like plasmas with central ion temperature $\sim$ 1.5 keV. Alcator C also has an extensive program dedicated to the study of lower hybrid heating and current drive and ion cyclotron heating.

The edge plasma in Alcator C is characterized by densities $n_{edge} \sim 10^{12}$–10^{14}/cm^3 with very short radial scrape-off lengths $\sim$ 0.3 cm. Early in the operating life of Alcator C, it was found that heat loading on secondary limiter surfaces was highly nonuniform. The mechanical failure of these 'virtual' limiters prompted the first extensive Langmuir and calorimeter probe work on Alcator C.[17] Another localized phenomenon in the edge plasma, later referred to as a MARFE, was detected on the inside density interferometer cord and on the visible continuum array.[3] The MARFE was found to grow in size and extent at higher densities coincident with a reduction in pulse gas fueling efficiency at these densities. Local radiated emission in the MARFE region was measured[2] to exceed 20 watts/cm^3. These results indicated at an early stage that edge plasma phenomena in Alcator C could be important and impact the operation of the machine.

The improvement in energy confinement due to pellet fueling emphasizes the role the edge plasma plays on gas fueled discharges. By directly fueling the center, neo-Alcator scaling is more closely followed at high densities.[16] The transport processes which normally fuel the center from gas puffing at the edge are bypassed in a pellet fueled plasma. Thus, the degradation of $\tau_E \propto n_e$ scaling

for strong gas puff discharges may be connected to edge conditions approaching some critical state.

The motivation for studying the edge plasma in Alcator C is dominated by the need to understand already identified phenomena such as MARFEs in addition to a more general characterization of the edge during routine operation, pellet injection and lower hybrid heating. For a doctoral thesis, the study of the edge plasma in Alcator C is also exciting in that the potential for identifying new phenomena exists. The limiter shadow plasma in Alcator C is, at least in principle, easily diagnosed by Langmuir probes. This thesis makes use of this fact and utilizes an edge plasma diagnostic system consisting of a poloidal array of 80 closely spaced Langmuir probes (DENSEPACK) to diagnose the limiter shadow plasma of Alcator C in detail.

1.4 Outline of Thesis

The results of this study are organized into twelve chapters. The chapters are grouped under four major divisions of *Introduction & Background*, *Experimental Apparatus & Data Reduction*, *Experimental Results*, and *Summary*.

Introduction & Background includes chapters 1–4. An overview of relevant edge plasma physics and experimentation is presented in chapter 2. As an introduction to edge modelling, a simple radial diffusion model and a diffusion plus convection model in the limiter shadow plasma is discussed in chapter 3. A set of reduced fluid equations used in later chapters to evaluate transport in the edge plasma is also presented. Chapter 4 focuses on the edge plasma in Alcator C from an experimental point of view. Topics included in this overview are: asymmetric limiter damage, first probe measurements, and MARFEs.

Chapters 5 and 6 are included in *Experimental Apparatus & Data Reduction*. Chapter 5 describes the principal edge diagnostics developed during the course of this thesis. A poloidal array of 80 Langmuir probes (DENSEPACK) is described in detail. Probe characteristic models used to analyze DENSEPACK data is presented in chapter 6. An extensive numerical algorithm developed to fit the large number of characteristics generated by DENSEPACK is also presented.

The main body of this thesis consists of chapters 7–11, *Experimental Results*. Chapter 7 describes the poloidal structure of density, temperature, and floating potential in the limiter shadow plasma. Mechanisms which might explain the observed asymmetries are discussed in chapter 8. Chapters 9–11 present data during routine ohmic, gas puff discharges, lower hybrid radio frequency heating, and pellet injection. The difference between MARFE and non-MARFE discharges is examined. The dependence of edge plasma parameters on central parameters is presented.

Finally, Chapter 12 restates the major findings of this thesis and offers some suggestions for future work.

CHAPTER 2

EDGE PLASMA PHYSICS

The edge plasma is easy to diagnose since, in many cases, a probe can be used to directly sample the plasma. However, the many processes occuring in the edge complicate the understanding of the overall picture. Sections 2.1–2.5 review some physical processes that occur in the edge plasma as background for discussion in the later chapters of this thesis. Section 2.6 points to some experimental techniques used in the study of edge plasma and reviews results that have been obtained using Langmuir probes in tokamaks.

2.1 Introduction

A fusion plasma is sustained by maintaining a balance between power input and power losses. The power input includes internal alpha particle heating, ohmic heating in a tokamak, neutral beam, and RF heating. Power losses take the form of bremsstrahlung radiation, impurity line radiation, charge exchange neutrals, conduction, and convection. The success of the tokamak magnetic geometry lies partly in the elimination of parallel conduction and convection losses by forcing all particles exiting the central region to pass perpendicular to a strong magnetic field.

In the edge plasma of a tokamak, this situation changes. Unlike the central plasma, parallel conduction and convection becomes a dominant transport mechanism in this region. Flux tubes which intercept limiters or divertor neutralizer plates are populated by particles which diffuse perpendicular to field lines from the central plasma. Parallel effusion driven by pre-sheath electric fields carries these particles to material surfaces where they can cause impurity release and material damage and ultimately reappear as neutral atoms.

All wall surfaces cannot be positioned exactly tangent everywhere to the last flux surface. Local hot spots from even the slightest misalignment can develop. Thus, a limiter or magnetic divertor system is used to preferentially unload particles and energy exiting the central plasma and protect the vacuum wall from thermal loading and high energy electron damage. Special geometries of these limiter and divertor systems are employed to reduce thermal loading to acceptable levels and to position the recycling region away from the central plasma.

The above picture points out a number of important processes which need to be considered when dealing with the edge plasma. The following sections discuss some basic concepts under the topics of electric sheath formation, plasma-surface interactions involved in particle recycling and impurity release, perpendicular transport, and radiation processes.

2.2 Sheath Formation

Any solid object immersed in a plasma will float to a potential that is different than the local plasma potential. The random flux of electrons exceeds the random flux of ions in a plasma by a ratio $\sqrt{\frac{m_i}{m_e}}$. At a material surface, the highly mobile electrons initially strike more frequently than ions until the object acquires a sufficiently negative charge to repel electrons and equalize the fluxes. A sheath region between the material surface and local plasma where this potential drop occurs is thereby established.

The problem of sheath formation was originally considered by Tonks and Langmuir[18] and has been examined by many since. In connection with probe data analysis, the sheath interface determines the rate of particle collection and must be understood in order to deduce unperturbed plasma parameters away from the probe. The sheath is important for plasma-wall interactions as well. Ion

sputtering, particle and energy fluxes on wall surfaces depend on the accelerating potentials in the sheath.

2.2.1 Description of Sheath

Stangeby[19] covers the essential features of the plasma-wall sheath and presents a relatively simple formulation for particle and energy fluxes. Figure 2.1 depicts an electrically floating plane surface exposed to a plasma on one side. The potential drop is typically a few κT_e and occurs mostly in a sheath region near the surface $\sim$ 10 debye lengths thick. The density at the sheath edge is depressed to about $\sim 1/2$ the unperturbed density. A pre-sheath electric field is also established. This potential drop is on the order of $\sim \frac{1}{2} \kappa T_e$ and extends a few ion mean free paths into the plasma. The action of this pre-sheath is to accelerate ions to the sound speed by the time they reach the sheath boundary.

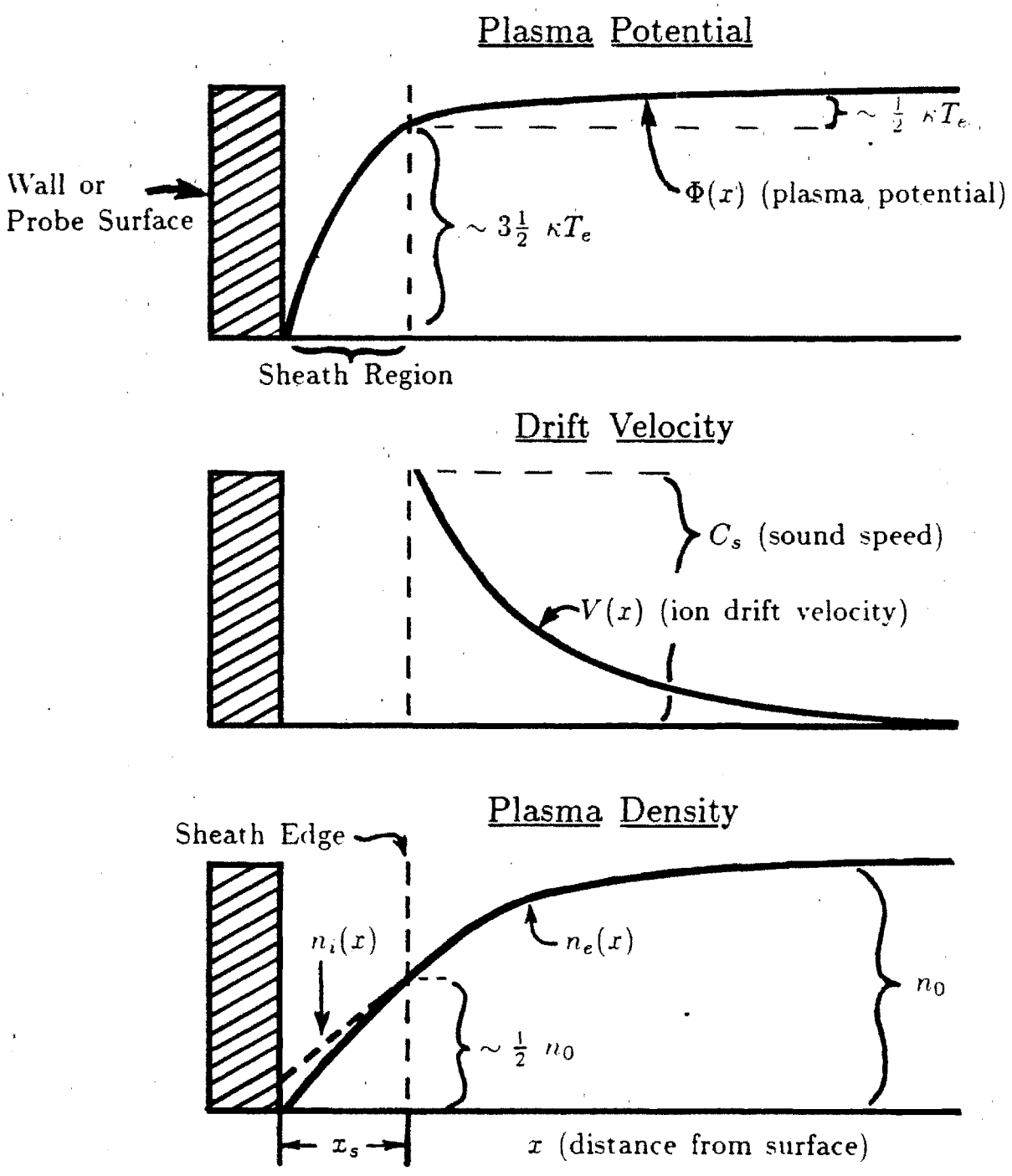

$x_s \approx 10\ \lambda_D$

Figure 2.1 Sheath at a Wall Surface

2.2.2 Particle Flux Through Sheath

The condition that ions arrive at the sheath with a bulk flow velocity on the order C_s is well established for both maxwellian and non-maxwellian ion distribution functions.* This constraint is referred to as the Bohm sheath criterion.[20] Because of the Bohm sheath criterion, electron and ion fluxes through the sheath to a locally 'floating' or unbiased wall surface can be simply estimated by

$$\Gamma_i = \Gamma_e \approx \frac{1}{2} n_0 C_s \tag{2.1}$$

where n_0 is the unperturbed density away from the surface.

2.2.3 Power Flux Through Sheath

Calculation of electron and ion power fluxes through the sheath is more complicated. Stangeby[21] most recently presented analytic relations for the floating potential and power fluxes to biased surfaces which include secondary electron emission and various T_i/T_e ratios. The total power flux through the sheath can be written as

$$P_{tot} \approx \delta_t \; T_e \; q \frac{n_0 C_s}{2} \tag{2.2}$$

---

* From analysis of waves in plasmas, the sound speed is given by $C_s = \sqrt{\frac{\kappa(T_e + \gamma T_i)}{m_i}}$, where γ ranges from 1 to 3 depending on thermodynamic state that is assumed for the ions (isothermal, one-dimensional adiabatic, etc.). For the case when $T_i = 0$, probe theory predicts that the ions arrive at the sheath edge with a sound speed flow velocity. For finite temperature ions this trend is still followed[81] although it is unclear what value of 'γ' should be used. For the discussion in this thesis, γ is taken as ≈ 1.

with $\delta_t \sim 5$–10 when $T_i \approx T_e$ and the surface is allowed to float. For an Alcator C edge plasma of $T_e \sim 10$ eV, $T_i \approx 2\ T_e$, and $n_e \sim 2 \times 10^{13}/\text{cm}^2$, $P_{tot} \approx 500$ watts/cm^2.

If the surface is biased to a more positive potential than the floating potential, the electron contribution to the heat flux increases dramatically. A factor of 5 increase in the power flux can easily result when the surface is biased at the plasma potential. This is exactly the problem encountered when operating a Langmuir probe in the electron saturation regime. Limiter surfaces can suffer from this power flux enhancement problem as well. Generally, a limiter will span large plasma density and temperature variations. A metallic limiter, being an equipotential surface, will be effectively biased at some locations more positively with respect to the local floating potential and in other locations more negatively. Local hot spots and places for unipolar arcing can develop in this way. Additional effects of non-ambipolar transport and charge separation due to $B \times \nabla B$ drifts can also contribute to the limiter-floating potential mismatch.

Ideally, one would like to use a non-conducting limiter to let the surface acquire the local floating potential everywhere. Alternatively, one might envision using a specially biased limiter such as that proposed by Motley.[22] Unfortunately, the thermal characteristics of non-conducting materials is never as good as metals, offsetting this advantage.

2.2.4 Effect of Magnetic Field

The above discussion has focused on a non-magnetized plasma or the variation along field lines in a 1-D magnetized plasma. In many instances, some sections of wall surfaces are parallel to field lines or intersect field lines at oblique angles. Daybelge[23] and Chodura[24,25] have considered oblique angle effects and concluded that although the sheath thickness along the B-field increases with

increasing deviation from perpendicular, the total potential drop remains insensitive to angle. However, with the surface aligned exactly parallel to the field, a positive wall potential can develop due to the larger ion versus electron gyro radii.

On probes, limiters, and divertor neutralizer plates, particle and energy removal along field lines dominates. Thus, the parallel or non-magnetized approximation for sheath formation and energy transport to these surfaces is well suited for describing these systems to first order. Further refinements in modelling parallel plasma flows and potential distributions at wall surfaces include an accounting for neutralization at the surface and the resultant cold ion refluxes.[26,27]

2.3 Plasma-Surface Interactions

Particles impinging on wall surfaces drive a number of wall related processes. Plasma-surface interactions in tokamaks is discussed in detail in a review by McCracken and Stott.[1] There are two primary categories into which plasma-wall interactions can be divided: recycling and impurity production mechanisms.

In the context of this thesis, recycling is important because it determines the strength of the particle source/sink in the edge. Asymmetric edge particle sources and sinks can lead to asymmetric edge parameters and vice versa. Impurity release from wall and limiter surfaces may be asymmetric as well. Locally enhanced impurity sources can greatly influence the intrinsic impurity level in a plasma. The identification of active impurity generation mechanisms has a high priority, particularly during RF current drive or heating. The first four subsections review the principal mechanisms involved in recycling. Impurity release mechanisms are similarly discussed in the remaining subsections.

2.3.1 Recycling: Particles on Wall

Recycling includes all processes which allow an ion incident on a wall surface to return to the discharge. When an ion or neutral strikes a wall surface it can experience elastic and inelastic scattering. As a result, the particle can *backscatter* or become *trapped* in the solid.

Backscattering is expressed in terms of a particle reflection coefficient R_p, and an energy reflection coefficient, R_E, which characterize the fraction of particle and energy reflected per incident particle, respectively. R_p and R_E increase with decreasing ion energy and increasing target atomic number. For a 10 eV incident ion, R_p is typically $\sim$ 0.8 for molybdenum and $\sim$ 0.5 for carbon. Most of the backscattered ions come off as neutrals carrying $\sim$ 50% of the incident ion energy. These neutrals have sufficient energy to stream back into the central plasma region and ionize or charge exchange there.

Trapping refers to all particles which do not backscatter. Hydrogen which becomes implanted in a solid is still highly mobile due to its large diffusion coefficient. Hydrogen atoms and molecules are eventually released by the solid at a later time. The effective hydrogen diffusion rate in a solid depends on the density of trapping sites from lattice imperfections and the temperature of the solid. Ion bombardment can produce damage sites and affect the overall diffusion rate over the course of time.

Ion impact itself can induce detrapping of hydrogen. This mechanism is expressed in terms of a cross-section for the expulsion of hydrogen per incident ion. Unlike diffusion, the release rate is not so strongly dependent on the temperature of the solid. At low temperatures where diffusion is low, ion-induced detrapping can still act to remove trapped hydrogen.

Both thermal desorption and ion-induced detrapping result in the release of hydrogen atoms with energies of a few eV or molecules with energies on the order of the wall temperature. The low transit velocity of these particles causes them to contribute more to local recycling near the surface.

2.3.2 Recycling: Neutral Transport and Ionization

Where the reflected flux of neutrals reappear as plasma ions depends on the location of the wall surface relative to the central plasma and the penetration depth of the neutrals before ionization. The transport and penetration of neutrals is governed by the rates of charge exchange and electron-impact ionization. For a less than 10 keV plasma, charge exchange is the dominant reaction for atomic hydrogen having a $\langle \sigma v \rangle_{cx}$ of $\sim 4 \times 10^{-8}$ cm^3/sec at 100 eV. In charge exchange, an electron is transferred from the neutral to a plasma ion. In this way, a hot plasma ion can change identity and become a fast neutral. Neutrals can be effectively transported in this manner over long distances before hitting a wall surface or becoming ionized.

Electron impact ionization of atomic hydrogen is also significant in this temperature range with a $\langle\sigma v\rangle_{ion}$ of $\sim 3\times10^{-8}$ cm^3/sec at 100 eV. For molecular hydrogen, electron impact ionization is the single most important process. The comparable charge exchange reaction for H_2 becomes significant only at plasma temperatures above $\sim$ 500 eV. A typical $\langle\sigma v\rangle_{ion}$ for H_2 at 100 eV is $\sim 5\times10^{-8}$ cm^3/sec. Since molecular charge exchange is much less probable than molecular ionization in the edge plasma, the molecular reflux component from wall surfaces contribute more to local recycling than to fueling the central plasma.

2.3.3 Recycling: Neutral Penetration

The problem of calculating neutral transport in a fusion plasma is a very difficult one. Because of the long mean free path of neutrals relative to the gradient scale lengths of plasma density and temperature, a fully kinetic description must be used. Analytic solutions to the neutral kinetic transport equations in simplified slab geometries have been obtained.[29] More typically, Monte Carlo techniques are employed for complicated geometries.[30,31]

Using a more simple-minded picture, the dependence of the effective penetration depth of neutrals on central density is easily obtained. The effective penetration depth, L_n, can be written as

$$L_n \sim \frac{V_{neutral}}{n_e\langle\sigma v\rangle_{ion}} \tag{2.3}$$

where $n_e\langle\sigma v\rangle_{ion}$ is the total ionization rate and $V_{neutral}$ is the effective velocity of the neutral including charge exchange transport. Letting $V_{neutral}$ correspond to a 100 eV neutral and using $\langle\sigma v\rangle_{ion}$ for a 100 eV background plasma,

$$L_n \sim \frac{2\times10^{14}}{n_{e(\mathrm{cm}^{-3})}} \quad \mathrm{cm}. \tag{2.4}$$

Thus, at high densities the neutrals will not penetrate as readily into the central plasma region. For Alcator C with $n_e \sim 2 \times 10^{14}/\text{cm}^3$, L_n from this scaling is only $\sim$ 1 cm. This exercise states the fundamental problem of the reduction in fueling efficiency at high discharge densities. Pellet fueling can overcome this problem and has been used in Alcator C with great success.

2.3.4 Recycling: Summary

In summary, a simple picture of recycling in a limiter bounded discharge depicted in Fig. 2.2 can be described. Ions arrive at the limiter through cross-field diffusion and parallel effusion. A fraction, R_p ($\sim$ 0.5–0.8 for 10 eV ions) is reflected back to the central plasma as neutrals retaining approximately one-half the incident ion energy. The remaining ions are trapped and re-released with low energy and ionize or charge exchange near the limiter surface. At the wall surface, the role of ions is replaced for the most part by incident neutrals. Backscattering, trapping and neutral-induced detrapping take place on the wall surface. Although the local recycling particle flux from the wall is much less than that from a limiter, the wall surface area is much larger. The total inventory of hydrogen adsorbed by the wall often exceeds the total number of ions in the discharge.

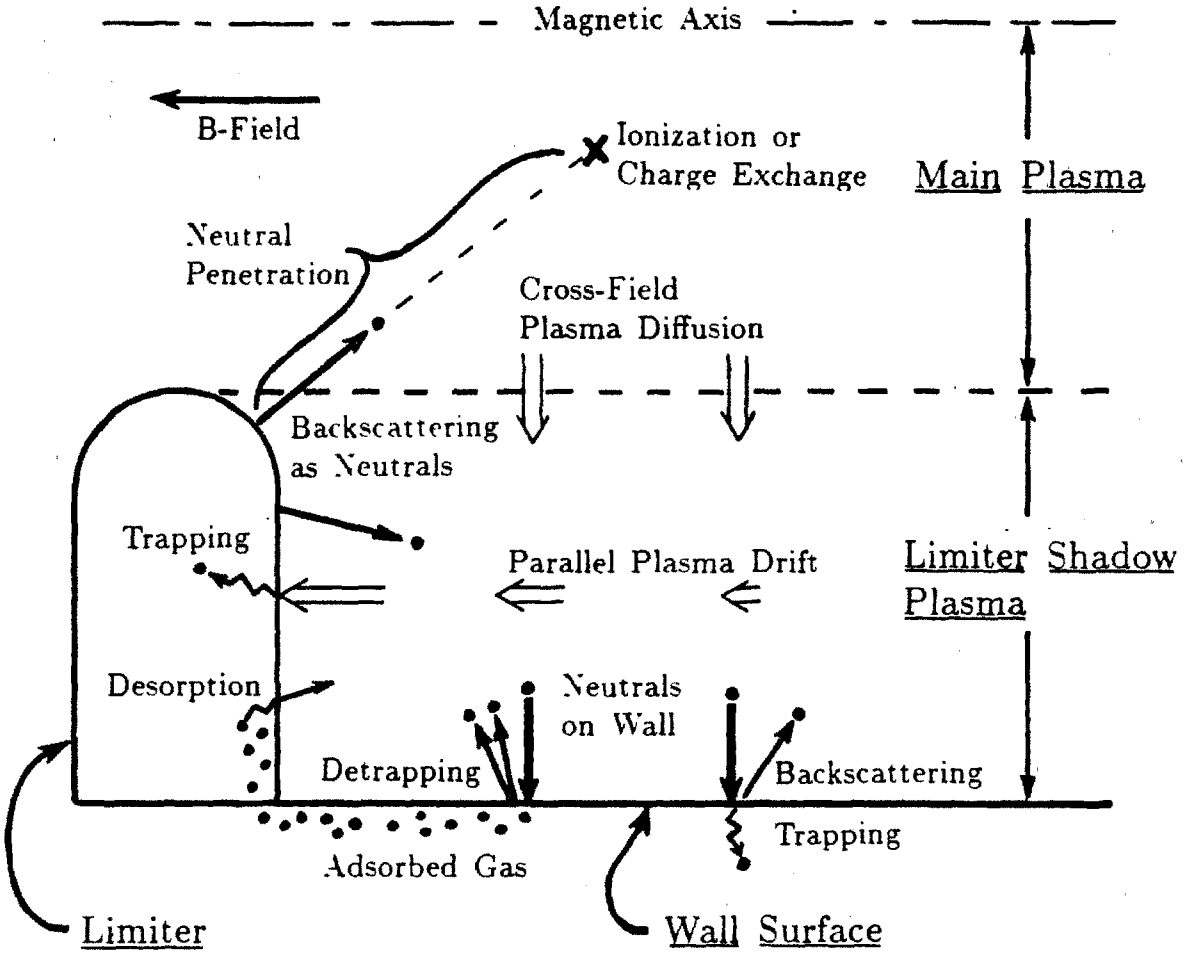

Figure 2.2 Recycling in a Limiter Bounded Discharge

2.3.5 Low-Z Impurity Release Mechanisms

Another consequence of plasma-wall interaction is the introduction of light impurity atoms on the wall surface into the plasma. The effect of these impurities in the plasma is to increase the central plasma Z_{eff} $(= \frac{\Sigma n_i Z_i^2}{\Sigma n_i Z_i})$, causing enhanced bremsstrahlung losses and line radiation in the cooler outer regions of the discharge. Although a cold, radiating plasma near wall surfaces is desirable to minimize thermal loading and sputtering, control of low-Z impurity influxes is necessary to avoid excessive central power loss and the propagation of a thermal collapse from the edge which can lead to a disruption or hard termination.[33]

Figure 2.3 illustrates processes which can lead to low-Z impurity release. Light impurities such as oxygen and carbon remain adsorbed on wall surfaces even in the cleanest vacuum systems. The surface bond can be chemical in nature or depend on weaker Van der Waal forces. Wall baking and discharge cleaning are techniques that are used to reduce the amount of adsorbed gas on wall surfaces. During the plasma discharge, the remaining impurities are available to be released by *thermal desorption* or *particle* and *photon-induced desorption.*

Another important light impurity release mechanism is *chemical desorption.* A chemical reaction between an incident ion or neutral and an adsorbed particle can result in a molecule which is less tightly bonded to the surface. The chemical erosion process that takes place can be quite important, particularly when the subtrate itself is made of a low-Z material. This mechanism is sometimes referred to as *chemical sputtering.*

In an effort to avoid high-Z contamination of the plasma, carbon materials are used widely in tokamaks for limiters and wall armor plates. Chemical sputtering of carbon can become an important contributor to carbon impurity levels in this case. Carbon-oxygen reactions yield carbon monoxide while carbon-hydrogen reactions result in methane and acetylene by-products.

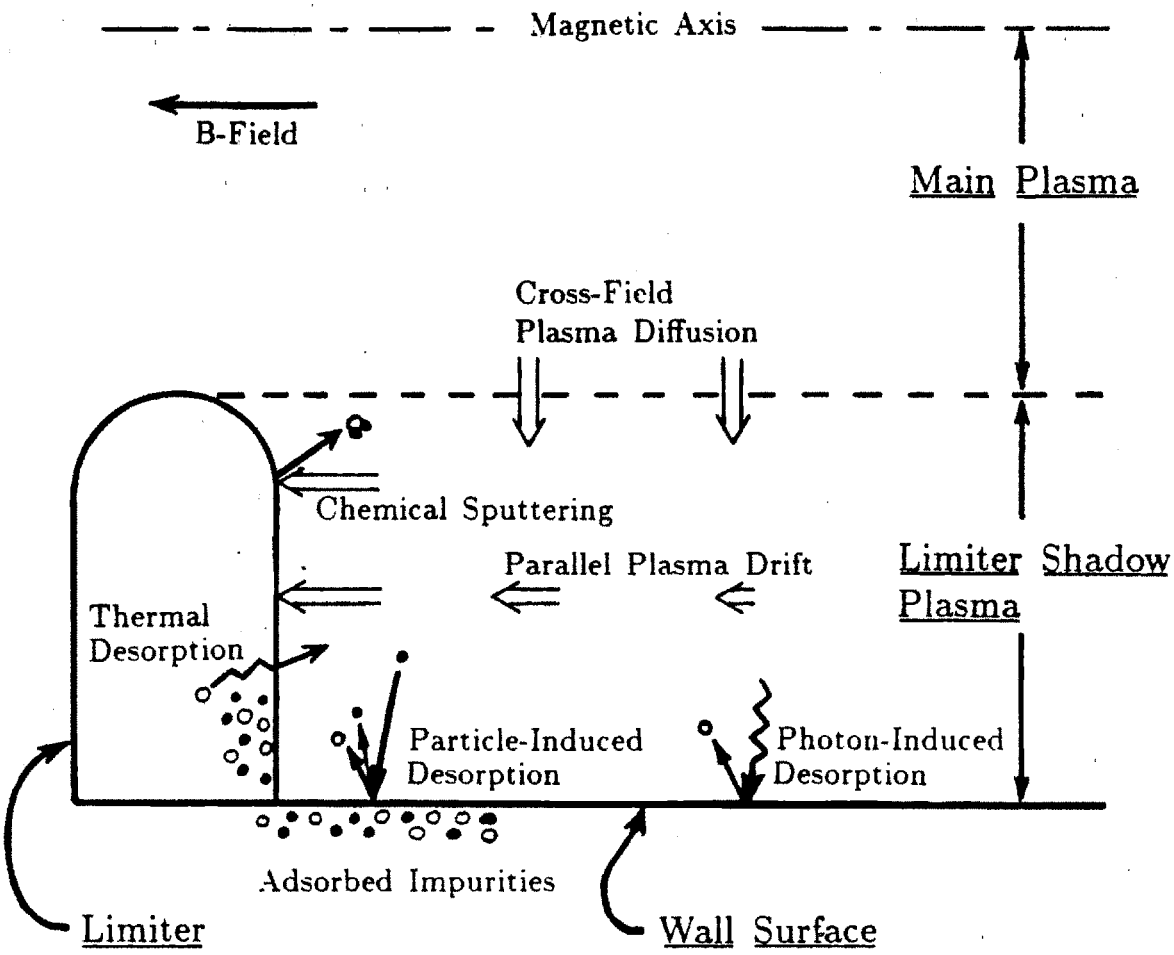

Figure 2.3 Low-Z Impurity Release Processes

2.3.6 High-Z Impurity Release Mechanisms

High-Z contamination of the central plasma can be a more serious problem in tokamaks. Even in the central plasma, high-Z impurities such as molybdenum and tungsten are not fully ionized, resulting in line radiation from electron transitions. In addition, Z_{eff} can become high with only minimal concentrations of these elements. The result of high-Z contamination can be large radiated power losses from the center leading to hollow temperature profiles, setting the stage for major disruptions.

The following discussion covers processes which cause atoms of the wall structural material itself to find their way into the plasma. For the most part, structural materials such as iron, nickel, molybdenum, and tungsten are high-Z materials although low-Z materials such as carbon are finding a wider use and are affected by the same processes. The dominant processes for present day tokamaks depicted in Fig. 2.4 include *evaporation*, *sputtering*, and *arcing*.

2.3.7 Impurity Release: Evaporation

Evaporation is simply the result of surface heating. The evaporation rate of a surface depends exponentially on the ratio of heat of sublimation to the surface temperature. Vapor pressures from evaporation span many decades from room temperature to melting point. It follows that higher melting point materials possessing higher heats of sublimation exhibit lower evaporation rates at a given temperature. At melting, vapor pressures on the order of 0.01–1 Torr are typical. For transient heat pulses, either a direct estimate or measurement of the power flux or a heat transfer analysis is required to calculate the surface temperature as a function of time. Change in thermal properties with temperature, radiation damage, and surface conditions need to be incorporated in such an analysis.

2.3.8 Impurity Release: Sputtering

Sputtering results from the direct interaction of energetic ions and neutrals on atoms in the solid matrix. An incident ion or neutral will produce a collision cascade with lattice atoms. Some of these atoms receive enough energy to overcome their binding energy and escape. The sputtering yield depends on how tightly bound the lattice atoms are (sublimation energy) and the momentum transferred from the incident particle to the lattice atoms. Thus, lower melting point materials sputter more easily, and low atomic mass ions such as hydrogen and helium are not as efficient in sputtering as heavier impurity atoms.

There is a sputtering threshold energy for incident particles below which no sputtering occurs. The threshold energy depends on the incident particle mass, M_1, target mass M_2, and sublimation energy, E_s, through the relation

$$E_{th} = \frac{E_s}{\gamma(1-\gamma)} \quad ; \quad \gamma = \frac{4M_1M_2}{(M_1+M_2)^2} \; . \tag{2.5}$$

For molybdenum, the threshold energies are 53, 94, and 176 eV for He^+, D^+, and H^+ respectively.

Sputtering yields depend on the angle of incidence of the impinging particle. For grazing incidence, sputtering rates increase by a factor of 10 or more. High perpendicular energy particles traveling along field lines to a wall surface can be major contributors to the sputtering yield.

An important effect occurs when the sputtering atoms are allowed to return as incident particles to the surface. The efficient momentum transfer of this *self-sputtering* can drive sputtering yields to exceed one atom per incident particle resulting in a runaway sputtering avalanche. A calculation of the overall sputtering yield must therefore take into account the impurity species and concentration near the surface by modelling impurity recycling and confinement.

The plasma sheath plays a particularly important role here since it allows a multiply charged ion to acquire energies exceeding many times the electron temperature as it crosses the sheath and strikes the solid. Control of the edge plasma electron temperature then becomes a critical issue when considering the sputtering erosion of wall surfaces in a near steady state fusion device.

2.3.9 Impurity Release: Arcing

Arcing can occur between a conducting surface and the local plasma. These single electrode, *unipolar arcs* are struck when a hot cathode spot is initiated on the surface causing a local emission of electrons. Once electrons are kicked out of the surface, the sheath potential accelerates them into the plasma. This emission slightly raises the potential of the entire solid. Electrons then can be replenished via conduction through the material from other areas of plasma contact where the reduced potential drop permits more electrons to be collected. An arc is sustained as long as it deposits sufficient power on the surface to maintain the hot cathode region. With a magnetic field, $J \times B$ forces can drive the arc and hot cathode spot along the surface. Arc tracks are often seen on large probes and limiter surfaces.

The erosion rate of the cathode surface due to an arc depends on the material and is generally found to be proportional to the current in the arc. Erosion rates of 0.05–0.14 atoms/electron are typical for molybdenum and carbon respectively. Material is removed as neutral vapor by evaporation or can be released as droplets and solid pieces.

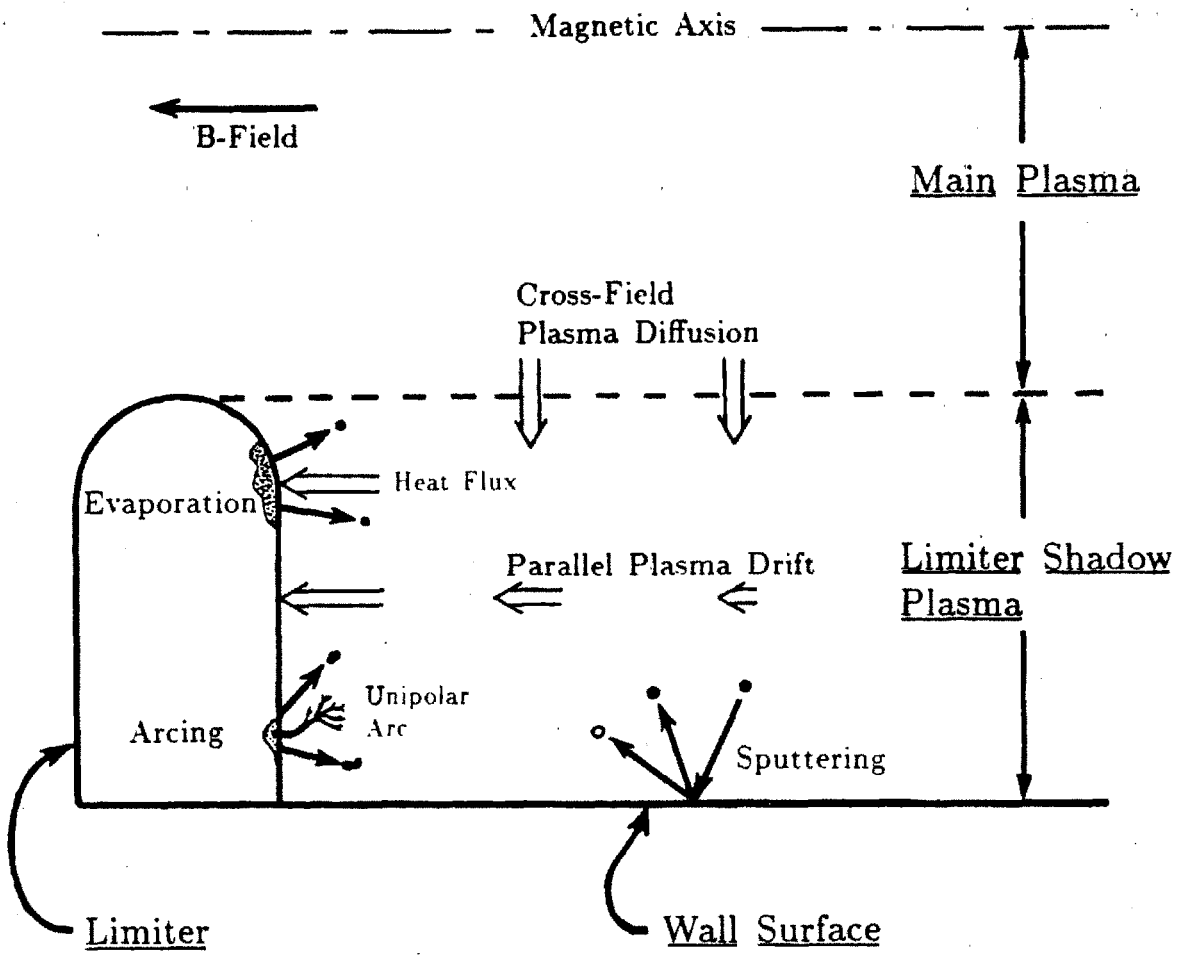

Figure 2.4 Wall Material Release Mechanisms

2.4 Perpendicular Transport

Particle and energy transport is a central issue in the study of thermonuclear plasmas. Early experiments in stellarators revealed that particle confinement for these machines scaled more like Bohm diffusion than the neoclassical rates.[34] More recent experiments in tokamaks have attained central confinement times which are much closer to neoclassical values.[16] Perpendicular ion conductivities of a few times neoclassical have been observed. However, edge plasma diffusion coefficients remain on the order of Bohm diffusion. There are several explanations for this departure from neoclassical confinement in magnetically confined plasmas. The following subsections discuss turbulence due to electrostatic and magnetic fluctuations, and convection cells as mechanisms which can drive anomalous transport.

2.4.1 Bohm Diffusion

The adherence of particle loss rates in early fusion experiments to the Bohm diffusion law,

$$D_B = \frac{T_{e\ (\mathrm{eV})}}{16 B_{\ (\mathrm{tesla})}} \quad \mathrm{m}^2/\mathrm{sec}. \tag{2.6}$$

is typically explained in terms of transport due to $\underline{E} \times \underline{B}$ drifts. The maximum potential variation in a plasma is limited by debye shielding to the local temperature

$$q\Phi_{max} \approx \kappa T_e \ . \tag{2.7}$$

Assuming a gradient scale length, λ,

$$E_{max} \approx -\frac{\kappa T_e}{q\lambda} . \tag{2.8}$$

Thus, $\underline{E} \times \underline{B}$ particle fluxes due to a perturbed Φ can be on the order of

$$\Gamma_\perp \approx n\frac{\underline{E} \times \underline{B}}{B^2} \approx -\frac{\kappa T_e n}{qB\lambda} \approx -\frac{\kappa T_e}{qB}\nabla n . \tag{2.9}$$

This is exactly the scaling for Bohm diffusion.

2.4.2 Perpendicular Particle Fluxes

A simple yet more rigorous formulation for the perpendicular particle flux in a collisional, magnetized plasma can be obtained through an MHD model. Consider perpendicular force balance and Ohm's law (neglecting Hall current and ∇P_e terms);

$$\underline{J} \times \underline{B} = \nabla P , \tag{2.10}$$

$$\underline{E} + \underline{V} \times \underline{B} = \underline{\underline{\eta}} \cdot \underline{J} . \tag{2.11}$$

Taking $\underline{B} \times$ (2.11) and substituting for $\underline{J} \times \underline{B}$ with (2.10),

$$\underline{V}_\perp = \frac{\underline{E} \times \underline{B}}{B^2} - \frac{\eta_\perp}{B^2}\nabla P \tag{2.12}$$

so that the perpendicular flux can be written as

$$\underline{\Gamma}_\perp = n\underline{V}_\perp = n\frac{\underline{E} \times \underline{B}}{B^2} - \frac{n\eta_\perp \kappa(T_i + T_e)}{B^2}\nabla n \tag{2.13}$$

with the assumption that T_i and T_e are independent of space. Letting $\underline{E} = \underline{E}_0 + \tilde{\underline{E}}_1$ where $\tilde{\underline{E}}_1$ is a fluctuating E-field with characteristic frequency ω ($\omega \ll \omega_{ci}$) and recognizing the classical diffusion coefficient, $D_{cl} = \frac{n\eta_\perp \kappa (T_i + T_e)}{B^2}$, Eq. 2.13 becomes

$$\underline{\Gamma}_\perp = n\frac{\underline{E}_0 \times \underline{B}}{B^2} + \left\langle \tilde{n}\frac{\tilde{\underline{E}}_1 \times \underline{B}}{B^2} \right\rangle - D_{cl}\nabla n \ , \tag{2.14}$$

where the notation $\langle\rangle$ denotes a time-average over the fluctuating quantitites. Thus the perpendicular particle flux in this analysis results from three contributing terms, a steady state $\underline{E}_0 \times \underline{B}$ term, a fluctuating $\tilde{n}\tilde{\underline{E}}_1 \times \underline{B}$ term, and a classical Fick's law diffusion term. (Hall current and ∇P_e terms can be incorporated into an effective $\underline{E}_0 \times \underline{B}$ term.)

Classical diffusion places a lower bound on the rate of particle loss. It is not surprising, therefore, that classical diffusion or neoclassical diffusion for a toroidal system is not typically observed. Fluxes due to time-varying E-fields in a turbulent plasma or relatively steady state E-fields in a convection cell can contribute to the particle fluxes and, as discussed in the following subsections, can dominate the overall particle loss rate.

2.4.3 Edge Plasma Turbulence

Density fluctuations have been recorded in many tokamaks through the use of microwave and CO_2 laser scattering[35,36,37], Langmuir probes[38,39], and visible light emission.[40] The results of these data suggest that plasma exhibits small scale fluctuations characteristic of a random 'turbulence'. The spatial extent of the turbulence is measured to be on the order of the ion gyro radius and the wavenumber and frequency spectra, $S(\mathbf{k}, \omega)$, are broad with no evidence of coherent modes. The spectral power, $P(\omega)$, is largest for frequencies $f \leq 200$

kHz. For frequencies above 200 kHz, $P(\omega)$ rolls off according to a power law, $P(\omega) \propto f^{-\gamma}$ with $\gamma \sim 2$–4.

The amplitude in the density fluctuations is found to vary most strongly with radius from $\tilde{n}/n \sim 0.01$ near the center to $\tilde{n}/n \sim 1.0$ at the wall and is relatively insensitive to the degree of collisionality, ν_{ei}/ν_{bounce}. The parameter ρ_s/L_n where $\rho_s = \frac{\sqrt{\kappa T_e/m_i}}{\omega_{ci}}$ and $L_n \sim n/\nabla n$ is found to be important in determining the level of density fluctuations. Larger values of ρ_s/L_n generally result in larger $\tilde{n}/n$.

Electrostatic potential fluctuations, $\tilde{\Phi}$, have also been detected using capacitive probes and Langmuir probes.[41] The spectral features of $\tilde{\Phi}$ are similar to $\tilde{n}$. A phase correlation between $\tilde{\Phi}$ and $\tilde{n}$ different than 90° can lead to turbulently driven transport through Eq. 2.14.

Particle fluxes due to $\tilde{n}$ and $\tilde{\Phi}$ have been evaluated using Eq. 2.14. For measured $\tilde{n}(\omega)$ and $\tilde{\Phi}(\omega)$, the corresponding perpendicular flux would be

$$\Gamma_{\perp}^{\tilde{n},\tilde{\Phi}} = -\int \frac{\tilde{n}(\omega)\nabla\tilde{\Phi}(\omega) \times \underline{B}}{B^2} \cos\gamma(\omega)\ \partial\omega \qquad (2.15)$$

where $\gamma(\omega)$ is the phase angle between $\tilde{n}$ and $\nabla\tilde{\Phi}$. Turbulent transport calculated this way has yielded fluxes which are consistent with the global particle confinement times.[42] Thus there is experimental evidence that $\underline{\tilde{E}} \times \underline{B}$ transport can dominate perpendicular particle fluxes and explain the Bohm-like diffusion rates in the edge plasma.

Drift waves are accepted as the most likely cause of microturbulence and anomalous transport in tokamaks. Quasilinear electrostatic drift wave theories have been used to estimate anomalous transport; however, it is recognized that the observation of a broad $S(\mathbf{k},\omega)$ in $\mathbf{k}$ and ω imply strong nonlinear coupling between many modes.[14]

2.4.4 Magnetic Fluctuations

Enhanced radial transport also results when the local magnetic field possesses a radial component, B_r, that allows particles to transit radially along field lines. In the design of an experimental magnetic fusion device, great care is taken to eliminate stray vacuum field lines and magnetic field ripple which can cause increased radial transport and mirror trapped particle losses.

The plasma itself can develop magnetic perturbations such as island formation in resistive MHD instabilities[43] which result in stochastic field line structures in the central plasma. In the turbulent edge plasma of tokamaks, radial magnetic field fluctuations, $\tilde{B}_r/B_T$, have been measured.[41] The finding is that $\tilde{B}_r/B_T$ decreases with increasing minor radius. In Macrotor, $\tilde{B}_r/B_T$ follows the density profile, going to zero at the wall and taking on a value $\tilde{B}_r/B_T \sim 5 \times 10^{-5}$ near $r/a \sim 0.5$. The low amplitude suggests that magnetic fluctuations are probably not responsible for the observed anomalous transport. However, in high β tokamaks $\tilde{B}_r/B_T$ may become more important.

2.4.5 $\underline{E} \times \underline{B}$ Cells

On a more macroscopic scale, spatial variations in Φ can lead to plasma convection eddies. The result can be enhanced particle and/or energy transport in a similar way that natural convection cools hot surfaces in air. There are a number of ways that Φ can be perturbed to drive $\underline{E} \times \underline{B}$ fluxes.

In the edge plasma of a tokamak where density gradients are sharp and parallel resistivity is high, $\underline{B} \times \nabla B$ particle drifts support poloidal variations in Φ. Pfirsch-Schlüter currents flowing along field lines in this resistive plasma do not cancel this potential completely. The resultant poloidal potential variation drives a radial Pfirsch-Schlüter plasma convection which increases the flux surface-averaged particle loss rate. This effect leads to the neoclassical correction of $D_{neo} \approx (1 + q^2) D_{cl}$ in the collisional plasma limit.[44] Φ on a circular flux

surface with a poloidally uniform density e-folding length, λ_n, can be estimated at the limiter radius, a, by[45]

$$\Phi(\theta) \approx -8.3 \times 10^{-10} \frac{n Z_{eff} a^4 \Lambda B}{I^2 R_0 T_e^{1/2} \lambda_n} \sin\theta \quad \text{(volts)} \tag{2.16}$$

with plasma current, I, major radius, R_0, and coulomb logarithm, Λ. Electron temperature, T_e, is in units of eV. All other quantities are in MKS units.

On flux tubes that intercept wall surfaces, Φ is determined by the wall-sheath potential drop plus any potential drop along the field line due to currents (such as Pfirsch-Schlüter) to the wall or limiter. In this case, the local electron temperature greatly influences Φ through an equation of the form

$$\Phi \approx 3.5\ T_e + \Phi_{wall} + \delta\Phi_{current} \ . \tag{2.17}$$

where the magnitude of the sheath drop is approximated to be a factor of ~ 3.5 times the local electron temperature. Thus, poloidal variations in T_e can drive radial particle fluxes on flux tubes that touch metallic surfaces. Spatial variations in T_e could be maintained by asymmetric heat fluxes from the plasma core, local radiative losses or spatially nonuniform power deposition from RF heating.[46]

At the interface between open and closed flux surfaces, E-fields can additionally arise from the potential mismatch between these two regions. In a collisional edge plasma, a transition must occur between the Pfirsch-Schlüter potential distribution in the interior region to the wall sheath dominated potentials in the wall or limiter shadow region. A sharp gradient in Φ can lead to large $\underline{E} \times \underline{B}$ velocities with velocity shear. Strong convective transport and conditions for shock formation[47] or Hemholtz instabilities[22,48] may form in this way.

A further complication arises when particle transport in the plasma center and/or edge is nonambipolar. Through the use of heavy ion beam probes, it has

been shown that the central plasma in a tokamak typically displays a negative plasma potential while the edge plasma shows a positive potential.[49] Transport mechanisms must be operating in the central plasma to initially remove ions more effectively than electrons thereby setting up such potentials. Nonambipolar transport has also been directly measured in the limiter shadow plasma through the use of probes.[50] Again, strong potential variations, this time driven by such transport mechanisms, can support $\underline{E} \times \underline{B}$ flows with strong velocity shear. Such a shear layer at the limiter radius with a corresponding reversal in poloidal flow velocity has been observed in the TEXT tokamak.[51,52]

2.5 Edge Plasma Radiation

Radiation is an important power loss mechanism in the edge plasma. Electrons moving through coulomb fields of ions radiate a bremsstrahlung continuum. More importantly, the low temperature in the edge plasma allows both hydrogen and low-Z impurity atoms to radiate via free-bound and bound-bound electron transitions.[53] Under certain conditions, the total radiated power density in the edge plasma can become as large as the power loss from parallel electron conduction. If the radiated power increases as the plasma temperature is lowered further, a radiation thermal instability can develop. The existence of this thermally unstable state is relevant to the formation of cold radiating plasmas near divertor plates[12] and MARFEs.[2,54,55]

2.5.1 Bremsstrahlung and Cyclotron Radiation

Bremsstrahlung and cyclotron radiation place a lower bound on the total radiated power from a plasma. Bremsstrahlung radiation classically arises from the acceleration of an electron in the coulomb field of an ion. The resulting bremsstrahlung continuum spans near infrared to X-ray wavelengths. In a high temperature, maxwellian plasma, the total power radiated in all wavelengths can be expressed as[56]

$$P_{br} = 5.35 \times 10^{-31} n_e \sum (n_i Z_i^2) T_e^{1/2} \quad \text{watts/cm}^3 \tag{2.18}$$

or

$$P_{br} = 5.35 \times 10^{-31} n_e^2 Z_{eff} T_e^{1/2} \quad \text{watts/cm}^3 \tag{2.19}$$

with T_e in units of keV and n_e in cm^{-3}.

Cyclotron radiation results from the centripetal acceleration of electrons about the confining magnetic field. Cyclotron radiation appears in the infrared and microwave regions of the spectrum and is emitted in discrete spectral lines which are harmonics of the electron cyclotron frequency. Unlike bremsstrahlung, the radiation can be reabsorbed in laboratory sized plasmas resulting in an *optically thick* plasma at that frequency. An approximate expression for cyclotron power in an *optically thin* plasma is

$$P_{cyc} \approx 5 \times 10^{-32} n_e^2 T_e^2 \qquad \text{watts/cm}^3 \tag{2.20}$$

with T_e in units of keV and n_e in cm^{-3}. For an optically thick plasma, the cyclotron emission from the surface is limited to the blackbody level.

2.5.2 Radiative Decay and Recombination

In the cooler edge region where a large population of electrons occupy bound states in hydrogen and impurity atoms, *radiative decay* and *recombination* are the dominant radiation power loss mechanisms. Photons are emitted through radiative decay when a bound electron jumps from an excited state to a lower energy level. Radiation from recombination results when a free electron is captured by an ion. A single photon with energy equal to the ionization potential plus electron kinetic energy can be produced (*radiative recombination*) or two photons totaling this energy can be emitted (*dielectronic recombination*).

In *coronal equilibrium*, radiative decay and recombination is balanced by electron impact excitation and electron impact ionization. A plasma can be considered to be in coronal equilibrium when photon re-absorption processes are negligible, impact *de-excitation* is small compared to radiative decay, the charge state densities are in steady state, and transport of charge states is negligible. In laboratory fusion plasmas, only the latter constraint is often violated. Thus, the

coronal equilibrium model forms the basis for estimating charge state densities and total radiated power in these plasmas.

Post, Jensen, *et al.*[57] have compiled tables of steady state cooling rates for elements in the range $2 \leq Z \leq 92$ based on a modified coronal equilibrium model. Total radiated power from this model includes radiative recombination, dielectronic recombination, radiative decay, and bremsstrahlung. For an impurity density, n_I, the total radiated power from all ionization states is written as

$$P_{rad} = n_e n_I f_I(T) \tag{2.21}$$

where n_e is the electron density and $f_I(T)$ is a cooling rate coefficient. $f_I(T)$ depends strongly on electron temperature, T, and on the details of the atomic level structure for each impurity. Reference [66] tabulates $f_I(T)$ for electron temperatures in the range 2 eV $< T <$ 200 keV and densities $n_e \leq 10^{16}/\text{cm}^3$.

Near wall surfaces, impurity transport and recycling can strongly influence the equilibrium charge state densities of an impurity species. The coronal approximation can underestimate the total radiated power in this instance. Carolan and Piotrowicz[58] have considered this problem and have calculated an impurity residence time, τ_{ss}, which an impurity must spend in the plasma before coronal equilibrium is established. Also included in this model is recombination via charge exchange with neutral hydrogen atoms.

2.5.3 Radiation Thermal Instability

The radiative cooling rate, $f_I(T)$, is a strong function of temperature. For light impurities such as carbon, nitrogen, and oxygen, $f_I(T)$ typically has a maximum around 7–10 eV. Consequently, an edge plasma with these impurities present and an electron temperature above 7–10 eV will radiate more power as the temperature is lowered. When radiation dominates the power balance, the electron temperature will be effectively clamped at the 7–10 eV level.

In the limiter shadow plasma where electron parallel conduction dominates the power balance, conditions for the onset of this thermal instability can be simply estimated. Consider electron parallel conduction and radiation in a 1-D time dependent electron energy equation[59]

$$\frac{3}{2}n\frac{\partial T}{\partial t} = \frac{\partial}{\partial z}\left(\kappa\frac{\partial T}{\partial z}\right) - \sum_{I=1}^{M} n_e n_I f_I(T) + Q_\perp \qquad (2.22)$$

where κ is the parallel electron thermal conductivity ($\kappa = \kappa_0 T^{5/2}$) and z is a coordinate along the magnetic field line. Radiation is included from M impurity species. A net energy source due to perpendicular heat transport is written as $Q_\perp$ (assumed to be independent of z and T).

Assume that $T = T_0(z)$ is the unperturbed temperature profile which solves Eq. 2.22 with $\frac{\partial T_0(z)}{\partial t} = 0$. Then, perturbing T such that

$$T = T_0(z) + T_1(z,t) \qquad (2.23)$$

$$T_1(z,t) = \sum_{j=-\infty}^{\infty} A_j e^{ik_j z - \alpha_j t} \qquad (2.24)$$

and plugging into Eq. 2.22 yields the parameters for thermal instability (growing T perturbation) for any k_j upon the condition that $Re\{\alpha_j\} > 0$. Using

this procedure, the following condition for instability of a given k_j perturbation results:

$$\frac{5}{2}\kappa_0 T_0^{1/2}\left[\frac{3}{2}\left(\frac{\partial T_0}{\partial z}\right)^2+T_0\frac{\partial^2 T_0}{\partial z^2}\right]-k_j^2\kappa_0 T_0^{5/2}-\sum_{I=1}^{M}n_e n_I\left.\frac{\partial f_I(T)}{\partial T}\right|_{T=T_0} > 0\ . \quad (2.25)$$

Consider the simplest unperturbed equilibrium, $T_0(z) = const.$, in the interval $0 \leq z \leq L$. In this case, Eq. 2.25 becomes

$$\sum_{I=1}^{M}n_e n_I\frac{\partial f_I(T)}{\partial T} < -k_j^2\kappa_0 T_0^{5/2}\ . \quad (2.26)$$

Fixing the perturbation to be zero at $z = 0$ and $z = L$ restricts the allowed k_js to be $k_j = \pi j/L$, $j \neq 0$, and sets $A_j = -A_{-j}$. Equation 2.26 can be most easily satisfied for the smallest $|k_j|$ perturbations, $k = \pm\pi/L$. Therefore, assuming that radiation is dominated by impurity species Z, the following instability condition results:

$$\left.\frac{\partial f_Z(T)}{\partial T}\right|_{T=T_0} < -\frac{\pi^2\kappa_0 T_0^{5/2}}{n_e n_Z L^2}\ . \quad (2.27)$$

Since $\frac{\partial f_Z(T)}{\partial T}$ is negative in the 10–100 eV range for light impurities, Eq. 2.27 can be satisfied in the edge plasma. This parallel thermal instability is suggested as the mechanism responsible for the MARFE phenomena[5] in Alcator C. A similar argument involving perpendicular electron conduction is used to explain the density limit in tokamaks.[33]

2.6 Edge Plasma Parameters in Tokamaks

The edge plasma in many tokamaks has been diagnosed with Langmiur probes. A review of some probe techniques and measurements in tokamaks is covered by Staib.[60] Edge plasma densities of range $n_e \sim 10^{10}$–$10^{14}/\text{cm}^3$ vary strongly between machines owing to the variation in central plasma densities. Electron temperatures in the edge plasma are not as sensitive to central parameters and are typically $T_e \sim 5$–50 eV. Table 2.1 reproduced from Table I in reference [74] displays characteristic values for edge plasma parameters in some tokamaks.

The radial density profile in the limiter shadow plasma of tokamaks is modelled well by a decaying exponential function. The density e-folding length, λ_n, characterizes the density gradients in the edge plasma and from a simple 1-D diffusion model of the scrape-off plasma (discussed later in section 3.1) and allows an estimate of the perpendicular particle diffusion rate. Diffusion measured in the edge plasma in this way is found to be highly anomalous and is most often reported as some fraction of the calculated Bohm diffusion rate.

High power fluxes on probe surfaces associated with high edge plasma densities in tokamaks such as Alcator C restrict the use of Langmuir probes as an edge diagnostic. The power flux to a floating surface given by Eq. 2.2 in section 2.2.3 demonstrates this problem. Near the limiter radius in Alcator C , $n_e \sim 10^{14}/\text{cm}^3$ and $T_e \sim 20$ eV. Equation 2.2 yields a power flux to a probe of $P_{tot} \approx 5\text{kW/cm}^2$. Molybdenum probes have been used to diagnose this plasma parameter range in Alcator C; however, probe melting usually occurs. Plasma parameters at minor radii less than the limiter radius are therefore inaccessible even with the use of tungsten probe tips. Unfortunately, interesting physics associated with MARFEs occurs at the limiter boundary interface in Alcator C. Conditions at the limiter edge can, at best, be extrapolated from measurements

in the limiter shadow region. In contrast, probes in a low-field, low-density tokamak such as Caltech, Macrotor, and Microtor, do not encounter the power flux constraint even at radii much less than the limiter or wall radius.

Enhanced heat fluxes (anomalous δ_t in Eq. 2.2) due to non-thermal electron tails can further restrict the use of Langmuir probes in tokamaks. On Macrotor and Microtor[61], δ_t factors on the order $\delta_t \sim 25$–100 have been measured and attributed to epithermal electron tails. Heat fluxes in the electron drift direction exceed those in the ion drift direction in Mactrotor by a factor of ~ 4, supporting this hypothesis.

Table 2.1 - Typical Edge Plasma Parameters in Some Tokamaks

Device	Boundary	B_t(T)	R(cm)	a(cm)	T_e(eV)	n_e(/cm^3)	λ_n(cm)	$D_\perp / D_B$	$\tilde{n}/n$	δ_t
Alcator A	poloidal limiter	6.0	54	10	10 – 12	7×10^{13}	~ 1	~ 1	~ 0.5	
Alcator C	poloidal limiter	10.0	64	16.5	10 – 20	10^{14}	~ 0.3	~ 1	0.5 – 0.7	
ASDEX	poloidal limiter	2.0	165	40	30	$< 3 \times 10^{11}$	2.5			
Caltech	outer limiter	0.36	45	16	10 – 25	$10^{11} - 10^{12}$	1.5	~ 1	~ 0.2	
DITE	bundle divertor	0.9 – 2.7	117	19 – 26	~ 25	$\sim 10^{12}$	~ 5		0.08-1.0	6 – 200
DITE	poloidal limiters	1.4 – 2.7	117	26	5 – 15	$< 2.5 \times 10^{12}$	$\sim 1 - 3$			
DIVA	poloidal divertor	0.8 – 2.0	60	10	15 – 80	$1 - 5 \times 10^{12}$		~ 0.1		15 – 20
JFT-II	rail limiters	1.7	90	25	30 – 50	$2 - 5 \times 10^{12}$	1.5 – 4.5	~ 1	≤ 0.1	3 – 20
Macrotor	rail limiter	0.3	90	45	20 – 40	$\sim 10^{11} - 10^{12}$	$\sim 7 - 10$	~ 2	0.05 – 0.3	~ 25
Microtor	rail limiter	2.0	30	10	20 – 40	$\sim 10^{11} - 10^{12}$	~ 1	~ 0.5	0.05 – 0.3	30 – 120
PDX	limiter or divertor	1.9	145	39	7 – 15	$3 \times 10^{10} - 10^{12}$	2 – 4			
PLT	mushroom limiters	1.7 - 1.9	130	40	5 - 40	$< 6 \times 10^{11}$	~ 4			
T-12	poloidal divertor	0.8	36	8	20 – 60	$< 10^{12}$	< 1	≤ 0.1		40 - 100
TFR 600	limiters	4.0	98	19	~ 10	$\sim 7 \times 10^{12}$	~ 1.8	≥ 1		~ 15

CHAPTER 3

EDGE PLASMA MODELS

There has been much effort devoted to the modelling of edge plasmas particularly in connection with divertor systems.[62-66] A complete edge plasma model must include particle, momentum, and energy balance with multiple ion species, electrons, and neutrals. Fortunately, radial plasma density profiles in the limiter shadow region of a tokamak can be simply modelled by considering only the ion species and invoking continuity to balance perpendicular diffusion with parallel flows to a limiter. Section 3.1 outlines this standard calculation which can be used to obtain an estimate of the global particle confinement time.

This simple radial diffusion model is lacking in that it assumes a poloidally symmetric edge plasma. Observations of MARFE phenomena and data presented later in this thesis will show that strong poloidal variations in density and temperature are maintained in the edge plasma of Alcator C. It has been suggested that sharp radial gradients in density and temperature may drive a strong Pfirsch-Schlüter convection in the edge plasma which causes a natural asymmetry.[45,67] Section 3.2 shows that the particle fluxes in the radial diffusion model are greatly modified when one includes bulk plasma flows due to Pfirsch-Schlüter convection. An estimate is made of the expected perturbation of the density and temperature profiles due to Pfirsch-Schlüter convection by considering the continuity and electron energy equations. The magnitude of both the density and temperature poloidal perturbations are found to scale very strongly with n/I, which is consistent with the observations of MARFE phenomena in Alcator C. This exercise emphasizes the possible role of $\underline{E} \times \underline{B}$ convection in the edge plasma and prompts a more detailed study of $\underline{E} \times \underline{B}$ convective transport in the limiter shadow plasma of Alcator C.

In order to investigate transport processes in the edge plasma of Alcator C in a more formal manner, a system of reduced transport equations appropriate for Alcator C edge plasma is identified in section 3.3. These equations were obtained in previous work[67,68] and are used to infer the magnitude of perpendicular transport from experimental data presented in later chapters.

3.1 A Simple Radial Diffusion Model

3.1.1 Radial Density Profile in the Limiter Shadow Plasma

Particle fluxes in the limiter shadow plasma can be simply modelled as shown in Figs. 3.1a–3.1c. The poloidal symmetry of the limiter geometry in a tokamak such as Alcator C (see Fig. 3.1a) suggests that only radial and toroidal particle fluxes need be considered in the limiter shadow plasma. Figure 3.1b illustrates perpendicular radial flows into the scrape-off plasma and parallel flows to limiter surfaces. The radial flow is assumed to be driven by a radial density gradient through Fick's law

$$\Gamma_r = -D_\perp \frac{\partial n}{\partial r} . \tag{3.1}$$

At the limiter, a sheath is formed. The pre-sheath electric fields accelerate ions so that they arrive at the limiter surface with the sound speed, C_s. Thus, the parallel flux to the limiter is some function of the distance along field lines, $S_\parallel$,

$$\Gamma_\parallel(S_\parallel) = n\, V_\parallel(S_\parallel) . \tag{3.2}$$

For the purposes of this simple analysis it is assumed that $n \approx const.$ while $V_{\|}$ most strongly varies along a field line. The simplest form for $V_{\|}(S_{\|})$ shown in Fig. 3.1c is

$$V_{\|}(S_{\|}) = \frac{S_{\|} C_s}{L} \tag{3.3}$$

where L is the distance from the symmetry point between limiters, $S_{\|} = 0$, to a limiter surface. A more careful consideration of parallel momentum leads to more complicated functions for $n(S_{\|})$ and $V_{\|}(S_{\|})$ (see sections 8.5.2 and 8.5.3). Nevertheless, equation 3.3 with $n \approx const.$ suffices for the present analysis. (Results from more detailed analyses can be incorporated in the model used in this chapter by replacing L by L_{eff} where $L_{eff} \approx 1.6\text{–}2 \times L$.)

a) Poloidal Cross-Section of Tokamak

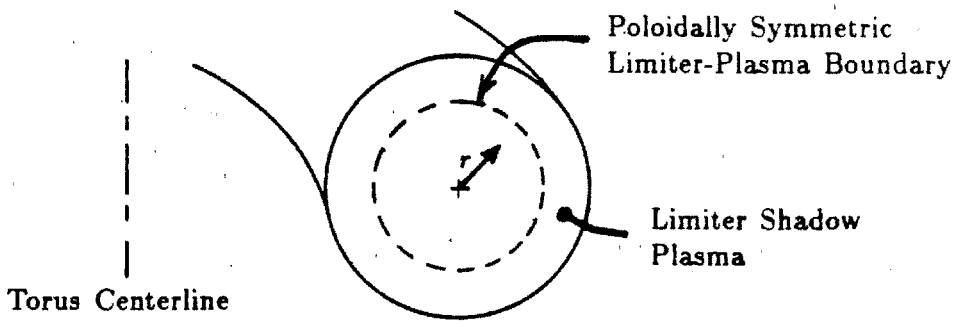

b) Perpendicular and Parallel Fluxes in Shadow Plasma

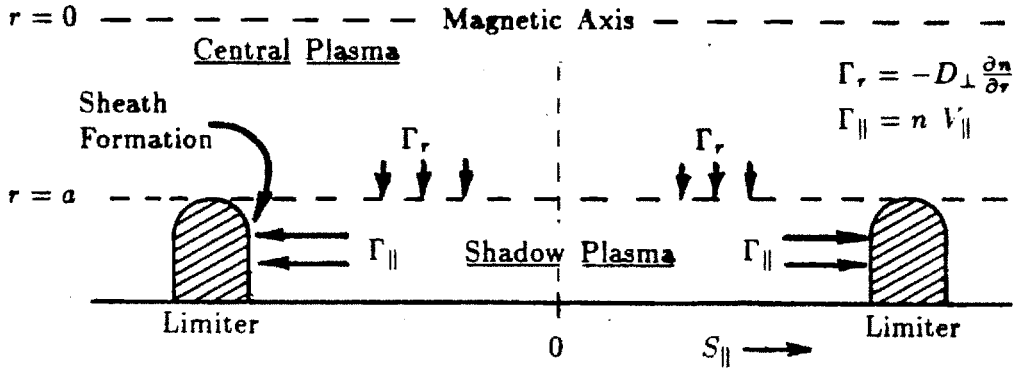

c) Parallel Flow to Limiter

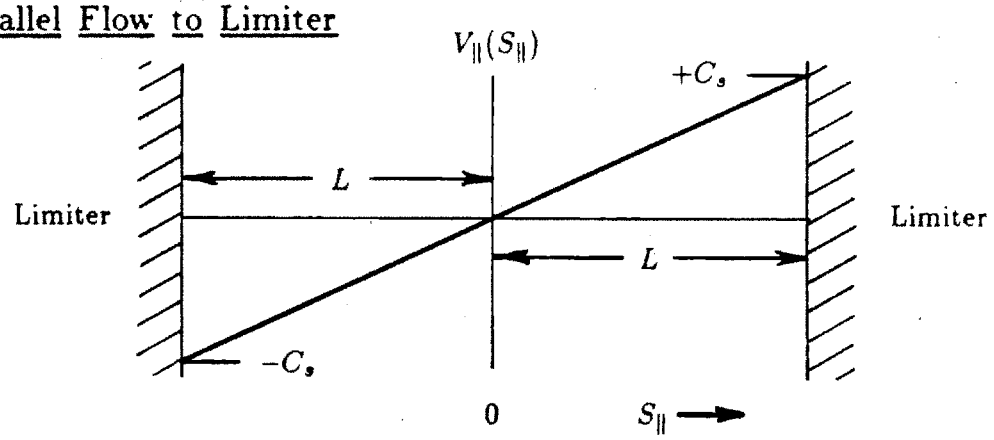

Figure 3.1 Simple 2-D Flow Model in Limiter Shadow Plasma

With this model for the particle fluxes, a radial density profile can be estimated. Continuity requires

$$\nabla \cdot \underline{\Gamma} \;=\; S \tag{3.4}$$

$$\nabla \cdot (\underline{\Gamma}_{\|} + \underline{\Gamma}_{\perp}) \;=\; n\; n_n \langle \sigma v \rangle_{ion} \tag{3.5}$$

where the source term, S, is due to ionization from background neutrals. Approximating the shadow plasma geometry as slab, and assuming uniformity in poloidal angle, Eq. 3.5 becomes

$$\frac{\partial}{\partial S_{\|}}\left(nV_{\|}\right) + \frac{\partial}{\partial r}\left(-D_{\perp}\frac{\partial n}{\partial r}\right) \;=\; n\; n_n \langle \sigma v \rangle_{ion}\;. \tag{3.6}$$

Further, assuming that $D_{\perp}$ is not a function of r,

$$\frac{nC_s}{L} - D_{\perp}\frac{\partial^2 n}{\partial r^2} \;=\; n\; n_n \langle \sigma v \rangle_{ion}\;. \tag{3.7}$$

Integrating for $n(r)$ and imposing the boundary conditions $n(r = a) = n_a$, $n(r \rightarrow \infty) = 0$, yields

$$n(r) \;=\; n_a e^{(a-r)/\lambda_n} \tag{3.8}$$

$$\lambda_n \;=\; \sqrt{\frac{D_{\perp}}{C_s/L - n_n \langle \sigma v \rangle_{ion}}} \tag{3.9}$$

when C_s/L and $n_n \langle \sigma v \rangle_{ion}$ are independent of radius.

An exponential variation of density with minor radius in a limiter shadow plasma similar to Eq. 3.8 is most often measured in tokamaks. Even with complicated limiter geometries or large probe systems where the effective 'L' length changes with radius, Eq. 3.7 models the radial density profile well when solutions in each region are matched with the appropriate boundary conditions.[69,70]

3.1.2 Estimating Perpendicular Diffusion

Once a measurement is made of the radial density profile and it is verified to be exponential, Eq. 3.9 can be used to estimate the perpendicular diffusion coefficient. Consider the ionization term and sound speed flow term in the denominator of Eq. 3.9. The perpendicular diffusion coefficient can be approximated as

$$D_\perp \approx \frac{\lambda_n^2 C_s}{L} \tag{3.10}$$

when

$$\frac{L\, n_n \langle \sigma v \rangle_{ion}}{C_s} \ll 1 \,. \tag{3.11}$$

For a 10–100 eV hydrogen plasma, $\langle \sigma v \rangle_{ion}/C_s \approx 3 \times 10^{-15}$ cm^2. Thus condition (3.11) becomes

$$L\, n_n \ll 3 \times 10^{14} \ \ /\mathrm{cm}^2 \,. \tag{3.12}$$

In Alcator C with $L \sim 100$ cm, Eq. 3.10 can be used to estimate $D_\perp$ as long as $n_n \ll 3 \times 10^{12}$ /cm^3.

3.1.3 Estimating Particle Confinement Time

The measurement of radial density profiles in the limiter shadow plasma allows an estimate of the global particle confinement time through the use of this radial diffusion model. Consider the time dependent continuity equation,

$$\frac{\partial n}{\partial t} + \nabla \cdot \underline{\Gamma} \;=\; n\; n_n \langle \sigma v \rangle_{ion} \;. \tag{3.13}$$

(No specification of particle species is made here; however, the electron density profile is most easily obtained with probes, independent of the edge Z_{eff}.) The neutral species obeys the similar equation

$$\frac{\partial n_n}{\partial t} + \nabla \cdot \underline{\Gamma}_n \;=\; -n\; n_n \langle \sigma v \rangle_{ion} \;. \tag{3.14}$$

Thus, in a steady state plasma or when $\frac{\partial}{\partial t} \rightarrow 0$, the plasma fluxes and neutral fluxes are related by

$$\nabla \cdot \underline{\Gamma} + \nabla \cdot \underline{\Gamma}_n \;=\; 0 \;. \tag{3.15}$$

At this time in a discharge we are interested in calculating the particle confinement time, τ_p. However, because of recycling and fueling implied by Eq. 3.15 the plasma density is not decaying in time. An estimate of τ_p can be obtained by considering the situation that would result when $n_n \rightarrow 0$. In the absence of a neutral species, Eq. 3.13 can be integrated over the total plasma volume to read

$$\frac{\partial}{\partial t} \int_{vol} n \; \partial V + \int_{surf} \underline{\Gamma} \cdot \partial \underline{S} \;=\; 0 \tag{3.16}$$

where the plasma surface is assumed to be coincident with the wall surface. The total number of particles would then decay in time. The characteristic time for this decay, τ_p, can then be written as

$$\tau_p = \frac{\int_{vol} n \; \partial V}{\int_{surf} \underline{\Gamma} \cdot \partial \underline{S}} \tag{3.17}$$

which requires an accounting of the total number of particles in the plasma and an estimate of the plasma flux to wall surfaces. The plasma flux to surfaces perpendicular to $\underline{B}$ can be obtained through measured radial profiles of $n(r)$ and $T(r)$ in the limiter shadow and the sound speed parallel flux condition of Eq. 2.1. If a significant density persists at wall radii where surfaces are parallel to $\underline{B}$, Eq. 3.1 in conjunction with Eq. 3.10 can be used to estimate the perpendicular flux contribution to $\int_{surf} \underline{\Gamma} \cdot \partial S$.

Alternatively, the plasma surface can be defined as the boundary at the limiter radius, $r = a$. In this case the total number of particles is simply

$$N_{tot} = 4\pi^2 R_0 \int_0^a n(r) \; r \; \partial r \tag{3.18}$$

for a specified central density profile, $n(r)$. The total flux through the surface at $r = a$ from (3.1), (3.8), and (3.10) is

$$\int_{surf} \underline{\Gamma} \cdot \partial \underline{S} = \frac{4\pi^2 \; R_0 \; a \; \lambda_n \; n_a \; C_s}{L} \tag{3.19}$$

In Alcator C, the central density profile follows a parabola to some power, γ,

$$n(r) \approx n_0 \left(1 - \frac{r^2}{a^2}\right)^{\gamma} \tag{3.20}$$

with n_0 being the peak plasma density on axis and $\gamma \sim 0.5 - 1.0$. Combining Eqs. 3.17–3.20,

$$\tau_p \approx \frac{n_0 \; L}{2(\gamma+1) \; \lambda_n \; n_a \; C_s} \tag{3.21}$$

where n_a is the density at the limiter radius extrapolated from probe measurements and C_s is an average sound speed in the limiter shadow plasma.

Finally, to arrive at a formulation of τ_p in terms of readily measured quantities, a relationship is needed between the peak plasma density, n_0, and the more often measured central line-averaged density, $\overline{n}_e$. For Alcator C central density profiles given by Eq. 3.20,

$$\overline{n}_e = \frac{1}{2a} \int_{-a}^{a} n_0 \left(1 - \frac{r^2}{a^2}\right)^{\gamma} \partial r \; . \tag{3.22}$$

Ratios of $\overline{n}_e/n_0$ for various parabola powers, γ, implied by (3.22) are plotted in Fig. 3.2. Now τ_p can be expressed as

$$\tau_p \approx \frac{\overline{n}_e \; L \; a}{2(\gamma+1) \; \lambda_n \; n_a \; C_s \; f(\gamma)} \tag{3.23}$$

with

$$f(\gamma) = \frac{\overline{n}_e}{n_0} \quad \text{(in Fig. 3.2).} \tag{3.24}$$

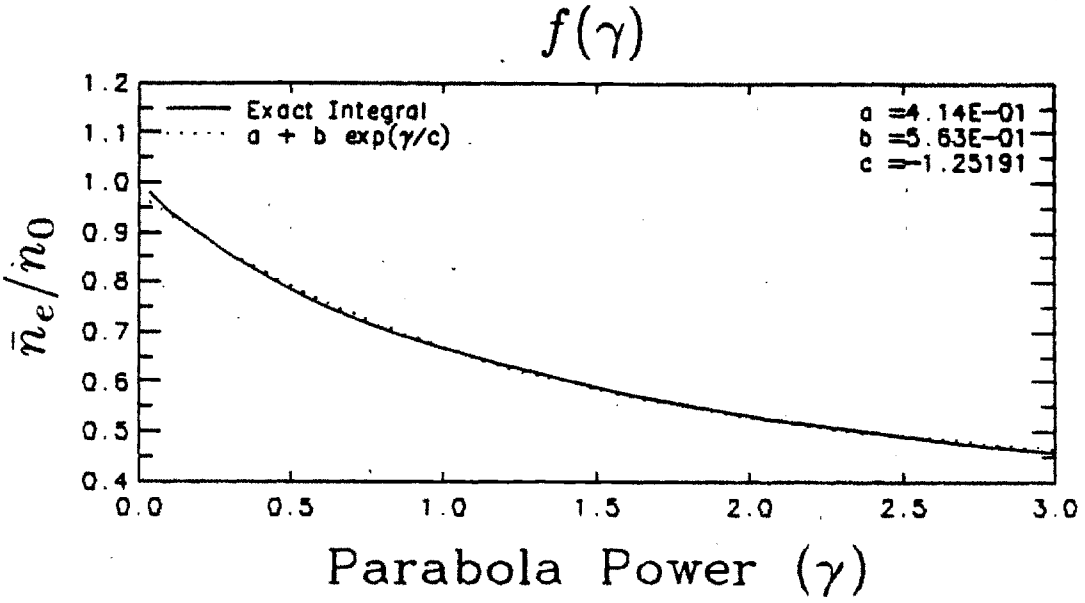

Figure 3.2 Ratio $\bar{n}_e/n_0$ vs. γ (central density parabola power)

3.2 A Diffusion Plus Pfirsch-Schlüter Convection Model

The diffusion model presented in the previous section made no statement about perpendicular convective flows that can occur in the edge plasma. The radial diffusion model mocks up the edge plasma density profiles well if convection is small compared to diffusion, or convection is along constant density surfaces. However, there are conditions when this is not the case, and perpendicular convective flows must be considered. Section 2.4.5 already outlined a number of ways in which $\underline{E} \times \underline{B}$ convection could be established in the edge plasma. Even in the absence of RF-induced eddies and potential mismatches from limiter surfaces, the toroidal effect of neoclassical Pfirsch-Schlüter convection remains. Pfirsch-Schlüter convection has been examined previously in connection with the MARFE phenomenon in Alcator C[45,67] and provides an example of a situation when convection can greatly influence the picture of particle and/or energy fluxes in the edge plasma.

3.2.1 Origin of Pfirsch-Schlüter Convection

The origin of Pfirsch-Schlüter plasma convection in a tokamak can be seen in Figs. 3.3a–3.3c. Due to the $1/R$ dependence of the magnetic field in a toroidal geometry, particles drift in the $q\underline{B} \times \nabla|\underline{B}|$ direction. At the plasma boundary where sharp density gradients arise, charge accumulation can occur. The rotational transform provides a path along magnetic field lines for currents to flow and short out the charge imbalance. These are the Pfirsch-Schlüter currents which flow out of the page in Fig. 3.3a at large major radii and into the page at small major radii. In the edge plasma, parallel resistivity can become large so that the charge separation is not cancelled completely by these currents. One can imagine a dipole-like field pattern as a result of this charge configuration such as that shown in Fig. 3.3b. An $\underline{E} \times \underline{B}$ convection pattern, Pfirsch-Schlüter convection, then arises as shown in Fig. 3.3c. This convection is across constant

density and temperature surfaces and therefore can influence the equilibrium density and temperature profiles under the appropriate conditions.

a) Pfirsch-Schlüter Currents

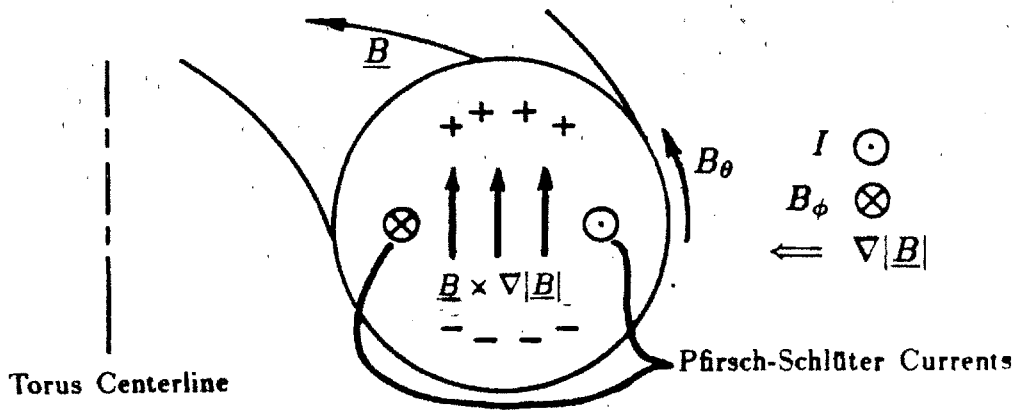

b) E-Fields

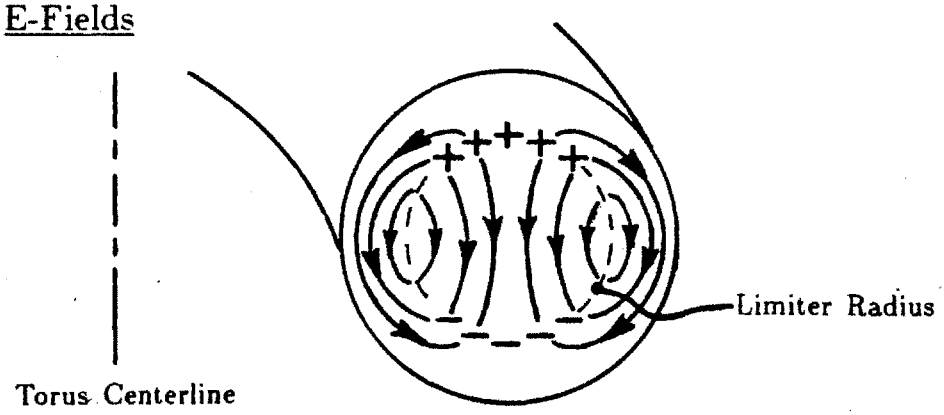

c) Pfirsch-Schlüter Convection Pattern

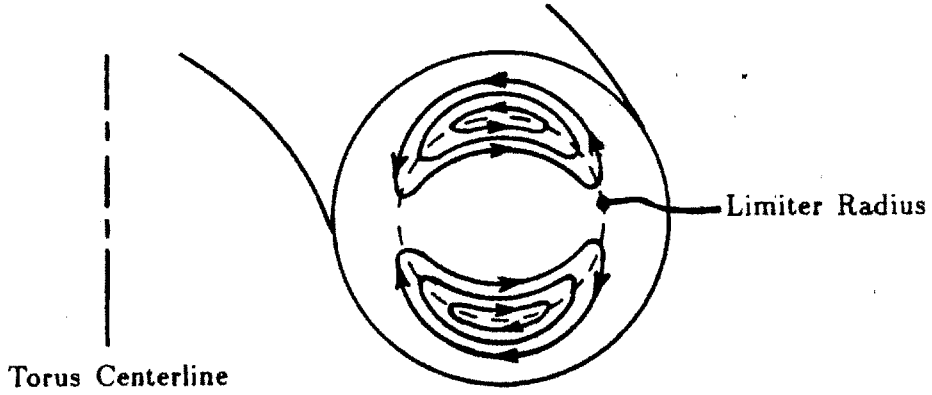

Figure 3.3 Origin of Pfirsch-Schlüter Convection

An analytic expression for the Pfirsch-Schlüter plasma convection in the limiter shadow plasma, $\underline{V}_\perp$, can be obtained as in Ref. [45] as follows: Let the pressure profile depend on radius only and require perpendicular force balance

$$\underline{J} \times \underline{B} = \nabla P \ . \tag{3.25}$$

The self-consistent pressure profile may depend on poloidal angle, but we are interested in examining only the magnitude and scaling of the Pfirsch-Schlüter convection. In the edge plasma, the $\underline{B}$ fields can be modelled by an equation of the form

$$\underline{B} = \underline{B}_0(r)/(1 + \epsilon \ cos\theta) \tag{3.26}$$

which satisfies $\nabla \cdot \underline{B} = 0$ in a toroidal coordinate system (Appendix A). Next, obtain $\underline{J}_\parallel$ which contains both Pfirsch-Schlüter and Ohmic heating currents from $\underline{J}_\perp$ above and the requirement

$$\nabla \cdot \underline{J}_\parallel + \nabla \cdot \underline{J}_\perp = 0 \ . \tag{3.27}$$

Ohm's law in the parallel direction is used to obtain the $\underline{E}$-field which drives the parallel current,

$$\underline{E}_\parallel = \eta_\parallel \underline{J}_\parallel \ . \tag{3.28}$$

The condition that $\nabla \cdot \underline{E} = 0$ can be used to reconstruct the electrostatic part of $\underline{E}$ from $\underline{E}_\parallel$. Finally the perpendicular Pfirsch-Schlüter flow velocity is obtained from perpendicular Ohm's law

$$\underline{V}_\perp = \frac{\underline{E} \times \underline{B}}{B^2} - \frac{\eta_\perp \nabla P}{B^2} \quad . \tag{3.29}$$

With the toroidal coordinate system and operators defined by Fig. A.1 in Appendix A, the above sequence leads to the following expressions for the perpendicular flow velocity to first order in ϵ $(= r/R_0)$:

<u>radial:</u>

$$V_r = -2\eta_\parallel \left(1 + \frac{B_\phi^2}{B_\theta^2}\right) \frac{B_\phi^2}{B^4} \frac{\partial P}{\partial r} \; \epsilon \; \cos\theta - \frac{\eta_\perp}{B^2} \frac{\partial P}{\partial r} - \frac{E_\phi^{oh} B_\theta}{B^2} \tag{3.30}$$

<u>poloidal component of perpendicular:</u>

$$V_{\perp\theta} = \frac{B_\phi}{B^2} \frac{\partial}{\partial r} \left[r \left(1 + \frac{B_\phi^2}{B_\theta^2}\right) 2\eta_\parallel \frac{\partial P}{\partial r} \frac{B_\phi}{B^2} \; \epsilon \; \sin\theta \right] + \frac{B_\phi}{B^2} \frac{\partial \Phi(r)}{\partial r} \tag{3.31}$$

<u>toroidal component of perpendicular:</u>

$$V_{\perp\phi} = -\frac{B_\theta}{B_\phi} V_{\perp\theta} \tag{3.32}$$

where $\Phi(r)$ is a superimposed electric potential that depends on radius only. $\Phi(r)$ results in a perpendicular rotation and can arise from non-ambipolar perpendicular fluxes which are left unspecified in this problem. Also, the perpendicular ion diamagnetic flow velocity not included in Eq. 3.29 can be incorporated into an effective $\Phi(r)$ term.

3.2.2 Scaling of Pfirsch-Schlüter Convection

In the radial direction, the total flow velocity given by Eq. 3.30 is made up of three terms. The first term looks similar to a diffusion term. After averaging over a flux surface, this first term combined with the second term leads to the Pfirsch-Schlüter neoclassical correction factor of $1+q^2$ times the classical diffusion coefficient. The last term is an $\underline{E} \times \underline{B}$ radial inward velocity due to the toroidal ohmic heating E-field included only for completeness in this model.

Since the perpendicular diffusion rate in the edge plasma is measured to be Bohm-like, exceeding the classical $2\eta_\perp n\kappa T/B^2$ value by orders of magnitude, the enhanced radial component of flux due to Pfirsch-Schlüter convection is not itself easily observed. However, it will be shown in later sections that this term has the potential to force a poloidally asymmetric perturbation to the density and temperature profiles.

The non-radial part of the Pfirsch-Schlüter perpendicular flow, on the other hand, can be much larger than the effective diffusion flow velocity as a consequence of the second derivative of the pressure profile with radius in Eq. 3.31. $V_{\perp\theta}$ can be simply scaled as follows: Let the edge radial density and temperature gradients be written as

$$\frac{\partial n}{\partial r} \approx \frac{n}{\lambda_n} \tag{3.34}$$

$$\frac{\partial T}{\partial r} \approx \frac{T}{\lambda_T} . \tag{3.35}$$

Since $\lambda_n, \lambda_T \ll a$, the radial derivatives of n and T dominate in Eq. 3.31. Approximating $B_\phi \approx B$, and allowing $\eta_\parallel \sim \eta_{\parallel 0}\ T_e^{-3/2}$, $V_{\perp\theta}$ can be written as

$$V_{\perp\theta} = \frac{4\ r^2\ \eta_\parallel\ n\ T_e\ sin\theta}{R_0\ B_\theta^2}\left(\frac{1}{\lambda_n}+\frac{1}{\lambda_T}\right)\left(\frac{1}{\lambda_n}-\frac{1}{2\lambda_T}\right) . \tag{3.36}$$

Finally, when $\lambda_n \ll 2\lambda_T$, $V_{\perp\theta}$ near the limiter radius reduces to

$$V_{\perp\theta} \approx 8.3 \times 10^{-10} \frac{n\ Z_{eff}\ a^4\ \Lambda\ sin\theta}{I^2\ R_0\ T_e^{1/2}\ \lambda_n^2} \quad \text{(m/sec)} \tag{3.37}$$

for plasma current, I, major radius, R_0, and coulomb logarithm, Λ. Electron temperature, T_e is in units of eV. All other quantities are in MKS units.

Equation 3.37 in conjunction with Eq. 3.30 describes the flow pattern depicted in Fig. 3.3c. In the limiter shadow region, $\frac{\partial^2 n}{\partial r^2}$ is positive and approximated by Eq. 3.7 in the previous section,

$$\frac{\partial^2 n}{\partial r^2} \approx \frac{n}{\lambda_n^2} \approx \frac{n\ C_s}{D_\perp\ L} . \tag{3.38}$$

The poloidal flow in this region always points to the inside of the torus through the $sin\theta$ dependence in (3.37).

Just inside the limiter radius where L $\rightarrow \infty$ in Eq. 3.7, $\frac{\partial^2 n}{\partial r^2}$ is negative and depends on the local neutral ionization source term

$$\frac{\partial^2 n}{\partial r^2} \approx \frac{n}{\lambda_n^2} \approx -\frac{n_n\ \langle \sigma v \rangle_{ion}}{D_\perp} . \tag{3.38}$$

The poloidal flow pattern therefore is opposite in this region and always points to larger major radii. Thus, two closed convection cells form as shown in Fig. 3.3c. An additional complication arises if the assumption $\lambda_n \ll 2\lambda_T$ is not satisfied. The point of $V_{\perp\theta}$ reversal then depends on gradients in temperature profile as well as the density profile such as in Eq. 3.36.

3.2.3 Magnitude of Pfirsch-Schlüter Convection in Alcator C

The magnitude of $V_{\perp\theta}$ can be estimated from Eq. 3.37; however, one must keep in mind that this is not necessarily the total poloidal or total perpendicular flow velocity. The total convective flow velocity can be formally written as

$$\underline{V} = V_r \hat{r} + (V_{\|\theta} + V_{\perp\theta}) \hat{\theta} + (V_{\|\phi} + V_{\perp\phi}) \hat{\phi} \tag{3.39}$$

with the understanding that $V_{\perp\theta}$ and $V_{\perp\phi}$ must satisfy Eqs. 3.31 and 3.32 in order to maintain the perpendicular force balance stated by (3.25). The parallel flow velocity does not enter into this perpendicular equilibrium and therefore must either be specified or determined by solving an appropriate parallel momentum equation. As a result, $V_{\|\theta}$ and therefore the total poloidal flow velocity is left undetermined in this model.

Although the velocity components cannot be uniquely stated, the magnitude of $V_{\perp\theta}$ places a restriction on the actual flow velocities which must exist to satisfy this toroidal equilibrium. Consider the case when the toroidal flow velocity is fixed to zero,

<u>Case 1:</u>

$$V_\phi(r,\theta) = 0 \tag{3.40}$$

implying

$$V_{\|\phi} = -V_{\perp\theta} \tag{3.41}$$

and therefore the total poloidal velocity is determined to be

$$V_\theta \;=\; (1+\frac{B_\theta^2}{B_\phi^2})\; V_{\perp\theta} \tag{3.42}$$

from the relationships for the parallel and perpendicular components discussed in Appendix B.

Similarly, when the total poloidal velocity is fixed to zero,

Case 2:

$$V_\theta(r,\theta) \;=\; 0\;, \tag{3.43}$$

the total toroidal flow velocity becomes

$$V_\phi \;=\; -(1+\frac{B_\phi^2}{B_\theta^2})\;\frac{B_\theta}{B_\phi}\;V_{\perp\theta}\;. \tag{3.44}$$

The actual poloidal and toroidal flow velocities in a real system will probably be some complicated function of radius and poloidal angle. Still, cases 1 and 2 determine the order of magnitude for convective flows in the edge plasma.

Notice that in case 1, the poloidal flow velocity is about the same magnitude as the poloidal component of perpendicular flow. This is expected since the perpendicular flow in a tokamak is mostly poloidal. On the other hand, case 2 forces the poloidal flow to be zero and requires the toroidal flow velocity to make up the necessary perpendicular flow. The net result is that the magnitude of the toroidal flow velocity is a factor B_ϕ/B_θ larger and allows the toroidal flow to acquire a significant fraction of the local sound speed.

Table 3.1 compares measured edge plasma parameters and calculated velocities for cases 1 and 2 for a typical Alcator C discharge. The sound speed, Bohm

diffusion coefficient, and effective radial diffusion velocity due to Bohm diffusion are included for reference. Note that although all flow velocities are under the sound speed, the toroidal flow can be a significant fraction of the sound speed and the poloidal flow is at least a few times larger than the effective radial diffusion velocity. Thus, the simple picture of plasma diffusing radially out of a cylindrical plasma column as presented in section 3.1 clearly *does not apply.* Plasma flow in the edge plasma region with sharp radial density gradients such as in Alcator C is dominated by flows perpendicular to $\hat{r}$ satisfying perpendicular equilibrium in a toroidal geometry and parallel momentum. The picture of perpendicular flows in the edge plasma then becomes like the flow pattern shown in Fig. 3.3c with a relatively weak radial flow pattern superimposed.

Table 3.1 - Estimate of Pfirsch-Schlüter Flows in the Alcator C Limiter Shadow Plasma

Edge Parameter	Measured Value
$n(r=a)$	$10^{14}/\text{cm}^3$
B_ϕ	8 tesla
I	380 kA
$T(r=a)$	20 eV
R_0	.64 m
a	.165 m
Z_{eff}	1.2
λ_n	.0025 m
λ_T	.0044 m
Transport Parameter	**Estimated Magnitude**
C_s	4.5×10^4 m/sec
D_{Bohm}	.16 m^2/sec
$V_{r\ Bohm}$	64 m/sec
$V_{\perp\theta}$MAX	285 m/sec
V_θMAX	285 m/sec
V_ϕMAX	5.0×10^3 m/sec

3.2.4 Poloidally Asymmetric Edge Plasma: Asymmetric Density

The implication of Pfirsch-Schlüter convection discussed in the previous section is that the edge plasma density and/or temperature profile can be perturbed from poloidal symmetry. Although it was already shown that the convective flux can easily dominate over the diffusive flux in the edge plasma, convection itself does not lead to particle or energy transport unless the flow is across a gradient, or the flow has a non-zero divergence. This fact is simply stated in the case of particle transport by the continuity equation which includes convection

$$\nabla \cdot (\underline{\Gamma}^D + \underline{\Gamma}^C) \;=\; S \tag{3.45}$$

$$\underline{\Gamma}^D \;=\; -D\nabla n \tag{3.46}$$

$$\underline{\Gamma}^C \;=\; n\,\underline{V} \tag{3.47}$$

so that

$$\nabla \cdot (-D\nabla n) + \underline{V} \cdot \nabla n + n\nabla \cdot \underline{V} \;=\; S\ . \tag{3.48}$$

To examine the influence that Pfirsch-Schlüter convection can have on the density profiles, consider a bulk flow velocity which is composed of a cross field Pfirsch-Schlüter convection calculated in section 3.2.2 plus a diamagnetic fluid velocity

$$\underline{V} \;=\; \frac{\underline{B} \times \nabla \Phi^{P.S.}}{B^2} \;+\; \frac{\underline{B} \times \nabla P_i}{q\ n\ B^2}\ . \tag{3.49}$$

The Pfirsch-Schlüter potential, $\Phi^{P.S.}$, is approximately

$$\Phi^{P.S.}(r,\theta) \approx K\ B_\phi\ \frac{\partial n}{\partial r}\ sin\theta \tag{3.50}$$

for nearly poloidally symmetric density profiles with

$$K = 8.3\times 10^{-10}\ \frac{Z_{eff}\ a^4\ \Lambda}{I^2\ R_0\ T_e^{1/2}} \tag{3.51}$$

in similar units as Eq. 3.37. Equation 3.50 requires that the temperature profile be uniform in space or slowly varying compared to n. Maintaining this assumption, we can now impose convection from (3.49) on Eq. 3.48 to examine the effect of these flows on the equilibrium density profile. In a $(\hat{r},\hat{\theta})$ plane slab geometry, with $\underline{B} = B_\theta\hat{\theta} + B_\phi\hat{\phi}$ and $\frac{\underline{B}\times\nabla|\underline{B}|}{B^2} = 0$, Eqs. 3.48–3.51 become

$$-D_\perp\frac{\partial^2 n}{\partial r^2} - \frac{D_\theta}{a^2}\frac{\partial^2 n}{\partial\theta^2} + K\ \Big(\frac{\partial^2 n}{\partial r^2}\Big)\frac{1}{a}\frac{\partial n}{\partial\theta}\ sin\theta - \frac{K}{a}\Big(\frac{\partial n}{\partial r}\Big)^2\ cos\theta$$

$$-\frac{K}{a}\Big(\frac{\partial^2 n}{\partial\theta\partial r}\Big)\frac{\partial n}{\partial r}\ sin\theta = S \tag{3.52}$$

with the approximation, $B_\phi \approx B$. $D_\perp$ and D_θ are assumed to be independent of space and D_θ includes perpendicular and parallel transport through the relationship

$$D_\theta = D_\perp\Big(\frac{B_\phi}{B}\Big)^2 + D_\parallel\Big(\frac{B_\theta}{B}\Big)^2\ , \tag{3.53}$$

where is it assumed for simplicity that the parallel transport process can also be written in the form of diffusion. The source term, S, can be approximated as

$$S \approx \frac{-n\ C_s}{L} \tag{3.54}$$

in the limiter shadow region ($r \geq a$) as suggested by Eq. 3.7 and the discussion in section 3.1.

Now, consider a perturbed density solution of the form

$$n(r,\theta) = n_0(r) + n_1(r,\theta) \tag{3.55}$$

$$n_0(r) = n_{a0} e^{(a-r)/\lambda_n} \tag{3.56}$$

$$n_1(r,\theta) = n_{a1}(\theta) e^{(a-r)/\lambda_n} \tag{3.57}$$

near the radial location $r \approx a$. With $|n_{a1}| \ll n_{a0}$, Eq. 3.52 reduces to

$$\frac{D_\theta}{a^2}\frac{\partial^2 n_{a1}}{\partial\theta^2} = -n_a \left(\frac{D_\perp}{\lambda_n^2} - \frac{C_s}{L}\right) - \frac{K\ n_{a0}^2}{a\ \lambda_n^2}\ cos\theta\ . \tag{3.58}$$

near $r \approx a$. λ_n is the unperturbed density scrape-off length and satisfies Eq 3.10.

$$\frac{D_\perp}{\lambda_n^2} - \frac{C_s}{L} = 0\ , \tag{3.59}$$

leaving a single term which drives a poloidal variation of n,

$$\frac{\partial^2 n_{a1}}{\partial\theta^2} = -\frac{a\ K\ n_{a0}^2}{D_\theta\ \lambda_n^2}\ cos\theta\ . \tag{3.60}$$

The density profile in the limiter shadow plasma is therefore perturbed by Pfirsch-Schlüter convection to a poloidally dependent profile of the form

$$n(r,\theta) \;=\; n_a(1+\delta_n cos\theta)\; e^{(a-r)/\lambda_n} \tag{3.61}$$

near the limiter radius with

$$\delta_n \;=\; \frac{K\; a\; n_a}{D_\theta\; \lambda_n^2}\;. \tag{3.62}$$

Parallel transport is much larger than perpendicular transport. As a first approximation, D_θ can be written as

$$D_\theta \;\approx\; D_\parallel\Big(\frac{B_\theta}{B}\Big)^2 \;\approx\; V_{thi}\;\lambda_{ii}\;\Big(\frac{B_\theta}{B}\Big)^2 \tag{3.63}$$

where λ_{ii} is the ion-ion mean free path. Using Eq. 3.51 for K, δ_n becomes

$$\delta_n \;=\; 5.0\times 10^{-18}\,\frac{Z^4\; a^7\; \Lambda^2\; n_a^2\; \sqrt{\mu}\; B^2}{I^4\; T_e^3\; R_0\; \lambda_n^2}\;. \tag{3.64}$$

The density at the limiter radius, n_a, is defined to be the electron density and Z in (3.64) includes the case of a $Z \neq 1$ ion species. μ is the ion mass in AMU and all other quantities are defined as in Eq. 3.37. This parameter, δ_n, is a measure of the perturbing effect of Pfirsch-Schlüter convection on a poloidally symmetric density profile. Values of δ_n for various edge parameters at the limiter radius in Alcator C are assembled in Table 3.2. Equation 3.61 is valid only for $\delta_n \ll 1$; however, Table 3.2 indicates that very large values of δ_n can easily be obtained in the edge, particularly at high densities and low currents.

Table 3.2 - Density Asymmetry Parameter, δ_n, for Various Edge Parameters in Alcator C

δ_n	n_a (m^{-3})	λ_n (m)	I (kA)	$\lambda_{ii}/\lambda_{\|}$
.024	10^{19}	.005	380	.10
.095	10^{19}	.0025	380	.10
.21	5×10^{19}	.005	500	.026
.60	5×10^{19}	.005	380	.020
.79	5×10^{19}	.0025	500	.026
2.4	5×10^{19}	.0025	380	.020
7.7	5×10^{19}	.005	200	.010
31	5×10^{19}	.0025	200	.010
124	10^{20}	.0025	200	.0052

Z_{eff}	a	Λ	μ	B	T_e	R_0
1.2	.165 m	11	1	8 tesla	15 eV	.64 m

The scaling of the density asymmetry parameter, δ_n, results from a combination of the Pfirsch-Schlüter convection scaling in Eq. 3.37 and the dependence of D_θ in Eq. 3.63. Care must be taken in using Eq. 3.64 for small n_a and high T_e since this result was derived using a collisional fluid model. The condition of sufficient ion-ion collisions for Eq. 3.64 to be valid can be stated as

$$\lambda_{ii} \ll \lambda_{\|} \tag{3.65}$$

where $\lambda_{\|}$ is the parallel density gradient scale length. From the poloidal variation in n suggested by Eq. 3.61, this condition becomes

$$\lambda_{ii} \ll \frac{a\ B}{B_\theta} \tag{3.66}$$

which leads to the constraint

$$4.8 \times 10^{10} \frac{I\ T_e^2}{Z^3\ a^2\ B\ n_e\ \Lambda} \ll 1 \tag{3.67}$$

at $r = a$. Table 3.2 includes $\lambda_{ii}/\lambda_{\|}$ for the displayed parameters, indicating that condition (3.67) is satisfied over the displayed range of parameters in the Alcator C edge plasma.

The density and current dependence of δ_n can be examined in more detail by noting that there is a relationship between the central plasma density, edge scrape-off length, and particle confinement time through Eq. 3.23. From neo-Alcator scaling at densities below $\overline{n}_e \approx 2 \times 10^{14}$ cm^{-3}, the energy confinement time scales with n, implying that the particle confinement time also scales roughly with n,

$$\tau_e \approx \tau_p/2 \propto n\ . \tag{3.68}$$

If the edge density follows the central density, then Eqs. 3.23 and 3.68 imply

$$\lambda_n \propto \frac{1}{n} . \tag{3.69}$$

This suggests that the asymmetry parameter depends more strongly on density than directly indicated in (3.64) and becomes

$$\delta_n \propto \frac{n^4}{I^4} . \tag{3.70}$$

This very strong n/I dependence is similar to the observed n/I threshold for the occurrence of a MARFE in Alcator C^5, and suggests a possible connection between poloidal asymmetries, MARFEs, and Pfirsch-Schlüter convection. Observations of MARFEs and MARFE threshold parameters are discussed in section 4.4.

A self-consistent calculation of Pfirsch-Schlüter convection for a poloidally asymmetric density profile which retains non-linear terms is needed to estimate more accurately the poloidal structure of the density profile for large values of δ_n. In addition, the equilibrium limiter shadow density profile depends on the details of the boundary condition at the limiter radius. The density profile in the limiter shadow region must be matched to solutions in the region $r < a$ where a net plasma source must be included. Further complications arise when the diffusion coefficients or source term are allowed to be some function of plasma density and/or spatial position. Nevertheless, from the perturbation analysis above, one expects that the edge plasma density in Alcator C can be greatly influenced by the presence of Pfirsch-Schlüter flows alone. The first order effect is a cosine perturbation that leads to a decrease in edge density at small major radii and an increase in edge density at large major radii. This perturbation has the potential

to saturate at very large amplitudes in Alcator C edge plasma. The very strong n^4/I^4 scaling points to a possible asymmetry threshold in n/I similar to the observed threshold for poloidally asymmetric edge conditions associated with a MARFE.

3.2.5 Poloidally Asymmetric Edge Plasma: Asymmetric Temperature

The temperature profile can be perturbed from poloidal symmetry by Pfirsch-Schlüter convection in a way analogous to the density profile. A poloidally perturbed temperature profile is perhaps a more interesting effect since it can lead to a poloidally localized radiative thermal instability in the edge plasma. Again, the observation of a poloidally localized, radiating edge region referred to as a MARFE in Alcator C suggests that some poloidally dependent cross field transport mechanism such as Pfirsch-Schlüter convection may indeed be active in the edge plasma.

The starting point for the calculation of perturbed T_e profiles in the limiter shadow plasma begins with the electron energy equation[59]

$$\frac{3}{2}n\frac{\partial T_e}{\partial t} + \frac{3}{2}n\underline{V}_e \cdot \nabla T_e + nT_e\nabla \cdot \underline{V}_e = -\nabla \cdot \underline{q}_e - Q_{rad} + \frac{\underline{R}\cdot\underline{J}}{q\ n} \qquad (3.71)$$

when electron viscosity and electron-ion energy transfer terms are small compared to conduction and convection terms.

In the perpendicular direction, the electron fluid velocity consists of Pfirsch-Schlüter convection, electron diamagnetic flow, and diffusion,

$$\underline{V}_{\perp e} = \frac{\underline{B}\times\nabla\Phi^{P.S.}}{B^2} - \frac{\underline{B}\times\nabla P_e}{B^2} - D_\perp\frac{\nabla_\perp n}{n}\ , \qquad (3.72)$$

while in the parallel direction, the electron velocity closely follows the ion flow velocity to limiter surfaces in order to maintain ambipolarity. As a result, $\underline{V}_{\|e}$ has a positive divergence in the limiter shadow plasma so that

$$n \ \nabla \cdot \underline{V}_{\|e} \ \approx \ \frac{n \ C_s}{L} \tag{3.73}$$

in a manner similar to Eq. 3.54. The density profile is assumed to be poloidally symmetric and given by Eq. 3.56. In a $(\hat{r}, \hat{\theta})$ plane slab geometry, with $\frac{\underline{B} \times \nabla |\underline{B}|}{B^3} = 0$, Eqs. 3.71–3.73 reduce in steady state to

$$-\frac{\partial}{\partial r}\left[\kappa_\perp^e \frac{\partial T_e}{\partial r}\right] \ - \ \frac{1}{a^2}\frac{\partial}{\partial \theta}\left[\kappa_\theta^e \frac{\partial T_e}{\partial \theta}\right] \ + \ \frac{3}{2}\frac{D_\perp n}{\lambda_n}\frac{\partial T_e}{\partial r} \ + \ \frac{3}{2}\frac{n^2 K}{a \ \lambda_n}\frac{\partial T_e}{\partial r} cos\theta$$

$$+ \ \frac{3}{2}\frac{n^2 K}{a \ \lambda_n}\frac{\partial T_e}{\partial \theta} sin\theta \ = \ -\frac{n \ T_e \ C_s}{L} \ - \ Q_{rad} \ + \ \frac{J_\|^2}{\sigma_\|} \tag{3.74}$$

where κ_θ^e is defined as

$$\kappa_\theta^e \ = \ \kappa_\perp^e \left(\frac{B_\phi}{B}\right)^2 \ + \ \kappa_\|^e \left(\frac{B_\theta}{B}\right)^2 . \tag{3.75}$$

K is defined previously in (3.51), and we have used the approximations $B_\phi \approx B$, and $D_\perp \gg D_\perp^{classical}$. Contributions from the $\nabla \cdot \underline{q}_{e\|}$ term arising from parallel temperature gradients and subtle changes in the parallel electron distribution function (important for maintaining the sheath) are neglected although they should be included in a more accurate model of the unperturbed electron temperature profile. Furthermore, neglecting $J_\|^2/\sigma_\|$ and Q_{rad} compared to nT_eC_s/L and dropping $-\frac{\partial}{\partial r}[\kappa_\perp^e \frac{\partial T_e}{\partial r}]$ relative to $\frac{3}{2}\frac{D_\perp n}{\lambda_n}\frac{\partial T_e}{\partial r}$ (valid if $\kappa_\perp^e$ is not highly anomalous), Eq. 3.74 becomes

$$-\frac{1}{a^2}\frac{\partial}{\partial\theta}\left[\kappa_\theta^e\frac{\partial T_e}{\partial\theta}\right] + \frac{3}{2}\frac{nD_\perp}{\lambda_n}\frac{\partial T_e}{\partial r} + \frac{3}{2}\frac{n^2K}{a\ \lambda_n}\frac{\partial T_e}{\partial r}cos\theta$$

$$+ \frac{3}{2}\frac{n^2K}{a\ \lambda_n}\frac{\partial T_e}{\partial\theta}sin\theta = -\frac{n\ T_e\ C_s}{L}\ . \tag{3.76}$$

In the absence of Pfirsch-Schlüter convection or when $K \rightarrow 0$, the T_e profile is poloidally symmetric and Eq. 3.76 reduces to

$$\frac{3}{2}\frac{nD_\perp}{\lambda_n}\frac{\partial T_e}{\partial r} = -\frac{nT_eC_s}{L} \tag{3.77}$$

so that

$$T_0 = T_a\ e^{2(a-r)/3\lambda_n}\ . \tag{3.78}$$

Thus, in the absence of radiation, the edge temperature radial scrape-off length is estimated to be

$$\lambda_T \approx \frac{3\lambda_n}{2}\ . \tag{3.79}$$

In a similar way that a perturbed density profile was obtained, the perturbed T_e solution to Eq. 3.75 near $r \approx a$ is found to be

$$T(r,\theta) = T_a\ (1 - \delta_T\ cos\theta - \frac{9}{16}\ \delta_T^2\ cos2\theta)\ e^{2(a-r)/3\lambda_n} \tag{3.80}$$

with

$$\delta_T \;=\; \frac{n_a^2 K a}{\lambda_n^2 \kappa_\theta} \;. \tag{3.81}$$

The temperature profile is therefore perturbed in a similar manner as the density profile. However, the perturbed temperature profile has an additional $cos2\theta$ term which does not appear in the density perturbation even when expanded to second order in δ_n.

δ_T and δ_n are simply related by

$$\delta_n \;\approx\; \sqrt{\frac{m_i}{m_e}}\; Z^2\; \delta_T \;. \tag{3.82}$$

The temperature perturbation is therefore not as large as the density perturbation for the same edge plasma parameters. This is because electron parallel conduction, $\kappa_{\|}^e$, is a factor of $Z^2\sqrt{m_i/m_e}$ larger than ion parallel conduction, $\kappa_{\|}^i$, and the ion parallel diffusion scales like $D_{\|}^i \approx \kappa_{\|}^i/n$.

δ_T can be evaluated numerically as

$$\delta_T \;\approx\; 1.1\times 10^{-19}\frac{Z^2\; n_a^2\; a^7\; \Lambda^2\; B^2}{\lambda_n^2\; I^4\; T_e^3\; R_0} \tag{3.83}$$

with similar units as in equation 3.64. This temperature asymmetry parameter, δ_T, is displayed in Table 3.3 for the same edge plasma conditions that were displayed in Table 3.2 for δ_n. As in the density calculation, the constraint stated in (3.67) must be satisfied in order that this fluid treatment be valid. The column, λ_{ii}/λ in Table 3.3 has not changed from Table 3.2 and indicates that indeed $\lambda_{ii} \ll \lambda$.

Table 3.3 - Temperature Asymmetry Parameter, δ_T, for Various Edge Parameters in Alcator C

δ_T	n_a (m^{-3})	λ_n (m)	I (kA)	$\lambda_{ii}/\lambda_{\|\|}$
.0004	10^{19}	.005	380	.10
.0015	10^{19}	.0025	380	.10
.0032	5×10^{19}	.005	500	.026
.0092	5×10^{19}	.005	380	.020
.012	5×10^{19}	.0025	500	.026
.037	5×10^{19}	.0025	380	.020
.12	5×10^{19}	.005	200	.010
.47	5×10^{19}	.0025	200	.010
1.9	10^{20}	.0025	200	.0052

Z_{eff}	a	Λ	B	T_e	R_0
1.2	.165 m	11	8 tesla	15 eV	.64 m

The condition that $\delta_T \ll 1$ for the perturbed T_e solution to be valid is more easily satisfied than the $\delta_n \ll 1$ condition for a wide range of edge parameters in Alcator C, yet at high densities and low plasma currents, the strong I and n scaling can still take over and cause δ_T to exceed 1. This implies that for some critical combination of edge plasma parameters corresponding to a critical δ_T, the temperature in the inside midplane region may be sufficiently depressed to cause a local radiation thermal instablity there. Certainly if a radiation thermal instability were to occur at all in the edge plasma, one would expect from this analysis that it would be initiated on the inside midplane where the lowest temperature occurs in Eq. 3.80.

Examining the density and current dependence of δ_T more closely, similar to the argument used in scaling δ_n, δ_T is found to have the same strong functional dependence on n/I,

$$\delta_T \propto \left(\frac{n}{I}\right)^4 . \tag{3.84}$$

This again suggests a possible connection between the perturbation in the temperature profile due to Pfirsch-Schlüter convection and the observed threshold n/I value that precipitates the onset of a MARFE in Alcator C.

3.3 Reduced Transport Equations for Alcator C Edge Plasma

The previous section emphasized the role that convection can play in the edge plasma. Pfirsch-Schlüter convection was examined in particular, and it was found that the edge density and temperature profiles could be perturbed from poloidal symmetry with amplitude characterized by parameters δ_n and δ_T. Motivated by the coincidence in the scaling of δ_n and δ_T with the observed MARFE threshold scaling, the role of convection in the edge plasma is now more carefully investigated.

With the assumption that the fluid description is valid in the edge plasma, a system of fluid equations accurately describing physics in the edge must retain terms as dictated by gradient scale lengths and characteristic parameters found there. Such a scaling of transport terms in the fluid equations for a collisional edge plasma has been performed before by Singer and Langer[71] in a somewhat general form. Nevertheless, their analysis requires that the parallel flow velocity be under the sound speed, a condition violated near limiter surfaces. In addition, toroidal symmetry is assumed, and perpendicular $\underline{E}\times\underline{B}$ convection is neglected in their ordering. The analysis in sections 3.2.4 and 3.2.5 implied that perpendicular convection terms can, in fact, be substantial enough to perturb the pressure profiles from poloidal symmetry.

This section restates a system of reduced transport equations appropriate for the particular conditions found in Alcator C edge plasma. This system of equations was obtained in earlier work[68] and provides a more formal basis for the evaluation of transport terms from experimental data in later chapters. The system includes a simpler subset of terms identified by Singer and Langer in that no neutral species is included. On the other hand, all explicit convection terms are retained.

First, characteristic parameters and scale lengths found in the Alcator C edge plasma are discussed. The fluid model is shown to be valid, and a sizing

of convection terms is obtained. Finally, the set of reduced transport equations is restated with some important points reviewed.

3.3.1 Characteristic Parameters in Alcator C Edge Plasma

From Langmuir probe measurements and spectroscopic observations of the MARFE phenomena on Alcator C, a picture of characteristic edge plasma parameters has emerged. The following list of parameters is compiled for the purpose of scaling terms in the fluid transport equations:

Edge Density and Temperature

Langmuir probe data obtained in the Alcator C limiter shadow plasma indicates that near the limiter radius,[17,72]

$$n_e \sim 10^{13} - 10^{14} \text{ cm}^{-3} \tag{3.85}$$

$$T_e \sim 7 - 20 \text{ eV} . \tag{3.86}$$

The ion temperature has been measured as well through the use of a gridded energy analyzer.[73] It is found that typically

$$T_i \approx 1 - 3 \times T_e \tag{3.87}$$

in the limiter shadow plasma.

For estimating the magnitude of transport parameters in the remaining sections of this chapter, values of $n_e \approx n_i \approx 10^{13} - 10^{14}$ cm^{-3}, $T_i \approx T_e \approx 7 - 20$ eV, $Z_{eff} \approx 1.2$, $B \approx 8$ tesla, $\Lambda \approx 10$, $\mu \approx 1$, $\epsilon = a/R_0 \approx .25$, $q_{lim} = \epsilon B/B_\theta \approx 3-8$. are taken as typical.

Gradient Scale Lengths

The presence of limiter surfaces in the edge plasma forces gradients to exist along $\underline{B}$. No direct measurement of the parallel gradient scale length of temperature or density along $\underline{B}$ has been made in Alcator C; however, from geometry a value for the parallel gradient scale length, $\lambda_{\|}$, can be estimated. Taking $\lambda_{\|} \approx 1/2$ the distance between limiters,

$$\lambda_{\|} \approx \frac{2\pi R_0}{4} \sim 100 \text{ cm} \tag{3.88}$$

when two full poloidal limiters are used in Alcator C.

In the radial direction, Langmuir probes provide information about gradients in temperature and density. Typically, quantities vary exponentially with radius so that

$$\frac{\partial n}{\partial r} \sim \frac{n}{\lambda_{nr}} \; ; \; \lambda_{nr} \sim 0.3 \text{ cm} \tag{3.89}$$

$$\frac{\partial T}{\partial r} \sim \frac{n}{\lambda_{Tr}} \; ; \; \lambda_{Tr} \sim 0.8 \text{ cm} \; . \tag{3.90}$$

Thus the characteristic radial gradient scale length can be taken as

$$\lambda_r \sim \lambda_{nr} \sim 0.3 \text{ cm} \; . \tag{3.91}$$

The poloidal gradient scale length was at first the most difficult to characterize in Alcator C edge plasma. Before the DENSEPACK experiment, the only information about poloidal gradients in the edge came from spectroscopic observations of the MARFE phenomenon. It was recognized that poloidal gradients

must exist in violation of the often assumed poloidal symmetry approximation. From vertical brightness profiles during MARFE phenomena, a half-width extent of $\sim$ 5 cm was taken to be the order of the poloidal gradient scale length,

$$\lambda_\theta \sim 5 \text{ cm} . \tag{3.92}$$

Data obtained from the more recent DENSEPACK Langmuir probe data array which directly samples the poloidal variation in n and T_e has subsequently verified this scale size for λ_θ used in Ref. [80].

Validity of Fluid Model

The fluid description of the edge plasma is valid when the plasma is magnetized, $\omega_{ce}\tau_e \gg 1$, $\omega_{ci}\tau_i \gg 1$, and particle mean free paths are short compared to characteristic gradient scale lengths. The magnetized plasma condition can be stated when $Z \approx 1$ as:

$$\omega_{ci}\tau_i = 2 \times 10^{15} \frac{T_{i(\text{eV})}^{3/2} \; B_{(\text{T})}}{\mu \; n_{i(\text{cm}^{-3})} \; \Lambda} \tag{3.93}$$

$$\omega_{ce}\tau_e = \sqrt{\frac{m_i}{m_e}} \; \omega_{ci} \; \tau_i . \tag{3.94}$$

For typical edge parameters,

$$\omega_{ci} \; \tau_i \approx 300 - 1.4 \times 10^4 \tag{3.95}$$

$$\omega_{ce} \; \tau_e \approx 1.3 \times 10^4 - 6.1 \times 10^5 , \tag{3.96}$$

and, as expected, the magnetized plasma condition is satisfied in Alcator C edge plasma.

The fluid model can be used to describe a plasma with gradients parallel to $\underline{B}$ as long as

$$\lambda_{ii} \approx \lambda_{ei} \ll \lambda_{\|} . \tag{3.97}$$

A useful formula for λ_{ii} is

$$\lambda_{ii} = 2.4 \times 10^{13} \frac{T_{i(\mathrm{eV})}^2}{Z^3 \; n_{e(\mathrm{cm}^{-3})} \; \Lambda} \quad \mathrm{cm} , \tag{3.98}$$

and typical values become

$$\lambda_{ii} \approx 0.7 - 56 \quad \mathrm{cm} . \tag{3.99}$$

Condition (3.97) is therefore satisfied over most of the density and temperature ranges at the limiter radius except when both T_i becomes large and n_e small.

In the perpendicular direction, the corresponding scale length constraint is on the relative size of the poloidal ion gyro radius and perpendicular gradient scale length,

$$\rho_p \approx \frac{B \; \rho_i}{B_\theta} \ll \lambda_\perp \sim \lambda_r . \tag{3.100}$$

ρ_p is evaluated as

$$\rho_p = 1.02 \times 10^{-2} \; \frac{q_{lim} \; \mu^{1/2} \; T_i^{1/2}{}_{(\mathrm{eV})}}{\epsilon \; Z \; B_{(\mathrm{T})}} \quad \mathrm{cm} \tag{3.101}$$

and typically,

$$\rho_p \approx 4.1 \times 10^{-2} - 2 \times 10^{-1} \quad \text{cm} \tag{3.102}$$

so that Eq. 3.100 is satisfied for edge plasma conditions except for the uppermost range on T_i values.

In conclusion, the plasma near the limiter radius in Alcator C is reasonably approximated as a collisional, two species fluid. Problems can arise when the ion temperature becomes large as is observed in some cases,[73] or the plasma density becomes much smaller than the density stated in (3.85).

Bulk Plasma Flows

In order to scale convection and viscosity terms in the fluid equations, an estimate is needed of the magnitude of ion and electron flow velocities. In the parallel direction, the ions can acquire the sound speed upon flowing to the limiter surface. Since the ions carry the bulk flow momentum in the MHD description, the size scaling for $\underline{V}_{||}$ is taken as

$$V_{||} \approx V_{i||} \approx C_s \; . \tag{3.103}$$

For the electrons, a similar sizing results in

$$V_{e||} \approx V_{i||} \approx C_s \; , \tag{3.104}$$

even though the electrons carry the plasma current. This is because the parallel drift velocity of the electrons due to parallel E-fields is well under C_s in the edge plasma.

Perpendicular to $\underline{B}$, the electrons and ions have a fluid flow velocity due to diffusion, $\underline{E} \times \underline{B}$ drifts, and diamagnetic flows. It can be shown that the diamagnetic electron and ion flow velocity contributions to the continuity and energy equations are small compared to diffusion and $\underline{E} \times \underline{B}$ velocity contributions. In the electron and ion energy equations, for example, diamagnetic components of $n\underline{V} \cdot \nabla T$ and $nT\nabla \cdot \underline{V}$ cancel with diamagnetic components of $\nabla \cdot \underline{q}$, leaving only terms which depend on $\frac{\underline{B} \times \nabla |\underline{B}|}{B^3}$. These remaining terms are down by at least a factor of ϵ from non-diamagnetic terms. Thus, only diffusion and $\underline{E} \times \underline{B}$ convection flows need be considered in these equations.

Experimentally, it is found that the cross field particle diffusion rate in the edge plasma is on the order of Bohm diffusion, implying a size scaling for $\underline{V}_\perp^D$ of

$$\underline{V}_\perp^D \approx \underline{V}_{\perp i}^D \approx \underline{V}_{\perp e}^D \approx -\frac{D^B \nabla_\perp n}{n} \tag{3.105}$$

$$V_r^D \approx \frac{10^4 \; T_{(\mathrm{eV})}}{16 \; B_{(\mathrm{T})} \; \lambda_{r(\mathrm{cm})}} \; \mathrm{cm} \tag{3.106}$$

$$V_\theta^D \approx \frac{10^4 \; T_{(\mathrm{eV})}}{16 \; B_{(\mathrm{T})} \; \lambda_{\theta(\mathrm{cm})}} \; \mathrm{cm} \tag{3.107}$$

and typically

$$V_r^D \approx 1.8 \times 10^3 - 5.2 \times 10^3 \quad \mathrm{cm/sec} \tag{3.108}$$

$$V_\theta^D \approx 100 - 300 \quad \mathrm{cm/sec} \; . \tag{3.109}$$

As an estimate of the perpendicular velocity due to $\underline{E} \times B$ convection, Pfirsch-Schlüter convection velocities obtained in section 3.2.2 can be used. The radial component is well under the diffusive velocity while the poloidal component can be

$$V_{\perp\theta}^{E\times B} \approx 1000 - 1.5 \times 10^5 \quad \text{cm/sec} \; . \tag{3.110}$$

3.3.2 Reduced Transport Equations

It is more convenient to write the two-fluid equations as a single MHD fluid with the usual definitions:

$$\underline{V} = \frac{n_i m_i \underline{V}_i + n_e m_e \underline{V}_e}{n_i m_i + n_e m_e} \approx \underline{V}_i \tag{3.111}$$

$$\underline{J} = q(Z n_i \underline{V}_i - n_e \underline{V}_e) \tag{3.112}$$

$$P = P_e + P_i = n_e T_e + n_i T_i \ . \tag{3.113}$$

Using the characteristic parameters discussed in the previous section, one can examine the magnitude of each term in the full MHD fluid equations. The following set of reduced MHD transport equations for a steady state edge plasma with no neutral species is thereby obtained:

Continuity

$$\nabla \cdot n \, \underline{V} = 0 \tag{3.114}$$

$$\nabla \cdot \underline{J} = 0 \tag{3.115}$$

Momentum

$$\underline{J} \times \underline{B} = \nabla_{\perp} P \tag{3.116}$$

$$m_i \; n \; (\underline{V} \cdot \nabla) V_{\parallel} = -\nabla_{\parallel} P \tag{3.117}$$

Ohm's Law

$$\underline{E}_{\perp} + \underline{V} \times \underline{B} = \frac{\nabla_{\perp} P_i}{q \; n} + \frac{\underline{J}_{\perp}}{\sigma_{\perp}^{*}} \tag{3.118}$$

$$\underline{E}_{\parallel} = \frac{\underline{J}_{\parallel}}{\sigma_{\parallel}} - \frac{\nabla_{\parallel} P_e}{q \; n} - 0.71 \frac{\nabla_{\parallel} T_e}{q} \tag{3.119}$$

Energy

$$\frac{3}{2} n \underline{V} \cdot \nabla T_e + n T_e \nabla \cdot \underline{V}_e = -\nabla \cdot \underline{q}_e - Q_{rad} + \frac{\underline{R} \cdot \underline{J}}{q \; n} \tag{3.120}$$

$$\frac{3}{2} n \underline{V} \cdot \nabla T_i + n T_i \nabla \cdot \underline{V} = -\nabla \cdot \underline{q}_i - \underline{\underline{\pi}} : \nabla \underline{V}_i + Q_{e \rightarrow i} \tag{3.121}$$

The continuity equations, (3.114)–(3.115), and perpendicular momentum equation, (3.116), are unaffected by the scaling of terms and have the familiar simple form. The parallel momentum equation, (3.117), retains the convective derivative of the parallel flow velocity since we are allowing $V_{\parallel} \approx C_s$ at some point in the plasma. Parallel viscosity in this equation can be significant at some locations where the convective derivative is small but is not included in (3.117) for simplicity.

Ion pressure gradients which drive the diamagnetic ion flow in perpendicular Ohm's law, (3.118), must be included. The classical perpendicular electron conductivity in (3.118) is small enough to ignore. However, taking $n\underline{B} \times$ (3.118) leads to an expression for the perpendicular particle flux which contains a classical diffusion term that depends on $1/\sigma_\perp$. Since it is known that perpendicular diffusion in the edge plasma greatly exceeds this classical value, the $\sigma_\perp$ term can be rewritten as an effective $\sigma_\perp^*$ term so that

$$\frac{n\ \nabla_\perp P}{\sigma_\perp^*\ B^2} \ = \ D_\perp^{meas} \nabla n \ , \tag{3.122}$$

and the diffusive flux agrees with experimental values. $\sigma_\perp^*$ can be considered as another way to represent a time averaged $\langle \tilde{n}\tilde{\underline{E}} \times \underline{B} \rangle$ term that would result when taking $\langle n\underline{B} \times (3.118) \rangle$ and accounting for turbulent transport driven by low frequency electrostatic fluctuations.

Parallel Ohm's law contains two additional non-standard terms. The $\nabla_\parallel P_e$ term cannot be ignored in the parallel electron momentum equation while the $0.71 \nabla_\parallel T_e$ term results from the thermal component, $\underline{R}_T$, of the electron-ion momentum transfer term, $\underline{R}$.

In the electron energy equation, (3.120), both viscosity and electron-ion energy transfer terms are dropped compared to the electron conduction term. Radiative energy losses must be included in this equation. Electron-ion friction heating, $\underline{R} \cdot \underline{J}$, is also included in (3.120). Parallel currents driven by parallel temperature gradients such as in Eq. 3.119 can lead to Joule heating that is on the same order as the $\nabla \cdot \underline{q}_e$ term in Eq. 3.120. Only when the parallel gradient scale length is large can this term be neglected.

Unfortunately, the ion energy equation is not simplified at all from this reduction process. Viscosity must be retained since the parallel flow velocity can have a high shear in the radial direction. The electron-ion energy transfer

term also becomes important relative to $\nabla \cdot \underline{q}_i$ in high density edge plasmas characteristic of Alcator C.

In summary, Eqs. 3.114–3.121 are identified as an appropriate set of MHD fluid equations which retain the dominant physics in Alcator C edge plasma. Parallel gradients in density in temperature and strong parallel and perpendicular plasma convection are considered. Since the purpose of obtaining these equations is to investigate transport in the edge plasma, the neutral particle species is neglected for simplicity. An additional observation is that diamagnetic flow velocities implied by Eqs. 3.118, 3.116, and 3.112 do not need to be included in Eq. 3.114 and Eqs. 3.120–3.121 as long as the diamagnetic components of $\nabla \cdot \underline{q}$ are also neglected.

CHAPTER 4

ALCATOR C EDGE PLASMA

This chapter traces the history of edge plasma phenomena in Alcator C. Asymmetric limiter damage, first probe measurements in Alcator C, evidence of MARFEs, and data from a Langmuir probe built to study the MARFE region are presented. These sections serve as an introduction and summary of observations in the Alcator C edge plasma before the DENSEPACK probe system was operated.

4.1 Alcator C Vacuum Vessel and Limiter Geometry

The Alcator C stainless steel vacuum chamber consists of six bellows sections welded to six wedge-shaped flanges forming a torus as shown in Fig. 4.1. The bellows wall radius is at $r \approx 19.0$ cm and the major radius of the tokamak is $R_0 = 64.0$ cm. Each wedge-shaped flange has a set of keyhole slots allowing perpendicular to $\underline{B}$ diagnostic access from top, bottom, and outside locations. Copper Bitter plates which make up the toroidal field magnets occupy the space between the stainless steel flanges.

A system of 'virtual' limiters is used to protect the vacuum bellows from thermal plasma loading and runaway electron damage. Each of the six ports has a set of four stainless steel virtual limiter rings extending into $r \approx 18.0$ cm as shown.

The main limiter structure in Alcator C consists of segmented molybdenum, carbon, or SiC coated carbon poloidal ring limiters. Typically, Alcator C operates with two sets of 16.5 cm radius limiters. A 16.5 cm limiter set is usually composed of two full poloidal ring segments that straddle the access keyholes as shown in Fig. 4.1. In this arrangement, the double limiter acts as a single

poloidal ring limiter at that port, yet it protects diagnostics in the vicinity of the keyhole.

Alcator C has also operated with single poloidal ring molybdenum limiters of smaller radii, $a = 13.0$ and $a = 10.0$ cm, in a series of size scaling experiments.[119] For these experiments, the smaller size limiter diaphragm was inserted between the 16.5 cm limiters at E-port.

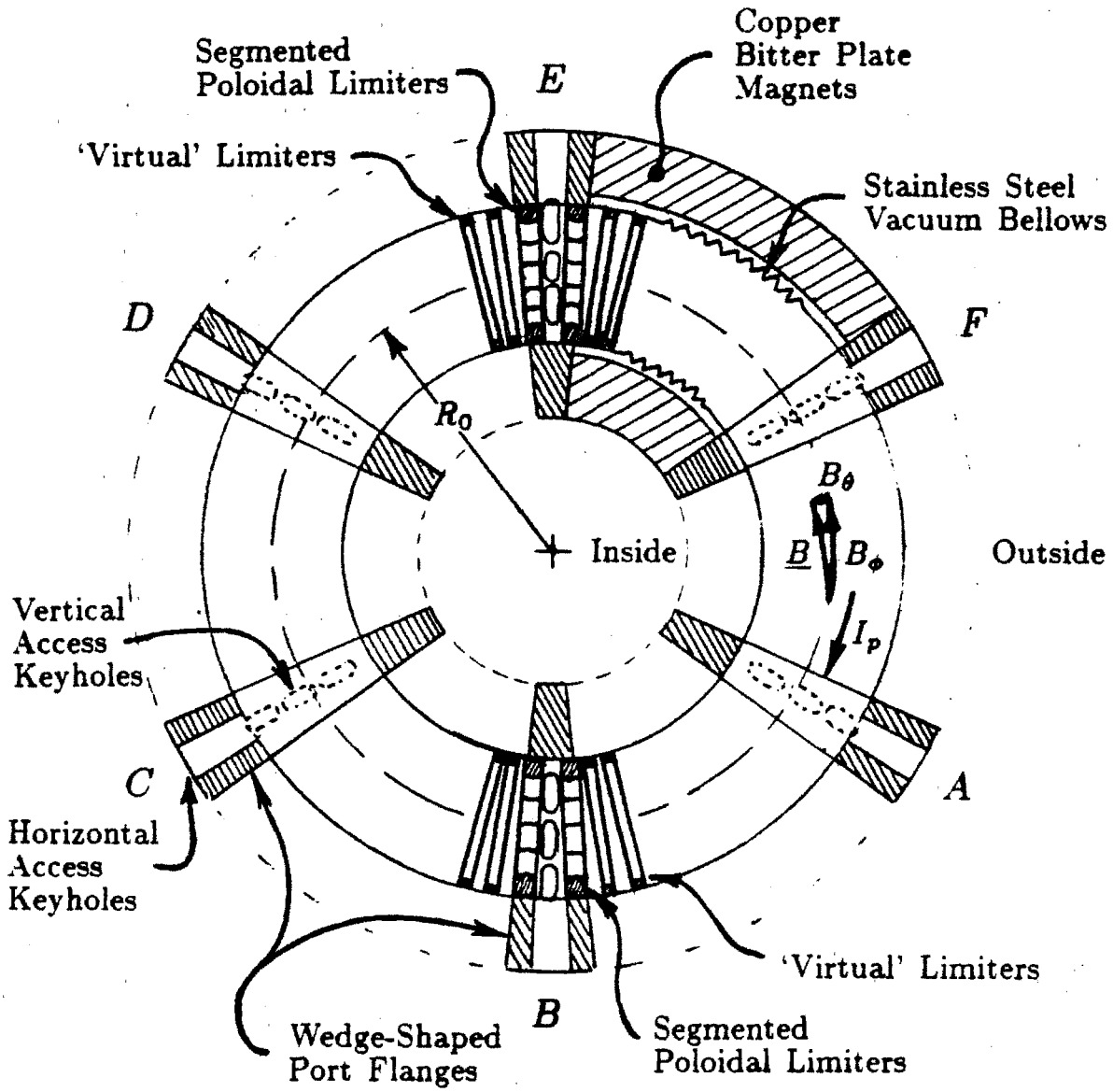

Figure 4.1 A Cut-away, Top View of Alcator C
Vacuum Vessel and Limiters

4.2 Asymmetric Limiter Damage

4.2.1 Qualitative Observations

Alcator C first began operating in the spring of 1978. At that time, a single 16.0 cm poloidal molybdenum limiter was used in E-port (see Fig. 4.1). However, it was found that this single limiter did not adequately unload the edge plasma energy and protect the vacuum wall. A virtual limiter in the adjacent F-port received a sufficiently high power flux to cause it to melt and become unwelded from the flange wall. The damage pattern indicated that the virtual limiter had received the most power flux on a location near the bottom of the poloidal cross-section. This was the first indication that the edge plasma in Alcator C was poloidally asymmetric, and it prompted the first series of Langmuir and heat flux probe measurements in Alcator C.[17]

One result of this study was that the high heat flux to the virtual limiter on F-bottom could be reduced by reversing the toroidal field direction and/or adding another full poloidal limiter. Consequently, Alcator C has since operated with at least two or more poloidal limiters when running discharges of minor radii $a \gtrsim 16.0$ cm.

Limiter damage in Alcator C has always been highly asymmetric. There are three distinct areas on a given limiter which show high power deposition: 1) at the upper-inside or 2) lower-inside poloidal positions depending on the limiter side (electron/ion drift), and 3) at the outside midplane position. These damage areas are most clearly seen on the 10 cm and 13 cm limiters which were used in the size scaling experiments. Figure 4.2 summarizes the damage observed on these limiters. Discharges were run with the toroidal B-field anti-parallel to the plasma current as shown in Fig. 4.1. These limiters consisted of 12 molybdenum block segments arranged about a 10 cm or 13 cm radius circle and pinned to a stainless steel back plate. Associated with the poloidal positions of enhanced

limiter damage are areas of deposited molybdenum extending to large minor radii on the stainless steel support plate.

On the side of the limiters which faced the electron drift direction, the damage pattern indicates that molybdenum blocks near the *upper* to *upper-inside* position received the highest power flux at large minor radii. Molybdenum blocks show a melted surface extending back from the limiter radius $\sim$ 1 cm. The radial extent of the molybdenum deposited on the stainless steel coincides with the severity of local molybdenum melting and aids in visualizing the poloidally asymmetric nature of the limiter damage.

On the ion side of the limiters depicted in Fig. 4.2, the pattern of damage is instead at *bottom* to *bottom-inside* locations. The sharp boundary of the deposited molybdenum seen at radii far into the limiter shadow is due the presence of 16.5 cm molybdenum limiters that remained in Alcator C during these discharges. Thus, the effects of highly asymmetric limiter damage extend at least $\approx$ 6 cm into the limiter shadow region.

The third area where the worst limiter melting and erosion occurred was on the outside midplane. For molybdenum limiters, this location typically displayed bulk melting, cracking and pitting of the limiter blocks. Carbon limiters did not show these bulk effects but appeared to be 'shaved down' at the outer midplane location. Carbon deposits on the vacuum wall were found toroidally about the limiter location and suggested that carbon was sputtered from the tip of the limiter and deposited there. This kind of damage was localized to an area at the limiter radius and did not extend into the limiter shadow or display an electron/ion side asymmetry as in the above two cases.

It is difficult to assess any more detail of the poloidal distribution of power flux on these limiters from the damage pattern alone. However, the above picture presents the overall trend. Unfortunately, the asymmetric deposition pattern which highlights the poloidal locations of damage to the molybdenum blocks can only be seen on the 10 cm and 13 cm limiters since the 16.5 cm limiters

have very little exposed stainless steel structure. However, the pattern of molten molybdenum on these limiters and the fact that the virtual limiters in F-port were damaged early in the operation of Alcator C with 16.0 cm limiters indicates that this kind of asymmetric power loading occurred for these larger minor radii limiters as well.

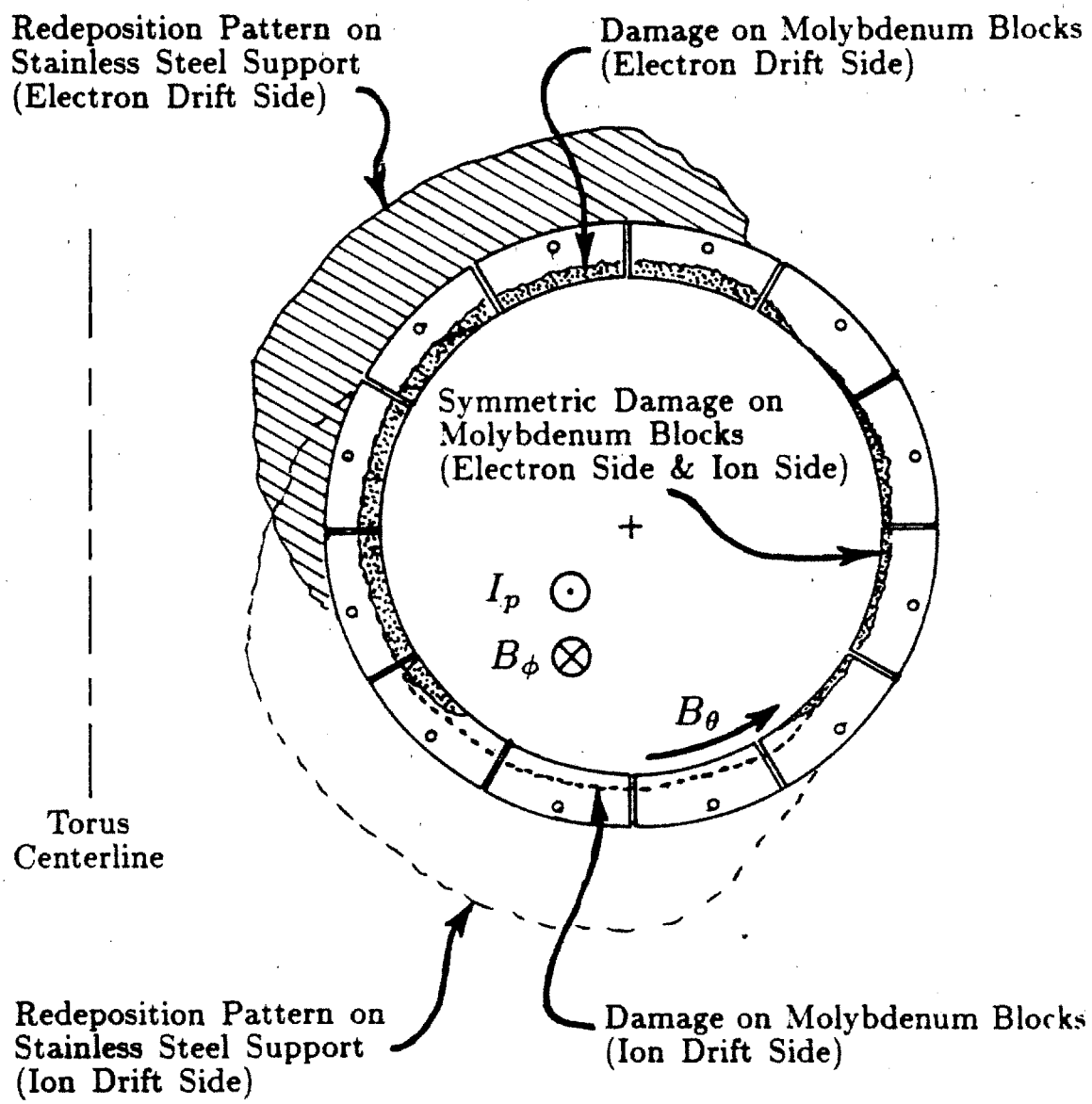

Figure 4.2 Summary of Limiter Damage Observations

4.2.2 Possible Reasons for Asymmetric Limiter Damage

The localized limiter damage on the outside midplane is most likely due to runaway electrons; however, the asymmetric damage on the molybdenum blocks is not so easily explained. Nevertheless, there are a number of possible explanations which come to mind.

Making the assumption that plasma density and temperature is constant on a flux surface, the asymmetric limiter damage might be explained in terms of displaced or distorted outer flux surfaces. Figure 4.2 illustrates the magnetic field direction and damage pattern for the 10 cm and 13 cm limiters. During a disruption or plasma termination, the plasma may crash inside. Alternatively, the plasma outer flux surfaces might be systematically misplaced by up to ~ 0.5 cm inside throughout the duration of many discharges. Such a shift of circular magnetic flux surfaces could allow the damage regions to be connected along a field line to large major radii regions of the plasma. Plasma could then diffuse from the inner flux surfaces onto these flux surfaces which intercept the limiter at the damage locations upon a single toroidal pass. However, the asymmetric damage extends too far into the limiter shadow. This is evident in the top and bottom damage locations and in the damage to the virtual limiters which cannot be explained by only an inward shift of circular flux surfaces. These points place in question the latter hypothesis of a badly positioned steady state plasma unloading preferentially at these locations.

Assuming that disruptions and/or plasma termination is not the cause of the limiter damage, one could consider non-circular outer flux surfaces. However, the limiter damage again extends well into the limiter shadow region, and the outer flux surfaces are measured to be very nearly circular.[77]

Finally, one could also consider a case when non-uniform density and/or temperature is allowed to occur on circular flux surfaces in the limiter shadow plasma. At this point in this discussion of edge asymmetries in Alcator C, the

only basis for making this assumption is on the theoretical estimate of asymmetrically perturbed density and temperature profiles in sections 3.2.4 and 3.2.5. However, Langmuir probe measurements made by the DENSEPACK probe array directly show that strong pressure asymmetries always occur in the edge plasma of Alcator C. A possible connection between asymmetric limiter damage and asymmetric edge plasma parameters is deferred to chapter 8 when DENSEPACK data can be suitably presented and discussed.

4.3 First Probe Measurements in Alcator C

4.3.1 Langmuir and Thermocouple Probes

The first investigation of poloidal asymmetries in Alcator C edge plasma was performed by Hayzen, Overskei, and Moreno.[17] The motivation for these experiments came from the observation of asymmetric damage to virtual limiter surfaces discussed previously. The experimental arrangement consisted of a series of thermocouple probes imbedded in molybdenum blocks as shown in Fig. 4.3. Langmuir probes were used at the same time and positioned near the set of molybdenum blocks at F-top in this figure and by themselves at other port locations. At two poloidal locations on the array, a pair of blocks were mounted in tandem to allow a comparison between the power flux on the ion and electron plasma current drift sides.

4.3.2 Experimental Results

Radial profiles of density and electron temperature were obtained using the two Langmuir probes at F-port and single Langmuir probes at other port locations. Figures 4.4*a* and 4.4*b* display the typical radial density and temperature profiles that were obtained during the steady state portion of the discharge.

These particular data were taken at D-bottom but are characteristic of the profiles at other locations. Central plasma parameters were $I_p \approx 250 - 300$ kA, $\overline{n}_e \approx 2 \times 10^{14}/\text{cm}^3$, and $B \approx 6$ tesla. For these experiments, the number of limiters as well as the toroidal field direction was changed. Data presented in Ref. [17] and reproduced in this section is for the three cases of: (1) a full 16.0 cm radius molybdenum ring limiter in both B and E-ports with reversed toroidal field direction ($\bullet$ in Fig. 4.1); (2) a single limiter in B-port with reversed toroidal field ($\circ$); and (3) a single limiter in B-port with forward toroidal field direction ($\times$).

Densities and temperatures inferred by the Langmuir probes were typically $n \sim 10^{11}$–$10^{14}/\text{cm}^3$ and $T_e \sim 7$–25 eV. The Langmuir probes were used in conjunction with the thermocouple probes to verify that the heat flux was primarily due to a thermal flux from the plasma and not due to a high energy electron or ion component of their distribution functions.

Noting the temperature rise of the molybdenum blocks after the discharge, the poloidal variation in the time integrated heat flux was obtained near the bottom of the vacuum chamber at F-port. Figure 4.4*c* shows the typical poloidal variation across the array for the three cases. Thermal fluxes on the order 50–300 kW/cm^2 were estimated at a minor radius of $r \approx 17$ cm. For all three cases, a variation of a factor of 20 or more over a poloidal extent of 60^0 was measured. Peak heat fluxes occurred near the 0^0 location in Fig. 4.4*c*, which corresponds to the very bottom location in F-port. The toroidal field direction and number of limiters changed the magnitude of the heat flux, but the poloidal shape remained unchanged.

The two sets of double molybdenum blocks provided information about the ion drift side versus electron drift side power loading. Figure 4.4*d* displays the ratio of electron side to ion side thermal loading on F-bottom, 5.7^0 outside. for cases (1) and (2). For case (3), the ratio is inverted. Unfortunately, data from case (3) does not extend inside $r \approx 17.5$ cm, yet there is a clear toroidal

asymmetry of a factor of 2 or more in the power flux which depends on the direction of the toroidal field. Furthermore, when two limiters are used as in case (1), the toroidal asymmetry increases to a factor of ~ 6 at a radius of 17 cm.

4.3.3 Possible Reasons for Asymmetric Power Loading

The poloidal and toroidal variation in heat flux to the array of molybdenum blocks is consistent with the limiter damage pattern discussed in section 4.2. Case (3) in Figs. 4.4*c* and 4.4*d* indicates that the highest power flux at the *F*-bottom location in the limiter shadow plasma is on the ion side and peaks near the bottom-center poloidal position. The damage pattern on the limiter and the molybdenum deposition pattern on the stainless steel support structure in Fig. 4.2 coincides with these heat flux measurements. The implication is that the asymmetric heat flux is not occurring only during a disruption or termination and is not a consequence of superthermal particle fluxes. The asymmetric heat flux and subsequent asymmetric limiter damage at large radii is more likely a consequence of poloidally and/or toroidally nonuniform edge plasma conditions existing throughout the duration of the discharge.

In Ref. [17], noncircular outer flux surfaces in Alcator C were considered in detail as a possible explanation for the observed poloidal and toroidal heat flux asymmetry. However, the flux surfaces displayed in Ref. [17] were obtained by modelling the single turn current in the toroidal field coil and computing the flux surfaces. Near the edge, the accuracy of the computation is uncertain. Direct measurements of the outer flux surfaces in Alcator C using a series of 12 poloidal flux loops has since indicated that these surfaces are very nearly circular[77]. Furthermore, if one assumes that flux surfaces are responsible for the heat flux asymmetry, then the flux plots in Ref. [17] are inconsistent with the measured poloidal variation in heat flux shown in Fig. 4.4*c* for case (3) with B_T

anti-parallel to I_p. The flux surfaces plotted in Ref. [17] with B_T anti-parallel to I_p are slightly elliptical so that a peak in the heat flux would be expected near the inside and outside midplane poloidal positions. However, the heat flux was still measured to have a maximum at the $\theta \approx 0^0$ position in this case (Fig. 4.4*c*). Finally, the limiter damage in Fig. 4.2 would require a very distorted outer flux surface to explain the $\gtrsim 1$ cm radial extent of the damage pattern at minor radii $r \approx 10$ cm. The hypothesis of a flux surface distorted to this degree is inconsistent with both the measured poloidal flux and the theoretical flux plots displayed in Ref. [17].

The conclusion drawn from looking at the limiter damage and heat flux measurements is that edge plasma conditions are most likely nonuniform on a flux surface in the limiter shadow plasma region of Alcator C. As indicated in the previous section, this hypothesis is consistent with the data obtained by the DENSEPACK Langmuir probe array and is discussed in detail in chapters 7 and 8.

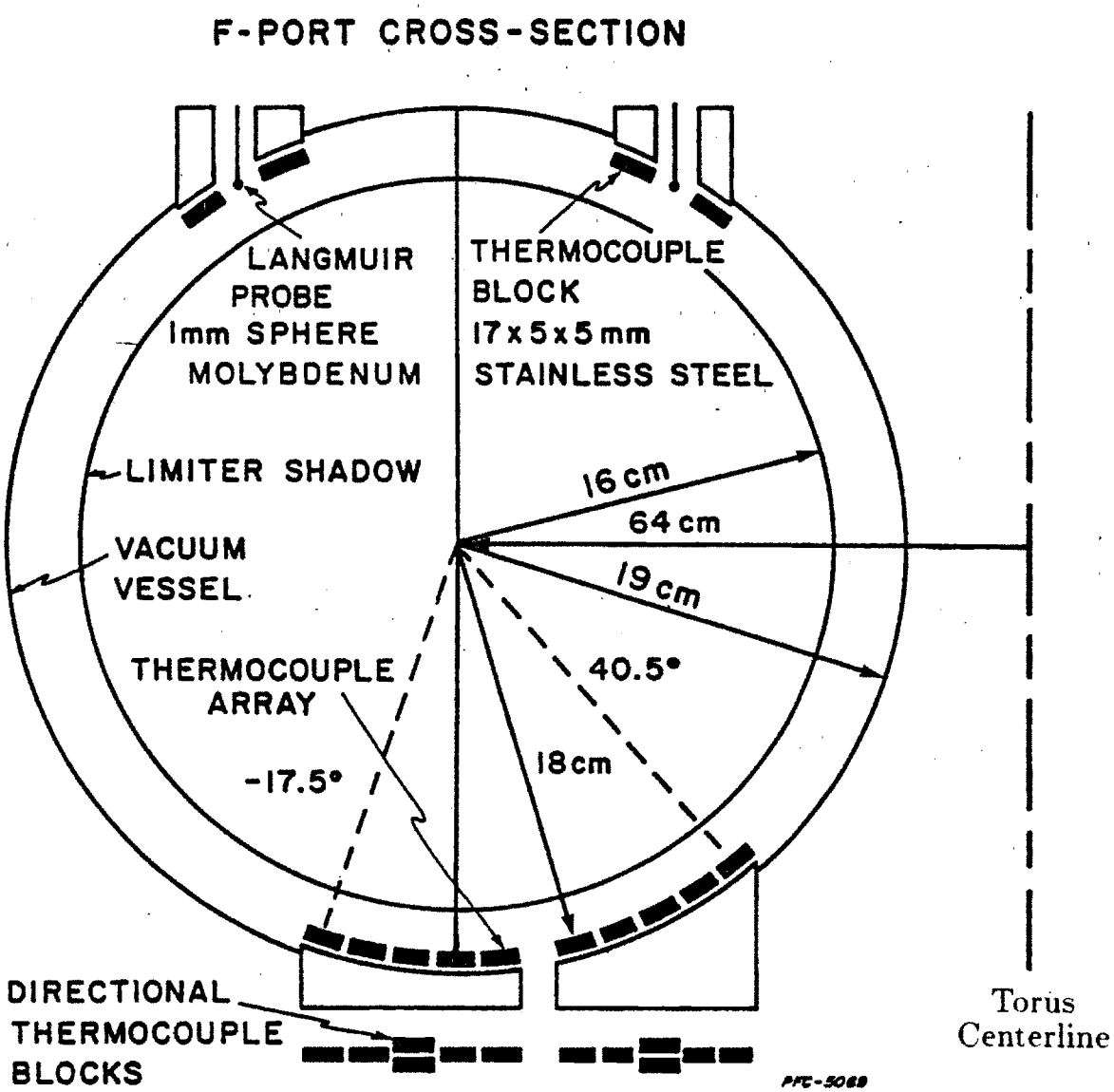

Figure 4.3 Langmuir and Thermocouple Probe Array in *F*-Port (from Ref. [17])

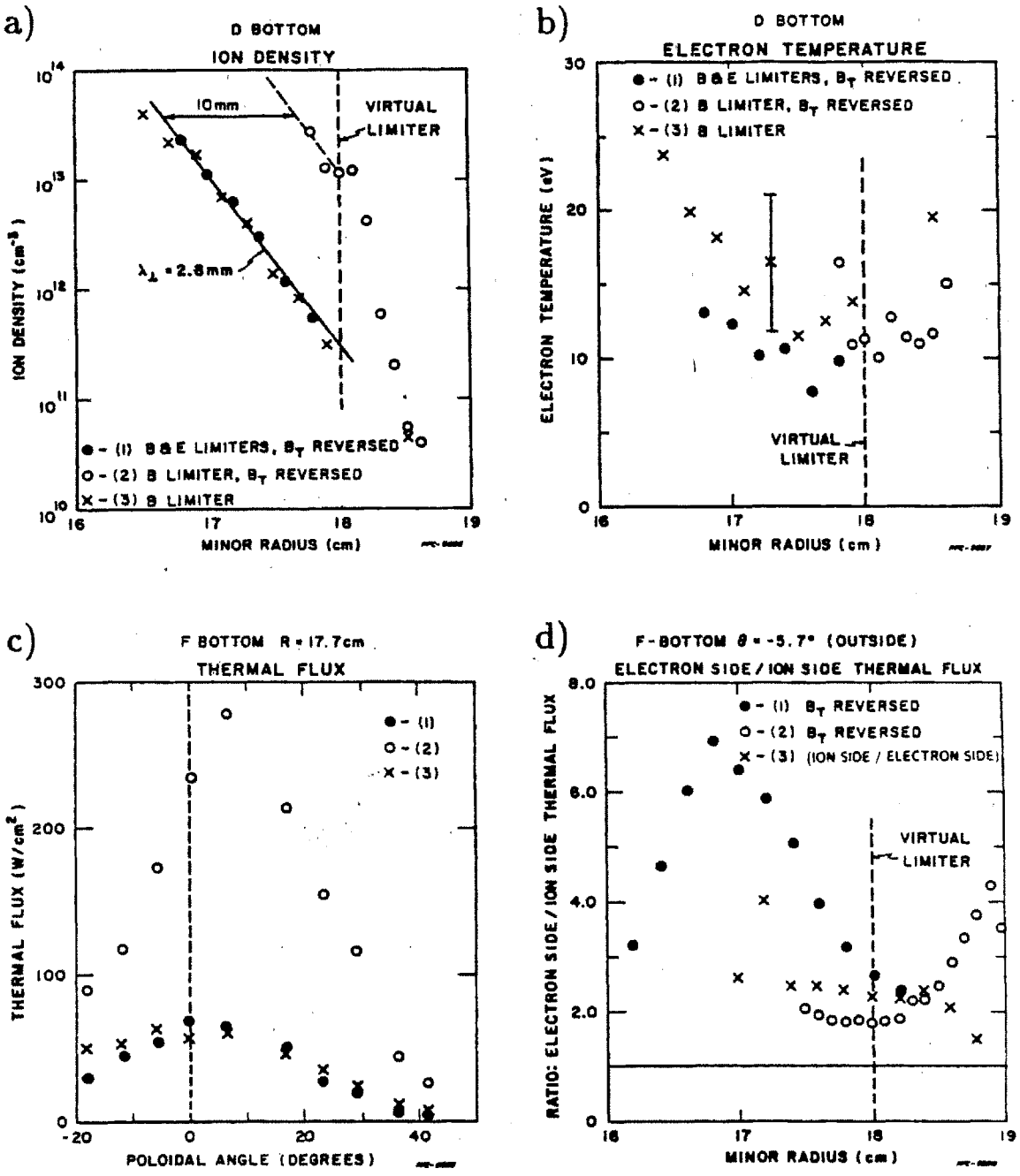

Figure 4.4 First Probe Measurements in Alcator C (from Ref. [17])

4.4 MARFES

The edge plasma in Alcator C can exhibit a strong poloidal asymmetry in local radiated power. At moderate to high densities and/or low plasma currents, a cooler, radiating plasma region forms typically just above the inside midplane of the torus extending $\approx 30^0$ in poloidal angle and 360^0 in toroidal angle. This phenomenon is referred to as a 'MARFE' in Alcator C[2,3,5,55] and a similar phenomenon in other tokamaks has since been detected.[6,54,120] This section reviews the principle observations of MARFEs in Alcator C as background for discussion in later chapters.

4.4.1 Asymmetric Edge Radiation

Diagnostic traces for a typical discharge which exhibited a MARFE at 120 ms are shown in Fig. 4.5. Central parameters for this discharge were $B \approx 8$ tesla, $\overline{n}_e \sim 2.5 \times 10^{14}$, $I_p \approx 400$ kA. The central line-averaged density vertical cord in trace (b) shows a smooth increase, leveling, and decay of plasma density, typical of all discharges. On the other hand, the inside vertical chord in trace (a) appears to be interrupted 120 ms into the discharge. At this time, the interferometer beam is scattered or refracted and not seen by the collection optics. The total radiated power as inferred by a bolometer looking along a vertical chord on the inside in trace (c) increases at 120 ms and remains at a higher level throughout the duration of the MARFE event. A similar time behavior is seen on non-spatially resolved H_α and C^{III} line emission in the remaining two traces.

The location of the MARFE region in the poloidal plane is obtained by simultaneously monitoring the enhanced emission on a vertically viewing bolometer array and a horizontally viewing visible continuum array. Figure 4.6 shows brightness profiles obtained by these two diagnostics for a non-MARFE and a

MARFE discharge. It is thereby determined that the radiating region is restricted to the upper-inside location of the poloidal cross-section as shown.

The toroidal extent of the emission region was investigated as well. A 16 chord horizontally viewing H_α array system (discussed in chapter 5) was used to obtain vertical brightness profiles as in Fig. 4.6 at different port locations. The radiating region was found to extend 360^0 toroidally and appeared to be toroidally symmetric, not following field lines.

It seemed curious that the MARFE region typically appeared on the upper-inside location rather than on the midplane or lower-inside locations. It was thought that the direction of the B-field might play a role similar to the way that it affects heat flux asymmetries discussed in the previous section. Consequently, for a limited number of discharges, the direction of the toroidal magnetic field was reversed while the vertical brightness profile was monitored using the same H_α array. The emission profile was found in fact to peak at the lower-inside position. However, there were a number of discharges where the emission profile peaked on the inside midplane or at the usual upper-inside position.

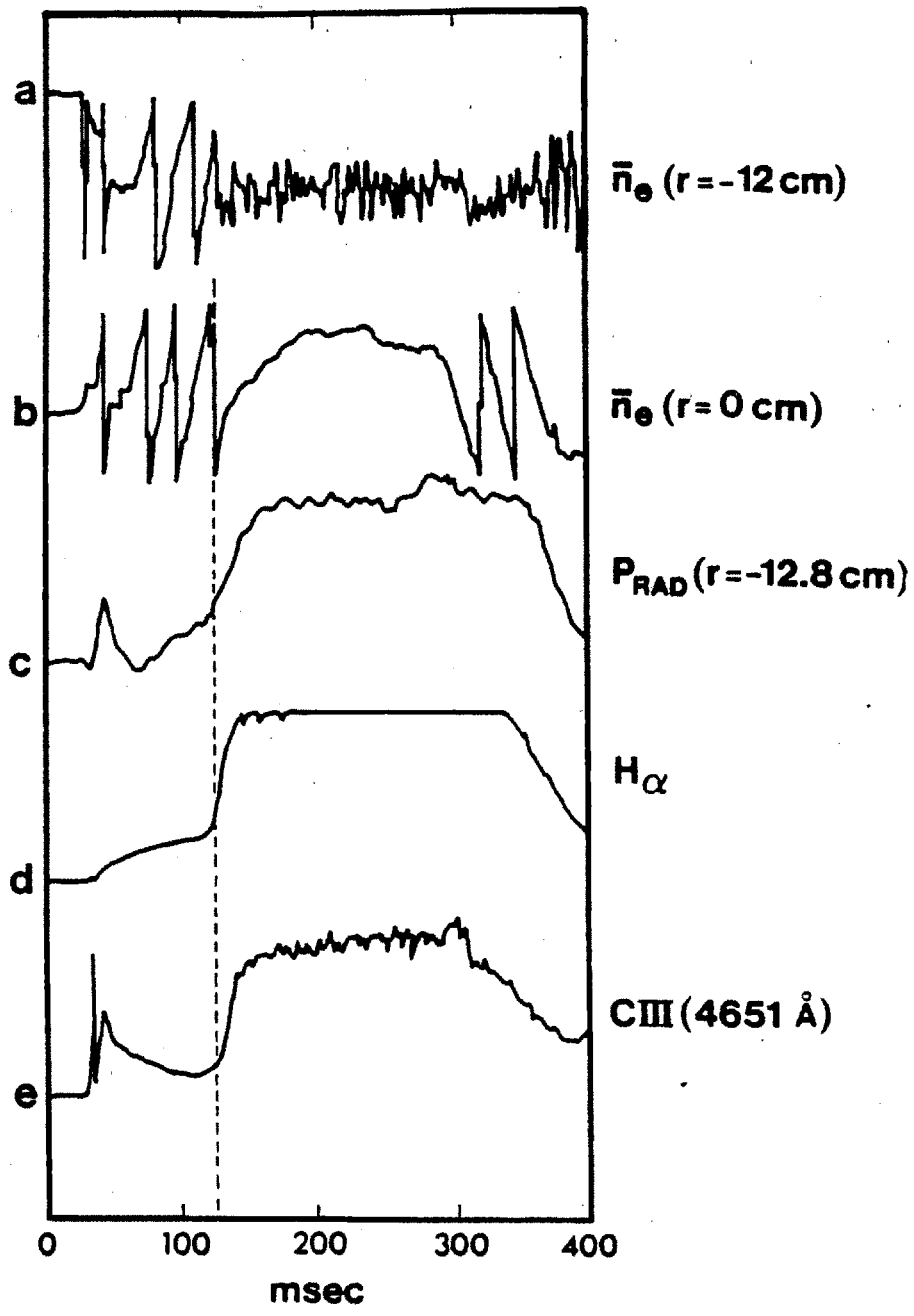

Figure 4.5 Diagnostic Traces During an Alcator C Discharge with a MARFE (from Ref. [5])

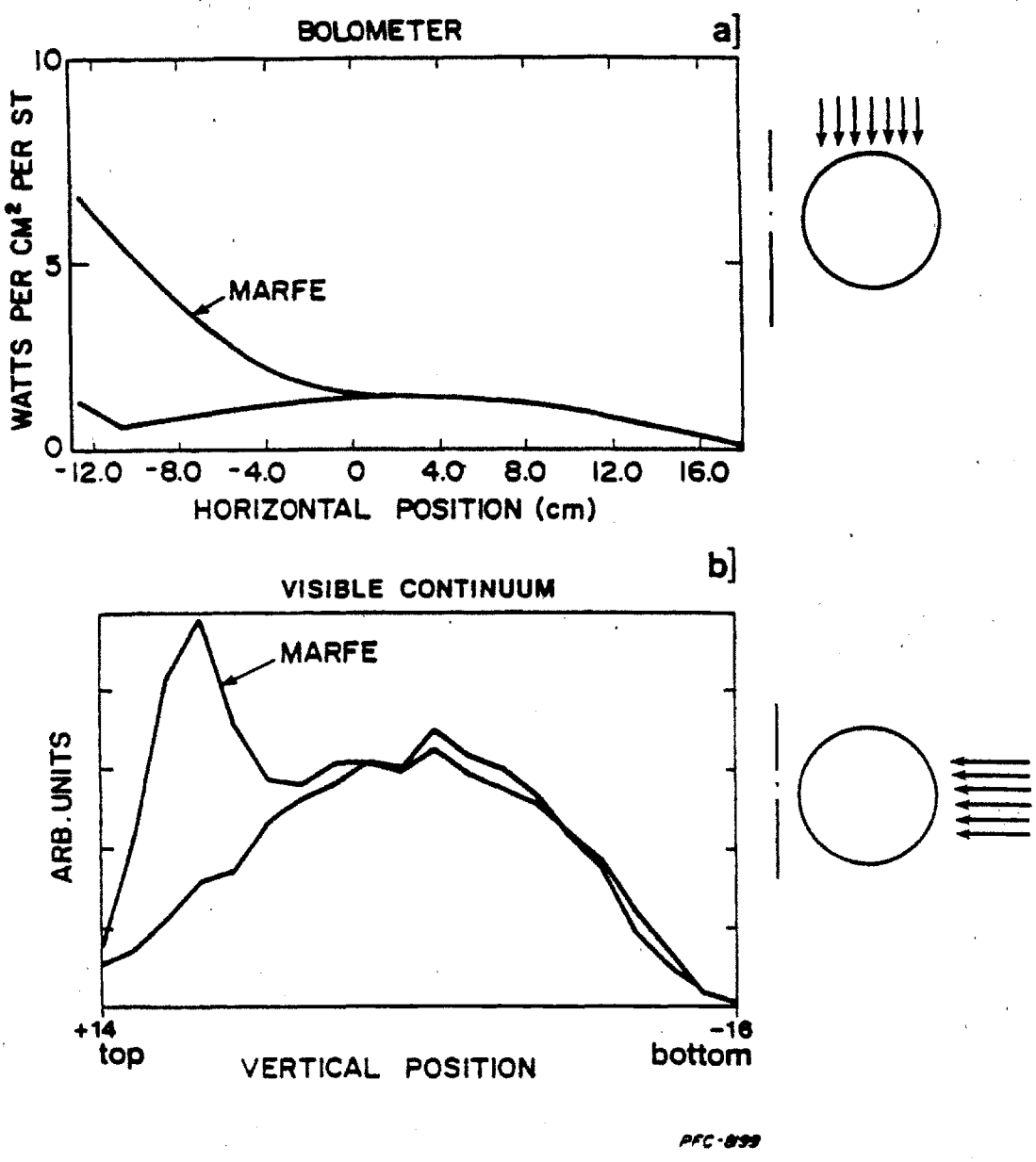

Figure 4.6 Location of Radiative MARFE Region in Alcator C (from Ref. [5])

4.4.2 Edge Density

The 'breakup' of the inside interferometer in Fig. 4.5 signifying the beginning of the MARFE suggests that edge density conditions change in conjunction with a MARFE. The most probable explanation outlined in Ref. [5] for the loss of signal is that during a MARFE a strong density gradient develops perpendicular to the path of the probe beam (wavelength = 119 μm). A perpendicular gradient of $\frac{\partial n}{\partial x_\perp} \gtrsim 10^{15}/\mathrm{cm}^4$ is sufficient to refract the interferometer beam out of the field of view of the detector.

The interferometer beams pass vertically between the limiter set in B-port (see Fig. 4.1). A very sharp radial density e-folding length in the limiter shadow is therefore expected since the effective 'L' length (see Eq. 3.9) is $L \approx 1.2$ cm in the gap between limiters. Scaling λ_n in this region (region A) from λ_n and L at non-limiter port locations region (B)

$$\lambda_n^A \approx \lambda_n^B \sqrt{\frac{L^A}{L^B}} \approx 0.3\sqrt{\frac{1.2}{100}} = 0.033 \text{ cm} . \tag{4.1}$$

Since the inside interferometer beam passes $\approx 45^0$ with respect to the radial direction, it might be possible to explain the 'break-up' as a refraction due to this sharp gradient. In this case, the condition for refraction of $\frac{\partial n}{\partial x_\perp} \gtrsim 10^{15}/\mathrm{cm}^4$ becomes

$$\frac{\partial n}{\partial x_\perp} \approx \frac{1}{\sqrt{2}} \frac{n_a}{\lambda_n} \approx 20\ n_a \gtrsim 10^{15}\ /\mathrm{cm}^4 \tag{4.2}$$

which could be satisfied at the limiter radius when the density there exceeds $n_a \gtrsim 5\times10^{13}/\mathrm{cm}^3$. However, there is other evidence suggesting that the refraction does not necessarily occur in the shadow region.

During the confinement size scaling experiments when single 10 cm and 13 cm minor radius poloidal limiters were inserted in E-port, MARFEs were observed. The corresponding inside interferometer channel for these geometries exhibited the same 'break-up' feature as previously shown in Fig. 4.5. Since there was negligible plasma between the limiter gap for these experiments, the short limiter shadow scrape-off length argument does not apply. It is more likely that the interferometer beam is being refracted at radii just inside the limiter radius.

Further evidence supporting this hypothesis comes from the observation of anomalously high line-averaged densities on the inside interferometer channel for some MARFE discharges. Figure 4.7 displays the interferometer output from three vertical chords at -12.0 cm, -6.0 cm, and $+1.3$ cm. Central plasma parameters were $B \approx 8$ tesla, $I_p \approx 200$ kA in a 16.5 cm radius plasma. The central interferometer channel displays a peak line-averaged density of $1.3 \times 10^{14}/\text{cm}^3$. The -6.0 cm channel in trace (b) peaks at a value of $1.2 \times 10^{14}/\text{cm}^3$, which is typical for the radial density profiles in Alcator C. Trace (c), on the other hand, records a line-averaged density at -12.0 cm which *exceeds the central chord value* by a factor of ~ 2 before the signal is lost. This implies that there exists a localized high density plasma region in the path of the beam. Furthermore, the detection of this high density plasma region *preceeds* the enhanced H_α emission and interferometer break-up which defines the beginning of a MARFE event.

The inside interferometer chord length in an $a = 16.5$ cm plasma is ~ 22 cm. It is not likely that this density asymmetry extends very far to inner flux surfaces where parallel transport is high. On the other hand, edge probe measurements do not record such a high density in the limiter shadow region. Therefore, in order to explain the high density recorded by the inside interferometer and yet retain poloidally symmetric inner flux surfaces, a poloidally asymmetric high density plasma must exist just inside the limiter radius. The high line integral density and subsequent refraction of the inside interferometer beam suggests that

a plasma density on the order $n \sim 10^{15}/\text{cm}^3$ over a distance of ~ 1 cm might be forming near the limiter radius. Such a situation of a high density plasma occurring near limiter surfaces has been observed in Doublet III.[4]

In summary, it is conceivable that highly asymmetric plasma density and sharp density gradients exist *inside* the limiter radius and are responsible for refracting the inside interferometer beam. In any case, the edge plasma density in Alcator C is found to be highly poloidally asymmetric in discharges which display a MARFE. The density asymmetry appears *before* the enhanced radiation is detected and implies that cooling via radiation of the MARFE region itself is not solely responsible for the density asymmetry.

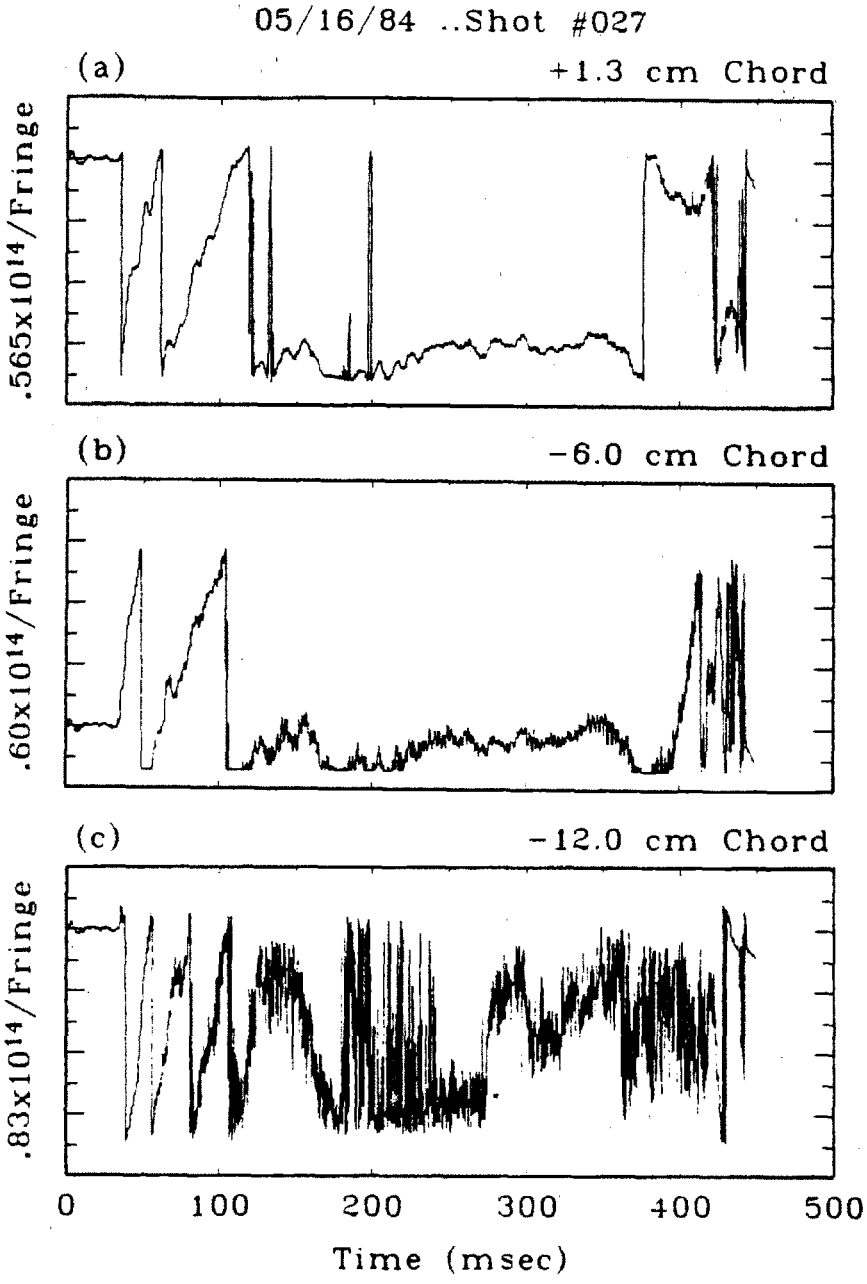

Figure 4.7 Line-Averaged Density from Interferometer at Three Vertical Positions

4.4.3 MARFE Probe

In order to investigate MARFE phenomena further, a Langmuir probe was constructed to directly sample plasma in the limiter shadow at the upper-inside location. The 'MARFE Probe' shown in Fig. 4.8 used the inside keyhole on the top of F-port. Radial profiles of ion density, electron temperature and fluctuations just before and during a MARFE are shown in Fig. 4.9. The ion density profile fits an exponential for both cases, but the scrape-off length increases almost a factor of 2 during a MARFE. The density at the limiter radius does not appear to change during the MARFE, whereas at larger minor radii, a dramatic density change takes place.

It should be pointed out that the absolute density calibration for the data shown here is uncertain. The densities displayed seem to be high, by a factor of 2–10, considering subsequent data taken by the DENSEPACK probe array at this same poloidal location (chapter 7). The MARFE probe collection area was not accurately known and/or incorrectly used in reducing this data. Nevertheless, this data does display the relative change in edge conditions during a MARFE.

The radial electron temperature profile in Fig. 4.9*b* also changes when a MARFE occurs. Without a MARFE, typical temperatures at the limiter radius are $\approx$ 20 eV. During a MARFE, the electron temperature falls to a $\approx$ 10 eV level. This is consistent with the hypothesis that a MARFE is a consequence of a local radiation thermal instability.

The fluctuation level in the ion saturation current collected by the MARFE probe is displayed versus radial position in Fig. 4.9*c*. The abscissa displays the RMS amplitude of the ion saturation current, J_{sat}, about the mean value normalized to the mean value for a sampling period of 10 ms. J_{sat} includes frequencies up to 10 KHz. Before a MARFE, the radial profile of fluctuations spans values of 0.06–0.25. During a MARFE, the fluctuation amplitude increases to 0.15–0.3 with some stray points around 0.4–0.5. This data suggests that there

might be a connection between the increased fluctuation level and the observed flattening of the radial density profile through increased turbulent transport. CO_2 laser scattering recorded a strong increase in the level of density fluctuations in the MARFE region.[5] Also, FIR laser absorbtion measurements indicated an anomalously high nonresonant absorbtion or scattering of FIR radiation just prior to and/or during the MARFE.[79] The latter measurement was made along a horizontal chord slightly above the plasma midplane.

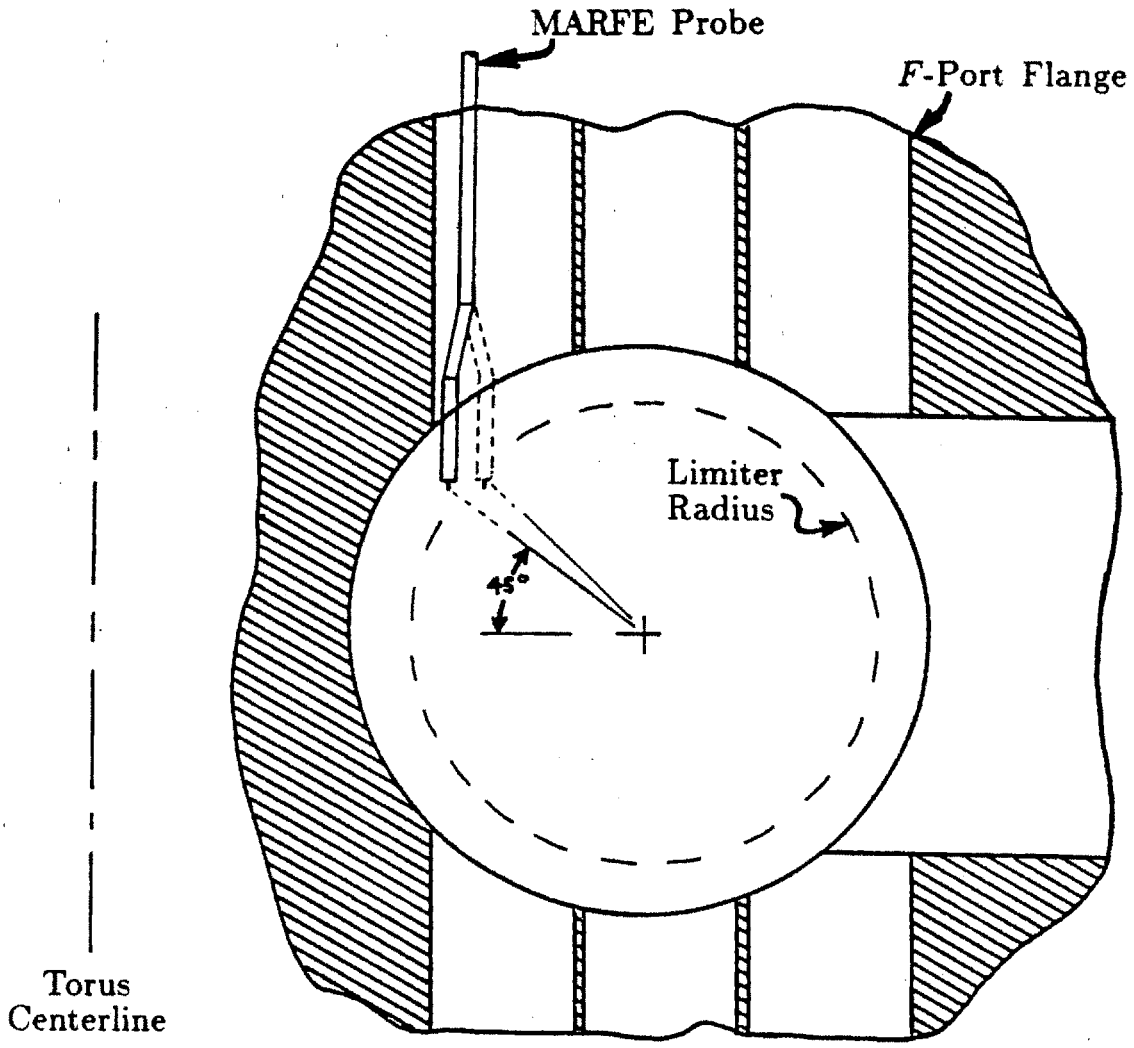

Figure 4.8 Location of MARFE Probe in *F*-Port

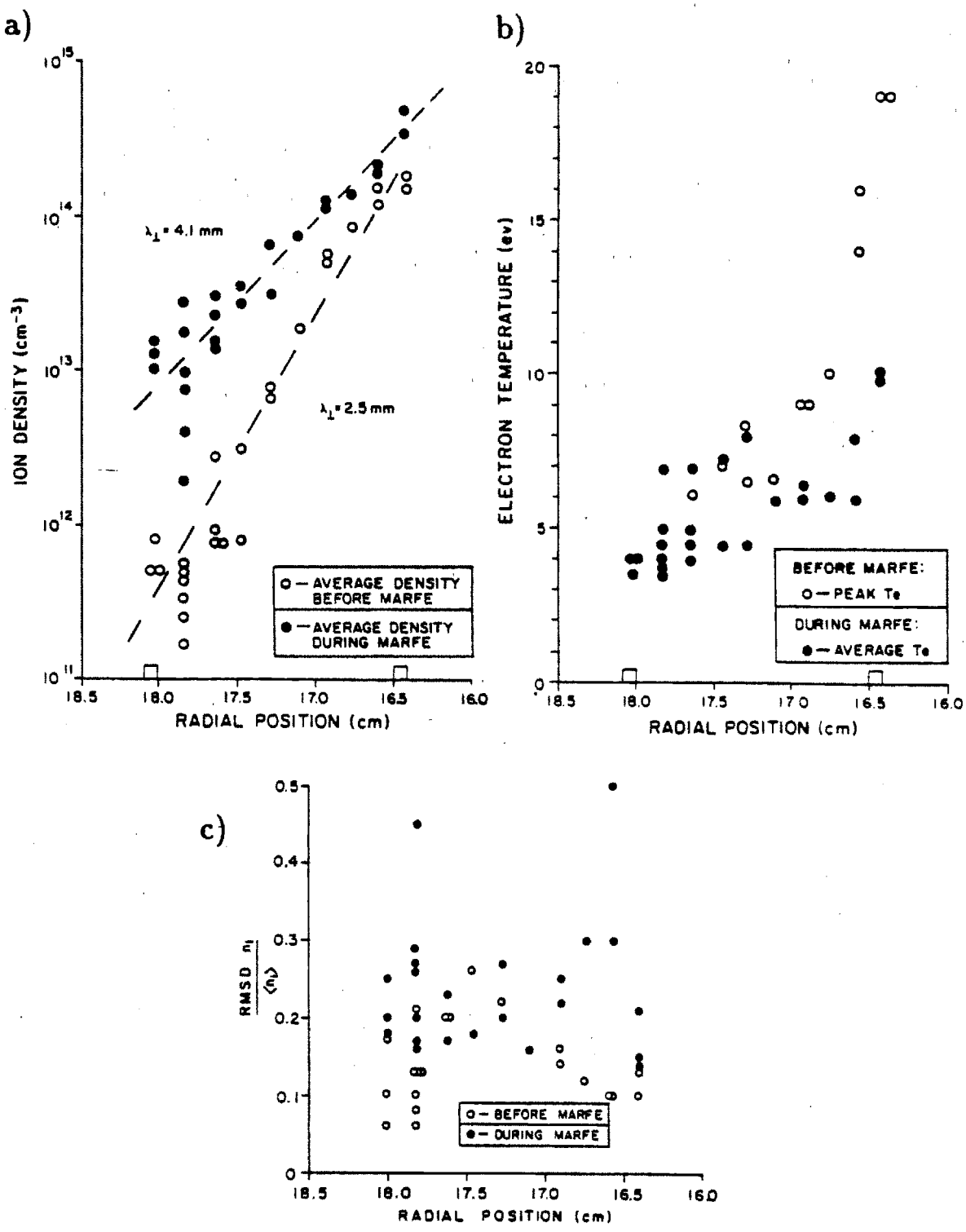

Figure 4.9 Density, Electron Temperature, and Fluctuations vs. Radius Inferred by MARFE Probe (absolute density uncertain)

4.4.4 MARFE Threshold Parameters

MARFEs do not occur in all discharges in Alcator C. There appears to be a fixed range of central plasma densities and currents where a MARFE does and does not occur. Holding the plasma current constant, the MARFE threshold central density can be found by raising the density until a MARFE is detected. Repeating this procedure for various currents allows a mapping of MARFE threshold central line-averaged densities, $\overline{n}_e(= n_m)$ and plasma currents, I_p, as is shown in Fig. 4.10. A constant n_m/I_p line passing through these data points is also shown and yields a value of

$$\left.\frac{n_m}{I_p}\right|_{thres.} \approx 5.4 \times 10^{11} \quad /\text{kA cm}^3 \tag{4.3}$$

It appears, therefore that a MARFE, occurs whenever the critical $\overline{n}_e/I_p$ value given by Eq. 4.3 was reached or exceeded. This result is similar to the observed $n\kappa/I_p$ scaling for the formation of cold, high density plasmas near the limiter in Doublet III[4] where κ is the vertical elongation. A critical value of $n\kappa/I_p$ inferred from Ref. [4] is

$$\left.\frac{n\kappa}{I_p}\right|_{thres.} \approx 9 \times 10^{10} \quad /\text{kA cm}^3 \tag{4.4}$$

which is similar to the Alcator C MARFE threshold relationship above.

It is possible to induce a MARFE at lower values of $\overline{n}_e/I_p$ than in Eq. 4.3 by the injection of low-Z gaseous impurities. As discussed in Ref. [5], a MARFE can be triggered by puffing nitrogen into a non-MARFE discharge. This result further supports the radiation thermal instability model and/or a Z-dependent asymmetric perpendicular transport such as Pfirsch-Schlüter convection discussed in chapter 3. A further discussion of MARFE threshold parameters relevant to data obtained by the DENSEPACK probe array is included in chapter 9.

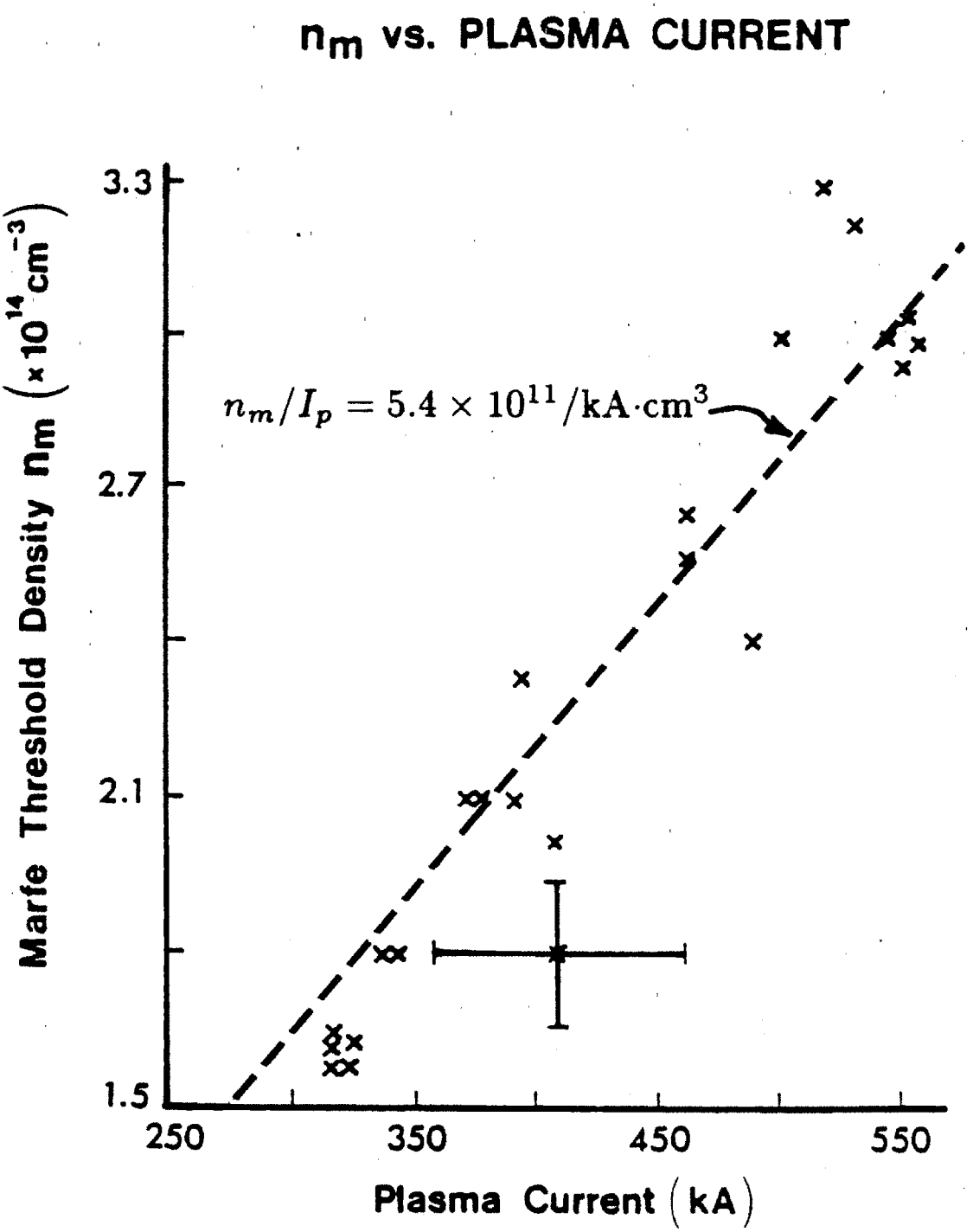

Figure 4.10 MARFE Threshold Density vs. Plasma Current

II EXPERIMENTAL APPARATUS

CHAPTER 5

EDGE PLASMA DIAGNOSTICS

As indicated in the previous chapter, the edge plasma of Alcator C exhibits strong poloidal asymmetries through non-uniform limiter power loading and enhanced edge radiation characteristic of a MARFE. The idea of a fixed array of Langmuir probes, 'DENSEPACK', grew from the need to map the poloidal variations in n and T over short distances in the limiter shadow plasma. DENSEPACK, a poloidal array of 80 Langmuir probes and the principal diagnostic developed during the course of this thesis, is described in detail in this chapter. A visible light imaging system was also developed to follow spatially the location and size of enhanced H_α emission in the edge. This system was used in conjunction with DENSEPACK to correlate changes in edge plasma parameters during the occurence of a MARFE. Other diagnostics which are described in remaining parts of this chapter include a system of twelve poloidal flux loops operated and analyzed by P. Pribyl[77] for outer flux surface shape and position.

5.1 DENSEPACK Hardware

5.1.1 Probe Array Structure

A system of 80 Langmuir probes, 'DENSEPACK', was used to study plasma in the limiter shadow region of Alcator C. The probe array shown in Fig. 5.1 and 5.2 consists of three different length molybdenum probes mounted with $\sim$ 1 cm poloidal spacing on a rigid stainless steel support ring. Plasma is sampled at minor radii 16.8, 17.2, and 17.6 cm over a poloidal angular extent of 360° excluding two $\sim$ 40° segments on top and bottom. The stainless steel support ring is divided into six segments which are inserted through the access keyhole slots and clamped into place with wedge-shaped expansion blocks. The outer radius of the support ring is designed to rest against the vacuum vessel wall, insuring that the ring structure is positioned accurately with respect to minor radius. The inner radius of the support ring is at 18.0 cm which coincides with the radial extent of the nearby virtual limiters.

Data aquisition electronics (discussed in section 5.1.4) allow 30 probes to be operated simultaneously. The goal was to map out any poloidal variations in plasma density and temperature, particularly during those discharges which exhibit a MARFE event. Through the use of fast analog-to-digital converters, this system was also used to look for large spatial scale fluctuation correlations between probes.

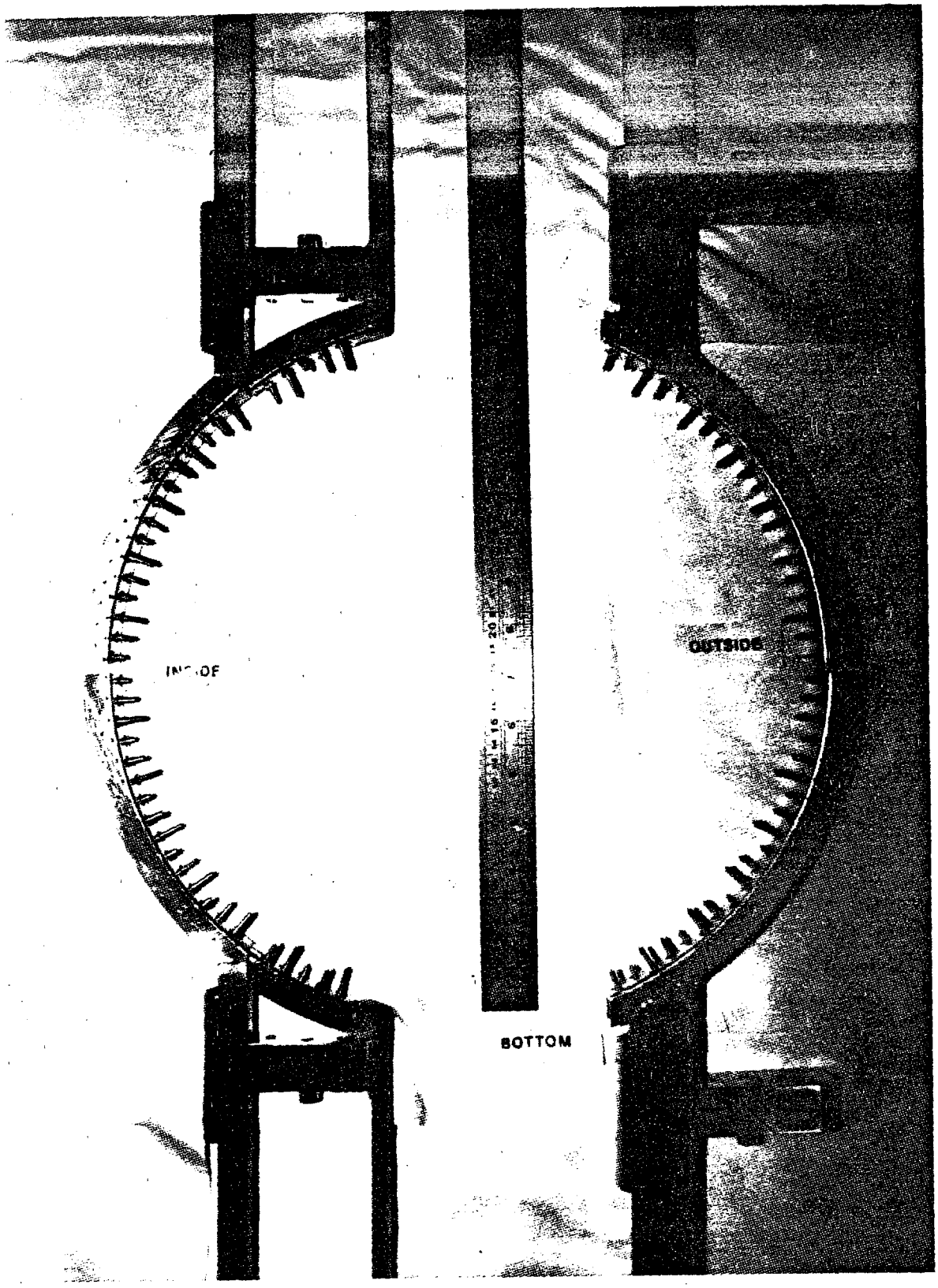

Figure 5.1 Photograph of DENSEPACK Before Installation

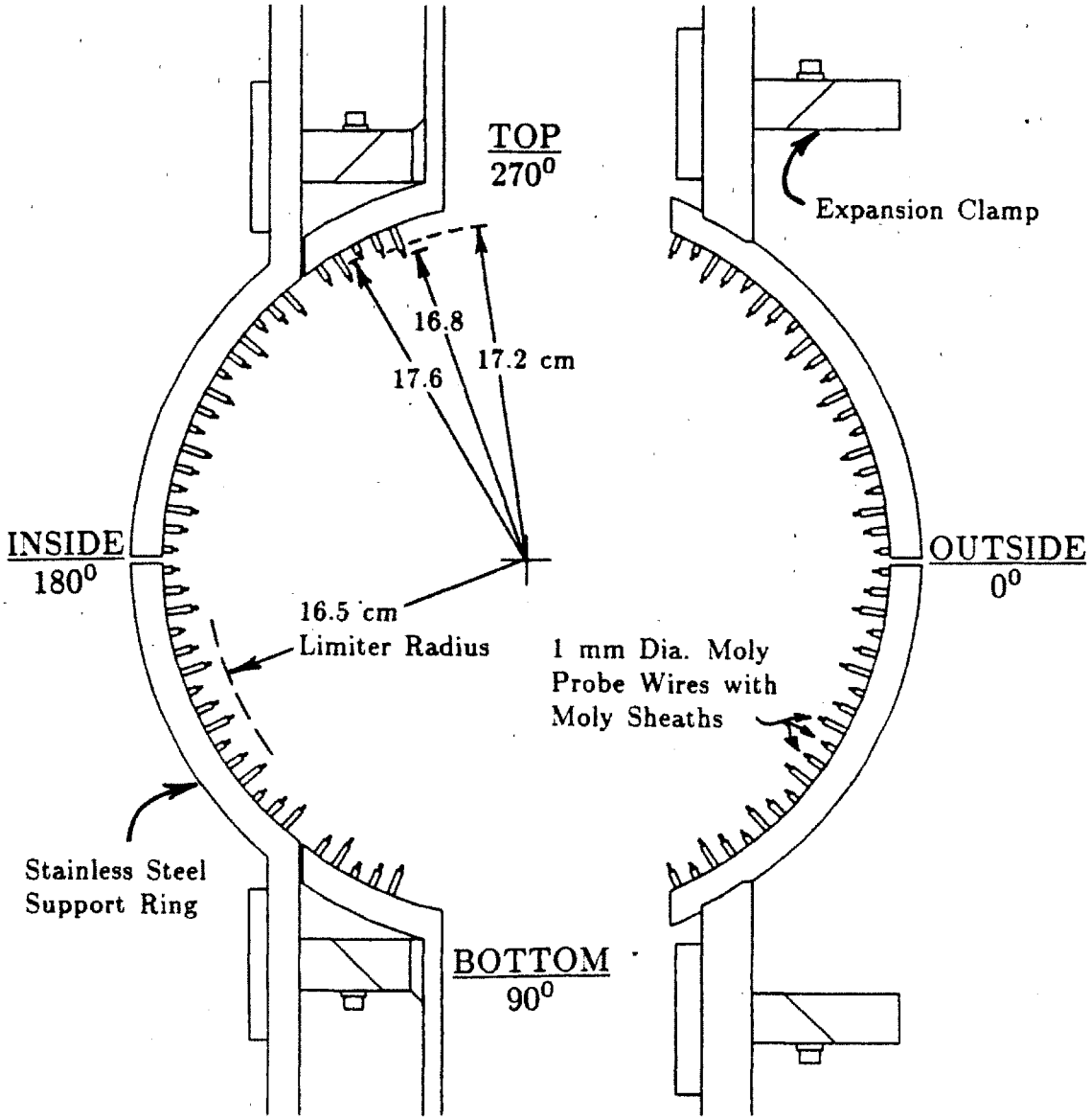

Figure 5.2 Schematic of DENSEPACK Probe Array

5.1.2 Shadow Plasma Geometry

Two physical configurations of both DENSEPACK and Alcator C's poloidal ring limiters were used. The first configuration, "*A*", is diagrammed in Fig. 5.3. In this configuration, the full array of probes is installed with both a complete and a partial (3/4) poloidal ring of carbon limiters located $\sim 60^{\circ}$ and $\sim 120^{\circ}$ toroidally away from DENSEPACK. The double limiter ring segments straddle the Lower Hybrid Radio Frequency (LHRF) waveguides and allow unimpeded launching of RF power in the electron drift direction for current drive. This limiter configuration scrapes off the plasma on the DENSEPACK half of the torus with poloidal uniformity. Consequently, poloidal variations in edge plasma parameters were studied using configuration *A*.

The exposed probe tip lengths were measured and recorded before installation. After ten run-days, DENSEPACK was inspected with a fiber optic scope. Only minor pitting and melting was observed on most of the probe tip surfaces. Partial melting of the molybdenum tip and molybdenum sheath tubing was detected on the upper and lower inside probes, particularly on the longest probes. Data obtained from these probes late in DENSEPACK operation is treated with caution due to the uncertainty in probe collection area. Plasma density inferred from these probes is taken as a lower limit since the probe area generally decreases with increasing damage. Parameters such as electron temperature and floating potential which do not depend on the collection area remain unaffected.

After fourteen run-days in configuration *A*, DENSEPACK was removed. A total of six damaged long probes on the upper and lower inside were cut and reworked as medium-length probes. DENSEPACK was re-installed and operated for 16 more run-days in configuration *B*.

Configuration *B*, shown in Fig. 5.4, utilized only the inside half of the array to make room for a LHRF waveguide on the outside. A small outside limiter segment (1/4 ring) was installed at D-port, and the limiters in the adjacent B-port were all changed to 3/4 rings. The pellet injector[87] was installed at E-port.

The primary focus of study with configuration B was on changes in edge plasma parameters during RF heating and pellet fueling.

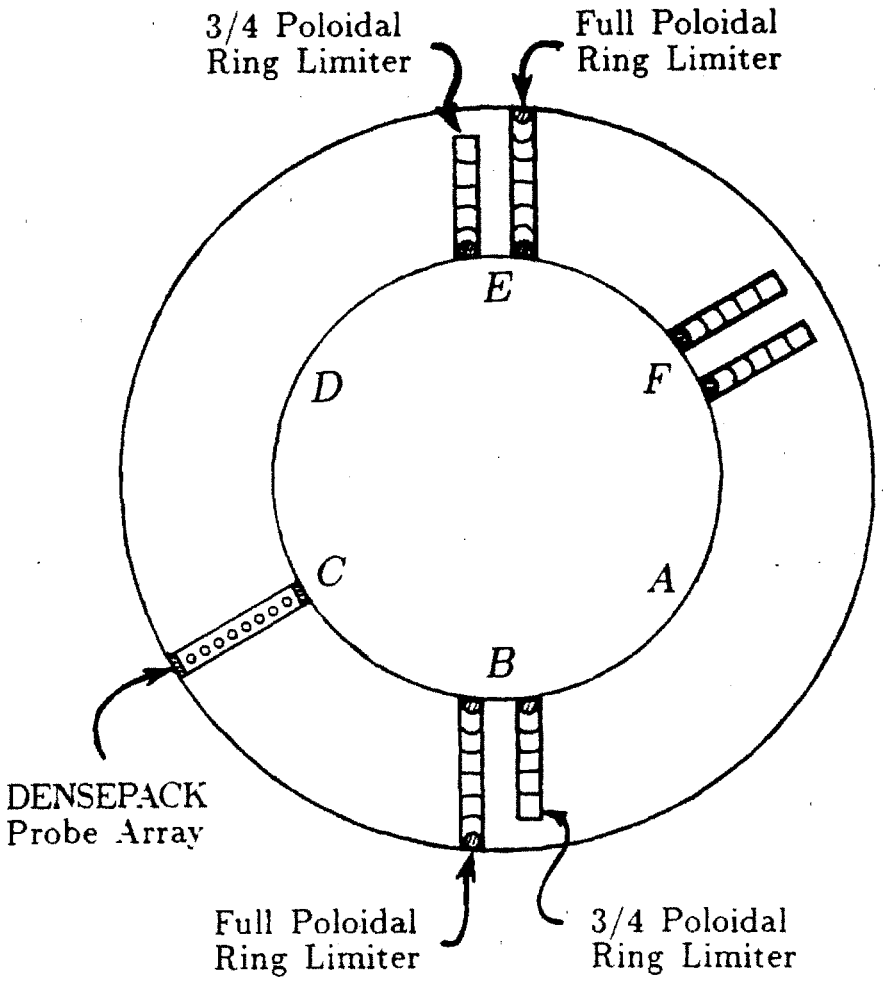

Figure 5.3 Cut-Away, Top View of Alcator C showing DENSEPACK and Limiter Configuration *A*

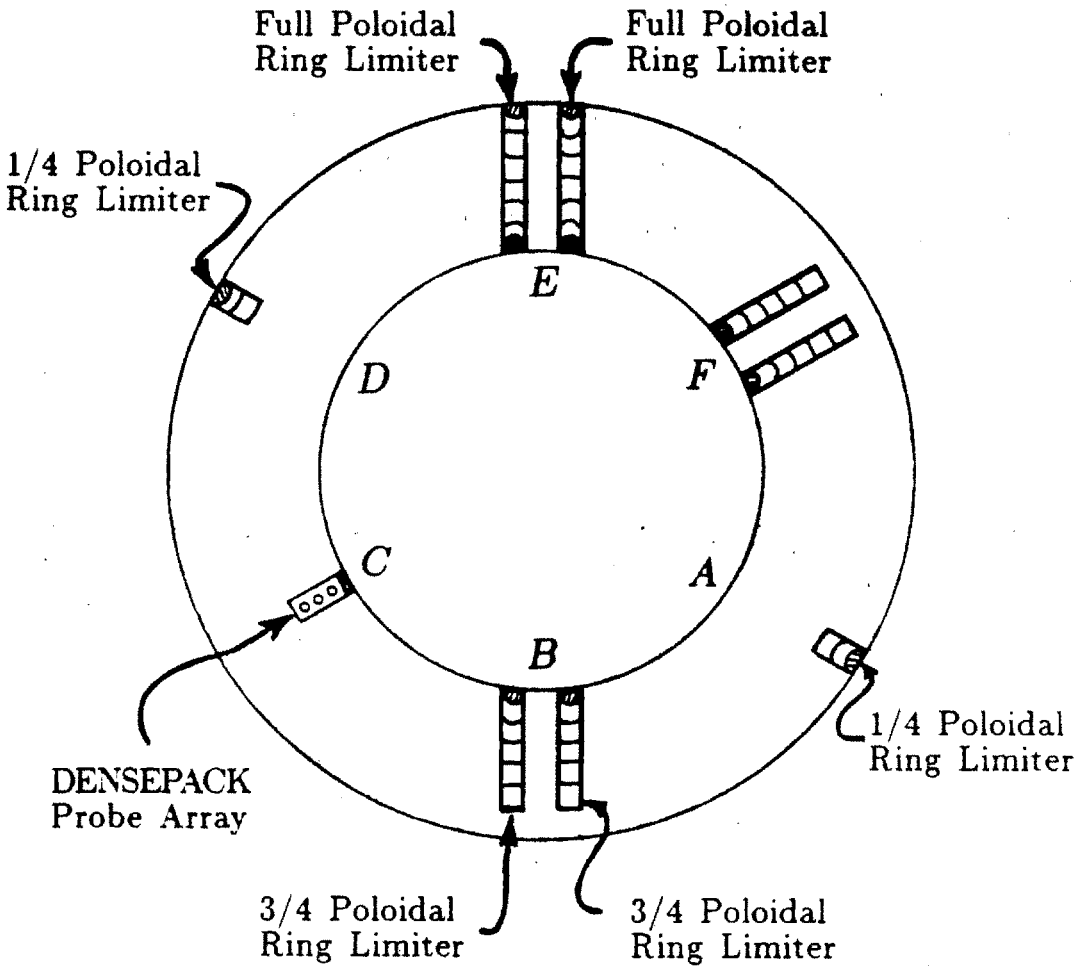

Figure 5.4 Cut-Away, Top View of Alcator C showing DENSEPACK and Limiter Configuration *B*

5.1.3 Detail of Probe Assembly

A close-up view of the upper-inside segment of the DENSEPACK probe assembly is shown in Figs. 5.5 and 5.6. Figure 5.7 shows a detailed schematic for the assembly of an individual probe. Each Langmuir probe consists of a 1 mm diameter molybdenum wire with an exposed length of $\sim$ 1 mm. The remaining wire length is insulated from plasma by a Al_2O_3 sleeve which is thermally protected by an outer, electrically-floating molybdenum sheath. A spring roll pin interlocks with a groove on the ceramic sleeve securing it to the stainless steel support ring. A small molybdenum button is e-beam welded to the molybdenum sheath and traps the sheath on another groove on the ceramic sleeve.

Current is carried in vacuum to each probe through a single conductor mineral insulated cable. A 0.032 inch diameter copper conductor size was chosen to minimize the voltage drop in the cable and provide a thermal conduction path for probe cooling between shots. A 850° C copper to molybdenum braze provides a good electrical and thermal connection between the probe wire and copper conductor. The other end of the mineral-insulated cable connects to high vacuum feedthroughs at the port access flange. Instrumentation cables carry current on the air side of the feedthroughs to probe driver and data aquisition electronics in a nearby isolated rack.

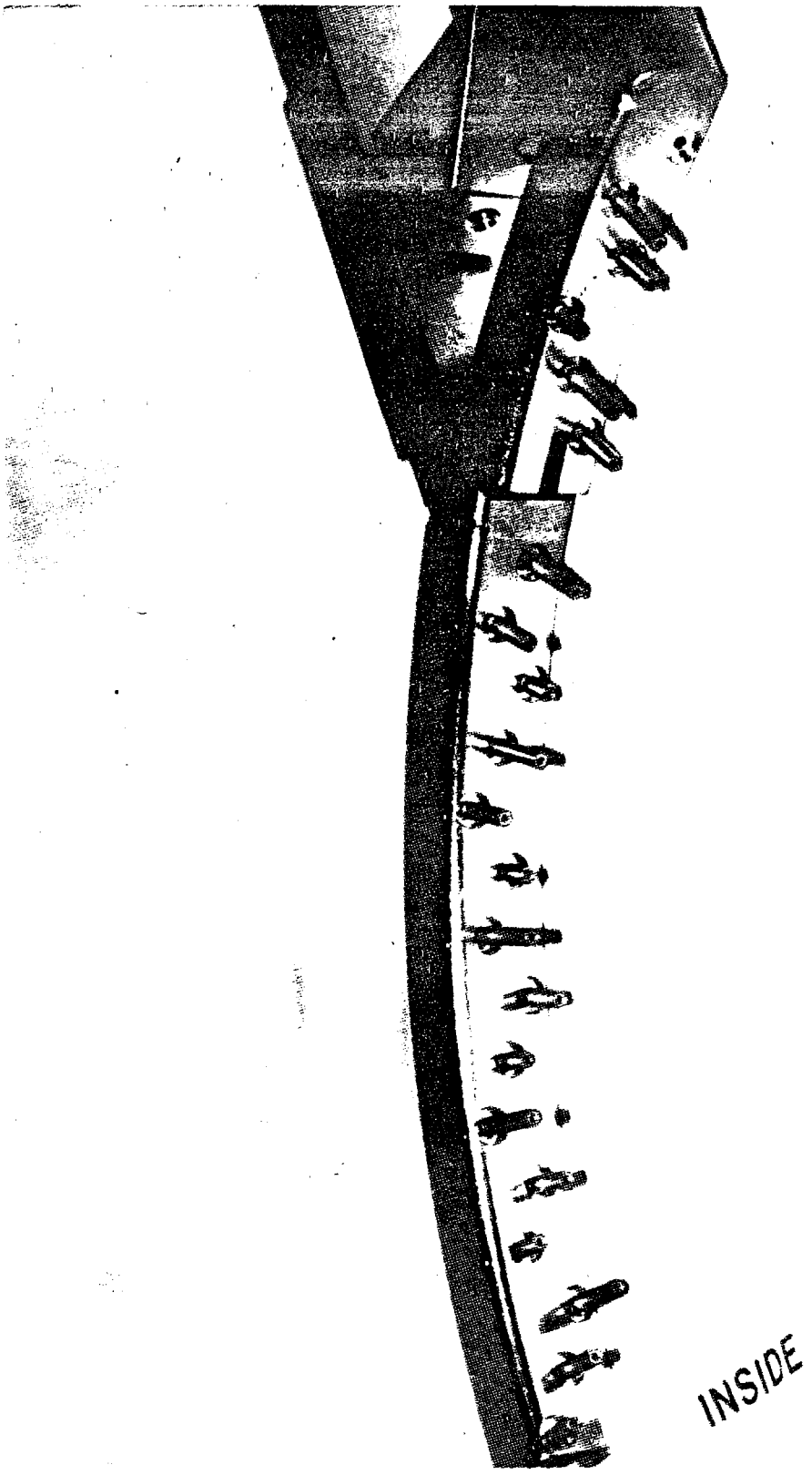

Figure 5.5 Close-Up Photograph of Upper-Inside Segment of DENSEPAC'K

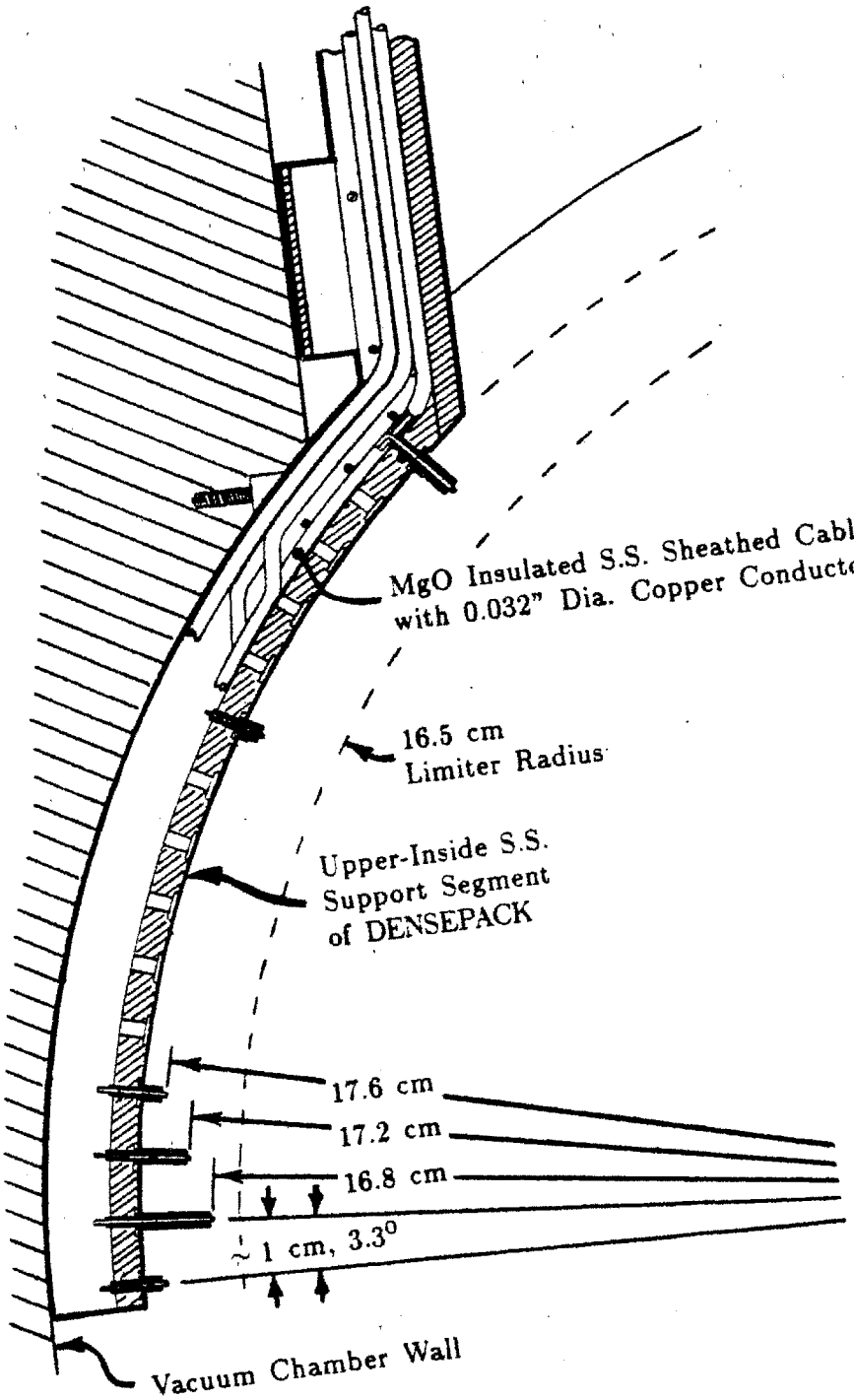

Figure 5.6 Schematic of Upper-Inside Segment of DENSEPACK

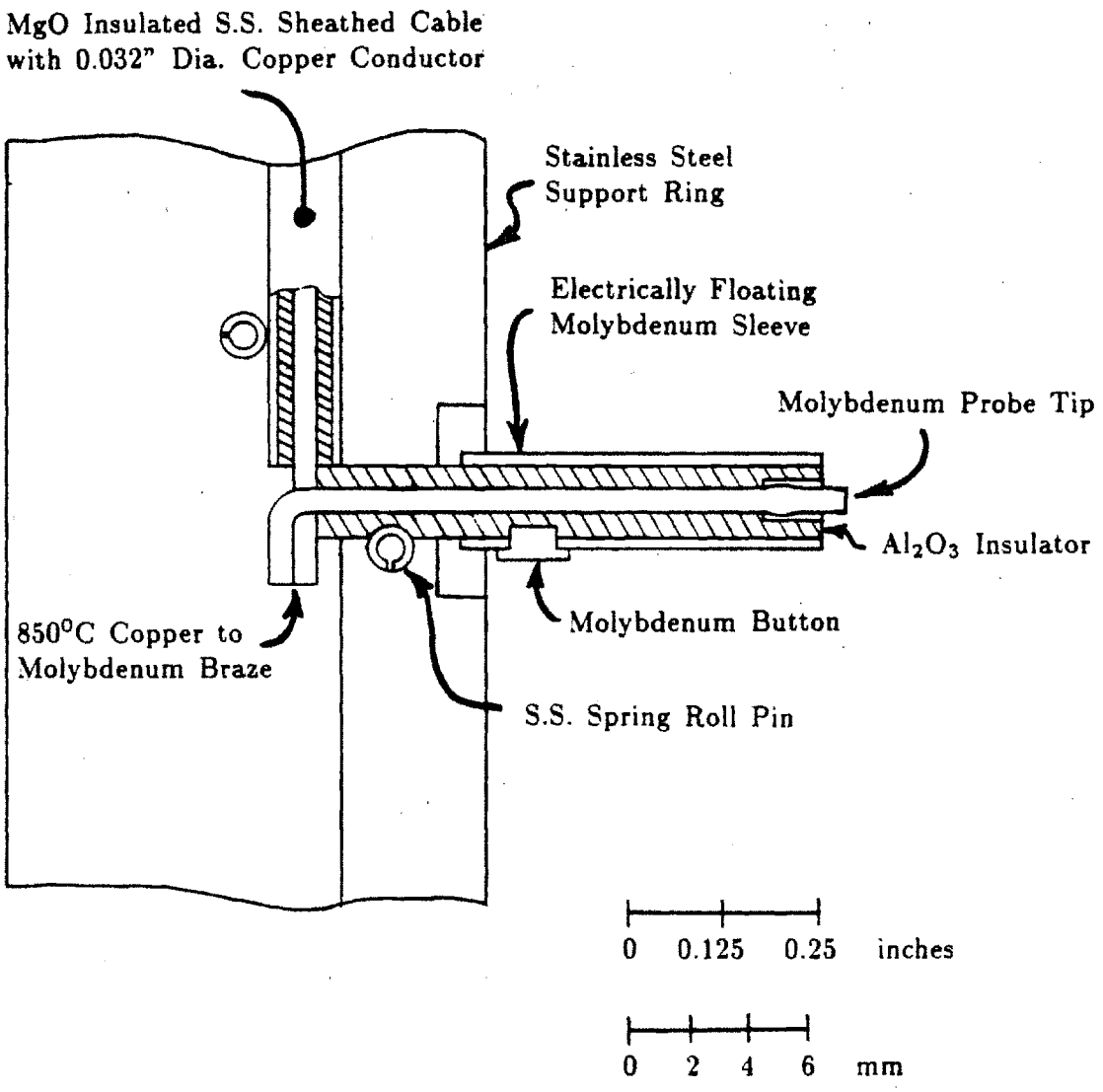

Figure 5.7 Detail of DENSEPACK Probe Assembly

5.1.4 Probe Driver and Data Acquisition Electronics

A conceptual diagram of the DENSEPACK probe electronics system is shown in Fig. 5.8. Probe voltage is maintained on a common feed line by two 1400 Watt TECRON 7570 audio amplifiers which are driven by two TEKTRONIX 502 function generators. The TECRON amplifiers provide up to 40 amps of total probe current in the range of ± 80 volts for frequencies less than 40 KHz. A triangular voltage waveform sweeping from -60 to +40 volts at 100 Hz was typically programmed to drive the Langmuir probes. Data was also taken with a 5 KHz sweep frequency although above 5 KHz, displacement current due to stray capacitance starts to appear as probe current on the current monitors. The electronics did not have any stray capacitance compensation since the system was designed to be operated at frequencies less than 5 KHz. In any case, whatever stray capacitance component remaining was numerically subtracted out during data processing.

Voltage outputs corresponding to the gang bias voltage and individual probe currents were digitized and stored by two types of CAMAC modules. Two LeCroy 8212 CAMAC units were used to store a total of 32 channels of data with a sampling rate of 10 KHz for 600 msec. Sixteen of these channels where also sampled at 1 MHz by four LeCroy 8210 units with an 8 msec storage capacity. Ten pole Tchebyshev-Ellipsoidal lowpass filters with a cutoff frequency of 416 KHz were inserted before the fast digitizers to suppress digital aliasing below -60 db for frequencies greater than 500 KHz.

The system was set up to drive 30 of the 80 Langmuir probes during a single discharge. Any combination of 30 probes could be selected via a patch panel located on the back of the electronics rack. Maximum currents drawn by the longest probes could sometimes exceed 2 amps. Each probe driver line had a 1–2 amp fuse in series with the probe for protection against shorted probe wires or to shut down the probe should it receive too much power flux.

A switch selectable current monitor load resistor was used to maintain the optimum signal to noise ratio over a wide range of collected current. The design criteria was to have a typical voltage drop across this resistor of ~ 1 volt. Due to large radial and poloidal variations in plasma density, a switch selectable resistance range of at least 1–200 ohms was necessary. Further details of the probe current monitor and bias voltage circuitry are outlined in Appendix C.

All probe driver and digital data storage electronics were grounded at the *C*-port, top location on Alcator C's vacuum vessel. This common ground point eliminated the need for isolation amplifiers and the associated loss of frequency response. A 5 KVA isolation transformer provided power to the insulated rack and cable trays. Digital data stored in the CAMAC units was read out by Alcator C's VAX computer between plasma shots via a fiber optic link.

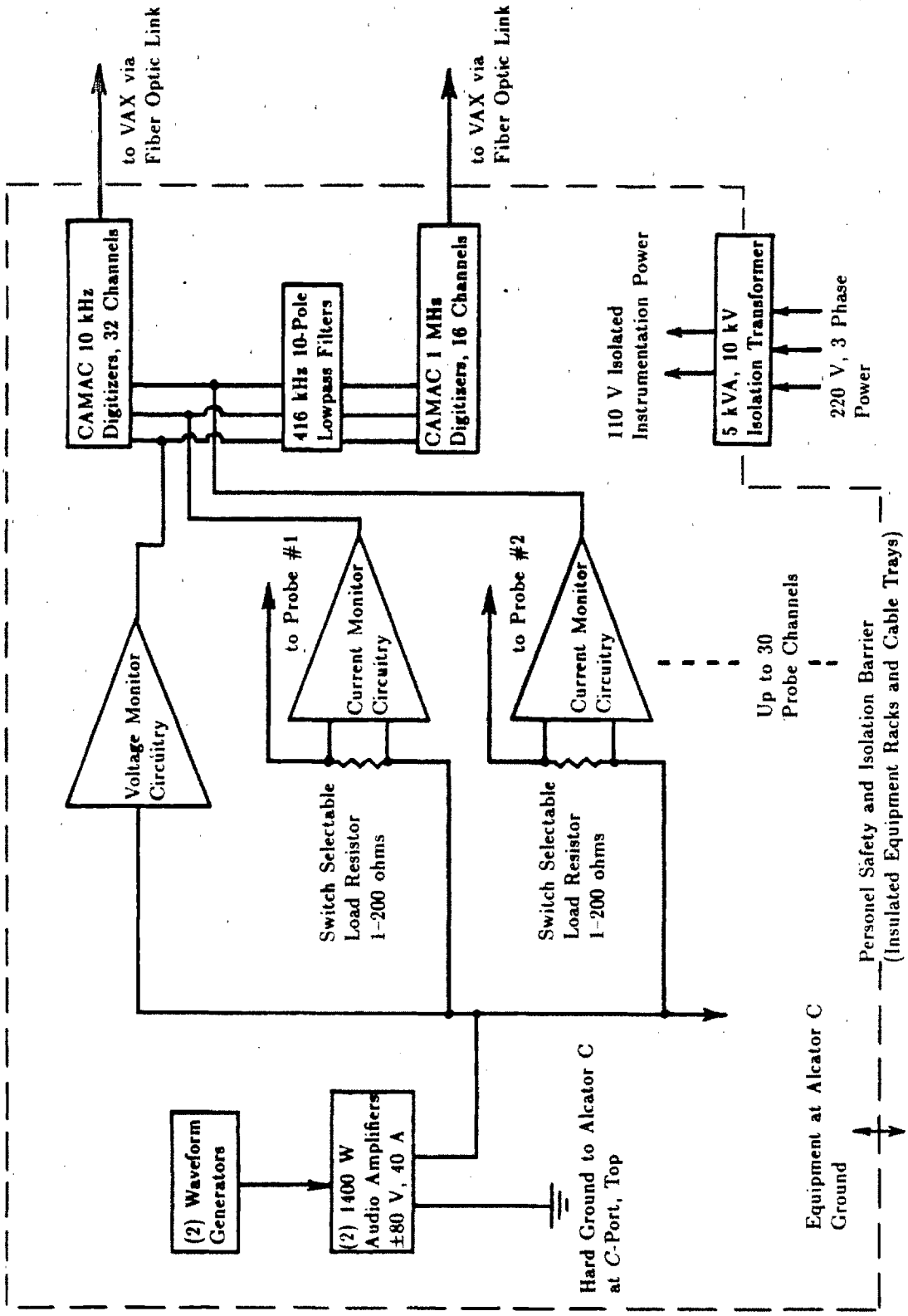

Figure 5.8 Probe Driver and Data Acquisition Electronics

5.1.5 Typical Raw Voltage and Current Traces from DENSEPACK

Each of the 30 driven DENSEPACK probes was operated in one of three modes: sweep mode, ion saturation mode, and floating potential mode. Figure 5.9 displays typical current and probe voltage traces that were recorded on the LeCroy 8212 Data Loggers for a $r = 16.8$ cm probe in sweep mode. A triangular bias voltage waveform of 100 Hz spanning +40 to −60 volts is used. Current collected by the probe displays the usual Langmuir characteristic from the begining of the discharge at 40 ms to the end at 490 ms. With a digitizer sampling rate of 10 kHz, 50 data points are recorded during a −60 V to +40 V or +40 V to −60 V sweep. A 1 Ω series load resistor was selected to monitor this probe current. Ion saturation is achieved around −15 to −25 volts and fluctuations in plasma density appear as 'hash' on the signal. Downward 'spikes' in the current trace can be seen as the probe is biased more positively to collect electrons. On closer inspection these 'spikes' have an exponential dependence on voltage and suggest a maxwellian distribution of electron particle velocities. Electron saturation is not achieved at the maximum positive potential of +40 volts. Maximum collection currents of ~ 1 amp become the limiting factor in setting the range of bias for electron collection. Further details of the probe characteristic and fitting technique can be found in chapter 6.

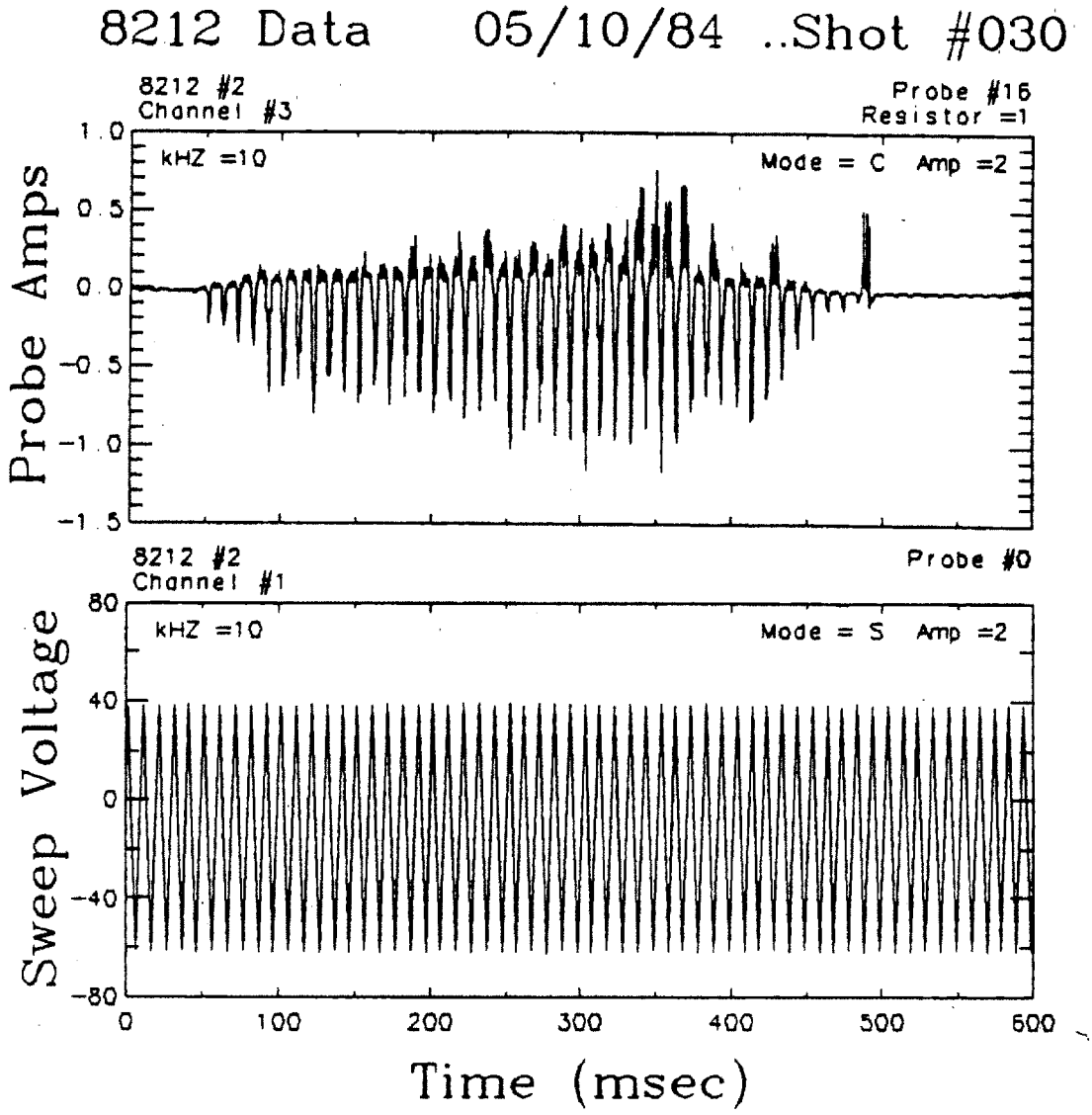

Figure 5.9 Raw Voltage and Current Traces from DENSEPACK

Figure 5.10 displays a typical probe current trace versus time for a probe biased in ion saturation mode and a typical probe voltage trace versus time in floating potential mode. In ion saturation mode, the TECRON amplifier was held at -60 volts throughout the duration of the discharge. Ion saturation mode was used primarily to record density fluctuations on the 1 MHz LeCroy 8210 digitizers. The probe floating potential displayed in Fig. 5.10 is obtained by disconnecting the probe from the main feed bus and monitoring the zero current or 'floating' probe potential. Both floating potential and ion saturation modes were not used as often as sweep mode was since the ion saturation current and floating potential could be deduced from the complete Langmuir characteristic.

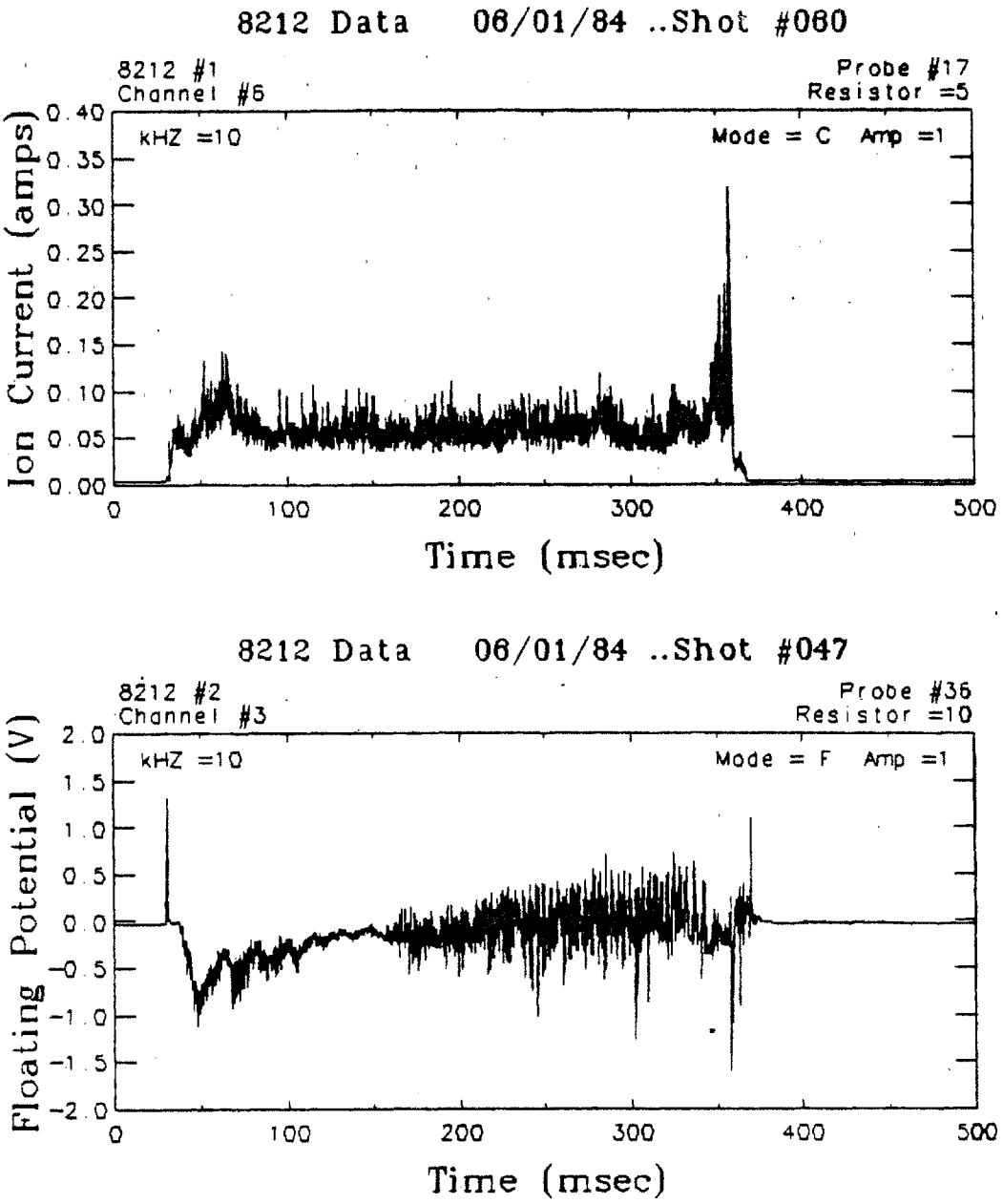

Figure 5.10 Ion Saturation Mode and Floating Potential Mode

5.2 H_α Camera Imaging System

A simple visible light imaging system illustrated in Fig. 5.11 was built to monitor non-uniformities in edge plasma radiation particularly during a MARFE event. A linear array of 16 silicon PIN photodiodes is positioned in the focal plane of a PENTAX K-1000 SLR camera body. Four LF347N quad FET input op-amps mounted in the camera back convert each diode current to an output voltage with a fixed gain of 1 volt/μamp. The signals are further amplified x1–x100 through a sixteen channel gain selectable amplifier box. Finally, the output signals are digitized and recorded in a Lecroy model 8212 CAMAC data logger. Data in each channel is digitized at 5 kHZ and stored for 400 ms.

The use of a standard PENTAX camera body as the base of the optical system allowed readily available SLR camera lenses to be utilized, eliminating the need for custom designed optics. Light passing through the lenses was focused onto the photodiode array just as it would normally focus on the film. In addition, a gradicule mask in the viewfinder enabled the 16 photodiodes to be aimed and focused onto the desired location in the plasma, thereby bypassing the usual uncertainty and complication associated with an external optical alignment procedure.

Since the system was based on glass optical elements and silicon photodiode detectors, any plasma emission in the visible wavelengths could be monitored. Typically, a 30 Å bandpass interference filter centered about λ = 6563 Å was placed in front of the lens to restrict the spectral response to the $3 \rightarrow 2$ hydrogen Balmer line transition, H_α. Weaker spectral lines such as from C^{III} could be monitored but the signal to noise ratio of the photodiode detector system became limiting. This system was also successfully used to record visible continuum emission in a 1000-600 Å region centered about λ = 5500 Å, similar to a 20 channel fiber optic system at Alcator C based on photomultiplier tubes.[88]

The camera system was compact and could be held in one hand. Consequently, it was easily moved and realigned at any available access port. Since the view of the plasma in Alcator C is through a narrow rectangular keyhole, a linear array of photodiodes was most appropriate. Lenses were selected to view the desired vertical extent when looking from an outside keyhole or in-out extent when looking through a top or bottom keyhole. Extender tubes were used for long focal length telephoto lenses in order to achieve the required close focusing distance. When the light emission became very bright, such as H_α emission at a limiter location, the camera could be 'stopped down' to avoid saturation and achieve the optimum dynamic range.

This camera system was primarily used to correlate spatial changes in H_α brightness with changes in edge plasma parameters detected by the DENSEPACK array. Brightness profiles from this H_α diagnostic along with DENSEPACK data during MARFE phenomena are presented in chapter 11.

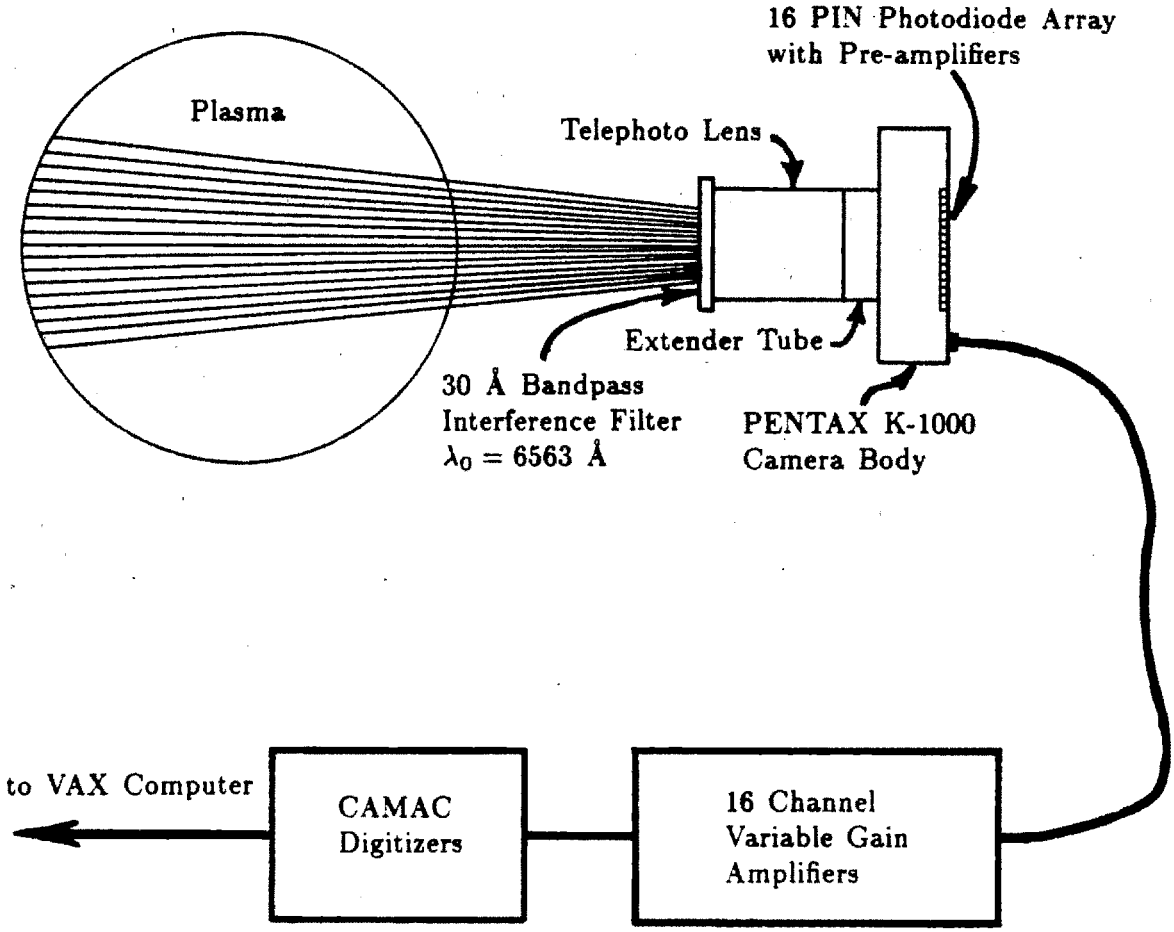

Figure 5.11 Schematic of H_α Camera System

5.3 Other Diagnostics

In addition to the usual traces of plasma current inferred from a Rogowsky coil and line averaged densities via a laser interferometer system, there are a number of other diagnostics which were relied upon in this study of the Alcator C edge plasma. Figure 5.12 displays output from other diagnostics that were recorded along with DENSEPACK probe data.

The inside interferometer cord at -12 cm in trace (c) was used to detect MARFE activity. The central soft X-ray channel, (d), and central visible continuum brightness, (e), were used to detect anomalous conditions such as a sudden increase in impurity concentrations due to a 'natural' impurity injection. In addition, the visible continuum brightness allowed an unambiguous following of the rapid density increase during a pellet injection. (The interferometer can change by an unknown number of fringes.) The output of a non-spatially resolving H_α detector, (f), was typically recorded to monitor MARFE activity. Finally, output from $\cos\theta$ and saddle coil magnetic pickup loops were processed to indicate the outer flux surface in–out, (g), and up–down, (h), plasma position.

One important result of the DENSEPACK probe study was that plasma pressure is not constant on a flux surface in the Alcator C limiter shadow plasma. In support of this finding is the data obtained by a series of twelve poloidal flux loops used to reconstruct the outer flux surface shape and position. Consquently, a brief discussion of the flux surface measurement and determination is in order.

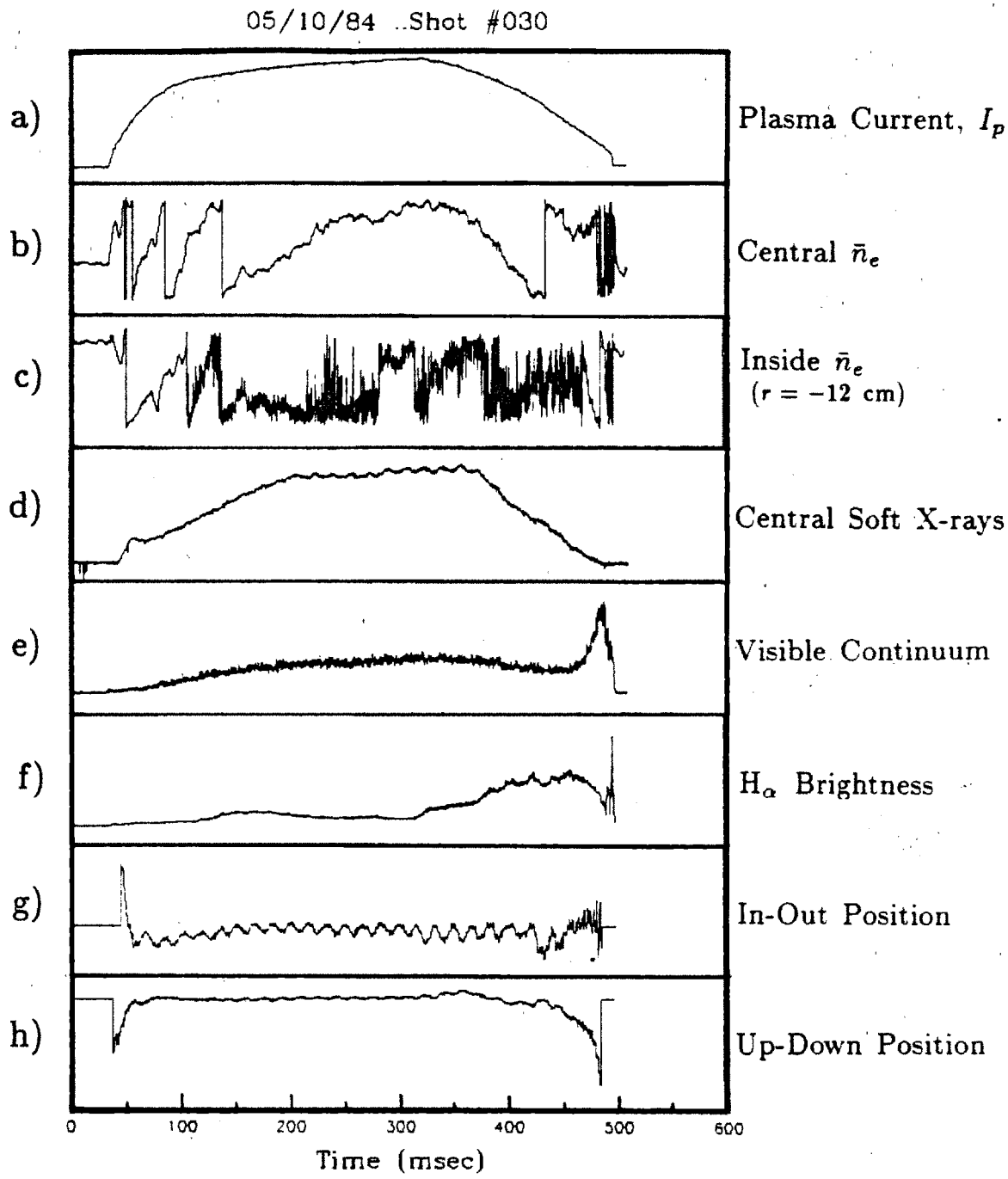

Figure 5.12 Other Diagnostic Traces Recorded Along with DENSEPACK

5.3.1 Outer Flux Surface Measurement

An array of twelve poloidal flux loops used to infer the outer magnetic flux surface shape is diagrammed in Fig. 5.13. Details of data analysis from this diagnostic are presented in Ref. [77].

The poloidal field pickup coils are located on the vacuum chamber surface and are absolutely calibrated to within $\sim 0.5\%$. Maxwell's equations are solved in toroidal coordinates and used to interpolate for the magnetic field between loops and in the vacuum region surrounding the plasma. This 'vacuum region' approximation is valid everywhere that there is no significant toroidal current which includes the region between the vacuum chamber wall and the limiter radius. Once the field is determined, the outer flux surfaces can easily be drawn.

Toroidal harmonic amplitudes of the poloidal field are fitted to the data from the twelve pickup loops. Consequently, the accuracy of the low order harmonics is very good and not sensitive to random errors in flux loop calibrations. The error in the inferred shape of the last closed flux surface (tangent to the limiter) is estimated to be less than 0.5 mm.[118] Plots of magnetic flux surfaces inferred by this diagnostic along with pressure surfaces inferred by the DENSEPACK probe array are included in chapter 8.

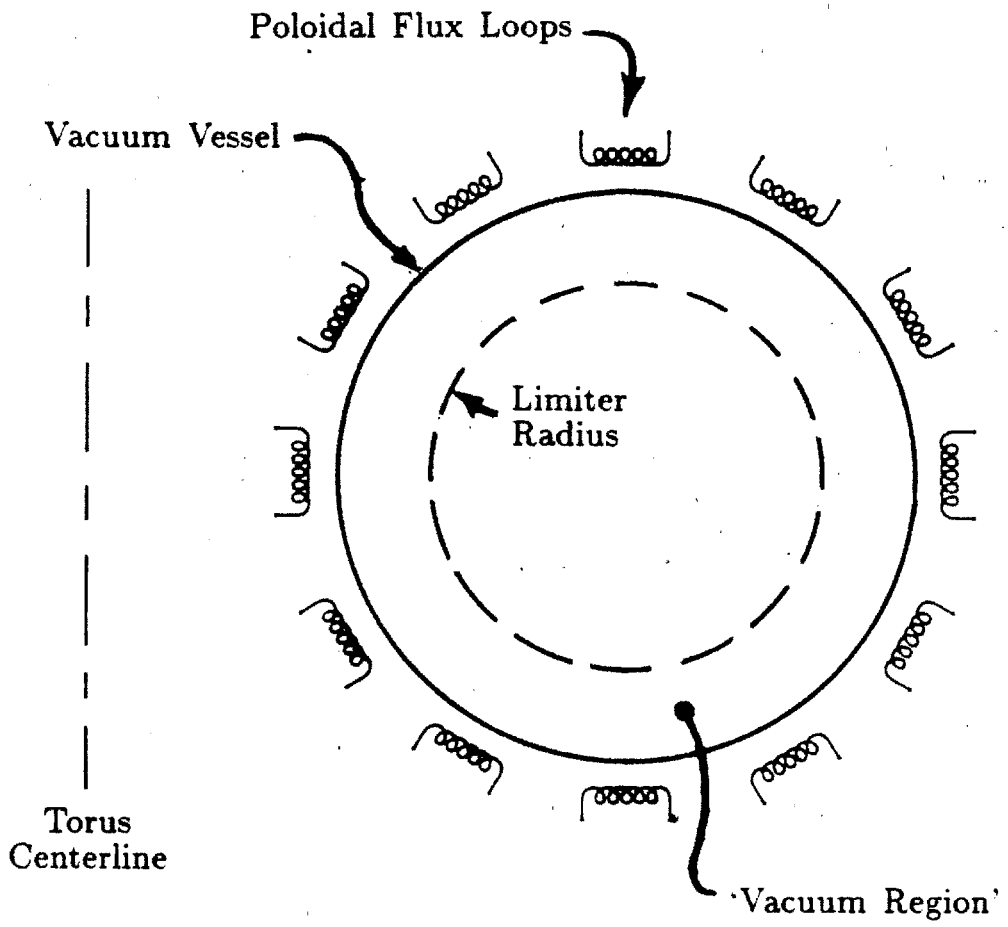

Figure 5.13 Poloidal Flux Loops for Outer Flux Surface Measurement

CHAPTER 6

DENSEPACK PROBE DATA ANALYSIS

In a typical plasma shot, DENSEPACK can generate over 100 Langmuir probe characteristics for each of the 30 data channels. Much effort was spent on developing a series of data processing programs and in particular a numerical algorithm to facilitate fitting many probe characteristics in a fast and reliable way. Section 6.1 outlines the overall data acquisition, display, and storage procedure which was needed in order to handle the high volume of data. Sections 6.2 and 6.3 discuss Langmuir probe characteristic models and fitting procedures which were used in DENSEPACK data analysis. A probe characteristic model based on the work of Stangeby[19] is presented which includes perpendicular diffusion into the particle collection flux tube. Appendix D includes more details of a fast numerical algorithm which was developed to infer density, electron temperature, floating potential, space potential, and estimates of the corresponding uncertainties from fitting the Langmuir characteristic.

6.1 Data Processing

Starting with the raw digital data stored in LeCroy 8212 and 8210 data loggers and producing a graphic display of constant density or temperature contours in the edge plasma in Alcator C involves the execution of a number of successive data reduction, archiving, and display programs. The multiple steps that occur in this data processing is presented chronologically in this section beginning with raw data acquisition and ending with a description of a DENSEPACK database program.

6.1.1 Raw Data Acquisition and Display

During an Alcator C run, data is archived and displayed as shown in Fig. 6.1. Diagram (*a*) depicts the flow of data during execution of a data aquisition program, 'PROBE', which is run after each shot. DENSEPACK data stored in CAMAC memory modules is read out, combined with other diagnostics' output, such as plasma current and density, and stored in a disk file. The DENSEPACK configuration and load resistor settings are read from a set-up file and saved as header information in the raw data file. A separate editor program allows information to be updated in the set-up file any time changes are made in the DENSEPACK hardware.

Between plasma shots, raw data stored in the disk files can be displayed in graphical form on the terminal, (*b*). A number of programs are available to display all 8212 channels, all 8210 channels, or all other diagnostic channels that were recorded for a quick check of the system's operation. Alternatively, any one channel can be displayed in detail.

a) Data Acquisition Between Shots

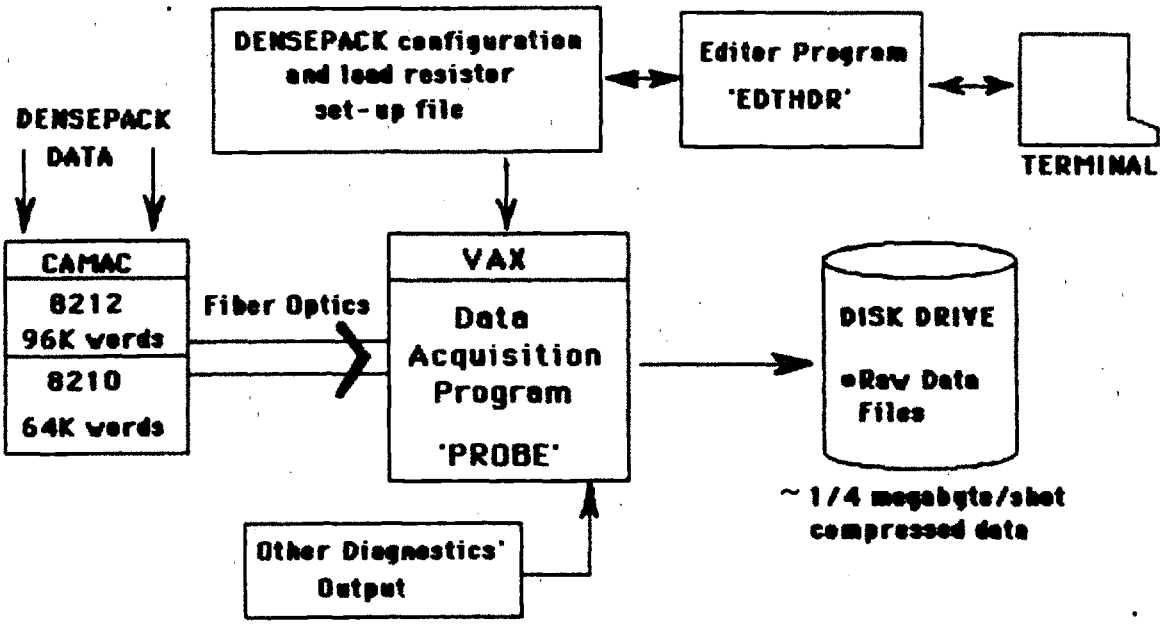

b) Raw Data Display Between Shots

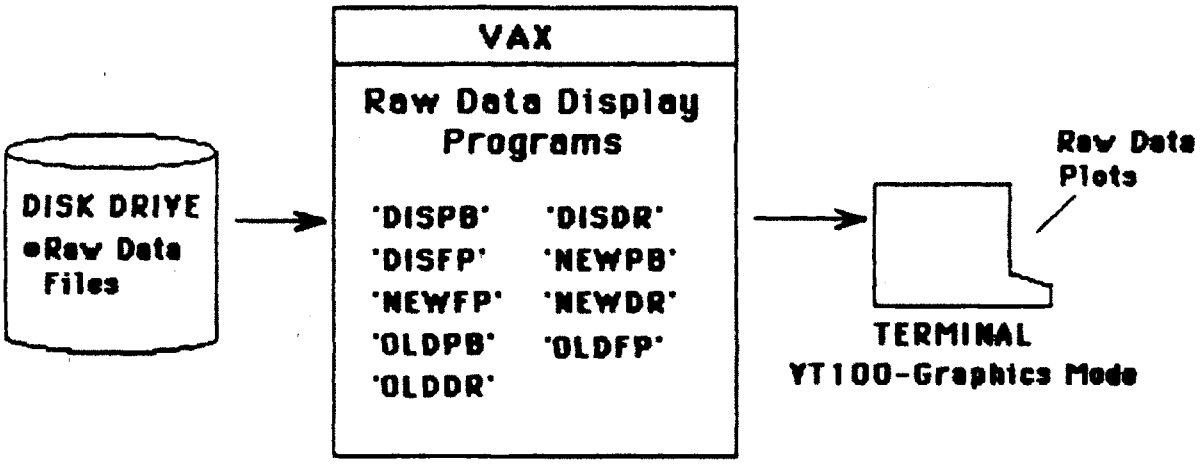

Figure 6.1 Data Acquisition and Display During An Alcator C Run

6.1.2 Data Reduction and Archiving

Figure 6.2 diagrams procedures used after a run to summarize, reduce, and archive data for later reference. A more tangible record of the raw data accumulated during the day is first produced using hardcopy programs, (*a*), which output all data channels on a three page summary for each shot.

The task of reducing raw probe data into plasma parameters such as density and temperature is then handled by the program 'DPACK' in Fig. 6.2, (*b*). The raw data files are read in, fitted, and a reduced data file is generated. Optimized fitting parameters and program control parameters are stored in a menu file. This allows the program to be easily executed as a batch job to process data from many plasma shots. Section 6.3 and Appendix D cover the data fitting section of the program 'DPACK' in more detail.

Once the probe data for a particular day is reduced, it is copied along with the raw data to magnetic tape for permanent storage, (*c*). A log file records the file names archived on a given tape volume for later reference. Data files on the disk drive are cleared to reserve space for new data.

a) Raw Data Hardcopy

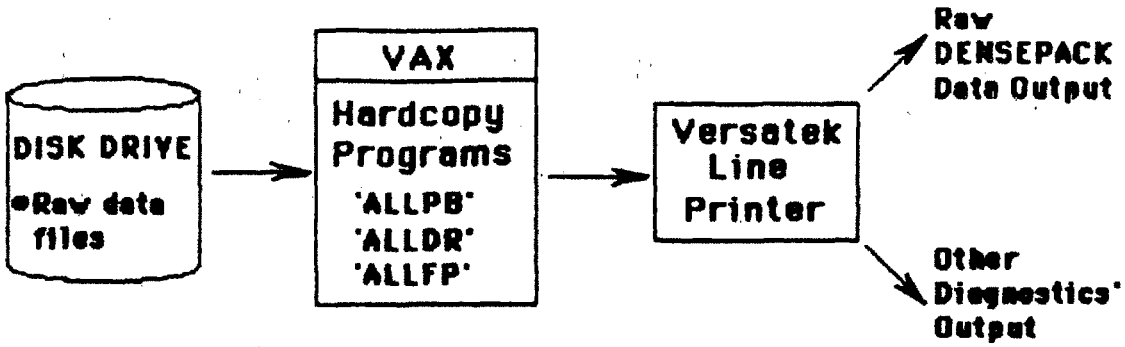

b) Data Reduction

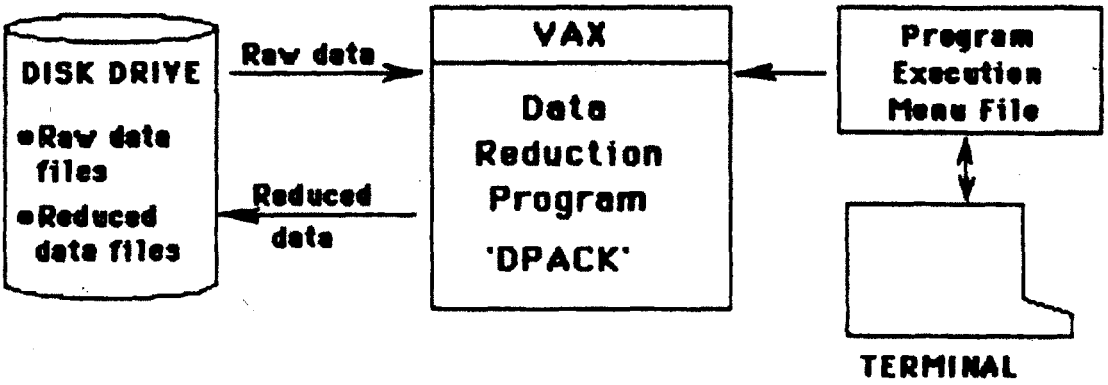

c) Archiving for Permanent Storage

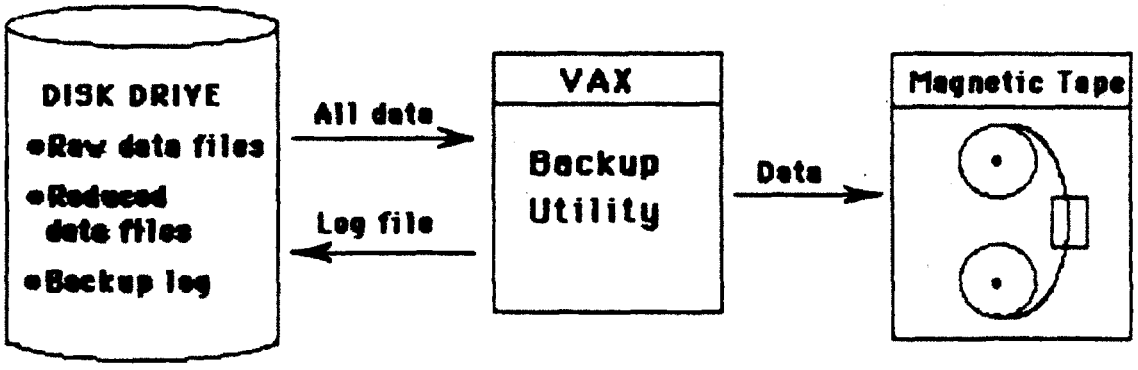

Figure 6.2 Data Reduction and Archiving

6.1.3 Reduced Data Display Programs

The benefit of reducing all the probe data beforehand in the program 'DPACK' is that the data can then be reviewed with fast, easy access and plotted in a number of different formats. Figure 6.3 shows a simple single channel display program, (*a*), and a more complex multiple probe, 3-D display program, (*b*). The multiple probe data display program, 'DPKPLOT', can plot directly inferred plasma parameters such as density, electron temperature, and floating potential as a function of time, radius, or poloidal angle. Three-dimensional surfaces or contour plots representing the data can be displayed.

The program also has the capability of plotting in the same 3-D or contour plot format quantities which are calculated from the reduced probe data. This feature was incorporated to study the particle and energy balance in the limiter shadow region. Terms in the continuity and energy equations can be computed directly from probe data and displayed versus spatial position.

The 'DPKPLOT' program is controlled via a menu file and all output can be directed to the terminal or sent to a graphics line printer. Most of the graphics is based on a software package obtained from NCAR.[89]

a) Single Probe Reduced Data Display

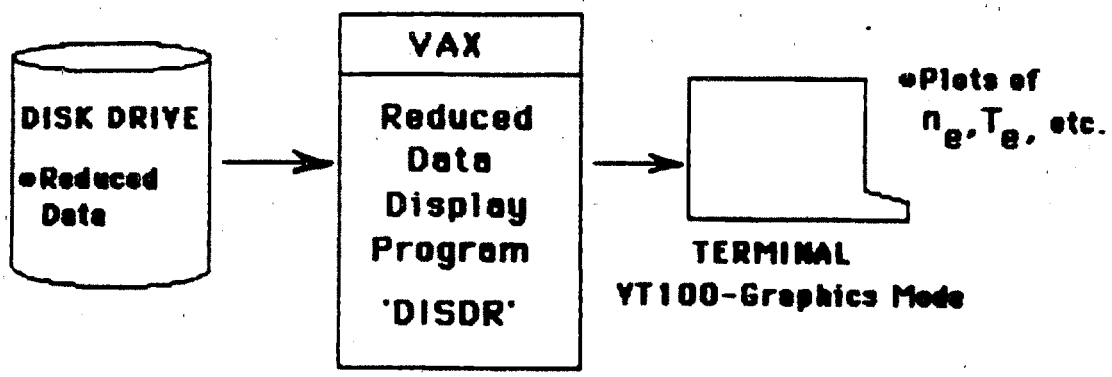

b) Multiple Probe 3-D Display Program

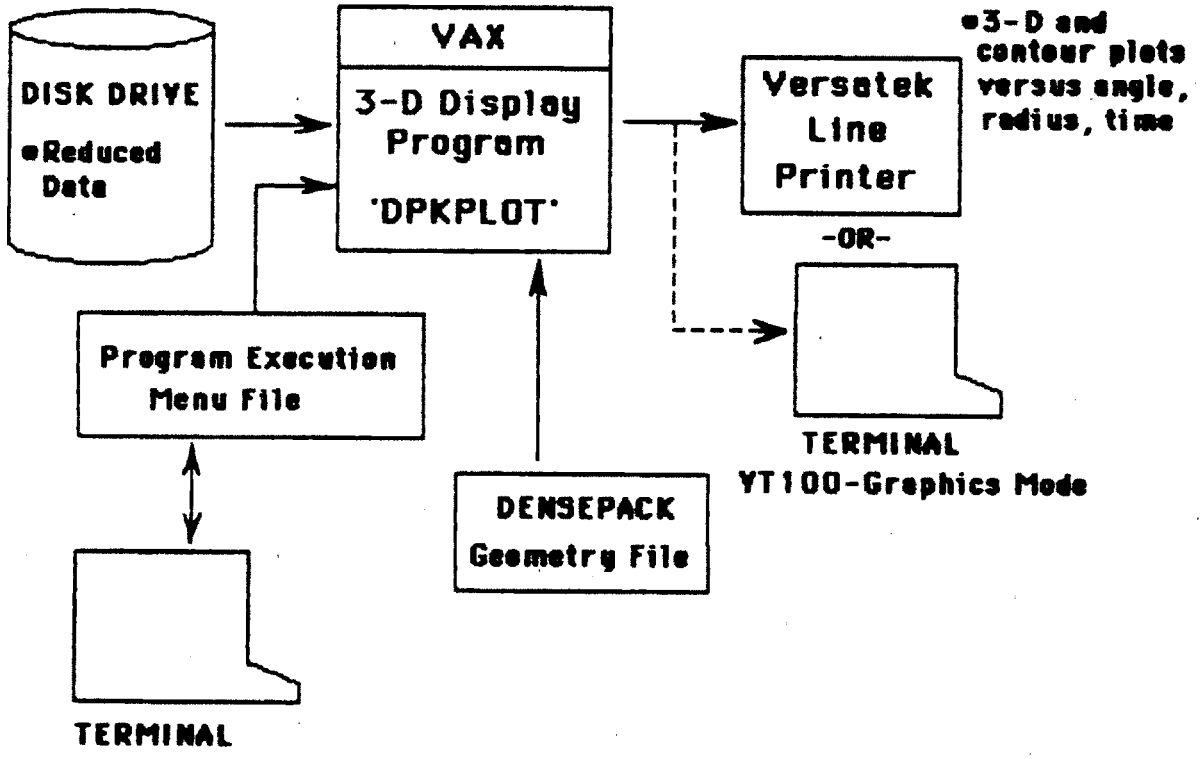

Figure 6.3 Reduced Data Display Programs

6.1.4 DENSEPACK Database Programs

Typically, one or two days of DENSEPACK data completely fill a magnetic tape reel. In order to correlate edge plasma parameters with central plasma parameters in a systematic way, a database generating program was written (DPKBASE). 'DPKBASE' summarizes DENSEPACK and central plasma parameter data from each discharge and writes it in a common database file. Figure 6.4 shows the operation of 'DPKBASE' and a corresponding database display program, 'DBPLOT'. The database file contains central and edge plasma parameters at four specifiable times during each plasma shot. The display program allows the user to choose any quantity in the database as the independent and dependent variable for a graph. Data before or after an event such as a pellet injection can be selected. Maximum and minimum value restrictions can be applied to any or all variables to 'window-in' on a particular subset of data. This feature allows the selection and plotting of shots with only certain plasma currents, densities, or horizontal position, for example. The program utilizes an advanced graphics package developed by McCool[90] which handles multiple labled axes and includes an extensive library of interactive features.

a) Data Base Generation Program

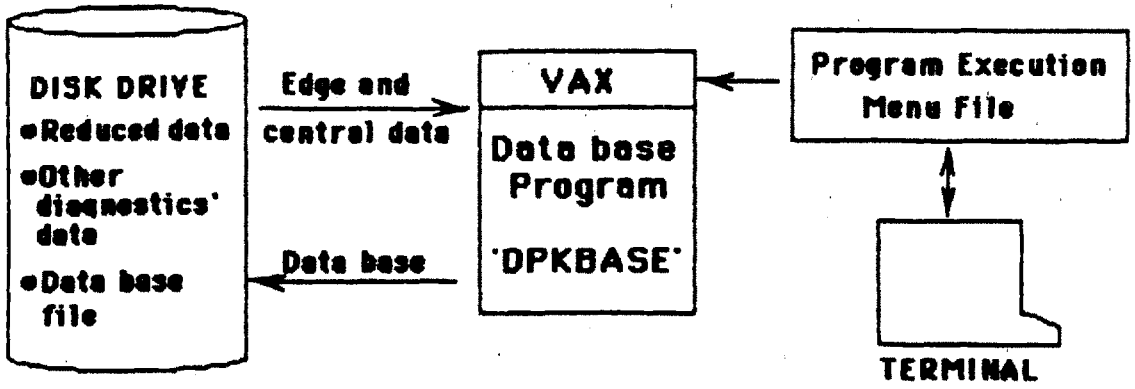

b) Data Base Program

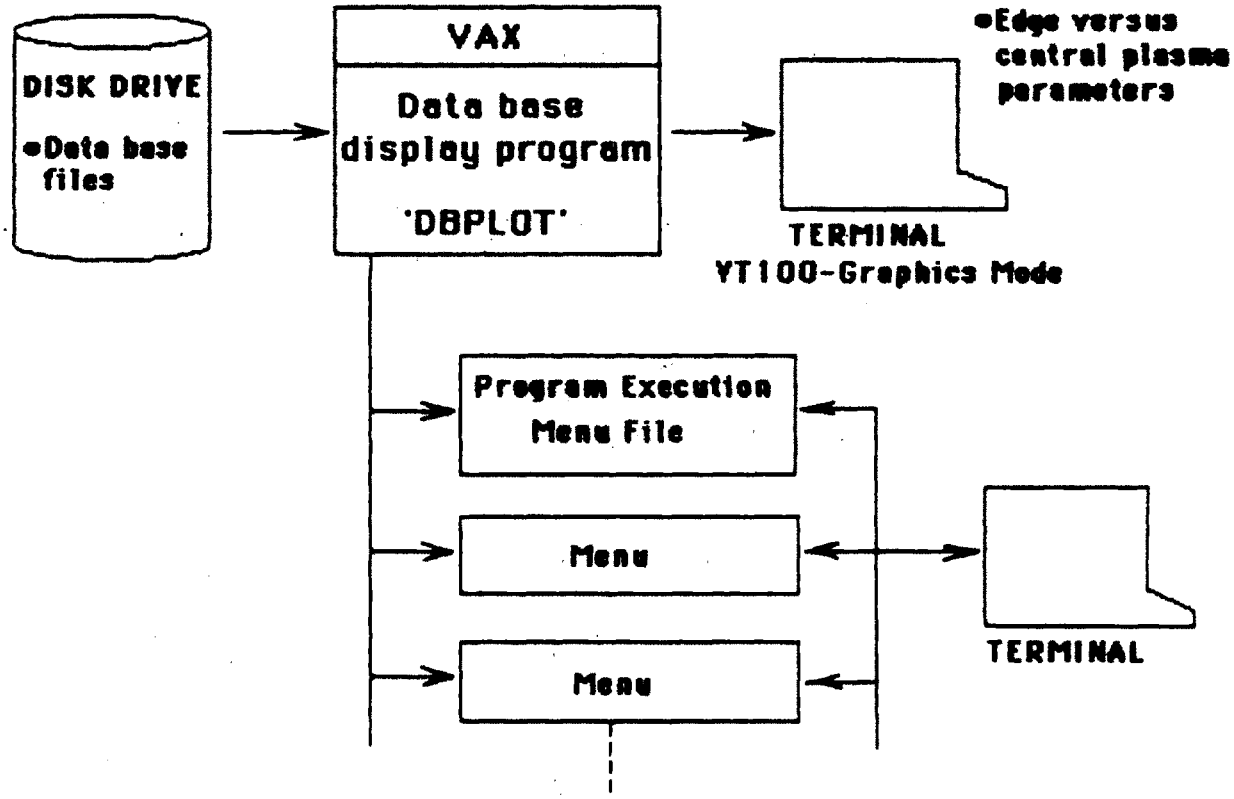

Figure 6.4 Database Generation and Display Programs

6.2 Probe Characteristic Models

There have been many treatments of the plasma-sheath problem published in connection with electric probes since Tonks and Langmuir. Unfortunately, no complete and rigorous theory exists to cover the many regimes that a Langmuir probe can operate. Nevertheless, there are a number of well established rules which govern the plasma near a metallic surface. The general features of a Langmuir probe characteristic can be understood in terms of these rules. Fortunately, when they are employed to analyze Langmuir probe data, they yield results which are typically accurate to within the experimental uncertainty of the data itself.

The first part of this section discusses relationships useful for Langmuir probe data analysis. A first-cut Langmuir probe characteristic model based on these relationships is stated. Some refinements of the probe model are then mentioned in a section on Langmuir probes in a magnetized plasma and in a section on a model developed by Stangeby.[19]

6.2.1 General Features of a Langmuir Probe Characteristic

As discussed in section 2.2, a consequence of a metallic surface in contact with a plasma is that a sheath region of a few debye lengths thick forms at the surface-plasma interface. For an electrically floating surface, the sheath potential drop acts to equalize the impinging electron and ion currents. A pre-sheath electric potential variation farther away from the surface is also established to insure that the ions arrive at the sheath edge with a velocity characteristic of the sound speed. This 'Bohm sheath criterion' must be satisfied in order for a stable sheath to exist. From both a collisionless-kinetic and a fluid treatment of the presheath, the density at the sheath edge is found to be approximately 1/2 the density far away from the probe. Thus, a simple estimate of electron and ion fluxes to a floating surface is

$$\Gamma_e \;=\; Z_i\;\Gamma_i \;\approx\; \frac{1}{2}\;n_0\;C_s\;, \qquad (6.1)$$

Where n_0 is the electron density far away from the probe, and Z_i is the ion charge.

When the surface is biased negatively with respect to the floating potential, electrons are repelled by the increased sheath drop, but ions arrive at the sheath edge with the same sound speed flow. Therefore, at large negative biases, one expects that only the ions will be collected at a 'saturated' rate

$$Z_i\;\Gamma_i \;\approx\; \frac{1}{2}\;n_0\;C_s\;. \qquad (6.2)$$

Biasing the surface more positively with respect to the floating potential reduces the sheath potential drop, allowing more electrons to be collected. For a maxwellian distribution of electrons, the collected electron flux will depend on the probe potential, V_p, relative to the plasma space potential far away, V_s, through a Boltzmann factor

$$\Gamma_e \;\approx\; \frac{1}{4}\;n_0\;\overline{C}_e\;\;e^{(V_p-V_s)/T_e}\;. \qquad (6.3)$$

For $V_p \geq V_s$, Eq. 6.3 breaks down since the electrons cannot be collected any faster then the unimpeded random flux,

$$\Gamma_{eMax} \;=\; \frac{1}{4}\;n_0\;\overline{C}_e\;, \qquad (6.4)$$

with $\overline{C}_e = \sqrt{8qT_e/\pi m_e}$. (Here and throughout this section the electron temperature is in eV and all other units are in MKS.) At these positive biases, the

sheath and the density around the probe can be greatly perturbed. In general, it is not easy to determine the proper value for n in Eq. 6.4.

The potential that a probe acquires when no net current is drawn is termed the 'floating potential', V_f. V_f can be simply estimated by setting equal Eqs. 6.1 and 6.3, resulting in

$$V_f \;=\; V_s \;-\; T_e \; ln\Big[\frac{2\; m_i}{\pi\; m_e}\Big]^{1/2} \;. \tag{6.5}$$

For hydrogen, the floating potential is approximately

$$V_f \;\approx\; V_s \;-\; 3.5\; T_e \;. \tag{6.6}$$

Equation 6.5 must be derived from a more complete model to predict accurately the floating potential in the presence of finite temperature ions or secondary electron emission from the probe surface.

In a magnetized plasma, any metallic surface extending over many ion Larmor radii will collect current primarily along the field lines. Thus, the surface can be considered to act as a one-dimensional probe which conceptually simplifies the geometry. The appropriate current collecting surface then becomes the total perpendicular projected area.

Combining Eqs. 6.1–6.3 for a plane collection area, A_p, yields a first-cut estimate for the probe characteristic

$$\frac{I(V_p)}{q\ A_p\ n_0} \approx \frac{1}{2}\ C_s - \frac{1}{4}\ \overline{C}_e\ e^{(V_p - V_s)/T_e} \quad ;\ \text{for}\ \ V_p < V_s \qquad (6.7)$$

$$\frac{I(V_p)}{q\ A_p\ n_0} \approx -\frac{1}{4}\ \overline{C}_e \quad ;\ \text{for}\ \ V_p \geq V_s\ , \qquad (6.8)$$

which is graphed in Fig. 6.5. Notice that there is a disagreement in the probe current predicted by Eqs. 6.7 and 6.8 at $V_p = V_s$. However, since $\frac{1}{4}\overline{C}_e$ is much larger than $\frac{1}{2}C_s$, the latter term can be neglected in the electron saturation regime. A more precise treatment would include finite temperature ion effects to properly match these two regimes.

When the probe is biased at the space potential, V_s, no sheath exists and the electrons are collected at the random flux rate in this simple theory. In practice, the sharp 'knee' at the space potential is not observed. A more typically observed curve for the electron saturation regime is sketched in Fig. 6.5. The location of the V_s point on the characteristic is therefore not well defined. In addition, the electron saturation flux given by Eq. 6.4 is rarely seen even for very large positive biases. This effect is due to the limited rate at which electrons can diffuse perpendicularly into the collecting flux tube. The following sections consider this and other effects as refinements to the characteristic model.

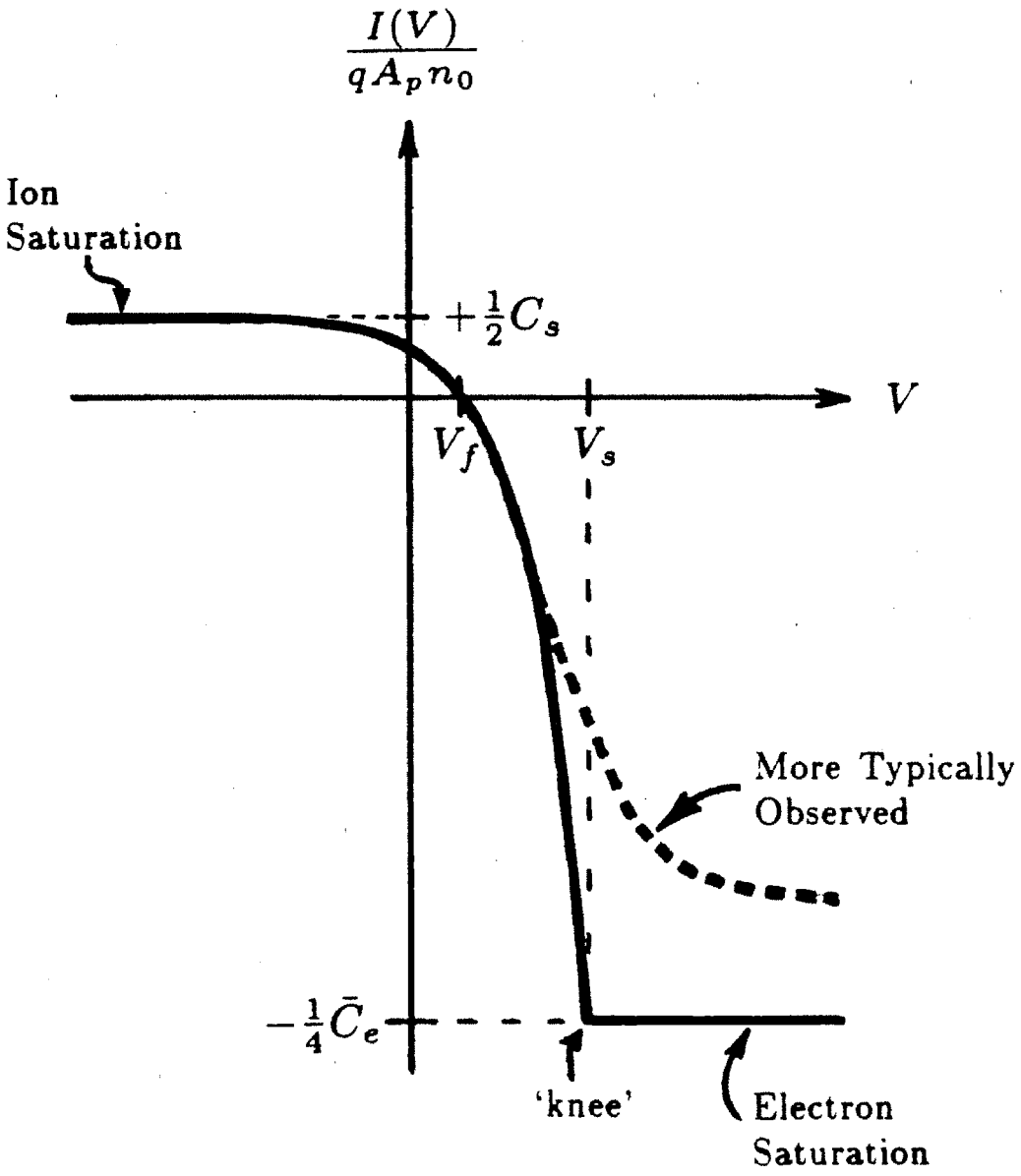

Figure 6.5 First-Cut Estimate of Langmuir Probe Characteristic

6.2.2 Langmuir Probe in a Magnetized Plasma

A probe immersed in a magnetized plasma collects particles along the magnetic field as shown in Fig. 6.6. The probe surface is a particle sink which is balanced by particle fluxes parallel and perpendicular to $\underline{B}$. The parallel mobility of particles is much greater than perpendicular mobility, causing the probe to collect particles primarily along a 'flux tube'. The implication is that the Langmuir probe does not sample plasma parameters immediately about the probe but rather samples average plasma parameters over a long parallel collection region. The parallel extent of this region, d, can be simply estimated by equating the perpendicular fluxes to the total current collected by a square probe with area s^2 as drawn in Fig. 6.6. Assuming that the characteristic density gradient scale length perpendicular to $\underline{B}$ is $\sim n/s$ and that Eq. 6.1 applies for a floating probe, one obtains the relation[70]

$$4\ D_\perp\ n\ d\ =\ \frac{1}{2}\ n\ C_s\ s^2\ . \tag{6.9}$$

Using the relationship for $D_\perp$ given by Eq. 3.10, d can be written as

$$d\ \approx\ \frac{L\ s^2}{8\ \lambda_n^2}\ . \tag{6.10}$$

For DENSEPACK probes with $s \approx 0.12$ cm, $L \approx 100$ cm, $\lambda_n \approx .3$ cm, d is approximately

$$d\ \approx\ 2\ \text{cm}\ . \tag{6.11}$$

When the probe is biased to collect electrons, the flux tube collection length increases. Consider a probe collecting the random electron flux of Eq. 6.4. The same analysis yields

$$d_e \approx \frac{\overline{C}_e\, d}{2\, C_s} \approx \sqrt{\frac{2\, m_i}{\pi\, m_e}}\, d \tag{6.12}$$

$$d_e \approx 69 \text{ cm} . \tag{6.13}$$

The condition that the flux tube just intercepts the limiter surface, $d_e \approx L$, places a restriction on the probe size relative to the scrape-off length,

$$s \approx \frac{\lambda_n}{2\mu^{1/4}} . \tag{6.14}$$

For a probe larger than the characteristic size given by Eq. 6.14, the flux tube can be bounded by a limiter. This may affect the rate of particle collection at some point on the *I-V* curve. Ideally, one would like the flux tube to never touch the limiter surface over the range of bias or always to intercept the limiter. In the latter case, the probe can act as a local limiter itself. In this case, the density depletion due to particles collected by the probe must be considered.[69,70]

An Alcator C hydrogen plasma with $\lambda \approx 0.3$ cm and $\mu \approx 1$ results in

$$s \approx 0.15 \text{ cm} . \tag{6.15}$$

DENSEPACK probes are small enough to be considered as a set of probes immersed in a infinitely large magnetized plasma over most of the bias range. In electron saturation, Eq. 6.14 indicates that this approximation starts to become marginally satisfied. This point is raised again later during electron saturation data analysis in section 7.2.5.

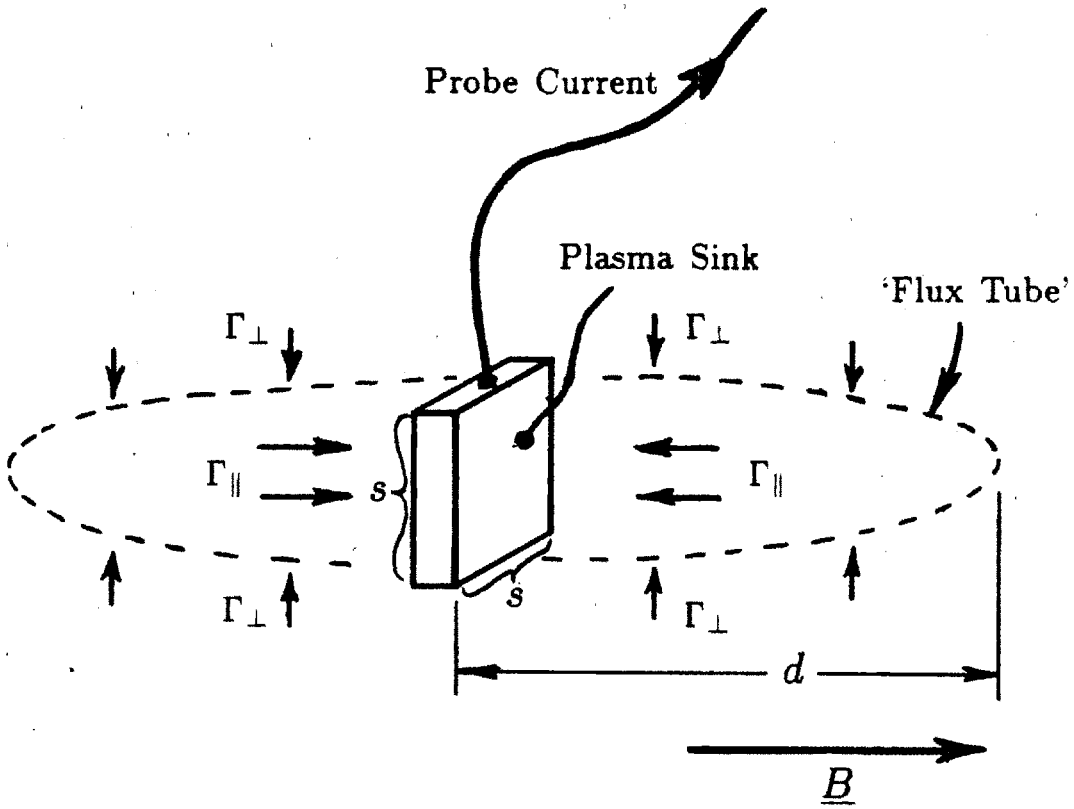

$\Gamma_\perp$ = Perpendicular Particle Fluxes

$\Gamma_\parallel$ = Parallel Particle Fluxes

Figure 6.6 Collection Flux Tube for Probe in Magnetized Plasma

6.2.3 Description of the Stangeby Model

Stangeby[19] has considered the problem of probes in a magnetized plasma in some detail. The approach is based primarily upon a two-species fluid treatment which is not rigorously correct in a nearly collisionless regime. Nevertheless, the essential features of a Langmuir probe characteristic are predicted. Further justification for using such a model lies in the fact that most results obtained by other authors who have used more elaborate kinetic treatments can be reproduced by this model in the appropriate limits. From the point of view of an experimentalist, Stangeby's model is attractive since it is relatively simple in form, covers the entire range of the probe characteristic, and incorporates such refinements as cross-field diffusion into the flux tube.

In this model, the electrons are assumed to be collisional up to the sheath edge while the ions are assumed to follow a Boltzmann relation. In the limit of electron saturation, the electron flux collected by the probe is shown to be reduced from the $n\ \overline{C}_e/4$ value to

$$\Gamma_{\|e} \;=\; \frac{1}{4}\ n_0\ \overline{C}_e\ \frac{r}{1+r} \tag{6.16}$$

similar to the analysis by Bohm[20] where the reduction factor, r, is defined as

$$r \;=\; \frac{16}{\pi}\ \frac{\lambda_{ei}\ \sqrt{\alpha}\ (1+\tau)}{s}\ . \tag{6.17}$$

The following definitions apply: λ_{ei} = electron mean free path, $\alpha = D_\perp/D_\|$, $\tau = T_i/T_e Z_i$, and s = effective probe diameter. The reduction factor, r, is a measure of how efficient perpendicular electron diffusion is in populating the flux tube. For a high magnetic field (low $D_\perp$) and/or large probe size, the electron saturation flux received by the probe can be significantly reduced.

The more general expression for electron collection at arbitrary probe bias involves accounting for the possibility of a potential 'hill' in the pre-sheath. Figure 6.7 illustrates the potential variation versus distance from a magnetized probe that was considered by Stangeby. The plasma space potential far away from the probe is taken as the zero voltage reference point. The potential hill aids in pulling electrons to the sheath edge against their collisional drag when the probe is biased to collect electrons preferentially. The Boltzmann relation for the ions in the pre-sheath allows a connection between the plasma density and electric potential at the hill crest through the ion temperature. Electrons experience a repulsive potential in crossing the sheath so that the flux collected is reduced by the usual Boltzmann factor, except that the potential drop now involves the difference between the hill potential and the probe potential. This formulation leads to the expression for the collected electron flux,

$$\Gamma_{\|e} \;=\; \frac{1}{4}\; n_0\; \overline{C}_e \Big[\frac{r}{1+re^{\eta_h-\eta_p}}\Big] \quad ;\; \text{for} \quad \eta_p \;\leq\; \tau\; ln\Big[\frac{1+r}{r}\Big]\;, \tag{6.18}$$

and

$$\Gamma_{\|e} \;=\; \frac{1}{4}\; n_0\; \overline{C}_e \Big[\frac{r}{1+r}\Big] \quad ;\; \text{for} \quad \eta_p \;>\; \tau\; ln\Big[\frac{1+r}{r}\Big]\;, \tag{6.19}$$

with the additional transcendental relationship for η_h,

$$\tau\; ln\big[r^{-1}\; e^{\eta_p-\eta_h}+1\big] \;=\; \eta_h\;. \tag{6.20}$$

η_p $(= V_p/T_e)$ and η_h $(= V_h\; T_e)$ are the normalized probe and hill potentials. When $\eta_p = \tau\; ln[(1+r)/r]$, the hill potential equals the probe potential, and the electrons arrive with the reduced random flux as in Eq. 6.19. For a given τ,

r, and η_p, η_h can be found using Eq. 6.20 and the corresponding $\Gamma_{\|e}$ found from 6.18 or 6.19. Notice that when $\tau \to 0$, η_h becomes zero. Furthermore, when $r \to \infty$, the simple expression for the electron flux in Eqs. 6.3 and 6.4 is recovered.

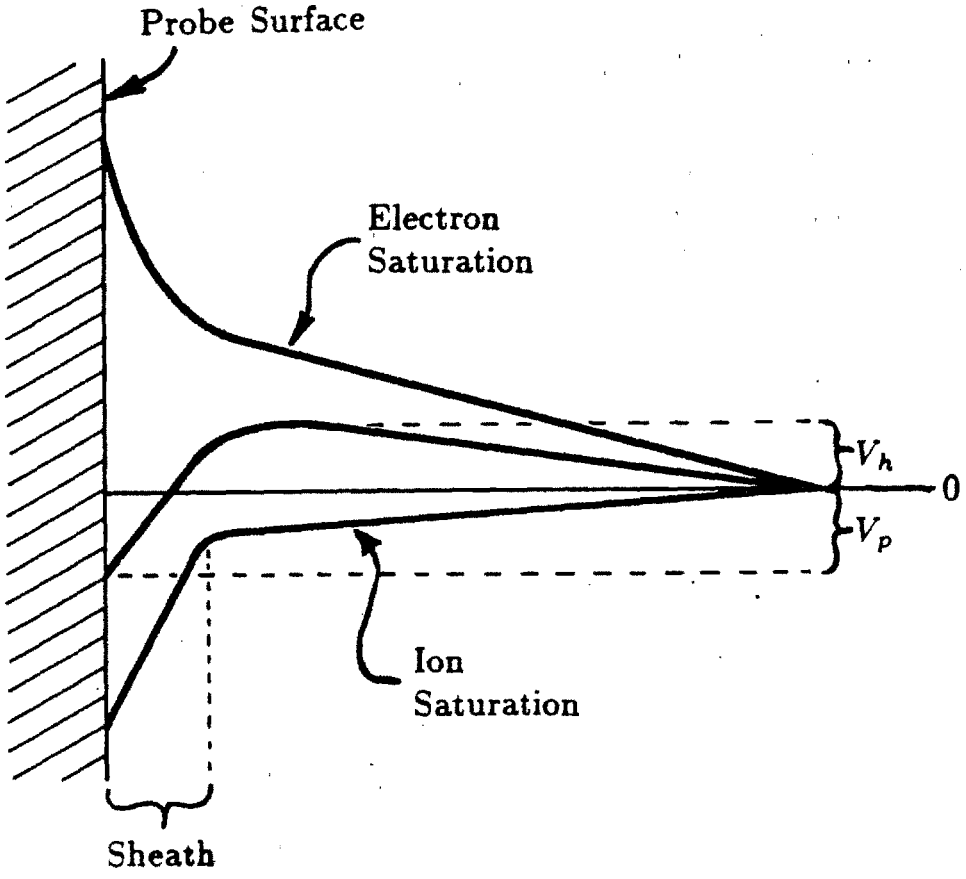

V_h = 'Hill' Potential
V_p = Probe Potential

Figure 6.7 Potential vs. Position for a Magnetized Probe (from reference [19])

The ion flux collected by the probe also depends upon the probe potential relative to the hill potential. At positive probe potentials when $\eta_p > \eta_h$ ($\eta_p > \tau\ ln[(1+r)/r]$), the ions arrive at the probe at the random rate reduced by the Boltzmann factor

$$Z_i\ \Gamma_i\ =\ \frac{1}{4}\ n_0\ \overline{C}_i\ e^{-\eta_p/\tau} \tag{6.21}$$

with $\overline{C}_i = \sqrt{8qT_i/\pi m_i}$. When $\eta_p < \eta_h$, the ions are repelled by the hill potential but accelerated to the probe by the sheath drop. The ion density at the hill crest is reduced by a Boltzmann factor so that the free streaming ion flux from this point to the probe is

$$Z_i\ \Gamma_i\ =\ f(\tau)\ n_0\ C_s^*\ e^{-\eta_h/\tau}\ . . \tag{6.22}$$

C_s^* is defined as $\sqrt{qZ_iT_e(1+\tau)/m_i}$, and the term $f(\tau)$ is included to allow the flux to agree with that obtained from a collisionless model of ion flow developed by Emmert *et al*.[81] $f(\tau)$ takes on values around $\sim 1/2$ as stated earlier in Eq. 6.2.

Equations 6.21 and 6.22 do not join smoothly at the point $\eta_p = \tau\ ln[(1+r)/r]$. Stangeby's model does not attempt to reconcile this difference by including a transition regime. Fortunately, the current collected by a Langmuir probe in the regime $\eta_p > \tau\ ln[(1+r)/r]$ is dominated by the electrons. The discontinuity in the total current due to the mismatch in the ion fluxes is therefore small enough to be neglected. In fact, it is a reasonable approximation to assume that Eq. 6.22 applies for the entire range of η_p.

6.2.4 Magnetized Langmuir Probe Characteristic

The total current collected by a Langmuir probe with projected area, A_p, can be obtained from Stangeby's magnetized probe model by combining Eqs. 6.18, 6.19, and 6.22, resulting in

$$\frac{I(\eta_p)}{q\ A_p\ n_0} = f(\tau)\ C_s^*\ e^{-\eta_h/\tau} - \frac{1}{4}\ \overline{C}_e\ \left[\frac{r}{1+re^{\eta_h-\eta_p}}\right] \tag{6.23}$$

when $\eta_p \leq \tau\ ln\left[\frac{1+r}{r}\right]$, and

$$\frac{I(\eta_p)}{q\ A_p\ n_0} = f(\tau)\ C_s^*\ e^{-\eta_h/\tau} - \frac{1}{4}\ \overline{C}_e\ \left[\frac{r}{1+r}\right] \tag{6.24}$$

when $\eta_p > \tau\ ln\left[\frac{1+r}{r}\right]$. The previously mentioned approximation for ion collection has been used in Eq. 6.24.

The Langmuir probe characteristic described by Eqs. 6.23 and 6.24 is plotted in Fig. 6.8 for various r parameters with $\tau \approx 2$ and $f(\tau) \approx 0.5$. Note that the characteristic in Fig. 6.5 is recovered for $r \to \infty$.

The probe floating potential of the Langmuir probe relative to the space potential is obtained from this model using Eqs. 6.23 and 6.20. The result is

$$\eta_f = \frac{V_f}{T_e} = \tau\ ln\left[1+\frac{\beta}{r}\right] + ln[\beta] \tag{6.25}$$

with

$$\beta = \frac{4\ f(\tau)\ C_s^*}{\overline{C}_e}\ . \tag{6.26}$$

In the limit that $f(\tau) \sim 1/2$, $T_i \to 0$, $Z_i = 0$, and $r \to \infty$, the earlier result for V_f in 6.5 is recovered.

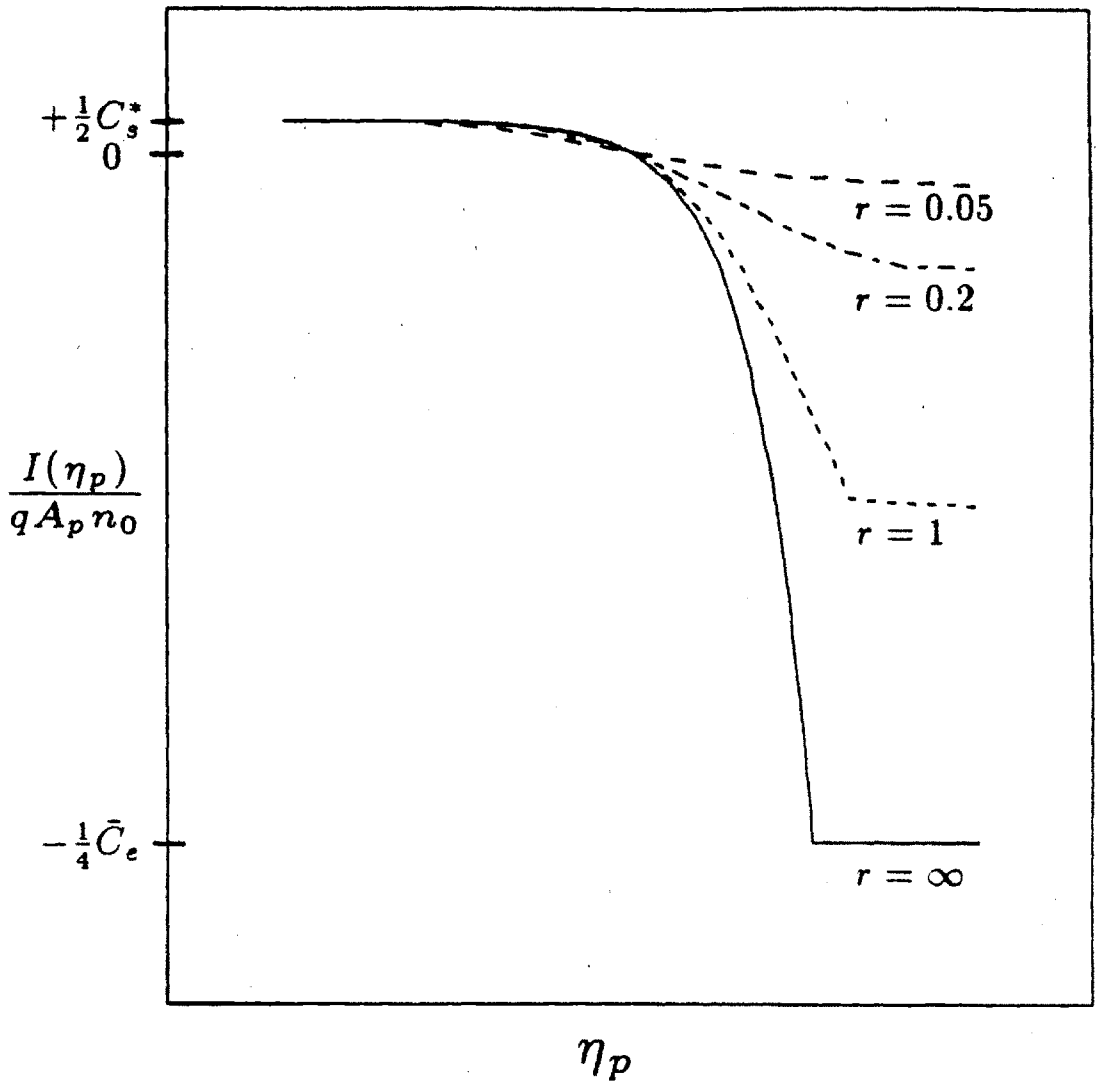

Figure 6.8 Magnetized Langmuir Probe Characteristic (Stangeby[19] model)

6.3 Fitting to the Langmuir Characteristic

The principle quantities which can be inferred from a Langmuir probe characteristic are ion saturation current, I_{sat}, electron temperature, T_e, and floating potential, V_f. Using the Stangeby model, it is also possible to obtain the reduction factor, r. These fitted values depend on the model that is selected for the characteristic and can also depend on the fitting technique that is used. When the probe is operated in a continuous ion saturation mode or continuous floating potential mode, measurements of $\tilde{I}_{sat}$ or $\tilde{V}_f$ can be obtained.

This section covers some important considerations in the fitting of Langmuir probe data starting with first the simple probe model and then the Stangeby model as was described in the previous section. Finally, techniques used to characterize fluctuating quantities such as $\tilde{n}$ and $\tilde{V}_s$ are discussed. Some comments about the optimum range of probe bias are included in closing.

6.3.1 A Typical DENSEPACK Langmuir Characteristic

Figure 6.9 shows a typical Langmuir characteristic from a probe on the DENSEPACK array during the steady state portion of the discharge. The trace was obtained by monitored current to the probe over a 10 msec period when the voltage was swept from -65 to $+40$ volts and back. The 8212 10 kHz digitizers record ≈ 100 data points at this time. The current-voltage data pairs are ordered according to voltage and displayed in Fig. 6.9 with straight lines connecting the points.

The ion saturation portion of the probe characteristic is clearly visible for probe voltages less than ~ -20 volts. In the range ~ -20 to $+20$ volts, the curve displays the electron transition regime and is approximated by an exponential function. At biases above $\sim +20$ volts, the trace deviates from a simple exponential and tends to flatten out. This suggests that electron saturation is being approached.

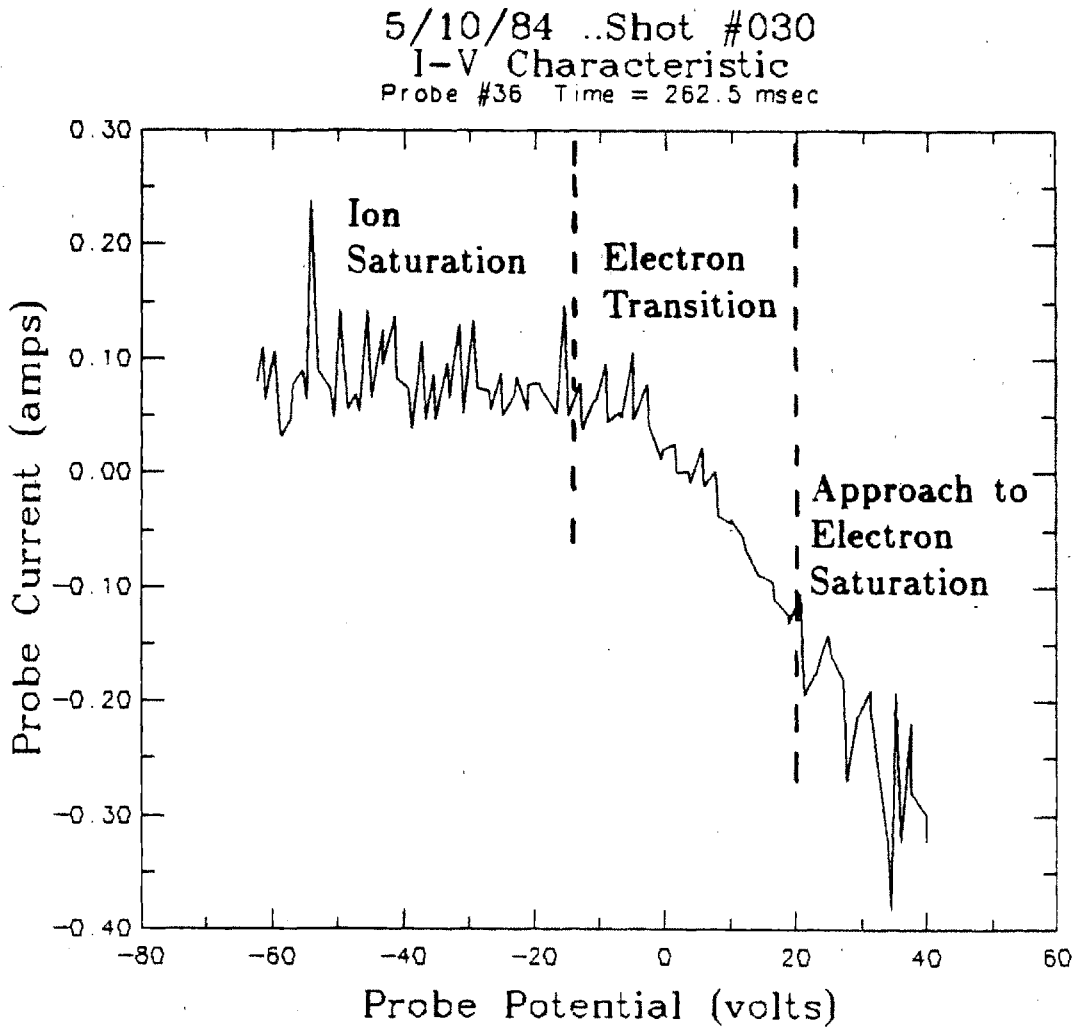

Figure 6.9 Typical DENSEPACK Langmuir Probe Characteristic

6.3.2 Estimating n_0, T_e from Simple Characteristic

The most straightforward approach in extracting plasma density and electron temperature from the probe characteristic is to use the simple model outlined in section 6.2.1. In this case, the measured I-V curve can be assumed to follow Eq. 6.7 within a random error, ϵ_r, up to some cut-off voltage, V_{knee}, where the model no longer applies:

$$\frac{I(V_p)}{q\ A_p\ n_0} \approx \frac{1}{2}\ C_s - \frac{1}{4}\ \overline{C}_e\ e^{(V_p - V_s)/T_e} \pm \epsilon_r \quad ; \quad \text{for} \quad V_p < V_{knee}\ . \tag{6.27}$$

The random error may be due to electronic noise or density fluctuations. In the latter case, the amplitude of ϵ_r is usually found to be proportional to the current as suggested by Fig. 6.9, but for simplicity it will be assumed independent of bias voltage in the following analysis. ϵ_r can be considered as a random error distributed according to a gaussian distribution with a standard deviation, σ_ϵ.

The strategy for fitting a probe characteristic is simply to select V_{knee} and find the best combination of n_0, T_e, and V_s that minimizes the difference between the data set and the ideal characteristic model. It is more convenient to write Eq. 6.27 for a discrete $\{I_i, V_{pi}\}$ data set as

$$I_i = I(V_{pi}) \approx I_{sat} - b\ e^{V_{pi}/T_e} \pm \epsilon_{ri} \quad ; \quad \text{for } V_{pi} < V_{knee} \tag{6.28}$$

since the ion saturation current, I_{sat}, is determined directly from the characteristic. Here, the space potential, V_s, is absorbed into the coefficient, b, and V_p is the bias voltage for each data point, i.

6.3.3 Estimating n_0, T_e: Logarithmic Approach

One procedure which is often used to estimate n_0 and T_e from a Langmuir trace utilizes the fact that only ion saturation current is sampled at large negative biases. An estimate of I_{sat} can therefore be made and subtracted from the characteristic at all probe voltages leaving only the exponential electron contribution. The electron temperature is simply determined by fitting a straight line to the logarithm of this difference. Once the temperature is known, the density can be inferred from I_{sat}. However, this procedure can lead into some problems particularly when ion saturation is not quite reached or the random error, σ_ϵ, in the data set is large.

Consider the estimate of I_{sat} as an average of k data points during the ion saturation portion of the characteristic,

$$I_{sat}^{est.} \approx \frac{1}{k} \sum_{i=1}^{k} I_i \pm \epsilon_{ri} \approx I_{sat} \pm \frac{\sigma_\epsilon}{\sqrt{k}} . \tag{6.29}$$

Including more data points reduces the uncertainty in $I_{sat}^{est.}$ by a factor $1/\sqrt{k}$ for random error contributions. Subtracting the data set given by Eq. 6.28 from $I_{sat}^{est.}$ and taking the log results in

$$ln(I_{sat}^{est.} - I_i) \approx ln\left[b\ e^{V_{pi}/T_e} \pm \epsilon_{ri} \pm \frac{\sigma_\epsilon}{\sqrt{k}}\right] . \tag{6.30}$$

When the exponential term dominates over the random error terms, a plot of Eq. 6.30 versus voltage yields a straight line with a slope characteristic of the inverse of the electron temperature. However for data points where the error terms become significant, Eq. 6.30 becomes independent of bias voltage. If these points are included in the straight line fit, the slope will become flatter and the electron temperature will be overestimated. In the extreme case when ϵ_{ri} dominates, a negative argument for the logarithm can result. This technique is

therefore limited on the low bias voltage side to data points where the exponential dominates and on the high bias voltage side by V_{knee}. Furthermore, a proper linear least square fitting treatment should include data weighting that is consistent with the logarithmic transformation.

6.3.4 Estimating n_0, T_e: Exponential Approach

A better approach is to accept the nonlinear nature of Eq. 6.28 and fit I_{sat}, b, and T_e simultaneously. The least squares fitting problem implied by Eq. 6.28 can be written as

$$\epsilon = \sum_{i=1}^{n} (I_i^{meas} - I_{sat} + b\ e^{V_{pi}/T_e})^2 \qquad (6.30b)$$

for n data points where I_i^{meas} is the measured current for each applied voltage, V_{pi}. The goal is to choose values of I_{sat}, b, and T_e that minimize the sum of the squared error, ϵ. At the optimum values of I_{sat} and b,

$$\frac{\partial \epsilon}{\partial I_{sat}} = 0 = \sum_{i=1}^{n} I_i^{meas} - n\ I_{sat} + b \sum_{i=1}^{n} e^{V_{pi}/T_e} \qquad (6.30c)$$

and

$$\frac{\partial \epsilon}{\partial b} = 0 = \sum_{i=1}^{n} e^{V_{pi}/T_e} I_i^{meas} - I_{sat} \sum_{i=1}^{n} e^{V_{pi}/T_e} + b \sum_{i=1}^{n} e^{2V_{pi}/T_e} . \qquad (6.30d)$$

From these two equations, I_{sat} and b can be solved for a given data set in terms of T_e. Thus, ϵ can be written in terms of T_e alone. A minimization of ϵ can therefore be performed by iteration of this single parameter. Once T_e is determined by this method, I_{sat} is readily obtained from Eqs. 6.30c and 6.30d.

This technique bypasses the undefined logarithm problem at negative biases, fits the data with uniform weighting, and does not require the Langmuir probe to operate at large negative biases in order to estimate I_{sat}. The only remaining problem lies in determining an appropriate high voltage cut-off value, V_{knee}.

The voltage at which Eq. 6.28 no longer descibes the electron collection part of the characteristic is a loose definition. Fortunately, it is only necessary

to obtain a rough estimate of this voltage, V_{knee}. The technique that is used for DENSEPACK data to estimate V_{knee} is based on an approach similar to the logarithmic fitting procedure outlined earlier. An estimate is made of the ion saturation current from the most negatively biased data. The new quantity, $Y_i = ln(I_{sat}^{est.} - I_i)$ as in Eq. 6.30, is calculated for all bias voltages. Only data points in which the exponential term dominates over the random error terms are accepted for negative biases. A plot of typical probe data processed in this way is presented in Fig. 6.10. At more positive biases, the curve deviates from this straight line and appears to follow another straight line. This tendency of the curve to exhibit a 'knee' is exploited to find a transition voltage, V_{knee}.

First, a value for V_{knee} is guessed. Then, straight lines are fitted to the data points $\{Y_i, V_{pi}\}$ on the left and right of V_{knee}. The intersection of these lines provides a new estimate for V_{knee}. The procedure is repeated until V_{knee} does not change or changes less than some minimum parameter. Characteristics in which V_{knee} cannot be determined in this way because of a bad probe bias range are discarded.

With V_{knee} determined, the three parameter non-linear fit of Eq. 6.28 can be applied to the data set. Figure 6.11 shows probe data and a corresponding fit using this method. The characteristic is fit well by an exponential up to V_{knee}. An estimate of I_{sat} and T_e is thereby obtained. The electron density can then be inferred by assuming a value for T_i (such as $T_i \approx 1\text{–}2 \times T_e$) and applying Eq. 6.27 for ion saturation.

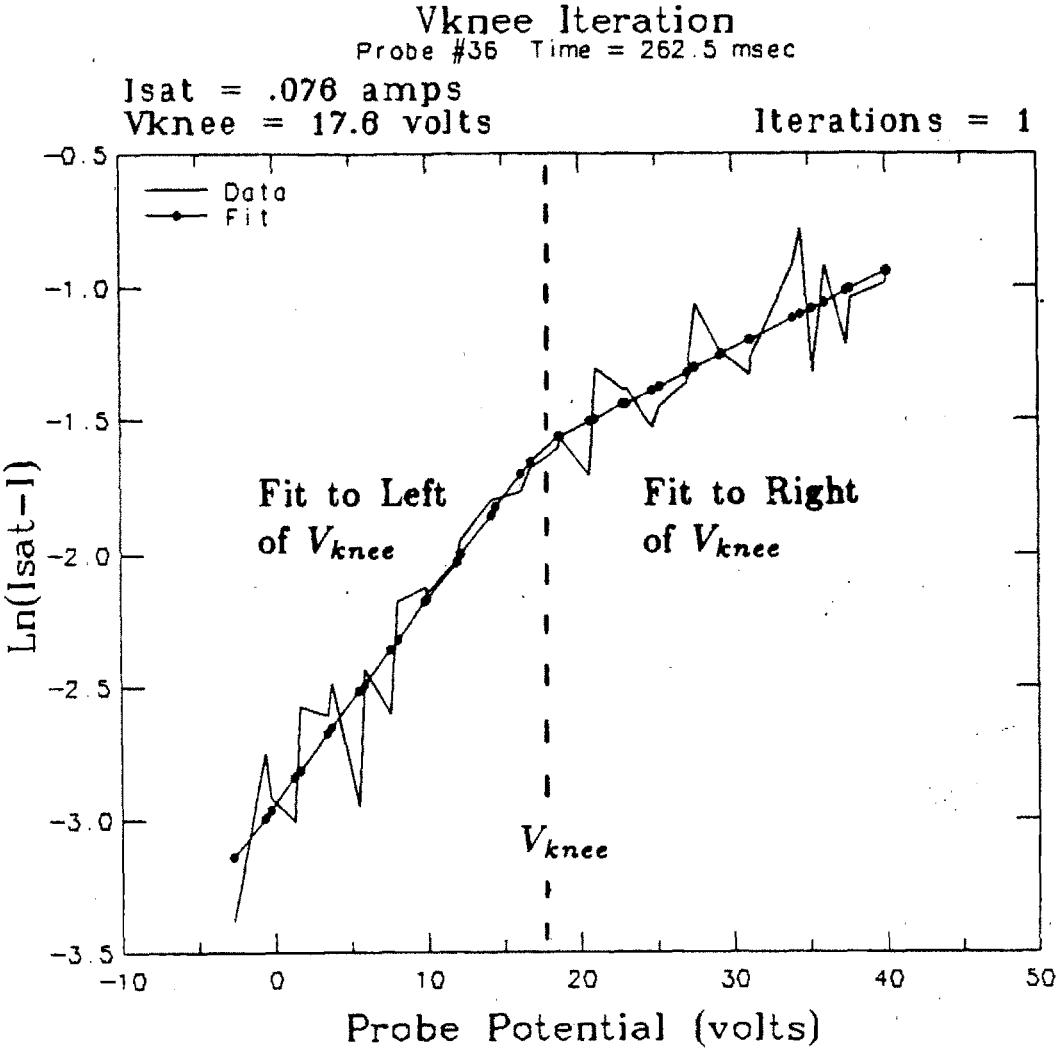

Figure 6.10 Iteration Process to Estimate V_{knee}

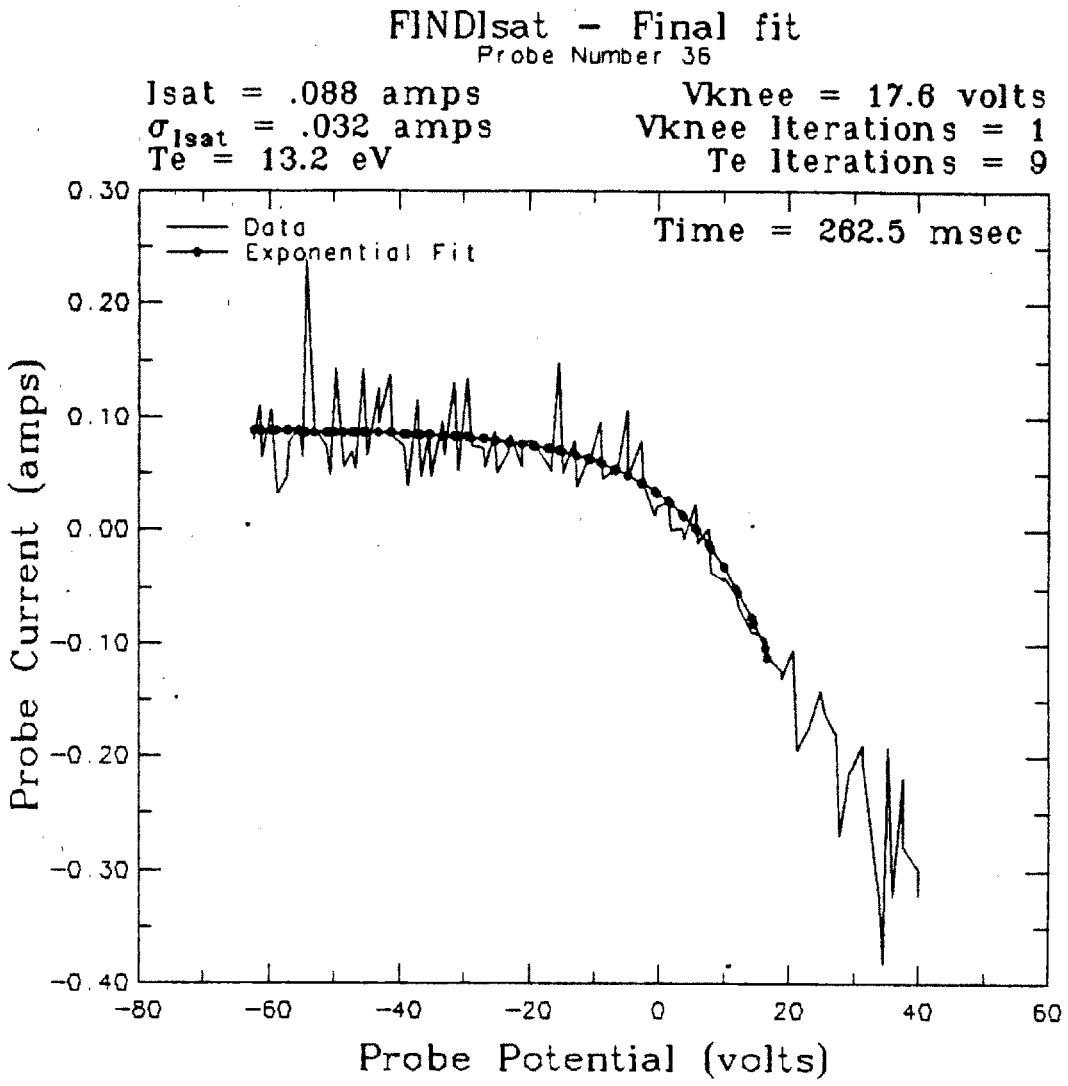

Figure 6.11 Exponential Fit to Langmuir Characteristic

6.3.5 Estimating n_0, T_e with finite r: Stangeby Model

The previous technique does not attempt to deal with the electron saturation portion of the characteristic. As discussed in section 6.2, the shape of the characteristic near electron saturation is determined by the rate of cross-field electron diffusion into the collecting flux tube. The reduction parameter, r, in Stangeby's model quantifies this effect. The previously discussed fitting technique leads to a reasonable estimate of the electron temperature; however, it is unsettling that points near electron saturation must be ignored. This section outlines a procedure that is used to fit n_0 and T_e to DENSEPACK data which attempts to include data points from the electron saturation portion of the probe characteristic.

The Stangeby model contained in Eqs. 6.23–6.26 can be written more conveniently as

$$I(\eta_p) \;=\; I_{sat}\left(e^{-\eta_h/\tau} \;-\; \frac{1}{\beta}\left[\frac{r}{1+r\;e^{\eta_h-\eta_p}}\right]\right) \tag{6.31}$$

when $\eta_p \leq \tau\; ln\left[\frac{1+r}{r}\right]$, and

$$I(\eta_p) \;=\; I_{sat}\left(e^{-\eta_h/\tau} \;-\; \frac{1}{\beta}\left[\frac{r}{1+r}\right]\right) \tag{6.32}$$

when $\eta_p > \tau\; ln\left[\frac{1+r}{r}\right]$. β is defined as

$$\beta \;=\; 4\; f(\tau)\; \sqrt{\frac{Z_i\;(1+\tau)\;\pi\;m_e}{8\;m_i}}\;, \tag{6.33}$$

and it is understood that η_p and η_h satisfy

$$\eta_p \;=\; \frac{V_p}{T_e}\;; \tag{6.34}$$

$$\eta_h \;=\; \tau \; ln\Big[r^{-1}\; e^{\eta_p - \eta_h} + 1\Big] \;. \tag{6.35}$$

For an assumed value of τ $(= T_i/T_e Z_i)$, an optimum combination of the parameters I_{sat}, T_e, and r can, in principle, be fit to probe data using Eqs. 6.31–6.35. This problem is complicated by the fact that $I(\eta_p)$ depends non-linearly on T_e and r with a transcendental relationship for the intermediate quantity, η_h. Also, the model equation changes form at $\eta_p = \tau \; ln\big[\frac{1+r}{r}\big]$. Nevertheless, there is a systematic way to arrive at optimum I_{sat}, T_e, and r values.

At large negative biases, the electron term vanishes in Eq. 6.31 and $\eta_h \rightarrow 0$. Thus, only the ion saturation current is collected. I_{sat} can therefore be determined independently of T_e and r using data at these biases in a way similar to Eq. 6.29. However, it is better not to rely on the probe achieving ion saturation at all. I_{sat} and a first guess estimate of T_e can be best obtained by using the exponential fitting procedure outlined in the previous section. In the limit that η_p becomes a large negative value, the exponential model and the Stangeby model must agree. Therefore, this value for I_{sat} is a good estimate. Now the non-linear fitting problem reduces to a two parameter iteration for the best combination of T_e and r with the first try value for T_e already determined.

A fast numerical algorithm (discussed in Appendix D) was written to iterate Eqs. 6.31–6.35 for an optimum combination of T_e and r. Figure 6.12 displays a typical fit to a complete DENSEPACK probe characteristic obtained in this manner. For this fit, it was assumed that $\tau \approx 2$. The reduction parameter, r, is found to be around 0.2, indicating that perpendicular diffusion into the flux tube is indeed important for DENSEPACK probe data.

The inferred values for the electron temperature using the Stangeby model is notably different than that obtained from the exponential model. For this fit, T_e is ≈ 8 eV, while for the same data fit by an exponential in Fig. 6.11, T_e is found to be ≈ 13 eV. It appears that the electron temperature inferred by the Stangeby technique is lower because, by including the r parameter, the fitting function rolls over more gently at lower T_e values. This implies that it may be necessary to incorporate such effects as a collecting flux tube into the data analysis. In any case, it demonstrates a situation where the electron temperature can be model-dependent.

Finally, with the electron temperature determined, the electron density can be obtained by this model. From the value of I_{sat}, n_0 can be calculated using

$$n_0 = \frac{I_{sat}}{q\ A_p\ f(\tau)\ C_s^*} \ . \tag{6.36}$$

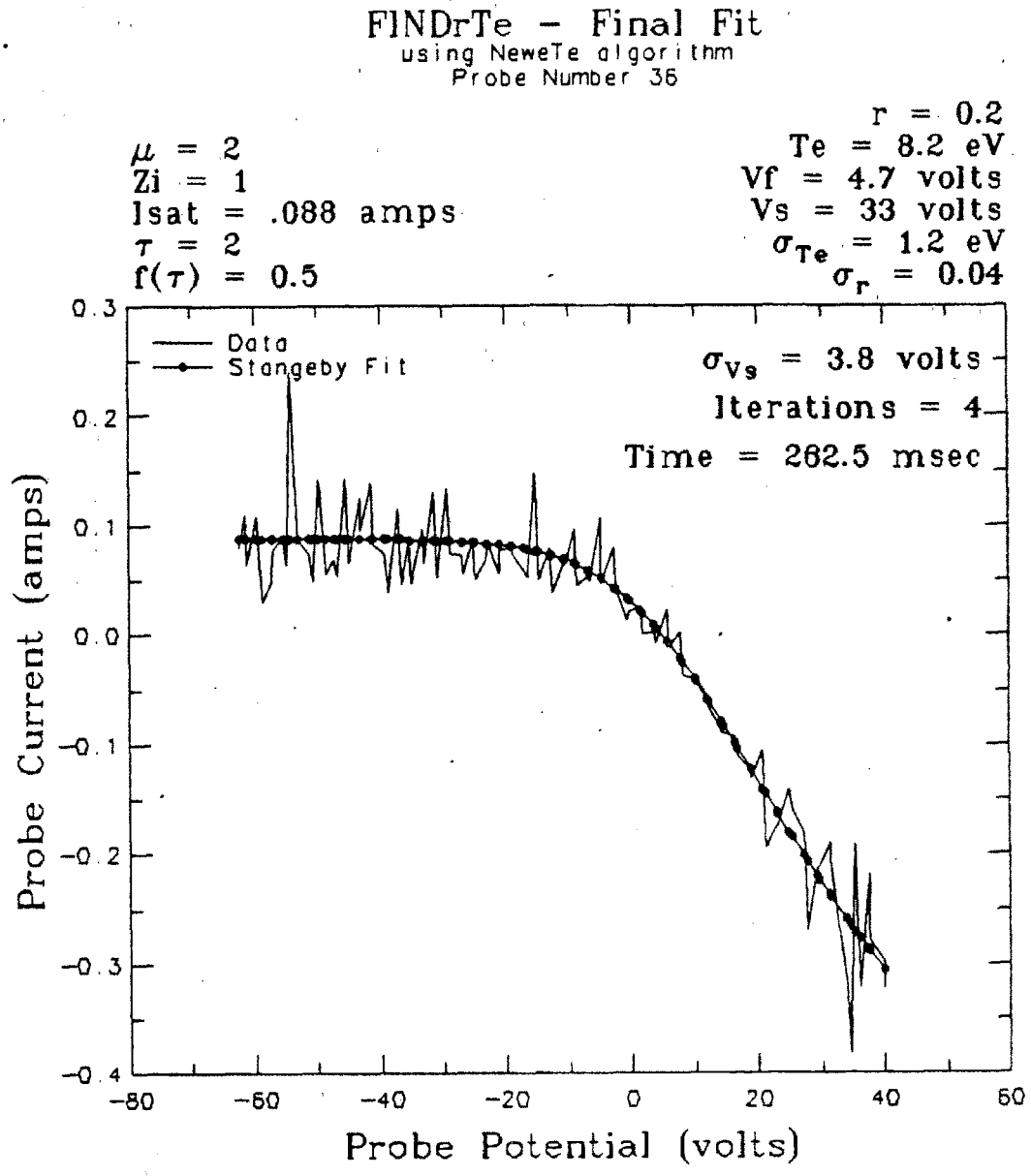

Figure 6.12 Fit to Full Langmuir Characteristic Using Stangeby's Model

6.3.6 Comparison of Exponential Model and Stangeby Model

As shown in Figs. 6.11 and 6.12, both the exponential and Stangeby probe characteristic models fit the data reasonably well. It is therefore difficult to readily eliminate one fitting procedure in favor of the other. However, the difference in the inferred T_e of 8 eV for the Stangeby model versus 13 eV for the exponential model is worrisome and places an emphasis on identifying the more accurate fitting model.

Recent results from a combination retarding field energy analyzer/Langmuir probe/heat flux probe diagnostic[94] operating in the Alcator C limiter shadow plasma offers more information on this problem. Data obtained simultaneously by the retarding field energy analyzer and Langmuir probe sections of this diagnostic show that in most, but not all cases, the electron temperatures inferred from the Langmuir probe using the exponential fitting algorithm more closely agree with the electron temperature inferred from the energy analyzer. The electron temperature obtained using the Stangeby model is consistently lower than the exponential model by $\approx$ 20–40%. In some cases the Stangeby model T_e more closely agrees with T_e from the analyzer, but the fits to the analyzer data may merely be coincidently low. It appears, therefore, that although the Stangeby model nicely reproduces the entire probe characteristic, the inferred temperature should not be taken as absolutely correct. Perhaps the physics in the model is not precise enough, or there are some systematic errors associated with energy analyzer and/or Langmuir probe electron temperatures.

No attempt is made to eliminate one fitting procedure in favor of the other in this thesis. Fortunately, temperatures obtained by either model show similar spatial and temporal variations, only differing in absolute magnitude. The temperature data is therefore treated with allowance for some systematic error. Typically, results from the exponential model could be predicted from the Stangeby model by multiplying T_e by a factor of 1.2–1.8. Both algorithms were

used in reducing DENSEPACK probe data. The particular fitting algorithm used to generate a given plot in this thesis is stated in the text.

One benefit in using the Stangeby model over the exponential model is that an estimate of the reduction parameter, r, is obtained. However, once again the absolute value of the r parameter obtained by Stangeby's model should be treated with caution. It is found for DENSEPACK data that the magnitude of r depends on the assumed ratio of T_i/T_e. Figure 6.13 illustrates two fits to the same probe data assuming $T_i/T_e = 1$ (a) and $T_i/T_e = 3$ (b). Note that the inferred electron temperature does not change significantly. However, the inferred r nearly doubles from 0.15 to 0.27.

It is interesting to note the r changes as τ changes to hold $\lambda_{ei}\sqrt{\alpha}$ roughly constant in Eq. 6.17. Thus, it may be still possible to extract information about $D_\perp/D_\parallel$ using Stangeby's model. The only drawback lies in obtaining a good estimate for the absolute value of T_e. Further comments on obtaining $D_\perp/D_\parallel$ from Stangeby's model is included in section 7.2 where 2-D plots of DENSEPACK results are presented.

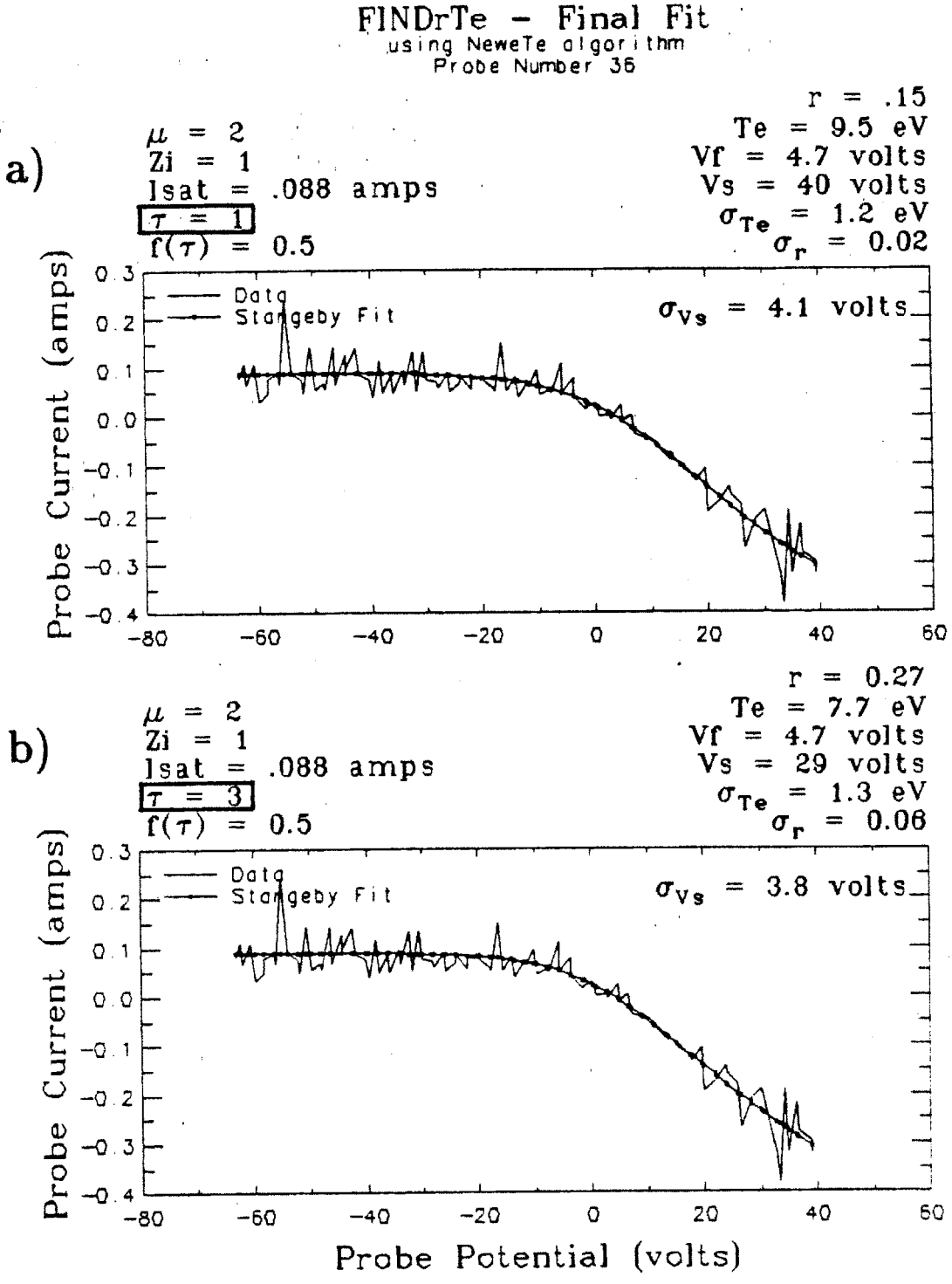

Figure 6.13 Sensitivity of Inferred T_e and r to Assumed T_i/T_e Ratio (Stangeby fit)

6.3.7 Fluctuating Quantities

When a probe is continuously biased in ion saturation mode or allowed to float, measurements of $\tilde{I}_{sat}$ or $\tilde{V}_f$ can be made. Experimental techniques for the study of fluctuations using probes have been employed extensively by Zweben[38,40,41,42] in recent pioneering work on turbulence in the edge of tokamak plasmas. The fluctuating quantity is typically recorded digitally on a fast data logger and fourier transformed to yield a fluctuation spectrum. Various statistical techniques[39,91,92] such as autocorrelation and crosscorrelation of probe signals can be employed to infer the wavenumber and frequency spectrum of the turbulence.

Fluctuations in the ion saturation current are in general due to fluctuations in density and temperature through Eq. 6.36. However, it has been shown by fast-sweeping Langmuir probes to infer electron temperature and by correlating $\tilde{I}_{sat}$ with visible light emission or CO_2 laser scattering that variations in I_{sat} are most likely due to density fluctuations and not temperature fluctuations. Thus, $\tilde{I}_{sat}$ obtained from probe data is often translated into $\tilde{n}_0$.

In a similar manner, fluctuations in V_f are sometimes assumed to be primarily due to fluctuations in V_s and not in T_e as is suggested by Eq. 6.6. It is therefore possible with a single Langmuir probe to obtain information about both $\tilde{n}$ and $\tilde{V}_s$, but not simultaneously. Ideally, one would like to record $\tilde{I}_{sat}$ and $\tilde{V}_f$ simultaneously in order to correlate density fluctuations with potential fluctuations and estimate a turbulent $\tilde{n}$, $\tilde{V}_s$ transport flux as discussed in section 2.4.3. However, this type of fluctuation analysis is beyond the scope of the present work with the DENSEPACK array. Fluctuation information obtained during the DENSEPACK experiment is limited primarily to recording the magnitude and spectral features of ion saturation current fluctuations.

Data obtained by DENSEPACK probes was processed to yield information about fluctuations in two ways. Since the primary goal of DENSEPACK was to record poloidal variations in density and temperature, the gang probe voltage was swept to generate Langmuir characteristics most of the time. Thus, the first way in which fluctuation information was obtained was to examine the ion saturation current during the portion of the characteristic when the probe was biased in ion saturation.

For some channels, fast LeCroy 8210 data loggers digitizing at 1 MHz recorded $\approx$ 1000 samples during the ion saturation portion of a sweep. Figure 6.14 displays a Langmuir sweep recorded by a 8210 fast digitizer. This characteristic includes $\approx$ 7,000 data points (shown here as dots) recorded during part of a 10 msec sweep. A fit based on the Stangeby model (solid line) is made to the data in order to demonstrate the goodness of fit for this case of very good statistics and to illustrate the level of fluctuation that typically occurs in the data sample. Data points in ion saturation indicated on this graph are typically fast fourier transformed in time to yield spectral information about the fluctuations.

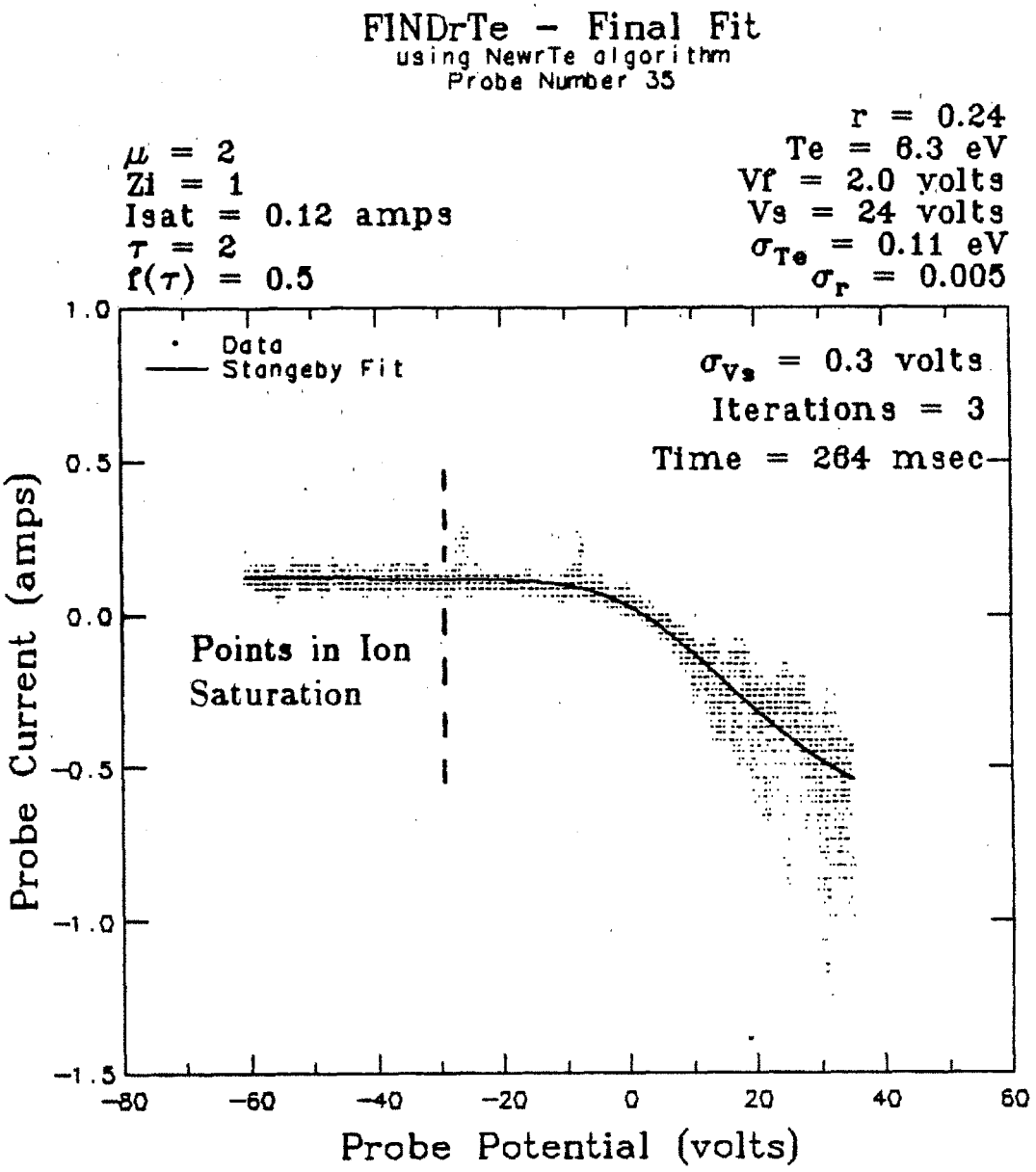

Figure 6.14 Langmuir Characteristic Recorded by 8210 Data Logger with Stangeby Fit

The ion saturation portion of the probe characteristic was also processed for all active probes using the data recorded by the 8212 data loggers. This data was not digitized fast enough to yield spectral information; however, an estimate of the RMS deviation in the ion saturation current about the mean was calculated. When divided by the average ion saturation current, this number quantifies the relative level of $\tilde{n}/n$ turbulence at that location in the plasma.

The second way in which fluctuations were examined was by holding the probes continuously in ion saturation. For a limited number of discharges, the probes were also allowed to float continuously to record floating potential fluctuations. However, both these measurements had the drawback that the density and temperature could not be simulatenously obtained, and therefore they were not performed very often.

6.3.8 Optimum Probe Bias Range and Waveform

One important decision that an experimentalist must make when designing a Langmuir probe system is choosing an optimum probe bias range and bias waveform. Ideally, one would like to record the complete probe characteristic slowly from large negative biases to large positive biases with very fine current and voltage resolution. In practice, however, the probe usually cannot withstand the power flux associated with drawing large currents, particularly in electron saturation. In addition, plasma parameters may be changing in time, forcing one to sweep the probe through a characteristic quickly. At the other extreme, a very fast changing probe voltage can result in displacement currents from stray capacitances to appear as probe signals.

Using the exponential or Stangeby model of the probe characteristic discussed earlier, it is not necessary to achieve full ion or electron saturation in order to infer plasma density and temperature. The probe bias range can be adjusted so that a relatively flat ion saturation begins to appear at the negative-most biases, and a deviation from exponential begins to appear at the positive-most biases. In this way, the exponential model or Stangeby model will yield a reasonable estimate for I_{sat}. Also, the algorithm will be able to find the 'knee' in the electron portion of the curve where the 'r' parameter begins to take over. This is the strategy that was used in operating DENSEPACK probes and yielded I-V characteristics such as in Fig. 6.12.

The sweep time and digitization rate should be chosen so that at least 50–100 data points are recorded during a single sweep. This allows good statistics and enables the fitting algorithms to converge reliably. A sweep time of 5–10 ms with 10 kHz digitizers was chosen for DENSEPACK probes. Over the 5–10 ms period, plasma parameters in the Alcator C edge plasma were roughly constant. This sweep rate was found to pose no capacitance coupling problems.

The shape of the probe bias waveform provides an additional degree of freedom. Waveforms from a pure sinusoid to a sawtooth have been used to sweep Langmuir probes. Since the electron temperature is the most uncertain parameter obtained from fitting to the probe characteristic, one would like to choose a bias waveform that aids the fitting algorithm in estimating T_e. The electron temperature is determined primarily by points in the transition region of the probe characteristic. An ideal waveform would therefore sweep slowly in this region, generating more data points there. Additionally, one would like to minimize the time spent in ion and electron saturation, thereby reducing the time-integrated heat flux to the probe.

Figure 6.15 displays three waveforms that could be used to bias a Langmuir probe. Although a sinusoidal waveform is pleasing in that it contains only one frequency component, it is not the best choice for a probe bias. Most of the time the probe is held in ion or electron saturation with a sinusoid. Few data points are sampled in the transition region. A better choice in this respect might be a triangular waveform or a special waveform as in Fig. 6.15 (b) and (c).

The RMS bias voltage about the mean is a simple figure of merit which can be used to compare the amount of time spent in ion or electron saturation relative to the time spent in the transition region for different waveforms. Using this criterion, nearly a factor of 2 reduction in the time-integrated heat flux can result by using a special waveform as in Fig. 6.15 (c).

For simplicity, a triangular waveform was used to drive the DENSEPACK probe array. However, with the advent of software programmable waveform generators, special waveforms of any shape can be used. In any case, it is advantageous to select a waveform that is symmetric in time. This allows the option for positive-going and negative-going sweeps to be folded together to form a single sweep. Fitting to this composite sweep, any capacitance coupling contributions in the data tend to cancel out.

a) Sinusoid

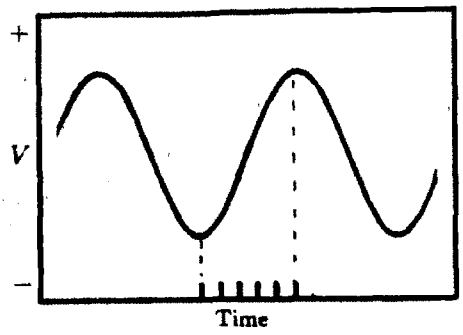

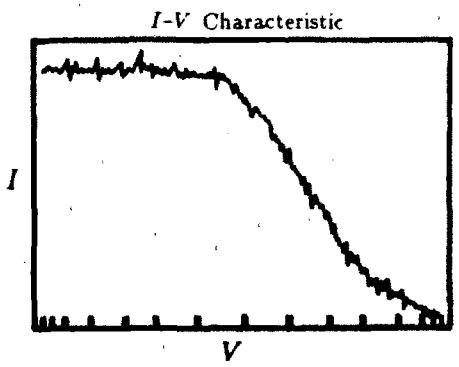

$V_{rms} = 0.577\ V_{max}$

b) Triangular

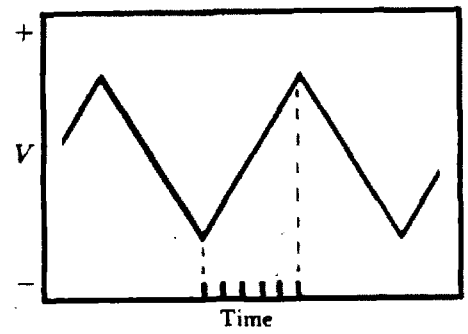

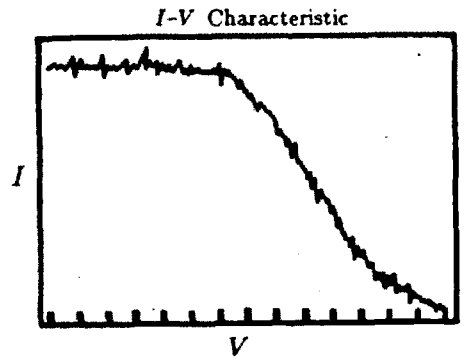

$V_{rms} = 0.707\ V_{max}$

c) Special (arcsine)

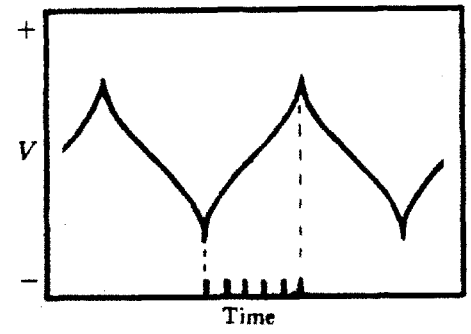

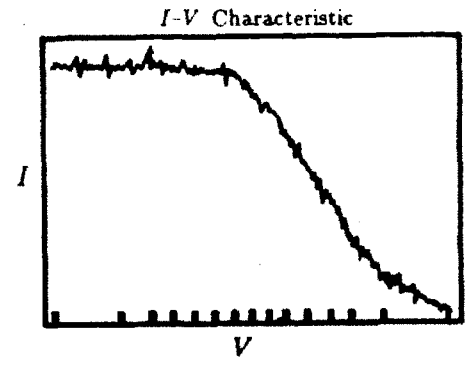

$V_{rms} = 0.435\ V_{max}$

Figure 6.15 Some Probe Bias Waveforms

III EXPERIMENTAL RESULTS

CHAPTER 7

POLOIDAL STRUCTURE OF LIMITER SHADOW PLASMA

The edge plasma in Alcator C was determined by DENSEPACK to be highly asymmetric independent of the occurence of a MARFE. A relatively high density and temperature plasma was detected on the top and bottom of the poloidal cross-section and the density scrape-off length was measured to be short on the inside (~ 0.15 cm) and long on the outside (~ 0.8 cm). In addition, the probe floating potential was found to depend on poloidal angle. A $-sin\theta$ variation was typically recorded, consistent in sign and magnitude with charge separation in the edge plasma due to $\underline{B} \times \nabla B$ particle drifts. This 2-D structure of the limiter shadow plasma as inferred from DENSEPACK is presented in sections 7.1 and 7.2.

The fluctuation spectrum in ion saturation current, $S(\omega)$, at various poloidal angles was also recorded for a number of shots. The probe spacing on the DENSEPACK probe array ($\sim$ 1 cm) was large compared to the typical spatial correlation length for fluctuations ($\sim 2\pi/k_\perp \approx 6\pi\rho_s \approx 0.1$ cm).[14] As a result, a cross-correlation of signals between probes did not reveal any significant coherence. It was also found that $\tilde{J}/\bar{J}$ ($\approx \tilde{n}/\bar{n}$) recorded at various poloidal angles did not vary in any systematic way, independent of central and edge plasma parameters. Fluctuation spectra and poloidal variations in $\tilde{J}/\bar{J}$ are presented in section 7.3.

7.1 Shadow Parameters versus Angle, Radius, and Time

The reduced DENSEPACK data file generated for each shot includes plasma density, electron temperature, and floating potential as a function of poloidal angle, minor radius, and time. Additional parameters which can be inferred are pressure, scrape-off length, and space potential. The reduction factor, r, obtained from the probe fitting algorithm is also recorded and offers information about perpendicular diffusion through Eq. 6.17.

Clearly, a presentation of all these edge parameters as a function of angle, radius, and time for various central plasma parameters can easily lead to a confused picture of the edge plasma. Consequently, this section focuses on the general spatial and temporal variation of limiter shadow plasma parameters in typical Alcator C discharges. A more detailed look at the poloidal structure during the steady state portion of the discharge is presented in section 7.2. The variation of edge parameters with changing central plasma parameters is presented later in chapter 9.

7.1.1 Edge Density

The plasma density in the limiter shadow region of Alcator C was found by DENSEPACK to be a strong function of poloidal angle. Figure 7.1 displays density at a radius of 16.8 cm versus poloidal angle and time as both a 3-D surface and a contour plot. The diagram of DENSEPACK indicates which probes were operating during this shot ($\circ$ and $\bullet$) and the poloidal location of probes at $r = 16.8$ cm which generated this data ($\bullet$). A single poloidal profile at 250 msec is also plotted. Central parameters were $\overline{n}_e \approx 2 \times 10^{14}/\mathrm{cm}^3$, $I_p \approx 350$ kA, $B_t \approx 8$ tesla, in deuterium plasma. Each data point was generated from a fit of two 5 msec Langmuir sweeps folded together. No poloidal or temporal smoothing was performed for the plots in this figure.

The most striking feature in this data is the poloidal variation of the density. Density maxima appeared on the top and bottom of the poloidal cross-section while minima appear on the inside and outside. The lowest densities for a given radius always appeared on the inside midplane. In fact, some probes along the inside wall were not used on this day because the collection current was found to be too low there.

There is no immediately obvious reason why the density should exhibit such a poloidal asymmetry. For this data and the data shown in the rest of this chapter, the limiter configuration was as shown in Fig. 5.3. Given that the limiters are poloidally symmetric, the edge plasma should be scraped off with poloidal uniformity. However, despite of this limiter configuration, it was found that the edge plasma displayed a strong poloidal asymmetry.

The sharpest poloidal gradient was detected by two probes near the 270^0 location. Density changed by $\sim 2 \times 10^{13}/\mathrm{cm}^3$ in a poloidal distance of ~ 3 cm. The poloidal structure was established quickly ($\lesssim 20$ msec) and persisted throughout the duration of the discharge. Data in Fig. 7.1 is cut-off in time for display purposes at 400 msec. The structure in the density profile at longer times during current ramp-down remains similar, displaying a smooth, decreasing level to plasma termination.

The two density peaks shown in Fig. 7.1 achieve roughly the same level. $n_e \approx 5 \times 10^{13}/\mathrm{cm}^3$. However, the usual value for the bottom peak was typically 20% lower than the top peak. When the toroidal field was reversed, the bottom peak became the larger in almost a symmetric way. This finding is reminiscent of up-down asymmetries in the edge impurity radiation on Alcator A[121] and PDX[122] as well as the pressure in the divertor chambers of ASDEX,[123] all of which depended on the direction of the magnetic field. Nevertheless, it should be pointed out that comparing density peaks measured by DENSEPACK can be misleading since the highest density might have occurred in the top and

bottom 40^0 gaps between probes. In any case this top-bottom variation was small compared to the dominant poloidal variation in density.

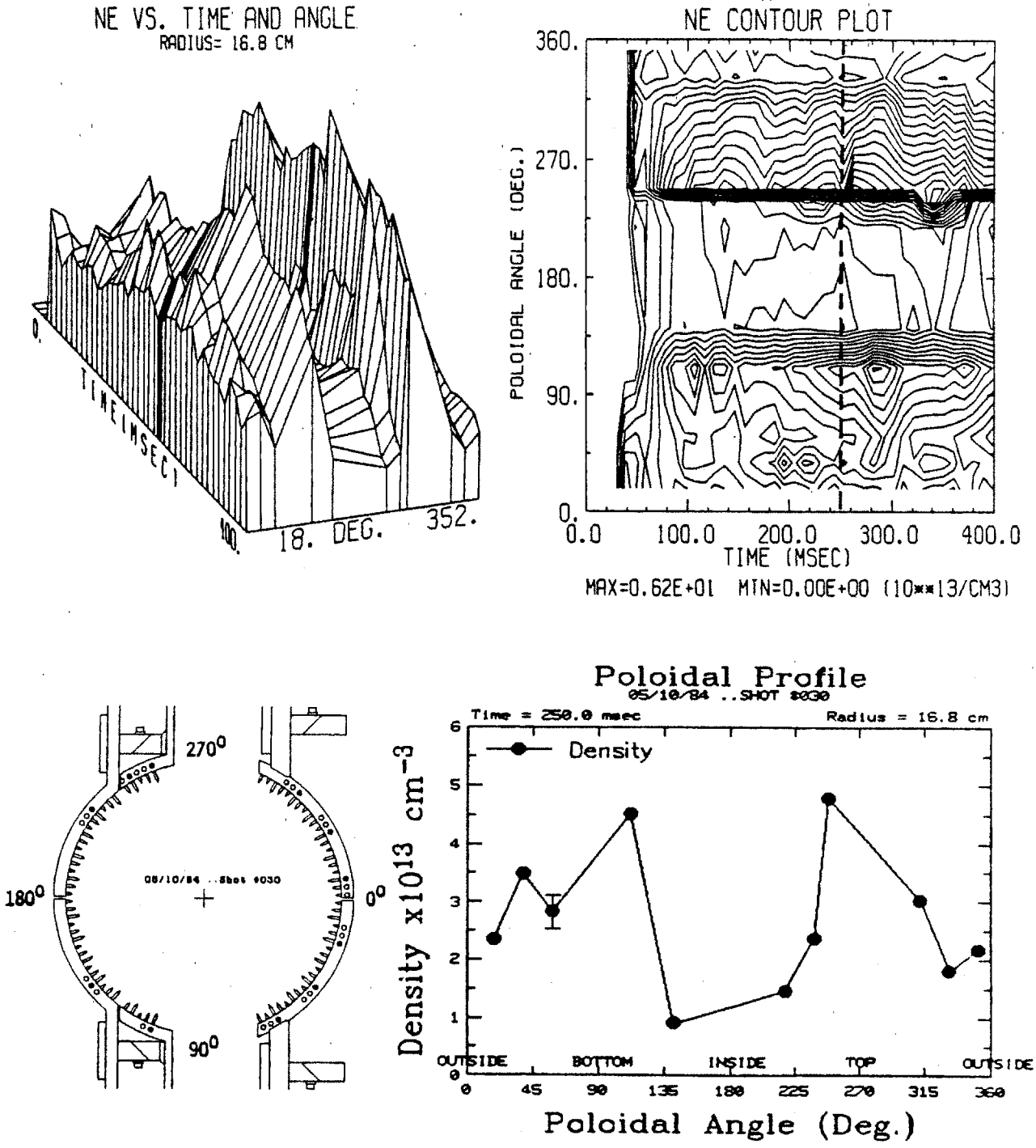

Figure 7.1 Density at $r = 16.8$ cm vs. Angle and Time

The poloidal asymmetry in density becomes more pronounced at larger minor radii. Figure 7.2 shows poloidal density profiles at 250 msec for the three DENSEPACK radii of 16.8, 17.2, and 17.6 cm in a $\overline{n}_e \approx 1.8 \times 10^{14}/\mathrm{cm}^3$, 200 kA, 8 tesla, hydrogen discharge. The positions of the probes on the DENSEPACK backbone that generated this data are also shown. The density scale for the 17.2 and 17.6 cm data is multiplied by factors of 2 and 4 respectively for ease of comparison. The density measured by probes near the inside midplane (180^0) at $r = 17.6$ cm is at or below a level of $7 \times 10^{10}/\mathrm{cm}^3$, while near the top and bottom locations the density is on the order $\sim 2 \times 10^{12}/\mathrm{cm}^3$. This is at least a factor of 25 density variation in poloidal angle at this radius.

The locations of the density maxima in poloidal angle appear to be a function of minor radius although the exact location is not easy to discern with this probe spacing. At $r = 17.6$ cm, the maximum density data points change location by $\approx 45^0$ relative to the 16.8 cm data, moving toward the outside midplane. This implies that the actual location of the density maximum changes from at least a few degrees to $\approx 45^0$ over a radial span of 0.8 cm. Unfortunately, the density maxima occur in the two regions where there are no probes. By biasing many close-spaced probes near these regions, it was found that the locations of the density maxima occurred in the gaps so that their positions still could not be resolved.

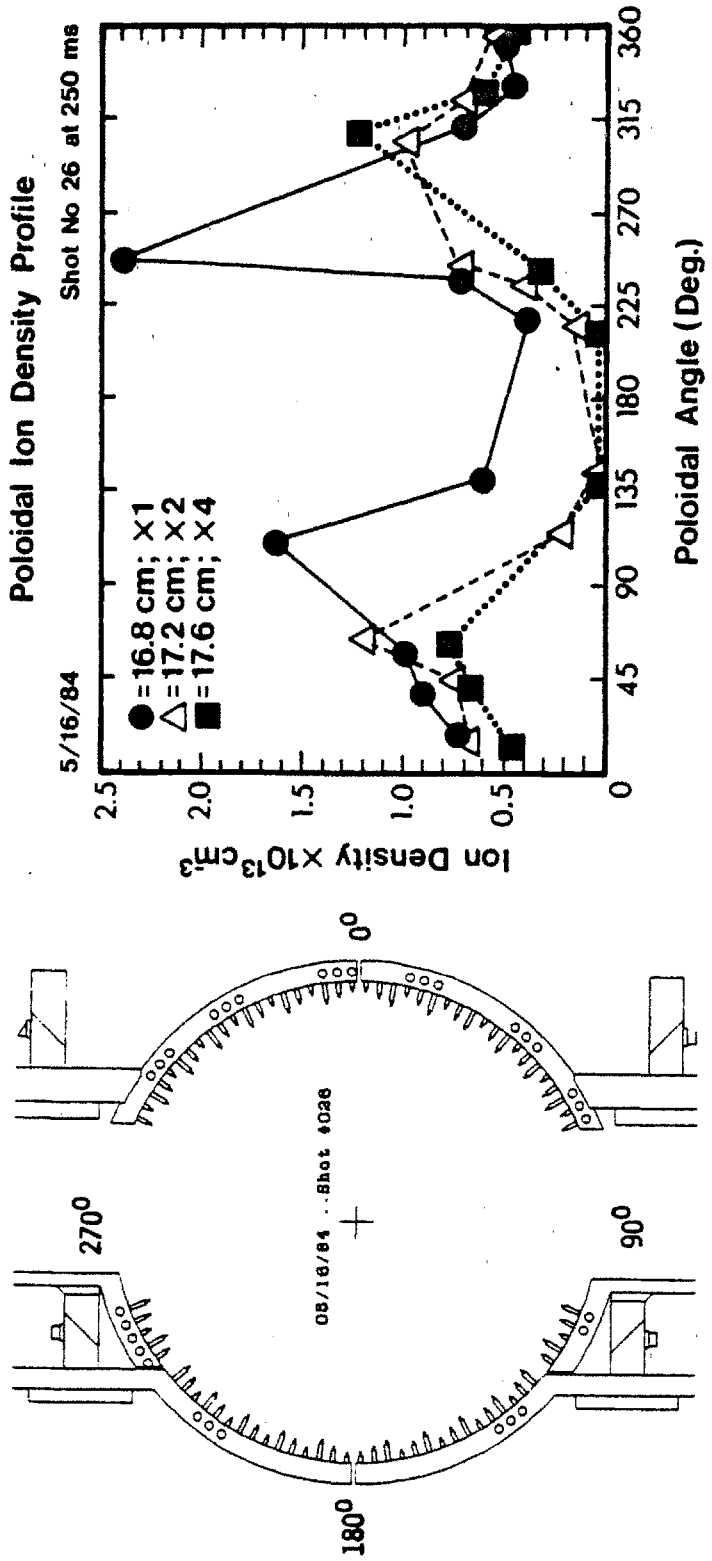

Figure 7.2 Limiter Shadow Density vs. Radius and Angle

The poloidal variation of plasma density along the inside wall is displayed with high spatial resolution at a radius of 16.8 cm in Fig. 7.3. The poloidal density gradient which appeared across only two probes in Fig. 7.1 is shown to be smoothly varying over three or more data points. This verifies that the density variation displayed previously is not due to a bad probe or some instrumental artifact.

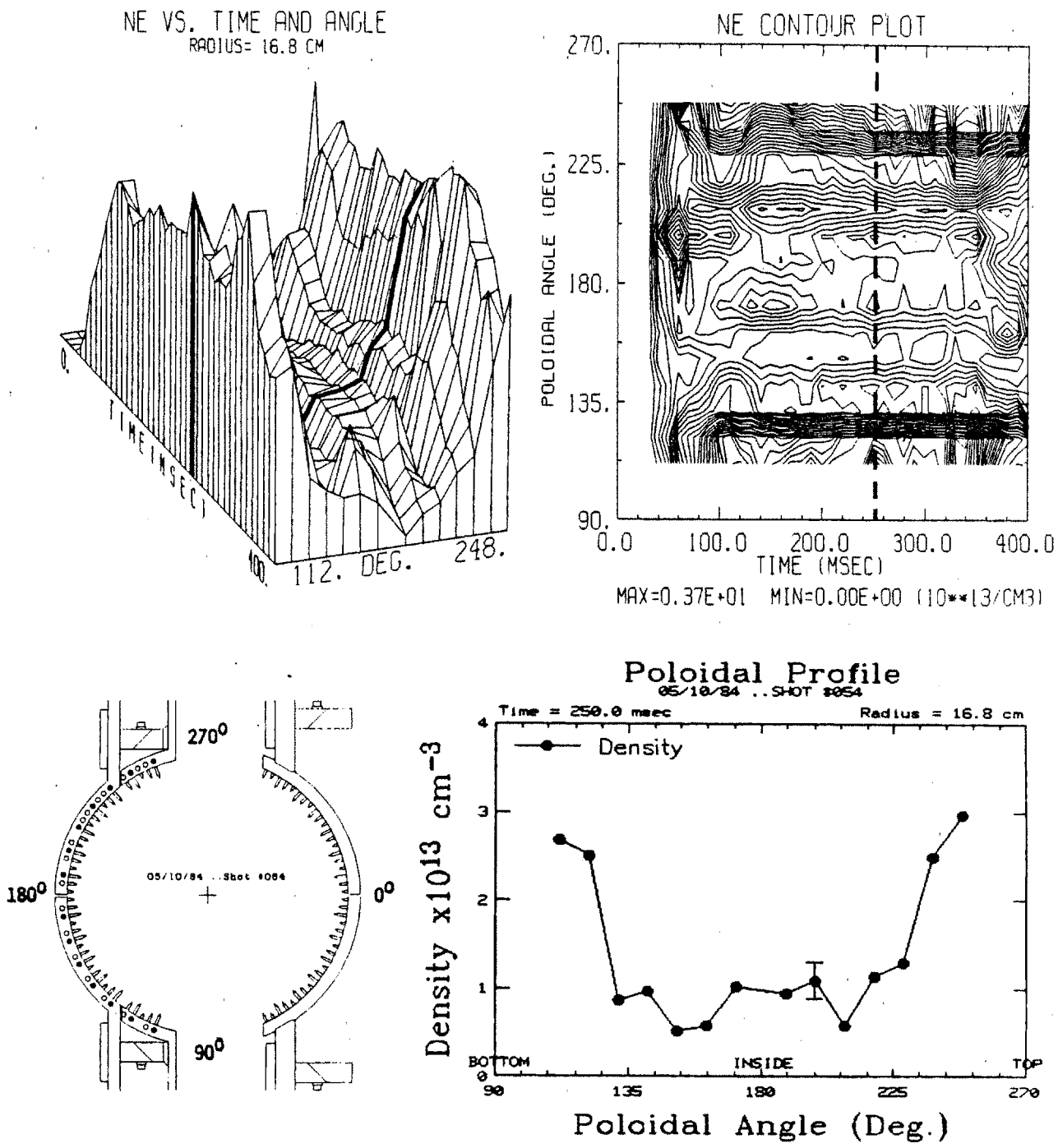

Figure 7.3 High Spatial Resolution of Plasma Density at $r = 16.8$ cm Along Inside Wall vs. Angle and Time

7.1.2 Temperature

The temperature profile in the limiter shadow plasma was found to exhibit a poloidal variation similiar to the density profile. Figure 7.4 shows plots of temperature data points in a similar format and for the same probe arrangement as displayed in Fig. 7.1. The temperature data points were obtained by performing a 20 msec time average of temperatures inferred by the Stangeby model (section 6.3.5).

One might expect that the temperature would exhibit a poloidal variation such that the plasma pressure remains relatively independent of angle. However, the reverse was found to be true. Poloidal positions of electron temperature maxima and minima coincide with locations of density maxima and minima.

A low temperature point always occurred on the inside. Figure 7.4 shows the lowest temperature at this radius occurring at $\theta \approx 225^0$. It is interesting to note that this is the typical poloidal position where the MARFE phenomenon occurs in Alcator C. In fact, this discharge happened to display a MARFE at this location throughout the duration of the shot. Nevertheless, in discharges in which a MARFE did not occur, this poloidal variation in temperature generally still existed. However, the minimum temperature in the non-MARFE case was not as low as ~ 5 eV at 16.8 cm as is displayed here.

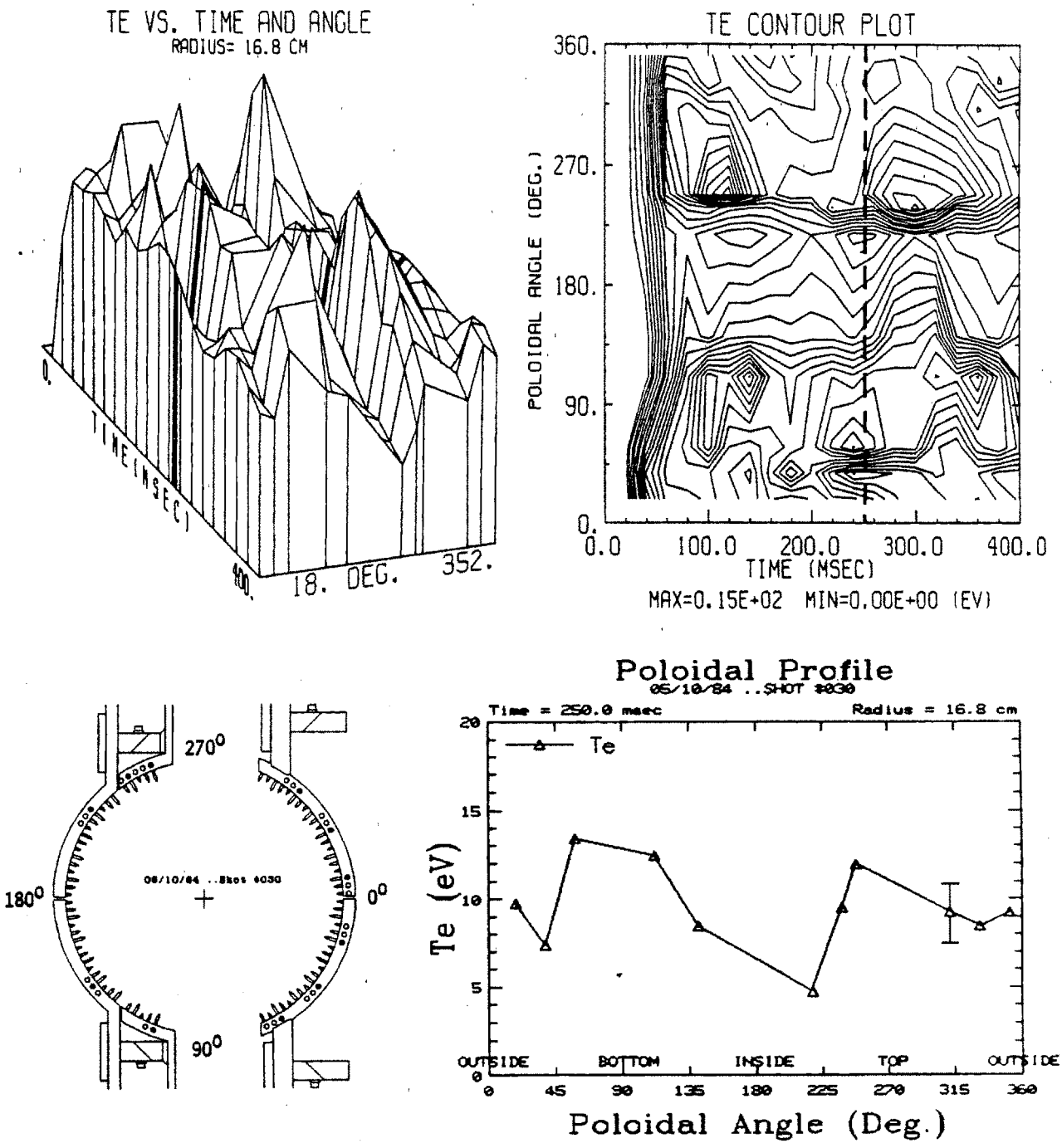

Figure 7.4 Electron Temperature at $r = 16.8$ cm vs. Angle and Time

The poloidal variation in electron temperature was not as dramatic as density. Contrary to the density variation, the poloidal variation in temperature became less pronounced at larger minor radii. Figure 7.5 displays poloidal electron temperature profiles at the three DENSEPACK radii. At 17.2 and 17.6 cm, most of the poloidal variation is within the experimental uncertainty, although there is a suggestion that the poloidal position of temperature maxima is a function of minor radius similar to the density in Fig. 7.2. In any case, the temperature was found to be a weak function of minor radius.

In some cases, the radial temperature profile appeared to invert. Data points at 315^0 in this figure show that the electron temperature increases in minor radius at this poloidal location. At first it was thought that there was a problem with the fitting algorithm or that one or two probes were mislabelled. Yet, no such problems were found, and this inverted temperature data remains as a curiosity. However, in most other discharges this feature was not seen.

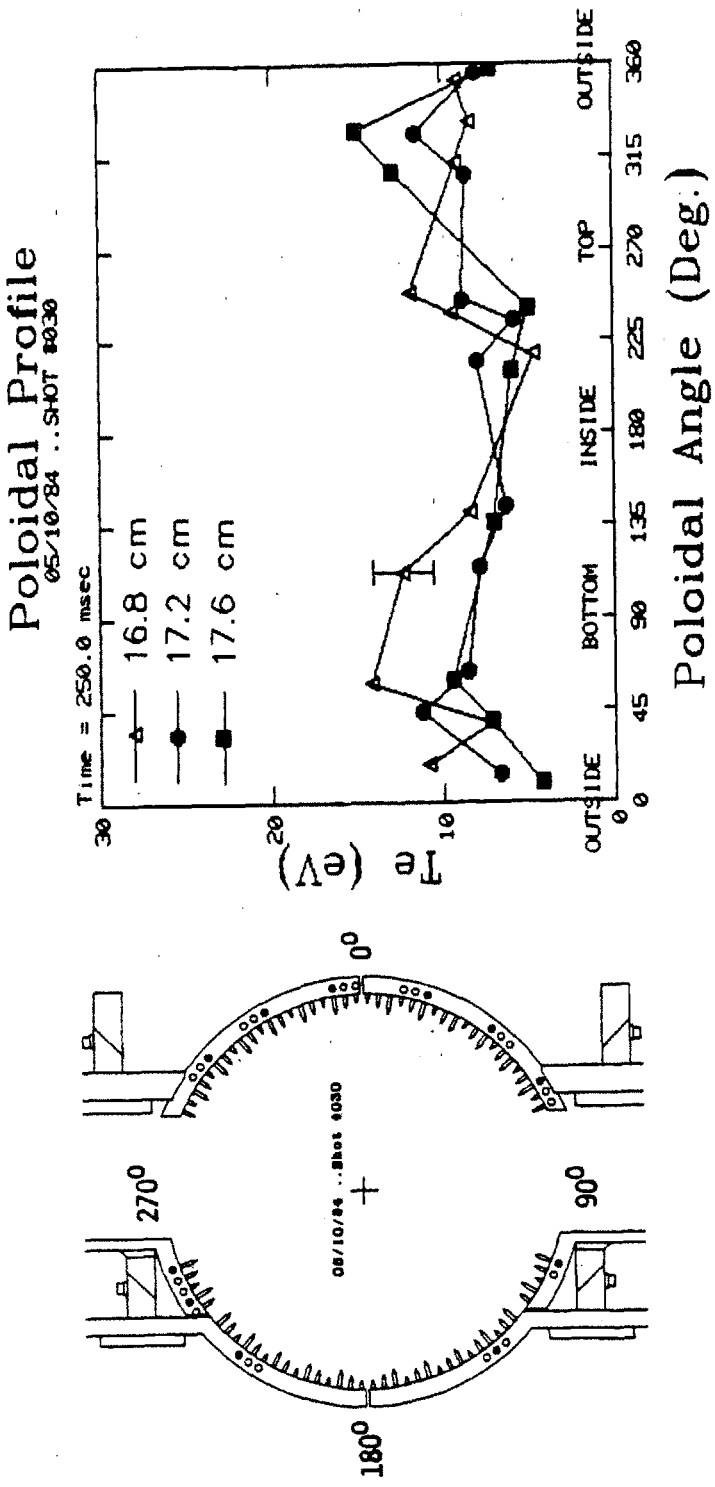

Figure 7.5 Limiter Shadow Electron Temperature vs. Radius and Angle

7.1.3 Pressure

Since the edge plasma density and temperature was asymmetric, it follows that the plasma pressure was asymmetric as well. The plasma pressure ($n \times T_e$) inferred from density and temperature data in Figs. 7.1 and 7.4 is plotted in Fig. 7.6. The poloidal structure in pressure is dominated by the density, although the temperature variation adds to the asymmetry.

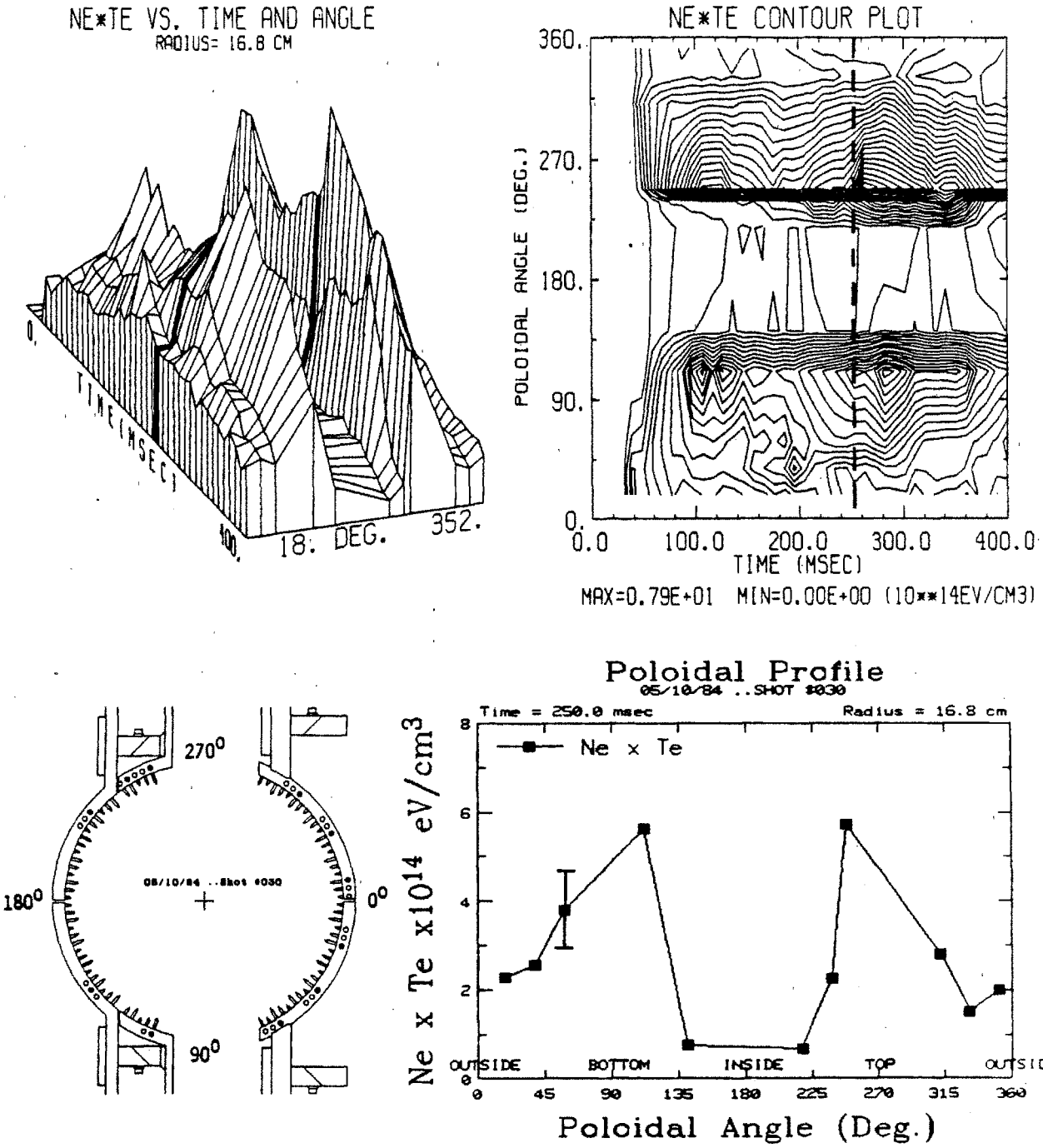

Figure 7.6 Plasma Pressure at r = 16.8 cm vs. Angle and Time

7.1.4 Density Scrape-off Length

With density at three radii being recorded simultaneously for a given shot, the density e-folding length as a function of poloidal angle could be estimated. Since the three radial measurements occurred at different poloidal angles, a linear interpolation scheme was used to estimate the radial density profile at a given angle. An exponential was then fit to these points versus radius to yield a scrape-off length. Figure 7.7 displays the result of this procedure. Again, a clear poloidal structure appears but with a different poloidal dependence.

While density and temperature data showed maxima near the top and bottom poloidal positions, this figure shows an overall scrape-off length maximum that is nearer to the outside. This is because the poloidal locations of the density maxima were found to be a function of minor radius. A factor of 5–10 variation in scrape-off length was recorded with the shortest scrape-off lengths occurring on the inside midplane ($\sim$ 0.1 cm). The poloidal structure appeared to be more like $cos\theta$ except for a slight relative minimum on the outside. The density and temperature profiles shown previously are more like $-cos2\theta$ with a deep absolute minimum on the inside.

The scrape-off length is related to the balance of parallel and perpendicular fluxes in the limiter shadow plasma. An accounting of these fluxes is often used to develop a simple expression for λ_n as derived previously in section 3.1.1. Although the connection length to the limiter, L, changes from $\sim$ 125 cm on the outside edge of the plasma to $\sim$ 73 cm on the inside, this cannot account for the observed factor of 5–10 variation in λ_n. Such a large poloidal variation in λ_n therefore suggests that the perpendicular and/or parallel transport processes that are active in the edge depend on poloidal location. The poloidal density and temperature profiles shown earlier suggested that this might be the case; however, the poloidal variation of the scrape-off length shown here more strongly supports this idea and is considered in more detail in chapter 8.

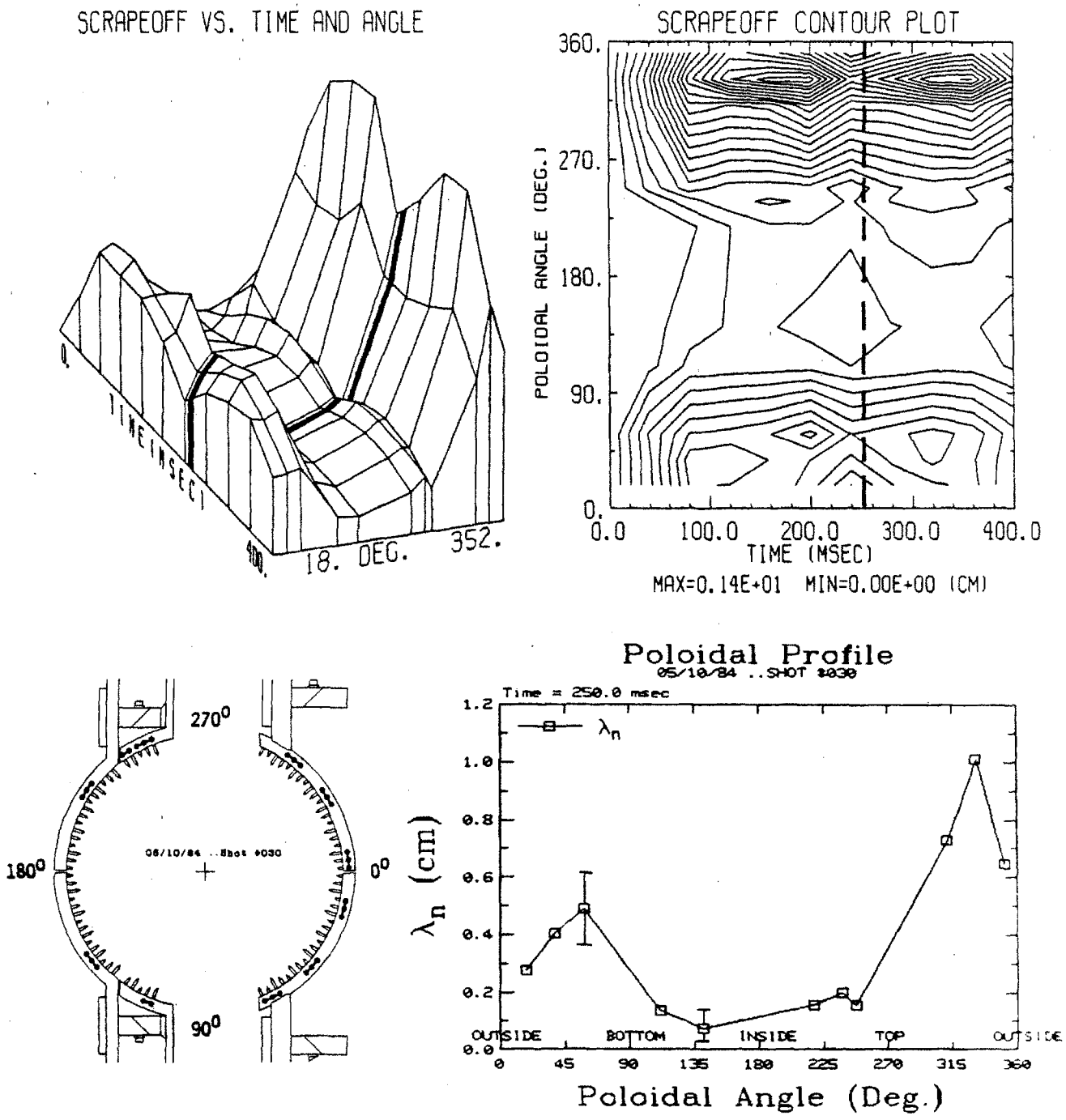

Figure 7.7 Density e-folding Length vs. Angle and Time

7.1.5 Floating Potential

In addition to recording density and temperature data, probe floating potentials were recorded on the DENSEPACK array. Figure 7.8 displays floating potential data in the standard format. Once again, a well defined poloidal variation was recorded for this edge parameter. Data is presented here using a 30 msec time average. The floating potential was found to vary in poloidal angle like $-sin\theta$, being negative at the bottom location and positive at the top. Typical extreme values at this radius were $\approx \pm$(8 to 15) volts. In addition, when the direction of the toroidal field was reversed, the poloidal variation changed to something more like $+sin\theta$ (dotted line in Fig. 7.8).

Unlike the density and temperature data shown previously, the poloidal structure in the floating potential can be simply explained at least to first order. The floating potential of a DENSEPACK probe relative to the limiter potential (taken as 0 volt reference by the electronics) is diagrammed in Fig. 7.9. The limiter is a perturbing structure and sets the local value of the space potential through the sheath drop to be roughly $\sim$ 3.5 T_e. However, $\underline{B} \times \nabla B$ charge accumulation can increase or decrease the space potential farther away from the limiter surface. At the probe surface another sheath drop of $\sim$ 3.5 T_e occurs. The floating potential of the probe relative to the limiter (Φ_f) therefore becomes

$$\Phi_f \approx \delta\Phi_s + 3.5\,(T_e^{limiter} - T_e^{probe})\,. \qquad (7.1)$$

If T_e along a field line varies little so that $T_e^{probe} \approx T_e^{limiter}$ then $\Phi_f \approx \delta\Phi_s$, and the spatial variation in the floating potential should reflect the spatial variation in the plasma potential due to effects such as $\underline{B} \times \nabla B$ particle drifts.

For the normal magnetic field direction, the direction of the $\underline{B} \times \nabla B$ drift in Alcator C is from the bottom to the top as in Fig. 3.3. The potential variation near the limiter radius, $\delta\Phi_s$, due to this charge separation goes like $-sin\theta$ and

can be estimated using Eq. 2.16. For Alcator C, potentials are obtained on the order $\sim \pm 8$ volts from Eq. 2.16 which is similar to the observed values. The result that the sign of the potential depends on the direction of $\underline{B}$ is also consistent with the $\underline{B} \times \nabla B$ drift explanation.

The assumption that $T_e^{probe} \approx T_e^{limiter}$ along a field line is not expected to be satisfied in general. The departure of the measured floating potential from a pure $-sin\theta$ variation may be reflecting this fact. Discharges shown in Fig. 7.8 were picked because they displayed the clearest $sin\theta$ structure. However, discharges can display a more distorted angular dependence of floating potential. This may be attributed to a non-negligible difference between the local probe and limiter electron temperatures.

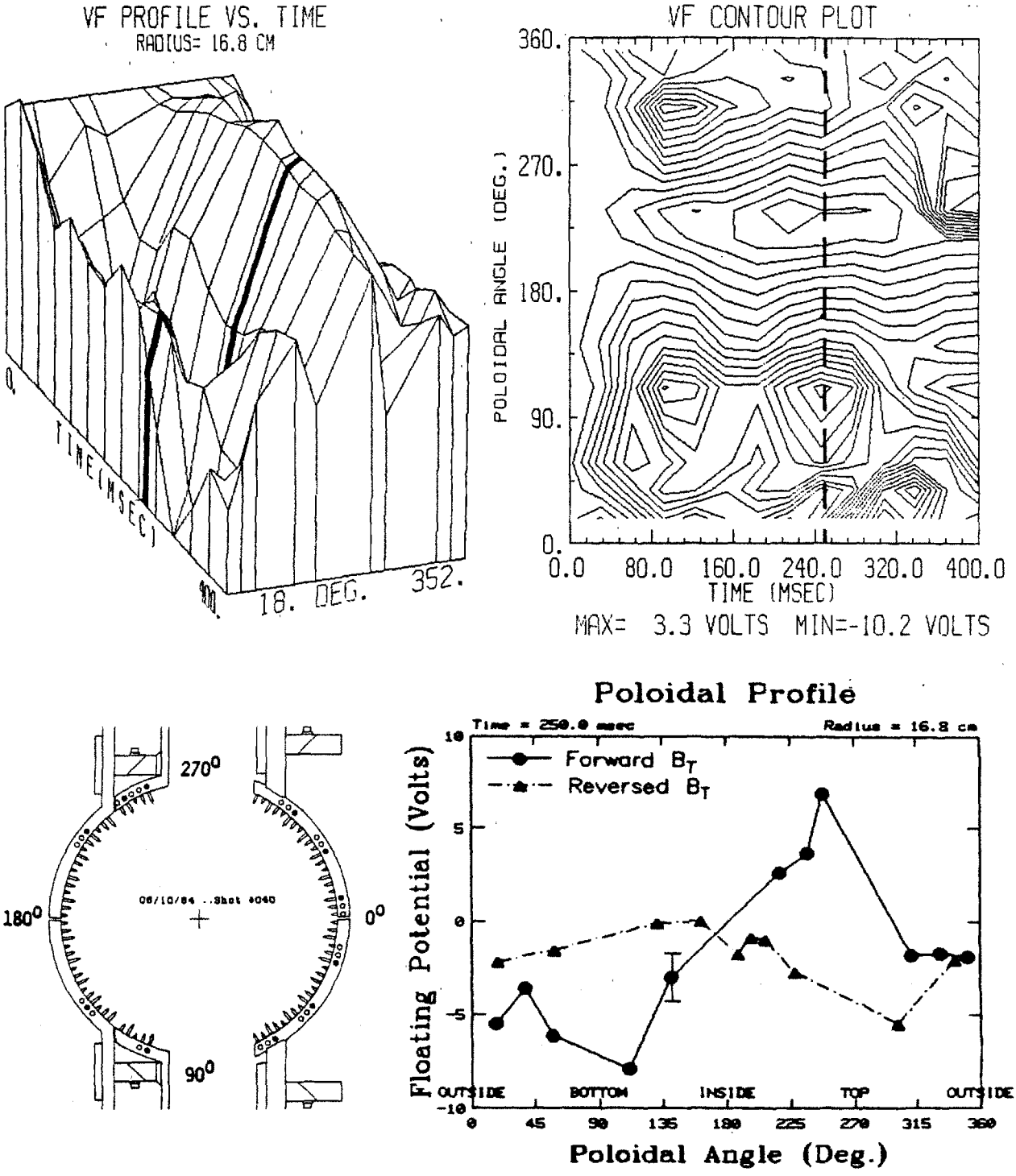

Figure 7.8 Floating Potential at $r = 16.8$ cm vs. Angle and Time

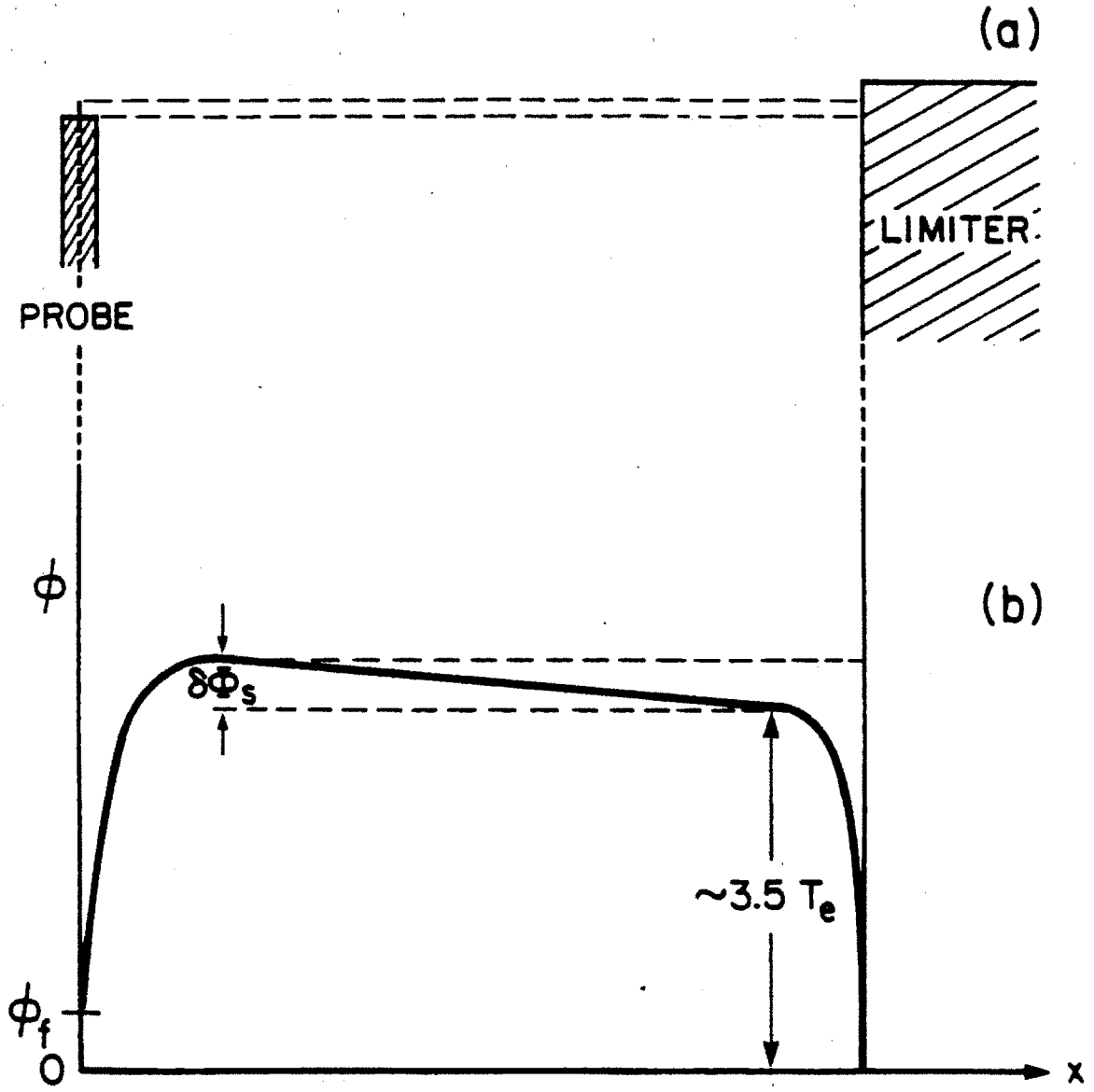

Figure 7.9 DENSEPACK Floating Potential Relative to the Limiter Potential

7.2 Poloidal Contours of Shadow Plasma Parameters

The 2-D structure of plasma parameters in the limiter shadow plasma can be most easily displayed at a specified time in the discharge as a contour plot in the (r, θ) poloidal plane. This section presents both measured and derived Alcator C limiter shadow plasma parameters in this format.

7.2.1 Coordinate System and Data Processing for Contour Plots

The DENSEPACK probe array samples plasma in a thin annular region as shown in Fig. 7.10 (*a*). In order to view contours of constant edge plasma parameters plotted on this poloidal cross-section, it is more convenient to artificially expand the radial dimension leading to a 'conformal mapping' as shown in Fig. 7.10 (*b*). The DENSEPACK probe locations for a particular discharge are shown on this conformal mapping in Fig. 7.11 (*b*). Data obtained by DENSEPACK during this discharge is displayed using the conformal mapping in subsequent sections. An example of density and temperature contour plots is shown in Fig. 7.12 and discussed in the next section.

In generating these plots, a fair amount of data processing was performed. First, the 3-D data arrays (angle, radius, time) were smoothed in time. Typically, a 40 msec time average was performed. Time smoothed data points near $t =$ 250 msec were then selected for plotting, reducing the plotting array to two dimensions. Next, an interpolation procedure was performed to fill data points between probe locations. A three radial node by 216 poloidal node mesh was thereby generated over the conformally mapped region. Finally, data on this mesh was smoothed in both radius and angle before contour plotting.

Data was smoothed in radius by fitting a straight line to the three radial points at each poloidal angle. An estimate of the uncertainty level in each parameter that was generated by the fitting algorithm was used in weighting this fit. The density was treated as a special case. Here, a fit was made to the

logarithm of the data since it was expected that the density varies in radius as an exponential instead of a linear function.

Data was repeatedly smoothed in angle by setting the value at a node to be equal to the average of neighboring nodes. The smoothing in poloidal angle was used to improve the aesthetic appearance of the plot. A high degree of poloidal smoothing tended to deemphasize the poloidal variation. On the other hand, without any smoothing, systematic and statistical variations in the data from adjacent probes could show up as fine structures in the contour plot. Such fine structures are misleading since error bars cannot be explicitly shown on these plots. By averaging in angle and fitting in radius, uncorrelated errors in measured parameters between probes tend to cancel out.

One way to overcome this spatial aliasing problem in poloidal angle is to monitor a region of closely-spaced probes on DENSEPACK, as was done to generate Fig. 7.3, and smooth this data over space. However, the trade-off is that a 360^0 poloidal mapping as shown here is too large to be covered with only 30 active probes. As a result, only low poloidal resolution ($\approx 30^0$), 360^0 poloidal plots will be shown in this section. Consequently, these plots should be taken only as an indication of the large spatial scale variation of plasma parameters in the limiter shadow region. The actual poloidal variations can be more abrupt than those plotted.

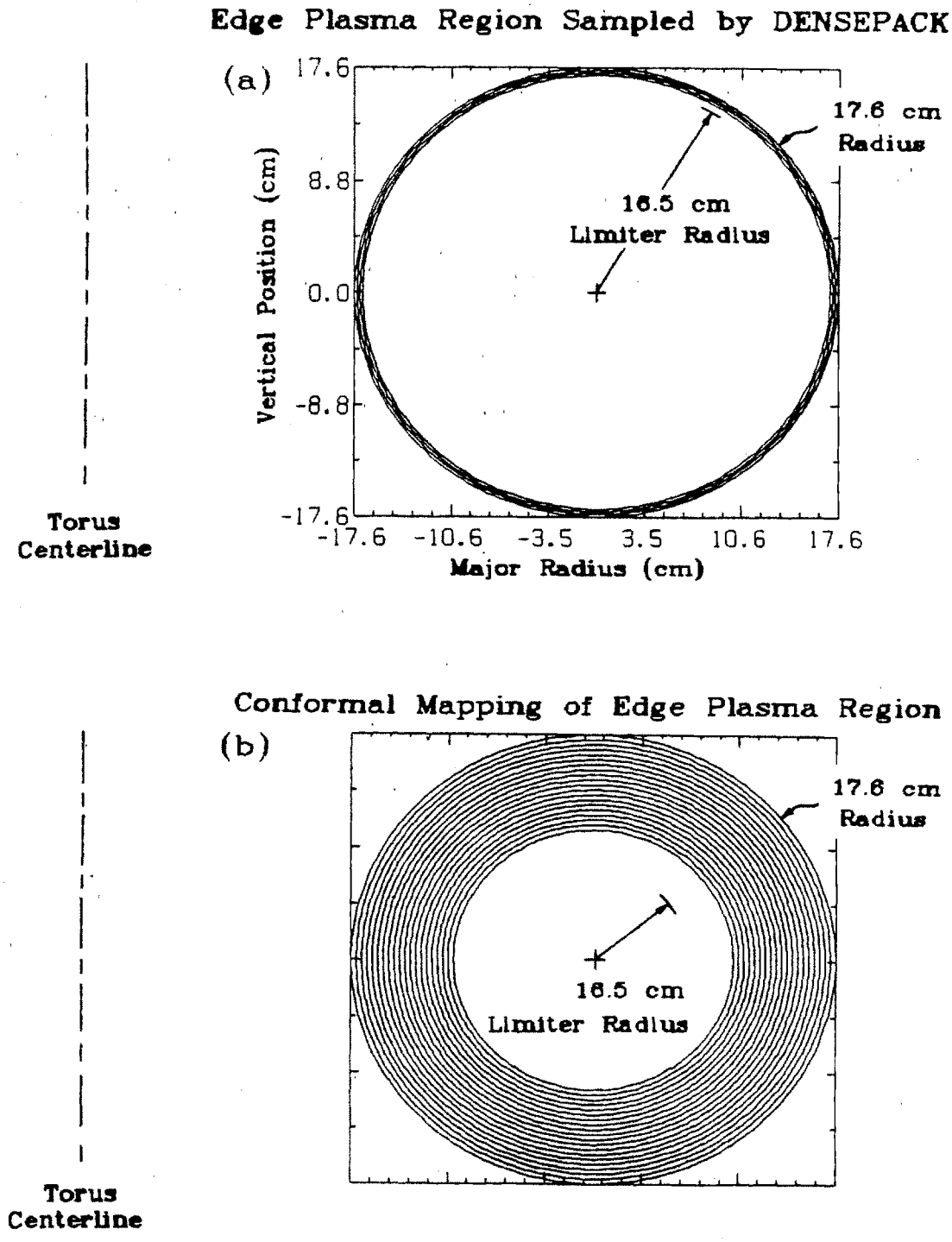

Figure 7.10 Shadow Plasma Region Sampled by DENSEPACK and Conformal Mapping

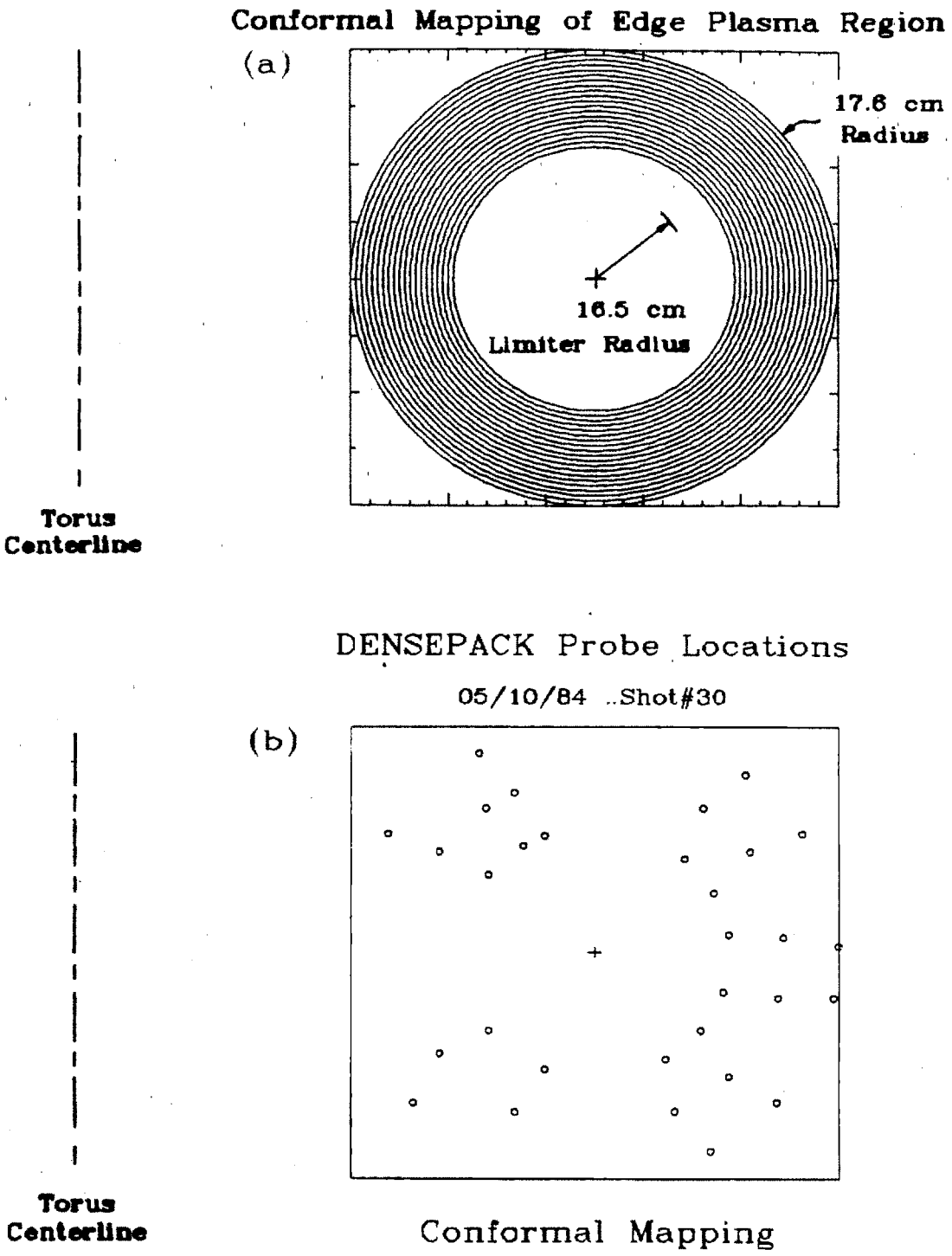

Figure 7.11 DENSEPACK Probe Locations on Conformal Mapping Region

7.2.2 Density and Temperature

The poloidal variation in density and temperature of Alcator C limiter shadow plasma is most clearly illustrated by this technique of contour plotting in Fig. 7.12. The data displayed here is taken at 250 msec from the same discharge as was shown in Fig. 7.1. Central plasma parameters are $\overline{n}_e \approx 2 \times 10^{14}/\ \mathrm{cm}^3$, $I_p \approx 350$ kA, $B_T \approx 8$ tesla, in deuterium plasma.

The density contour plot in Fig. 7.12 (a) shows the two density lobes on the top and bottom of the poloidal cross-section. A marked poloidal asymmetry is seen extending well into the limiter shadow plasma. The density contour labelled .800 ($\times 10^{13}/\mathrm{cm}^3$) maps the density asymmetry a full 360^0 in poloidal angle. The smallest minor radius that this contour approaches is $r \approx 16.9$ cm near the lower-inside position. The largest radius is $r \approx 17.5$ cm near the upper-outside position, indicating an effective total radial displacement from circular of ~ 0.6 cm. By extrapolation to smaller minor radii, it appears that higher density contours, such as those near the density maxima, may experience a much larger radial displacement versus poloidal angle, extending inside the limiter radius. However, there is no way to verify this directly by using DENSEPACK probes.

The temperature contour plot in Fig. 7.12 (b) also shows a poloidal variation extending into the shadow plasma. The dashed lines were drawn in by hand to aid in visualizing the poloidal variation. Although the isotherms must form a closed loop encircling the plasma, this representation is not unique.

The most interesting poloidal variation in temperature occurs at smaller minor radii where the most reliable data points are obtained via the fitting algorithm. A temperature variation from ~ 11 eV near maxima at the top and bottom to ~ 5.5 eV near a minimum on the upper-inside occurs at the innermost probe radius. The location of a temperature minimum (labeled 'L') at the upper-inside position is coincident with the typical location of the enhanced H_α emission associated with the MARFE. This discharge displayed a MARFE.

Other discharges which did not display a MARFE still displayed a temperature minimum at this location although it was not as low as ~ 5.5 eV.

It should be pointed out that the Stangeby algorithm was used to generate this temperature data. When the exponential fittng technique is used, T_e values scale up uniformly by about a factor of 1.5. (See section 6.3.6.)

(a) Constant Ne ($x10^{13}/cm^3$)

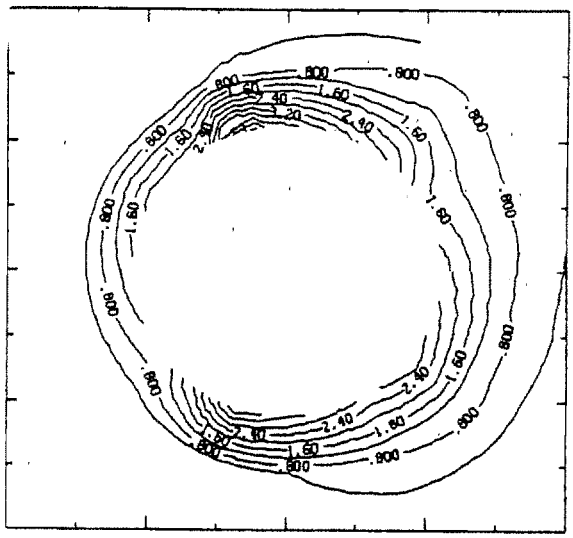

Torus Centerline

Conformal Mapping

(b) Constant Te (eV)

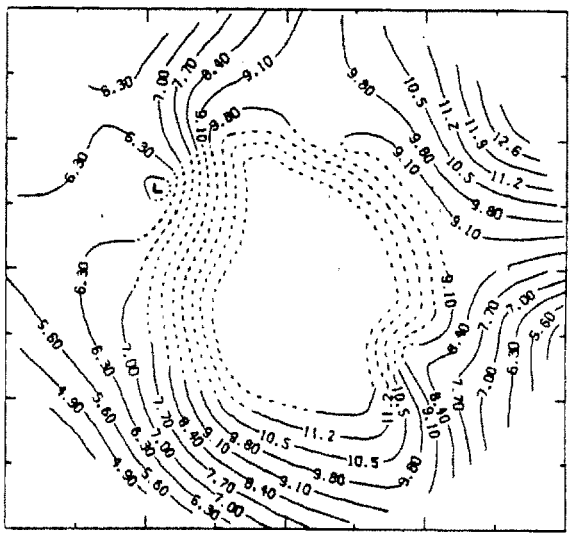

Torus Centerline

Conformal Mapping

Figure 7.12 Density and Temperature Conformal Contour Plots

7.2.3 Pressure

Contours of constant logarithm of density and plasma pressure are shown in Fig. 7.13. Both contours are similar as expected, since the density variation in radius and angle dominates over the temperature variations. The temperature variation acts to enhance the pressure variation slightly.

The logarithmic plots directly display the poloidal variation in density and pressure scrape-off length since the spacing between the contours is proportional to the e-folding length. As shown previously, the density or pressure scrape-off length is 4–5 times longer on the outside than on the inside midplane. This scrape-off length variation is found to persist at least out to the largest DENSEPACK radius of 17.6 cm, a full 1 cm beyond the limiter radius.

As a consequence of the scrape-off asymmetry, the logarithm of the pressure becomes poloidally more asymmetric at large minor radii. At a radius of 17.6 cm, the pressure varies from $nT_e \approx 7 \times 10^{12}$ eV/cm^3 near the upper-outside position to $nT_e \approx 10^{11}$ eV/cm^3 on the inside midplane. This pressure ratio of ≈ 70 is much larger than the pressure ratio of ~ 7 at $r = 16.8$ cm shown previously in Fig. 7.6. However, the poloidal variation of the absolute pressure difference is greater at 16.8 cm radii.

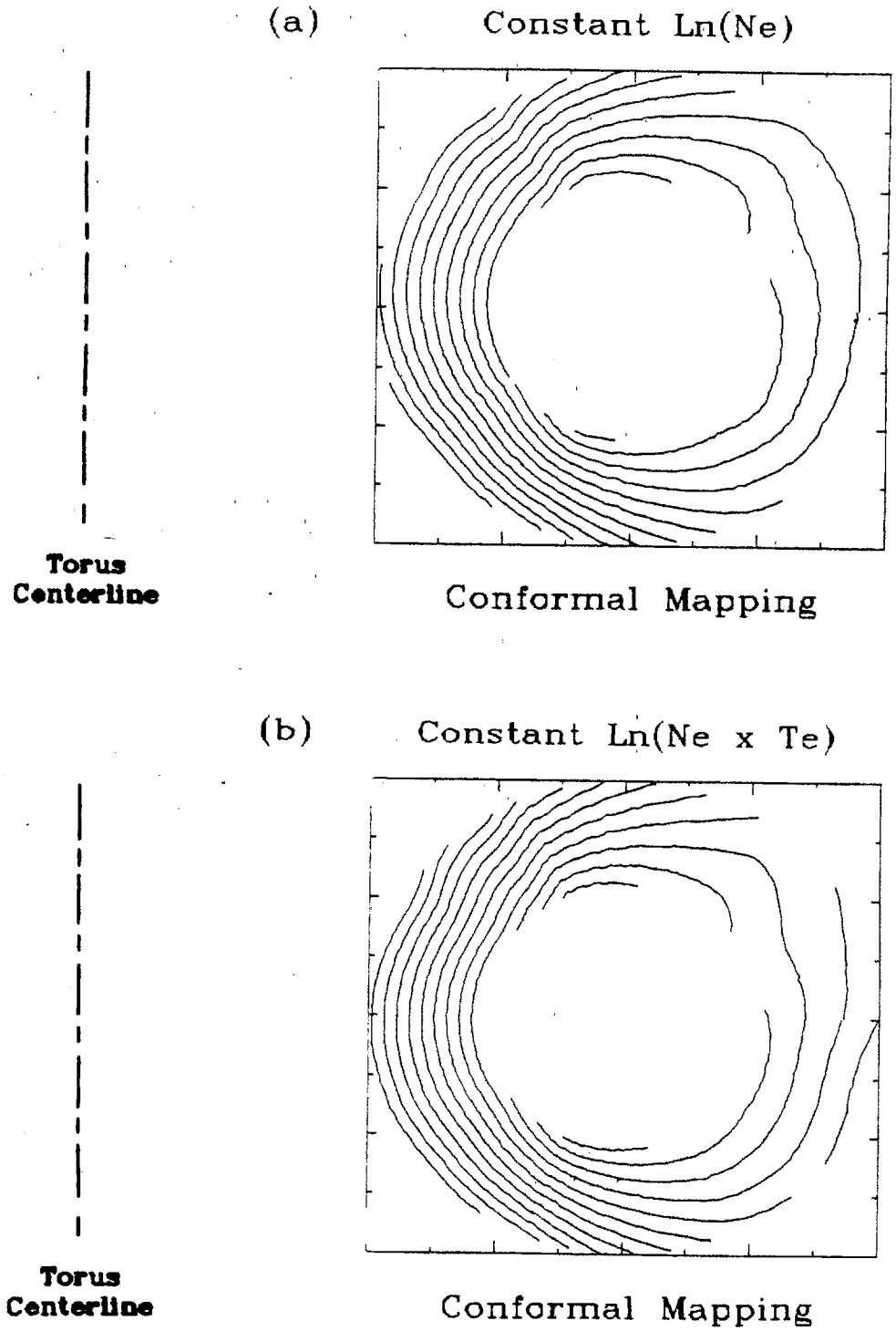

Figure 7.13 Logarithm of Density and Pressure Conformal Contour Plots

7.2.4 Floating Potential and Space Potential

A conformal contour plot of floating potential in the shadow plasma is shown in Fig. 7.14 (a). The floating potential measurement is not sensitive to systematic errors from probe collection area variation as the density measurement is and Φ_f is not subject to uncertainties in the probe fitting technique as T_e is. Consequently, no smoothing in angle or fitting in radius is performed on this data. However, the usual 40 msec time average is applied to reduce the statistical error from fluctuations.

The overall structure of floating potential in Alcator C discharges consistently showed more positive floating potentials near the top of the poloidal cross-section for this toroidal B-field direction. When the B-field was reversed, more positive potentials appeared near the bottom location. There was also a finer detail structure which disrupted this pure sinusoidal appearance in both radius and angle. Sharp spatial variations in the floating potential over distances on the order of the probe spacing are seen in Fig. 7.14 (a). This is somewhat expected because the electron temperature is found to vary in space, and Φ_f depends on the local T_e through Eq. 7.1. Since the probe spacing limits the spatial resolution, the actual spatial structure can be finer in some locations than is displayed here.

An important point that Fig. 7.14 (a) makes is that in the limiter shadow plasma, where field lines intercept a grounded limiter surface, a steady state floating potential variation was maintained by some process. The overall floating potential variation can be explained in terms of $\underline{B} \times \nabla B$ particle drifts across a pressure gradient. The detail structure appears to be related to temperature variations although some other process such as non-ambipolar perpendicular transport cannot be ruled out.

In principle, the local plasma space potential can be obtained from the electron temperature and floating potential. Relative to the limiter potential (defined as 0 volt reference), the local space potential is roughly given by Eq. 6.5. A finite r parameter and ion temperature can be included in the space potential calculation through Eqs. 6.25–6.26. Figure 7.14 (*b*) shows poloidal contours of space potential using the latter correction and Stangeby's fit for the electron temperature. Here, the usual smoothing in angle and radius is performed.

Because of the strong dependence on the electron temperature, the space potential contour plot looks similar to the electron temperature plot. Unfortunately, the accuracy of the space potential is also no better than the accuracy of the inferred electron temperature. Using temperatures obtained from the exponential fitting algorithm, the space potential contours in Fig. 7.14 (*b*) become a factor of 1.2–1.5 larger. This estimate of V_s is limited further by the uncertainty of the ion temperature which was assumed to be $\approx 2 \times T_e$ for this plot. Nevertheless, a number of important points can be made from Fig. 7.14 (*b*).

First, it can be simply stated that near steady state radial and poloidal plasma potential variations existed in the limiter shadow plasma of Alcator C. The existence of steady state potential variations imply that steady state E-fields perpendicular to $\underline{B}$ must also exist in the shadow plasma. From Fig. 7.14 (*b*), the peak magnitudes of these E-fields were at least $\gtrsim 15$ V/cm in the radial direction and $\gtrsim 2$ V/cm in the poloidal direction. The $\underline{E} \times \underline{B}$ convection velocity of particles in the shadow plasma implied by these potential measurements are

$$V_r \approx \frac{E_\theta}{B} \approx 2.5 \times 10^3 \quad \text{cm/sec} \tag{7.2}$$

$$V_\theta \approx \frac{E_r}{B} \approx 2 \times 10^4 \quad \text{cm/sec} \; . \tag{7.3}$$

An effective radial velocity due to diffusion, $V_r \approx D_\perp/\lambda_n$, can be estimated from an average density e-folding length of $\lambda_n \approx 0.25$ cm for this discharge (Fig. 7.7). Using Eq. 3.10 for $D_\perp$,

$$V_r^D \approx \frac{\lambda_n C_s}{L} \approx 5.6 \times 10^3 \text{ cm/sec} . \quad (7.4)$$

Thus, the potential variation in the limiter shadow plasma can result in $\underline{E} \times \underline{B}$ flow velocities which are significant compared to the effective radial diffusion velocity. This leads one to suspect that $\underline{E} \times \underline{B}$ convection may be acting in a self-consistent manner to perturb the edge plasma density and temperature profiles from poloidal symmetry in a way analogous to the diffusion plus convection model discussed in section 3.2. The possible impact of this inferred $\underline{E} \times \underline{B}$ convection in the edge plasma is discussed further in chapter 8.

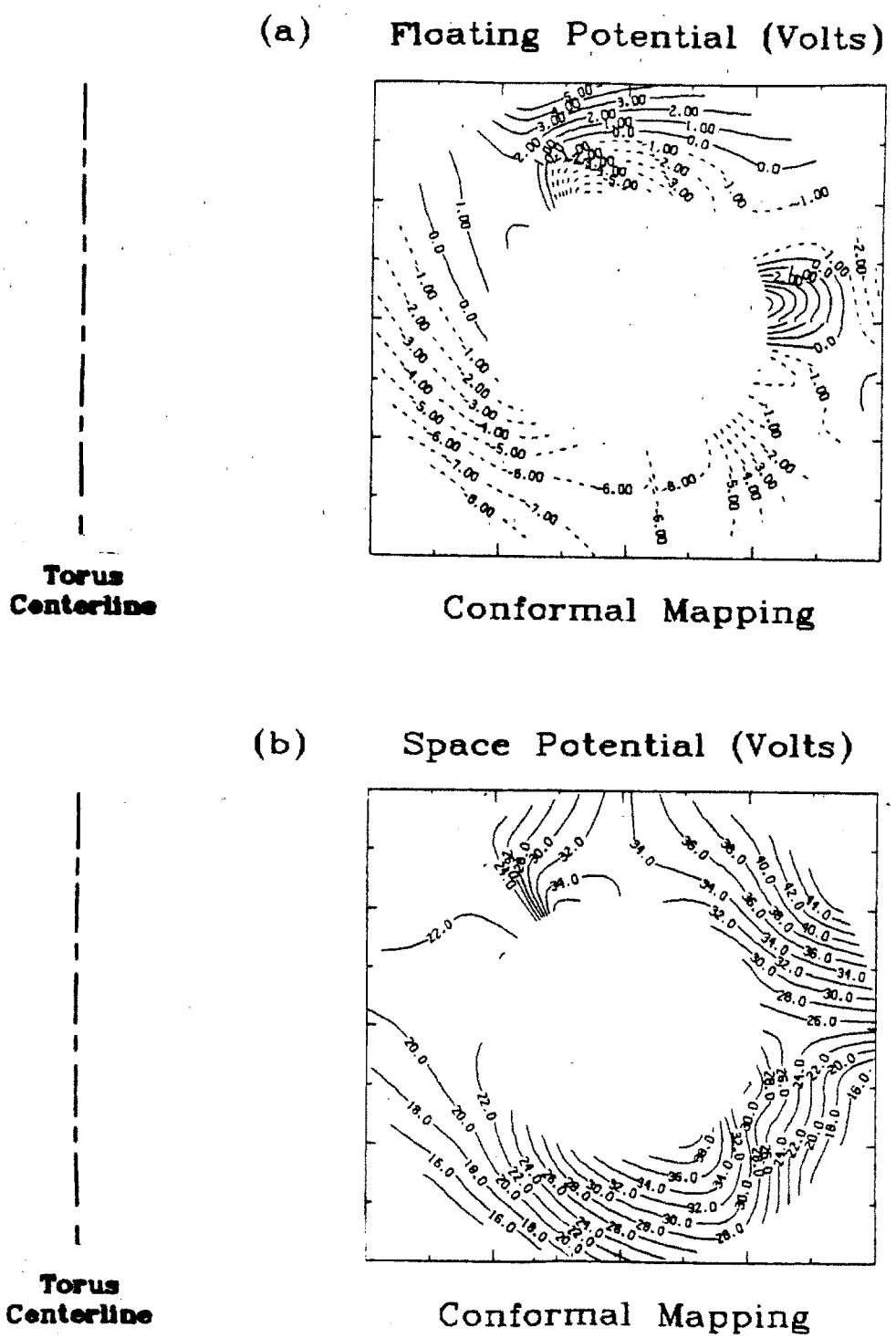

Figure 7.14 Floating Potential and Space Potential Conformal Contour Plots

7.2.5 Reduction Parameter: $D_\perp$

The Stangeby fitting algorithm arrives at an estimate of the reduction factor, r, for each Langmuir characteristic. Insofar as the reduction parameter is theoretically related to parallel and perpendicular diffusion coefficients through Eq. 6.17, the magnitude and spatial variation of r bears attention. Figure 7.15 shows a conformal contour plot of the reduction parameter fitted from the Stangeby algorithm. The usual spatial and temporal smoothing was performed.

The plot in Fig. 7.15 displays an unexpectedly narrow range of r with only a gentle spatial variation. Assuming that $D_{\|} = \lambda_{ei}\overline{C}_e/4$, similar to the analysis by Bohm,[20] Eq. 6.17 can be written as

$$r = \frac{32}{\pi\ s}(1+\tau)\sqrt{\frac{D_\perp\ \lambda_{ei}}{\overline{C}_e}} \tag{7.5}$$

showing the explicit dependence of r on $D_\perp$ and λ_{ei}. It has already been stated in section 6.3.6 that even though τ $(= T_i/T_e)$ must be assumed, the r parameter obtained for a given characteristic via the Stangeby algorithm is found to depend on τ such that the quantity $\sqrt{D_\perp \lambda_{ei}/\overline{C}_e}$ is roughly constant. Thus, it is only necessary to fix τ to some value (here, $\tau = 2$), not worrying about the true T_i/T_e ratio, in order to compare relative r values over the poloidal cross-section.

The electron-ion mean free path can be expressed as

$$\lambda_{ei} = 4.5 \times 10^{13}\ \frac{T_{e\,(\mathrm{eV})}^2}{Z_{eff}\ n_{(\mathrm{cm}^{-3})}\ \Lambda} \quad \mathrm{cm}\ , \tag{7.6}$$

allowing for impurity ion species through Z_{eff}. In Fig. 7.12, the plasma density was shown to vary over the poloidal cross-section from a maximum of $n \approx 5 \times 10^{13}/\mathrm{cm}^3$ to a minimum of $n \approx 10^{11}/\mathrm{cm}^3$. Consequently, with T_e varying at most by a factor of 2. λ_{ei} given by Eq. 7.6 should change by at least two orders

of magnitude over the poloidal plane. If all other parameters remain relatively constant in space, Eq. 7.5 would predict that r should vary by at least an order of magnitude over the poloidal cross-section. However, Fig. 7.15 clearly indicates that this is not the case. In fact, what little spatial variation in r that is displayed in Fig. 7.15 is, in some instances, opposite to the expected scaling of r through λ_{ei}.

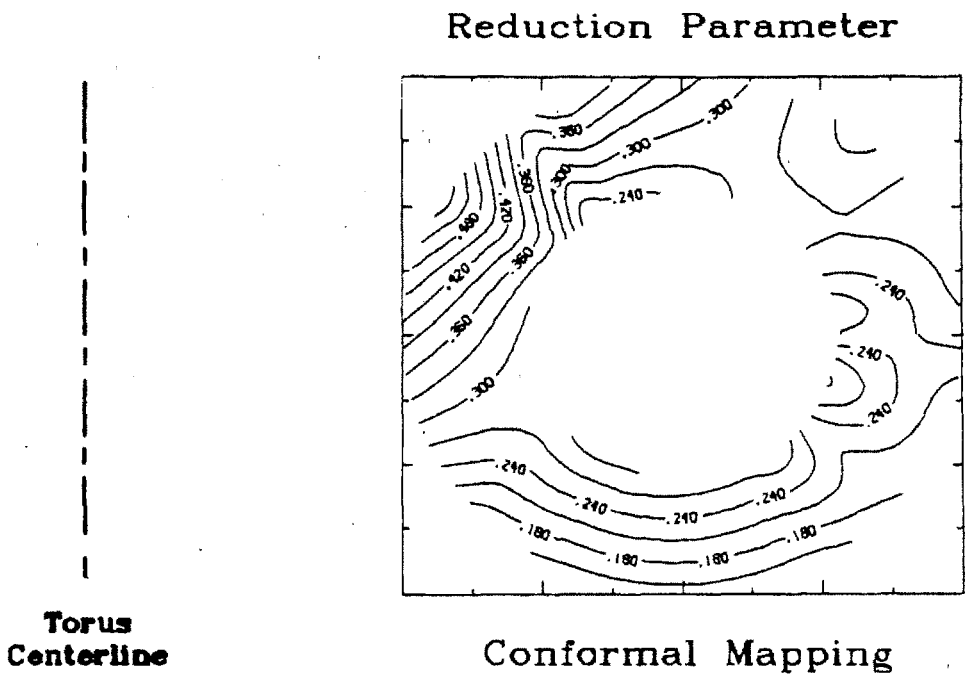

Figure 7.15 Reduction Parameter Conformal Contour Plot

There are a number of possible reasons for this apparent contradiction. First, the simplest conclusion to draw is that Eq. 7.5 does not properly include the physics that gives rise to a reduced electron saturation value. The argument that is used in obtaining Eq. 7.5 simply involves conservation of particles with parallel and perpendicular diffusion. A Fick's law formulation of diffusion is valid when the particle mean free path is short compared to the density gradient scale length or characteristic dimension of the region considered. In the perpendicular direction, the electron Larmor radius is much smaller than the probe size, validating the use of a perpendicular diffusion model. In the parallel direction, the situation is different. At the limiter radius where $n \approx 5 \times 10^{13}/\ \mathrm{cm}^3$, $T_e \approx 15$ eV, Eq. 7.6 predicts $\lambda_{ei} \approx$ 10–15 cm so that the limit $\lambda_{ei} \ll L$ ($L \approx 100$ cm, distance to limiter) is satisfied. Farther out in radius where the density drops off exponentially, this inequality is reversed so that $\lambda_{ei} \gg L$. Thus, a parallel diffusion model, and therefore Eq. 7.5, is not valid over the entire shadow plasma region. Before returning to this point later in this discussion, other possible explanations are now considered.

Another explanation of this apparent contradiction is that maybe the r parameter as inferred from the probe characteristic is not reliable. However, this point is easy to dismiss. The variation in r sweep to sweep for a given probe during a discharge is typically $\lesssim 0.07$. The r parameter is uniquely determined for each probe characteristic and is not very sensitive to noise or changes in probe bias. There may be a systematic error in r of up to a factor of 2 due to the characteristic model and the fact that electron saturation is not actually achieved by the probe. Nevertheless, the uncertainty in the fit of r is found to be much too small to account for the unseen order of magnitude variation that one would expect from Eq. 7.5.

Upon accepting that Eq. 7.5 is valid and that r is being accurately determined at least within some systematic error, another possibility is that $D_\perp$, λ_{ei}, and $\overline{C}_e$ are indeed changing in such a way as to keep r nearly constant in

space. This hypothesis is not so unreasonable since typical values for $D_\perp$ in the edge plasma are far from classical. The appropriate value for the electron mean free path may not be the classical λ_{ei} value but rather some anomalously small value due to the same turbulent processes that drive an anomalous $D_\perp$. In this way, $D_\perp$ and λ_e in Eq. 7.5 could be coupled so that r appears independent of space. However, one problem with this explanation is that an anomalously short electron mean free path would necessarily imply an anomalously large parallel electron resistivity. This is inconsistent with the observed agreement of the floating potential variation with an estimate based on classical resistivity and $\underline{B} \times \nabla B$ drifts in section 7.1.5.

Our attention therefore returns to Eq. 7.5 and to the question of validity. The distance to the limiter is shorter than the electron mean free path over much of the limiter shadow plasma. This implies that in electron saturation the particle collection 'flux tube' can intercept the limiter surface. The rate of electron diffusion to the probe surface is affected by this change in geometry. It is expected that the role of λ_{ei} should somehow be replaced by L in Eq. 7.5. Appendix E considers this case of electron collection when $\lambda_{ei} \ll L$. Assuming that the density along a field line in the flux tube is approximately constant, an effective reduction parameter is found to be

$$r = \frac{\delta}{1-\delta} \tag{7.7}$$

with

$$\delta = \frac{2}{\beta s} \frac{I_1(\beta s)}{I_0(\beta s)} \tag{7.8}$$

and

$$\beta = \sqrt{\frac{\overline{C}_e}{2\ \pi\ L\ D_\perp\ (1+\tau)}} \tag{7.9}$$

where I_n is a hyperbolic Bessel function of order n, and s is the length of one side of a square probe collection plate. When $\beta s \gtrsim 8$, Eqs. 7.7–7.9 can be approximated as

$$r \approx \frac{2}{\beta s} = \frac{1}{s}\sqrt{\frac{8\ \pi\ L\ D_\perp\ (1+\tau)}{\overline{C}_e}}\ . \tag{7.10}$$

Note that from this analysis, λ_{ei} does not appear in the expression for r. As expected, L takes the place of λ_{ei} in this formulation. The net result is that r is more nearly independent of position in the poloidal plane, which is consistent with what is experimentally observed. Nevertheless, a problem still arises in comparing the expected value of r from Eqs. 7.7–7.10 with the measured values.

From Eq. 7.10 and measured values of r between 0.1–0.5, one expects that βs be $\approx$ 4–20. Using the estimate of $D_\perp$ given by Eq. 3.10, βs can be written as

$$\beta s \approx 3.3\ \frac{s}{\lambda_n}\frac{\mu^{1/4}}{(1+\tau)^{3/4}}\ . \tag{7.11}$$

With $s \approx 0.15$, $\tau \approx 2$, $\mu \approx 2$, and typical λ_n values of $\approx$ 0.2–0.5 (see Fig. 7.7), βs is estimated to be around 0.6–1.5, which is a factor of 10 below the expected values. For comparison, Eq. 7.5, evaluated near the limiter radius where $\lambda_{ei} \approx 15$ cm, is also off by a factor of 10, predicting r values of ≈ 2. It appears that there is either some gross systematic error in fitting r from the data, which is highly unlikely, or that Eqs. 7.5 and 7.10 are incorrect and need to include some anomaly factor.

It is beyond the scope of this thesis to investigate the possible mechanisms for this anomaly. Since Eq. 7.10 scales more favorably in radius than Eq. 7.5, a semi-empirical approach can be taken based on Eq. 7.10 to express r. Introducing an empirical factor, A, r can be written as

$$r \approx \frac{A}{s}\sqrt{\frac{2\,\pi\,D_{\perp}\,(1+\tau)}{\overline{C}_e}} \tag{7.12}$$

so that $D_{\perp}$, L, $\overline{C}_e$, and r agree with typical experimental values. Unfortunately, due to the uncertainty in this model, r cannot be used to independently infer a value for $D_{\perp}$ as was initially suggested at the beginning of this section. All that can be safely said about r from DENSEPACK data at this time is that Eq. 7.12 is consistent with an anomaly factor, A, equal to ≈ 0.1.

7.3 Fluctuations

In addition to recording time averaged quantities such as density and temperature shown in the previous sections, the DENSEPACK hardware was also configured to record high frequency fluctuations in the ion saturation current collected by 15 of the 30 active probes. Data from these probes was sampled at 1 MHz for 8 msec during the steady state portion of the discharge by LeCroy model 8210 data loggers. Spectral analysis techniques were performed on this data to infer fluctuation power spectra and to look for coherent modes appearing across probes.

Section 7.3.1 presents ion saturation current fluctuation spectra and autocorrelation time histories typical of the edge plasma sampled by DENSEPACK. The fluctuation power spectra were found to exhibit no discernable features and are typical of the broad-band 'turbulence' that is generally found in the edge plasma of tokamak discharges. In addition, no coherent modes were detected between probes, consistent with expected spatial correlation lengths for fluctuations. Section 7.3.2 focuses on the fluctuation amplitude in ion saturation current which is characterized by the quantity $\tilde{J}/\bar{J}$. An important result is that unlike the time averaged quantities, n and T_e, $\tilde{J}/\bar{J}$ did not depend in any systematic way on poloidal location in the limiter shadow plasma.

7.3.1 $\tilde{J}$ Power Spectra and Correlations

Data sampled and recorded at 1 MHz was analyzed using Fourier transform methods. When a DENSEPACK probe was biased in sweep mode, a data sample of typically 1024 or 2048 points during the ion saturation part of the characteristic was used (see Fig. 6.13). For operation in continuous ion saturation, all 8192 data samples (8K, 10 bit words) are used in the spectral analysis.

The first step in this analysis was to compute the Fourier transform of the ion saturation data samples. This was done by employing a fast Fourier transform (FFT) algorithm on suitably 'prepared' ion saturation data. The data was 'prepared' by first subtracting any linear trend. In this manner, the D.C. level and any slow time (2–8 msec) variation was removed. Then, the time sample was multiplied by a Hanning function to minimize frequency artifacts in the transform due to 'leakage'.[96] Finally, the time series was doubled in length by appending it with zeros. This technique defined the signal to be zero outside the time window of measurement and made the autocorrelation and crosscorrelation calculations evaluated in the frequency domain agree with comparable calculations using the time series data directly. The resultant FFT of this time series, $s(t)$, was a discrete representation of the Fourier transform for a continuous, finite length, time series,

$$S(f_n) = \sum_{k=0}^{N-1} s(kT)\ e^{-i2\pi f_n kT} \quad ;\ n = 0, 1,\ \ldots\ N-1 \tag{7.12}$$

$$\approx \int_{-\infty}^{\infty} s(t)\ e^{-i2\pi f_n t}\ \partial t \quad ;\ f_n = \frac{n}{N\ T}\ , \tag{7.13}$$

as long as the highest frequency component in $s(t)$ was less than the Nyquist sampling rate, $f_c = 1/2T$, where T is the sample time interval. Ten pole, Tchebyshev-ellipsoidal, lowpass filters with a cutoff frequency of 416 kHz were inserted before the fast digitizers to insure that the recorded signal was at least 60 db down for frequencies above the Nyquist limit of $f_c = 500$ kHz. However, it was found in most cases that spectra naturally rolled off at high frequencies to avoid significant aliasing even without filtering.

Once the Fourier transform was calculated, the discrete power spectrum, $P(f_n)$ was simply estimated by computing

$$P(f_n) \;=\; S(f_n)\; S^{*}(f_n)\;. \qquad (7.14)$$

Figure 7.16 displays a typical power spectrum of ion saturation fluctuations from DENSEPACK probes. This power spectrum was obtained from an ion saturation current time series of 2048 points. A numerical Gaussian filter in frequency with a half width of ≈ 1 kHz was used to smooth the spectrum. The spectrum displays no evidence of any clear modes localized in frequency. The fluctuations appear as a broad-band 'turbulence' and exhibit a bandwidth and roll-off similar to the spectra obtained using probes by Zweben.[38] The effect of the 416 kHz lowpass filter is seen on the semi-log plot in Fig. 7.16 (a) at frequencies above 400 kHz, indicating the level of digital noise for this spectrum.

The power spectrum can be characterized by the same parameters as those used by Zweben, namely, a critical frequency, f_{crit}, below which the power spectra are relatively flat and above which the power rolls off as $P(f) \propto f^{-\alpha}$. The exponent, α, was found to be in the range 1–3 for DENSEPACK data, similar to Zweben's result. The critical frequency as defined by Zweben appeared similar. The 'flat' region in DENSEPACK's data was in the range $f < f_0$ where $f_0 \approx$ 10–20 kHz. Typically, 80–85% of the fluctuation power was at frequencies below 50 kHz.

Power spectra obtained from probes at different poloidal locations were compared to search for a spatial dependence of the fluctuation spectrum. The spectrum was found to be very similar at all poloidal locations. The only notable difference from probe to probe was the rate of high frequency roll-off. For the same shot, α was found to be on the lower limit, ~ 1, for some probes and on the upper limit, ~ 3, for others. However, no systematic relationship between spatial position and α was detected.

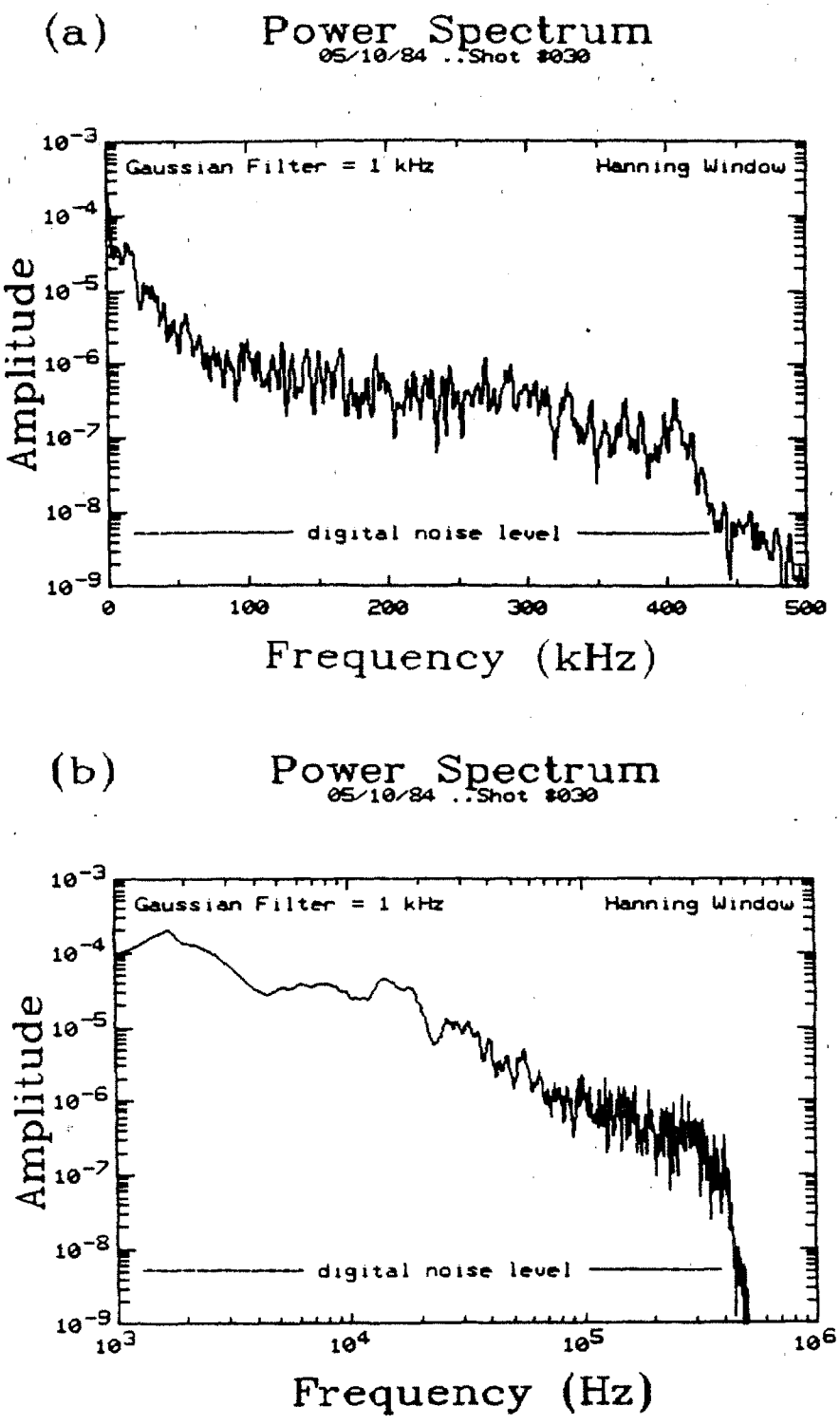

Figure 7.16 Typical $\tilde{J}$ Power Spectrum from DENSEPACK

Cross-correlations and auto-correlations of probe signals can be computed efficiently using Fourier transform techniques. A time delay correlation between two signals, $x(t)$ and $y(t)$, defined by the continuous integral,

$$C(\tau) \;=\; \int_{-\infty}^{\infty} x(t)\; y(t+\tau)\; \partial t \;, \tag{7.15}$$

is simply the inverse Fourier transform of the cross-power spectrum,

$$C(\tau) \;=\; \int_{-\infty}^{\infty} X(f)\; Y^{*}(f)\; e^{i2\pi f\tau}\; \partial f \;. \tag{7.16}$$

In an analogous way, the discrete time delay correlation which approximates Eq. 7.15,

$$C(kT) \;=\; \sum_{l=0}^{N-1} x(lT)\; y((k+l)T) \;, \tag{7.17}$$

can be obtained from the inverse FFT,

$$C(kT) \;=\; FFT^{-1}\Big\{X(f_n)\; Y^{*}(f_n)\Big\} \tag{7.18}$$

$$\;=\; \frac{1}{N}\sum_{n=0}^{N-1} X(f_n)\; Y^{*}(f_n)\; e^{i2\pi k f_n} \;. \tag{7.19}$$

When $x(kT) = y(kT)$, then $C(kT)$ becomes the discrete representation of the autocorrelation, which is the inverse FFT of the discrete power spectrum.

The correlation function, $C(kT)$, was computed in this manner to obtain autocorrelation and crosscorrelation functions between 15 active probes on the DENSEPACK array. A typical autocorrelation function calculated from the power spectrum shown in Fig. 7.16 is plotted in Fig. 7.17. The $\sin(at)/at$ structure in Fig. 7.17 (a) is due to wiggles in the low frequency end of the power spectrum. With more data samples, this feature disappears. Figure 7.17 (b) shows the autocorrelation on an expanded time scale. As shown here, it is found that typical autocorrelation times are on the order $\tau_{corr} \approx$10–20 μsec.

Cross-correlations of probe signals yielded no coherence even for adjacent probes except during a subset of shots in which a global mode referred to as 'MARFE oscillations' appeared (chapter 11). This result is consistent with the accepted spatial correlation length for fluctuations.[14] From probe and electromagnetic scattering measurements, the power spectrum in perpendicular wavenumber, $P(\mathbf{k}_\perp)$, peaks around $k_\perp \rho_s \approx 0.3$ where ρ_s is the ion Larmor radius evaluated at the electron temperature. For Alcator C edge plasma where $B \approx 8$ tesla and $T_e \approx 15$ eV, this implies a fluctuation correlation length of $\lambda_{corr} \approx 0.1$ cm. The closest DENSEPACK probe spacing was ~ 1 cm. Probes at the same minor radius location were spaced poloidally by ~ 3 cm (see Fig. 5.6). Thus, it is not expected that there be any significant coherence in ion saturation fluctuations between probes on the DENSEPACK array.

One other way in which a coherence might be detected between probes is when the plasma has a bulk flow velocity directed from one probe to another. If the time for a volume of plasma to move from probe to probe is less than the autocorrelation time, τ_{corr}, then some degree of coherence would be displayed by the crosscorrelation function. With a probe spacing of ≈ 3 cm, this would necessitate a flow velocity of $V_\perp \approx 3 \times 10^5$ cm/sec. However, the estimated spatial correlation length for fluctuations of $\lambda_{corr} \approx 0.1$ cm implies that this velocity vector must align within 2^0 of a straight line path connecting two probes. Thus, it is unlikely that a correlation between probes would be detected even if such

a flow velocity in the edge plasma exists.

There were a number of discharges during reversed toroidal magnetic field operation that displayed a global, low frequency ($\approx$ 270 Hz) mode referred to as 'MARFE oscillations'. In this case, crosscorrelations yielded coherence between all probes. This phenomenon is presented separately in chapter 11 as part of a discussion of MARFEs. It appears to be related to changes in macroscopic plasma equilibrium, and so it is not included in this section on fluctuations.

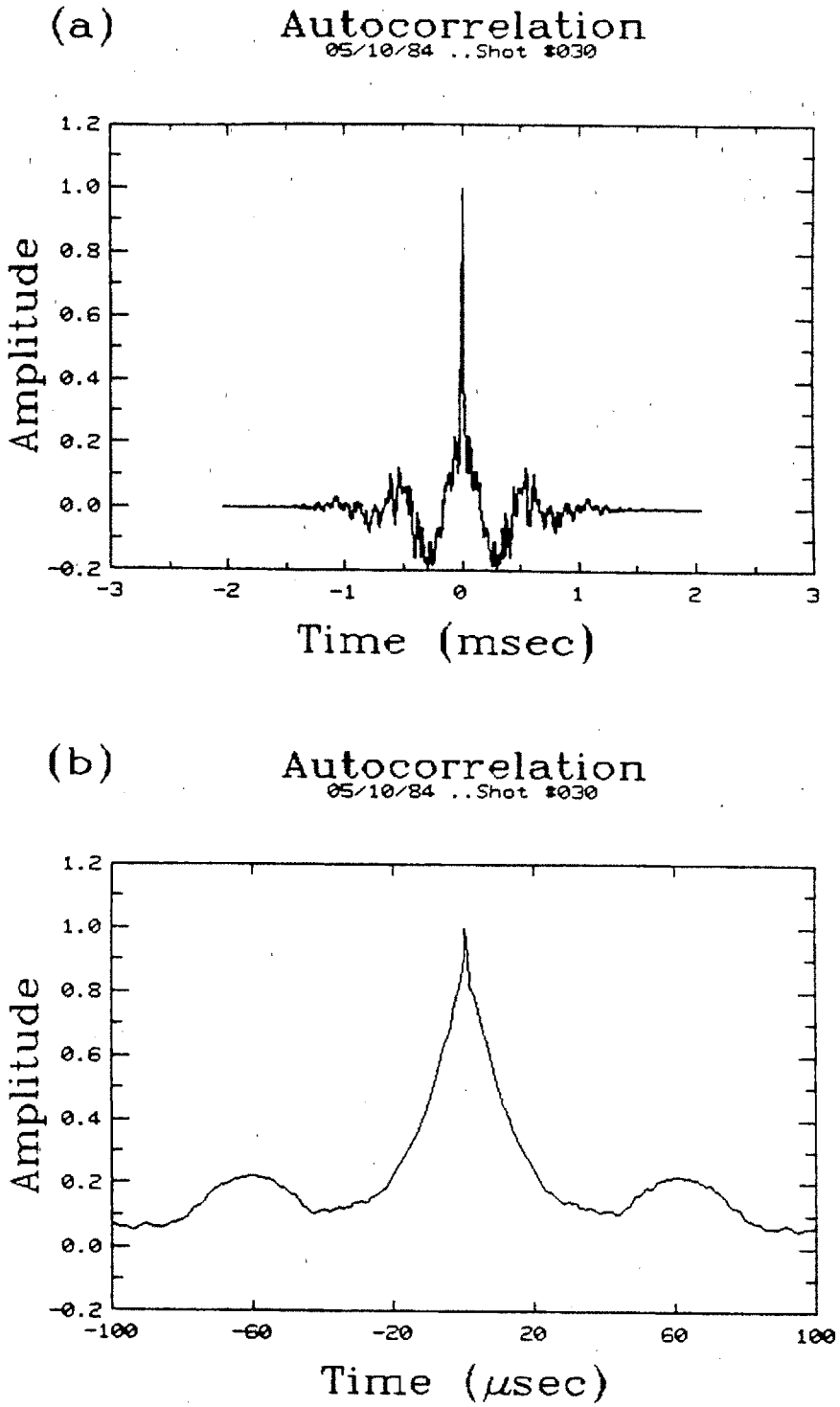

Figure 7.17 Typical Autocorrelation Function for DENSEPACK Probes

7.3.2 Spatial Dependence of $\tilde{J}/\bar{J}$

The ion saturation current fluctuation level can be characterized by the total energy in the fluctuations for a sample time period. Alternatively, one can compute the root mean square (RMS) fluctuation amplitude and parameterize the fluctuation level in terms of this quantity. The RMS is defined for a discrete time series $(s(kT);\ k = 0, N)$ as

$$\text{RMS} = \sqrt{\frac{1}{N}\sum_{k=0}^{N-1} s^2(kT)}\ , \tag{7.20}$$

and for discrete functions, the following version of Parseval's theorem applies:

$$\sum_{k=0}^{N-1} s^2(kT) = \frac{1}{N}\sum_{n=0}^{N-1} S(f_n)S^*(f_n) \tag{7.21}$$

$$= \frac{1}{N}\sum_{n=0}^{N-1} P(f_n)\ , \tag{7.22}$$

as long as $S(f_n)$ is an accurate representation of the discrete Fourier transform of $s(kT)$. Thus, the RMS fluctuation level for a finite time data sample is simply related to the integral of the power spectrum or to the time-averaged power in the fluctuations.

The relative fluctuation level in ion saturation current collected by probes, $\tilde{J}$, is most conveniently expressed in terms of the time averaged ion saturation current, $\bar{J}$, through the ratio $\tilde{J}/\bar{J}$. Here, and throughout the remainder of this thesis, $\tilde{J}$ is defined as the RMS fluctuation level about the mean of the ion saturation current. $\tilde{J}/\bar{J}$ therefore can be calculated from

$$\bar{J} = \frac{1}{N}\sum_{k=0}^{N-1} J(kT) \tag{7.23}$$

and

$$\tilde{J} = \sqrt{\frac{1}{N}\sum_{k=0}^{N-1}\left[J(kt)-\bar{J}\right]^2}\ . \tag{7.24}$$

When electron temperature fluctuations are small, ion saturation current fluctuations are proportional to density fluctuations allowing $\tilde{J}/\bar{J}$ to be interpreted as $\tilde{n}/\bar{n}$.

For DENSEPACK, $\tilde{J}/\bar{J}$ was calculated using both fast sampled 1 MHz data and slower sampled 10 kHz data. Since the power spectrum indicates that ion saturation current fluctuations appear as a random turbulence, one expects that $\tilde{J}/\bar{J}$ inferred from the 1 MHz data and from the 10 kHz data should in principle agree when the analog bandwidth of the two systems is the same. More formally, when the data is sampled over many autocorrelation times so that the uniform sample time interval cannot 'lock in phase' with fluctuations, a truly 'random' sampling is obtained. This criterion was easily satisfied by both the 8210 and 8212 data retrieval systems. However, discrete Fourier transforms computed from the 10 kHz data were not accurate since frequency components in the data exceed the Nyquist limit for this case.

The LeCroy 8212 10kHz digitizers had an analog bandwidth of $\sim$ 50 kHz while the bandwidth of the fast, 1 MHz, 8210 modules was limited only by the lowpass filters at 416 MHz. Thus, $\tilde{J}/\bar{J}$ computed from Eqs. 7.23 and 7.24 includes contributions from essentially the entire fluctuation spectrum for the fast loggers. On the other hand, data from the slow loggers includes only a range of 0–50 kHz.

$\tilde{J}/\bar{J}$ was computed for ion saturation data recorded simultaneously by 8210 and 8212 data loggers. It was found that $\tilde{J}/\bar{J}$ from the 10 kHz data was typically 80–85% of the $\tilde{J}/\bar{J}$ computed from the 1 MHz data. This is consistent with

the result presented in the previous section, i.e. 80–85% of the power in the fluctuations occurred for frequencies under 50 kHz. When every 100^{th} point of the 1 MHz data sample was used to compute $\tilde{J}/\bar{J}$, simulating an 'effective' 10 kHz data sample, no statistically significant difference was found between this value and the $\tilde{J}/\bar{J}$ calculated using all the data points. This is expected since this 'effective' 10 kHz data sample was not analog bandwidth limited as the actual 10 kHz data was.

In summary, the relationship of $\tilde{J}/\bar{J}$ calculated from the 10 kHz data logger system to $\tilde{J}/\bar{J}$ calculated from the 1 MHz system can be simply stated as

$$\left.\tilde{J}/\bar{J}\right|_{10\ \mathrm{kHz}} \approx 0.80\text{–}0.85\ \left.\tilde{J}/\bar{J}\right|_{1\ \mathrm{MHz}} \tag{7.25}$$

where the factor, 0.80–0.85, is attributed to the analog bandwidth of the 10 kHz data and the power distribution in frequency of the fluctuations. This result in itself is not interesting enough to demand so much attention. The relationship in Eq. 7.25 is most useful in connecting fluctuations recorded by the slower data logger system to the virtually unlimited bandwidth fluctuation level recorded by the fast 8210 data logger system. The 8212 data logger system recorded 30 probe signals simultaneously over the duration of the shot whereas the 8210 system recorded only 15 probes for $\sim$ 8 msec. Thus, a more complete mapping of fluctuations versus poloidal position could be made from the 8212 data once the relationship in Eq. 7.25 was found to hold true.

Figure 7.18 displays $\tilde{J}/\bar{J}$ computed from both 10 kHz and 1 MHz data as a function of poloidal angle for two DENSEPACK radii of 16.8 cm and 17.2 cm. The 10 kHz data represents an average of $\tilde{J}/\bar{J}$ over 16 sweeps which span 80 msec during the steady state portion of the discharge (t = 250 msec). The 1 MHz $\tilde{J}/\bar{J}$ is from $\sim$ 1000 points during a single sweep around t = 250 msec. As indicated above, the 10 kHz data points are typically 80–85% of the 1 MHz points, independent of poloidal angle. The data at 16.8 cm, shown in Fig. 7.18

(a), was recorded with a better signal to noise level than the 17.2 cm data (b) so that the error bars for this data are smaller. For both radii, there appears to be little or no systematic variation in the value of $\tilde{J}/\bar{J}$. The 16.8 cm data does show some poloidal variation, suggesting that minima in $\tilde{J}/\bar{J}$ may occur near the top and bottom poloidal locations. However, this trend is not observed in the 17.2 cm data where the relative fluctuation level is found to vary in a way that appears to be independent of angle.

The key point that is made in Fig. 7.18 is that although the density was found to vary by a factor of 5–10 over poloidal angle (section 7.1), the quantity $\tilde{J}/\bar{J}$ showed no variation that coincided with the density variation. Perhaps more importantly, the scrape-off length was shown in section 7.1 and 7.2 to vary in angle by at least a factor of 2–4 and yet $\tilde{J}/\bar{J}$ showed no correlation with this spatial dependence.

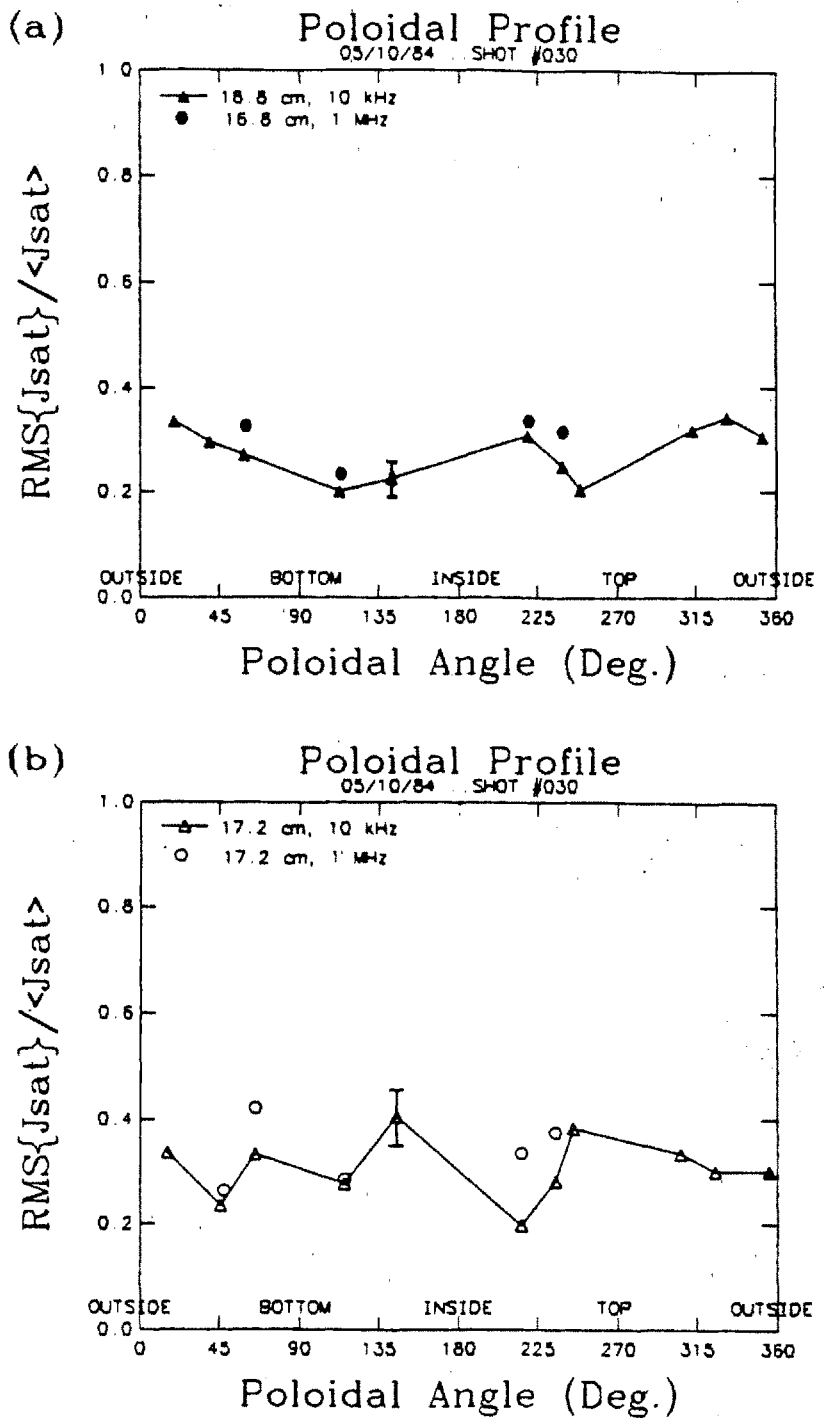

Figure 7.18 Example of RMS Fluctuation Level ($\tilde{J}/\bar{J}$) vs. Poloidal Angle

CHAPTER 8

MECHANISMS SUPPORTING POLOIDAL ASYMMETRY

Even in the absence of the enhanced H_α emission signifying a MARFE event, the edge plasma in Alcator C maintains a strongly asymmetric structure. The question of why the edge plasma should exhibit such a strong poloidal asymmetry arises. This chapter identifies five possible explanations for the measured asymmetry: 1) systematic errors in measurement due to incorrect installation of DENSEPACK and/or edge plasma perturbation by DENSEPACK, 2) noncircular magnetic flux surfaces, 3) spatially dependent diffusion, 4) spatially dependent convective transport, and 5) parallel plasma flows.

Section 8.1 considers incorrectly installed DENSEPACK probe array hardware and DENSEPACK as a perturbing 'limiter'. The possibility that systematic errors in DENSEPACK data appeared as a poloidal asymmetry was checked and eliminated.

At first, it was thought that the outer magnetic flux surfaces were noncircular so that plasma was being scraped off nonuniformly on the circular poloidal ring limiters. Section 8.2 presents magnetic flux surface measurements which show that this was not the case. The outer flux surfaces in Alcator C were measured to be very nearly circular. Even for a well-centered discharge, the edge plasma somehow maintained pressure asymmetries on magnetic flux surfaces. In reviewing previous measurements of edge plasma in Alcator C (chapter 4), it was found that edge plasma asymmetries detected previously also violated magnetic flux surfaces, supporting this result.

Section 8.3 discusses the possibility that spatially dependent diffusion caused the asymmetries. Measurements of $\tilde{J}/\bar{J}$ from DENSEPACK show that the fluctuation amplitude was nearly independent of space. Thus, in order to maintain this argument, one must require that the relative phase of $\tilde{n}$ and $\tilde{\Phi}_s$ fluctuations

be dependent on spatial position. Unfortunately, no such simultaneous measurements of $\tilde{n}$ and $\tilde{\Phi}_s$ versus poloidal position in Alcator C are available at this time.

Section 8.4 considers perpendicular convective transport in the edge plasma as a mechanism to support asymmetries. Motivated by the Pfirsch-Schlüter plus convection model outlined in section 3.2, perpendicular $\underline{E} \times \underline{B}$ convection as inferred from DENSEPACK data is examined. Perpendicular convection terms in the reduced transport equations (section 3.3) are estimated to scale the importance of this convection in the edge plasma. It is shown that although $\underline{E} \times \underline{B}$ particle transport can be significant compared to the rate of particle loss to the limiter, it possesses neither the magnitude nor the structure needed to simply explain the observed density asymmetry in the limiter shadow plasma. $\underline{E} \times \underline{B}$ electron energy transport is shown to be even less important compared to parallel power fluxes to the limiter. Thus, perpendicular transport estimated in this model only perturbs the edge and does not, by itself, explain the asymmetric equilibrium that is established. However, it is pointed out that for $r \lesssim a$, where the metallic limiter can no longer 'short out' the plasma potential, and there is no parallel transport to limiter surfaces, $\underline{E} \times \underline{B}$ fluxes may play a more dominant role. DENSEPACK data combined with observations of MARFE phenomena suggest that strong poloidal asymmetries also exist in this plasma region ($r \lesssim a$).

Finally, parallel convection in the edge plasma is considered in section 8.5. Independent of the mechanism by which plasma parameters are maintained to be nonuniform on a flux surface, bulk plasma flows along $\underline{B}$ can be driven by such asymmetries.[99] Although parallel plasma flows can affect the ion saturation current collected by a Langmuir probe, it is shown that the asymmetries detected by DENSEPACK cannot be attributed to a misinterpretation of data due to such flows. However, it is suggested that data from the thermocouple array presented in chapter 4 can be explained in terms of poloidally asymmetric transport and/or parallel flows. Recently, data obtained using a two-sided en-

ergy analyzer/Langmuir probe/heat flux probe[73,97,98,106] lends support to this hypothesis. Asymmetric limiter damage discussed in section 4.2 can also be explained in terms of parallel plasma flows in the edge plasma. The required parallel flow pattern is shown to be consistent with the poloidally asymmetric perpendicular transport inferred by DENSEPACK extending inside the limiter radius.

8.1 Check of Systematic Errors

When data from the DENSEPACK array first indicated such strong poloidal asymmetries, it was suspected that the array was either incorrectly installed or that the probes were perturbing the edge plasma. The following two subsections address these points.

8.1.1 DENSEPACK Installation

The DENSEPACK probe array consisted of fixed length molybdenum probes mounted on segments of a stainless steel support ring (Figs. 5.1 and 5.2). The array was installed one section at a time and clamped to Alcator C's vacuum vessel flange. The complete support ring assembly was designed to rest against the vacuum wall, insuring that the segments lay on a circular arc about the vacuum chamber center. The poloidal ring limiter system in Alcator C was also designed to rest against the vacuum wall. Thus DENSEPACK was constructed to sample plasma on circles which were concentric with the limiter.

One possibility for the observed systematic variation in edge plasma parameters is that the DENSEPACK hardware was incorrectly installed. If the backbone structure of DENSEPACK was in fact elliptical, density and temperature differences on the same length probes would be detected.

The position of DENSEPACK was checked during a vacuum break midway through its operation when the full array of probes was installed. A fiber optic scope was inserted into the vacuum chamber to view the position of the backbone along the vacuum wall. It was found that the stainless steel ring segments were flush against the wall as designed. Thus it was concluded that DENSEPACK was indeed sampling plasma along concentric circles of radii 16.8, 17.2, and 17.6 cm.

The fact that the density scrape-off length was found to be a function of angle further verifies that the edge plasma was truly asymmetric and that the DENSEPACK backbone was not in a displaced position. No simple displacement in DENSEPACK can account for the variation in the radial gradient of density measured by DENSEPACK.

8.1.2 DENSEPACK Perturbations

Another possible way in which DENSEPACK itself could systematically cause a poloidal asymmetry to be detected was that the probe array perturbed the edge plasma. From Fig. 8.1, one can see that there are no probes over a $\sim 40^0$ segment at the top and bottom locations. These are exactly the positions where plasma density and temperature maxima were found to exist. This raised concern that perhaps DENSEPACK, with its densely-packed probes, was acting as a limiter and reducing the plasma density and temperature from the unperturbed values.

In order to test this hypothesis, the molybdenum casing of a gridded energy analyzer[73] was inserted in the gap between probes at the top location as shown in Fig. 8.1. Normally the energy analyzer probe was pulled back and oriented to collect plasma. In this case, it was turned 90^0 to expose its maximum area to the plasma and act as a local 'limiter'. It was found that even when this 'limiter' was inserted to a radius of 16.7 cm, the poloidal profile of edge plasma parameters inferred by DENSEPACK remained unchanged. The projected area

of this 'limiter' was much larger than the area of DENSEPACK probes and yet no perturbation in the edge parameters was detected. This was strong evidence to support the conclusion that DENSEPACK itself was not perturbing the edge plasma in a way to cause the measured asymmetries.

An additional argument similar to the one stated in the previous section could be used. Even if DENSEPACK was perturbing the edge plasma, the poloidal variation in the scrape-off length cannot be simply explained. It is not likely that the same physical arrangement of probes on the inside and outside positions of the torus would lead to dramatically different gradients in the radial density profile. It was therefore concluded that poloidal asymmetries detected by DENSEPACK were due to true asymmetries appearing in the limiter shadow plasma of Alcator C.

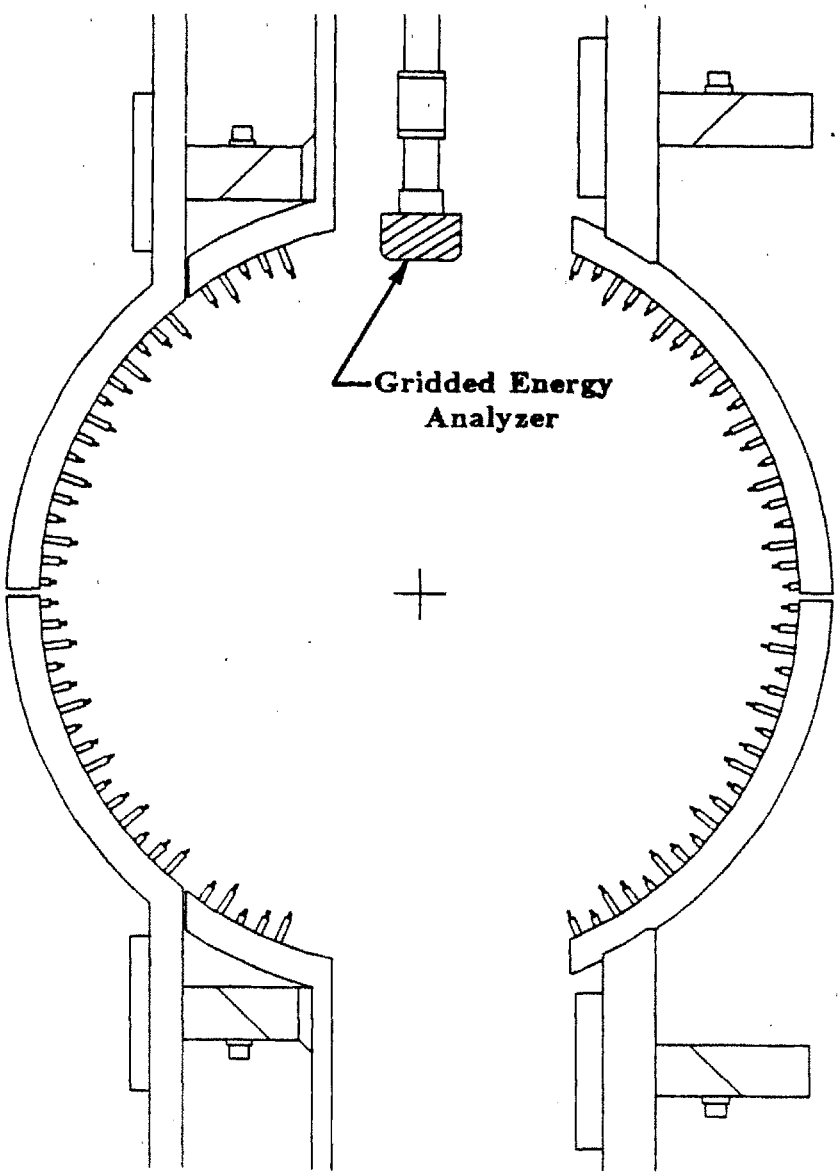

Figure 8.1 Test of DENSEPACK Perturbing Edge Plasma

8.2 Magnetic Flux Surfaces

Perhaps the simplest explanation for the observed poloidal pressure asymmetries is that the outer magnetic flux surfaces in Alcator C were not circular and did not align with the limiters. This type of argument was used in Ref. [15] in an attempt to explain the heat flux asymmetries in Alcator C. However, as discussed in section 4.3, this explanation was not consistent with the reversed field data in Ref. [15] and with asymmetric limiter damage. It is now shown in a more direct way that the outer magnetic flux surface shape in Alcator C was very close to circular and could not explain the observed variation of plasma pressure using the usual argument that $n \times T = const.$ on a non-circular flux surface.

8.2.1 Measurement of Outer Magnetic Flux Surfaces

The outer magnetic flux surface shape was measured in Alcator C by a series of 12 poloidal flux loops.[77] In the limiter shadow plasma, where negligible current flows, vacuum Maxwell's equations could be used to interpolate for the magnetic field in that region (section 5.3.1). In this manner, outer flux surfaces could be drawn by plotting surfaces of constant flux.

In order to compare magnetic flux surfaces obtained from the poloidal flux loops with pressure surfaces obtained from DENSEPACK, the magnetic data was processed in the following way. First, values of magnetic flux were interpolated and read at the probe locations as shown in Fig. 7.11*b*. Then, contours of constant flux were generated from this data in the same way that contours of constant density and temperature were generated from DENSEPACK data except that no smoothing was done. The result was a conformally mapped flux plot as shown in Fig. 8.2*a*. In processing the magnetic data in the same way as the probe data, any systematic 'artifacts' that might be introduced in data processing would appear in the same way on both plots. This data was obtained

simultaneously with the pressure data inferred from DENSEPACK which is shown for reference in Fig. 8.2*b*.

8.2.2 Comparison of $n \times T_e$ Surfaces with Flux Surfaces

The magnetic flux surfaces and plasma pressure surfaces ($n \times T_e$) shown in Fig. 8.2 clearly show that pressure was not constant on a flux surface in the limiter shadow plasma. The flux surfaces show only a minor distortion from circular whereas the pressure plot is far from circular. The most dramatic departure from $n \times T_e = const.$ is at large minor radii. A flux contour near the maximum radii sampled by DENSEPACK traverses many pressure contour lines as it encircles the plasma. The variation in pressure along these contours easily exceeds a pressure ratio of 50:1.

Even when the plasma position was moved in-out or up-down so that the outer flux surfaces shifted relative to the surfaces shown in Fig. 8.2*a*, the picture in Fig. 8.2 still held true. Although in these cases the pressure surfaces shifted slightly, it was found that the pressure profiles consistently violated $n \times T_e = const.$ on a flux surface and exhibited the same poloidally asymmetric structure.

The conclusion drawn from this data was that there were processes active in the limiter shadow plasma that supported pressure asymmetries on a flux surface. This is not so surprising in view of the fact that MARFEs were found early in the operation of Alcator C to be toroidally symmetric, violating the local rotational transform (section 4.4).

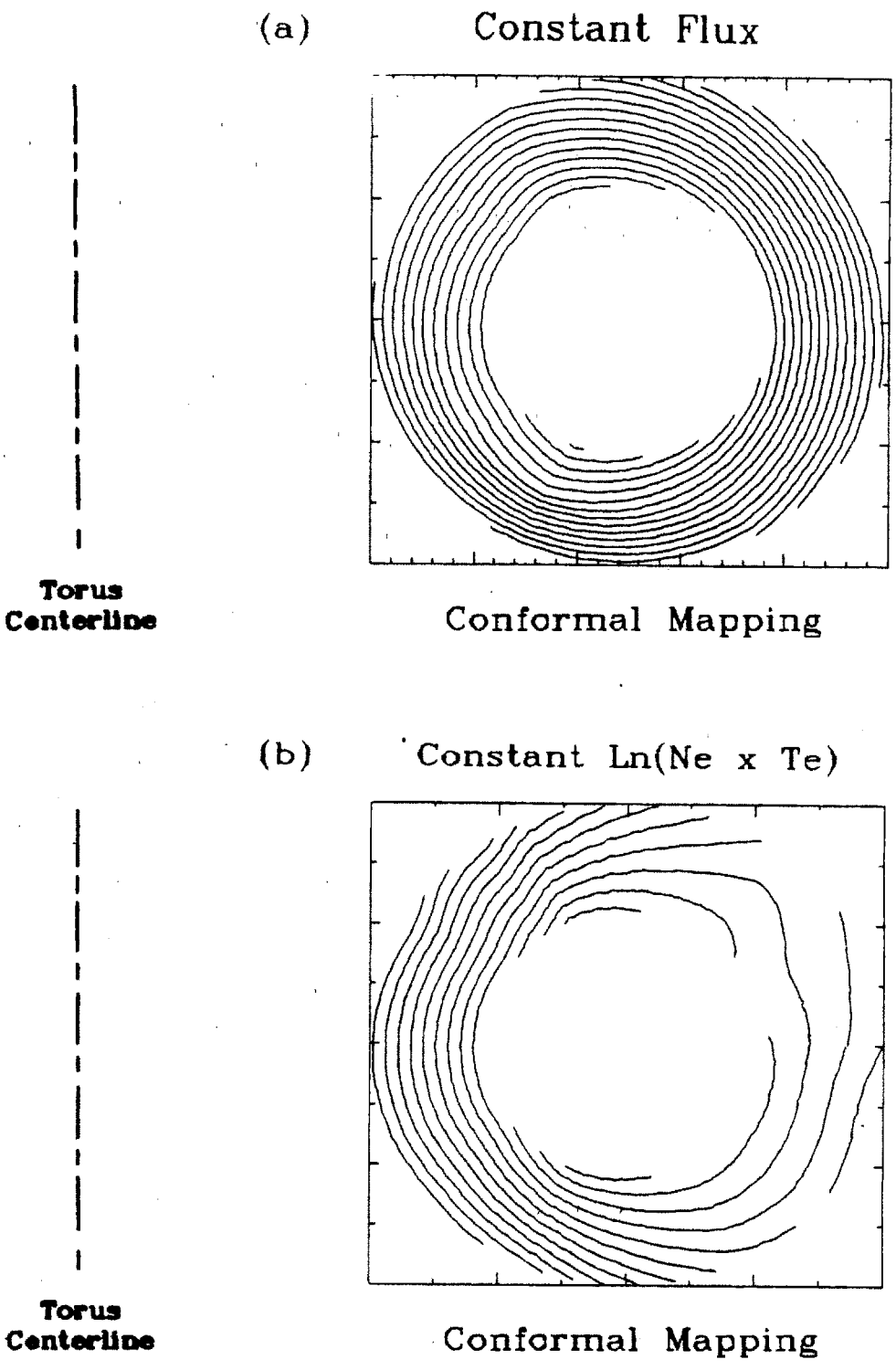

Figure 8.2 Flux Surfaces and Constant Pressure Surfaces Conformal Mapping

8.3 Spatially Dependent Diffusion

In searching for mechanisms to explain the observed density and temperature asymmetries on a flux surface in the limiter shadow plasma, one can consider the possibility that plasma transport is a function of space. Spatially non-uniform sources and sinks can also be considered. The radiation term in the electron energy equation is an example of such a local sink which can disturb the electron temperature profile and lead to a radiation thermal instability (section 2.5.3). The continuity equation, which provides an accounting of the local plasma density, can also include an ionization source term and recombination sink term.

Since the most marked poloidal asymmetry occurs in the density profile, the continuity equation bears the most immediate attention. For typical edge plasma temperatures of 5–25 eV, recombination is negligible. As argued in section 3.1, ionization can also be neglected in the limiter shadow plasma of Alcator C. Thus, neutrals and associated source and sink terms in the continuity equation can be ignored. The only dominant terms remaining in the continuity equation are convection and diffusion.

A system of reduced transport equations appropriate for conditions in the edge plasma which neglect the neutral species was presented previously in section 3.3. This section and sections 8.4 and 8.5 draw on these equations as a model of plasma transport near the limiter radius in Alcator C.

8.3.1 Scrape-off Length Variation: $D_\perp(\theta)$

The first complication considered in modelling transport in the Alcator C limiter shadow plasma is that the cross-field diffusion rate is some function of space. The 2-D diffusion model discussed in section 3.1.1 can be extended to a 3-D model that includes a poloidal variation of the diffusion coefficient. In this new model, plasma is convected to the limiter surfaces along field lines as before

and the plasma density is assumed to be approximately toroidally symmetric ($\frac{\partial}{\partial \phi} \rightarrow 0$). However, the perpendicular flux due to diffusion is written with a poloidal dependence as

$$\underline{\Gamma}_{\perp} \;=\; -D_{\perp}(\theta)\;\nabla_{\perp} n \;=\; -D_{\perp}(\theta)\;\left[\frac{\partial n}{\partial r}\hat{r} \;+\; \frac{B_{\phi}^{2}}{B^{2}}\frac{1}{r}\frac{\partial n}{\partial \theta}\hat{\theta}\right] \tag{8.1}$$

where a cylindrical (r, θ, ϕ) coordinate system is used. The continuity equation can therefore be written as

$$\nabla \cdot \Gamma_{\perp} \;=\; -\nabla \cdot \Gamma_{\parallel} \tag{8.2}$$

$$-D_{\perp}(\theta)\;\frac{\partial^{2} n}{\partial r^{2}} \;-\; \frac{1}{r}\frac{\partial}{\partial \theta}\left[D_{\perp}(\theta)\;\frac{B_{\phi}^{2}}{B^{2}}\frac{1}{r}\frac{\partial n}{\partial \theta}\right] \;\approx\; -\frac{n\;C_{s}}{L(\theta)} \tag{8.3}$$

where the divergence of the parallel flow to the limiter is approximated as the value from the 2-D model. The fact that the parallel connection length, $L(\theta)$, depends on poloidal angle is explicitly shown for clarity. Since radial derivatives dominate, Eq. 8.3 reduces to

$$D_{\perp}(\theta)\;\frac{\partial^{2} n}{\partial r^{2}} \;\approx\; \frac{n\;C_{s}}{L(\theta)} \tag{8.4}$$

which yields the same exponential density dependence in radius except that the scrape-off length depends on angle. A poloidal density profile at the limiter radius, $n_{a}(\theta)$, and a density of zero at $r \rightarrow \infty$ can be specified as the boundary conditions so that

$$n(r) \;=\; n_{a}(\theta)\;e^{(a-r)/\lambda_{n}(\theta)} \tag{8.5}$$

$$\lambda_n(\theta) = \sqrt{\frac{L(\theta)\ D_\perp(\theta)}{C_s}}\ . \tag{8.6}$$

Thus, the first order response of a poloidally symmetric plasma to a poloidally dependent perpendicular diffusion coefficient is a local adjustment of the radial scrape-off length. The density at the limiter radius is not directly determined by $D_\perp$ but is obtained by matching the fluxes crossing from the central plasma into the limiter shadow plasma. Consequently, poloidal variations in density offer no unambiguous information about $D_\perp$. However, λ_n is readily determined from DENSEPACK data and can be directly related to $D_\perp$ through Eq. 8.6.

As shown in section 7.14, the scrape-off length was found to be a strong function of angle in Alcator C edge plasma. From the simple model outlined above, such a variation in the scrape-off length could be due to a poloidally dependent diffusion coefficient through Eq. 8.6. A poloidal variation of factors of 5–10 in scrape-off length implies factors of 12–50 variation in $D_\perp$ even when accounting for a factor of $\sim$ 2 variation in $L(\theta)$. Including poloidal diffusion terms in Eq. 8.4 only results in a reduction of the poloidal variation of the plasma density. Thus, a factor of 12–50 variation in $D_\perp$ represents the minimum variation required to explain the poloidal variation in λ_n.

Given that the anomalous level of $D_\perp$ observed in the edge plasma of tokamaks is due to turbulence, one would expect that a factor of 12–50 variation in $D_\perp$ would show up as some variation in the fluctuation level characterized by $\tilde{J}/\bar{J}$. However, Fig. 7.18 shows no clear evidence of any systematic poloidal variation in $\tilde{J}/\bar{J}$.

The conclusion is that either $D_\perp$ changes in space independent of the relative power in the fluctuations characterized by $\tilde{J}/\bar{J}$ or that some other mechanism is responsible for the poloidal asymmetries. It is unlikely that $D_\perp$ departs

so markedly from some spatially uniform value implied by the spatially uniform level of $\tilde{J}/\bar{J}$, especially when it is so widely accepted that fluctuations are responsible for the anomalously high value for $D_\perp$. This inconsistency prompts the following discussions of other mechanisms which could cause the edge density profile to be asymmetric.

8.3.2 Scrape-off Length Variation: Directed $\tilde{n}$, $\tilde{\Phi}_s$ Fluxes

Another possibility is that edge plasma turbulence in Alcator C does not lead to a purely isotropic diffusion flux but rather a directed, time averaged $\langle \tilde{n}\ \underline{\tilde{E}} \times \underline{B} \rangle$ flux as discussed in section 2.4.2. In this case, the level of $\tilde{J}/\bar{J}$ is not important in determining the magnitude of the perpendicular flux. Instead, the relative phase of $\tilde{n}$ and $\nabla_\perp \tilde{\Phi}_s$ determines the magnitude and direction of this time averaged 'diffusive' flux. Such fluctuation induced particle fluxes due to $\tilde{n}$ and $\tilde{\Phi}_s$ have been detected in the edge plasma of other tokamaks[14] and estimated through the use of Eq. 2.15.

A possible scenario which could explain the measured poloidal variation in the density profile is that coherent components of $\tilde{n}, \tilde{\Phi}_s$ fluctuations are phased differently at various poloidal angles in the limiter shadow plasma. These fluctuation induced particle fluxes can then add or subtract to the local, purely diffusive flux, depending on the poloidal position.

More formally, one can divide the perpendicular fluxes into two components: namely, a part that includes an isotropic diffusion and a part that results from phase correlated $\tilde{n}, \tilde{\Phi}_s$ fluctuations,

$$\underline{\Gamma}_\perp = \underline{\Gamma}_\perp^D + \underline{\Gamma}_\perp^{\tilde{n},\tilde{\Phi}} \tag{8.7}$$

$$\underline{\Gamma}_\perp^D = D_\perp \nabla_\perp n \tag{8.8}$$

$$\underline{\Gamma}_{\perp}^{\tilde{n},\tilde{\Phi}} \;=\; \int \frac{\tilde{n}(\omega)\;\underline{B}\times\nabla\tilde{\Phi}_s(\omega)}{B^2}\;cos\gamma(\omega)\;\partial\omega\;. \tag{8.9}$$

Here, the directed turbulent flux is assumed to be dependent on poloidal angle. On the other hand, $D_\perp$ is no longer assumed to be a function of space. Incorporating $\underline{\Gamma}_{\perp}^{\tilde{n},\tilde{\Phi}}$ into Eq. 8.2 results in

$$-D_\perp\;\frac{\partial^2 n}{\partial r^2}\;+\;\nabla_\perp\cdot\underline{\Gamma}_{\perp}^{\tilde{n},\tilde{\Phi}}(\theta)\;=\;-\frac{n\;C_s}{L(\theta)}\;. \tag{8.10}$$

Performing $\nabla\cdot$[Eq. 8.9], one obtains

$$\begin{aligned}\nabla\cdot\underline{\Gamma}_{\perp}^{\tilde{n},\tilde{\Phi}} \;=\; &\int\Big[\frac{\underline{B}\times\nabla\tilde{\Phi}_s(\omega)}{B^2}\Big]\cdot\nabla\tilde{n}(\omega)\;cos\gamma(\omega)\;\partial\omega\\ &+\int 2\;\tilde{n}(\omega)\;\nabla\tilde{\Phi}_s(\omega)\cdot\Big[\frac{\underline{B}\times\nabla|\underline{B}|}{B^3}\Big]\;cos\gamma(\omega)\;\partial\omega\;.\end{aligned} \tag{8.11}$$

The second term on the right hand side of Eq. 8.11 can be neglected compared to the first term since $\nabla\tilde{n}/\bar{n}$ is much larger than $\nabla|\underline{B}|/|\underline{B}|$. Equation 8.10 can now be written with an effective source term due to correlated $\tilde{n},\tilde{\Phi}_s$ fluctuations as

$$-D_\perp\;\frac{\partial^2 n}{\partial r^2}\;=\;-\frac{n\;C_s}{L(\theta)}\;+\;n\;S^{\tilde{n},\tilde{\Phi}}(\theta) \tag{8.12}$$

where

$$S^{\tilde{n},\tilde{\Phi}}(\theta)\;=\;-\int\Big[\frac{\underline{B}\times\nabla\tilde{\Phi}_s(\omega)}{B^2}\Big]\cdot\frac{\nabla\tilde{n}(\omega)}{\bar{n}}\;cos\gamma(\omega)\;\partial\omega \tag{8.13}$$

and $\bar{n}$ is the time averaged density ($= n$ unless otherwise noted).

The solution to Eq. 8.12 is also an exponential in radius except that now the radial e-folding length is

$$\lambda_n(\theta) = \sqrt{\frac{D_\perp}{C_s/L(\theta) - S^{\tilde{n},\tilde{\Phi}}(\theta)}} . \tag{8.14}$$

Thus, the density scrape-off length depends on the relative sign and magnitude of $S^{\tilde{n},\tilde{\Phi}}(\theta)$ compared to $C_s/L(\theta)$. In view of the fact that potential and density fluctuations occur over very short spatial correlation lengths (~ 0.1 cm for Alcator C), it is possible that $S^{\tilde{n},\tilde{\Phi}}(\theta)$ can be large enough to explain the observed density asymmetry. Ideally, $\nabla\tilde{n}/\bar{n}$ and $\nabla\tilde{\Phi}_s$ should be measured at various poloidal locations in order to compute $S^{\tilde{n},\tilde{\Phi}}(\theta)$. Unfortunately, no simultaneous measurements of $\nabla\tilde{n}/\bar{n}$ and $\nabla\tilde{\Phi}_s$ have been made in Alcator C edge plasma.

In conclusion, transport due to $\tilde{n}, \tilde{\Phi}_s$ fluctuations is identified as a candidate mechanism which might explain the poloidal asymmetries in Alcator C edge plasma. Since no data exists at this time to support or refute the above model, the importance of $\tilde{n}, \tilde{\Phi}_s$ transport must be left as an open question which may be answered in some future work. Keeping this in mind, other candidate mechanisms can still be investigated. The following two sections consider the possible role of bulk plasma convection in the edge plasma of Alcator C.

8.4 Perpendicular Convection

In addition to fluctuations in plasma density and potential, the edge plasma exhibits non-zero time averaged components of n and Φ_s. Poloidal profiles of such near steady state quantities were presented in detail in section 7.2. The fact that the edge plasma can maintain near steady state gradients in Φ_s prompts one to consider the impact that $\underline{E} \times \underline{B}$ bulk plasma flows may have on the equilibrium density and temperature profiles.

Section 7.2.4 already showed that typical gradients in Φ_s inferred from DENSEPACK data suggest $\underline{E} \times \underline{B}$ convection velocities which can be significant compared to the effective radial flow velocity due to diffusion alone. Thus, it may indeed be possible for these flows to influence the equilibrium profiles in a way analogous to the Pfirsch-Schlüter convection plus diffusion model discussed in section 3.2.

In principle, it is possible to infer 2-D $\underline{E} \times \underline{B}$ flow patterns from DENSEPACK data. From these flow patterns and the already inferred 2-D density and temperature profiles, perpendicular convection terms in the reduced fluid transport equations can be evaluated. In this way, the impact of $\underline{E} \times \underline{B}$ convection as it affects density and temperature in the limiter shadow plasma can be investigated. This approach is used in the following subsections to estimate the magnitude of convection terms in both the continuity and electron energy equations.

8.4.1 Convection Terms versus Non-Convection Terms

The purpose of this subsection is to compare the relative magnitude of perpendicular convection terms in the continuity and electron energy equations to other terms in these equations. The approach is first to obtain simplified continuity and electron energy equations which retain the dominant terms for an edge plasma that is nearly poloidally symmetric. In doing this, the set of reduced fluid transport equations presented in section 3.3 is used. Once this is done, the magnitude of the convection terms can be compared to typical magnitudes of non-convection terms in these equations. The goal is to see if perpendicular convection in the Alcator C edge plasma is sufficiently strong to perturb poloidally symmetric profiles into the observed asymmetric structure.

Starting from Eqs. 3.114 and 3.120, the continuity and electron energy equations can be written with explicit convective and diffusive transport terms as

$$\nabla \cdot \underline{\Gamma}^D \; + \; \underline{V}^C \cdot \nabla n \; + \; n \; \nabla \cdot \underline{V}^C \; = \; 0 \tag{8.15}$$

$$\begin{aligned} \frac{3}{2} \; \underline{\Gamma}_e^D \cdot \nabla T_e \; + \; n \; T_e \nabla \cdot \frac{\underline{\Gamma}_e^D}{n} \; + \; \frac{3}{2} \; n \; \underline{V}_e^C \cdot \nabla T_e \\ + \; n \; T_e \nabla \cdot \underline{V}_e^C \; = \; -\nabla \cdot \underline{q}_e \end{aligned} \tag{8.16}$$

where $\underline{\Gamma}^D$ is the particle flux due to diffusion, and $\underline{V}^C$ is some convection velocity. From the MHD fluid model, $\underline{V} \approx \underline{V}_i$, while $\underline{V}_e$ is given by Eq. 3.112. The radiation term normally in Eq. 8.16 has been dropped in order to consider only the impact of convection on the electron temperature profile. By the same argument, the ohmic heating term is also neglected.

The perpendicular convection in Eqs. 8.15 and 8.16 is assumed to arise from $\underline{E} \times \underline{B}$ and diamagnetic particle drifts. Taking $\underline{B} \times$[Eq. 3.118], and using

Eqs. 3.112 and 3.116, one obtains both contributions for the convection part of the perpendicular velocities,

$$\underline{V}_{\perp}^{C} = \frac{\underline{B} \times \nabla \Phi_s}{B^2} + \frac{\underline{B} \times \nabla P_i}{q\ n\ B^2} \tag{8.17}$$

$$\underline{V}_{e\perp}^{C} = \frac{\underline{B} \times \nabla \Phi_s}{B^2} - \frac{\underline{B} \times \nabla P_e}{q\ n\ B^2} \tag{8.18}$$

where $\underline{E}$ is written as $-\nabla \Phi_s$.

In the parallel direction, the bulk plasma accelerates to the sound speed along field lines as it approaches the limiter surface. This effect leads to a local plasma sink term in the continuity equation (section 3.1.1) of order

$$\nabla_{\parallel} \cdot n\ \underline{V}_{\parallel}^{C} \approx \frac{n\ C_s}{L} . \tag{8.19}$$

In the electron energy equation, a similar scaling for the divergence of the parallel flow is

$$n\ T_e\ \nabla_{\parallel} \cdot \underline{V}_{\parallel}^{C} \approx \frac{n\ T_e\ C_s}{L} . \tag{8.20}$$

Incorporating Eqs. 8.17–8.20 into 8.15 and 8.16 yields

$$\nabla \cdot \underline{\Gamma}^{D} + \left[\frac{\underline{B} \times \nabla \Phi_s}{B^2}\right] \cdot \nabla n + 2\ n\ (\nabla \Phi_s + \nabla P_i) \cdot \left[\frac{\underline{B} \times \nabla |\underline{B}|}{B^3}\right] \approx -\frac{n\ C_s}{L} \tag{8.21}$$

$$\frac{3}{2}\,\underline{\Gamma}^D\cdot\nabla T_e \;+\; n\,T_e\,\nabla\cdot\frac{\underline{\Gamma}^D}{n} \;+\; \frac{3}{2}\,n\left[\frac{\underline{B}\times\nabla\Phi_s}{B^2}\right]\cdot\nabla T_e$$
$$+\;2\,n\,T_e\left[\nabla\Phi_s - 4.92\nabla T_e - 2.42T_e\nabla ln(n))\right]\cdot\left[\frac{\underline{B}\times\nabla|\underline{B}|}{B^3}\right]$$
$$+\;\frac{3}{2}\,n\,\underline{V}^C_{\|}\cdot\nabla_{\|}T_e \;+\nabla\cdot\left(-\kappa^e_{\|}\nabla_{\|}T_e - \kappa^e_{\perp}\nabla_{\perp}T_e\right) \;\approx\; -\frac{n\,T_e\,C_s}{L}\,. \tag{8.22}$$

The numerical factors in this equation come from combining terms and using Braginskii's transport coefficients.[59]

$\frac{\underline{B}\times\nabla|\underline{B}|}{B^3}$ terms in Eqs. 8.21 and 8.22 are small compared to $\frac{\underline{B}\times\nabla\Phi_s}{B^2}$ terms and can be neglected. At the symmetry point between limiters, one expects that $\nabla_{\|}T_e \approx 0$ and $\nabla_{\|}n \approx 0$ so that parallel heat conduction and convection can be ignored. In the case where strong poloidal asymmetries develop, this approximation cannot be made. However, here we are considering the case of a nearly poloidally symmetric edge plasma. Furthermore, $\nabla\cdot\kappa_{\perp}\nabla_{\perp}T_e$ is neglected relative to $\underline{\Gamma}^D_{\perp}\cdot\nabla_{\perp}T_e$ since density gradients greatly exceed temperature gradients and perpendicular diffusion is always anomalously large.

With these approximations, the continuity and electron energy equations reduce to

$$\nabla_{\perp}\cdot\underline{\Gamma}^D \;+\; \left[\frac{\underline{B}\times\nabla\Phi_s}{B^2}\right]\cdot\nabla n \;\approx\; -\frac{n\,C_s}{L} \tag{8.21}$$

$$n\,T_e\,\nabla_{\perp}\cdot\frac{\underline{\Gamma}^D}{n} \;+\; \frac{3}{2}\,\underline{\Gamma}^D_{\perp}\cdot\nabla_{\perp}T_e \;+\; \frac{3}{2}\,n\left[\frac{\underline{B}\times\nabla\Phi_s}{B^2}\right]\cdot\nabla T_e \;\approx\; -\frac{n\,T_e\,C_s}{L}\,. \tag{8.22}$$

A similar version of these two equations appeared earlier as Eqs. 3.52 and 3.74 when Pfirsch-Schlüter convection was considered as a possible perpendicular transport mechanism. However, we are interested in these somewhat more

general equations in order to insert values for $\nabla\Phi_s$ inferred directly from the DENSEPACK probe array.

DENSEPACK data shows that radial density profiles in the limiter shadow plasma are modelled well as a local exponential with an e-folding length that depends on angle,

$$n(r,\theta) \approx n_a(\theta)\ e^{(a-r)/\lambda_n(\theta)} . \tag{8.23}$$

Assuming that diffusion is not a function of space, and using the fact that radial gradients are much larger than poloidal gradients, the continuity equation can be approximated as

$$-\frac{D_\perp\ n}{\lambda_n^2(\theta)} + \left[\frac{\underline{B}\times\nabla\Phi_s}{B^2}\right]\cdot\nabla n \approx -\frac{n\ C_s}{L(\theta)} . \tag{8.24}$$

In a similar manner, modelling $T_e(r,\theta)$ as

$$T_e(r,\theta) \approx T_{ea}(\theta)\ e^{(a-r)/\lambda_T(\theta)} , \tag{8.25}$$

the electron energy equation can be approximated as

$$-\frac{3}{2}\ \frac{D_\perp\ n\ T_e}{\lambda_n(\theta)\ \lambda_T(\theta)} + \frac{3}{2}\left[\frac{\underline{B}\times\nabla\Phi_s}{B^2}\right]\cdot\nabla T_e \approx -\frac{n\ T_e\ C_s}{L(\theta)} , \tag{8.26}$$

since for exponential density gradients, $\nabla\cdot(\underline{\Gamma}_\perp^D/n) = 0$.

The impact of $\underline{E}\times\underline{B}$ convection on the density and temperature profiles in the limiter shadow plasma can now be seen from Eqs. 8.24 and 8.26. In the absence of an $\underline{E}\times\underline{B}$ convection, these equations reproduce the unperturbed profiles

as derived previously in sections 3.2.4 and 3.2.5 for Pfirsch-Schlüter convection. Therefore, in order for the perpendicular convection terms to significantly perturb the density or temperature profiles, they need to be the same order of magnitude as other terms in these equations. Using the local sink term in these equations as a comparison, it is required that

$$|\epsilon_n| \approx 0.1 - 1 \tag{8.27}$$

for perpendicular convection in the continuity equation to be important where

$$\epsilon_n \equiv \frac{L \left[\frac{\underline{B} \times \nabla \Phi_s}{B^2}\right] \cdot \nabla n}{n \, C_s} \, . \tag{8.28}$$

Similarly for perpendicular convection to be important in the electron energy equation,

$$|\epsilon_T| \equiv \left| \frac{\frac{3}{2} \, L \left[\frac{\underline{B} \times \nabla \Phi_s}{B^2}\right] \cdot \nabla T_e}{T_e \, C_s} \right| \approx 0.1 - 1 \, . \tag{8.29}$$

One can therefore examine $|\epsilon_n|$ and $|\epsilon_T|$ as inferred from DENSEPACK data to assess the impact of $\underline{E} \times \underline{B}$ convection on the edge plasma.

Finally, λ_n can be estimated in terms of ϵ_n from Eq. 8.24 when ϵ_n is only a function of poloidal angle as

$$\lambda_n(\theta) = \frac{\lambda_{n0}(\theta)}{\sqrt{1 + \epsilon_n(\theta)}} \, , \tag{8.30}$$

where λ_{n0} is defined as the scrape-off length for the case no convection with poloidally symmetric diffusion, $\lambda_{n0}(\theta) = \sqrt{D_\perp L(\theta)/C_s}$. Thus, perpendicular convection is another process which can result in a density scrape-off length that

depends on angle. Should ϵ_n approach -1, a very long scrape-off length would result. On the other hand, if ϵ_n is $+1$, the scrape-off length becomes a factor of $1/\sqrt{2}$ shorter.

The next step in this analysis is to determine the $\underline{E} \times \underline{B}$ flow field and ∇n, ∇T_e vector fields so that ϵ_n and ϵ_T can be calculated.

8.4.2 $\underline{E} \times \underline{B}$ Flow Fields

Two-dimensional $\underline{E} \times \underline{B}$ flow fields in the limiter shadow plasma of Alcator C can be inferred from DENSEPACK data. Since $\underline{E} = -\nabla \Phi_s$, one first needs an estimate of the spatial variation of Φ_s. The local plasma space potential can be estimated from the probe floating potential and the local temperature through Eq. 6.5,

$$\Phi_s \approx \Phi_f + 3.5\, T_e \,. \tag{8.31}$$

Once $\Phi_s(r,\theta)$ is obtained from DENSEPACK data, the perpendicular $\underline{E} \times \underline{B}$ velocity due to space potential variations,

$$\underline{V}_\perp^S \equiv \frac{\underline{B} \times \nabla \Phi_s}{B^2} \,, \tag{8.32}$$

can be computed. Since $\underline{V}_\perp^S$ is perpendicular to both $\underline{B}$ and $\nabla \Phi_s$, and $\underline{B}$ is mostly toroidal, the $\underline{E} \times \underline{B}$ flow field closely follows surfaces of constant Φ_s. Figure 8.3*a* shows a typical $\underline{E} \times \underline{B}$ flow field as determined from surfaces of constant Φ_s plotted in the usual conformal mapping format (see section 7.2.1).

In computing ϵ_T as defined in Eq. 8.29, the total $\underline{E} \times \underline{B}$ convection velocity need not be calculated. Using Eq. 8.31,

$$\frac{\underline{B} \times \nabla \Phi_s}{B^2} \cdot \nabla T_e \approx \frac{\underline{B} \times \nabla (\Phi_f + 3.5\ T_e)}{B^2} \cdot \nabla T_e = \frac{\underline{B} \times \nabla \Phi_f}{B^2} \cdot \nabla T_e \equiv \underline{V}_\perp^f \cdot \nabla T_e \quad . \tag{8.33}$$

Thus, the component of perpendicular convection that affects the temperature profile, $\underline{V}_\perp^f$, is due to floating potential variations alone. Figure 8.3*b* shows the $\underline{E} \times \underline{B}$ flow field that results from just floating potential variations.

Both flow fields in Fig. 8.3 exhibit a complex spatial structure. $\underline{V}_\perp^f$ is particularly interesting since the flow pattern possesses a radially inward component on the inside and a radially outward component at the top-outside and bottom-outside locations. This suggests that the flow field may be responsible for the observed density and/or temperature asymmetry. However, as shown in the next subsection, the impact of this convection on the equilibrium density and temperature profiles is small compared to the rate of particle and energy losses to the limiter. Thus, these flows merely perturb the plasma in the limiter shadow region and do not explain the highly asymmetric equilibrium.

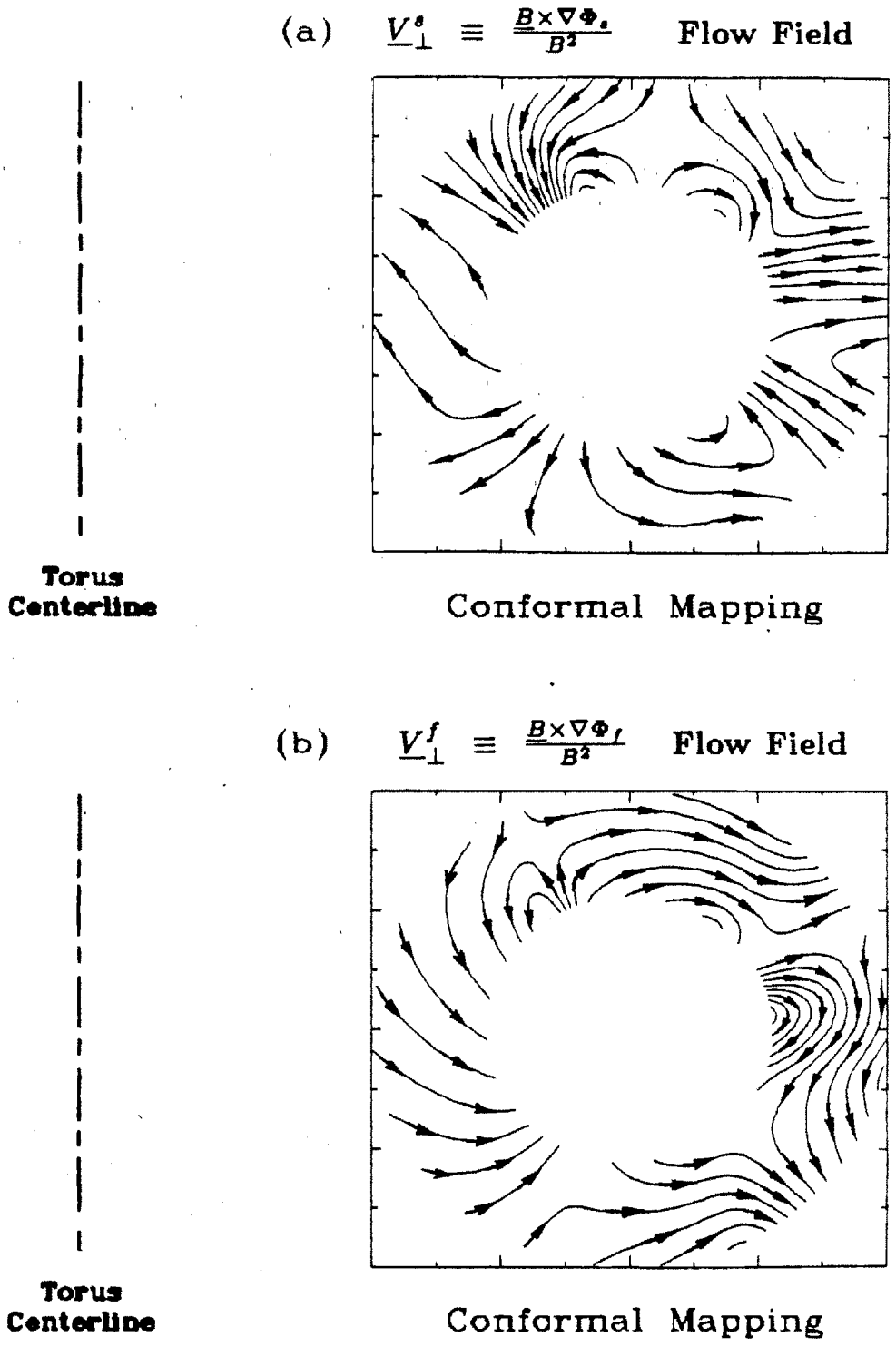

Figure 8.3 $\underline{E} \times \underline{B}$ Flow Fields

8.4.3 Magnitude of Perpendicular Convective Transport

The magnitude of the perpendicular convection term and parallel flow divergence term in the continuity equation (8.24) can be estimated from DENSEPACK data. Figure 8.4 displays conformally mapped contours of nC_s/L and $\frac{B\times\nabla\Phi_*}{B^2}\cdot\nabla n$.

nC_s/L is simply computed from the local density and temperature. The distance to the limiter, L, depends on poloidal angle and is taken into account for this plot. Since the strongest variation of nC_s/L is through n, this quantity generates contours which are similar to the constant density contours (Fig. 7.12).

The perpendicular convective transport term, $\frac{B\times\nabla\Phi_*}{B^2}\cdot\nabla n$, plotted in Fig. 8.4*b* is obtained by computing the local perpendicular convection and gradient in n. This term displays a more detailed structure in poloidal angle. All parameters used in computing these terms are smoothed in poloidal angle, and gradients are computed as an average over many data points. The idea is to look for large spatial scale variations in these terms which may correlate with the general structure of the observed density asymmetry.

The ratio of these two terms, ϵ_n, is plotted in Fig. 8.5. Typical values of ϵ_n range $\sim \pm 0.15$. This indicates that perpendicular convective particle transport in the shadow plasma is indeed significant enough not to be ignored. However, as indicated from both the poloidal variation and magnitude of ϵ_n, this convection does not simply explain the observed poloidal density asymmetry.

From Eq. 8.30, a variation of ϵ_n from -0.15 to $+0.15$ implies a scrape-off length variation of only $\approx 15\%$. In addition, the areas of positive ϵ_n and negative ϵ_n do not coincide with the poloidal variation of the scrape-off length or density (Fig. 7.13). Therefore, it is concluded from this simple model that although perpendicular convective particle transport can perturb the edge density profile, it cannot explain the observed asymmetry in density.

A similar analysis can be performed to estimate values for ϵ_T over the poloidal cross-section. Comparing Eq. 8.28 with 8.29, one can readily see that $|\epsilon_T| \ll |\epsilon_n|$ since gradients in T_e are typically much smaller than gradients in n, and only floating potential variations drive $\underline{E} \times \underline{B}$ flows that affect the temperature profile. Computing ϵ_T from DENSEPACK data, it is indeed found that $|\epsilon_T| \ll |\epsilon_n|$ with typical values of $|\epsilon_T| \lesssim 0.02$. Perpendicular convective electron energy transport is therefore only a small perturbation compared to the total energy balance in the limiter shadow plasma of Alcator C.

In conclusion, the analysis of DENSEPACK data outlined in this section indicates that although $\underline{E} \times \underline{B}$ particle transport in the limiter shadow plasma can be significant compared to the loss rate of particles to the limiter, it is not sufficient to explain the observed poloidal density asymmetry in any simple way. In addition, it is found that $\underline{E} \times \underline{B}$ electron energy transport is negligible compared to energy fluxes to the limiter and therefore does not directly influence the equilibrium electron energy balance of the shadow plasma. Thus, the role of $\underline{E} \times \underline{B}$ fluxes in this region is secondary in nature. Such fluxes may act to perturb the edge plasma and cause other mechanisms such as a local radiation thermal instability to occur, although there is no way to directly test this hypothesis with DENSEPACK.

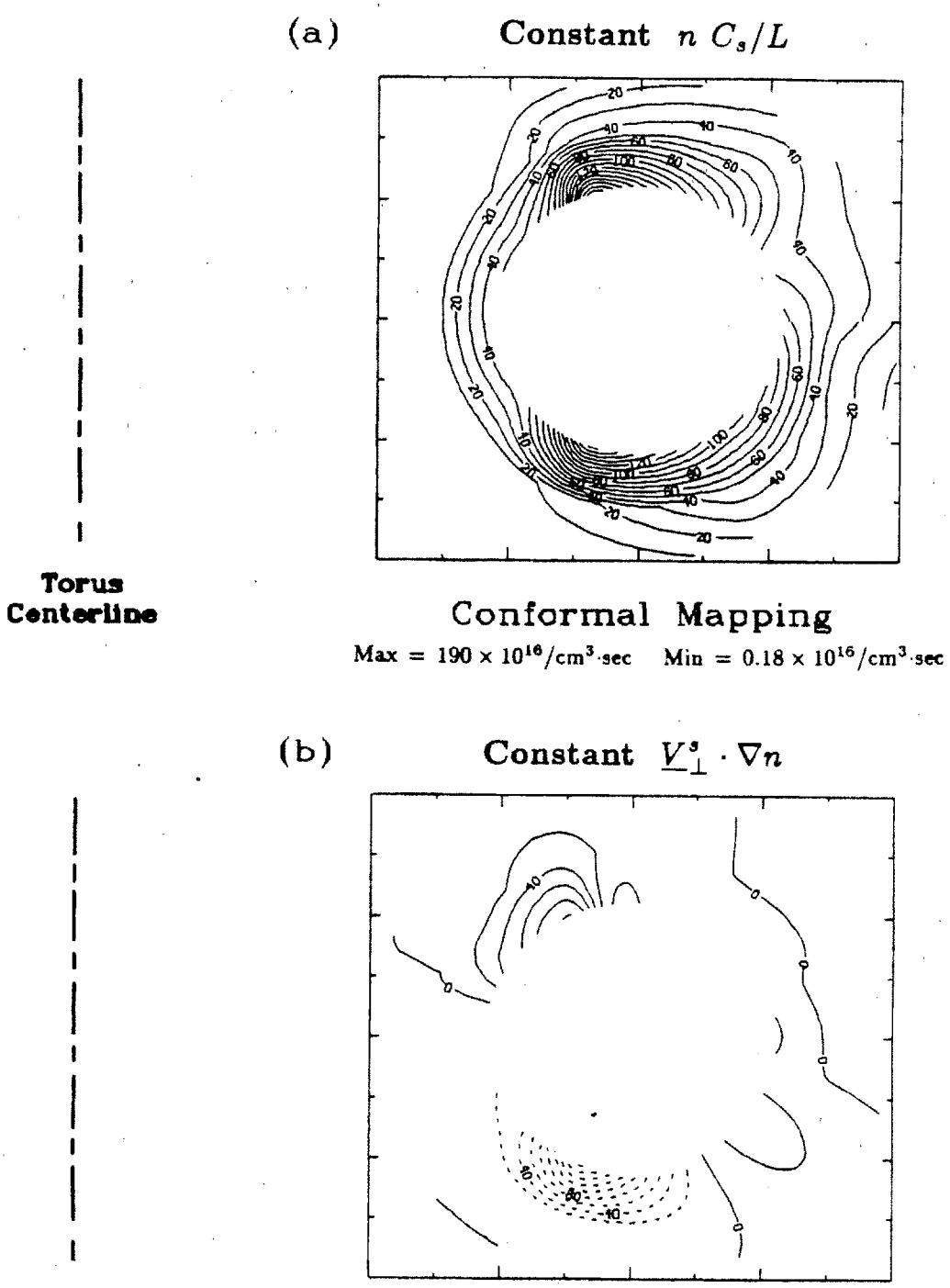

Figure 8.4 nC_s/L and $\frac{B \times \nabla \Phi_s}{B^2} \cdot \nabla n$
Conformal Mapping

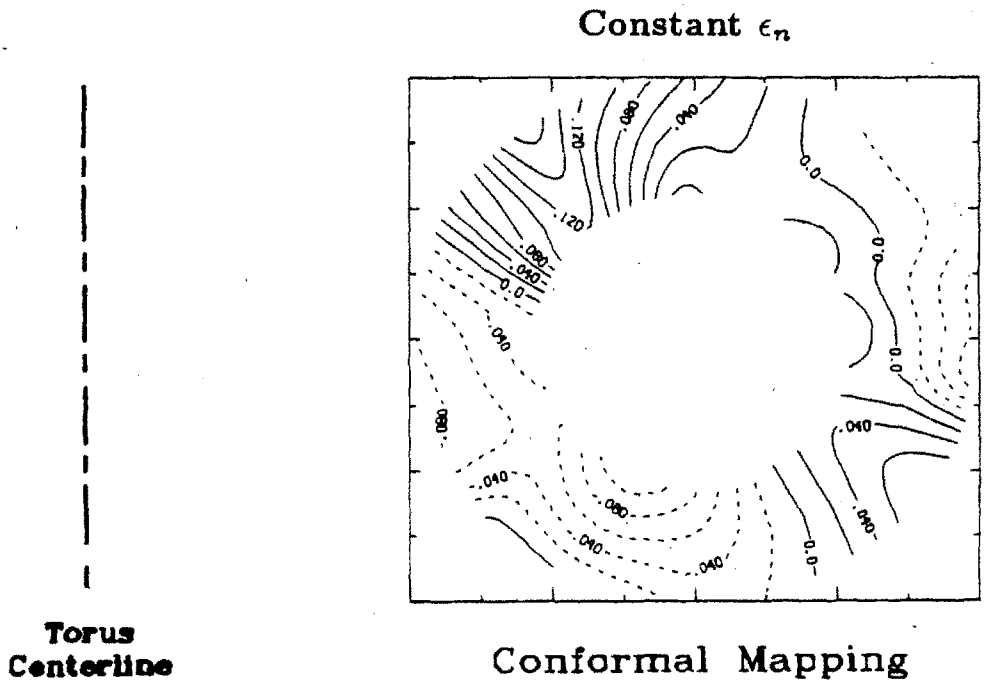

Figure 8.5 ϵ_n Conformal Mapping

8.4.4 Poloidal Asymmetries Inside the Limiter Radius

The above analysis of perpendicular transport processes is restricted to the limiter shadow plasma sampled by DENSEPACK. However, there is strong evidence that poloidal asymmetries are not restricted to this region and can appear on closed flux surfaces inside the limiter radius.

From the density profiles and scrape-off lengths measured by DENSEPACK, the poloidal variation in the density profile can be extrapolated to the limiter radius. Figure 8.6 shows a density scrape-off length profile and the density profile at $r = 16.5$ cm (limiter radius) that results from this procedure. Note that even at the limiter radius, the density retains the same asymmetric structure and exhibits at least a factor of 2 variation over poloidal angle. Note also that the density maxima are shifted to the small major radius side of the top and bottom locations. The values of these maxima are very large at $n_e \approx 10^{14}/\text{cm}^3$ compared to the central line-averaged density, $\bar{n}_e \approx 2 \times 10^{14}/\text{cm}^3$. Thus, the edge plasma just inside the limiter radius must also support strong poloidal asymmetries.

The asymmetries detected during MARFE phenomena are consistent with these observations from DENSEPACK. At the onset of a MARFE, a buildup of density is typically detected at the smaller major radius edge of tokamak plasmas by density interferometer measurements.[4-6,124] In Alcator C, the line-averaged density along the inside vertical chord can approach or exceed the central line-averaged density (section 4.4.2). Comparing the path of this inside interferometer beam (-12 cm inside the magnetic axis) with the poloidal density profile at the limiter radius shown in Fig. 8.6*b*, one can see that it passes through high density and steep poloidal density gradient plasma (dashed lines in Fig. 8.6*b*). However, the line-integral of this density in the limiter shadow plasma is not nearly enough to account for the observed density buildup along this chord. Consequently, the density asymmetry must not only extend inside the limiter radius, $r \lesssim a$, but also be more pronounced there.

The radiating MARFE region coincident with these events is observed to be strictly toroidally symmetric, not following field lines. Furthermore, this radiating region is found to extend slightly inside the limiter radius where field lines are not intercepted by limiter surfaces. This is further evidence of a poloidally asymmetric plasma existing on closed flux surfaces inside the limiter radius.

The implication of these observations combined with DENSEPACK data is that perpendicular transport in both the limiter shadow and a small annular region inside the limiter radius is highly poloidally asymmetric. Gradients are thereby supported along field lines. The resulting picture is an edge plasma that displays poloidal asymmetries yet retains toroidal symmetry.

Transport modelling of the edge plasma region just inside the limiter radius is more complex than the limiter shadow plasma. One must now include neutral ionization source terms which could be neglected in the shadow plasma of Alcator C. In addition, steady state $\underline{E} \times \underline{B}$ fluxes may be more important. The poloidal limiter which was present during the DENSEPACK experiment is not available to 'short out' E-fields in this region. An additional consequence can be a sharp potential mismatch between the limiter shadow plasma and the plasma just inside limiter radius. The limiter as such an electrically perturbing structure has been considered in the past.[22,102]

Unfortunately, this plasma region is difficult to diagnose. Nevertheless, whatever transport processes which are active in this region result in a poloidally asymmetric density boundary condition for the limiter shadow plasma.

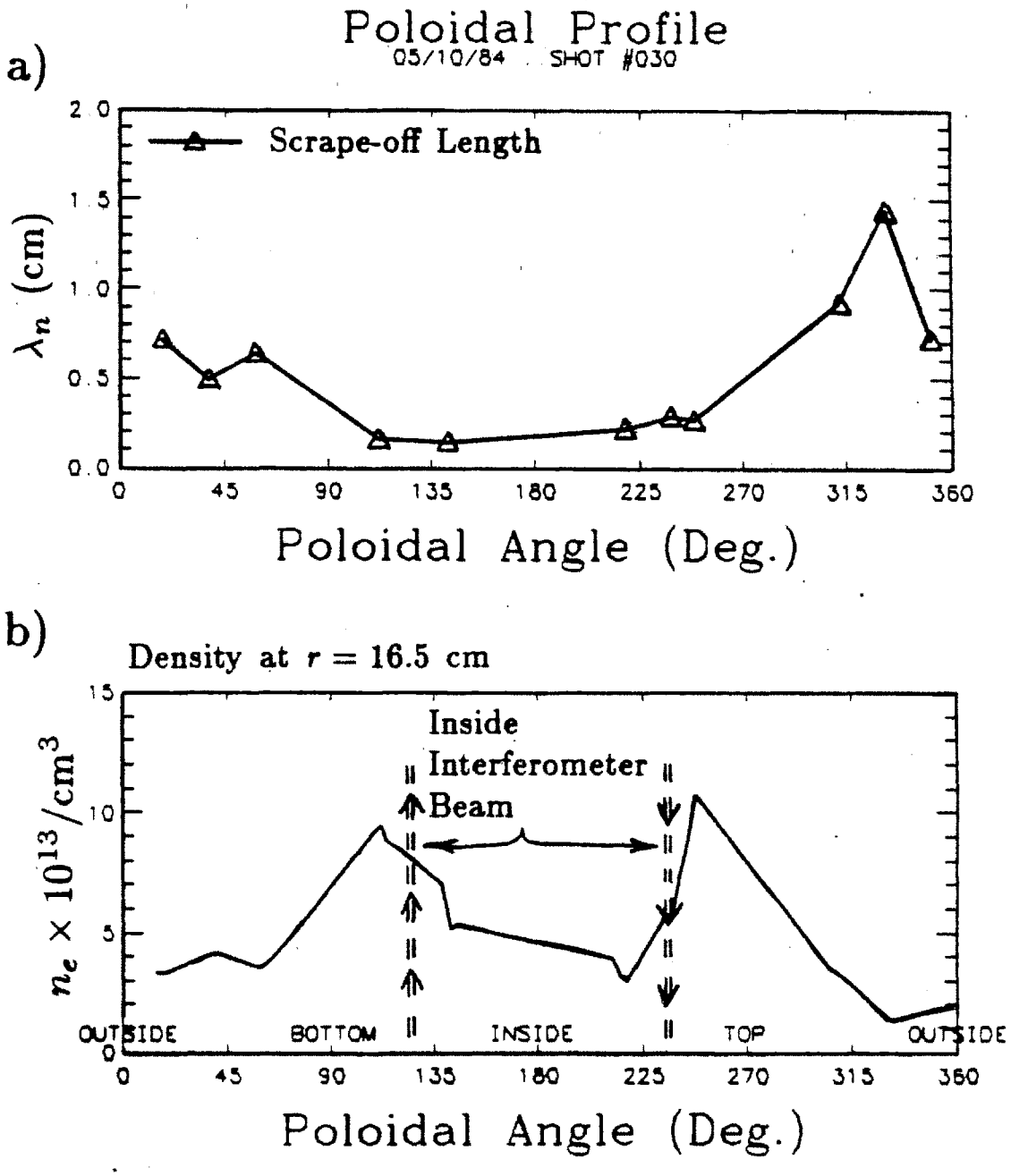

Figure 8.6 Poloidal Profile of Density e-folding Length and Density at the Limiter Radius

8.4.5 Refinements to Perpendicular Transport Model

It is possible to consider cases in which the local plasma sink term in the limiter shadow plasma is not simply nC_s/L as modelled here but some more complicated function of space. Clearly, edge plasma conditions differ near a limiter surface so that such a modification is needed in a more accurate description of the shadow plasma. Where this sink term is smaller, $\underline{E} \times \underline{B}$ convection as considered above can possibly play a more important role.

There is also the question of whether the shadow plasma retains the observed poloidal structure at various toroidal locations. Observations of MARFE phenomena indicate that a level of toroidal symmetry exists, although at limiter locations, the MARFE H_α emission is always recorded to be much higher, indicating that the poloidal structure may change there.

An additional unknown in the above perpendicular transport model is the parallel convection velocity. It has been assumed up to now that the parallel flow uniformly accelerates to the sound speed at the limiter surface with poloidal symmetry. However, since it has been shown that pressure is not necessarily constant on a flux surface, parallel flows can be driven which can greatly distort this picture. The following section considers such parallel flows which may be present in the Alcator C limiter shadow plasma. A possible consequence of such parallel flows is an asymmetric power loading of limiter and probe surfaces in Alcator C.

8.5 Parallel Convection

Section 3.1 considered a simple 2-D diffusion model for the shadow plasma where perpendicular diffusion was assumed to be independent of space and the local sink term from parallel convection was approximated as a spatially independent quantity, $-nC_s/L$. However, section 8.2.2 pointed out that plasma pressure contours in the poloidal plane of the limiter shadow plasma are highly asymmetric, deviating from flux surfaces. Furthermore, data presented in section 8.4.4 indicated that asymmetries exist inside the limiter radius. This implies that perpendicular transport processes are dependent on space and, in particular, poloidal angle. Therefore, a model which accurately predicts density and flow velocities along field lines in the limiter shadow plasma must include spatially varying effective particle source terms from perpendicular convection and diffusion. Unfortunately, a completely rigorous model which includes these effects is inherently three-dimensional and too complicated for this present analysis, particularly in view of the accuracy and spatial extent of the DENSEPACK data set. Nevertheless, a number of simple observations based on asymmetries detected by DENSEPACK are made in the following subsections.

From observations of MARFE phenomena, it has been established that the edge plasma exhibits toroidal symmetry, at least in the MARFE region. The implication of this combined with DENSEPACK data is that plasma pressure gradients occur along field lines in the edge plasma. From the parallel momentum equation, subsection 8.5.1 will show that such pressure gradients can result in parallel flows which achieve near-sonic speeds even in the absence of a limiter surface. It is suggested that parallel flows in the shadow plasma may scrape off plasma in a toroidally asymmetric way and might account for the asymmetric limiter damage (section 4.2) and the results from directional thermocouple probes shown earlier (section 4.3).

In order to further investigate this hypothesis, parallel flows along a flux tube to limiter and probe surfaces is modelled in subsections 8.5.2 and 8.5.3 using

the reduced fluid transport equations with the approximation that $T_e \approx const.$ along a field line. It is shown that plasma will indeed scrape off in a toroidally asymmetric way if particles diffusing into a flux tube carry a non-zero, total parallel momentum. Such an analysis is typically used to estimate the Mach number of the unperturbed plasma flow field in divertors from two-sided probe data.[103,104]

The fact that the plasma density inferred by a Langmuir probe can depend on the bulk plasma flow velocity prompts one to consider such parallel flows in the interpretation of DENSEPACK data. Using the parallel flow models, subsection 8.5.4 shows that unless the parallel plasma flow field in the vicinity of the probes significantly exceeds Mach 1, the asymmetric density previously inferred from DENSEPACK data cannot be explained as a misinterpretation of the data due to such flows.

Recently, the directional Langmuir probe part in a multiple edge probe diagnostic[73,97,98] has detected ion drift side/electron drift side asymmetries in the rate of ion saturation current collection. The asymmetries detected by this probe are found to depend on the relative direction of the toroidal magnetic field and the plasma current. Subsection 8.5.5 suggests that such asymmetries and the observed scaling with magnetic field direction might be explained in terms of the poloidally asymmetric perpendicular transport inferred by DENSEPACK and/or parallel plasma flows. Such parallel flows may arise in an attempt to equalize density on a flux surface in the edge plasma. Subsection 8.5.6 notes that the directional thermocouple probe data may be explained by the same argument, supporting the original hypothesis presented in section 4.3 that asymmetric heat fluxes might be a consequence of an asymmetric edge plasma.

Finally, a possible connection is made between the asymmetric limiter damage pattern (section 4.2) and the asymmetries detected by the DENSEPACK probe array. Subsection 8.5.7 shows that the asymmetric limiter damage pattern can only be explained by this model if near-sonic parallel flows occur in the

plasma region $r \lesssim a$ since poloidally asymmetric perpendicular transport alone cannot produce this result. Such a hypothesis of parallel flows is found to be consistent with the asymmetric perpendicular transport inferred by DENSEPACK and the previous discussion in section 8.4.4 which pointed to strong poloidal asymmetries also occurring in the edge plasma region, $r \lesssim a$.

The starting point in these analyses of parallel flows is a consideration of the parallel momentum equation.

8.5.1 Parallel Force Balance with Near-Sonic Flows

Using the reduced fluid transport equations presented in section 3.3.2, the parallel momentum equation is simply

$$m_i\ n\ (\underline{V}_\perp \cdot \nabla_\perp)\underline{V}_\parallel\ +\ m_i\ n\ (\underline{V}_\parallel \cdot \nabla_\parallel)\underline{V}_\parallel\ =\ -\nabla_\parallel P\ , \tag{8.34}$$

or equivalently,

$$m_i\ n\ (\underline{V}_\perp \cdot \nabla_\perp)\underline{V}_\parallel\ =\ -\nabla_\parallel(P\ +\ \frac{1}{2}\ m_i\ n\ V_\parallel^2)\ +\ \frac{1}{2}\ m_i\ V_\parallel^2\ \nabla_\parallel n\ . \tag{8.35}$$

In the absence of the left hand side, Eq. 8.35 reduces to a version of Bernoulli's equation for fluid flow. For an incompressible fluid, i.e $n = const$, the thermal energy plus directed kinetic energy would be constant along a field line. Rewriting Eq. 8.34,

$$\begin{aligned}(\underline{V}_\perp \cdot \nabla_\perp)\underline{V}_\parallel\ +\ \frac{1}{2}\ \nabla_\parallel V_\parallel^2\ &=\ -\frac{\nabla_\parallel P}{m_i\ n} \\ &=\ -C_s^2\ \nabla_\parallel ln(n)\ -\ \nabla_\parallel C_s^2\end{aligned} \tag{8.36}$$

with the definition $C_s^2 \equiv \frac{T_e+T_i}{m_i}$. For the moment, considering a flow field which is uniform in the perpendicular direction so that the $(\underline{V}_\perp \cdot \nabla_\perp)\underline{V}_\parallel$ term can be neglected, Eq. 8.36 can be used to obtain a relationship for the parallel Mach number, M $(= V_\parallel/C_s)$,

$$\nabla_\parallel M^2 \; + \; (M^2+2)\nabla ln(T_e+T_i) \; + \; 2 \; \nabla_\parallel ln(n) \; = \; 0 \; . \qquad (8.37)$$

Thus, a plasma flow along field lines is driven by pressure variations through Eq. 8.37.

Ideally, one would like to know n, T_e, and T_i along $\underline{B}$ in order to estimate the variation in M from Eq. 8.37. Lacking this data, an assumption must be made about the parallel variation in n, T_e, and T_i, or equivalently, if one uses the DENSEPACK data in the poloidal plane, an assumption must be made about toroidal variations in these quantities. Since MARFEs are observed to be a purely toroidal band of radiating plasma, the simple assumption can be made that the edge plasma is toroidally symmetric in n, T_e, and T_i over the entire edge plasma. Near a limiter surface, this assumption is not expected to hold true since a density variation can occur as the plasma accelerates to the sound speed. Nevertheless, if the assumption of toroidal symmetry is made, parallel gradients in edge quantities can be simply estimated from poloidal variations as recorded by DENSEPACK and the direction of $\underline{B}$.

Proceeding with this assumption, DENSEPACK probe data indicates that $\nabla_\parallel ln(T_e+T_i) \approx \nabla_\parallel ln(T_e)$ is typically smaller than $\nabla_\parallel ln(n)$ so that Eq. 8.37 can be approximated as

$$M^2 \; - \; 2 \; ln(n) \; \approx \; constant \qquad (8.38)$$

along a field line. Therefore variations in $ln(n)$ alone most strongly influence the parallel Mach number in the edge plasma.

Figure 8.7*a* displays a conformal mapping contour plot of constant $ln(n)$ as inferred from DENSEPACK. Figure 8.7*b* superimposes circular contours representing constant flux (dashed lines on this same plot). From these plots, it is found that $ln(n)$ can vary by ~ 3 or more on a flux surface. Equation 8.38 predicts a variation in M of ~ 2.4 for this $ln(n)$ variation along field lines. Thus, typical density variations along field lines can easily lead to parallel flows approaching Mach 1 in a plasma region that is not necessarily near a limiter surface. Since it is found that maxima and minima in T_e follow maxima and minima in n, including T_e and T_i ($\approx 2 \times T_e$) variations, as in Eq. 8.37, only leads to a prediction of even sharper changes in flow velocities along $\underline{B}$.

The above analysis relies on assuming toroidal symmetry in n and inferring $\nabla_{\|} ln(n)$ from DENSEPACK data. In actuality, the density asymmetry is probably a result of poloidally asymmetric perpendicular transport which is strong enough to maintain poloidal density variations despite parallel transport. Thus, a better model might be obtained by assuming that the effective *particle source term* due to perpendicular convection and diffusion varies in poloidal angle yet is toroidally symmetric. The following sections use this assumption to examine in a more quantitative way the parallel flows along flux tubes that intercept probe and limiter surfaces.

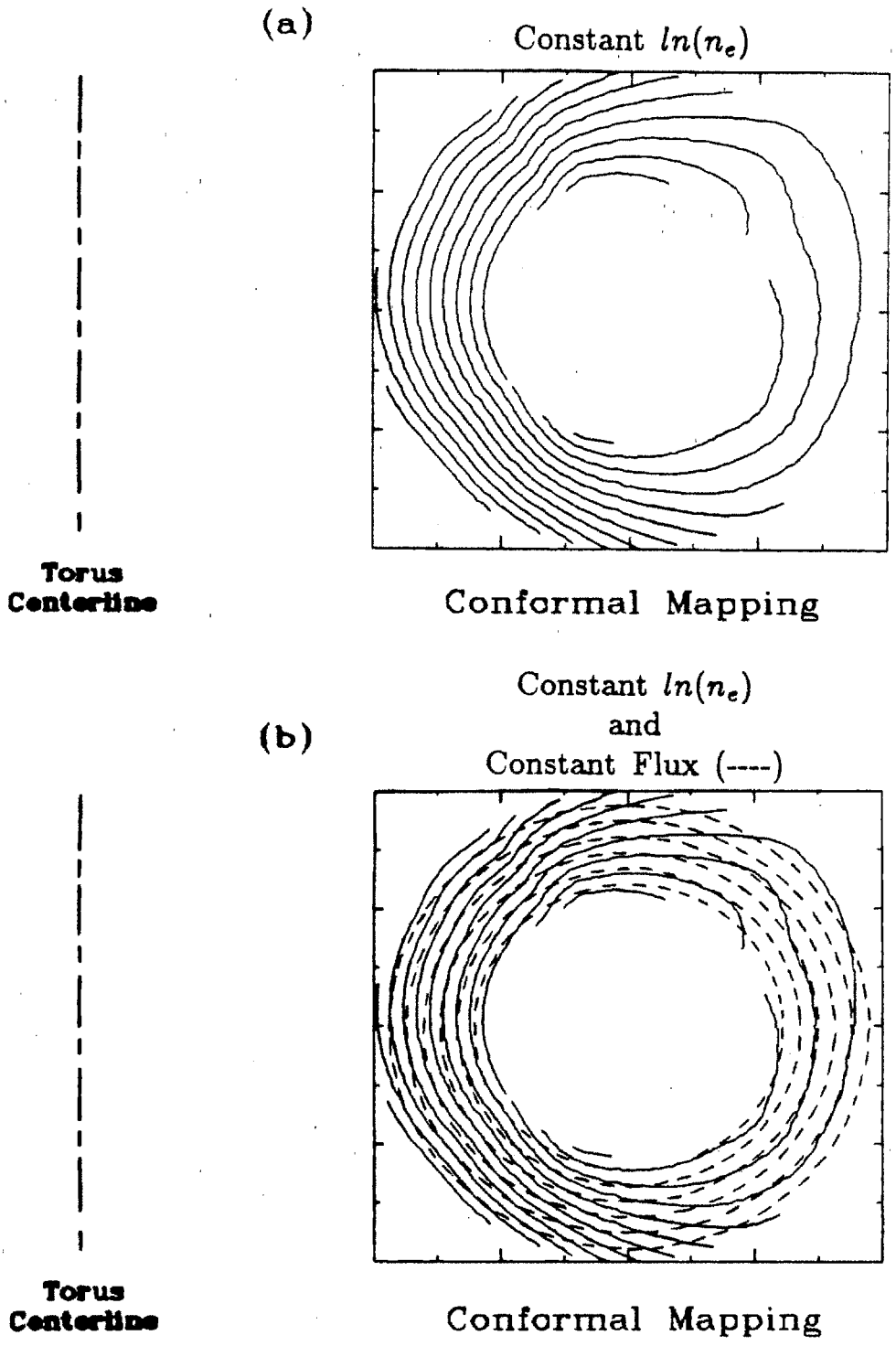

Figure 8.7 Constant $ln(n)$ and Constant Flux Conformal Mapping

8.5.2 Simple Model for Parallel Flows Between Collection Surfaces

The parallel continuity equation can be written to include an effective source term as

$$\begin{aligned} \nabla_{\parallel} \cdot n\underline{V}_{\parallel} &= -\nabla_{\perp} \cdot n\underline{V}_{\perp} \\ &= S \end{aligned} \tag{8.39}$$

or defining z to be the coordinate along $\underline{B}$,

$$\frac{\partial (nMC_s)}{\partial z} = S \ . \tag{8.40}$$

For simplicity, it is assumed that $\partial T/\partial z$ terms can be neglected compared to $\partial n/\partial z$ terms, or equivalently, the sound speed is constant along a field line. In this case, Eq. 8.38 also holds true (still neglecting $\underline{V}_{\perp} \cdot \nabla_{\perp}$ term). Combining Eq. 8.40 and 8.38,

$$\left(M \ e^{-M^2/2} \right|_{M_1}^{M_2} = \frac{1}{n_0 \ C_s} \int_{z_1}^{z_2} S \ \partial z \tag{8.41}$$

where n_0 is the plasma density at some point that $M = 0$. At the limiter sheath, the Mach number must be $|M| = 1$. Setting $M_1 = -1$ and $M_2 = +1$ at the limiter locations, $z = \pm L$, yields

$$0.61 \ \frac{n_0 \ C_s}{L} = \frac{1}{2 \ L} \int_{-L}^{L} S \ \partial z \ . \tag{8.42}$$

Thus, the effective perpendicular source averaged along a flux tube, $\langle S \rangle$, must satisfy the condition,

$$\langle S \rangle = 0.61 \ \frac{n_0 \ C_s}{L} \ . \tag{8.43}$$

When the source term varies along the field line (poloidally asymmetric in this toroidally symmetric model), the Mach number can approach unity far away from the limiter surface. Figure 8.8 plots Mach number, density, and source term versus parallel position using Eq. 8.41 for the case of a constant source (a), and a spatially non-uniform source (b). Figure 8.8b is set up to coincide with a flux tube in the Alcator C limiter shadow plasma that passes from the inside midplane location ($-L$), where a minimum perpendicular source is expected, to a point near the top of the poloidal cross-section, where S is found to be larger. Note that no matter how the source is distributed along the flux tube, the particle flux to each surface, nC_s, is always equal. This is because Eq. 8.38 forces a one-to-one correspondence between flow velocity and density. Since the Mach number at these surfaces is forced to be unity from the sheath condition, the density at both surfaces must be the same. The spatial variation in S is handled by the parallel flow accelerating to near sound speeds farther away from one surface than the other. The point where $M = 0$ simply becomes the 'center of mass' location of S.

This picture changes when including cross field momentum transport as would arise through the $\underline{V}_\perp \cdot \nabla_\perp$ term in Eq. 8.36. If particles carry a non-zero net momentum as they appear in the flux tube, the pressures, and therefore densities, at the two surfaces will be unequal. The following section considers a simple version of this case.

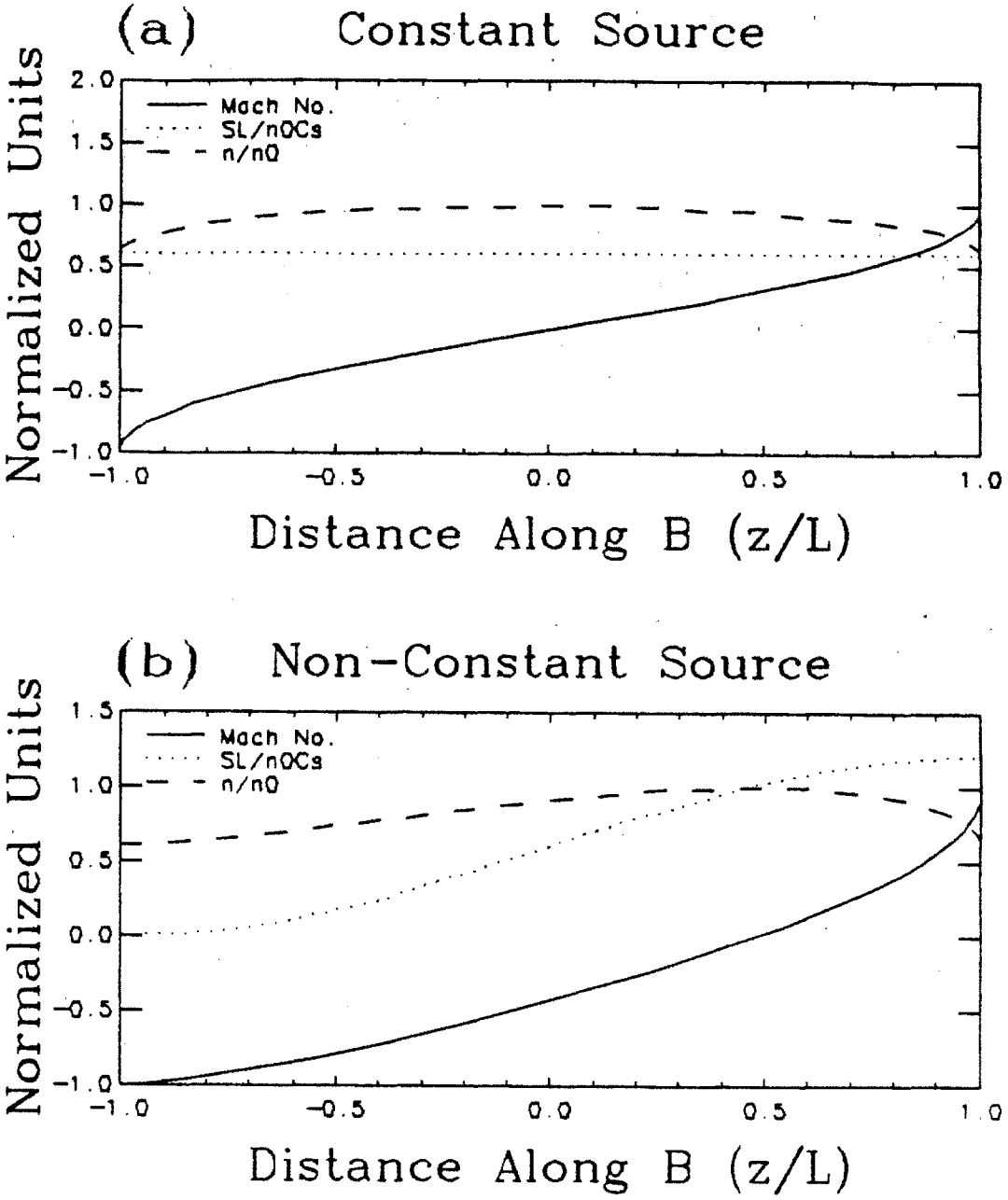

Figure 8.8 Mach Number, Density, and Source Along $\underline{B}$ (no parallel momentum source)

8.5.3 Estimating Parallel Flows with $\|$ Momentum Source

The problem of estimating particle fluxes along a flux tube when perpendicular transport carries parallel momentum into this region has been considered before. Stangeby[103] treats the case of a probe surface immersed in a drifting plasma and uses an MHD fluid analysis similar to the following approach.

Neglecting $\nabla_{\|} ln(T_e + T_i)$ as before, but retaining the $\underline{V}_{\perp} \cdot \nabla_{\perp}$ term, the parallel momentum equation reads as

$$\frac{(\underline{V}_{\perp} \cdot \nabla_{\perp})M}{C_s} + \frac{1}{2}\frac{\partial M^2}{\partial z} + \frac{\partial ln(n)}{\partial z} = 0 \ . \tag{8.44}$$

Unfortunately, introducing the $(\underline{V}_{\perp} \cdot \nabla_{\perp})$ term makes the model two-dimensional. However, following the analysis by Stangeby, this term can be approximated by a momentum source term,

$$\frac{(\underline{V}_{\perp} \cdot \nabla_{\perp})M}{C_s} \approx \frac{S\ (M - M_0)}{n\ C_s} \ , \tag{8.45}$$

for the case when the flux tube is adjacent to a uniformly flowing plasma with a specified parallel Mach number, M_0. Here, S is the same local particle source due to perpendicular transport as was in the continuity equation. Particles appear in the flux tube at a rate S carrying parallel momentum, $m_i M_0 C_s$.

Using Eqs. 8.45, 8.44, and 8.40, an equation similar to 8.41 can be obtained for this model,

$$\left(\frac{M}{1 + M^2 \quad M_0 M} \right|_{M_1}^{M_2} = \frac{1}{n_0\ C_s} \int_{z_1}^{z_2} S\ \partial z \ . \tag{8.46}$$

A relationship for n versus Mach number is also obtained,

$$n(M) = \frac{n_0}{1 + M^2 - M_0 M} \quad . \tag{8.47}$$

With the condition that $|M| = 1$ at the sheath edge, Eq. 8.46 results in

$$\frac{4}{4 - M_0^2} = \frac{1}{n_0 \; C_s} \int_{-L}^{L} S \; \partial z \quad . \tag{8.48}$$

Thus, the flux tube averaged source, $\langle S \rangle$, is constrained to be

$$\langle S \rangle = 0.5 \; \frac{n_0 \; C_s}{L} \cdot \left(\frac{4}{4 - M_0^2} \right) \quad . \tag{8.49}$$

When $M_0 = 0$, $\langle S \rangle$ is reduced slightly compared to that predicted by the momentum source-free model in Eq. 8.43. This is because particles now must accelerate from rest to the collection surfaces. $\langle S \rangle$ can be larger when $|M_0| > 0$. For $|M_0| = 1$, the flux tube averaged source term and therefore total particle loss rate to the surfaces increases by a factor of 4/3.

8.5.4 Toroidally Asymmetric Fluxes to Limiters and Probes

Fluxes to limiter or probe surfaces can be estimated from the parallel flow with momentum source model using the condition that $|M| = 1$ and Eq. 8.47,

$$\Gamma(z = -L) = -\frac{n_0\ C_s}{2 + M_0} \tag{8.50}$$

$$\Gamma(z = L) = \frac{n_0\ C_s}{2 - M_0}\ . \tag{8.51}$$

Figure 8.9 plots $M(z)$, $n(z)$, and $S(z)$ computed from Eqs. 8.46 and 8.47 for the same two source functions as in Fig. 8.8 with $M_0 = 0.5$. Note that now the fluxes to the probe surfaces (nC_s) are no longer equal. When $|M_0| \approx 1$, one side of the probe or limiter surface can receive three times the particle flux as the other. This is in contrast to the results obtained in section 8.5.3 where no momentum source was included.

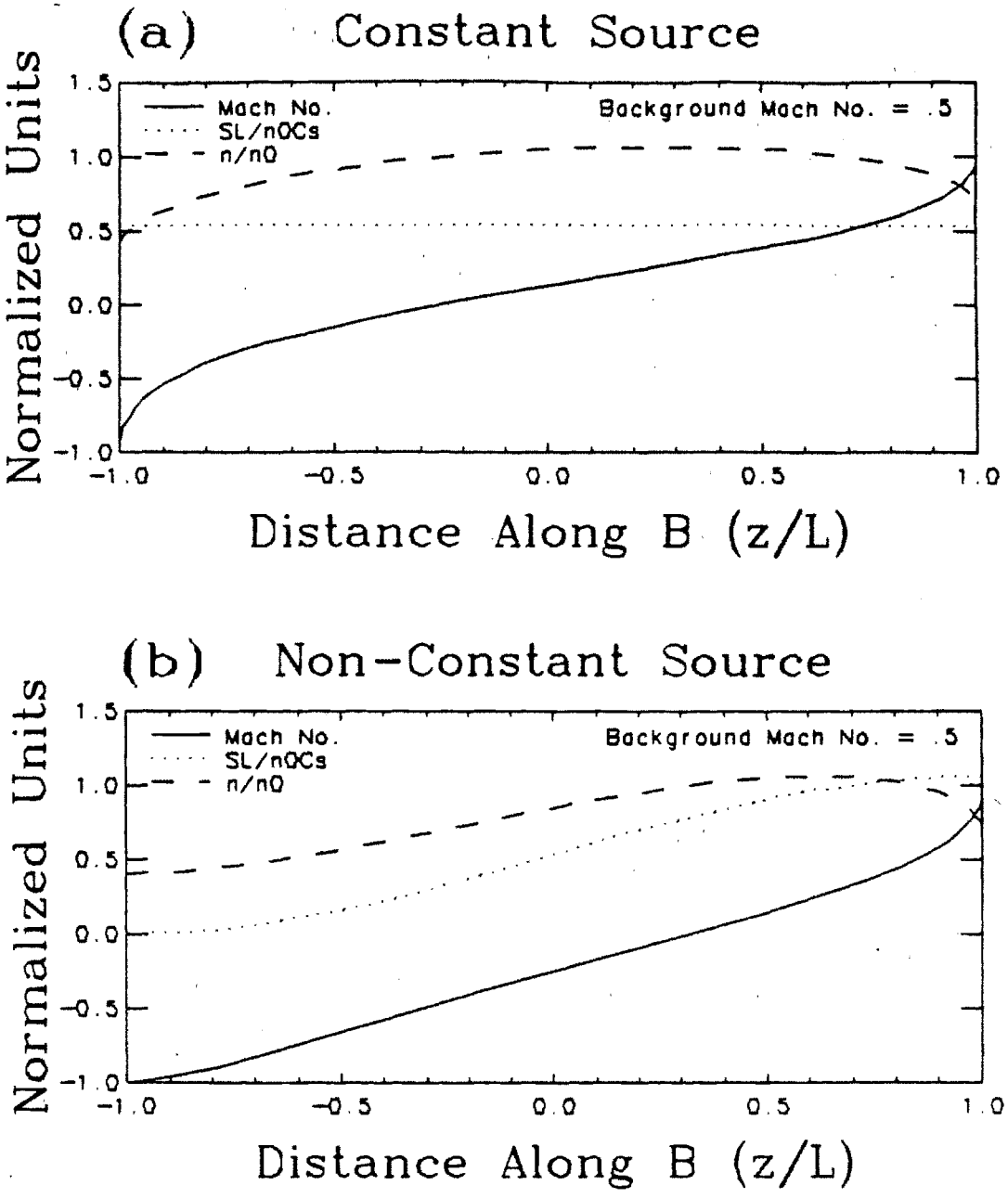

Figure 8.9 Mach Number, Density, and Source Along $\underline{B}$ (with parallel momentum source)

Stangeby[103] uses the above relationships to suggest that uniform plasma drift velocities, $M_0 C_s$, can be inferred using a two-sided Langmuir probe. In this case, the ratio of ion saturation currents collected by identical probes on sides facing upstream (u) and downstream (d) would be

$$\frac{I^u_{sat}}{I^d_{sat}} = \frac{2 + |M_0|}{2 - |M_0|} \; . \tag{8.52}$$

Note that for a single Langmuir probe that collects current from both sides, the total ion saturation current is obtained from Eqs. 8.50 and 8.51 as

$$\begin{aligned} I_{sat} &= \frac{q\ A}{2}\ \frac{n_0\ C_s}{2 + M_0} + \frac{q\ A}{2}\ \frac{n_0\ C_s}{2 - M_0} \\ &= \frac{1}{2} q\ A\ n_0\ C_s\ \left(\frac{4}{4 - M_0^2}\right) \; . \end{aligned} \tag{8.53}$$

Comparing this to Eq. 6.27 used for DENSEPACK data reduction, one can see that at $|M_0| = 0.5$ an error of 7% is introduced in the inferred unperturbed density. Systematic errors from probe area variations, probe fitting uncertainties, etc., can combine to yield a $\gtrsim 10\%$ uncertainty in computing n_0. Thus, the effect of plasma streaming by DENSEPACK probes can be typically ignored in comparison.

In the worst case when $|M_0| \to 1$, a 30% error in n_0 would result. Although this leads to a non-negligible error in the calculated n_0, it does not explain the $\times 10$ or more variation in n_0 found using the data analysis technique which ignored flows. Therefore, assuming that this model is at least approximately correct, the poloidal variation in n_0 cannot be simply attributed to a data interpretation problem from plasma streaming past DENSEPACK probes.

8.5.5 Directional Probe Results

Recently, a multiple probe diagnostic has been operated in Alcator C edge plasma.[73,94] A two-sided combination Langmuir probe/retarding field energy analyzer/heat flux probe has been used to obtain plasma density, electron temperature, ion temperature, and total heat flux in the directions parallel and anti-parallel to $\underline{B}$. A complete description of the results from this diagnostic is forthcoming.[106] Nevertheless, the two-sided Langmuir probe part of this diagnostic has already yielded important information about asymmetries in the Alcator C edge plasma.

The position of the gridded energy analyzer shown in Fig. 8.1 is the same poloidal position of this multiple probe diagnostic in Alcator C. The probe head shown in Figs. 8.10 and 8.11 has two Langmuir probes, one facing in the electron drift direction and one facing in the ion drift direction. Figures 8.10 and 8.11 trace the flux tubes which intercept the probe back to the limiter surfaces for the case of forward toroidal field (8.10) and reversed toroidal field (8.11). Figures 8.10*a* and 8.11*a* are views looking down on the top half of the vacuum chamber with the torus straightened into a cylinder and flattened. Figures 8.10*b* and 8.11*b* show projections of flux tubes sampled by the two-sided Langmuir probe on DENSEPACK $ln(n)$ and flux surface conformal mappings.

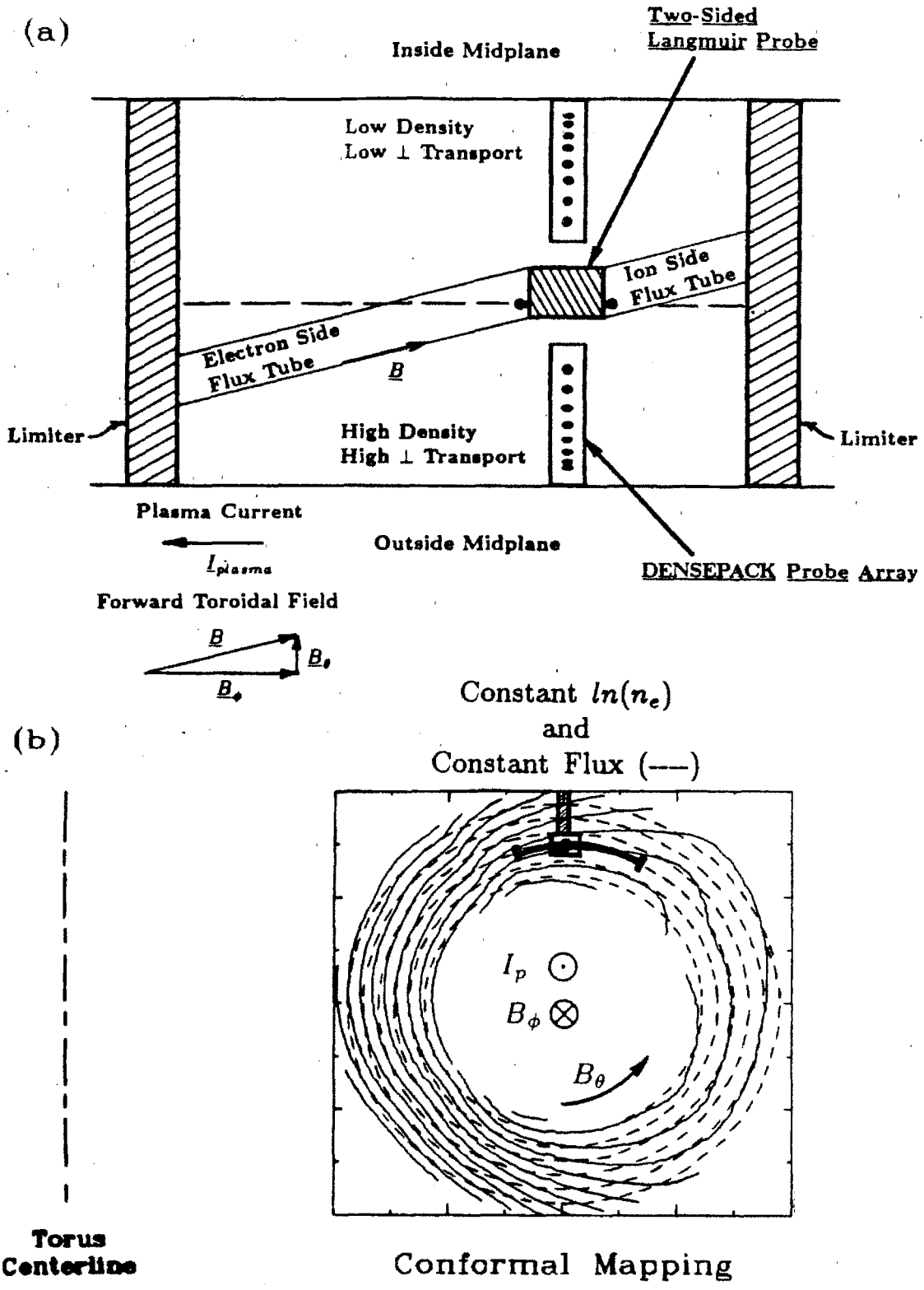

Figure 8.10 Flux Tubes Sampled by Two-Sided Langmiur Probe (forward toroidal field direction)

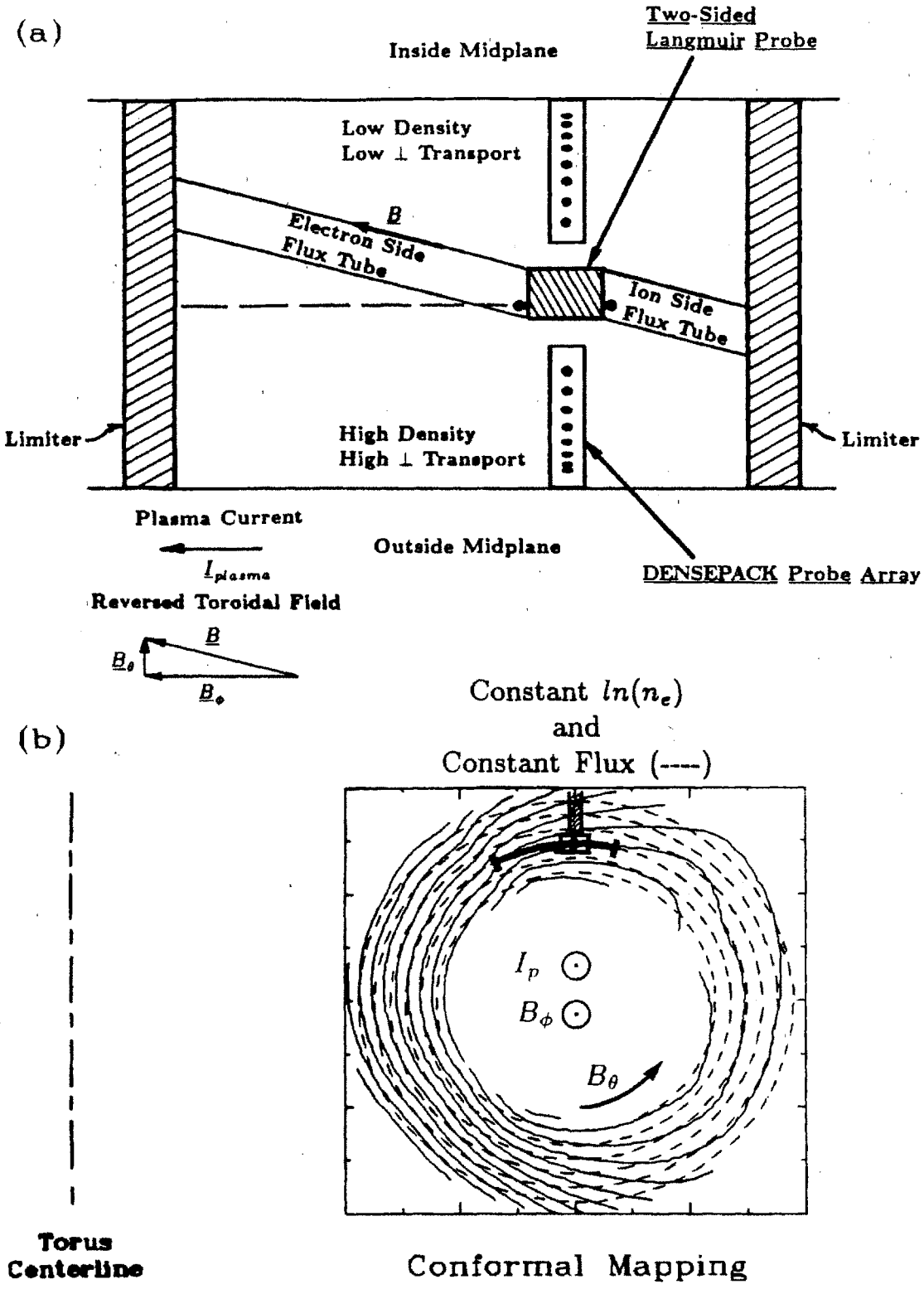

Figure 8.11 Flux Tubes Sampled by Two-Sided Langmiur Probe (reversed toroidal field direction)

Figure 8.12 shows a variation in ion saturation current collected from the ion and electron drift sides of the probe. Here, the ratio of ion saturation current collected from the electron drift side divided by ion saturation current collected from the ion drift side is plotted versus radius for both toroidal field directions. All discharges shown are similar in central parameters to the one which generated the $ln(n)$ conformal mapping, namely, I_p ~300–370 kA, $\bar{n}_e$ ~1.7–2.2×10^{14}/cm^3.

For the forward field direction (8.12*a*), one can see that nearly a factor of 100 more current is collected on the electron drift side than the ion drift side as the limiter radius (r = 16.5 cm) is approached. At larger minor radii, the ratio drops to ~ 10. For the case of reversed toroidal field (8.12*b*) the probe collects more on the ion drift side near the limiter radius. Again, at larger minor radii the probe reverts back to collecting a ratio of ~ 10 more on the electron drift side.

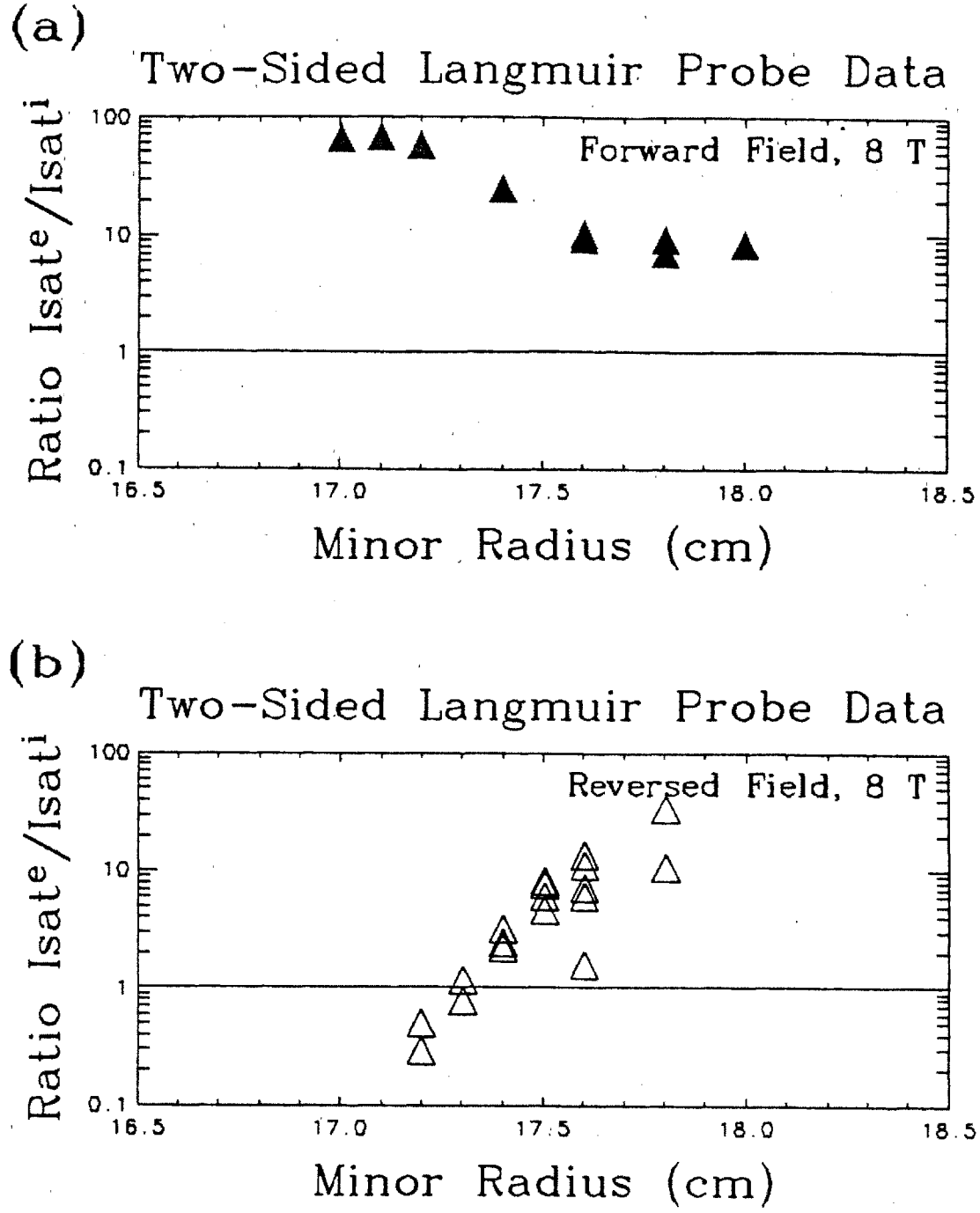

Figure 8.12 Ratio of Ion Saturation Currents Collected by Two-Sided Probe

As seen in Figs. 8.10 and 8.11, DENSEPACK data implies that the flux tubes sampled by the probe intersect plasma regions of varying density and perpendicular transport. In Fig. 8.10 with a forward toroidal field direction, the long flux tube intersects a region where the plasma density and scrape-off length are measured to be high. On the other hand, when the toroidal field is reversed, (8.11), the long flux tube samples a plasma region of lower density and shorter scrape-off length. Thus, it is expected that conditions measured on the ion drift side and electron drift side of the probe should be different and affect in some way the current collected by the probe.

The asymmetry measured by the two-sided Langmuir probe can be explained at least qualitatively in terms of the flux tubes sampled by the probe and the poloidal asymmetries in perpendicular transport which are found by DENSEPACK to exist in Alcator C shadow plasma. Figure 8.13 shows schematically the two-sided Langmuir probe inserted between limiters in Alcator C. Plasma in the long flux tube region, A', is sampled by the probe on the electron drift side. Similarly, plasma in region B' is sampled by the probe on the ion drift side. Regions A' and B' are populated by particles diffusing perpendicular from regions A and B respectively. Ion saturation currents collected by the two Langmuir probes depend on two effects: 1) the rate of perpendicular transport into the collection flux tube and 2) on any parallel flows which occur outside these flux tubes. Such a parallel flow which can be driven by asymmetries in the edge plasma is labelled as V_0 in Fig. 8.13.

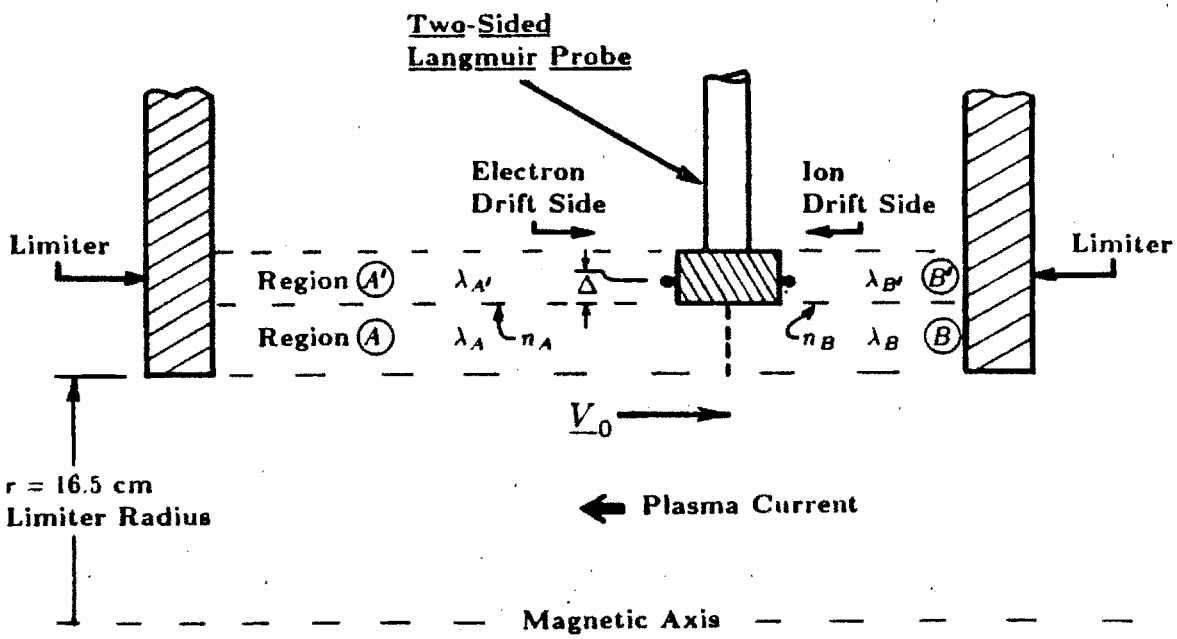

$$I_{sat}^{A'}/I_{sat}^{B'} \approx \frac{n_A}{n_B} e^{\Delta(1/\lambda_{B'} - 1/\lambda_{A'})}$$

Figure 8.13 Particle Flux Model for Two-Sided Langmuir Probe

The first effect can be examined in terms of the densities and density scrape-off lengths measured by DENSEPACK. For simplicity, consider the densities at the probe head edge and radial scrape-off lengths characteristic of regions A and B to be n_A, λ_B, and n_B, λ_B. The scrape-off lengths in regions A' and B' can be simply scaled from λ_A and λ_B using the connection lengths in these regions,[69,107]

$$\lambda_{A'} \approx \lambda_A \sqrt{\frac{2}{3}} \tag{8.54}$$

$$\lambda_{B'} \approx \lambda_B \sqrt{\frac{1}{3}} \, . \tag{8.55}$$

The densities along flux tubes intercepted by the Langmuir probe tips, $n_{A'}$, $n_{B'}$, can be estimated from

$$n_{A'} \approx n_A \, e^{-\Delta/\lambda_{A'}} = n_A \, e^{-1.22\Delta/\lambda_A} \tag{8.56}$$

$$n_{B'} \approx n_B \, e^{-\Delta/\lambda_{B'}} = n_B \, e^{-1.73\Delta/\lambda_B} \tag{8.57}$$

where Δ is the distance from the probe's leading edge to the Langmuir probe tip. Δ for this probe is ~ 0.5 cm.

Using the parallel flow model outlined in section 8.5.2 which includes no momentum source, the ion saturation current to each probe side is approximately

$$I^e_{sat} \approx 0.61 \, A \, n_A \, C_s \, e^{-1.22\Delta/\lambda_A} \tag{8.58}$$

$$I^i_{sat} \approx 0.61 \, A \, n_B \, C_s \, e^{-1.73\Delta/\lambda_B} \tag{8.59}$$

or the ratio is simply

$$I^e_{sat}/I^i_{sat} \approx \frac{n_A}{n_B}\, e^{\Delta(1.73/\lambda_B - 1.22/\lambda_A)} . \tag{8.60}$$

If the edge plasma were poloidally symmetric, then $n_A \approx n_B$ and $\lambda_A \approx \lambda_B$. In this case, taking a typical value recorded by DENSEPACK of $\lambda \approx 0.3$ cm yields

$$I^e_{sat}/I^i_{sat} \approx 2.3 \quad \text{(poloidally symmetric case)} . \tag{8.61}$$

Now consider the case of poloidal density asymmetries with a forward toroidal field direction as diagrammed in Fig. 8.10. From Figs. 7.7 and 7.2, $\lambda_A \sim 0.4$ cm, $\lambda_B \sim 0.2$ cm, and $n_A/n_B \sim 1.4$ which yields

$$I^e_{sat}/I^i_{sat} \approx 20 \quad \text{(forward field case)} . \tag{8.62}$$

For reversed field, regions A and B are interchanged implying $n_A \leftrightarrow n_B$ and $\lambda_A \leftrightarrow \lambda_B$. This results in

$$I^e_{sat}/I^i_{sat} \approx 0.41 \quad \text{(reversed field case)} . \tag{8.63}$$

Notice that these estimates are on the same order as the observed ratios of I^e_{sat}/I^i_{sat} displayed in Fig. 8.12 for $r \approx 17.2$ cm. Thus, it is possible that poloidally asymmetric perpendicular fluxes can contribute to two-sided asymmetries measured by this diagnostic. The fact that the magnitude of the observed two-sided asymmetries agrees with this rough calculation corroborates the asymmetries detected by the DENSEPACK array and offers a simple explanation for the dependence of the two-sided asymmetries on the relative direction of $\underline{B}$ and

I_p. However, this is not the only mechanism which can yield a two-sided asymmetry.

Parallel plasma flow is the second mechanism which can result in the observed two-sided asymmetry in this fluid model. As shown in sections 8.5.2–8.5.4, a flux tube will be preferentially unloaded at one end if particles diffusing into the region carry non-zero parallel momentum. Unfortunately, the simple model developed in section 8.5.4 is valid only for a small probe surface (relative to the scrape-off length). In the case of a large probe, such as in the two-sided Langmuir probe system discussed above, the formulation for the ratio of ion saturation currents in Eq. 8.52 does not apply. Nevertheless, the qualitative feature of particles being scraped-off preferentially at one end of the flux tube is still expected to hold true.

Since plasma is sampled ~ 0.5 cm behind the leading edge of this probe, any two-sided asymmetry which might be detected from parallel flows is expected to be enhanced. The ratio of ion saturation currents approaching ~ 3 in equation 8.52 for $M_0 \rightarrow 1$ is expected to be much greater at a point ~ 0.5 cm behind the probe's leading edge. Thus, the magnitude of two-sided asymmetries detected by this diagnostic may also be explained in terms of parallel plasma flows in the edge plasma.

A quantitative analysis of this effect requires the use of a 2-D transport model to properly include the effect of this 'large probe'. However, such an analysis is beyond the scope of this present work. Further analysis of asymmetries detected by this diagnostic will soon be available in Ref. [125].

8.5.6 Directional Thermocouple Probe Results

Section 4.3 reviewed some early probe measurements made in Alcator C as an introduction to the Alcator C edge plasma. In particular, it was pointed out that the directional thermocouple probes recorded a factor of 2 or more

directional asymmetry in the heat flux to probes at the F-bottom port location. Figure 4.4 showed the ratio of electron drift side to ion drift side heat fluxes for the case of forward and reversed toroidal field directions. The result is reminiscent of the ion saturation current ratios displayed in Fig. 8.12. For the thermocouple probes at F-bottom, a similar picture of particle collection flux tubes as in Figs. 8.10a and 8.11a can be constructed. However, since the view is now looking up from the bottom of the vacuum chamber, the plasma current in the picture is reversed. As a result, flux tubes for probes on the bottom with reversed field look exactly like those for probes at the top with the forward toroidal field direction. With this in mind, the thermocouple probe asymmetries measured early in Alcator C operation are consistent with the recent two-sided Langmuir probe results. It appears therefore that the hypothesis stated in section 4.3 of heat flux asymmetries in the Alcator C edge plasma being most likely a consequence of poloidally nonuniform edge conditions is supported.

8.5.7 Asymmetric Limiter Damage: Parallel Flows for $r \lesssim a$

Asymmetric damage on the limiters was discussed previously in section 4.2. Since the explanation of the damage pattern in terms of outer flux surface shape and/or position was placed in question, poloidal asymmetries of the edge plasma are now examined as another possible cause.

The analysis of asymmetric limiter damage is simpler than the analysis of the two-sided Langmuir and thermocouple probe data. Figure 8.14 shows a cross-sectional view of the Alcator C vacuum chamber including limiter shadow plasma regions labled A' and B'. The sketch in Fig. 4.2 indicates that high damage areas on the molybdenum blocks of 10 cm and 13 cm limiters occurred on the electron drift side for a limiter segment near the top-inside poloidal position and on the ion drift side for a limiter segment near the bottom-inside. These damage

areas are indicated for the top-inside and bottom-inside limiter parts shown in Fig. 8.14.

The edge plasma flow models discussed in sections 8.5.2 and 8.5.3 pointed out that no matter how spatially non-uniform the cross field particle transport rate is into regions A' and B', particle fluxes to the bounding surfaces are forced to be equal unless the perpendicularly transported particles carry a non-zero net parallel momentum. Thus, in order to explain the preferential limiter loading on one side of the flux tube using this fluid model, plasma just inside the limiter radius must possess a non-zero, flux tube averaged flow velocity. The required average plasma flow in regions A and B is labelled as V_A and V_B in Fig. 8.14.

The hypothesis of plasma flows occuring in the plasma region, $r \lesssim a$, implies that poloidal pressure asymmetries must not be restricted to the shadow plasma but must also extend somewhat into this region. In discussing the behavior of the inside edge interferometer chord signal during MARFE phenomena in Alcator C (section 4.4.2), it was pointed out that this diagnostic sometimes records line averaged densities that exceed the central cord line averaged value before the signal 'breaks up' from the MARFE. It was concluded at that time that poloidally asymmetric density profiles may exist inside the limiter radius. The discussion of DENSEPACK data extrapolated to the limiter radius in section 8.4.4 also supports this hypothesis.

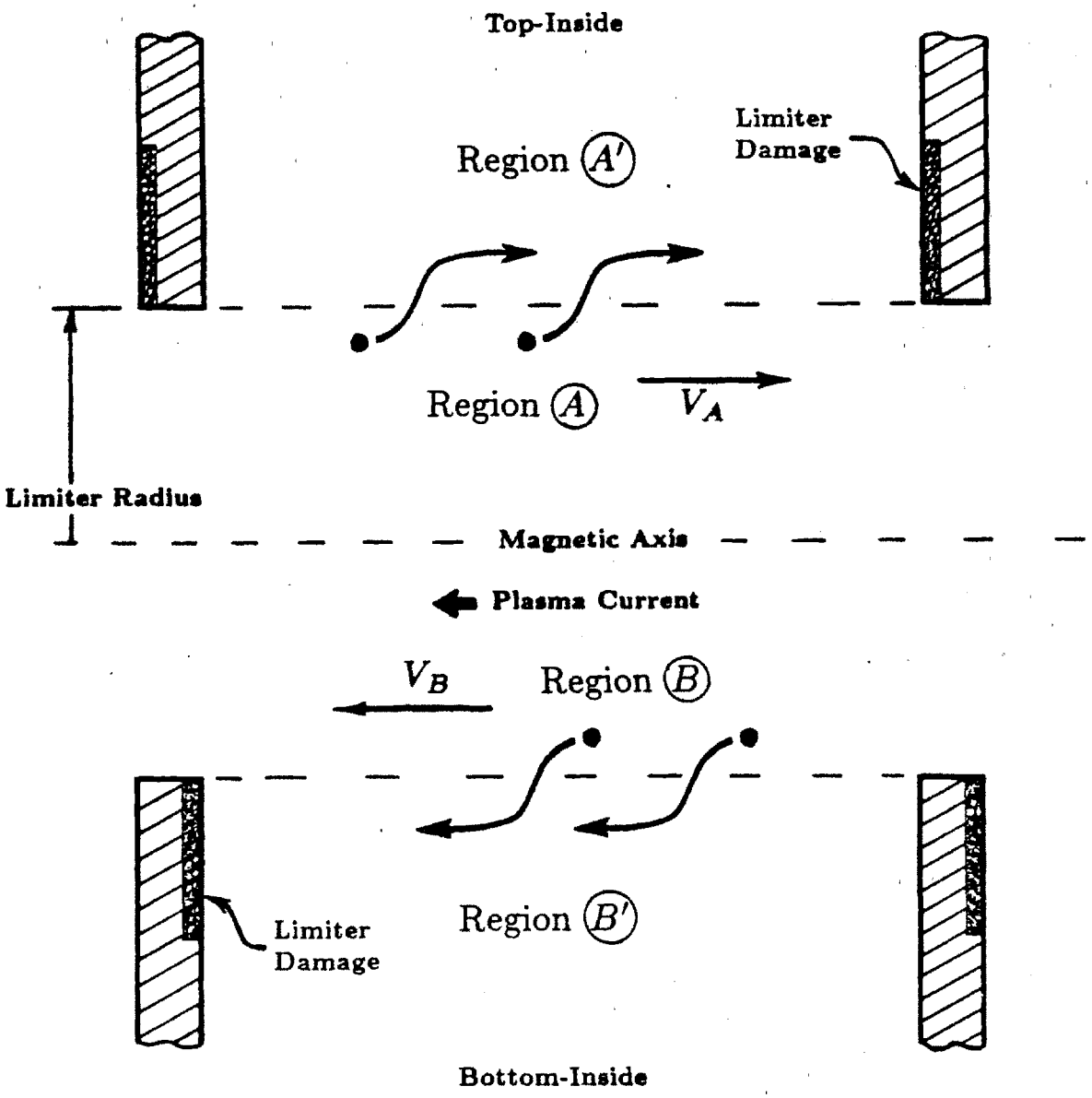

Figure 8.14 Asymmetric Scrape-off of Limiter Shadow Plasma

This idea of poloidally asymmetric plasma parameters occuring inside the limiter radius can be investigated further in connection with trying to explain the toroidally asymmetric limiter damage. Figure 8.15 proposes a scenario where parallel plasma flows in the region $r \lesssim a$ attempt to equalize the density in this plasma region. Radial scrape-off lengths inferred from DENSEPACK data indicate that perpendicular transport is highest on the outside midplane and lowest on the inside midplane. Consequently, it is expected that a parallel transport of particles from high perpendicular particle source regions to low source regions occurs. A poloidal projection of these expected parallel flows, V_A and V_B, is shown in Fig. 8.15*b*. Since these flows are constrained to be on field lines, the toroidal direction of the flow depends on the direction of the toroidal field relative to the plasma current. Figure 8.15*a* traces these flows along $\underline{B}$ for the case of forward toroidal field direction. The view shown here is looking at plasma inside the limiter radius with the eye positioned at the vacuum vessel wall. The limiter position and areas of damage on the stainless steel support structure is indicated in both figures. Note that the direction of V_A and V_B is exactly what is needed to explain both the toroidal location and poloidal extent of the asymmetric limiter damage.

If the $(\underline{V}_\perp \cdot \nabla_\perp)\underline{V}_\parallel$ term in the parallel momentum equation is neglected, one obtains Eq. 8.38 which can be used to roughly scale the magnitude of this parallel flow. Equation 8.38 shows that merely a factor of 1.6 variation in n along a field line leads to parallel flow velocities on order of Mach 1. Thus, it is relatively easy for parallel flows on the order of the sound speed to exist in the plasma region just inside the limiter radius. In addition, since temperature decreases with increasing minor radii, particles having Mach 1 flow velocity in the plasma region $r \lesssim a$ can cross field diffuse into the shadow plasma and appear as Mach > 1 particles there. Furthermore, including the viscosity term in the parallel momentum equation (which may be needed for this case of sharp radial variations of the parallel flow) only leads to a further enhancement of parallel

momentum transport into the shadow plasma region. A strong parallel momentum source for flux tubes in the shadow plasma is therefore readily obtained as a consequence of poloidally asymmetric pressure profiles.

Finally, notice that although the limiter damage is localized to different poloidal regions on the two sides, the total damage area on one side is approximately equal to the damage area on the other side. Thus it appears that if parallel flows are responsible for the asymmetric limiter damage, they do not exhibit a preferential toroidal direction. This is expected since there is no mechanism to impart a non-zero toroidal momentum to the total volume integral of these parallel flows.

In summary, it is possible that poloidal asymmetries in the plasma region just inside the limiter radius are responsible for the toroidally asymmetric and poloidally localized damage seen on Alcator C limiter and vacuum vessel structures. A fluid model, which includes a parallel momentum source from perpendicularly transported particles, predicts toroidally asymmetric fluxes to limiter surfaces when parallel plasma flows exist in the plasma region just inside the limiter radius. Assuming that the poloidally asymmetric perpendicular transport as detected by DENSEPACK extends inside the limiter radius, such parallel flows are likely and consistent in direction and spatial extent with those necessary to explain the asymmetric limiter damage, even when the outer flux surfaces are perfectly aligned with the poloidal limiters.

In closing, it should be pointed out that parallel flows can also be driven by misaligned outer flux surfaces. A flow pattern of parallel flow similar to that outlined above can result when the flux surfaces are shifted to small major radii with respect to the limiters. Thus, the asymmetric heat loading detected far into the limiter shadow plasma can arise from parallel plasma flows driven by both mechanisms. However, parallel flows driven by poloidally asymmetric transport may always be present whereas plasma flows driven by misaligned flux surfaces can be eliminated by careful positioning of the plasma.

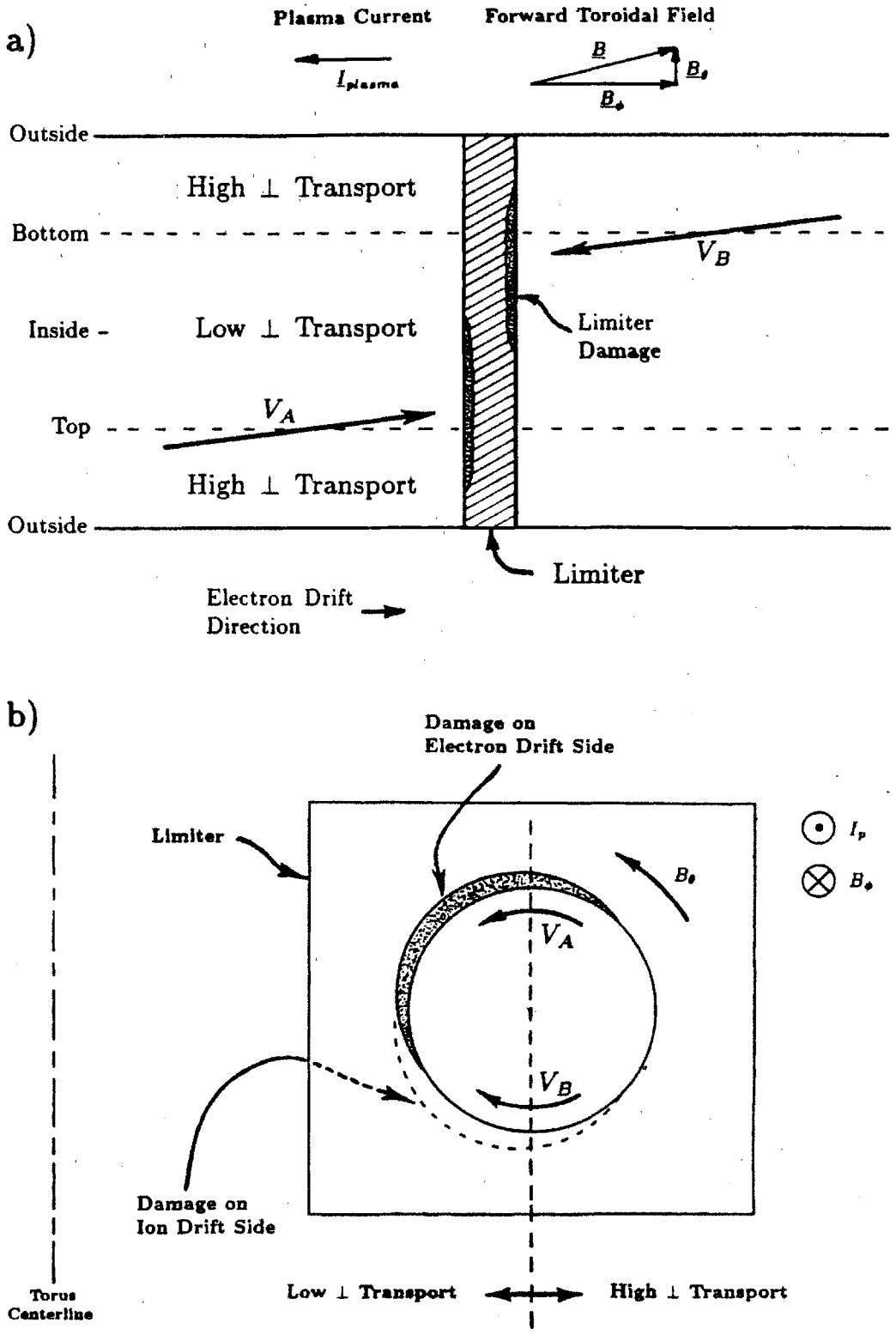

Figure 8.15 Parallel Plasma Flows in the region $r \lesssim a$

v.2 of 2

Poloidal Asymmetries in the Limiter Shadow Plasma of the Alcator C Tokamak

LaBombard, Brian

May 1986

Plasma Fusion Center
Massachusetts Institute of Technology
Cambridge, MA 02139

This work was supported by the U.S. Department of Energy Contract No. DE-AC02-78ET51013. Reproduction, translation, publication, use and disposal, in whole or in part by or for the United States government is permitted.

VOLUME II of II

CHAPTER 9

EDGE VERSUS CENTRAL PARAMETERS: OHMIC, GAS FUELED DISCHARGES

The DENSEPACK data presented in chapters 7 and 8 was obtained during only a few plasma discharges. Although these discharges were chosen for display because they represented the most typical conditions that exist in the Alcator C edge plasma, one would like to know how edge conditions change when central plasma parameters such as line-averaged density, plasma current, toroidal field, and fill gas are varied. In addition, it is of particular interest to examine the degree of edge plasma poloidal asymmetry versus these central quantities.

Clearly, it is not possible to display edge plasma parameters versus central parameters in the same detail as was shown in chapter 7. Consequently, DENSEPACK data is presented in this chapter in a more condensed format that shows the general trend of edge versus central dependences. To accomplish this, data was processed in two ways.

First, all discharges in which DENSEPACK data was recorded were summarized in a DENSEPACK database file. Central and edge plasma quantities were recorded at four selected times during the steady state portion of the discharge. Maxima, minima, and poloidal averages of density, temperature, scrape-off length, etc., obtained from DENSEPACK along with central line-averaged density, plasma current, plasma position, etc., were recorded in this file. Data entries in the file could be scanned and plotted to look for edge versus central plasma scalings. Section 9.1 discusses the organization of the DENSEPACK database and outlines calculations of perpendicular diffusion coefficients and particle confinement times. The results of this database survey for typical ohmic, gas-fueled discharges in which the entire 360^0 DENSEPACK ring was used is the primary focus of the remainder of this chapter.

One important result of this survey was that similar edge plasma parameters occurred at various central densities and currents as long as the combination of central quantities, $\bar{n}_e/I_p$, was held roughly fixed (section 9.2). It was found that a critical value of $\bar{n}_e/I_p$ determined which scaling law the edge density obeyed. Two distinct edge density scaling laws were identified coincident with two regimes: a non-MARFE regime, and a MARFE regime.

$\bar{n}_e/I_p$ appeared to be important for other edge plasma parameters as well. Poloidally averaged values of n_e, T_e, V_f, $\tilde{J}/\bar{J}$, etc. are plotted versus $\bar{n}_e/I_p$ in section 9.3. A clearer connection between the MARFE threshold and the edge density scaling laws is made in this section.

The magnitude of the edge plasma density asymmetry was found to be relatively insensitive to central parameters in contrast to what was expected in the Alcator C edge plasma. However, temperature and floating potential asymmetries were found to change, decreasing at high values of $\bar{n}_e/I_p$. These dependences are shown versus $\bar{n}_e/I_p$ in the final section, 9.4.

DENSEPACK data was also processed in a a way which retained information about faster time variations in edge parameters. Maxima, minima, and poloidal averages of various edge quantities were recorded continuously over the entire duration of the discharge. This yielded short time resolution ($\sim$ 5 msec) traces of these quantities for discharges which exhibited fast changes in central parameters, such as during pellet injection or lower hybrid current drive. Chapter 10 presents results from these discharges in which data from only the inside half ring of DENSEPACK was available. A comparison is made between these discharges and the ohmic, gas-fueled discharges discussed in this chapter.

The starting point in this presentation of edge versus central plasma parameter scalings is a brief description of the DENSEPACK database.

9.1 DENSEPACK Database

9.1.1 Database Quantities

A summary of central and edge plasma parameters was tabulated for all discharges in which DENSEPACK was operating. Table 9.1 lists the various quantities that were recorded for each discharge in addition to the toroidal magnetic field and fill gas. All quantities in table 9.1 resulted from a $\sim$ 20 msec time average centered about four different sample times during the discharge. The four time values shown here were most typically used although they could be varied.

For DENSEPACK variables, maximum, minimum, and average values over poloidal angle were recorded along with angular positions of two relative maxima and minima. In addition, n_e, T_e, V_f, and $\tilde{J}/\bar{J}$ were recorded at the DENSEPACK radii of 16.8, 17.2, and 17.6 cm. The density scrape-off length, λ_n, was inferred from an exponential fit to the data at the three radii, and n_a was obtained by extrapolating along this exponential back to the limiter radius.

The quantities $n_a \times \lambda_n$ and γ were recorded to enable an estimate of the global particle confinement time, τ_p. As described in section 3.1.3, the central density profile was assumed to follow a parabola in minor radius raised to some power, γ.

An estimate of the perpendicular diffusion coefficient, $D_\perp$, was also made from the poloidally averaged scrape-off length data to look for systematic variations with central parameters. The following two subsections describe the relationships that were used in estimating both $D_\perp$ and τ_p from DENSEPACK database entries.

Table 9.1 - DENSEPACK Database Quantities

DENSEPACK Variable	Description
n_e	Electron Density
T_e	Electron Temperature
V_f	Floating Potential
$\tilde{J}/\bar{J}$	Ion Saturation Fluctuation
λ_n	Density Scrape-off Length
n_a	Density at Limiter Radius
$n_a \times \lambda_n$	Limiter Density × Scrape-off Length

X

Time (msec)
200
250
300
350

X

Radii (cm)
16.8
17.2
17.6

X

Quantity
Maximum Value
Minimum Value
Poloidal Average
θ_1 Maxima Location
θ_2 Maxima Location
θ_1 Minima Location
θ_2 Minima Location

Central Variable	Description
$\bar{n}_e$	Central Line-Averaged Density
I_p	Plasma Current
In/Out	In-Out Position
Up/Down	Up-Down Position
q_L	MHD q at Limiter Radius
γ	Central Density Parabola Power

X

Time (msec)
200
250
300
350

9.1.2 Perpendicular Diffusion, $D_\perp$

The perpendicular diffusion coefficient, $D_\perp$, can be estimated using Eq. 3.10,

$$D_\perp \approx \frac{\lambda_n^2 \, C_s}{L} , \tag{9.1}$$

with the assumption that the neutral density is low enough so that condition 3.11 holds.

For the purposes of examining edge versus central plasma scalings, $D_\perp$ was estimated from Eq. 9.1 using the poloidally averaged scrape-off length. The sound speed, C_s in Eq. 9.1, was estimated from poloidally averaged temperatures at two radii, $r = 16.8$ and 17.2 cm,

$$C_s = \sqrt{\frac{(\langle T_e \rangle_{ave}@\ 16.8 \ + \ \langle T_e \rangle_{ave}@\ 17.2)(1+\tau)}{2\ m_i}} , \tag{9.2}$$

where $\tau \equiv T_i/T_e \sim 2$. The connection length, L, was taken as 100 cm.

9.1.3 Particle Confinement Time, τ_p

As described in section 3.3.3, the global particle confinement time, τ_p, can be estimated from probe measurements in the limiter shadow plasma. Data presented in chapter 7 showed that the edge plasma is highly asymmetric in poloidal angle. Thus, an estimate of τ_p from a single radial density profile obtained at one poloidal location can be misleading. DENSEPACK circumvents this problem by covering most of the (r,θ) poloidal plane.

A proper formulation for τ_p when the edge plasma is poloidally asymmetric proceeds exactly as presented earlier, except that the surface integral in Eq. 3.19

must be performed over the poloidally varying quantity, $\lambda_n \times n_a$. C_s also varies in poloidal angle through the variation in $\sqrt{T_e}$. However, this variation is small enough to be ignored considering the accuracy of the data set.

τ_p can therefore be approximated as

$$\tau_p \approx \frac{\bar{n}_e \; L \; a}{2 \; (\gamma + 1) \; \langle \lambda_n n_a \rangle_{ave} \; C_s \; f(\gamma)} \tag{9.3}$$

where $\langle \lambda_n n_a \rangle_{ave}$ is a poloidal average of scrape-off length times density at the limiter radius. For the database survey, C_s as defined by Eq. 9.2 was used. $f(\gamma)$ was numerically approximated as the exponential plus offset function shown in Fig. 3.2.

9.1.4 Units of DENSEPACK Database Quantities

Many plots of the data accumulated in this database will be presented in the sections to follow. For convenience of display, the database quantities are scaled so that they fall in the range 0.1–10. Table 9.2 lists the units associated with each variable. Unless otherwise specified, these units apply for all variables shown on graphs and referenced in the text in both this chapter and chapter 10.

In addition, some labelling on graphs in the following sections does not employ superscipts, subscripts, or Greek characters. Consequently, a quantity such as $\bar{n}_e/I_p$ is denoted as 'NeBar/Ip' on these graphs. Table 9.2 shows variable names, descriptions, and associated alternate 'plot variable' names. These definitions apply for the remainder of this thesis.

Table 9.2 - Units of DENSEPACK Database Variables

DENSEPACK Variable	Alternate Name	Description	Units
n_e	Ne	Electron Density	$1 \times 10^{13}/\text{cm}^3$
T_e	Te	Electron Temperature	eV
V_f	Vf	Floating Potential	volts
$\tilde{J}/\bar{J}$	DJ	Ion Saturation Fluctuation	$\times 1$
λ_n	Scrape	Density Scrape-off Length	cm
n_a	Na	Density at Limiter Radius	$1 \times 10^{13}/\text{cm}^3$
$n_a \times \lambda_n$	NaScrape	Limiter Density $\times$ Scrape-off Length	$1 \times 10^{13}/\text{cm}^2$
Central Variable	**Alternate Name**	**Description**	**Units**
$\bar{n}_e$	NeBar	Central Line-Averaged Density	$1 \times 10^{14}/\text{cm}^3$
I_p	Ip	Plasma Current	kA
$\bar{n}_e/I_p$	NeBar/Ip		$1 \times 10^{12}/\text{cm}^3\text{-kA}$
In/Out	InOut	In-Out Position	cm ($+ \rightarrow$ out)
Up/Down	UpDown	Up-Down Position	cm ($+ \rightarrow$ up)
q_L	qL	MHD q at Limiter Radius	$\times 1$
γ	Gamma	Central Density Parabola Power	$\times 1$
B	Bt	Toroidal Magnetic Field	tesla

9.2 $\bar{n}_e/I_p$ Scaling of Edge Parameters

As expected, edge plasma density and temperature were found to be most sensitive to central line-averaged density and plasma current. Toroidal magnetic field and fill gas species were found to influence slightly the parameters in the edge. Up-down position of the outer magnetic flux surfaces never varied more than ~ 2 mm and so was treated as essentially fixed. On the other hand, the in-out position could vary by more than 5 mm from shot to shot and therefore was treated as a central plasma variable. Still, edge parameters where found to be relatively insensitive to in-out position except for extreme values (± 0.8 cm or more). This was found to hold especially true for the poloidally averaged quantities.

Since the edge plasma was found to be most strongly dependent on the central density and current, discharges of various fill gases and toroidal magnetic fields could be grouped together and examined for $\bar{n}_e$ and I_p dependences. An interesting result was that the edge plasma depended on $\bar{n}_e$ and I_p in a way that implies that the combined quantity, $\bar{n}_e/I_p$, could be used to parameterize the edge plasma state. Furthermore, above a critical value of $\bar{n}_e/I_p$, edge parameters, particularly density, exhibited a different scaling. The critical value of $\bar{n}_e/I_p$ inferred from DENSEPACK data coincided with the $\bar{n}_e/I_p$ threshold for MARFEs as presented in section 4.4.

It is interesting to note that measurements in other tokamaks have also identified the quantity $\bar{n}_e/I_p$ to be important in the scaling of edge parameters. A discussion of DENSEPACK data scalings and some observations in the edge of other tokamaks is presented in the subsections to follow. First, some general observations on the scaling of the poloidally averaged edge density in Alcator C versus central $\bar{n}_e$ and I_p are presented.

9.2.1 $\bar{n}_e$ & I_p Scaling of Edge Density: General Observations

Figure 9.1 plots angle averaged edge plasma density at the DENSEPACK radii of r = 16.8, 17.2, and 17.6 cm versus central $\bar{n}_e$ for a restricted range of plasma currents, 280 kA $< I_p <$ 309 kA. Hydrogen and deuterium plasmas run at 6 and 8 tesla are included in this plot. It is not surprising to find that the edge density increases as the central density increases. However, density at r = 16.8 cm increases nonlinearly with $\bar{n}_e$ for low values of $\bar{n}_e$. As later plots will show, this resulted in shorter scrape-off lengths at high $\bar{n}_e$ but also higher particle loss rates (shorter τ_p) due to the increased plasma density at the limiter radius.

The MARFE threshold $\bar{n}_e/I_p \approx 0.6$ (in database units) is also indicated on this plot. Note that the nonlinear dependence of edge density versus central density is diminished above this threshold. As later analysis will show, the poloidally averaged edge density in this regime is sensitive to I_p but relatively insensitive to central $\bar{n}_e$.

Figure 9.2 shows a more unexpected trend. The same three densities are plotted in this graph but versus plasma current, for the restricted range of densities, $1.6 \times 10^{14}/\mathrm{cm}^3 < \bar{n}_e < 1.7 \times 10^{14}/\mathrm{cm}^3$. Again hydrogen and deuterium discharges at 6 and 8 tesla are included. The plasma density at all radii is generally found to decrease with increasing plasma current. This is particularly apparent for the density at r = 16.8 cm. A factor of two increase in I_p causes roughly a factor of two decrease in edge density at all radii. However, for currents below the indicated threshold, the data points begin to deviate from this trend. The edge density actually increases with plasma current in this regime, $\bar{n}_e/I_p \gtrsim 0.6$.

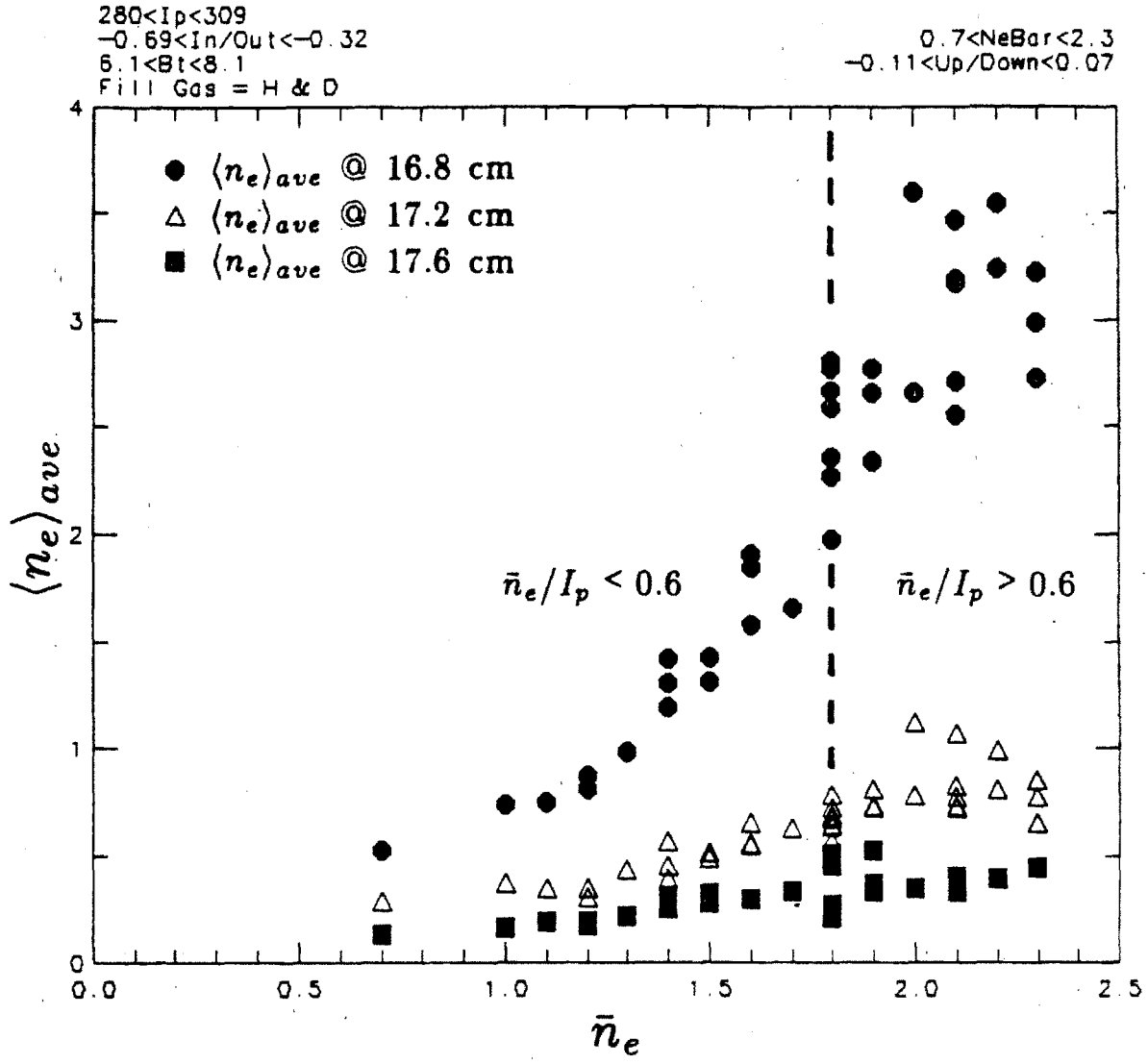

Figure 9.1 Edge Density, $\langle n_e \rangle_{ave}$, vs. Central $\bar{n}_e$

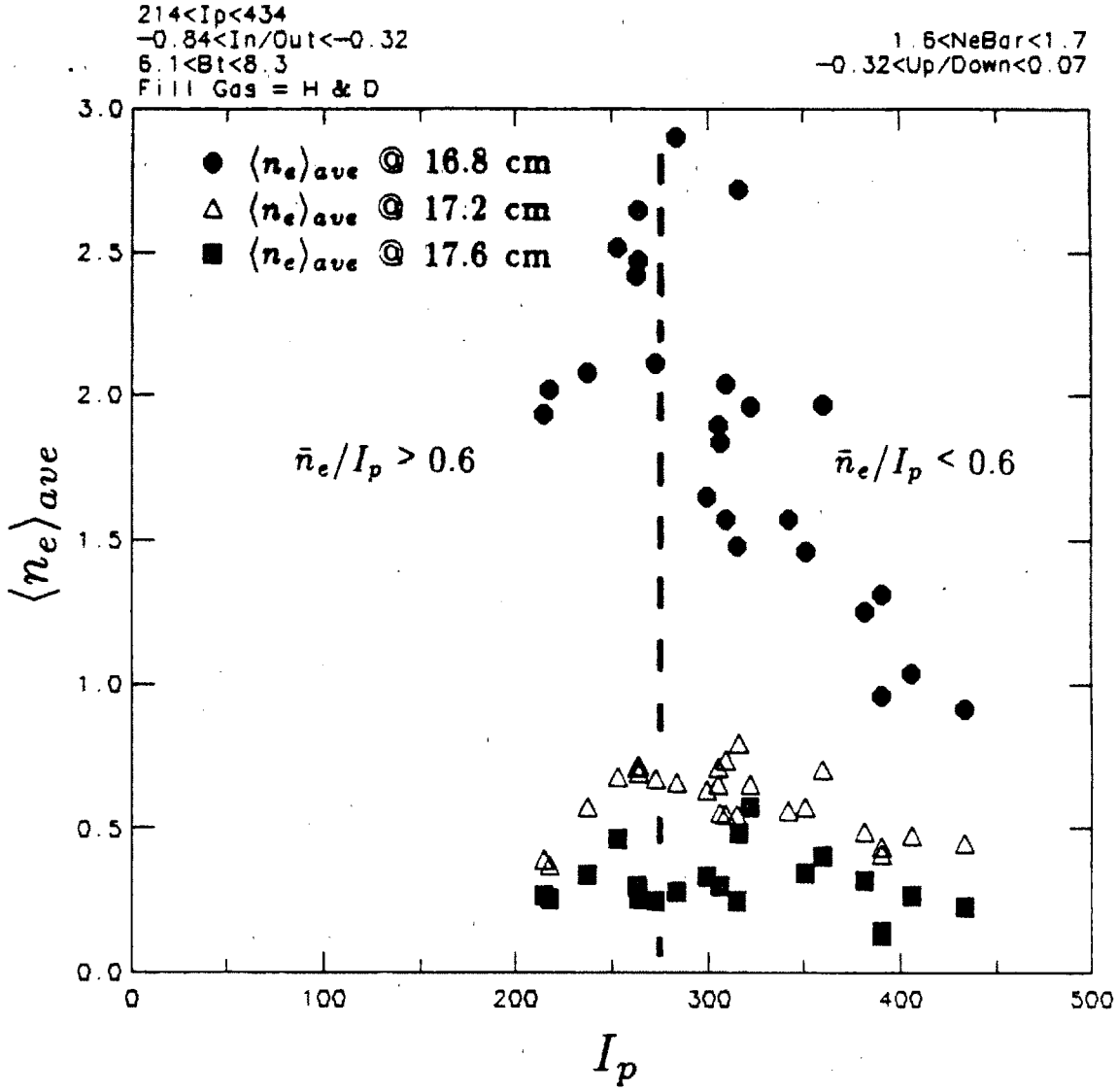

Figure 9.2 Edge Density, $\langle n_e \rangle_{ave}$, vs. Plasma Current

In the regime $\bar{n}_e/I_p \lesssim 0.6$, the relationship of edge density increase for increasing $\bar{n}_e$ and decrease for increasing I_p implies that the edge density at some radial location can be held fixed for multiple combinations of $\bar{n}_e$ and I_p. From the results shown in Figs. 9.1 and 9.2, one may deduce that the edge density itself simply depends on this same combination of central parameters, $\bar{n}_e/I_p$.

Pursuing this idea further, Fig. 9.3 plots poloidally averaged edge density at the three DENSEPACK radii versus $\bar{n}_e/I_p$. The discharges are restricted to hydrogen at 6 tesla although there is no explicit restriction on the range of plasma currents and densities. Again, the MARFE threshold, $\bar{n}_e/I_p \approx 0.6$, is indicated. In addition, data obtained from three types of discharges are indicated on the 16.8 cm data points: *a*) discharges which displayed a MARFE during the data sample time (clear MARFE case), *b*) discharges which displayed a MARFE at some time other than the data sample time ('partial' MARFE case), and *c*) discharges which displayed no MARFE. Note that these three types of discharges recorded by DENSEPACK observed the $\bar{n}_e/I_p$, MARFE threshold scaling law.

Poloidally averaged edge density at all three radii, shown in Fig. 9.3, closely track a smooth curve verus $\bar{n}_e/I_p$ for $\bar{n}_e/I_p \lesssim 0.6$. Above $\bar{n}_e/I_p \approx 0.6$, edge density data points scatter and a close relationship with $\bar{n}_e/I_p$ is no longer seen.

The implication of Figs. 9.1–9.3 is that the edge density obeys two separate scalings with central plasma density and current, depending on the magnitude of the critical parameter, $\bar{n}_e/I_p$, typically associated with the onset of MARFE phenomena. The next section extracts more information about edge density versus central plasma parameter scalings for the two regimes by employing multiple parameter, nonlinear regression analysis techniques.

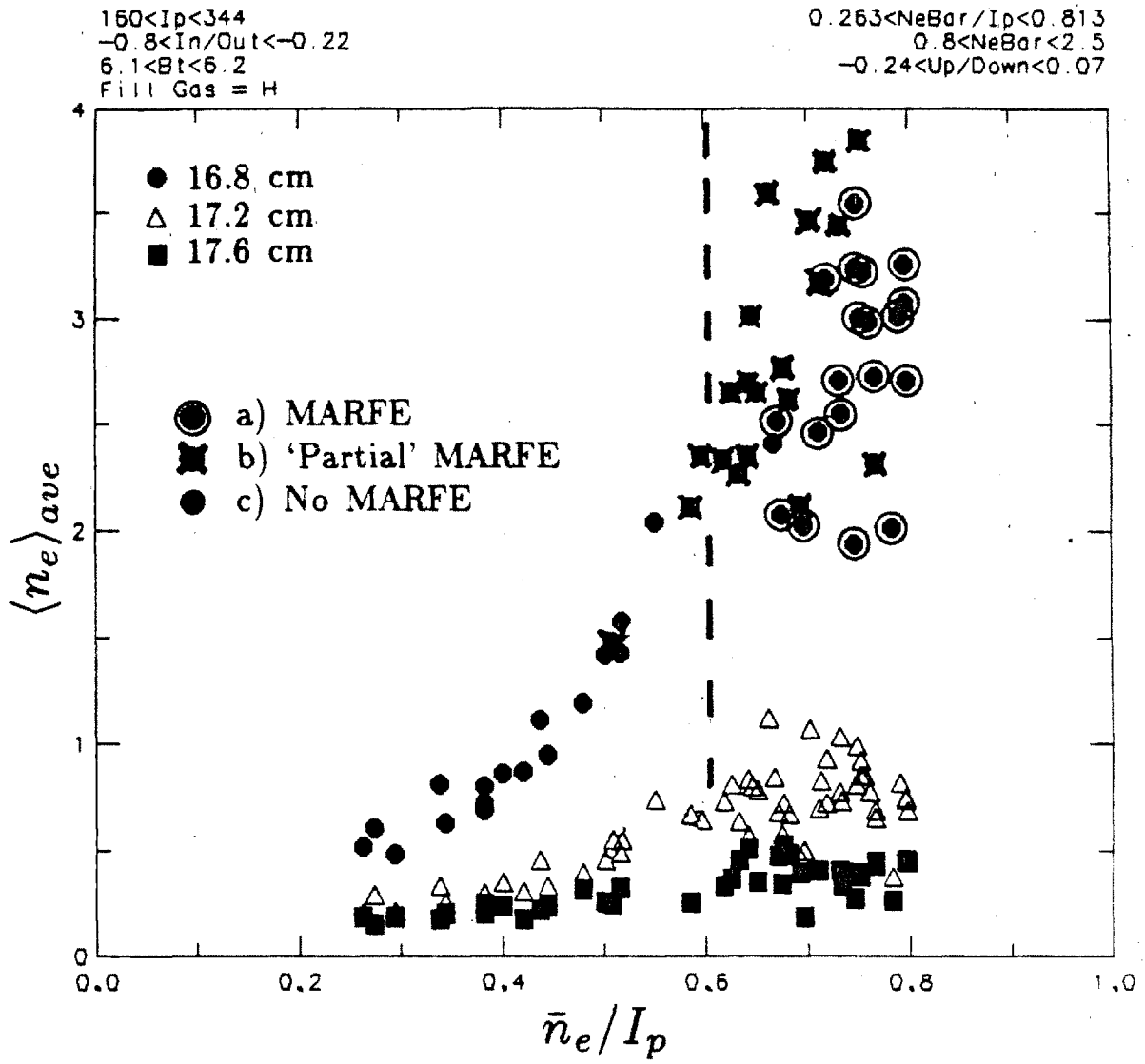

Figure 9.3 Edge Density, $\langle n_e \rangle_{ave}$, vs. $\bar{n}_e / I_p$

9.2.2 $\bar{n}_e$ & I_p Scaling of Edge Density: Regression Analysis

Figure 9.3 implies a nonlinear relationship between edge density and some combination of line-averaged density and plasma current. In general, this data can be fitted with equal accuracy to an unlimited number of functions of $\bar{n}_e$ and I_p. However, a simple function of a few variables is the most desirable. A search for a relatively simple functional form that still had enough freedom to adequately describe the observed trends was therefore performed.

To further simplify this fitting problem, the data set was divided into two regimes: a non-MARFE regime and a MARFE regime. The density data from each regime was treated separately and a best fitting functional form was selected independently for each. The first part of this discussion of the regression analysis only deals with data sampled in the absence of a MARFE.

Figure 9.4 plots poloidally averaged edge density at $r = 16.8$ cm versus a fitted function of the form

$$\langle n_e \rangle_{ave} = C\ \bar{n}_e^{\alpha}\ I_p^{\beta} \tag{9.4}$$

where C, α, and β are determined by regression analysis. The data was selected from only hydrogen, 6 tesla discharges in order to eliminate any effects due to gas species or toroidal field (section 9.3).

The general trend of increasing edge density with increasing central density or decreasing plasma current is reproduced by this regression although this three parameter function has trouble matching the overall grouping of the data points. The data points appear to curve away from the straight line that corresponds to perfect agreement.

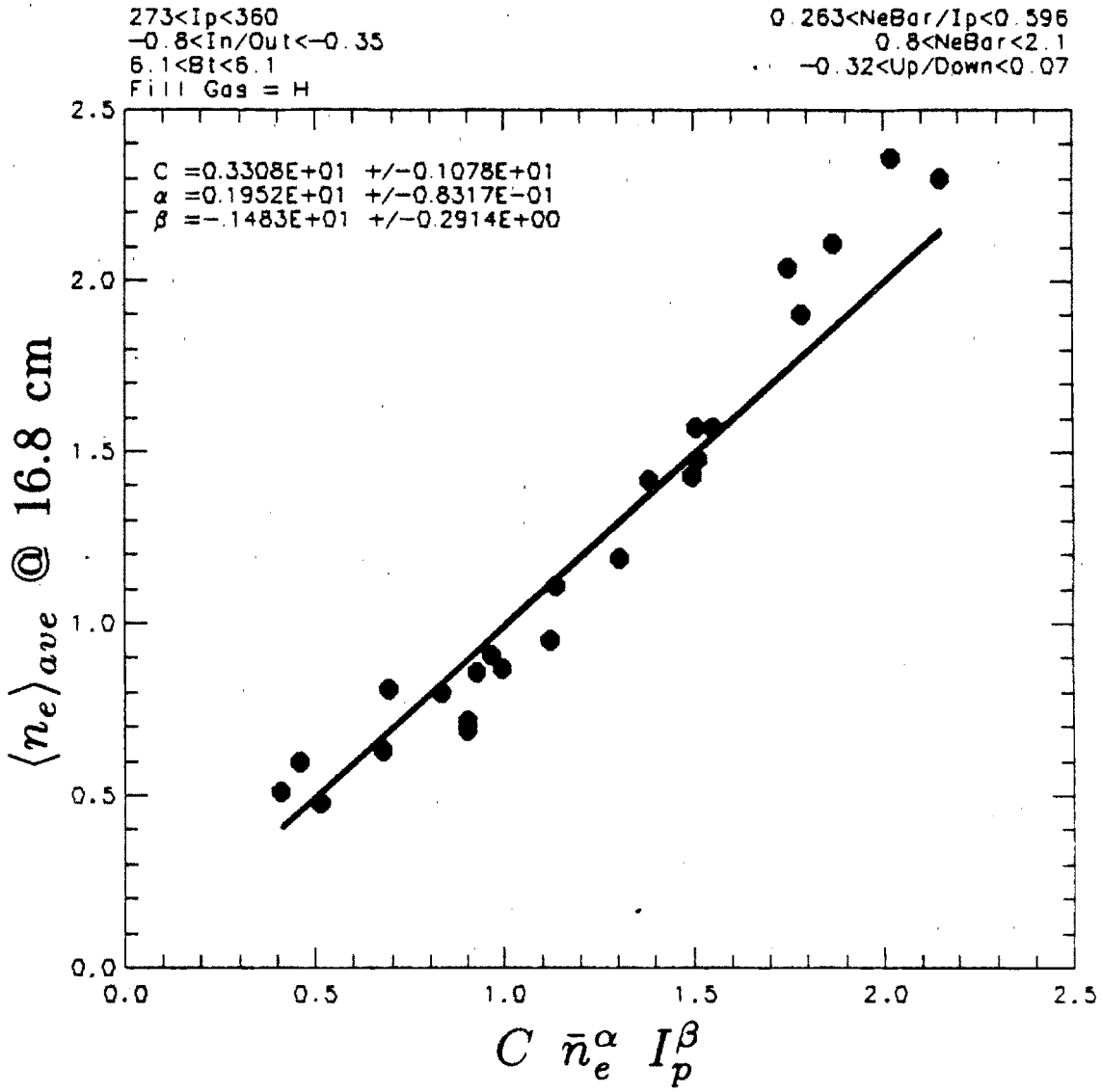

Figure 9.4 $\langle n_e \rangle_{ave}$@ **16.8 cm Regression Analysis using Fitting Function in Equation 9.4, Non-MARFE Regime**

The uncertainties displayed beside each fitted parameter in Fig. 9.4 and the figures to follow are estimated standard deviations. These were obtained by successively perturbing each data point and re-fitting the perturbed data. The total uncertainties for the fitted parameters were then obtained by summing the contributions from each perturbation.[93] The magnitude of the estimated standard deviations depends on the assumed standard deviation for the probe density data. Nevertheless, they provide a measure of the relative accuracy between parameters and between fitting functions.

A better fit to the data in Fig. 9.4 was obtained when a fourth parameter was included in the fitting function. Fig. 9.5 displays the agreement to a fitting function of the form

$$\langle n_e \rangle_{ave} = \bar{n}_e \left(a + b\, \bar{n}_e^{\alpha}\, I_p^{\beta} \right) . \tag{9.5}$$

The data points are now more uniformly distributed about the perfect agreement line. Notice that again the edge density depends on some positive power in $\bar{n}_e$ ($\alpha \approx 4.2$) and on some negative power in I_p ($\beta \approx -5.5$).

The functional form of Eq. 9.5 was chosen so that $\langle n_e \rangle_{ave} \rightarrow 0$, as $\bar{n}_e \rightarrow 0$, similar to Eq. 9.4. Equation 9.5 is also conceptually pleasing in that it contains both a linear and a nonlinear term in $\bar{n}_e$. From the fit, one can see that at low values of $\bar{n}_e$, the edge density is modelled to increase linearly with $\bar{n}_e$. For values of $\bar{n}_e$ near the limit, $\bar{n}_e / I_p \approx 0.6$, the edge density increases nonlinearly with $\bar{n}_e$. The range of $\bar{n}_e$ in the data set includes both extremes. Therefore, by including both terms, a better fit to the data was attained.

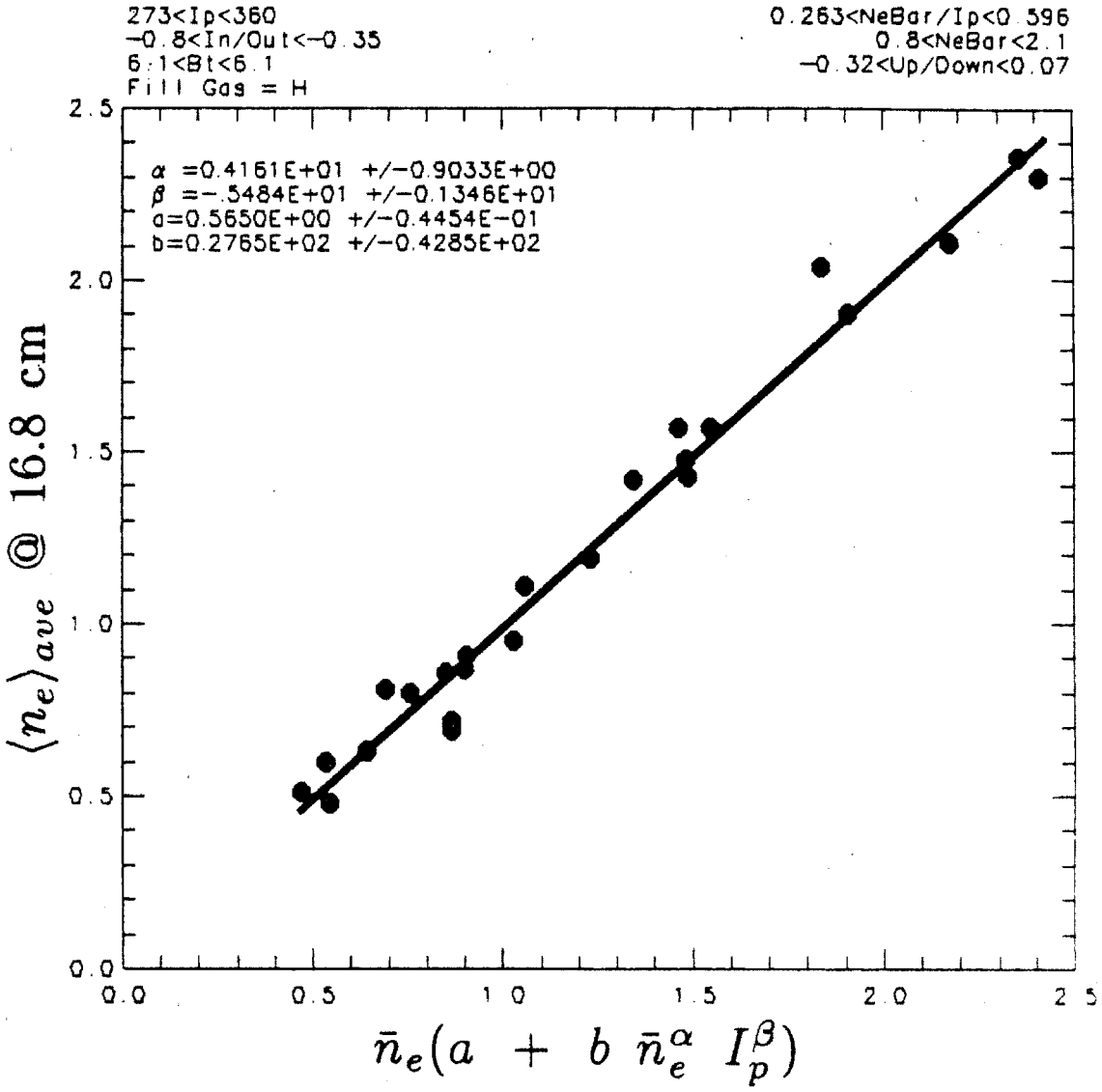

Figure 9.5 $\langle n_e \rangle_{ave}$@ **16.8 cm Regression Analysis using Fitting Function in Equation 9.5, Non-MARFE Regime**

The estimated uncertainty in coefficient b is large since for a given fit it depends exponentially on the values of α and β which also have some uncertainty. However, the important functional dependences are contained in a, α, and β which have reasonably small estimated standard deviations ($\lesssim 20\%$).

The values and uncertainties of α and β displayed in Fig. 9.5 suggest that one can force a requirement that $\beta = -\alpha$ and still obtain a good fit to the data set. Figure 9.6 plots the data against this less general function of $\bar{n}_e$ and I_p,

$$\langle n_e \rangle_{ave} = \bar{n}_e \left[a + b \left(\bar{n}_e / I_p \right)^{\alpha} \right] , \tag{9.6}$$

which now contains an explicit $\bar{n}_e/I_p$ dependence. As shown in Fig. 9.6, the data is modelled well by Eq. 9.6, verifying that the additional parameter, β, could indeed be set to $-\alpha$ within the accuracy of the data set. Thus, the initial observation that the edge density depended strongly on the value of $\bar{n}_e/I_p$ for the non-MARFE regime was borne out in this more rigorous regression analysis.

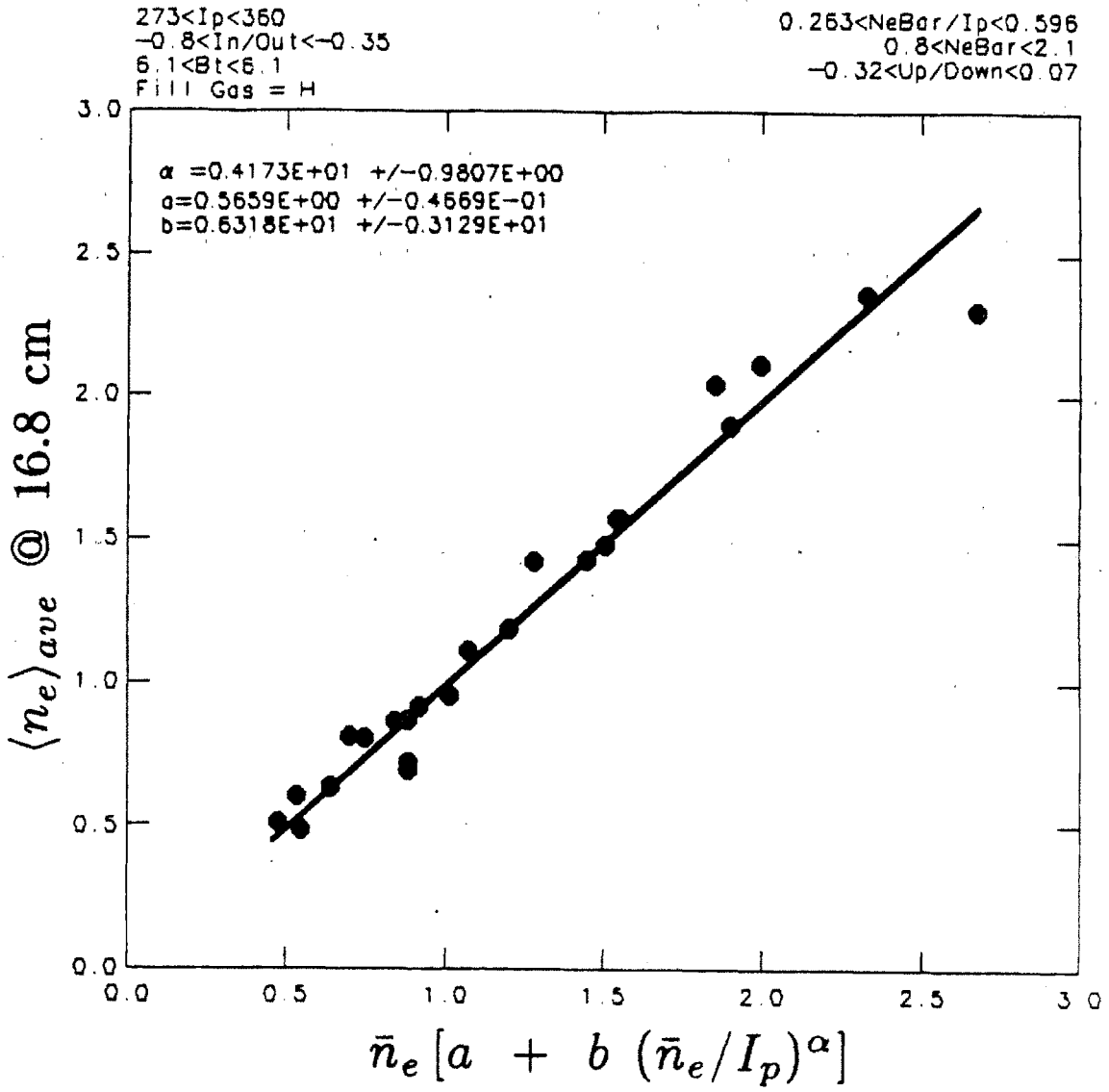

Figure 9.6 $\langle n_e \rangle_{ave}$@ 16.8 cm Regression Analysis using Fitting Function in Equation 9.6, Non-MARFE Regime

Figure 9.7 plots all the hydgrogen, 6 tesla data points against a fit that is similar to the one shown in Fig. 9.6. It is clear that the functional form given by Eq. 9.6 does not universally apply over the entire range of $\bar{n}_e/I_p$. Our attention therefore shifts to the data points obtained in the regime when $\bar{n}_e/I_p \gtrsim 0.6$ or in the MARFE regime.

For these data points, a regression analysis approach similar to the one used in the non-MARFE regime was employed. Figure 9.8 plots poloidally averaged edge density data at $r = 16.8$ cm obtained only when a MARFE was present during the time of data sampling. The abscissa in Fig. 9.8 is the predicted density from a fitted function of the form of Eq. 9.4. For the sake of clarity, only hydrogen, 6 tesla discharges are shown as in earlier plots.

The scatter in the data points is larger in this regime. A better regression fit was obtained when points from other discharges of various gas species and toroidal magnetic fields are included; however, the discussion of this more complete analysis is deferred until section 9.3.

The principal point made by Fig. 9.8 is that the edge density in the MARFE regime no longer scales by some positive power in $\bar{n}_e$ and some negative power in I_p. The edge density scaling is now dominated by the magnitude of the plasma current alone. Higher plasma currents allow higher edge densities when $\bar{n}_e/I_p \gtrsim 0.6$, and higher central densities do not directly affect the edge density in this regime.

Thus it is clear that the value of $\bar{n}_e/I_p$ not only enters directly into the scaling of edge plasma parameters in some cases but also determines which scaling law the edge density follows. $\bar{n}_e/I_p$ has been identified in other tokamaks as an important edge density scaling parameter. The next section considers some of these observations.

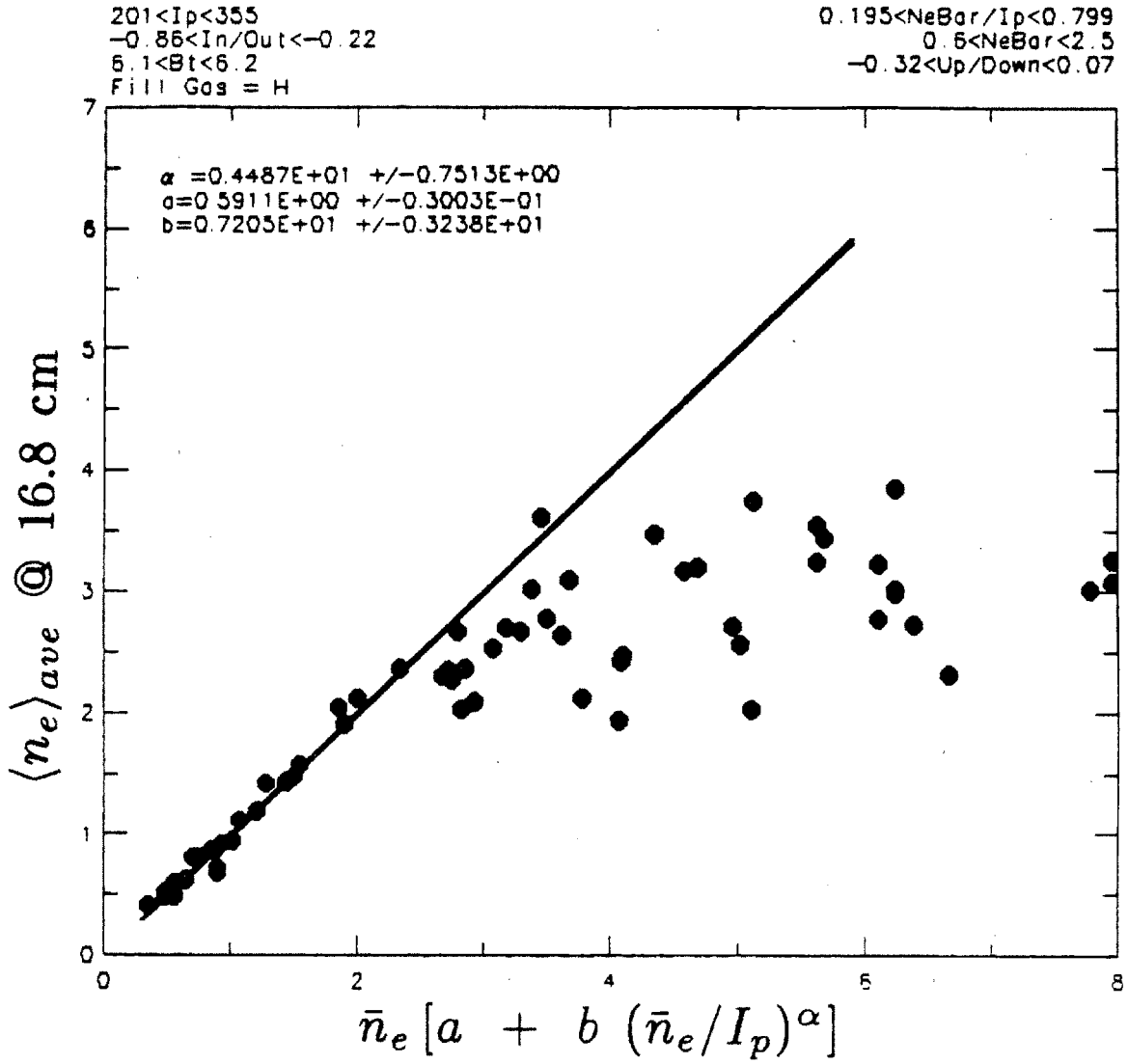

Figure 9.7 $\langle n_e \rangle_{ave}$@ 16.8 cm vs. Fitting Function in Figure 9.6, All Hydrogen, 6 tesla Data Points Included

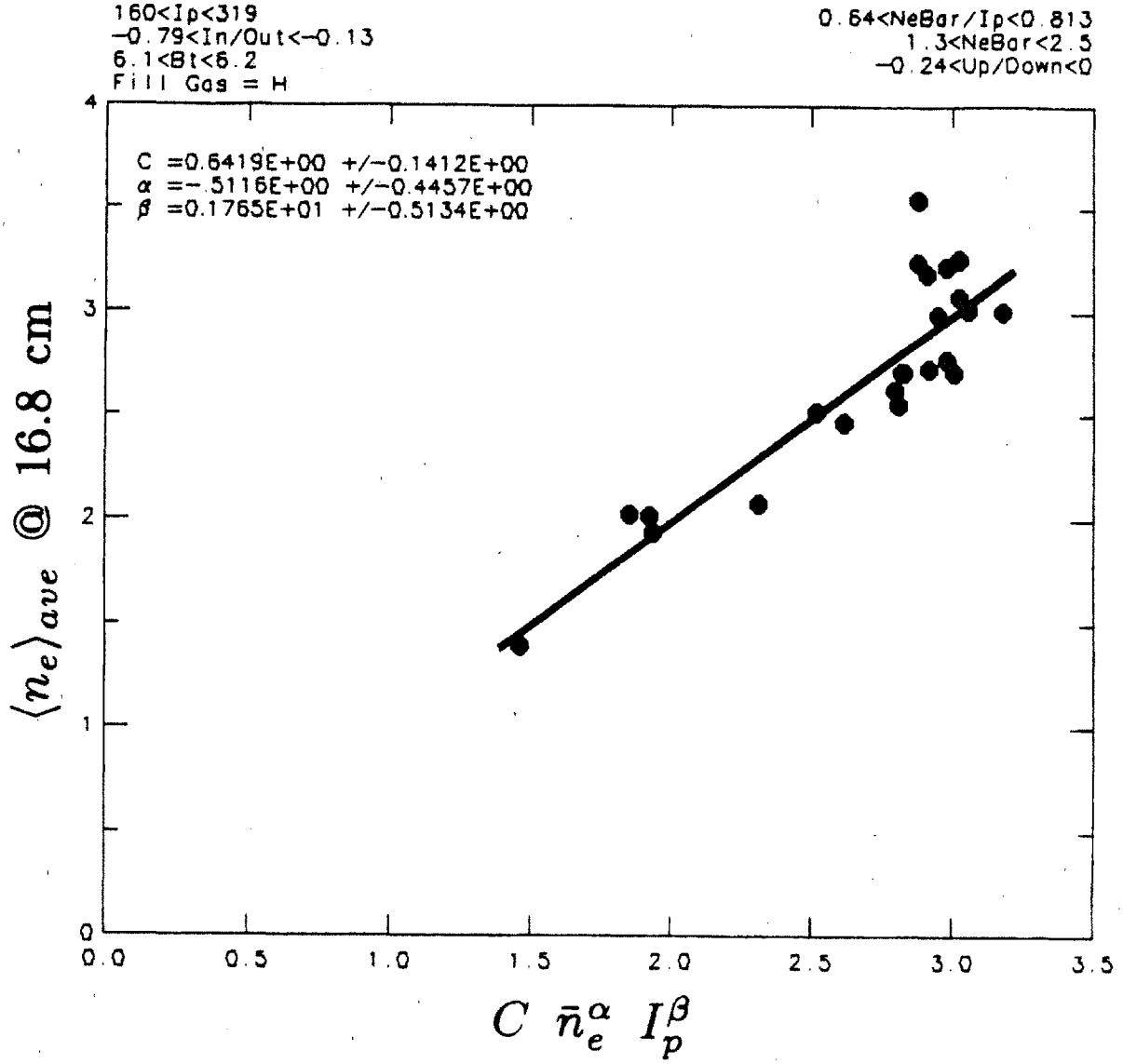

Figure 9.8 $\langle n_e \rangle_{ave}$@ 16.8 cm Regression Analysis using Fitting Function in Equation 9.4, MARFE Regime

9.2.3 $\bar{n}_e/I_p$ Scaling of Edge Density in Other Tokamaks

The scaling of edge parameters with central density and inverse plasma current has been seen in other tokamaks. This has been through indirect observations such as the onset of MARFE phenomena and/or the approach of a density limit in ohmic discharges or through more direct observations such as probe or H_α measurements in the edge.

As discussed in chapter 4, the density and current threshold for MARFE phenomena reported in Alcator C and Doublet III followed an approximate $\bar{n}_e/I_p$ scaling law. MARFE phenomena is now being identified in other tokamaks and is generally associated with the approach of a density limit. For ohmic heated discharges, the maximum density that can be attained is dependent on the plasma current. This result is usually seen in a 'Hugill' plot which shows achievable tokamak densities and currents on a $1/q$ versus $\bar{n}_e R/B_t$ diagram. A boundary of $\bar{n}_e/I_p \approx const.$ is a straight line on this plot which can define the tokamak density limit and/or the onset of MARFE discharges. For Alcator C, the MARFE threshold can be written in terms of Murakami number, m ($= \bar{n}_e R/B_T \times 10^{19}/\mathrm{m}^2$ tesla), as[111]

$$1/q \approx 0.11\ m \quad \text{(Alcator C MARFE threshold)} \tag{9.7}$$

Recently, ASDEX has reported similar results for ohmic discharges,[112]

$$1/q \approx 0.06\text{–}0.08\ m \quad \text{(ASDEX MARFE threshold).} \tag{9.8}$$

Thus, in terms of parameterizing the edge state, the quantity $\bar{n}_e/I_p$ works well.

More direct measurements of edge parameters have also identified $\bar{n}_e/I_p$ as important. Edge Langmuir probe measurements on the Frascati tokamak[113]

show that the same edge density at a given radius can be maintained by multiple combinations of central densities and plasma currents. The importance of this result is recognized with edge density control for optimum lower hybrid wave coupling.[113]

H_α measurements also generally show a $\bar{n}_e/I_p$ dependence. TFTR reports τ_p inferred by H_α measurements decreasing with $\bar{n}_e$ but increasing with I_p.[109] The implication is that the particle recycling coefficient depends on $\bar{n}_e/I_p$.

Thus, the magnitude of $\bar{n}_e/I_p$ appears to be important in defining the plasma edge state. Measurements from DENSEPACK support this observation. Not only is the edge density affected by the value of $\bar{n}_e/I_p$, but other edge parameters tend to group according to the value of $\bar{n}_e/I_p$.

9.2.4 Plotting T_e, V_f, $\tilde{J}/\bar{J}$, and All Edge Parameters vs. $\bar{n}_e/I_p$

The edge parameters T_e, V_f, and $\tilde{J}/\bar{J}$ were found to depend on $\bar{n}_e$ and I_p in a way that is similar to the edge density dependence on $\bar{n}_e/I_p$ or at least in a way that allows them to be plotted unambiguously versus $\bar{n}_e/I_p$.

It is found that discharges with high I_p or low $\bar{n}_e$ generally exhibit higher temperatures at $r = 16.8$ cm than discharges with low I_p or high $\bar{n}_e$. This is similar to a functional dependence on $\bar{n}_e/I_p$ observed for the edge density. At larger minor radii, $r = 17.2$ and 17.6 cm, the dependence of T_e on I_p is weak if detected at all. T_e at these radii actually tends to increase with increasing $\bar{n}_e$. However, because little if any I_p dependence is detected for this data, one can still plot T_e versus $\bar{n}_e/I_p$ and obtain a grouping of points that has the same, if not less, scatter than would result from plotting against $\bar{n}_e$ alone. However, one would not be able to deduce a scaling relationship that depends explicitly on $\bar{n}_e/I_p$ from this T_e data set.

As the following sections will show, the floating potential, V_f, and normalized ion saturation current fluctuation level, $\tilde{J}/\bar{J}$, show clearer trends with $\bar{n}_e$ and I_p. Thus, all parameters in the edge appear to be affected in some way by the value of $\bar{n}_e/I_p$. By plotting edge parameters versus $\bar{n}_e/I_p$, typical measured values can be summarized for discharges with a wide range of central plasma currents and densities. Consequently, more subtle dependencies on fill gas species and magnetic field, can be identified.

The following section makes use of this idea to plot DENSEPACK measurements versus $\bar{n}_e/I_p$ for various central plasma parameters.

9.3 Poloidally Averaged Edge Parameters vs. $\bar{n}_e/I_p$, B, and Gas

This section presents poloidally averaged edge parameters as inferred by DENSEPACK versus central line-averaged densities and plasma currents. Hydrogen and deuterium discharges run in 6 and 8 tesla toroidal fields are included. For convenience, most data are plotted versus $\bar{n}_e/I_p$. Results from a regression analysis are also summarized for the edge density data at radii $r = 16.8$ and 17.2 cm, and for densities extrapolated to the limiter radius, $r = 16.5$ cm.

9.3.1 Edge Density: Regression Analysis

As outlined in section 9.2.2, regression analyses using a variety of fitting functions were performed on the poloidally averaged density data. These regression analyses were extended to include discharges with hydrogen and deuterium fill gasses at 6 and 8 tesla magnetic fields. The results of these analyses are summarized first for the non-MARFE regime, $\bar{n}_e/I_p \lesssim 0.6$, and then for the MARFE regime, $\bar{n}_e/I_p \gtrsim 0.6$.

A. Non-MARFE Regime ($\bar{n}_e/I_p \lesssim 0.6$)

The best fitting function for edge density scaling in this regime was found to be

$$\langle n_e \rangle_{ave} = \bar{n}_e \left(a + b \left(\bar{n}_e/I_p \right)^{\alpha} B^{\gamma} \mu^{\delta} \right) , \tag{9.9}$$

where B is the toroidal magnetic field and μ is the atomic mass of the discharge gas species. The strongest dependence was found to be on $\bar{n}_e/I_p$, B, and μ, in that order. A magnetic field term and/or gas term was also tried as a multiplier on the right hand side of Eq. 9.9 but both resulted in negligibly small dependencies (exponent $\rightarrow 0$). It should be pointed out that data from only two

different gasses and two different toroidal magnetic fields were included in this regression. Thus, the functional dependence of Eq. 9.9 on B and μ (strictly power law in second term) is only a matter of convenience and does not represent any relationship inferred from the data. On the other hand, as discussed in section 9.2.2, the functional dependence of Eq. 9.9 on $\bar{n}_e$ and I_p does represent the data over a large variation in $\bar{n}_e$ (factor of ~ 5) and a smaller variation in I_p (factor of ~ 2).

Figure 9.9 displays poloidally averaged density data at $r = 16.8$ cm against the fitting function given by Eq. 9.9. All hydrogen, deuterium, 6 and 8 tesla points are included on this plot although only non-MARFE data points are fitted. This figure demonstrates that the function in Eq. 9.9 models the edge density scaling well for a variety of discharges. The uncertainty in all three exponents is estimated to be around the $\pm$ 10–20% level.

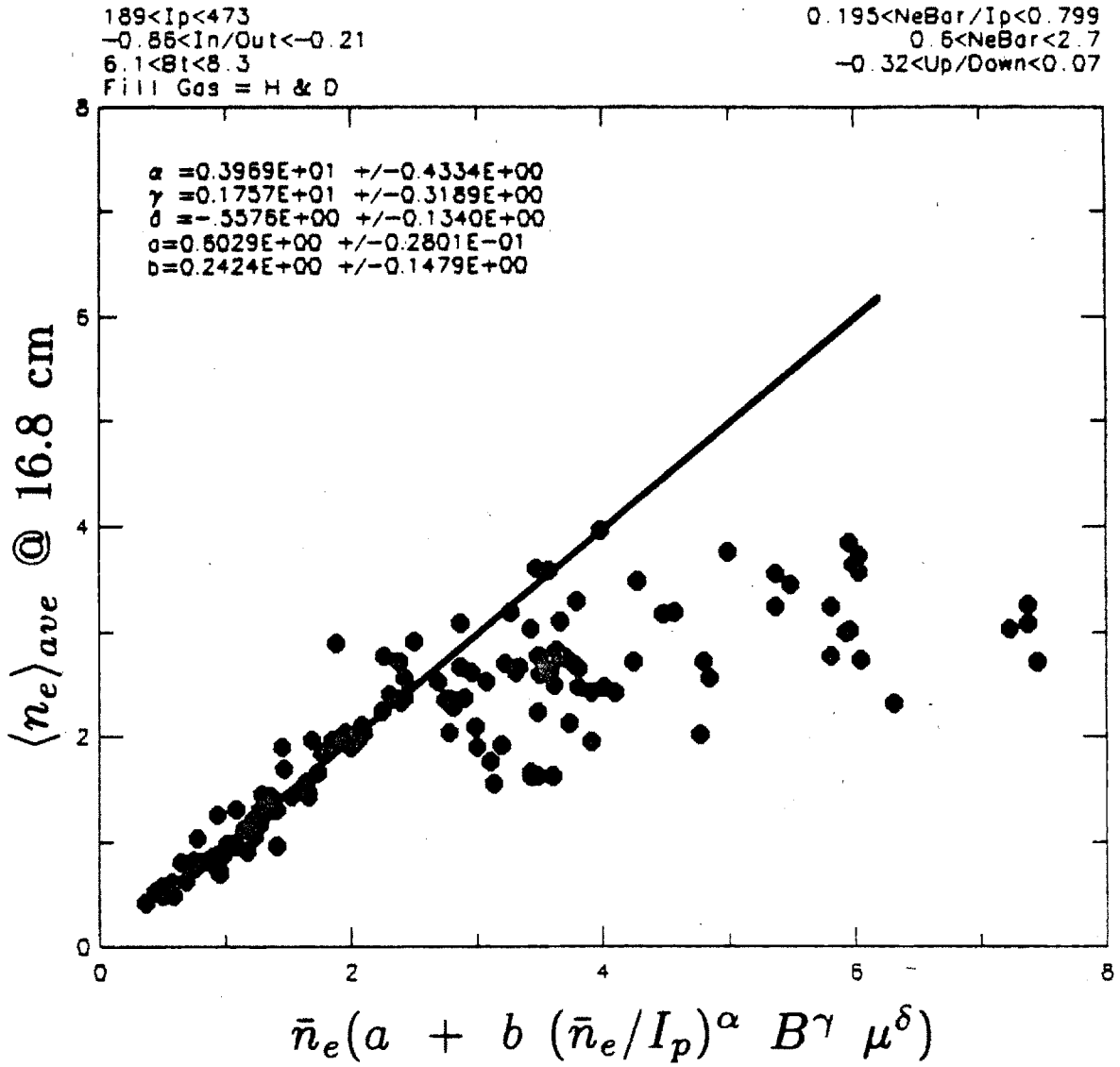

Figure 9.9 $\langle n_e \rangle_{ave}$@ **16.8 cm Regression Analysis using General Fitting Function in Equation 9.9, Non-MARFE Regime**

B. MARFE Regime ($\bar{n}_e/I_p \gtrsim 0.6$)

For discharges which displayed a MARFE during the data sample time ($t =$ 250 msec), the best edge density fitting function was found to be

$$\langle n_e \rangle_{ave} \;=\; C\; I_p^{\beta}\; \mu^{\delta}\;. \tag{9.10}$$

Inclusion of $\bar{n}_e$ and B terms showed that the edge density does not depend on these parameters within the accuracy of the data. The strongest dependence was found to be on I_p. It is interesting that in this regime the edge density was found to be proportional to some function of μ whereas in the non-MARFE regime, the density scaling analysis indicated that such a multiplier was inappropriate. Again the power law dependence on μ used here is assumed and cannot be verified from this data which includes only two gas species.

Figure 9.10 displays poloidally averaged density data at $r = 16.8$ cm against the fitting function given by Eq. 9.10. All points are during a MARFE in hydrogen and deuterium plasma at 6 and 8 tesla. The wide range of plasma currents in this data set, 134 kA $\leq I_p \leq$ 361 kA, is seen to strongly affect the edge density through the positive β exponent, $\beta \approx 1.4$. The I_p dependence of the edge density in this regime as first presented through Fig. 9.8 is now more clearly evident.

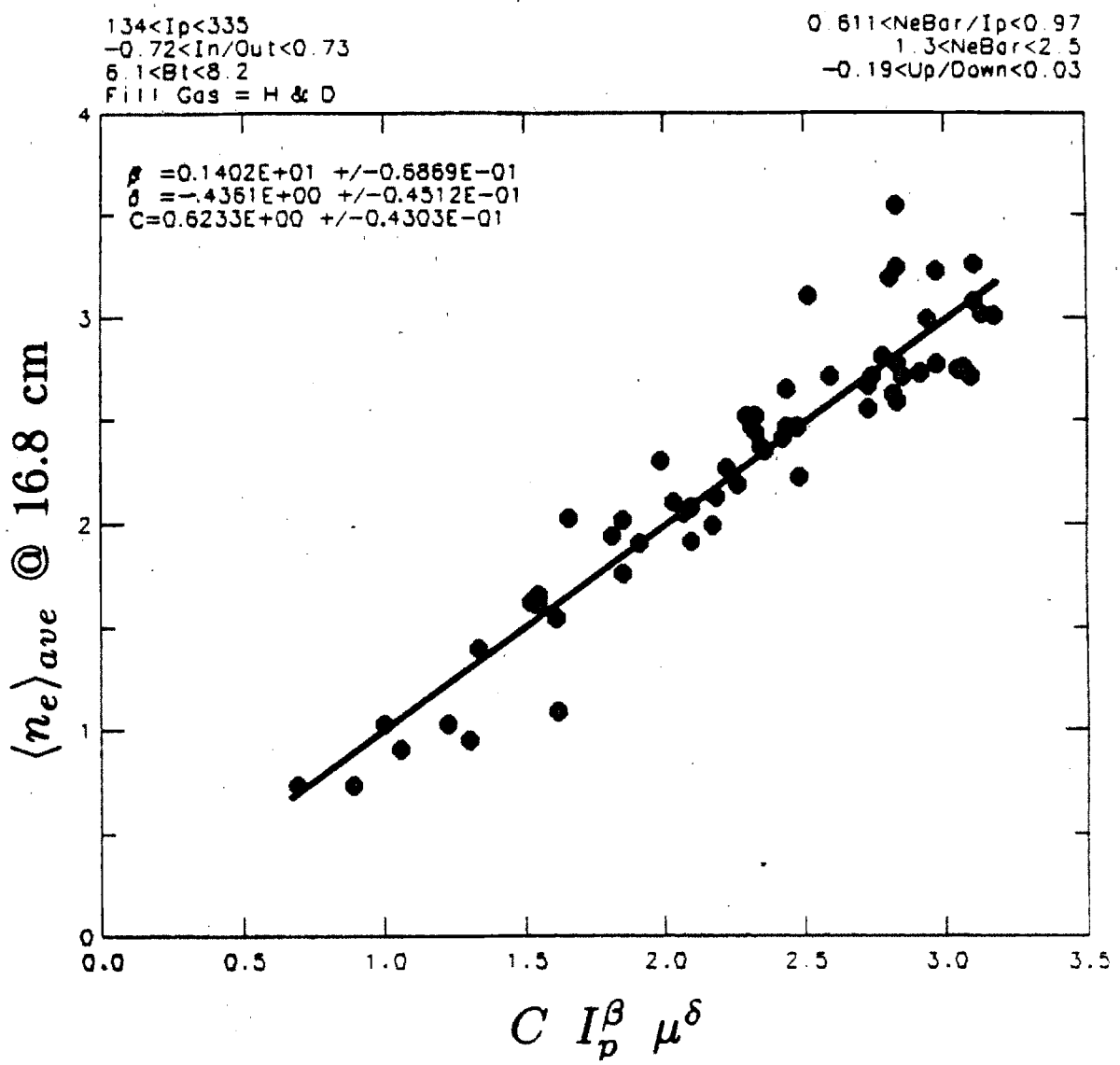

Figure 9.10 $\langle n_e \rangle_{ave}$@ **16.8 cm Regression Analysis using General Fitting Function in Equation 9.10, MARFE Regime**

C. Summary of Edge Density Scalings from Regression Analysis

The regression parameters for poloidally averaged densities at $r = 16.5$, 16.8, and 17.2 cm which result from best fits of Eqs. 9.9 and 9.10 are summarized in tables 9.3 and 9.4. Degenerate cases in which δ and/or γ are forced to zero are also included.

Table 9.3 - Edge Density Regression Parameters for non-MARFE Regime ($\bar{n}_e/I_p \lesssim 0.6$)

Full Regression	a	b	α	γ	δ
$\langle n_e \rangle_{ave}$ @ 16.5 cm	1.2 ± .070	.92 ± .52	5.1 ± .67	1.9 ± .36	−.96 ± .16
$\langle n_e \rangle_{ave}$ @ 16.8 cm	.60 ± .028	.24 ± .15	4.0 ± .43	1.7 ± .32	−.56 ± .13
$\langle n_e \rangle_{ave}$ @ 17.2 cm	.29 ± .087	.40 ± .58	5.3 ± 1.0	.94 ± .69	.012 ± .28

Regression, $\delta = 0$	a	b	α	γ
$\langle n_e \rangle_{ave}$ @ 16.5 cm	1.0 ± .063	3.7 ± 1.6	4.6 ± .49	1.0 ± .22
$\langle n_e \rangle_{ave}$ @ 16.8 cm	.57 ± .029	.54 ± .27	3.8 ± .41	1.3 ± .24
$\langle n_e \rangle_{ave}$ @ 17.2 cm	.29 ± .0076	.39 ± .48	5.4 ± .84	.95 ± .48

Regression, $\delta = 0$, $\gamma = 0$	a	b	α
$\langle n_e \rangle_{ave}$ @ 16.5 cm	.99 ± .059	25. ± 5.9	4.3 ± .41
$\langle n_e \rangle_{ave}$ @ 16.8 cm	.57 ± .029	6.6 ± 1.4	3.8 ± .40
$\langle n_e \rangle_{ave}$ @ 17.2 cm	.29 ± .0074	2.7 ± 1.1	5.5 ± .75

Fitting Function:

$$\langle n_e \rangle_{ave} = \bar{n}_e \left[a + b \, (\bar{n}_e/I_p)^{\alpha} \, B^{\gamma} \, \mu^{\delta} \right] \quad (\times 10^{13}/\mathrm{cm}^3)$$

$\bar{n}_e$ - in units of $10^{14}/\mathrm{cm}^3$

I_p - in units of 10^2 kA

B - in units of tesla

μ - in units of AMU

Table 9.4 - Edge Density Regression Parameters
for MARFE Regime ($\bar{n}_e/I_p \gtrsim 0.6$)

Full Regression	c	β	δ
$\langle n_e \rangle_{ave}$ @ 16.5 cm	1.6 ± .11	1.3 ± .070	−.61 ± .045
$\langle n_e \rangle_{ave}$ @ 16.8 cm	.62 ± .043	1.4 ± .069	−.44 ± .045
$\langle n_e \rangle_{ave}$ @ 17.2 cm	.19 ± .012	1.3 ± .065	−.21 ± .043

Regression, $\delta = 0$	c	β
$\langle n_e \rangle_{ave}$ @ 16.5 cm	1.1 ± .058	1.6 ± .053
$\langle n_e \rangle_{ave}$ @ 16.8 cm	.52 ± .027	1.5 ± .052
$\langle n_e \rangle_{ave}$ @ 17.2 cm	.17 ± .009	1.3 ± .052

Fitting Function:

$$\langle n_e \rangle_{ave} = c\ I_p^{\beta}\ \mu^{\delta} \qquad (\times 10^{13}/\mathrm{cm}^3)$$

I_p - in units of 10^2 kA

μ - in units of AMU

9.3.2 Edge Density: Regression Results, MARFE Threshold

The fitted functions presented in tables 9.3 and 9.4 completely describe the poloidally averaged edge density in Alcator C over the entire operating range recorded by DENSEPACK. It is useful to plot the edge density predicted by these regression analyses versus $\bar{n}_e$ for various I_p. Figure 9.11 plots the fitted functions in this way for density at $r = 16.8$ cm during hydrogen, 8 tesla discharges. For a given plasma current, the density predicted by both scaling laws must match at some value of $\bar{n}_e$. The transition point between scaling laws is therefore independently determined with no explicit mention of the critical value of $\bar{n}_e/I_p$. These transition densities for various plasma currents are connected by a solid line in Fig. 9.11.

Figure 9.11 illustrates an interesting dependence of edge density on central $\bar{n}_e$ and I_p which was true for all radii. For a fixed plasma current, the edge density depended nonlinearly on the central density until a critical value of $\bar{n}_e$ (or edge density) was reached. A further increase in $\bar{n}_e$ did not directly result in an increase in edge density. This transition is coincident with the occurence of a MARFE in Alcator C and suggests that the MARFE itself is a consequence of this high $\bar{n}_e$, low I_p regime (chapter 11).

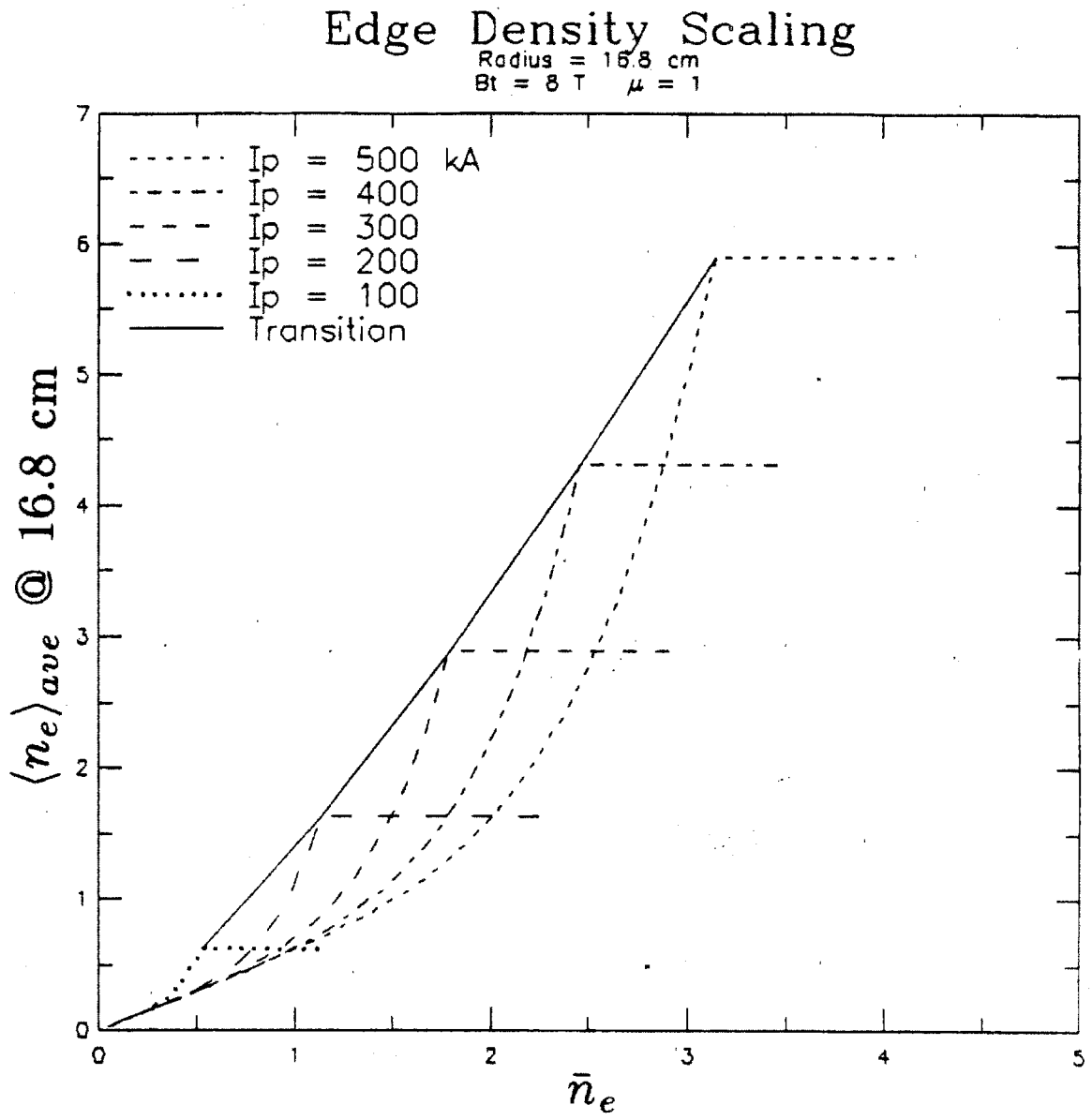

Figure 9.11 $\langle n_e \rangle_{ave}$@ **16.8 cm Predicted from Regression Analysis vs.** $\bar{n}_e$ **for Various** I_p

The density–current transition line can be examined further. Figure 9.12 plots the transition points identified in Fig. 9.11 versus I_p. It is not expected that they should fall along a straight line as shown, considering that they result from the matching of two highly nonlinear functions of $\bar{n}_e$ and I_p. Nevertheless, this line is almost precisely the MARFE threshold $\bar{n}_e$–I_p line presented in Ref. [5] and reproduced in Fig. 4.19. A similar result can be obtained using $r = 16.5$ and 17.2 cm data.

Figure 9.13 re-plots the MARFE threshold data from Ref. [5] along with a simple linear regression fit to the data points. This fit is seen to be markedly similar to a linear regression fit performed on the density scaling thresholds in Fig. 9.12. Thus, it is clearly established that the transition in the edge density scaling is a consequence of the edge plasma approaching a regime which is dominated by edge physics associated with MARFE phenonema.

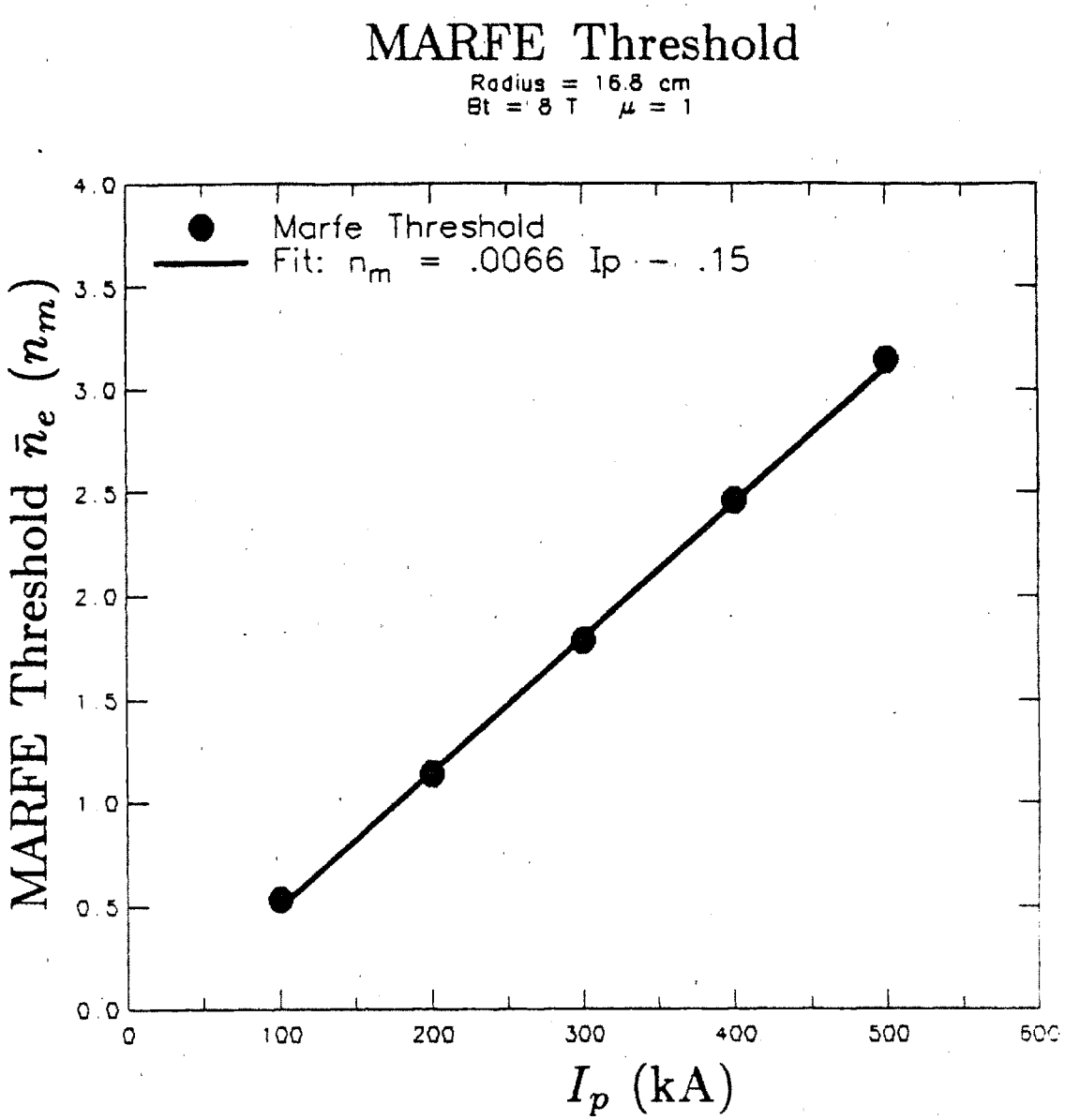

Figure 9.12 Transition Values of $\bar{n}_e$ & I_p for $\langle n_e \rangle_{ave}$@ **16.8 cm Scaling Law Predicted from Regression Analysis**

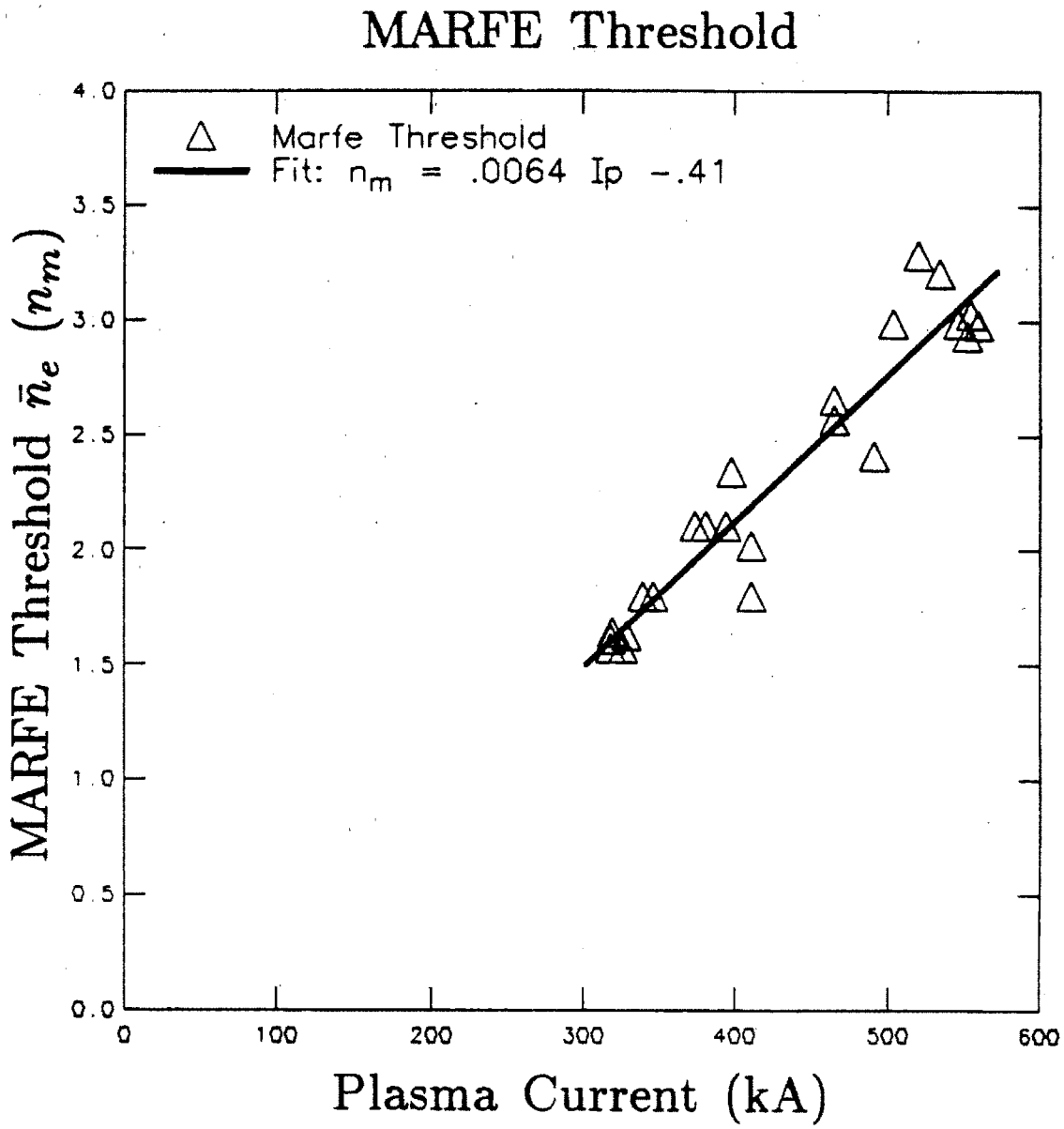

Figure 9.13 MARFE Threshold $\bar{n}_e$ and I_p Data (Ref. [5]) with Linear Fit

9.3.3 Density Scrape-off Length

The edge plasma density e-folding length averaged over poloidal angle is plotted versus $\bar{n}_e/I_p$ for hydrogen, 6 and 8 tesla discharges in Figs. 9.14*a* and 9.14*b* and for deuterium, 6 and 8 tesla discharges in Figs. 9.15*a* and 9.15*b*. The general trend is decreasing λ_n for increasing $\bar{n}_e/I_p$. Except for the hydrogen, 8 tesla data, there is no systematic difference between scrape-off lengths obtained in hydrogen versus deuterium, 6 versus 8 tesla discharges.

The scrape-off length obtained for the hydrogen, 8 tesla discharges is typically 20% lower than the three other cases. This data was taken last in this series of gas and field scans when the probe array began to show evidence of damage. Thus, there may be systematic errors introduced from unknown probe collection areas in this data which could account for the observed discrepancy in λ_n.

The dependence of λ_n on $\bar{n}_e/I_p$ can be connected with the edge density scaling laws developed in the previous sections. The poloidally averaged scrape-off length should be closely related to a scrape-off length calculated from the poloidally averaged edge densities. That is

$$\langle\lambda_n\rangle_{ave} \approx \bar{\lambda}_n = \frac{17.2 - 16.8}{ln(\langle n_e\rangle_{ave}@16.8/\langle n_e\rangle_{ave}@17.2)} \quad \text{(cm)} . \tag{9.11}$$

Using the regressions in tables 9.3 and 9.4 ($\delta = 0$, $\gamma = 0$),

$$\bar{\lambda}_n = \frac{0.4}{ln\left[\frac{0.57+6.6(\bar{n}_e/I_p)^{4.3}}{0.29+2.7(\bar{n}_e/I_p)^{5.5}}\right]} \quad \text{(cm)} \tag{9.12}$$

for $\bar{n}_e/I_p \lesssim 0.6$ and

$$\bar{\lambda}_n = \frac{0.4}{ln\left[\frac{0.52\ I_p^{1.5}}{0.17\ I_p^{1.3}}\right]} \approx 0.38 \text{ cm} \qquad (9.13)$$

for $\bar{n}_e/I_p \gtrsim 0.6$.

For small $\bar{n}_e/I_p$, Eq. 9.12 predicts that $\bar{\lambda}_n$ asymptotes to ≈ 0.6 cm. For large $\bar{n}_e/I_p$, Eq. 9.13 shows that $\bar{\lambda}_n$ should saturate at $\bar{\lambda}_n \approx 0.38$ cm. In between, $\bar{\lambda}_n$ depends predominantly on $\bar{n}_e/I_p$.

Figures 9.14 and 9.15 closely track this dependence on $\bar{n}_e/I_p$. The scrape-off length in Fig. 9.14*a* asymptotes to $\langle\lambda_n\rangle_{ave} \approx 0.65$ and $\langle\lambda_n\rangle_{ave} \approx 0.45$ for low and high values of $\bar{n}_e/I_p$ respectively.

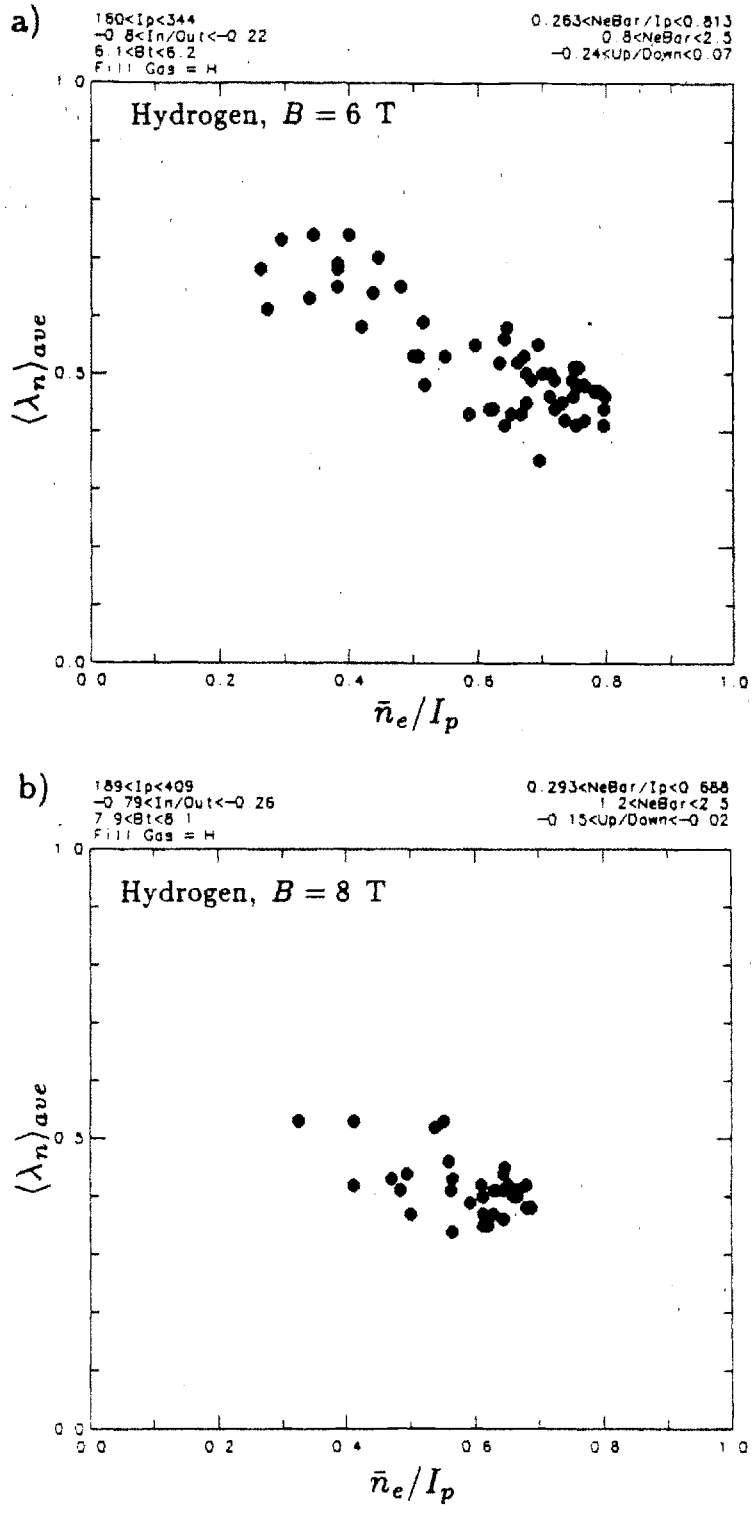

Figure 9.14 $\langle\lambda_n\rangle_{ave}$ **vs.** $\bar{n}_e/I_p$ **for Hydrogen Discharges in 6 and 8 tesla Toroidal Magnetic Fields**

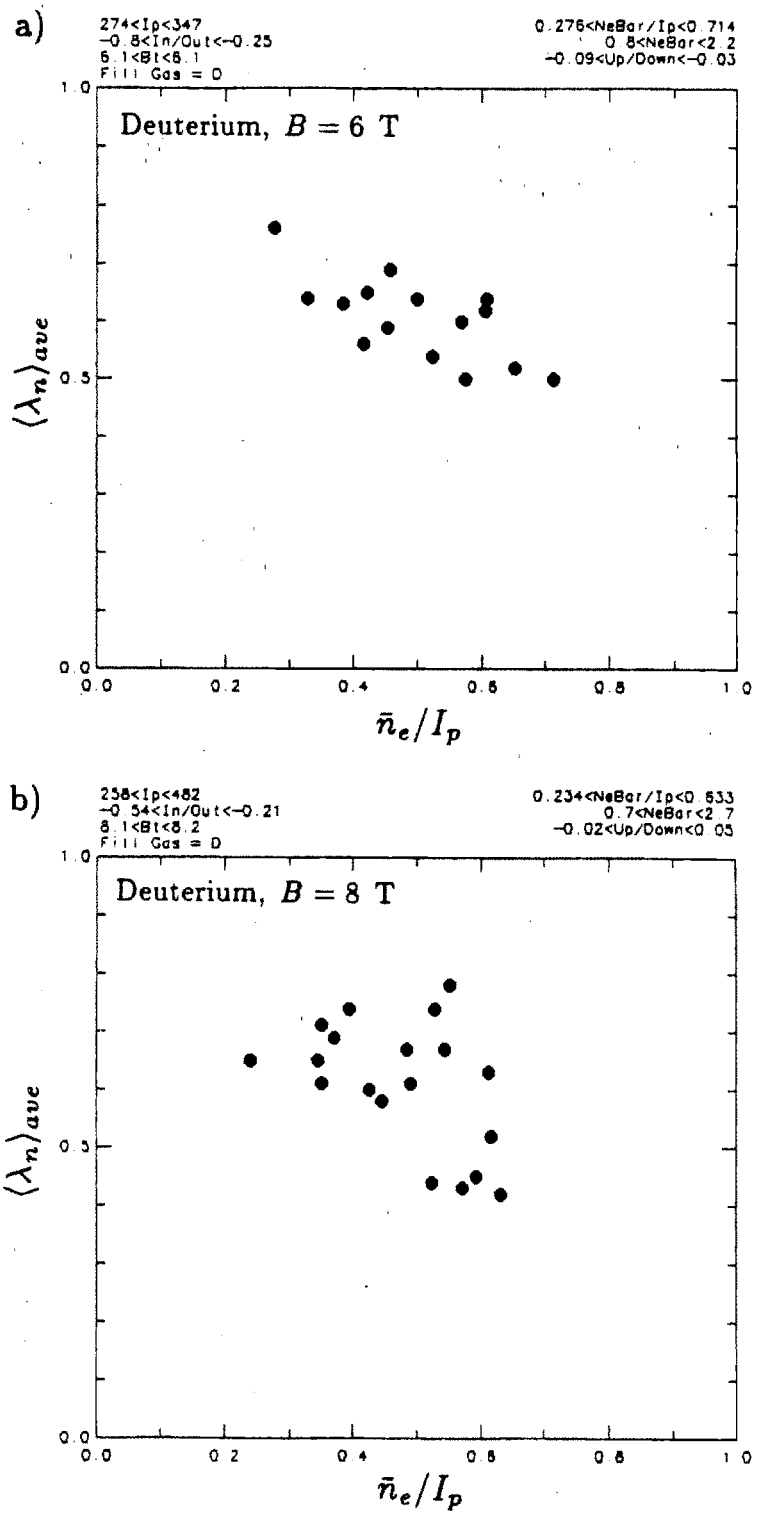

Figure 9.15 $\langle\lambda_n\rangle_{ave}$ **vs.** $\bar{n}_e/I_p$ **for Deuterium Discharges in 6 and 8 tesla Toroidal Magnetic Fields**

9.3.4 Edge Temperature

Electron temperature averaged over poloidal angle for DENSEPACK radii of $r = 16.8$, 17.2, and 17.6 cm is displayed versus $\bar{n}_e/I_p$ in Figs. 9.16 and 9.17. The general trends in temperature versus $\bar{n}_e/I_p$ persist for hydrogen, deuterium, 6 and 8 tesla discharges. The magnitudes are also similar in all cases except for the hydrogen, 8 tesla data which remains suspect.

An interesting result is that $\langle T_e \rangle_{ave}$ at $r = 16.8$ cm decreases while $\langle T_e \rangle_{ave}$ at $r = 17.2$ and 17.6 cm increases as $\bar{n}_e/I_p$ is increased. Furthermore, $\langle T_e \rangle_{ave}$ at $r = 17.2$ and 17.6 cm becomes indistinguishable at high values of $\bar{n}_e/I_p$. Thus, one can see that the average radial temperature gradient generally decreases as $\bar{n}_e/I_p$ increases.

Because of the large scatter in the data set, no regression analysis was performed on the $\langle T_e \rangle_{ave}$ data. In any case, the data is fairly well summarized versus $\bar{n}_e/I_p$ in Figs. 9.16 and 9.17. Note that the general trend of decreasing $\langle T_e \rangle_{ave}$ versus $\bar{n}_e/I_p$ at $r = 16.8$ cm is coincident with the edge plasma approaching a radiation-unstable, MARFE-prone regime.

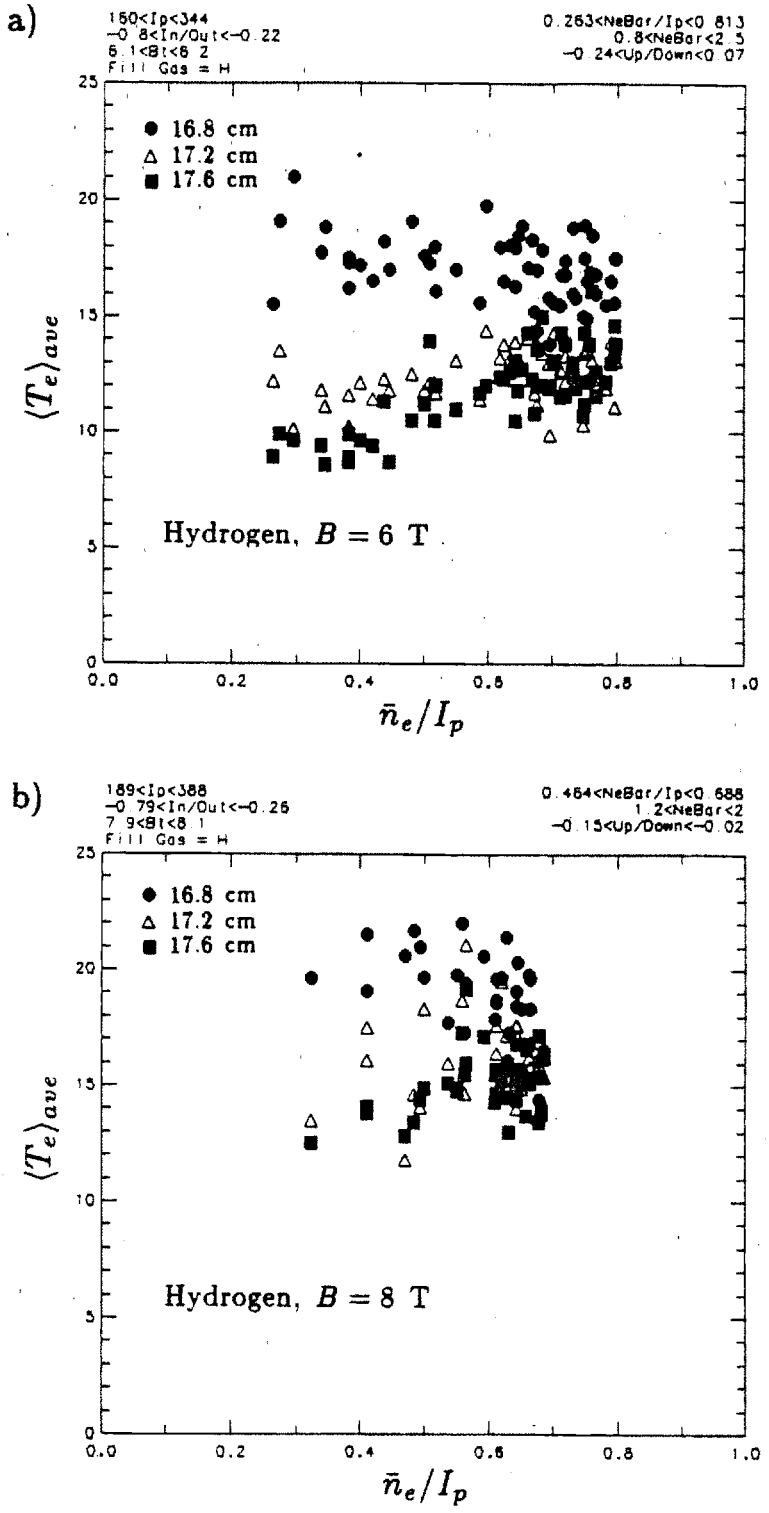

Figure 9.16 $\langle T_e \rangle_{ave}$ **vs.** $\bar{n}_e / I_p$ **for Hydrogen Discharges in 6 and 8 tesla Toroidal Magnetic Fields**

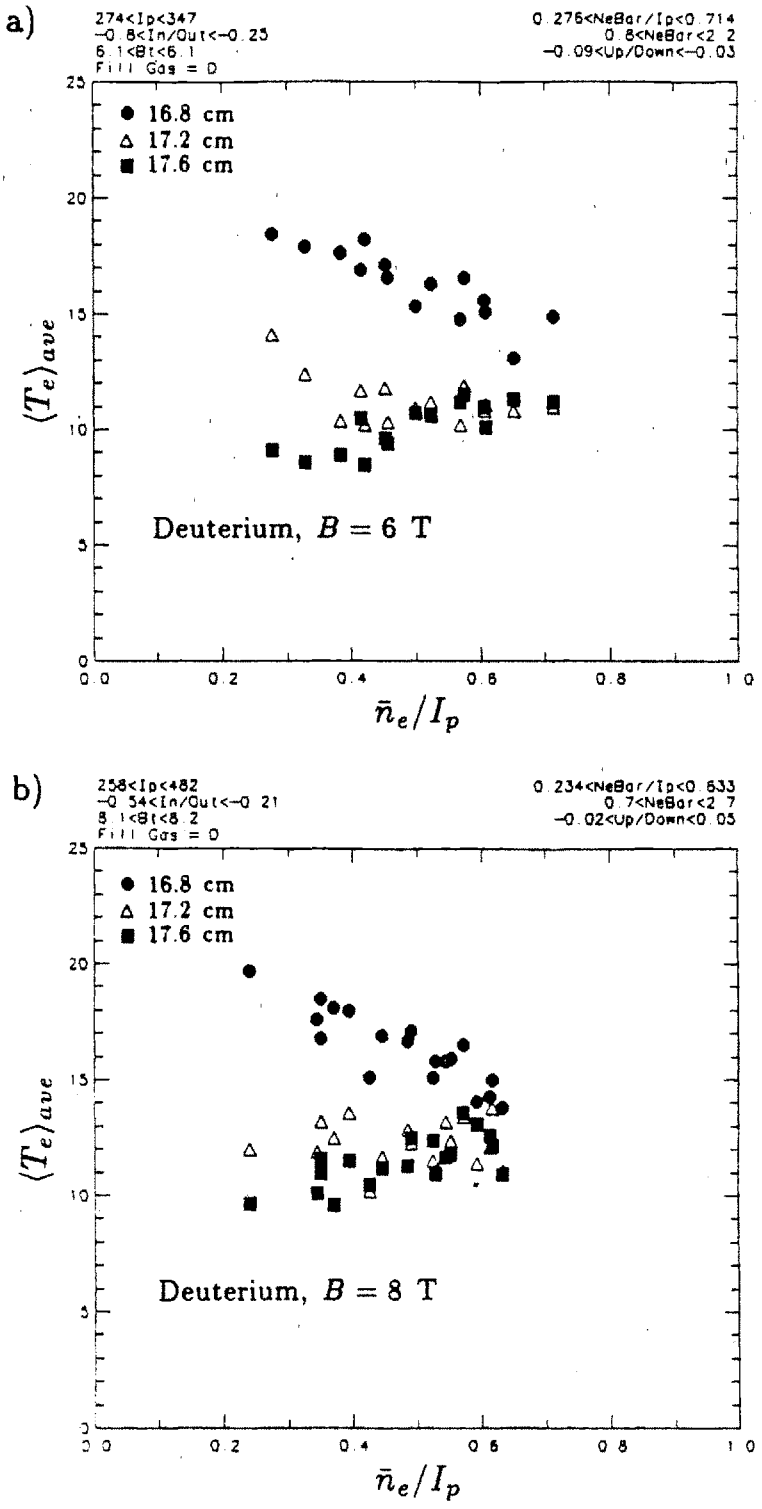

Figure 9.17 $\langle T_e \rangle_{ave}$ **vs.** $\bar{n}_e/I_p$ **for Deuterium Discharges in 6 and 8 tesla Toroidal Magnetic Fields**

9.3.5 Floating Potential

DENSEPACK probe floating potentials averaged over poloidal angle are displayed in Figs. 9.18 and 9.19 for the same set of discharges displayed in the previous sections. Although the scatter is large, there is a clear trend in $\langle V_f \rangle_{ave}$ versus $\bar{n}_e/I_p$ for all three radii. $\langle V_f \rangle_{ave}$ is found to decrease nearly linearly with $\bar{n}_e/I_p$. A linear least squares fit line is superimposed on the data for each radius to emphasize this point. Again the hydrogen, 8 tesla data shows a different character than the other three types of discharges and is questionable.

Another clear, reproducible trend evident in these data is the inversion of the average radial gradient in floating potential versus $\bar{n}_e/I_p$. For low values of $\bar{n}_e/I_p$, the poloidally averaged floating potential is generally higher at $r = 16.8$ cm than at $r = 17.2$ or 17.6 cm. As $\bar{n}_e/I_p$ is increased, the floating potential at all radii falls. However, the floating potential at $r = 16.8$ cm falls faster so that for $\bar{n}_e/I_p > 0.5$–0.6 the average floating potential at this radius is below the floating potential at the other two radii. It is interesting that the cross-over point occurs near the critical value of $\bar{n}_e/I_p$ identified for the Alcator C edge plasma, namely, $\bar{n}_e/I_p \approx 0.6$.

From Fig. 7.9 and the discussion in section 7.1.5, the probe floating potential relative to the limiter potential is

$$V_f \approx \delta\Phi_s + 3.5\ (T_e^{limiter} - T_e^{probe}) \qquad (9.14)$$

where $\delta\Phi_s$ is the change in plasma potential along a field line connecting the probe and limiter. $\delta\Phi_s$ can arise from $\underline{B} \times \nabla B$ particle drifts or non-ambipolar perpendicular particle transport. One would expect that the poloidally averaged floating potential at some radius should also follow Eq. 9.14,

$$\langle V_f \rangle_{ave} \approx \langle \delta\Phi_s \rangle_{ave} + 3.5\ (\langle T_e \rangle_{ave}^{limiter} - \langle T_e \rangle_{ave}^{probes}) \ . \qquad (9.15)$$

By up-down symmetry, $\underline{B} \times \nabla B$ contributions to $\langle \delta\Phi_s \rangle_{ave}$ average to zero. The only remaining contributor to $\langle \delta\Phi_s \rangle_{ave}$ is then non-ambipolar transport.

The decrease in floating potential with $\bar{n}_e/I_p$ can be reconciled with the electron temperature measurements and Eq. 9.15. If, for the moment, one assumes that $\langle \delta\Phi_s \rangle_{ave}$ is fixed at some value, independent of $\bar{n}_e/I_p$, then changes in $\langle V_f \rangle_{ave}$ and $\langle T_e \rangle_{ave}^{probes}$ with $\bar{n}_e/I_p$ imply something about changes in $\langle T_e \rangle_{ave}^{limiter}$. More specifically, in order for $\langle V_f \rangle_{ave}$ to decrease for increasing $\bar{n}_e/I_p$, the temperature difference, $\langle T_e \rangle_{ave}^{probes} - \langle T_e \rangle_{ave}^{limiter}$ must increase with increasing $\bar{n}_e/I_p$.

Because of the factor of ~ 3.5 in Eq. 9.15, the floating potential is sensitive to small changes in this temperature difference. A change in floating potential of 10 volts implies a temperature difference increase of ~ 3 eV. This means that a temperature depression along a field line to the limiter of ~ 0 eV for low $\bar{n}_e/I_p$ increasing to ~ 3 eV at high $\bar{n}_e/I_p$ could completely explain the observed floating potential variation versus $\bar{n}_e/I_p$ for $r = 16.8$ cm. Smaller parallel gradients in T_e could explain the floating potential at other radii.

Sizing typical power fluxes in the edge plasma, one can make a connection between increasing parallel gradients in T_e with increasing values of $\bar{n}_e/I_p$. By matching heat conducted to the limiter along field lines to heat transmitted through the sheath, a relationship between edge density and temperature and the temperature gradient along a field line can be obtained. Stangeby uses this approach to estimate values of n and T that indicate when parallel gradients become important in the edge power balance. This condition is stated as[108]

$$\frac{L_{(\mathrm{cm})}\ n_{(\mathrm{cm}^{-3})}}{T_{e\,(\mathrm{eV})}^2} \gtrsim 8 \times 10^{12} \tag{9.16}$$

which becomes satisfied at $r = 16.8$ cm for typical Alcator C edge values, $\langle n_e \rangle_{ave} \approx 2.5 \times 10^{13}/\mathrm{cm}^3$, $\langle T_e \rangle_{ave} \approx 18$ eV, $L \approx 100$ cm.

Higher $\bar{n}_e/I_p$ results in higher edge densities (in non-MARFE regime) and allows Eq. 9.16 to be more easily satisfied. Consequently, a steeper temperature drop along field lines to the limiter is expected. This is consistent with the observation of a lowering floating potential and the relationship between parallel T_e gradients and V_f suggested by Eq. 9.15.

The appearance of parallel temperature gradients is also important for the development of a localized radiation thermal instability or MARFE. If the parallel heat conduction in the edge is very good, any parallel temperature perturbation will be quenched and will not result in a radiation unstable plasma. This condition was stated more quantitatively earlier in section 2.5.3. Thus, in order to observe a MARFE, one must be able to sustain a perturbed parallel temperature profile. The observation of decreasing $\langle V_f \rangle_{ave}$ as the MARFE regime in Alcator C is approached suggests through Eq. 9.16 that parallel temperature gradients are indeed becoming larger and perhaps more easily perturbed as $\bar{n}_e/I_p$ increases.

For completeness, one should also consider the $\bar{n}_e/I_p$ dependence of the $\langle \delta\Phi_s \rangle_{ave}$ term in Eq. 9.15. However, non-ambipolar transport is very difficult to quantify or to scale with edge densities and temperatures. Perhaps the parallel electron temperature variations dominate Eq. 9.15 and lead to the observed floating potential scaling indicated above, but this alone is no rigorous basis for concluding that changes in ambipolar transport does not occur with changing edge densities and temperatures. However, further investigation of non-ambipolar effects is beyond the scope of this present work.

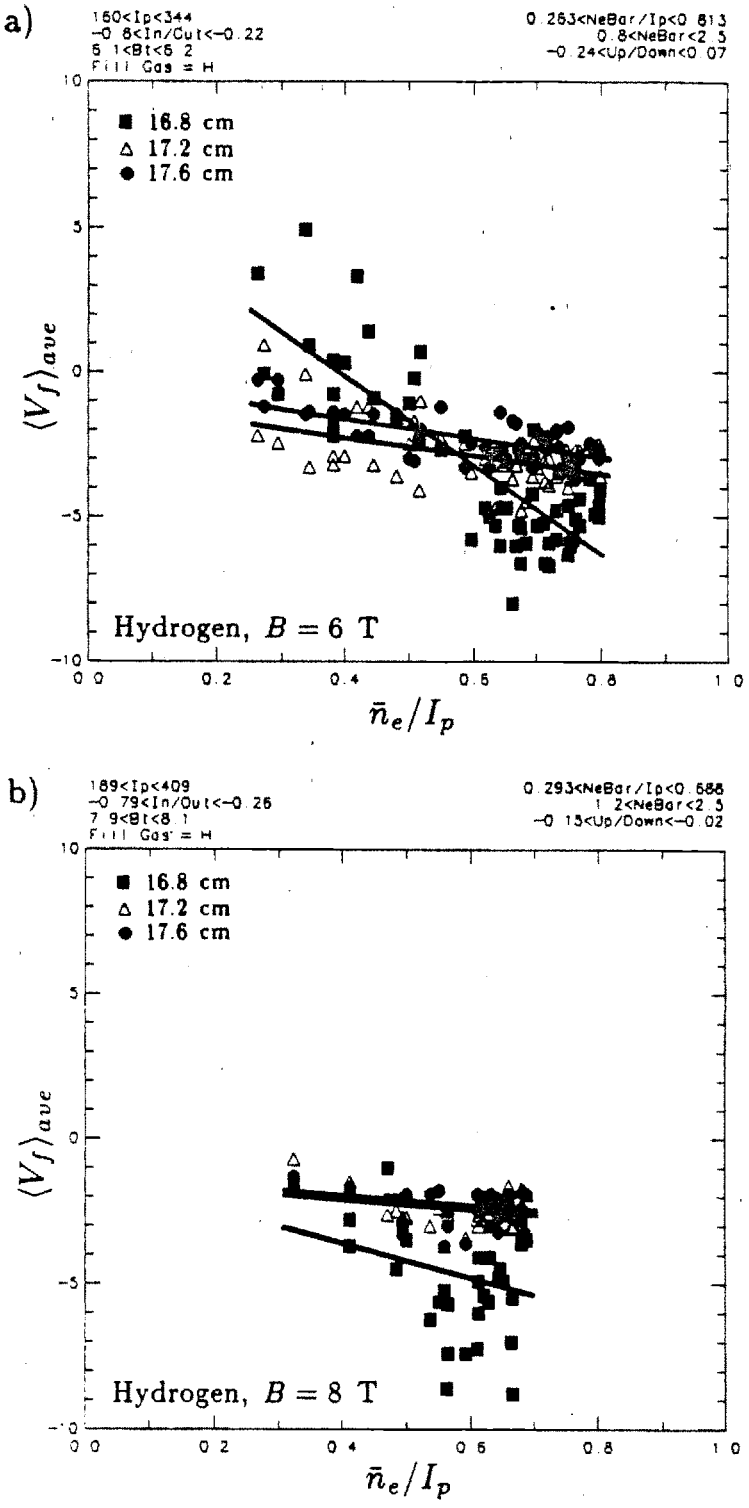

Figure 9.18 $\langle V_f \rangle_{ave}$ **vs.** $\bar{n}_e/I_p$ **for Hydrogen Discharges in 6 and 8 tesla Toroidal Magnetic Fields**

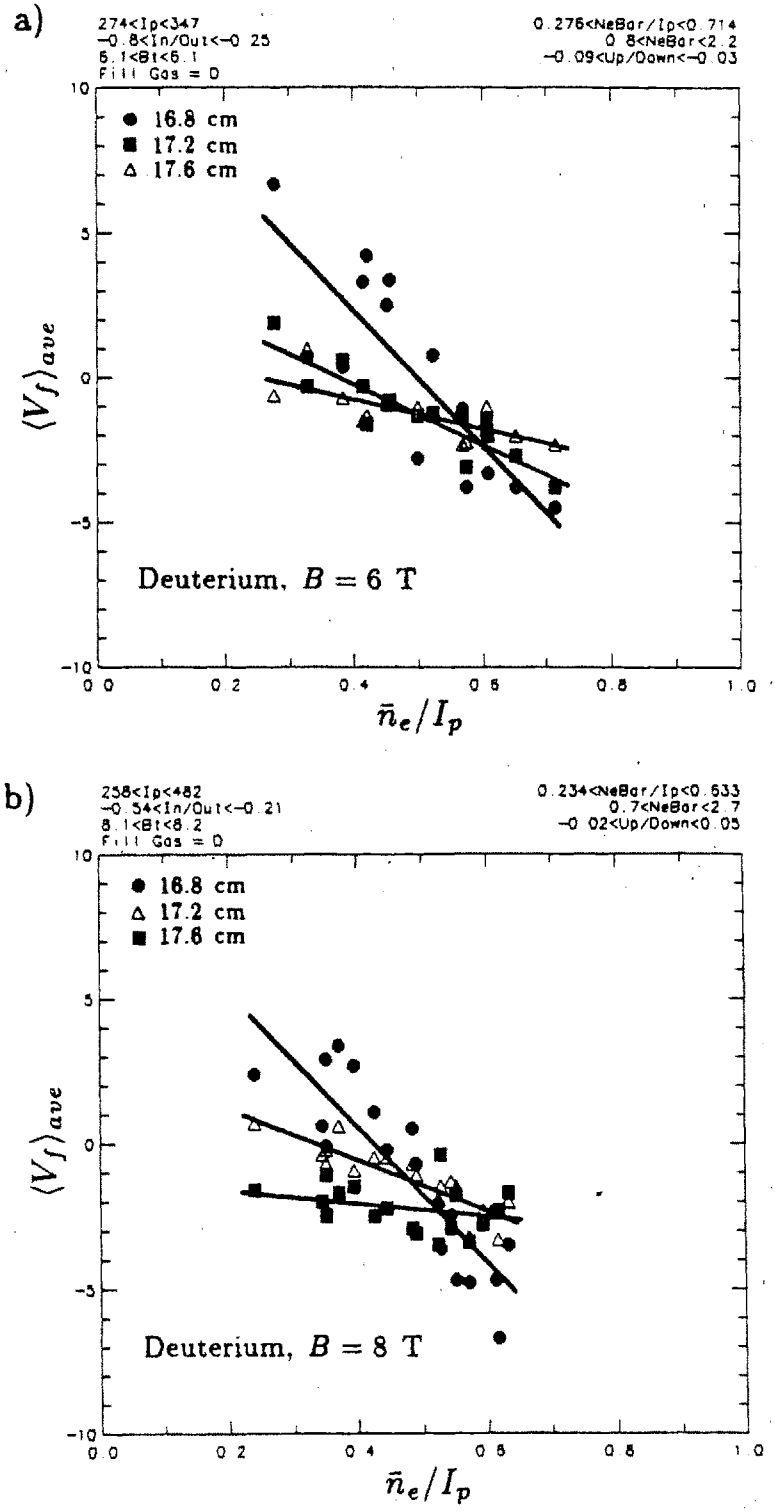

Figure 9.19 $\langle V_f \rangle_{ave}$ **vs.** $\bar{n}_e / I_p$ **for Deuterium Discharges in 6 and 8 tesla Toroidal Magnetic Fields**

9.3.6 Fluctuations

Figures 9.20 and 9.21 display the normalized fluctuation amplitude in the ion saturation current averaged over poloidal angle, $\langle \tilde{J}/\bar{J} \rangle_{ave}$, versus $\bar{n}_e/I_p$ for the three DENSEPACK radii. Unlike other edge quantities reported in the previous sections, magnitudes of $\langle \tilde{J}/\bar{J} \rangle_{ave}$ are found to depend slightly on the gas species. At $\bar{n}_e/I_p \approx 0.4$, hydrogen, 6 tesla data show $\langle \tilde{J}/\bar{J} \rangle_{ave}$@17.2 ≈ 0.30 whereas deuterium, 6 tesla data is higher at $\langle \tilde{J}/\bar{J} \rangle_{ave}$@17.2 ≈ 0.35. The magnetic field does not appear to change the magnitude of $\langle \tilde{J}/\bar{J} \rangle_{ave}$ as evidenced by Fig. 9.21. Recall that the hydrogen, 8 tesla data should be treated with caution.

All these fluctuation data were obtained from the 10 kHz digitizers. To obtain the full bandwidth fluctuation amplitude, one should multiply these values by a factor ≈ 1.2 (see section 7.3.2).

The overall dependence of $\langle \tilde{J}/\bar{J} \rangle_{ave}$ on $\bar{n}_e/I_p$ is clear for the hydrogen data in Fig. 9.20. The fluctuation amplitude for this data generally decreases with increasing $\bar{n}_e/I_p$. On the other hand, the deuterium data shows only a slight hint of decrease for increasing $\bar{n}_e/I_p$.

The relative level of $\langle \tilde{J}/\bar{J} \rangle_{ave}$ between the three radii remains constant independent of gas, field, or $\bar{n}_e/I_p$. Typically, fluctuations at $r = 17.2$ cm are 22–26% higher than at $r = 16.8$ cm. Fluctuations at $r = 17.6$ cm are higher still at roughly 34-38% above the level at $r = 16.8$ cm.

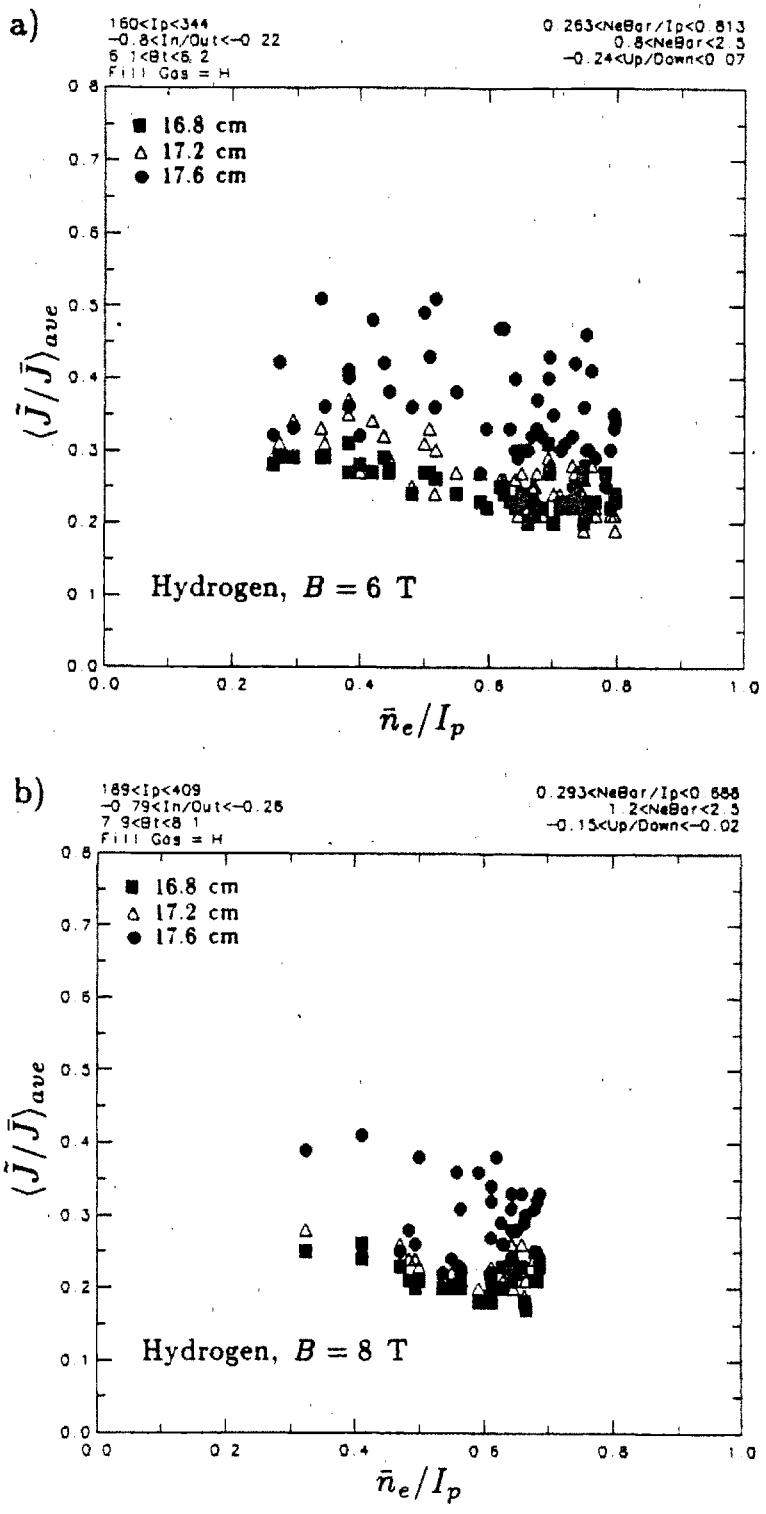

Figure 9.20 $\langle \tilde{J}/\bar{J} \rangle_{ave}$ **vs.** $\bar{n}_e/I_p$ **for Hydrogen Discharges in 6 and 8 tesla Toroidal Magnetic Fields**

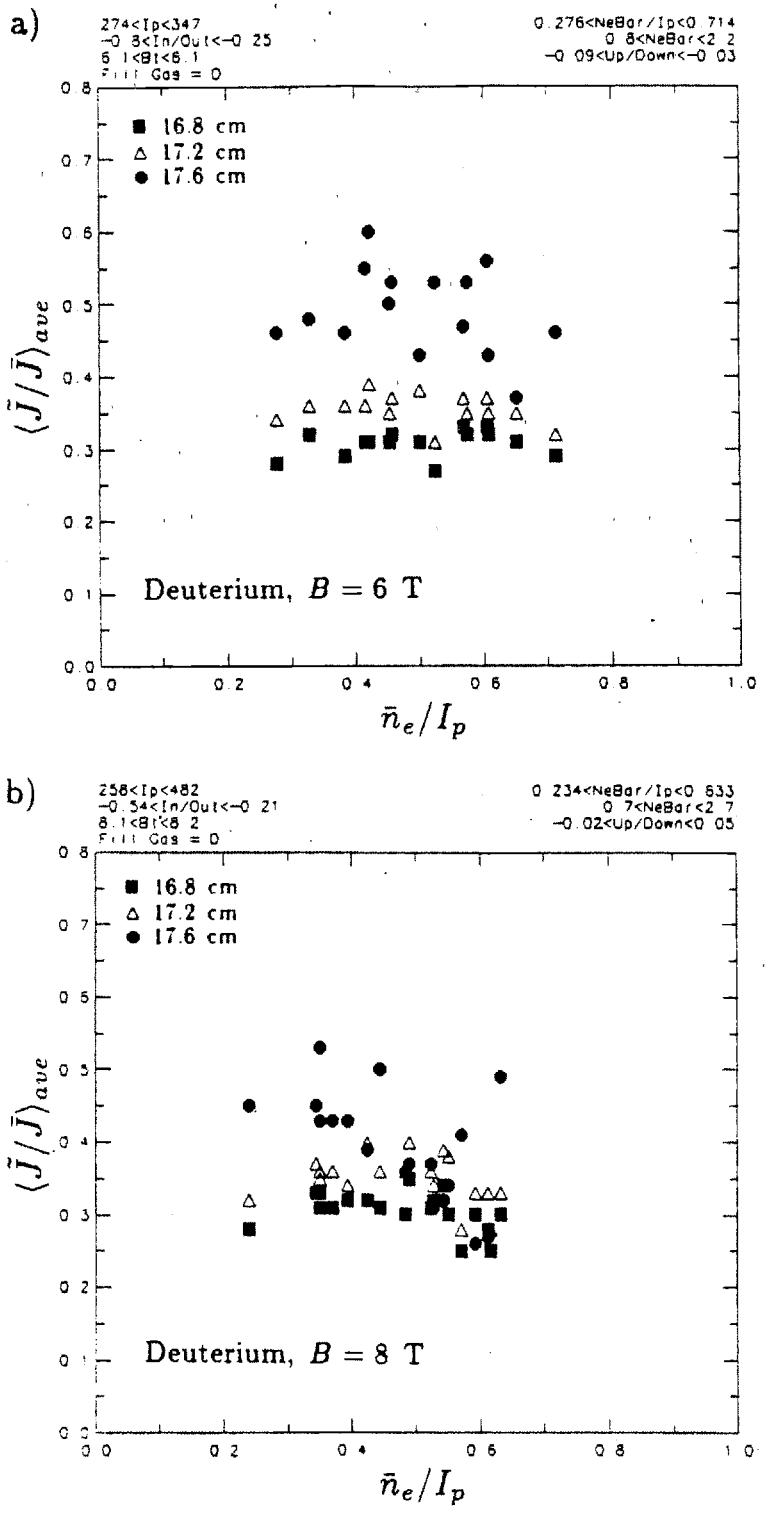

Figure 9.21 $\langle \tilde{J}/\bar{J} \rangle_{ave}$ **vs.** $\bar{n}_e/I_p$ **for Deuterium Discharges in 6 and 8 tesla Toroidal Magnetic Fields**

9.3.7 Perpendicular Diffusion

The perpendicular diffusion coefficient can be estimated using Eq. 9.2 and the measurements of λ_n and T_e reported in the previous sections. The best data recorded by DENSEPACK was obtained early in its operation during hydrogen, 6 tesla discharges. Figure 9.22 plots $D_\perp$ inferred from this data versus $\bar{n}_e/I_p$. The trend of $D_\perp$ falling with $\bar{n}_e/I_p$ is due to λ_n becoming small at high $\bar{n}_e/I_p$.

For reference, the level of Bohm diffusion, D_B, (Eq. 2.6) is also shown. Note that this value is quite low compared to the average diffusion coefficient computed from Eq. 9.2.

One possible explanation for this high estimated value of $D_\perp$ relative to D_B is the approximations implicit in Eq. 9.2. First, a value of $T_i \approx 2 \times T_e$ was assumed in computing the sound speed. However, this could only account for up to a factor of $\sqrt{3}$ overestimate in $D_\perp$ compared to D_B which is evaluated using the electron temperature alone.

Second, the model itself used in deriving Eq. 9.2 comes into question. As indicated in section 3.1.1, L can be replaced by $L_{eff} \approx 1.6\text{–}2 \times L$ when parallel flows are more carefully modelled. This can result in a additional factor of $\sim 1/2$ in the right hand side of Eq. 9.2. Yet, this alone is not enough to account for the high value of $D_\perp$ relative to D_B. In addition, Section 3.1.2 showed that the above formulation for $D_\perp$ is valid only if the neutral density satisfies Eq. 3.12. However, this condition is expected to be satisfied in Alcator C edge plasma. One can further argue that the scaling of λ_n versus $\bar{n}_e/I_p$ shown in Fig. 9.14*a* is inconsistent with the idea that high neutral densities are present which invalidate Eq. 9.2.

Consider λ_n given by Eq. 3.9 which includes neutral ionization. At low central plasma densities, one expects that the edge neutral density will also be low. At high central plasma densities, particularly in the MARFE regime, one expects the edge neutral density to be high. Equation 3.9 predicts that λ_n should

increase as the neutral density increases. However, the observation is that λ_n decreases for increasing central densities. Thus, neutrals appear to play no direct role in defining the value of λ_n and can be ignored. Equations 3.10 and 9.2 are therefore valid approximations in this respect.

It is interesting that both $D_\perp$ and $\langle \tilde{J}/\bar{J} \rangle_{ave}$ tend to fall with increasing $\bar{n}_e/I_p$. Perhaps this is an indication that fluctuations are directly responsible for the average value of $D_\perp$ and λ_n found in the edge.

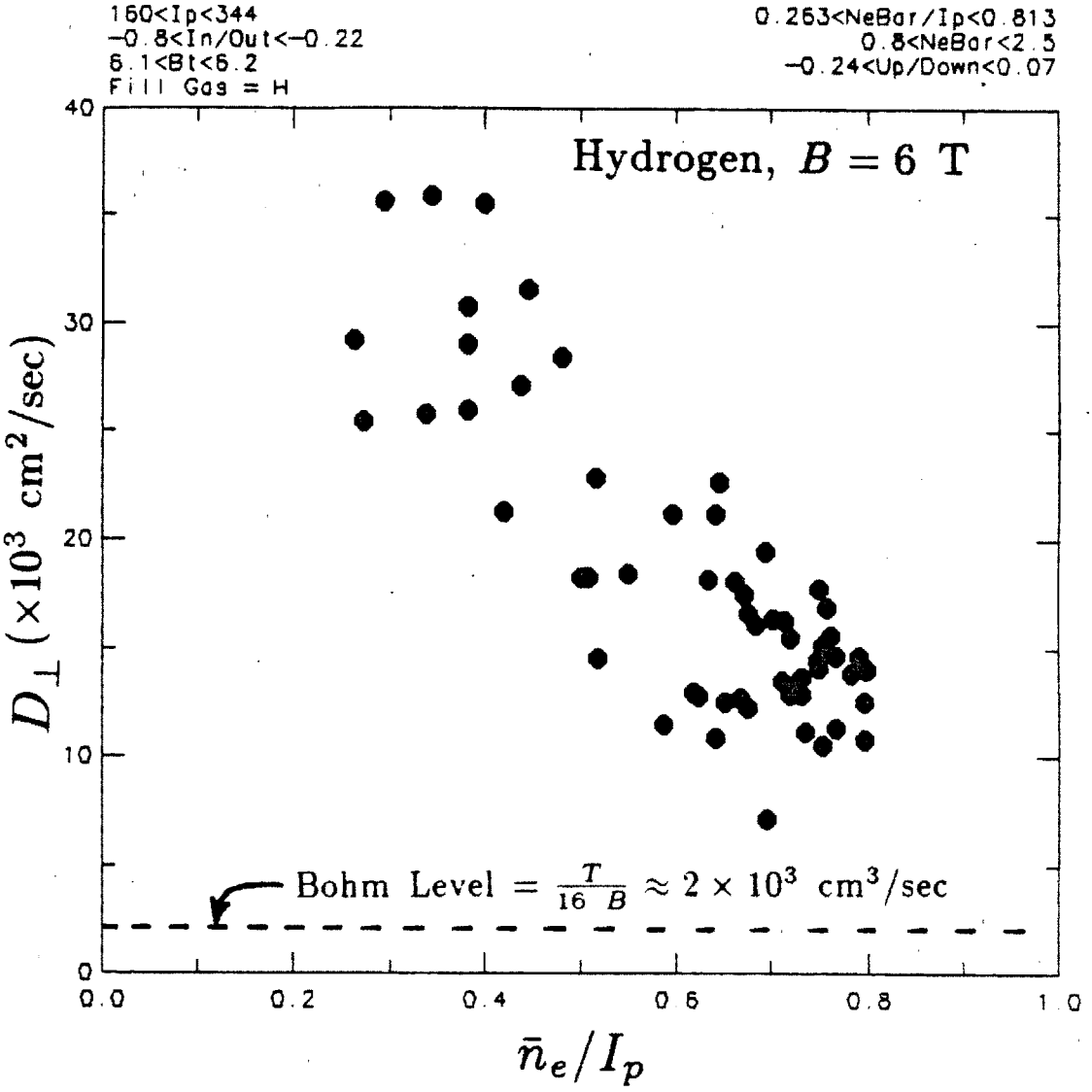

Figure 9.22 Estimated $D_\perp$ vs. $\bar{n}_e/I_p$ for Hydrogen Discharges in 6 tesla Toroidal Magnetic Field

9.3.8 Global Particle Confinement Time

The final parameter to be reported in this section on edge versus central parameter scalings is the global particle confinement time, τ_p. Figures 9.23 and 9.24 display τ_p versus $\bar{n}_e/I_p$ computed from Eq. 9.3 for the same four data sets shown in earlier sections. As discussed previously, the hydrogen, 8 tesla data should be treated as unreliable. Nevertheless, τ_p inferred from this data is displayed in Fig. 9.23*b*. Typical T_p values obtained in this manner are in the range 0.5–2 msec.

The general trend is a reduction in τ_p for increasing $\bar{n}_e/I_p$. τ_p reduces by a factor of $\sim 1/2$ as $\bar{n}_e/I_p$ scans from ~ 0.4 to ~ 0.7. Also, the deuterium data shows roughly a uniform factor of $\sim \sqrt{2}$ higher particle confinement times than the hydrogen data. Both these observations can be traced back to the input parameters in Eq. 9.3.

It was shown earlier that density, temperature, and scrape-off length are very similar for hydrogen and deuterium discharges in both 6 and 8 tesla fields. Thus, the $\sim \sqrt{2}$ larger values for τ_p in deuterium over hydrogen come from the C_s term in Eq. 9.3. It is difficult to assess whether this $\sqrt{2}$ increase in τ_p for deuterium is real or just a consequence of the model used to derive τ_p . A further uncertainty in the absolute magnitude of τ_p arises from the model used to derive Eq. 9.3. Setting $L \rightarrow L_{eff} \approx 1.6\text{–}2 \times L$ as suggested in section 3.1.1 leads to an increase in the inferred τ_p of up to a factor of ~ 2. Nevertheless, the scaling of τ_p with $\bar{n}_e/I_p$ is not sensitive to these type of assumptions in Eq. 9.3.

The reduction in τ_p as $\bar{n}_e/I_p$ increases can be understood from the scaling of edge parameters presented in earlier subsections. τ_p, as calculated by Eq. 9.3, depends most strongly on the ratio of the central line-averaged density to the edge density.

Using the fitted functions for edge density presented in section 9.3.1, the dependence of τ_p on $\bar{n}_e$ and I_p can be examined more closely. From Eqs. 9.3, 9.9–9.13, and tables 9.3 and 9.4,

$$\tau_p \approx A \frac{ln\left[\frac{0.57+6.6(\bar{n}_e/I_p)^{3.8}}{0.29+2.7(\bar{n}_e/I_p)^{5.5}}\right]}{0.99+25(\bar{n}_e/I_p)^{4.3}} \tag{9.17}$$

for $\bar{n}_e/I_p \lesssim 0.6$ and

$$\tau_p \approx B \frac{\bar{n}_e}{I_p^{1.3}} \tag{9.18}$$

for $\bar{n}_e/I_p \gtrsim 0.6$, where A and B are weak functions of $\bar{n}_e/I_p$. Thus, as $\bar{n}_e/I_p$ is increased, τ_p falls quickly according to Eq. 9.17 until the transition, $\bar{n}_e/I_p \approx 0.6$, is reached. After this point, τ_p begins to rise gradually with $\bar{n}_e/I_p$ according to Eq. 9.18. This behavior is evident in Figs. 9.23 and 9.24. The drop in τ_p as the MARFE threshold is approached indicates that the MARFE state is characterized by a high edge plasma recycling (low τ_p).

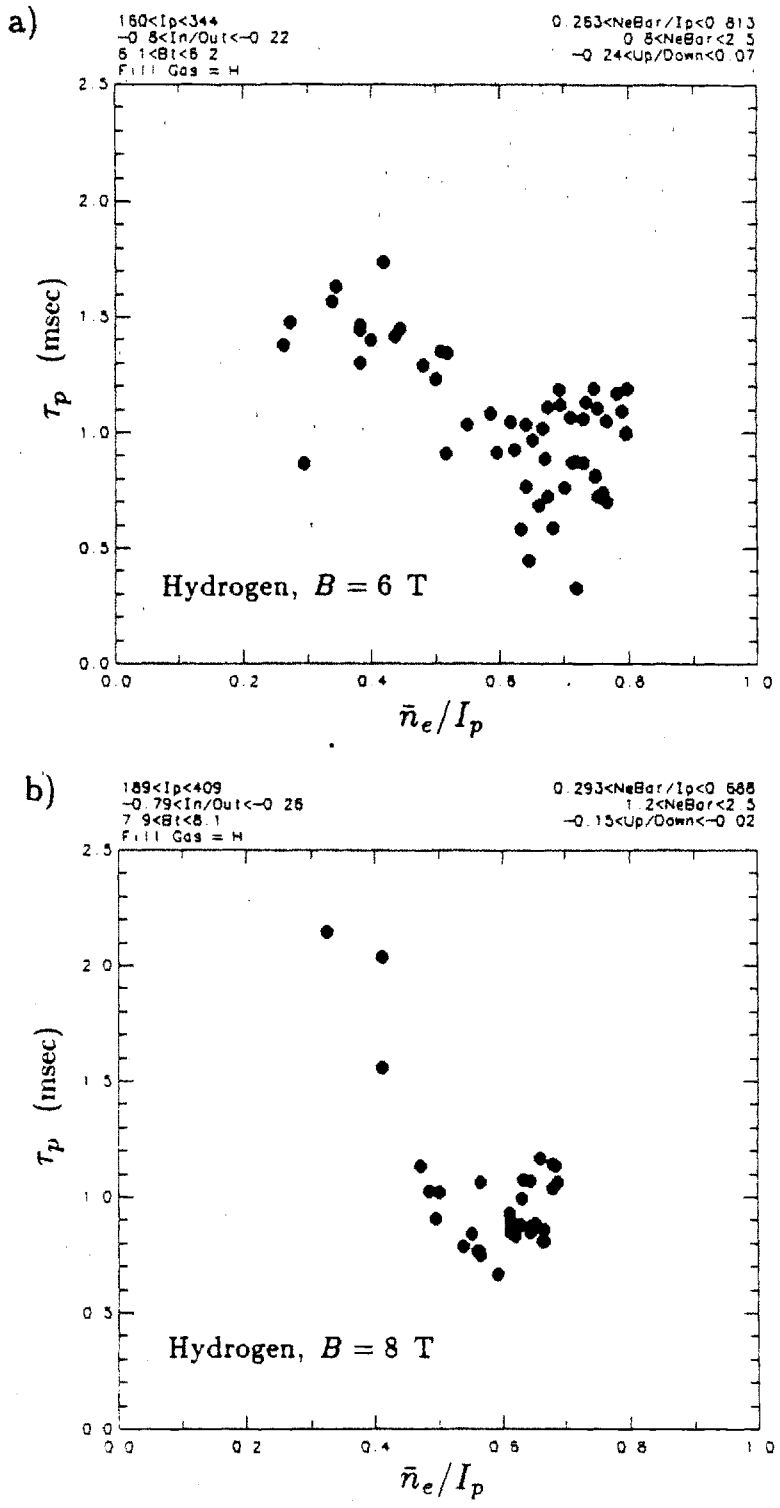

Figure 9.23 Estimated Global τ_p vs. $\bar{n}_e/I_p$ for Hydrogen Discharges in 6 and 8 tesla Toroidal Magnetic Fields

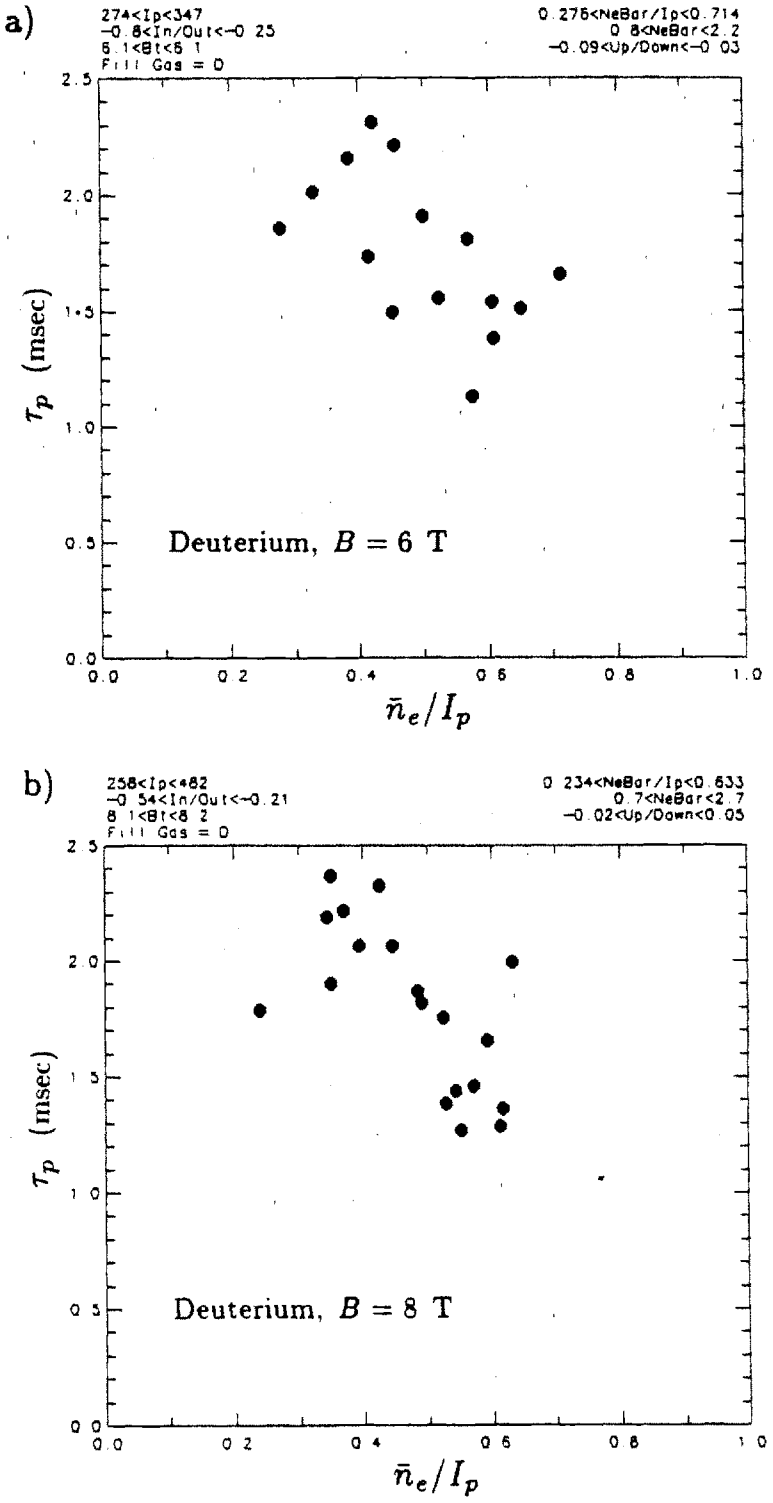

Figure 9.24 Estimated Global τ_p vs. $\bar{n}_e/I_p$ for Deuterium Discharges in 6 and 8 tesla Toroidal Magnetic Fields

9.4 Poloidal Asymmetries vs. $\bar{n}_e/I_p$, B, and Gas

This section focuses on poloidal asymmetries in edge parameters measured by DENSEPACK and their scaling with central plasma parameters. Poloidal maxima and minima in density, scrape-off length, and temperature normalized to the poloidal average are displayed versus $\bar{n}_e/I_p$. This normalization removes the overall edge plasma scaling covered in the previous section and leads to a simpler presentation of the relative asymmetry. For floating potential data, the poloidal maximum minus the minimum for a given radius is plotted. Poloidal locations of maxima and minima for all these edge parameters are also plotted versus $\bar{n}_e/I_p$. Since no systematic dependence is found on gas or magnetic field, hydrogen discharges at 6 tesla and deuterium discharges at 6 and 8 tesla are combined in each plot.

Measurements of poloidal maxima or minima for a given radius involve only one Langmuir probe. Consequently, these data show more scatter than the poloidally averaged data presented earlier. In addition, the measurements of density and temperature minima were found to be slightly dependent on the in-out plasma position. This is because these minima typically occur on the midplane (chapter 7). To account for the position dependence, the data was modeled as,

$$Y^i_{meas} \approx Y^i_0 \left(1 + a\ \mathrm{InOut} + b\ \mathrm{InOut}^2\right) \quad (i = 1, 2, \ldots n)\ , \tag{9.19}$$

where a and b are fitted coefficients. The position corrected data values, Y^i_0, are displayed in this section. Eq. 9.19 results in at most a 20% correction.

9.4.1 Density Asymmetry versus $\bar{n}_e/I_p$

Figures 9.25–9.27 plot normalized poloidal maxima and minima in density versus $\bar{n}_e/I_p$ for two DENSEPACK radii, $r = 16.8$ and 17.2 cm, and for density extrapolated to the limiter radius, $r = 16.5$ cm. The maximum to average density ratio, $n_e^{max}/\langle n_e \rangle_{ave}$, is relatively insensitive to $\bar{n}_e/I_p$ with only the $r = 16.8$ cm data showing a slight increase with $\bar{n}_e/I_p$. Typical values are $n_e^{max}/\langle n_e \rangle_{ave} \approx$ 1.5–2.5 for all three radii. The minimum to average density ratio, $n_e^{min}/\langle n_e \rangle_{ave}$, shows more of a dependence with $\bar{n}_e/I_p$, generally lowering at high $\bar{n}_e/I_p$, except for the $r = 17.2$ cm data which remains fixed to a very low value, ≈ 0.05–0.15. Thus, the strong poloidal asymmetry in density outlined in chapter 7 persists for all values of $\bar{n}_e/I_p$. There is only a slight increase in this normalized asymmetry at high values of $\bar{n}_e/I_p$. Note that discharges in the MARFE ($\bar{n}_e/I_p \lesssim 0.6$) and non-MARFE regimes ($\bar{n}_e/I_p \gtrsim 0.6$) show no obvious difference in the normalized density asymmetry.

Poloidal locations of density maxima and minima for $r = 16.8$ and 16.5 cm are indicated in Figs. 9.28*a* and 9.28*b*. The solid points on these plots represent positions of high density while the open points designate low density. As shown in chapter 7, the density minima on the inside (180^0) and outside (0^0,360^0) locations are similar in magnitude for $r \approx 16.8$ cm. However, due to the short scrape-off length on the inside, minima there are always the lowest for $r \gtrsim 17.2$ cm. Note that the angular positions of all these extrema remain the same for any value of $\bar{n}_e/I_p$. Again, data points in the MARFE versus non-MARFE regime do not indicate any shift in the overall density asymmetry.

The density asymmetry data combined with the scalings presented in the previous sections indicate that poloidal variations in density at a given radius follow a relationship,

$$n_e(\theta) \approx \langle n_e \rangle_{ave} \, f(\theta) \, , \tag{9.20}$$

where $f(\theta)$ is a function of poloidal angle that looks like the profiles in Fig. 7.2. For the density at $r = 16.8$ cm, $f(\theta)$ has the properties

$$f(\theta)\big|_{max} \approx 2.0 \; ; \tag{9.21}$$

$$f(\theta)\big|_{min} \approx 0.5 \; . \tag{9.22}$$

The absolute density asymmetry at $r = 16.8$ cm therefore scales as

$$n_e^{max} - n_e^{min} \approx 1.5 \; \langle n_e \rangle_{ave} \; . \tag{9.23}$$

Using the fitted functions in tables 9.3 and 9.4, one obtains

$$n_e^{max} - n_e^{min} \approx 1.5 \; \bar{n}_e \; (.6 \; + \; .24 \; (\bar{n}_e/I_p)^{4.0} \; B^{1.7} \; \mu^{-.56}) \quad (\times 10^{13}/\mathrm{cm}^3) \tag{9.24}$$

for $\bar{n}_e/I_p \lesssim 0.6$, and

$$n_e^{max} - n_e^{min} \approx 1.5 \; (.62 \; I_p^{1.4} \; \mu^{-.44}) \quad (\times 10^{13}/\mathrm{cm}^3) \tag{9.25}$$

for $\bar{n}_e/I_p \gtrsim 0.6$. These scalings indicate that although the normalized density asymmetry is relatively constant over the range of $\bar{n}_e/I_p$, the absolute density asymmetry is a strong function of $\bar{n}_e/I_p$.

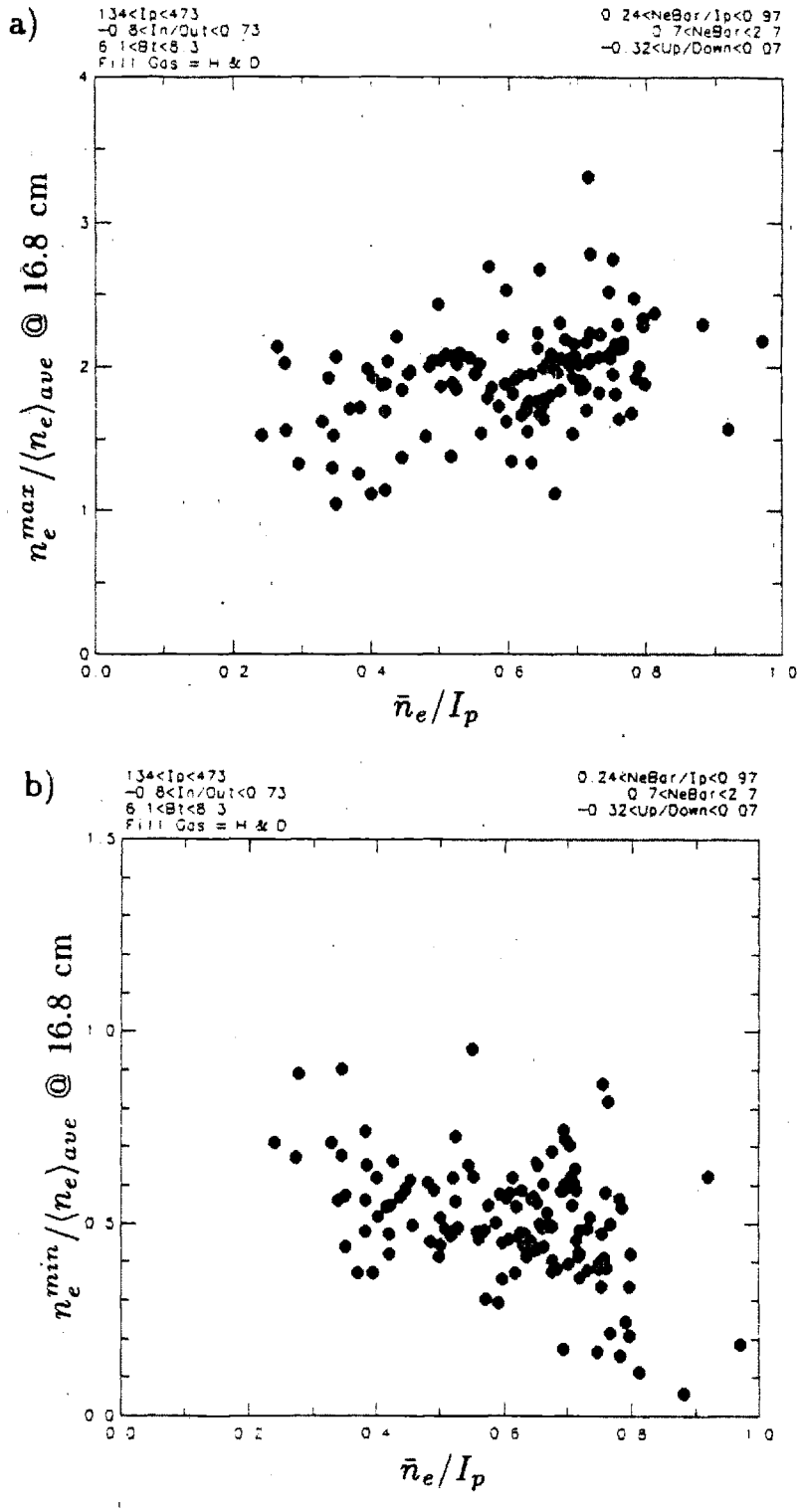

Figure 9.25 Density Asymmetry Relative to Poloidally Averaged Density at $r = 16.8$ cm vs. $\bar{n}_e/I_p$

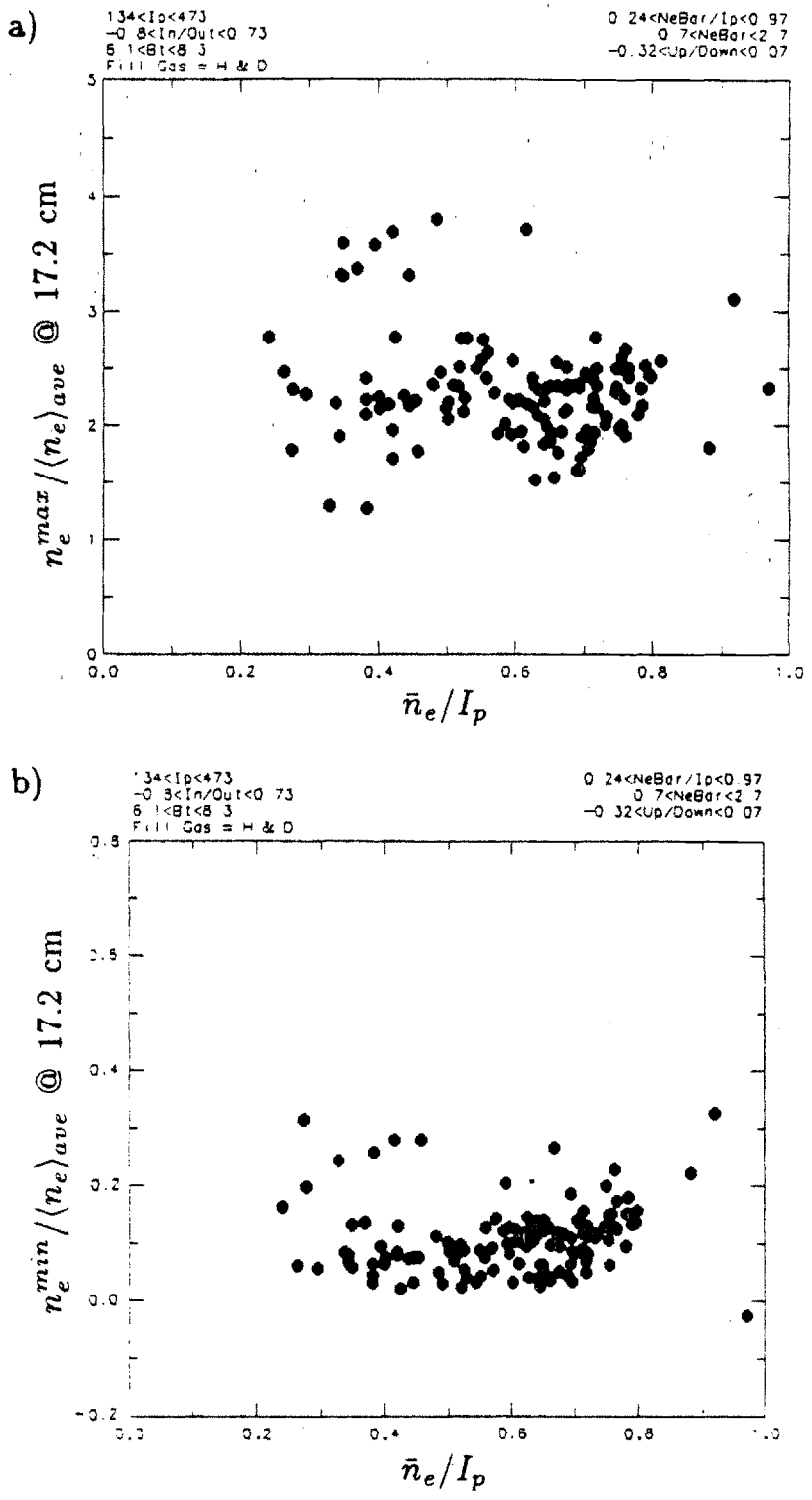

Figure 9.26 Density Asymmetry Relative to Poloidally Averaged Density at $r = 17.2$ cm vs. $\bar{n}_e/I_p$

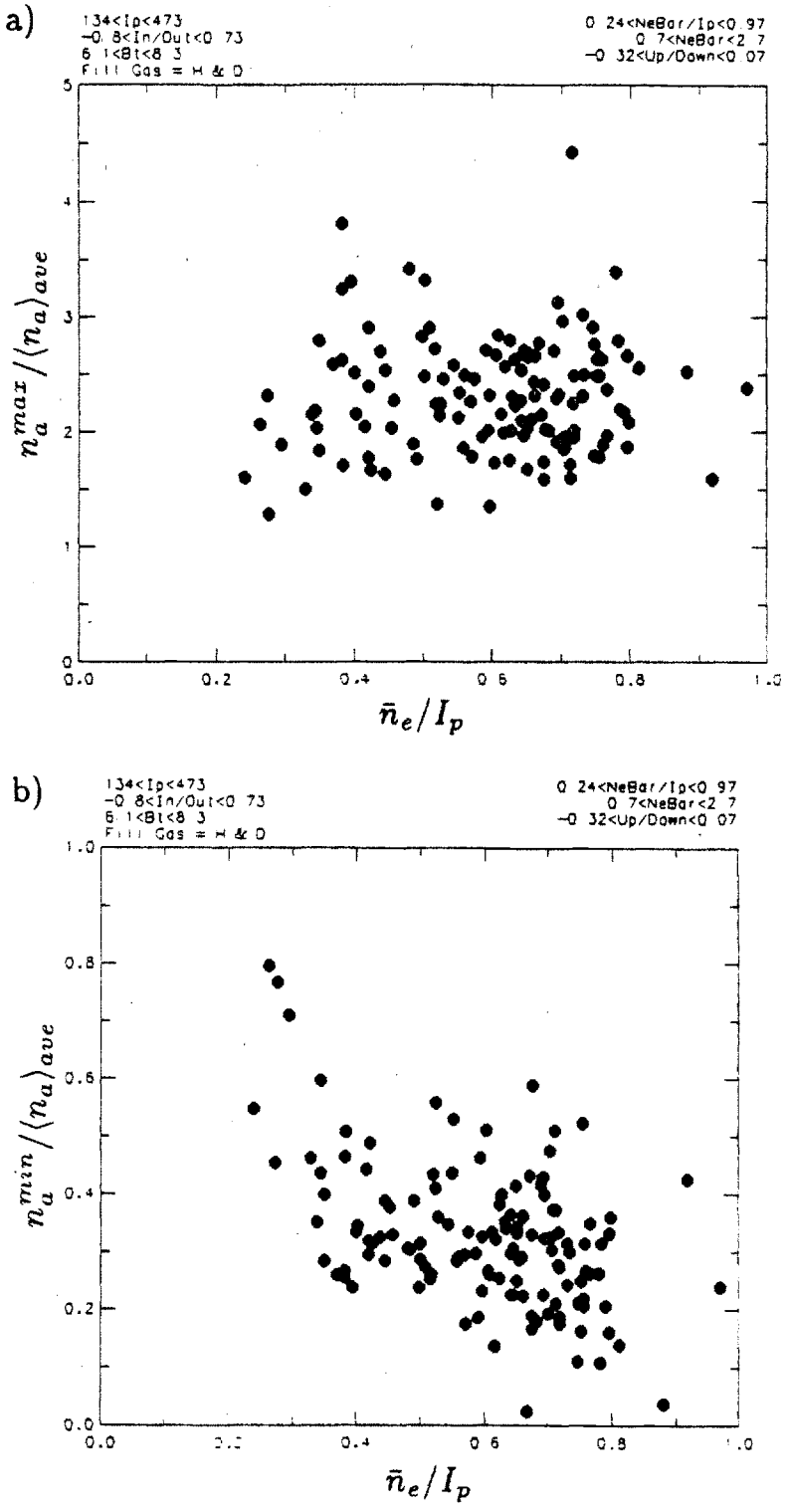

Figure 9.27 Density Asymmetry Relative to Poloidally Averaged Density Extrapolated to $r = 16.5$ cm vs. $\bar{n}_e/I_p$

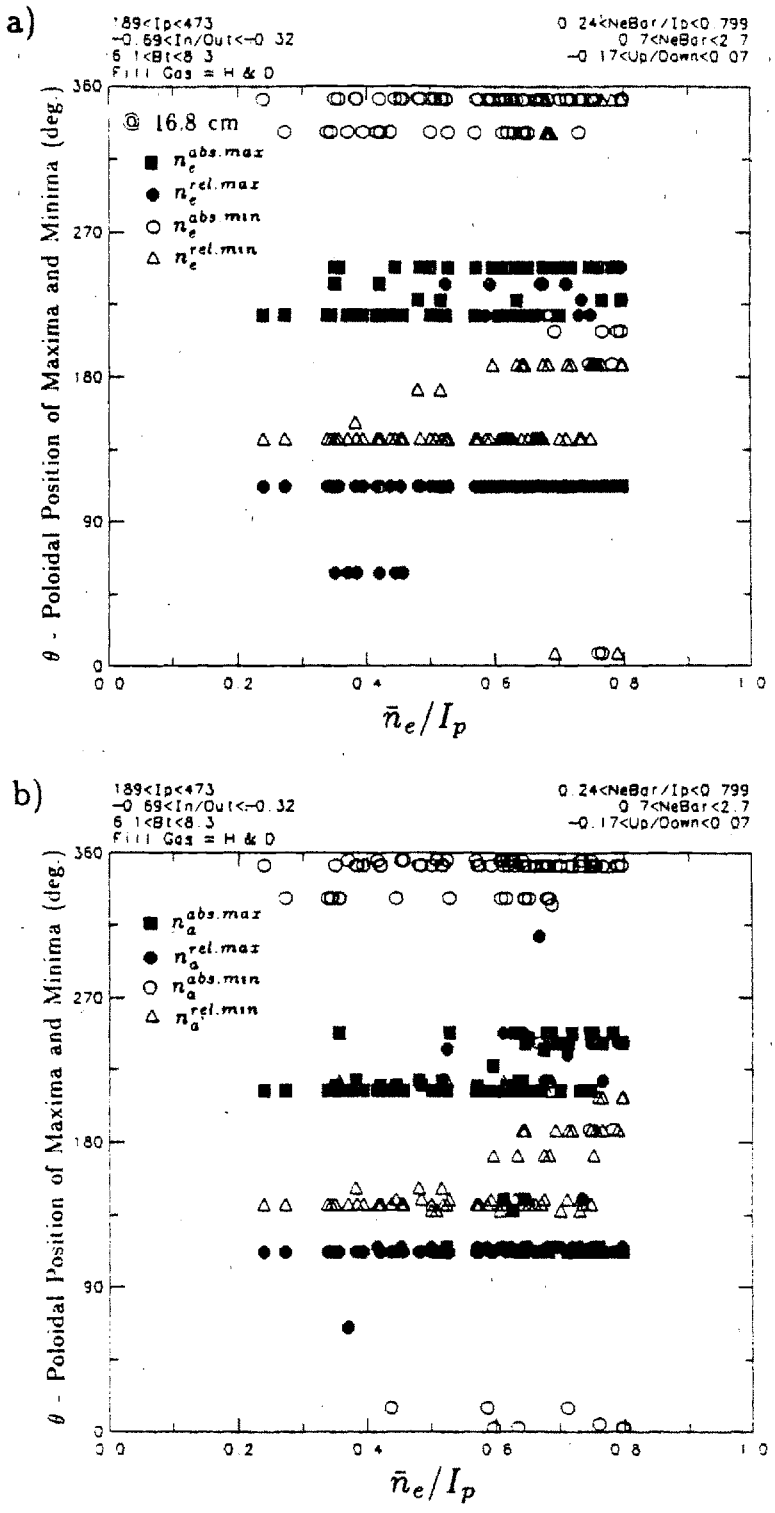

Figure 9.28 Poloidal Locations of Density Maxima and Minima vs. $\bar{n}_e/I_p$ for $r = 16.5$ and 16.8 cm

9.4.2 Density Asymmetry: Comparison with Asymmetry Model

Equation 9.20 can be contrasted with the simpler form used to investigate poloidal density asymmetries in section 3.2.4,

$$n(r,\theta) \approx n_0(r) + n_1(r,\theta) \tag{9.26}$$

where n_1 is a small density perturbation compared to n_0. Clearly Eq. 9.26 did not correctly model the observed density asymmetry. Nevertheless, it does allow an identification of asymmetric driving terms for the case of a nearly symmetric edge density. These same driving terms are expected to be active in the case of a fully developed, large poloidal density perturbation when Eq. 9.26 no longer applies. However, at this level of perturbation, the magnitude of the asymmetry itself can determine the average edge density.

The density asymmetry model presented in section 3.2.4 identified Pfirsch-Schlüter convection as a possible mechanism which can lead to poloidally asymmetric density profiles. In this model, asymmetric fluxes driven by $\underline{E}\times\underline{B}$ Pfirsch-Schlüter convection are balanced by diffusion parallel to the field lines. The resulting poloidal density perturbation depends on $\cos\theta$, and the degree of asymmetry is found to depend on the value of δ_n where

$$\delta_n \propto \frac{n_a^2 \sqrt{\mu} B^2}{I_p^4 T_e^3 \lambda_n^2} . \tag{9.27}$$

This scaling of δ_n compares favorably with the scaling of the absolute density asymmetry given by Eq. 9.24, although it is not expected to agree exactly. Both equations show a strong dependence on $\bar{n}_e$ (or n_a) and an inverse dependence on I_p. Thus, it is possible that a poloidally asymmetric driving mechanism such as Pfirsch-Schlüter convection can lead to strong poloidal asymmetries and explain

the observed edge density scaling. At least it is recognized that particle transport along field lines is not high enough compared to perpendicular transport processes to force complete poloidal symmetry in the edge plasma.

9.4.3 Temperature Asymmetry versus $\bar{n}_e/I_p$

Figures 9.29 and 9.30 show normalized maxima and minima in electron temperature recorded at r = 16.8 and 17.2 cm respectively versus $\bar{n}_e/I_p$. The asymmetry for the temperature is similar to the density asymmetry. Ratio of maximum to average temperatures are typically $T_e^{max}/\langle T_e\rangle_{ave} \approx$ 1.1–1.7 for both radii. However, both normalized temperature minima are in the range $T_e^{min}/\langle T_e\rangle_{ave} \approx$ 0.5–0.8, unlike the very low relative density minimum at r = 17.2 cm.

The temperature asymmetry is also relatively insensitive to $\bar{n}_e/I_p$. However, contrary to the density data, there is evidence of a slight decrease in the relative temperature asymmetry for high $\bar{n}_e/I_p$. This is seen in the lowering $T_e^{max}/\langle T_e\rangle_{ave}$ in Fig. 9.29*a*.

The poloidal locations of temperature extrema in Fig. 9.31 show no obvious dependence on $\bar{n}_e/I_p$. Here, open points denote low temperature measurements and solid points correspond to high temperature locations. The pattern is similar to the one presented earlier for density. Again the MARFE versus non-MARFE regimes show no change in the temperature asymmetry. However, as discussed in section 9.3.4, there is a trend of lowest temperature data points at the upper-inside location (MARFE location) becoming even lower as $\bar{n}_e/I_p$ is decreased.

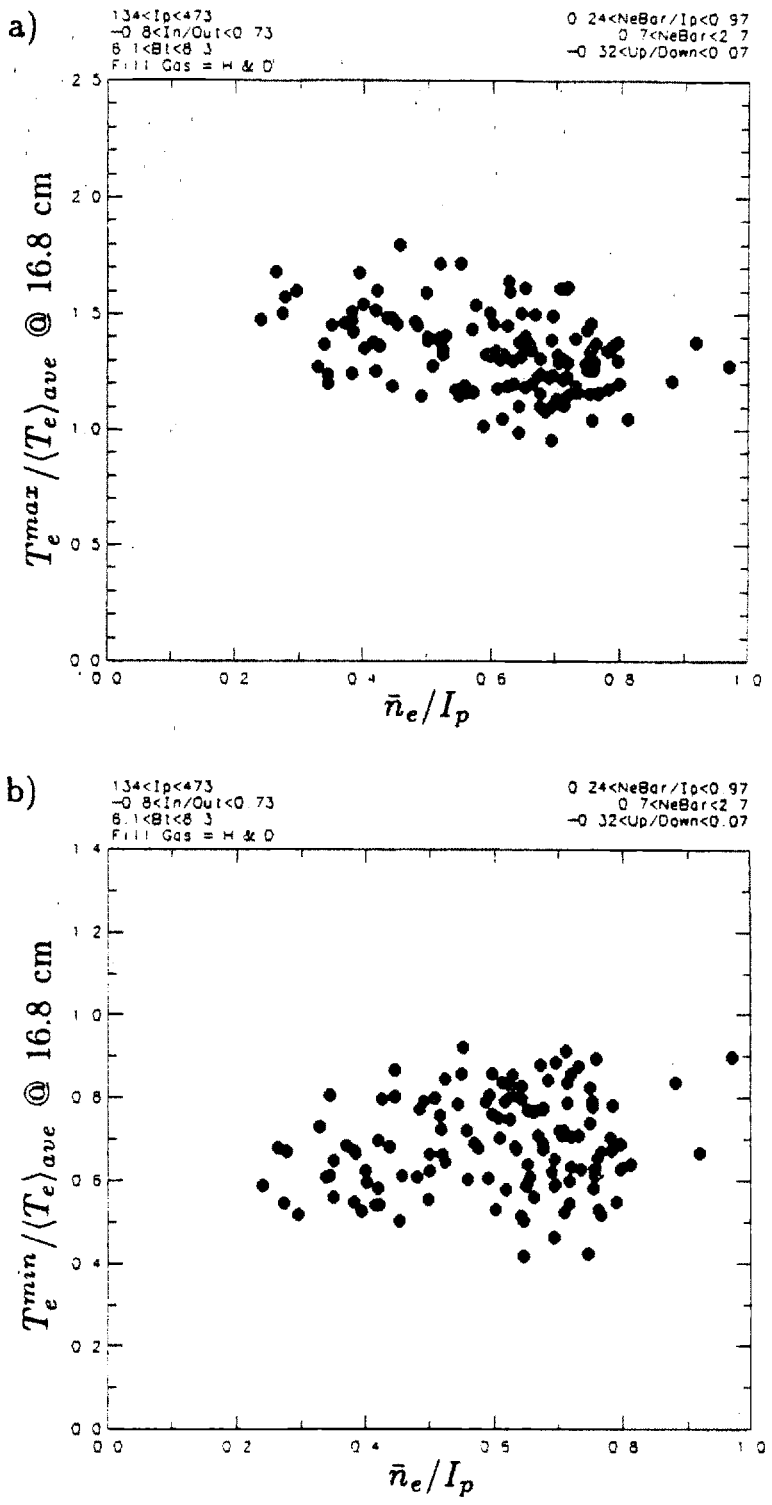

Figure 9.29 Temperature Asymmetry Relative to Poloidally Averaged Temperature at $r = 16.8$ cm vs. $\bar{n}_e/I_p$

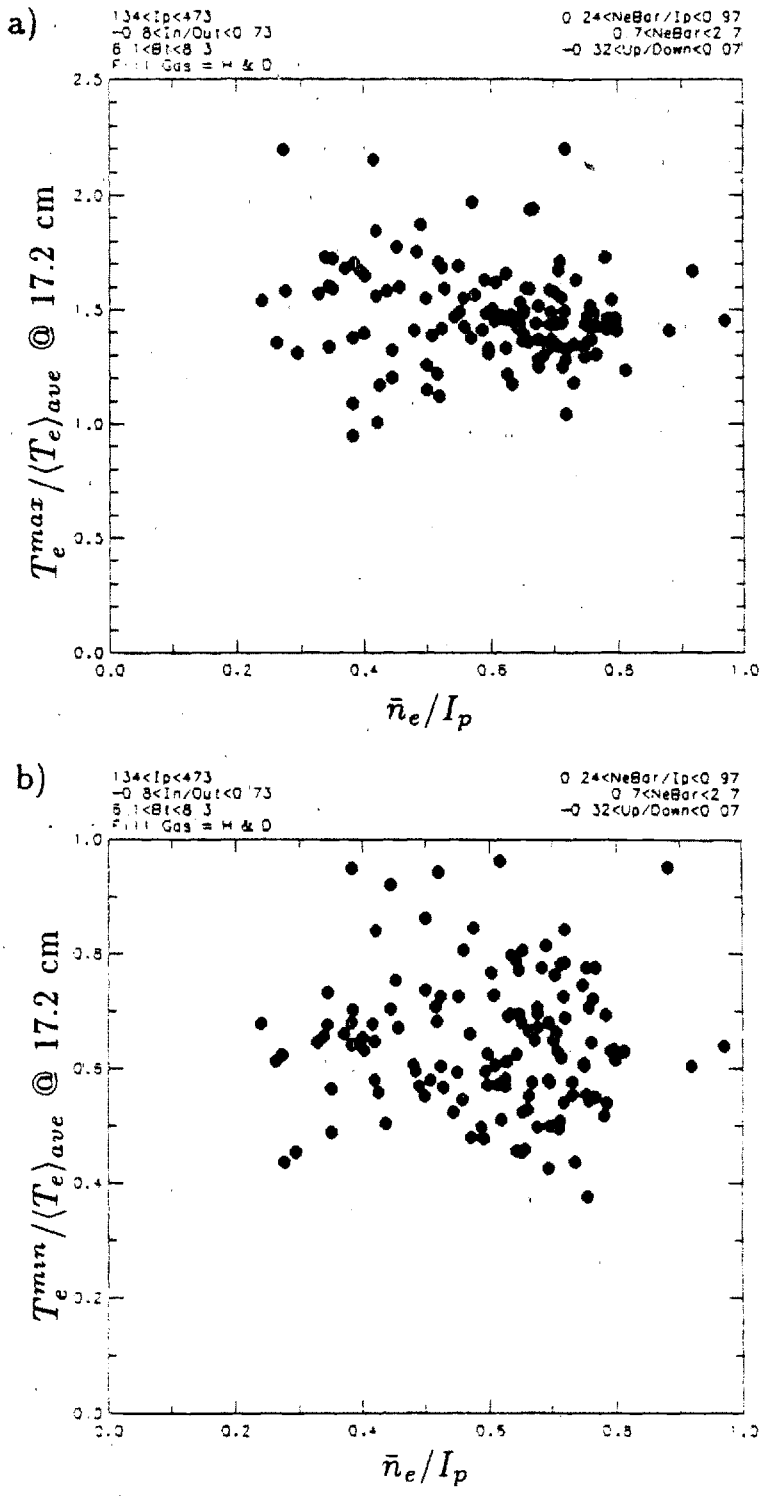

Figure 9.30 Temperature Asymmetry Relative to Poloidally Averaged Temperature at $r = 17.2$ cm vs. $\bar{n}_e/I_p$

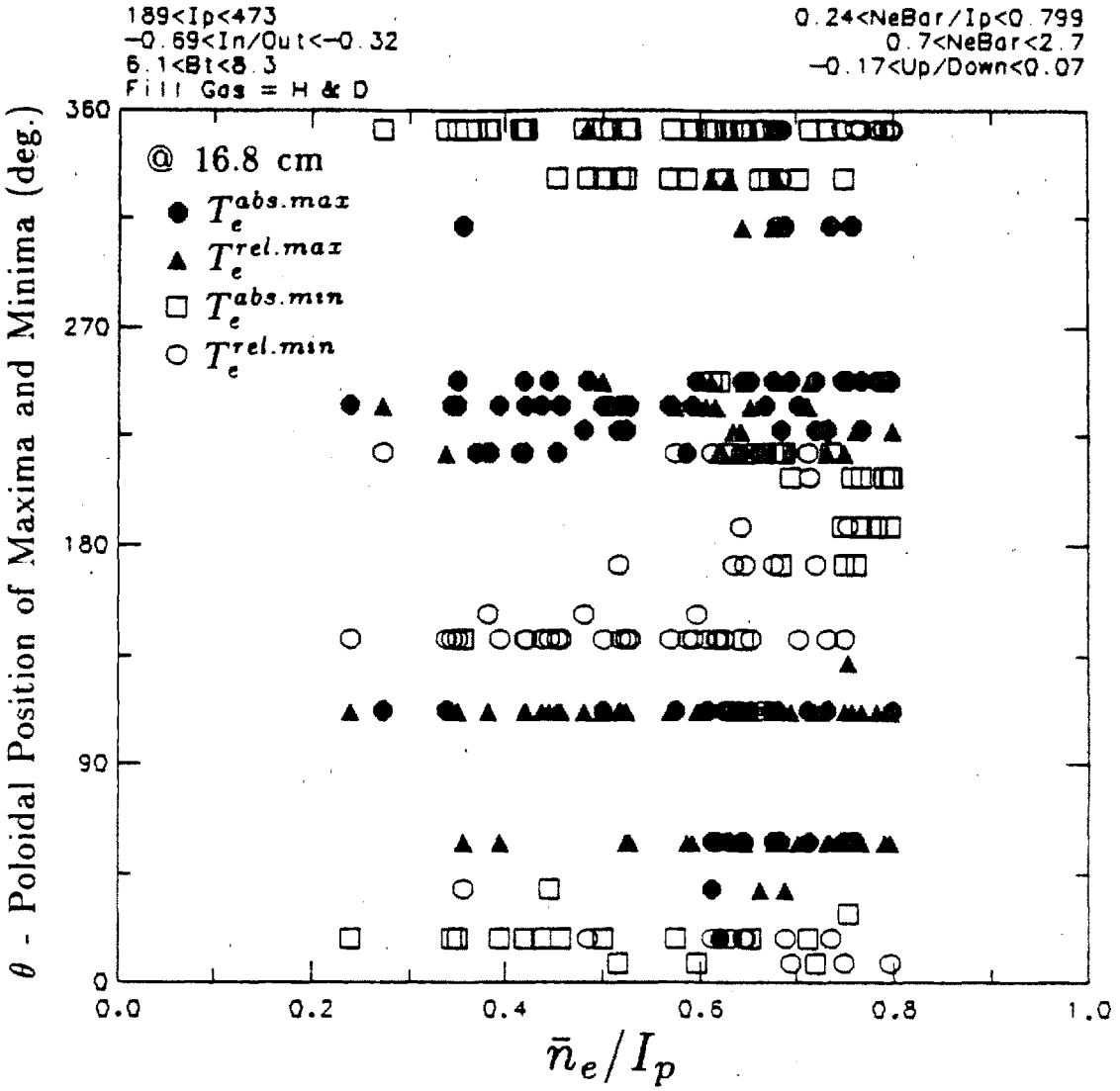

Figure 9.31 Poloidal Locations of Temperature Maxima and Minima vs. $\bar{n}_e/I_p$ for $r = 16.8$ cm

9.4.4 Scrape-off Length Asymmetry versus $\bar{n}_e/I_p$

Normalized maxima and minima in density scrape-off length is plotted versus $\bar{n}_e/I_p$ in Figs. 9.32*a* and 9.32*b*. Typical values range $\lambda_n^{max}/\langle\lambda_n\rangle_{ave} \approx 1.5$–$2.5$, $\lambda_n^{min}/\langle\lambda_n\rangle_{ave} \approx 0.3$–$0.5$, with no apparent correlation with $\bar{n}_e/I_p$.

As indicated in chapter 7, the poloidal structure of the scrape-off length profile is different than the density or temperature profile. Poloidal locations of maxima and minima in λ_n are indicated versus $\bar{n}_e/I_p$ in Fig. 9.33. The scrape-off length minima are always near the inside midplane. The factor of ~ 5 variation in scrape-off length from inside to outside is maintained for all values of $\bar{n}_e/I_p$.

The non-MARFE versus MARFE regime ($\bar{n}_e/I_p \lesssim 0.6$ or $\gtrsim 0.6$) does not show any difference in these plots except perhaps in the $\lambda_n^{min}/\langle\lambda_n\rangle_{ave}$ data which shows more scatter in the MARFE regime.

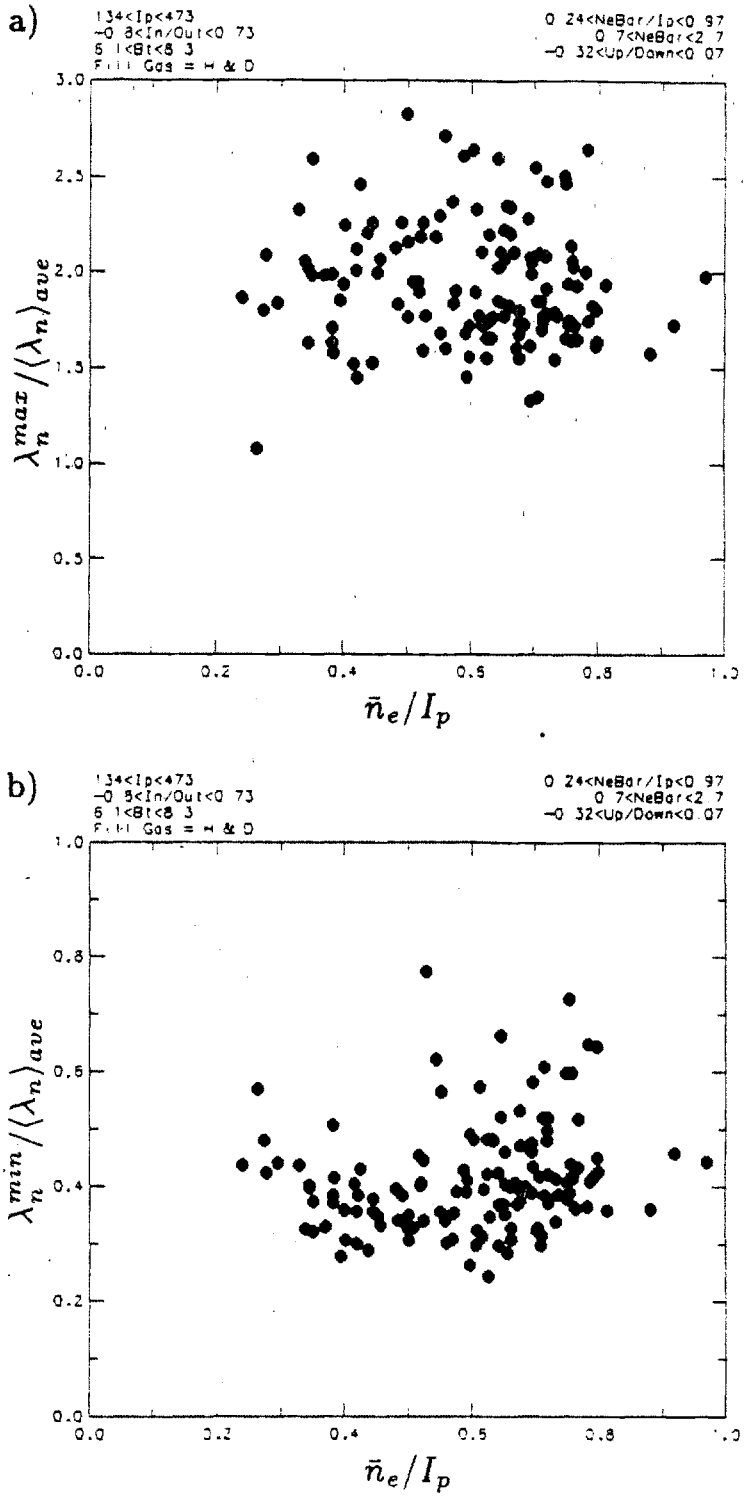

Figure 9.32 Scrape-off Length Asymmetry Relative to Poloidally Averaged Scrape-off Length vs. $\bar{n}_e/I_p$

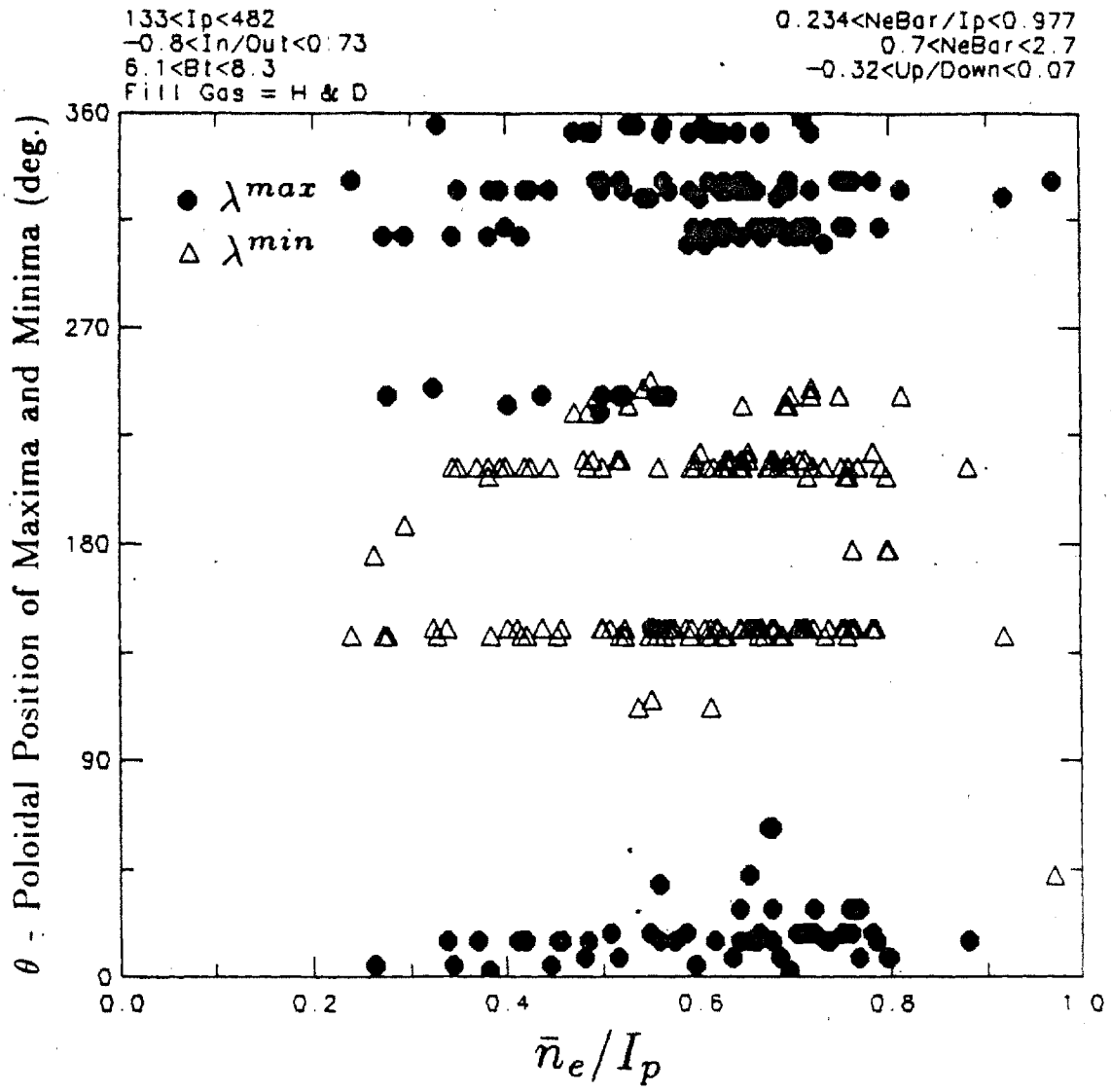

Figure 9.33 Poloidal Locations of Scrape-off Length Maxima and Minima vs. $\bar{n}_e/I_p$

9.4.5 Floating Potential Asymmetry versus $\bar{n}_e/I_p$

DENSEPACK probe floating potentials show the strongest asymmetry variation with $\bar{n}_e/I_p$ of all the edge parameters measured. Figures 9.34*a* and 9.34*b* plot maximum minus the minimum floating potential values in poloidal angle versus $\bar{n}_e/I_p$. Figure 9.35 shows that the maximum floating potential occurs near the top of the poloidal cross section (270°) and the minimum near the bottom (90°), independent of $\bar{n}_e/I_p$. The difference of this top-bottom potential can range from 5–25 volts for low values of $\bar{n}_e/I_p$ but drops to ~ 5 volts at $r = 17.2$ cm and ~ 7 volts at $r = 16.8$ cm for $\bar{n}_e/I_p \gtrsim 0.7$.

The probe floating potential is related to the electron temperature near the probe, the electron temperature near the limiter surface, and changes in plasma potential due to non-ambipolar fluxes through Eq. 9.14. Thus, it is difficult to identify the dominant mechanism which would explain this change in V_f with $\bar{n}_e/I_p$.

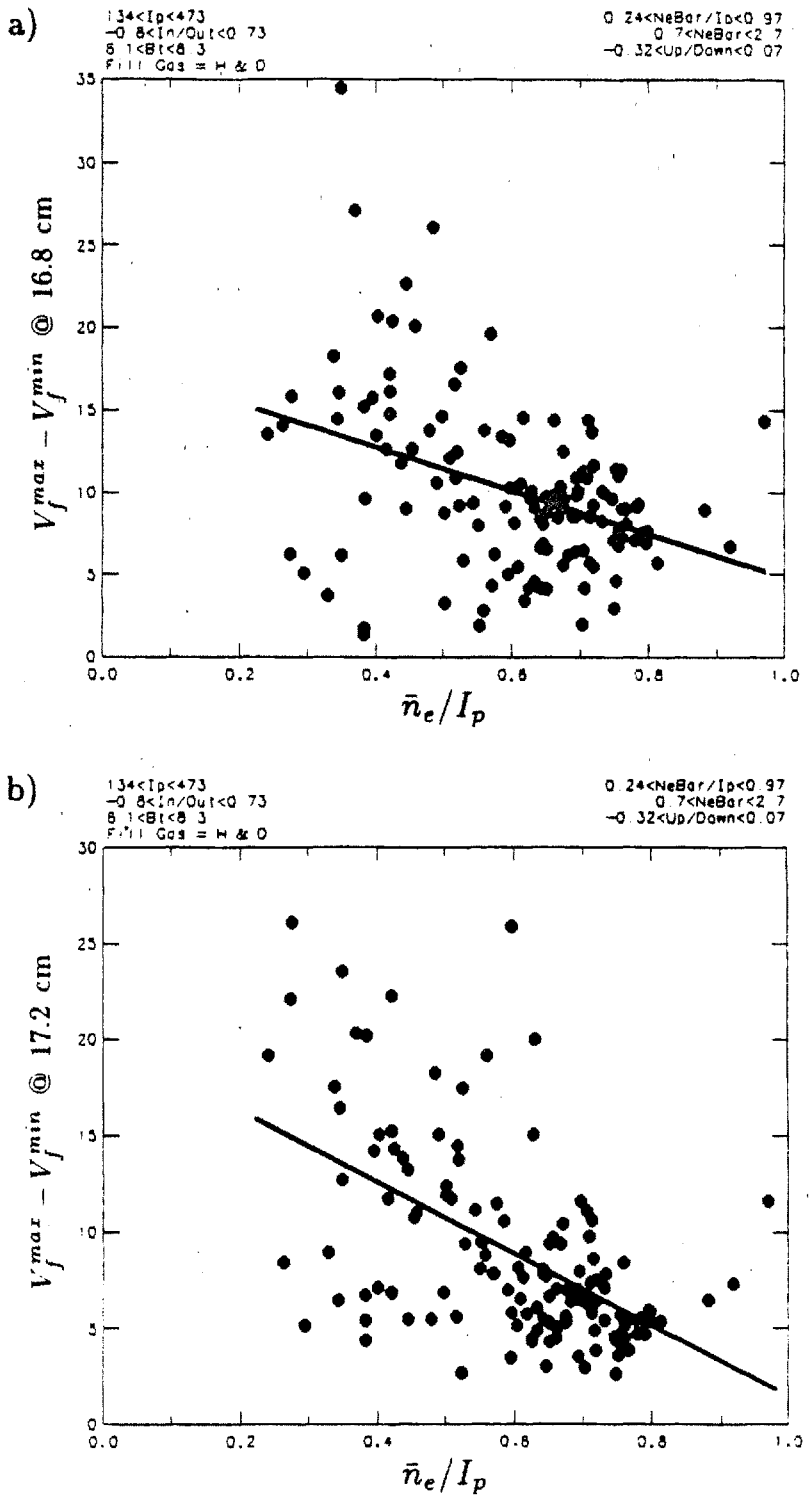

Figure 9.34 Poloidal Maximum Minus Poloidal Minimum Floating Potential vs. $\bar{n}_e/I_p$

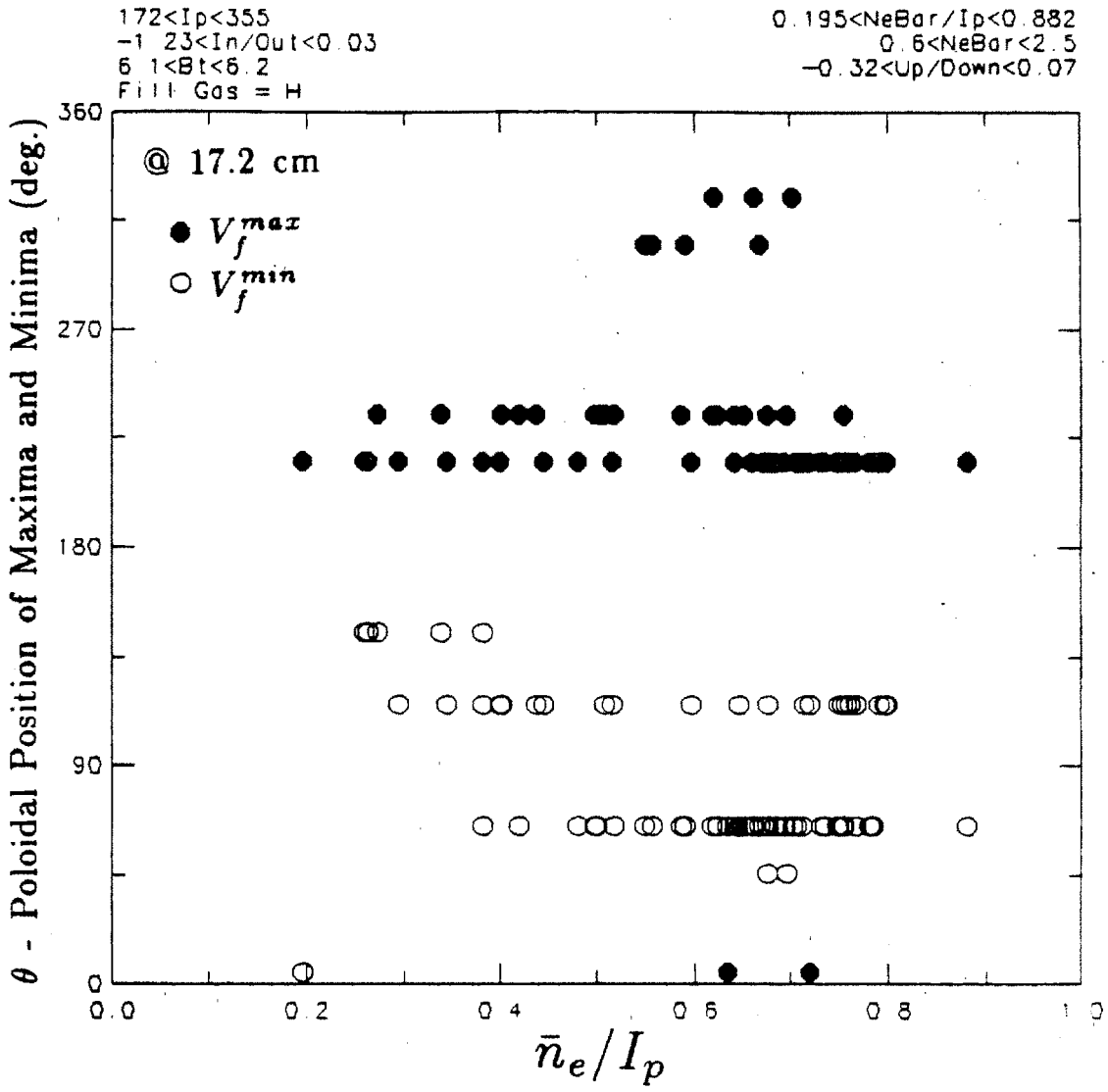

Figure 9.35 Poloidal Locations of Floating Potential Maxima and Minima vs. $\bar{n}_e/I_p$

CHAPTER 10

EDGE VERSUS CENTRAL PARAMETERS: LHRF HEATED AND PELLET FUELED DISCHARGES

In addition to the ohmic, gas fueled discharges reported in the previous chapter, data was recorded by the inside half of the DENSEPACK probe array during Lower Hybrid Radio Frequency (LHRF) heating and pellet fueling. During LHRF heating, edge densities and temperatures were found to increase uniformly by ~50% and ~25% respectively over the values measured during ohmic heating alone. The result was a relative reduction in the global particle confinement time and an increased power loading on limiter surfaces. Section 10.1 presents changes in edge parameters during LHRF heating and discusses some implications of increased edge particle and energy fluxes on impurity production rates.

Following pellet injection, the edge plasma was found to achieve one of two states. For small increases in central line-averaged density, the change in edge plasma parameters for changing central parameters followed the ohmic, gas fueled relationships presented in the previous chapter. However, for large increases in central $\bar{n}_e$ resulting from pellet injection, the final edge plasma state deviated from the gas fueled scaling laws. The edge plasma in this new regime was characterized by lower densities at all radii for the same central $\bar{n}_e$. The result was an increase in the global particle confinement time. Section 10.2 presents DENSEPACK data before and after pellet injection. Changes in global particle confinement time are plotted versus relative pellet size. It is shown that a relative density increase due to pellet injection of $\Delta\bar{n}_e/\bar{n}_e \gtrsim 1$ is required to attain the high particle confinement time regime.

10.1 Change in Edge Parameters During LHRF Heating

The experimental arrangement of DENSEPACK during the LHRF heating experiment is shown as configuration 'B' in Fig. 5.4. Lower hybrid waveguides were located in B, C, and F port locations. The effects of LHRF on edge plasma parameters were found to be independent of which Lower Hybrid launcher was active. For all the LHRF and pellet discharges, only the inside half of DENSEPACK was used. Consequently, poloidal averages (notated as $\langle\ \rangle_{ave}$ or $\langle\ \rangle$) of edge plasma parameters recorded in the database corresponded to a spatial average over only the inside half of the array.

10.1.1 Time Evolution of Edge Density and Temperature

Figure 10.1 shows the time evolution of spatially averaged density and electron temperature at $r = 17.2$ cm during a LHRF pulse. Central parameters for this data and all data presented in this section are $1 \lesssim \bar{n}_e \lesssim 2$ ($\times 10^{14}/\mathrm{cm}^3$), $300 \lesssim I_p \lesssim 400$ (kA) in deuterium plasma. Note the marked rise in edge density ($\sim 60\%$ change) and temperature ($\sim 40\%$ change) during the time when all three waveguides are fired (580 kW total).

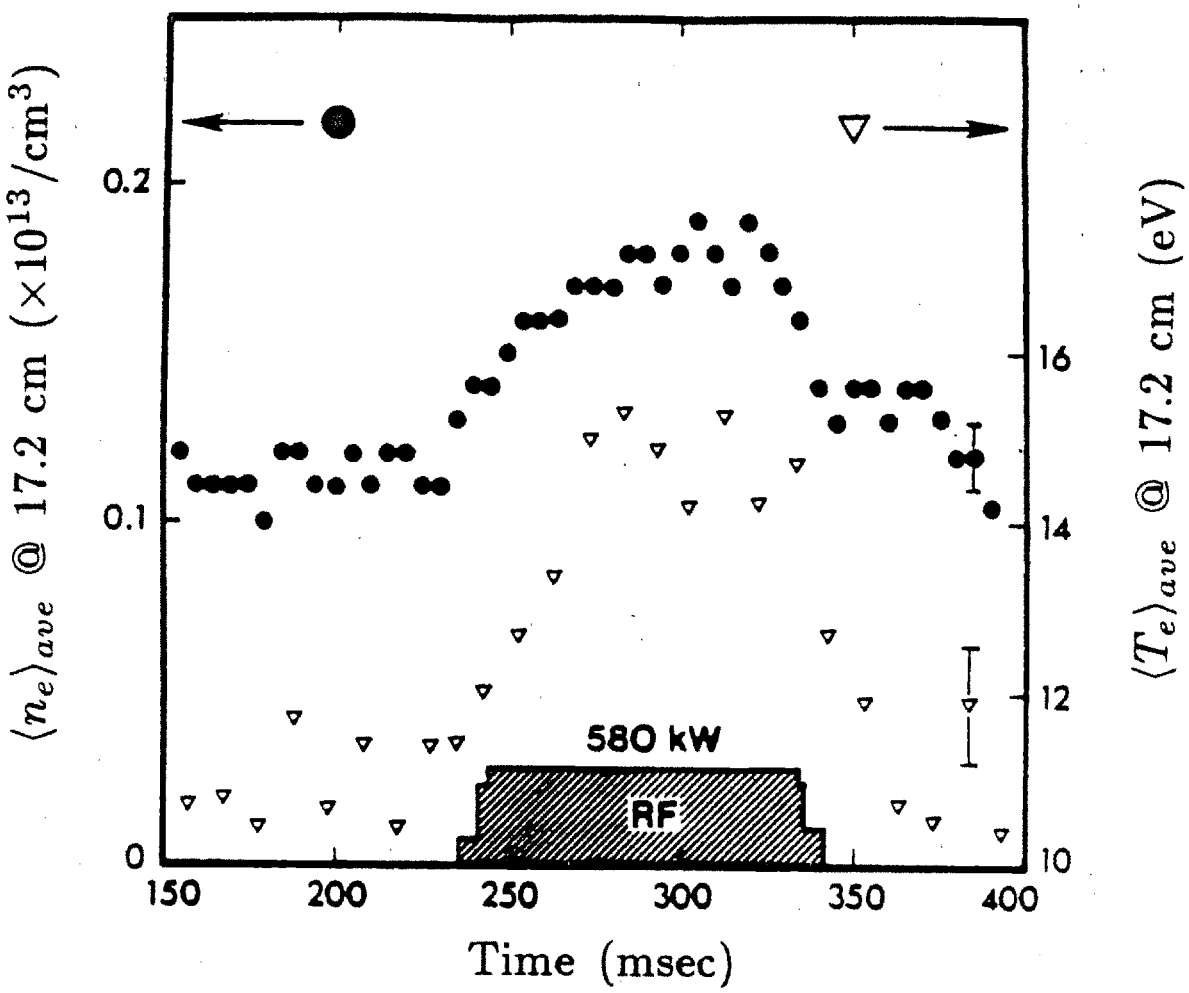

Figure 10.1 Time Evolution of Edge Density & Temperature at $r = 17.2$ cm During Lower Hybrid Heating

10.1.2 Change in Density, Temperature, and Particle Confinement

Edge plasma parameters for a range of injected LHRF powers were recorded in the DENSEPACK database. Figures 10.2–10.4 plot changes in poloidal averages of edge density, temperature, and scrape-off length for the inside section of the DENSEPACK array along with an estimate of the global particle confinement time as a function of LHRF power. In all cases there is a monotonic increase in the magnitude of change versus LHRF power.

The edge density increases $\sim 75\%$ at the highest LHRF powers with data at larger radii showing the largest percentage increase (Fig. 10.2). Changes in edge temperature show a similar trend with $\Delta\langle T_e\rangle_{ave}/\langle T_e\rangle_{ave}$ typically $\sim 30\%$ at the highest powers (Fig. 10.3). Some points at zero RF power are included for reference and indicate the change in edge parameters that can occur between the 'before' and 'during' sample times due to changes in central parameters alone.

The change in angle averaged, normalized ion saturation fluctuation amplitude, $\tilde{J}/\bar{J}$, ($0.1 \lesssim f \lesssim 50$ kHz) is plotted versus RF power for the three DENSEPACK radii in Fig. 10.4. A trend of a reduction in $\tilde{J}/\bar{J}$ during the edge density increase that occurs with LHRF heating is evident. However, the decrease in $\tilde{J}/\bar{J}$ is too small to be attributed to a constant level of $\tilde{J}$ and an increase in $\bar{J}$ from the increased edge density and temperature that occurs during RF heating.

The density scrape-off length plotted in Fig. 10.5*a* only slightly increases with RF power ($\sim 10\%$). Consequently, the density extrapolated to the limiter radius (Fig. 10.5*b*) exhibits roughly the same percent increase as the density in the shadow plasma ($\sim 50\%$). The result of the increased plasma density at the limiter radius combined with the increased electron temperature in the shadow plasma leads to a reduction in the global particle confinement time. Figure 10.5*c* shows an estimated $\sim 40\%$ decrease in τ_p at the highest LHRF powers. Assuming that the change in edge parameters measured by the inside section of

DENSEPACK applies to the entire poloidal extent of the shadow plasma, these data indicate that the total edge particle and energy flux changes during LHRF heating.

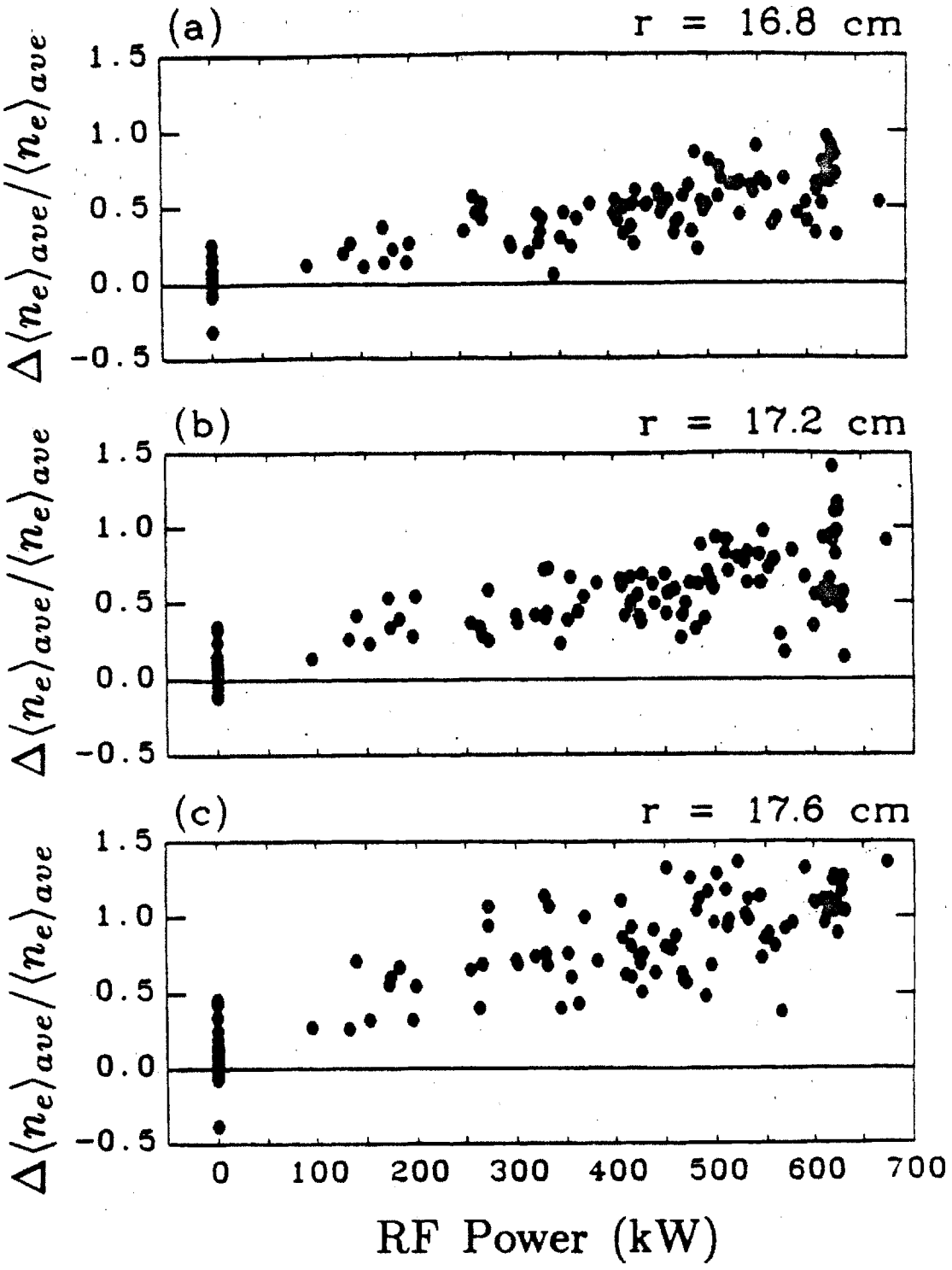

Figure 10.2 Fractional Change in Edge Density vs. RF Power

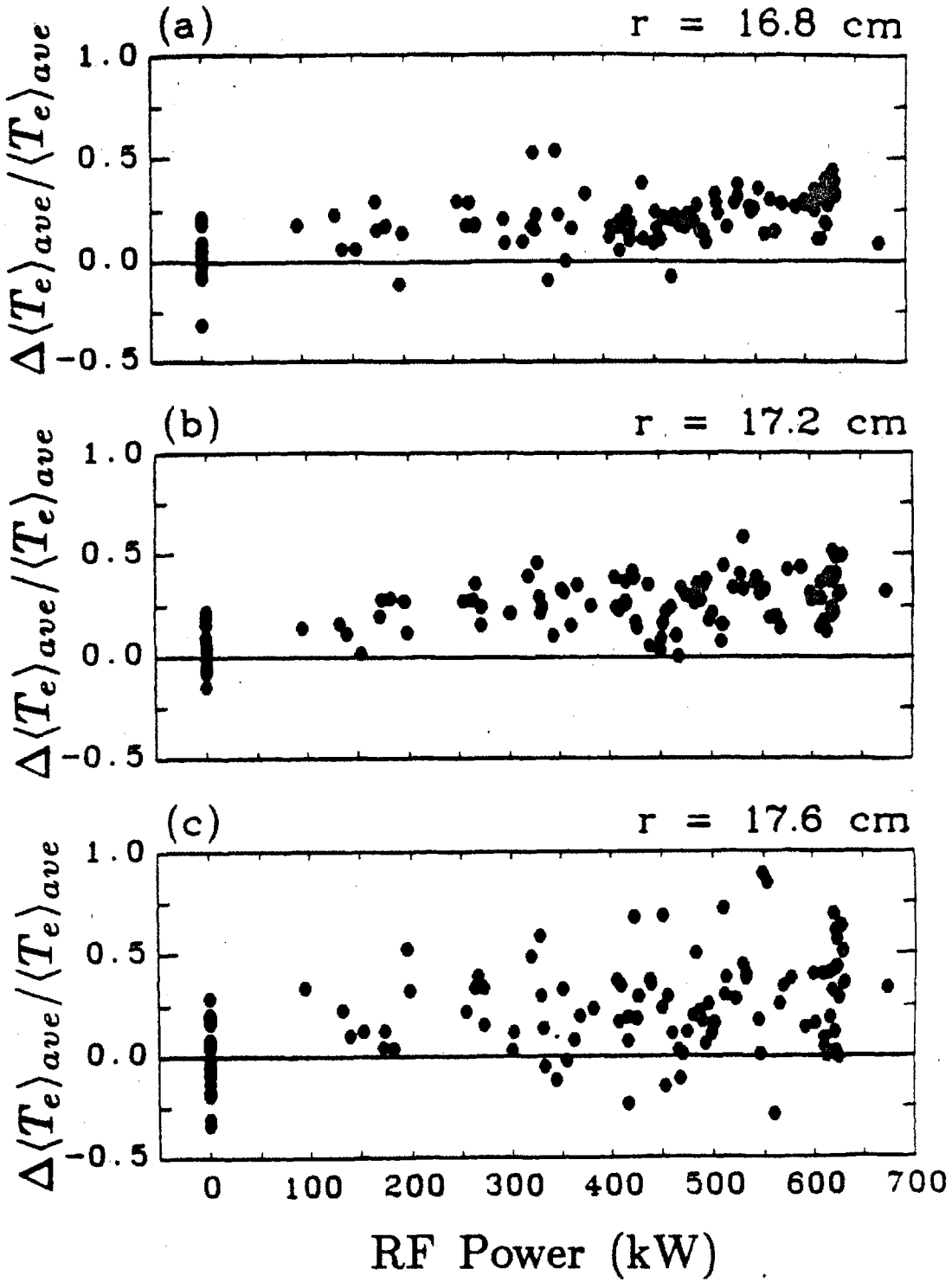

Figure 10.3 Fractional Change in Edge Temperature vs. RF Power

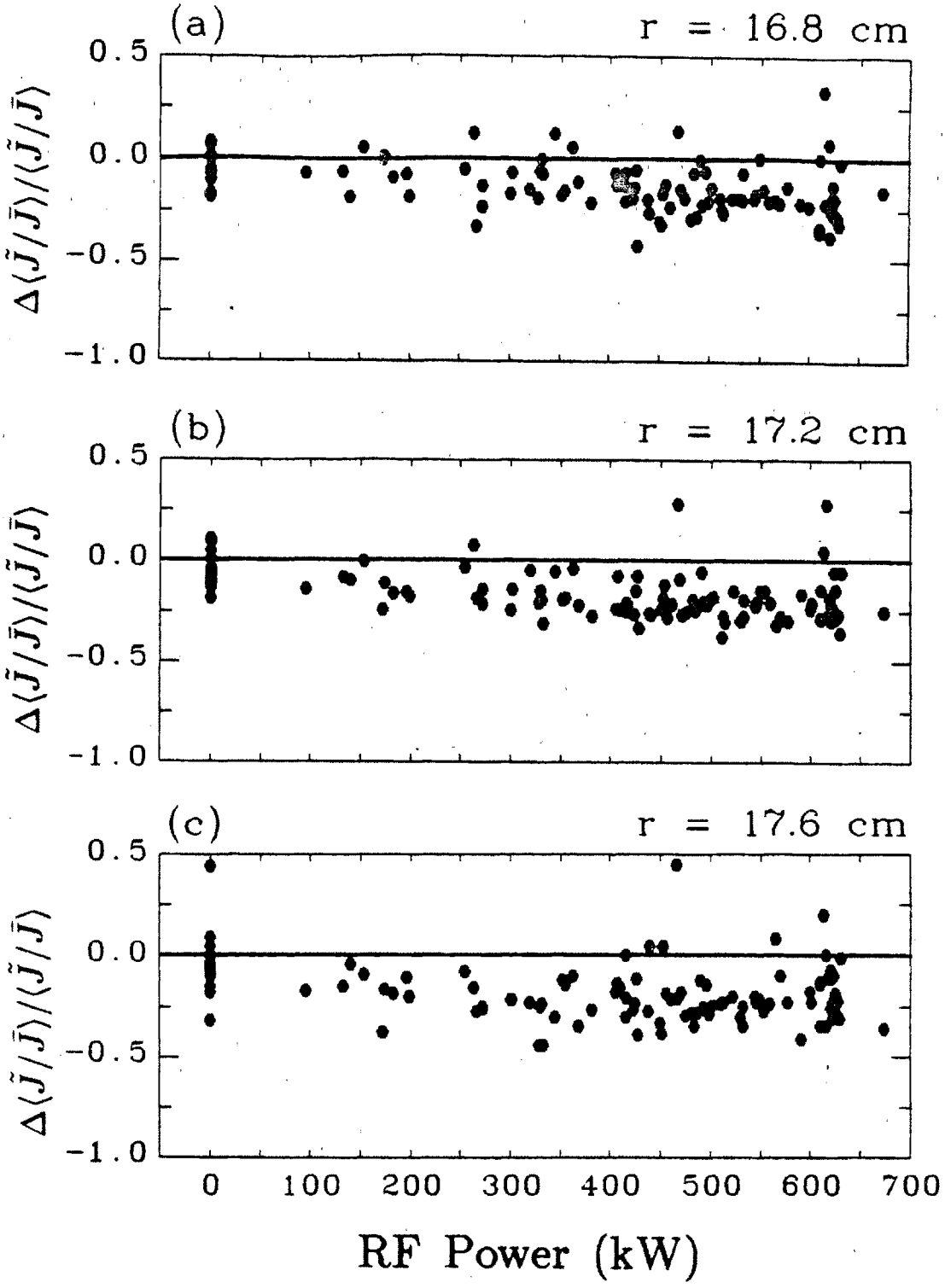

Figure 10.4 Fractional Change in Normalized Fluctuation Amplitude vs. RF Power

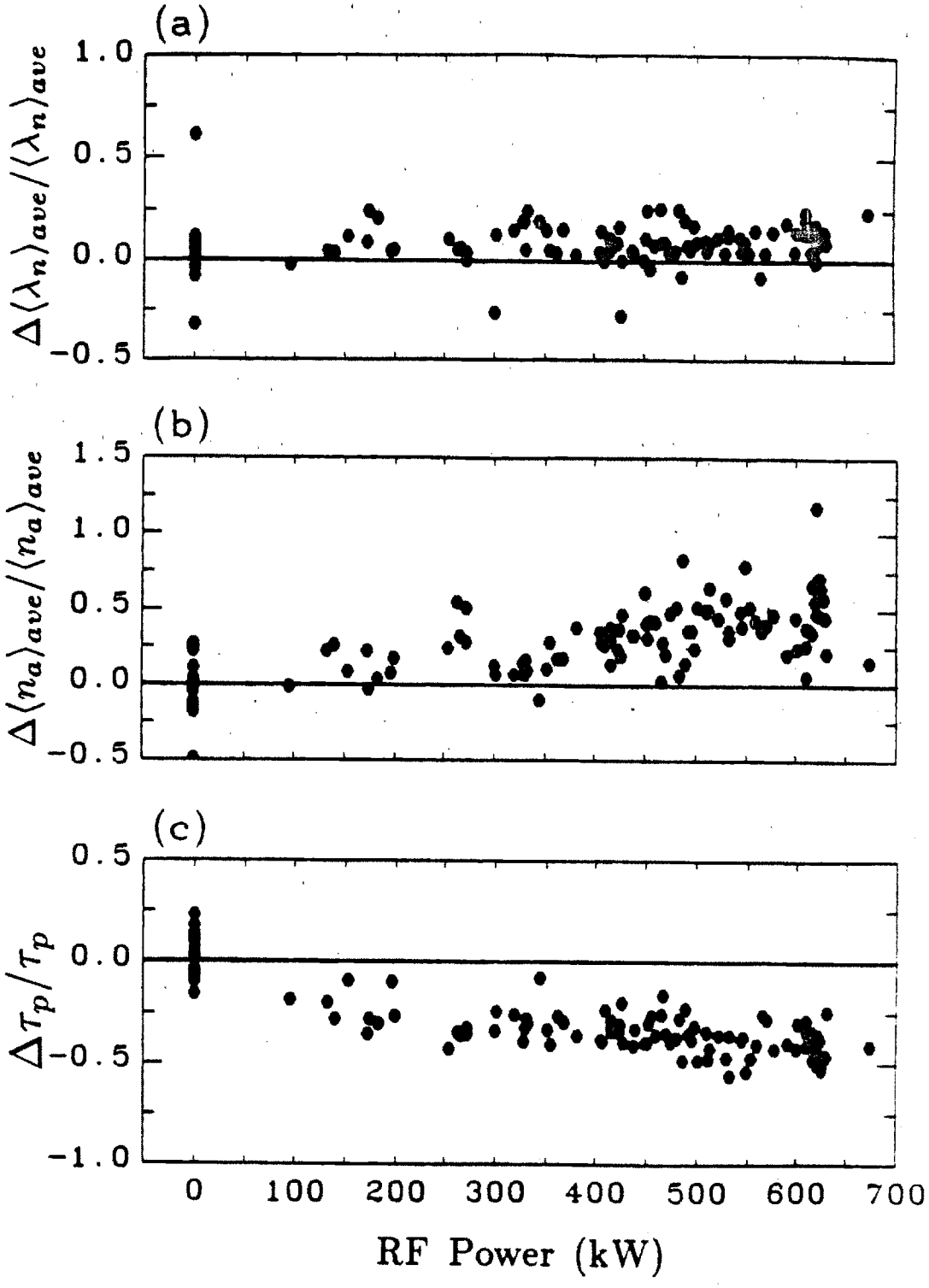

Figure 10.5 Fractional Change in Scrape-off Length, Density at the Limiter Radius, and Particle Confinement Time vs. RF Power

10.1.3 Edge Plasma Power Balance and Impurity Production

As discussed in section 2.2.3, the total power flux to a limiter surface can be expressed as

$$P_{tot} \approx \delta_t \, T_e \, q \, \frac{n_0 \, C_s}{2} \propto T_e^{3/2} n_0 \, . \tag{10.1}$$

For these LHRF heated discharges, the ohmic input power was $\sim$ 600–800 kW. Thus, the additional LHRF power leads to roughly a factor of $\sim$ 2 increase in the total input power with $P_{rf} \approx 650$ kW. Equation 10.1 predicts that the factor of $\sim$ 1.5 increase in edge density and $\sim$ 1.2 increase in edge electron temperature recorded by DENSEPACK for this level of LHRF heating also leads to an increase in power loading on limiter surfaces of approximately a factor of 2. Thus, the measured change in edge plasma parameters during LHRF heating is consistent with edge power balance considerations.

The increase in edge density and temperature and associated increase in power flux to limiter surfaces can affect the rate of impurity release through evaporation, sputtering, and/or arcing. For values of RF power, $P_{rf} < 550$ kW, it is found that impurity density increases during LHRF heating can be attributed to a rise in thermal sputtering rates from the increased edge densities and electron temperatures.[100,114] For values of $P_{rf} > 550$ kW, limiter evaporation due to non-thermal electrons generated during the LHRF heating process takes over, and the direct impact of increasing edge densities and temperatures on impurity production becomes secondary in importance.

10.2 Change in Edge Parameters Following Pellet Injection

Pellet injection experiments were performed with the inside half of the DENSEPACK array installed in 'C' port as shown in Fig. 5.4. The injector located at 'E' port was capable of pneumatically launching frozen H_2 and D_2 pellets along the major radius of Alcator C at velocities approaching 900 m/sec.[87] The number of gas atoms in a single pellet corresponded to roughly the total number of ions in an Alcator C plasma with line-averaged electron density of $\bar{n}_e \approx 1\text{–}2\times10^{14}/\text{cm}^3$.

Ablation of the pellet near the center of the plasma discharge leads to a rapid increase ($t \lesssim 100$ μsec) in the total particle inventory. This method of 'pellet fueling' is inherently more efficient than gas fueling since the particles are deposited directly in the central plasma region. The inside probes of the DENSEPACK array were used to record changes in edge parameters during pellet injection with the idea of characterizing edge plasma conditions of pellet fueled versus gas fueled discharges.

Probes at $r = 16.8$ cm which were damaged during the first phase of operation (configuration 'A' in Fig. 5.3) were converted to sample plasma at $r = 17.2$ cm prior to the pellet fueling experiments. Thus, most of the data collected by the inside half of DENSEPACK during pellet injection was at $r = 17.2$ cm. Consequently, poloidally averaged plasma parameters obtained at this radius are the primary focus of the presentation in this section.

10.2.1 Departure of Edge Density from Gas Fueled Scaling

Figure 10.6 plots inside, poloidally averaged density data at $r = 17.2$ cm before and after pellet injection versus $\bar{n}_e/I_p$. Data points from hydrogen and deuterium pellets injected into an 8 tesla deuterium plasma are included. Some data points from strictly gas fueled hydrogen plasmas at 6 tesla obtained early in the operation of DENSEPACK are also combined with this data and indicate

that edge conditions did not change when the pellet injector was installed. Data points obtained just before pellet injection or during gas fueling alone are shown as solid circles. Open triangles designate points obtained following pellet injection. A solid line connects these initial and final states when both were sampled for the same discharge.

As discussed in chapter 9, edge plasma parameters for ohmic, gas fueled discharges are found to depend on the combination of central variables, $\bar{n}_e/I_p$. The inside, poloidally averaged density at $r = 17.2$ cm measured before pellet injection follows the same ohmic, gas fueled scaling relationship with $\bar{n}_e$ and I_p that was inferred from the full poloidal array. Figure 10.7 overlays the regression fitted functional form presented earlier in tables 9.3 and 9.4 for density at $r = 17.2$ cm. The magnitude of this curve is scaled to match these lower densities detected by the inside segment of DENSEPACK. Central parameters used to determine the shape of this curve are $I_p = 370$ kA and $B = 8$ tesla in deuterium plasma. Note that the pre-pellet data points follow this curve, and the usual transition to the MARFE scaling regime near $\bar{n}_e/I_p \approx 0.6$ is evident.

In contrast, edge densities following pellet injection fall into one of two catagories: those which continue to follow the gas fueled relationship (type I), and those which depart from the gas fueled scaling law (type II). Figure 10.7 shows these two cases clearly with the type II pellet fueled data points grouped well below the gas fueled points that correspond to the same $\bar{n}_e/I_p$. No systematic distinction can be made between the type I or II points and the pellet fuel (H_2 or D_2).

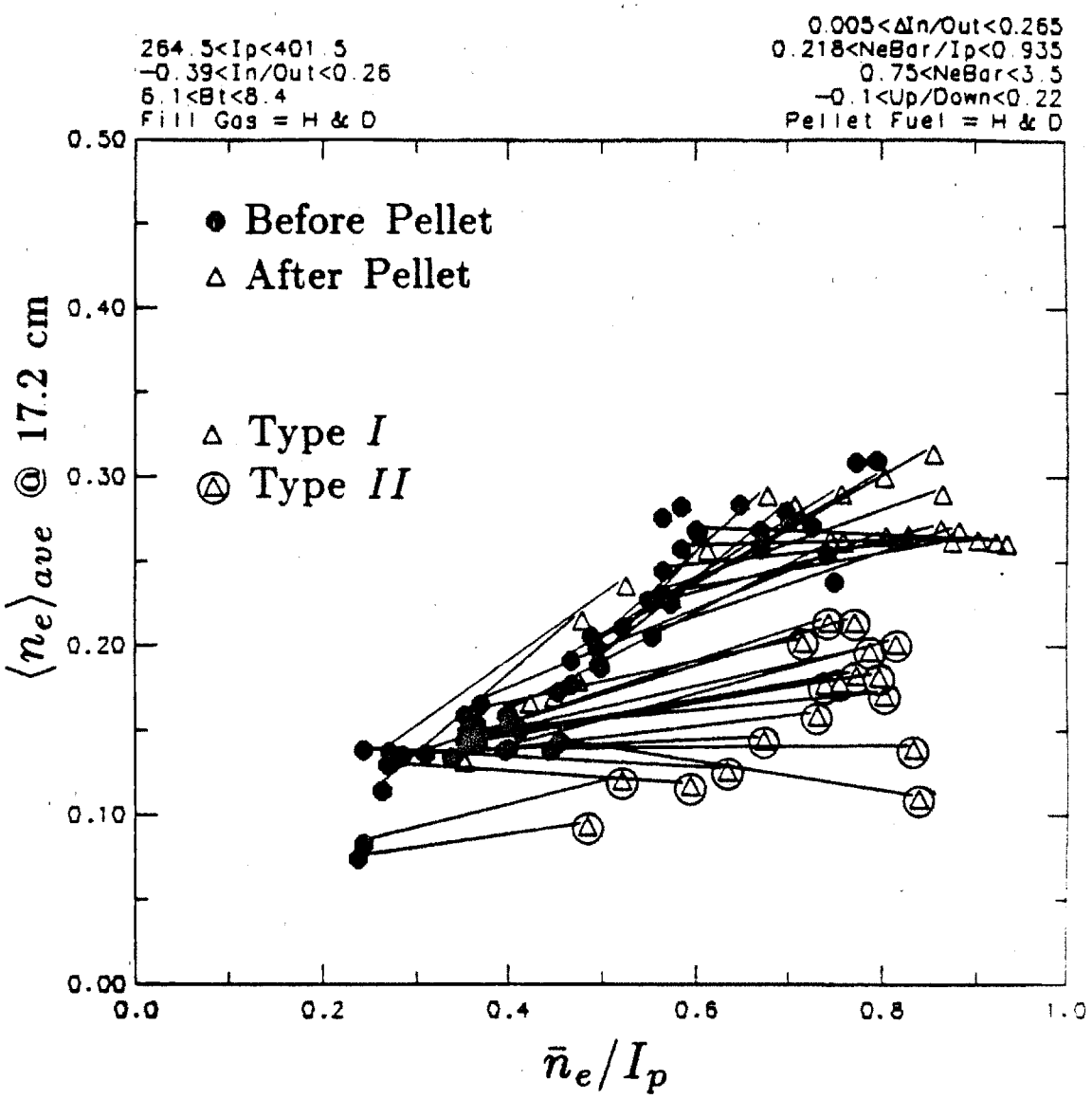

Figure 10.6 Poloidally Averaged, Inside Density at $r = 17.2$ cm Before and After Pellet Injection vs. $\bar{n}_e/I_p$

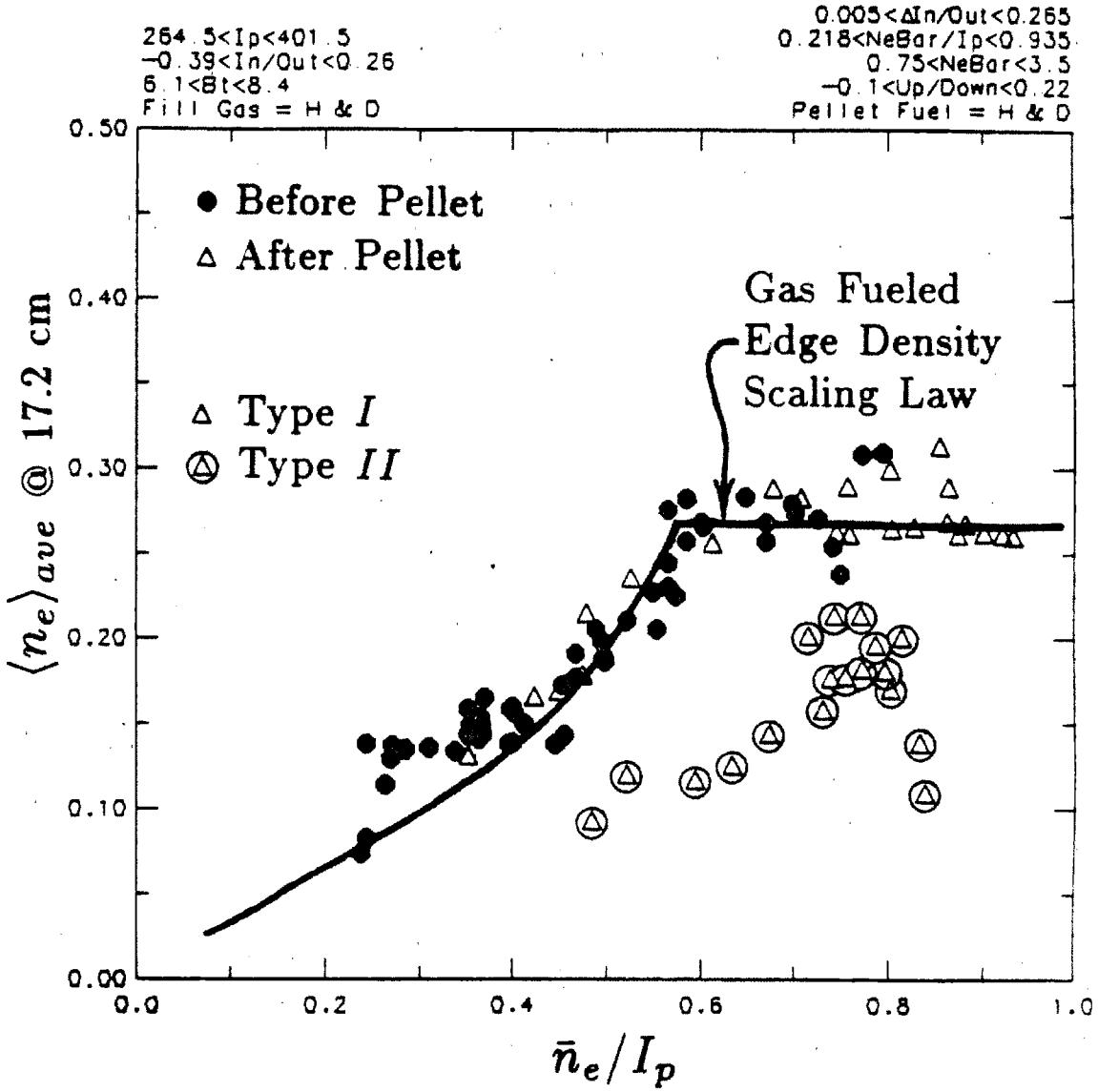

Figure 10.7 Same as Fig. 10.6 with Ohmic, Gas Fueled Edge Density Scaling Law (chapter 9) Overlayed

10.2.2 Change in Temperature, Scrape-off Length, & Confinement

Poloidally averaged electron temperature and density scrape-off length measured before and after pellet injection are shown versus $\bar{n}_e/I_p$ in Figs. 10.8 and 10.9 respectively. The electron temperature data points do not show any significant difference between pellet fueled and gas fueled discharges. The scrape-off length shows a slight increase following pellet injection; however, there is no obvious distinction between the type I and type II points identified in Fig. 10.6.

As a consequence of the low edge density yet high central $\bar{n}_e$ achieved during type II pellet injection, the global particle confinement time (τ_p) increases dramatically for these discharges. Figure 10.10 plots particle confinement time estimated by Eq. 9.3 before and after pellet injection versus $\bar{n}_e/I_p$. Note that the type II pellet fueled discharges display the highest achievable τ_p values. Since this estimate of τ_p is based on inside probe measurements alone, the absolute magnitude is not accurate. When the longer density scrape-off lengths on the outside of the tokamak are included in this calculation, τ_p reduces to the values shown previously in Figs. 9.23 and 9.24. However, the relative increase in τ_p following pellet injection in Fig. 10.10 does reflect the relative increase in global particle confinement time that would be observed by using data from the full DENSEPACK probe array. The only implicit assumption is that relative changes in edge parameters detected by the inside array occur uniformly over the full poloidal extent of the edge plasma.

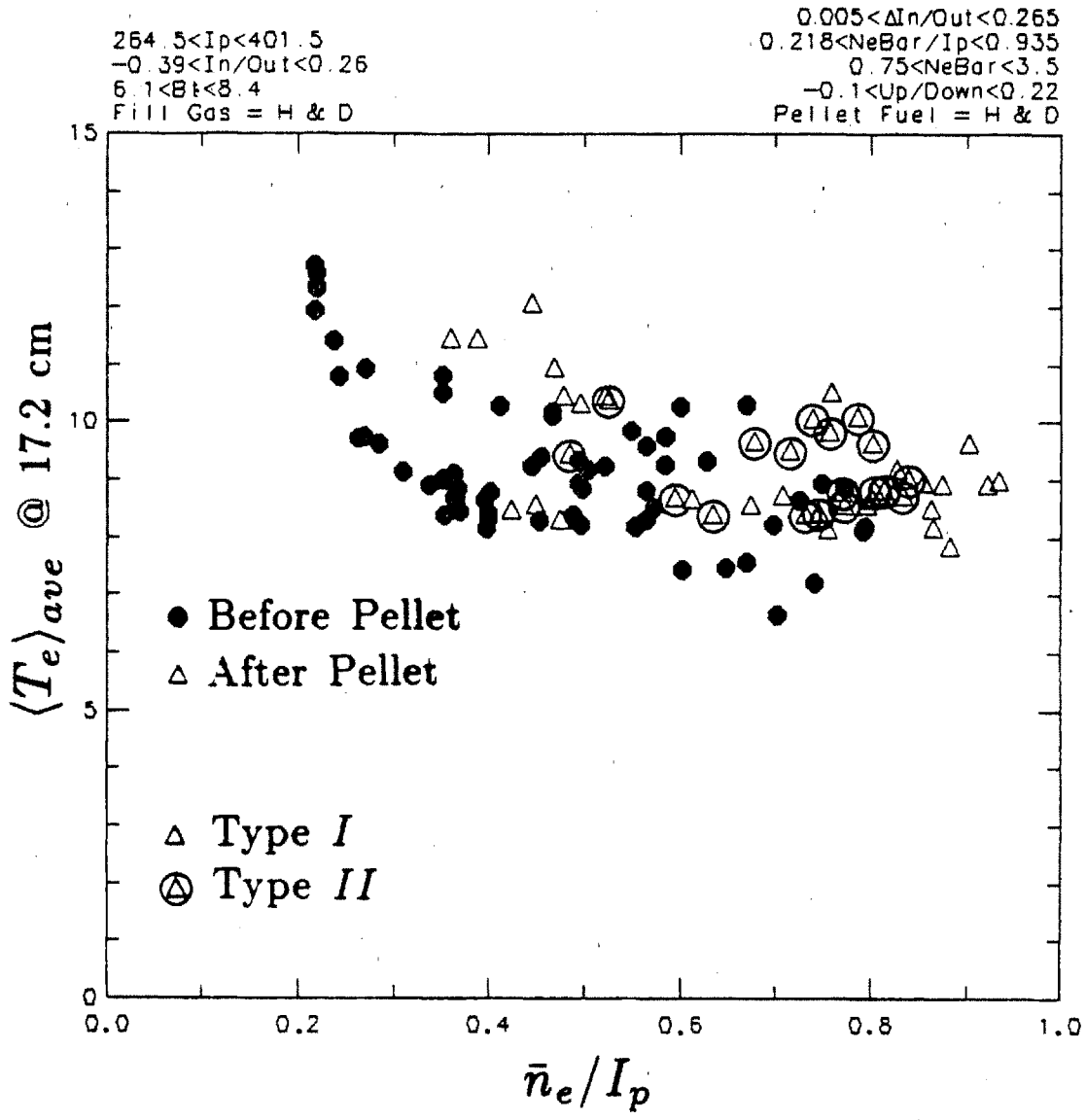

Figure 10.8 Poloidally Averaged, Inside Electron Temperature at $r = 17.2$ cm Before and After Pellet Injection vs. $\bar{n}_e/I_p$

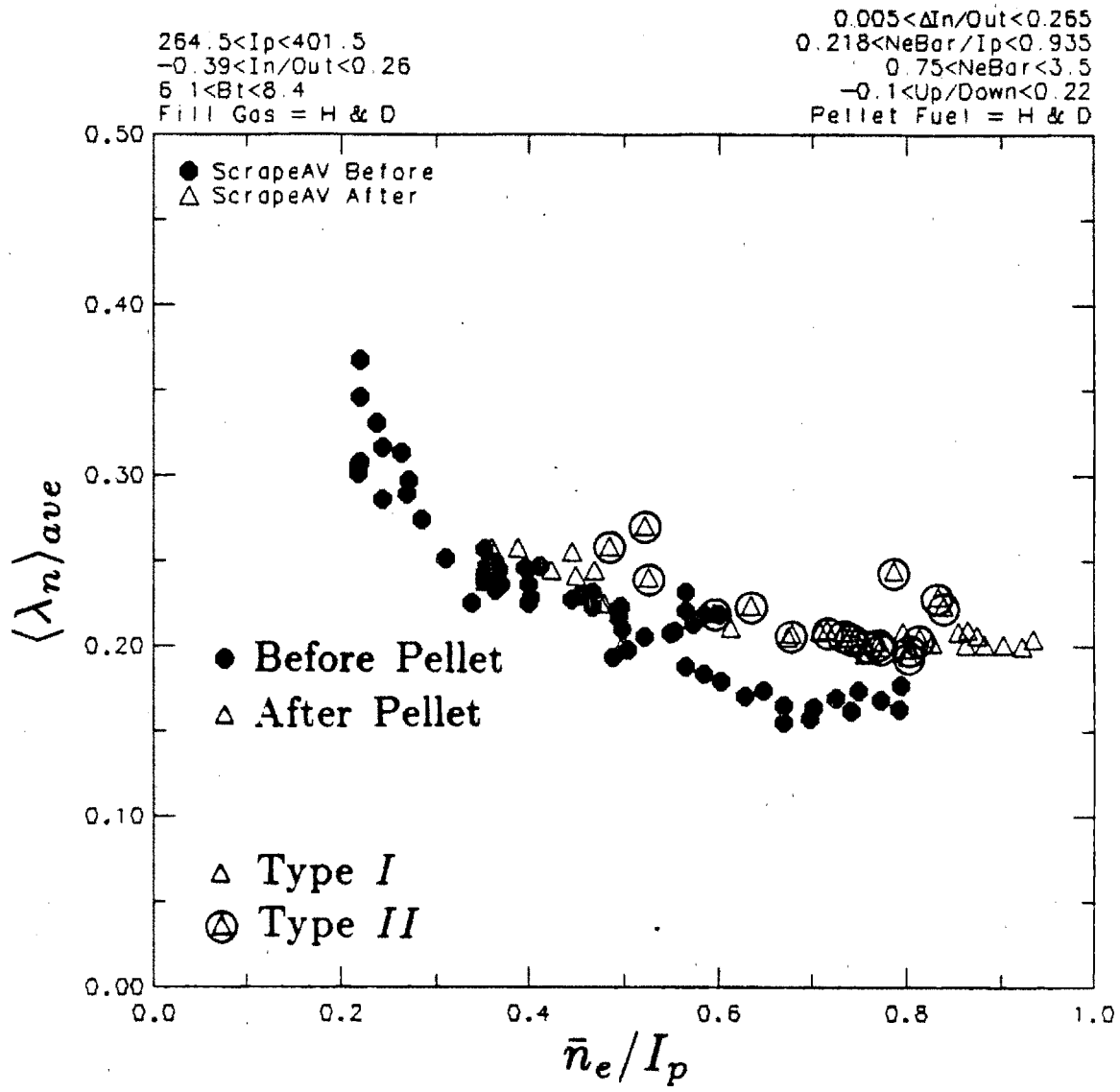

Figure 10.9 Poloidally Averaged, Inside Scrape-off Length Before and After Pellet Injection vs. $\bar{n}_e/I_p$

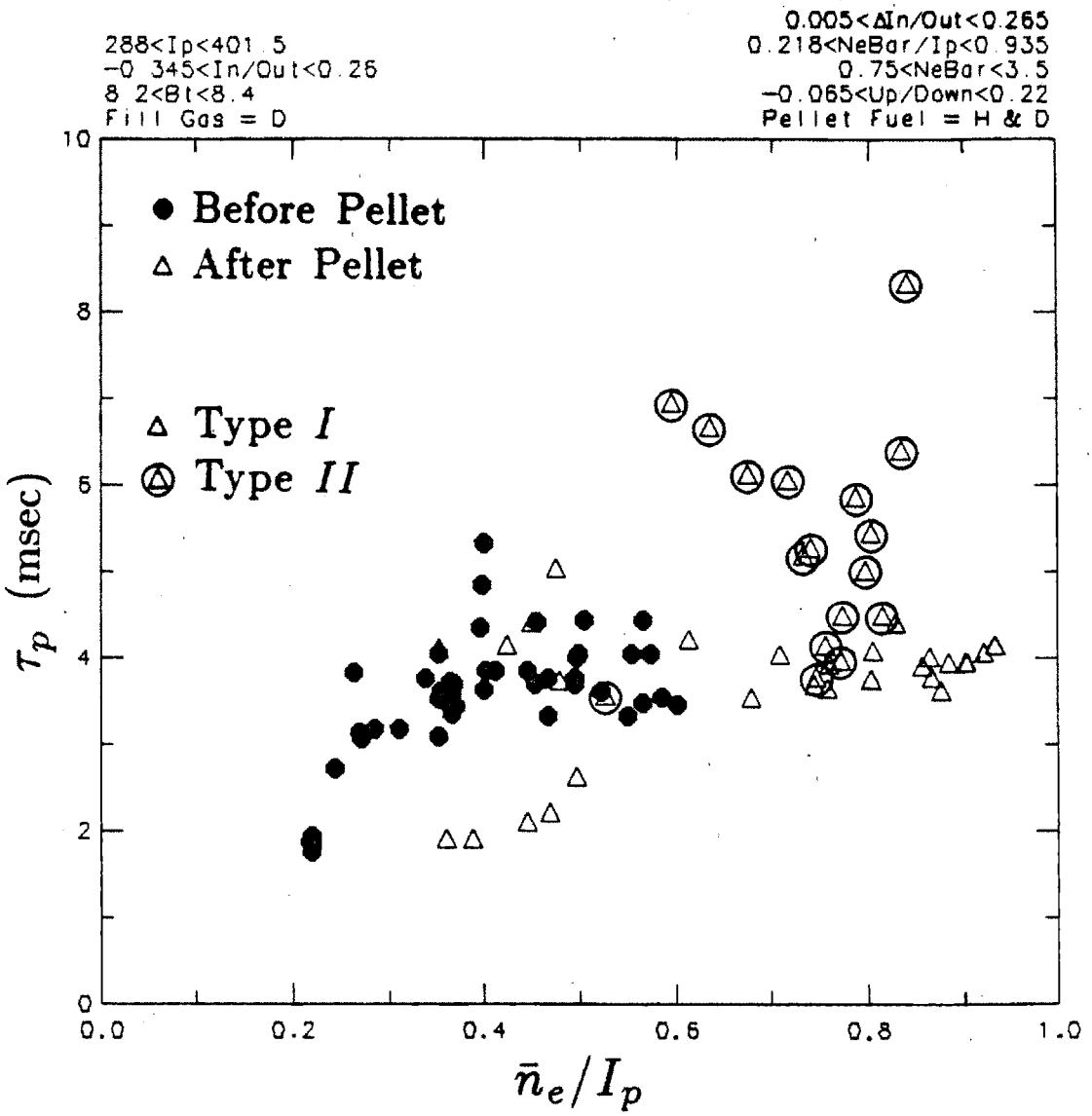

Figure 10.10 Global Particle Confinement Time Estimated from Inside Probes Before and After Pellet Injection vs. $\bar{n}_e/I_p$

10.2.3 Change in Particle Confinement Time versus Pellet Size

It is interesting that some pellet fueled discharges attain high particle confinement times while other discharges show no change. This type of threshold behavior has been detected in the change in central particle transport following a pellet injection.[115,116] It has been suggested that the pellet size relative to the target plasma density plays a role in determining whether or not the plasma attains the high central confinement mode.

With this idea in mind, the relative change in τ_p for the pellet fueled data points in Fig. 10.10 is plotted versus relative pellet size in Fig. 10.11. Here, relative pellet size is parameterized as $\Delta\bar{n}_e/\bar{n}_e$, the change in line-averaged density during pellet injection normalized to the line-averaged density prior to pellet injection. As shown, the high τ_p mode is indeed accessible only to discharges with $\Delta\bar{n}_e/\bar{n}_e \gtrsim 1$. The relative increase in global particle confinement time exceeds 100% in some cases. No discharges with $\Delta\bar{n}_e/\bar{n}_e \lesssim 1$ attain the enhanced τ_p regime.

The observation of a reduced edge density and enhanced particle confinement time when $\Delta\bar{n}_e/\bar{n}_e \gtrsim 1$ for pellet fueled discharges is also consistent with observations of central density profiles. When $\Delta\bar{n}_e/\bar{n}_e \gtrsim 1$, the density profile becomes more peaked following pellet injection.[117] The radial dependence of the central density profile for these cases can be described by Eq. 3.20 with $\gamma \approx 0.5$ prior to pellet injection (gas fueled profile) and γ approaching ~ 2 following pellet injection. This observation of peaked density profiles agrees with the measurement by DENSEPACK of an edge density that is lower after pellet injection than would be expected with gas puffing alone.

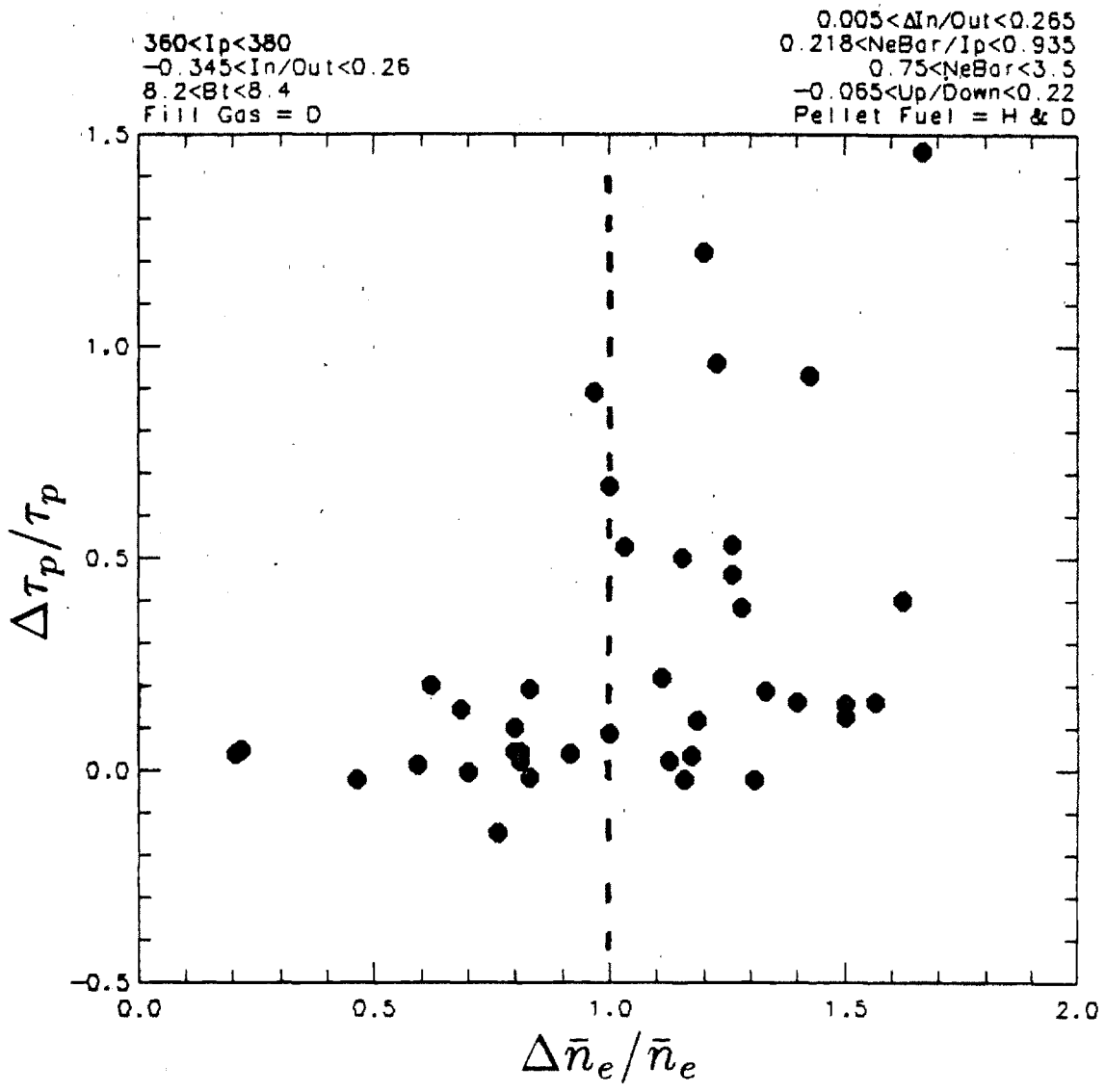

Figure 10.11 Relative Change in Global Particle Confinement Time Before and After Pellet Injection vs. Relative Pellet Size

The fact that γ changes during pellet injection adds some uncertainty to the estimate of τ_p from DENSEPACK data. Equation 9.3 accounts for the total inventory of particles in the plasma by modelling the density profile as a parabola to some power, γ. A change in γ of $0.5 \rightarrow 2$ yields a decrease in τ_p of $\sim 25\%$ when all other quantities in Eq. 9.3 are held fixed. In order to estimate a lower bound on the change in particle confinement time during pellet injection, values of $\gamma \approx 0.5$ prior to pellet injection and $\gamma = 2$ after pellet injection were used to compute confinement times for those discharges which showed an increased τ_p. Thus, the changes in τ_p displayed in Figs. 10.10 and 10.11 represent lower limits and may be higher if the actual central profile is flatter than is assumed ($\gamma < 2$).

CHAPTER 11

MARFES

A primary goal of the DENSEPACK probe experiment was to study the temporal and spatial evolution of the MARFE phenomena in Alcator C edge plasma. However, strong poloidal asymmetries were detected by the DENSEPACK probe array independently of the occurence of a MARFE. The MARFE was detected in the shadow plasma as only a relatively slight perturbation to this already poloidally asymmetric equilibrium. As a result, the main focus of the edge plasma study using DENSEPACK probes shifted from examining MARFEs to studying the dominant, poloidal asymmetries in density and temperature and identifying mechanisms which might support such asymmetries (chapters 7–8). This chapter now returns to the topic of MARFEs in Alcator C and examines edge plasma parameters measured by DENSEPACK within this radiating plasma region located on the inside of the torus.

At this point in this thesis, the difference between MARFE and non-MARFE discharges as detected by the DENSEPACK array has only been presented in terms of the transition between edge versus central plasma parameter scalings above $\bar{n}_e/I_p \approx 0.6$ (chapter 9). As shown in the previous chapter, pellet injection can cause an initially MARFE-free discharge to enter the MARFE regime. Pellet injection therefore provides a means of studying the difference in edge parameters with and without a MARFE in a single discharge. Section 11.1 makes use of pellet injection to examine edge plasma parameters detected by the inside segment of DENSEPACK during a MARFE. A slight rearrangement of the poloidal density asymmetry was found to occur. This led to an increase in plasma density and scrape-off length near the usual, upper-inside MARFE location. Thus, the single Langmuir probe measurements reported earlier in section 4.4.3 were reproduced by the DENSEPACK probe array.

Section 11.2 introduces a new edge plasma phenomenon, a 'MARFE oscillation', which is simultaneously detected by the DENSEPACK probe array and the H_α camera system (described in section 5.2). During reversed toroidal field operation, some discharges displayed a MARFE with a clear ~ 265 Hz up-down oscillation in the H_α brightness profile. This 'MARFE oscillation' provided a unique opportunity to correlate changes in H_α emission with changes in density and temperature in this 'moving' MARFE region. It was found that a local density increase and temperature decrease corresponded to a local enhancement in H_α emission, consistent with a radiation thermal instability model for MARFE formation (section 2.5.3).

The fact that this radiating plasma region was found oscillate in up-down position implies that local particle and energy transport to the MARFE changed as the MARFE evolved. A simple model is that a local thermal instability initially grows but is quenched after a period of time and causes an adjacent plasma region to become unstable. The timescale for this relaxation process (~ 2 msec) and spatial amplitude of the radiating region ($\sim$ 17 cm) suggests that perpendicular transport is important in defining the MARFE boundary.

Finally, section 11.3 includes some closing remarks on asymmetries and MARFE phenomena in Alcator C and other tokamaks.

11.1 Density Asymmetry of MARFE versus Non-MARFE Discharges

11.1.1 Inside Edge Density Before and After Pellet-Induced MARFE

Pellet injection can cause the edge plasma of Alcator C to change abruptly from a non-MARFE state to a MARFE state. This effect was used to examine the edge plasma during MARFE and non-MARFE conditions in a single discharge.

Figures 11.1 and 11.2 plot the time evolution of edge plasma density sampled at $r = 17.2$ and $r = 17.6$ cm by the inside probes of the DENSEPACK array during a pellet-induced MARFE. Density versus time and poloidal angle is represented as both a three-dimensional surface and a contour plot in the top half of Figs. 11.1 and 11.2. The schematic drawing of DENSEPACK in the lower left corner shows which probes were active during the data collection (solid dots). Profiles of density versus poloidal angle at $t = 220$ msec and $t = 280$ msec are shown in the lower right corner. Central plasma parameters are $\bar{n}_e \approx 2.2 \times 10^{14}/\text{cm}^3$ before and $\bar{n}_e \approx 3.7 \times 10^{14}/\text{cm}^3$ during the MARFE with $I_p \approx 375$ kA, $B \approx 8$ tesla in a deuterium discharge.

Pellet injection and the subsequent MARFE activity occurs at $t = 250$ msec as indicated on the contour plots. This MARFE displays exactly the same characteristics as a gas fueled MARFE previously discussed in section 4.4. The MARFE turns on abruptly as the central $\bar{n}_e/I_p$ value increases suddenly from $\bar{n}_e/I_p \approx 0.58$ to $\bar{n}_e/I_p \approx 0.98$ (database units) and remains present for the remainder of the discharge.

Independent of the MARFE, the edge density profiles exhibit the usual strong poloidal asymmetry: density maxima near the top ($\theta \approx 250^0$) and bottom ($\theta \approx 115^0$) of the poloidal cross section and a density minimum near the inside midplane ($\theta \approx 180^0$). For this particular discharge, the peak densities near the top are uniformly higher than those near the bottom. However, this up-down asymmetry is much larger than is typically observed with the full array and with poloidally symmetric ring limiters installed (chapter 7). This apparent up-down

asymmetry may be due to uncertain probe area or to the poloidally asymmetric limiters which were installed for this set of experiments (configuration 'B' in Fig. 5.4).

During the MARFE, the poloidal edge density profile is perturbed from the pre-MARFE structure. A reduction in plasma density occurs on probes sampling near the top location at the start of the MARFE and remains for the duration of the MARFE. At the same time, an increase in plasma density is observed near $\theta \approx 205^0$ on the $r = 17.2$ and particularly $r = 17.6$ cm probes. This is the same location where the enhanced H_α emission associated with the MARFE was observed.

This 'filling in' of the poloidal density asymmetry at large minor radii during the MARFE results in a local increase in the density scrape-off length (λ_n). Figure 11.3 shows this more clearly by plotting the poloidal variation of λ_n versus time in the same format that density was previously shown. A 'bump' in the scrape-off length at $t \gtrsim 250$ msec is seen near $\theta \approx 205^0$, corresponding to the MARFE location. A larger increase in λ_n occurs for $t \gtrsim 360$ msec which can be attributed to an 'end of shot' MARFE which is typically seen in Alcator C discharges. At this time, the plasma current begins to ramp down, $\bar{n}_e/I_p$ increases, and the MARFE region expands to fill the entire inside region of the edge plasma.

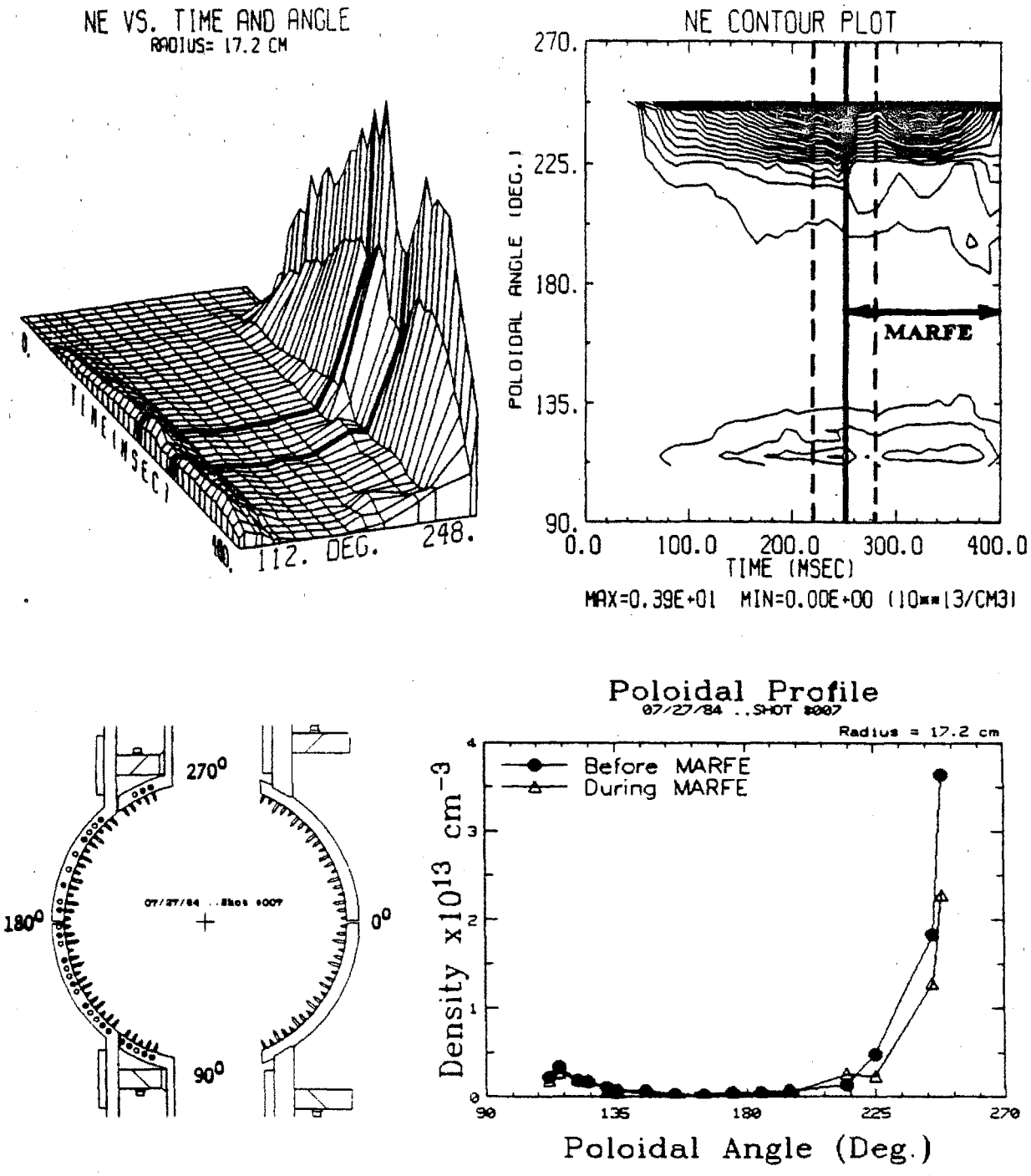

Figure 11.1 Inside Edge Density at $r = 17.2$ cm vs. Time and Angle During Pellet-Induced MARFE

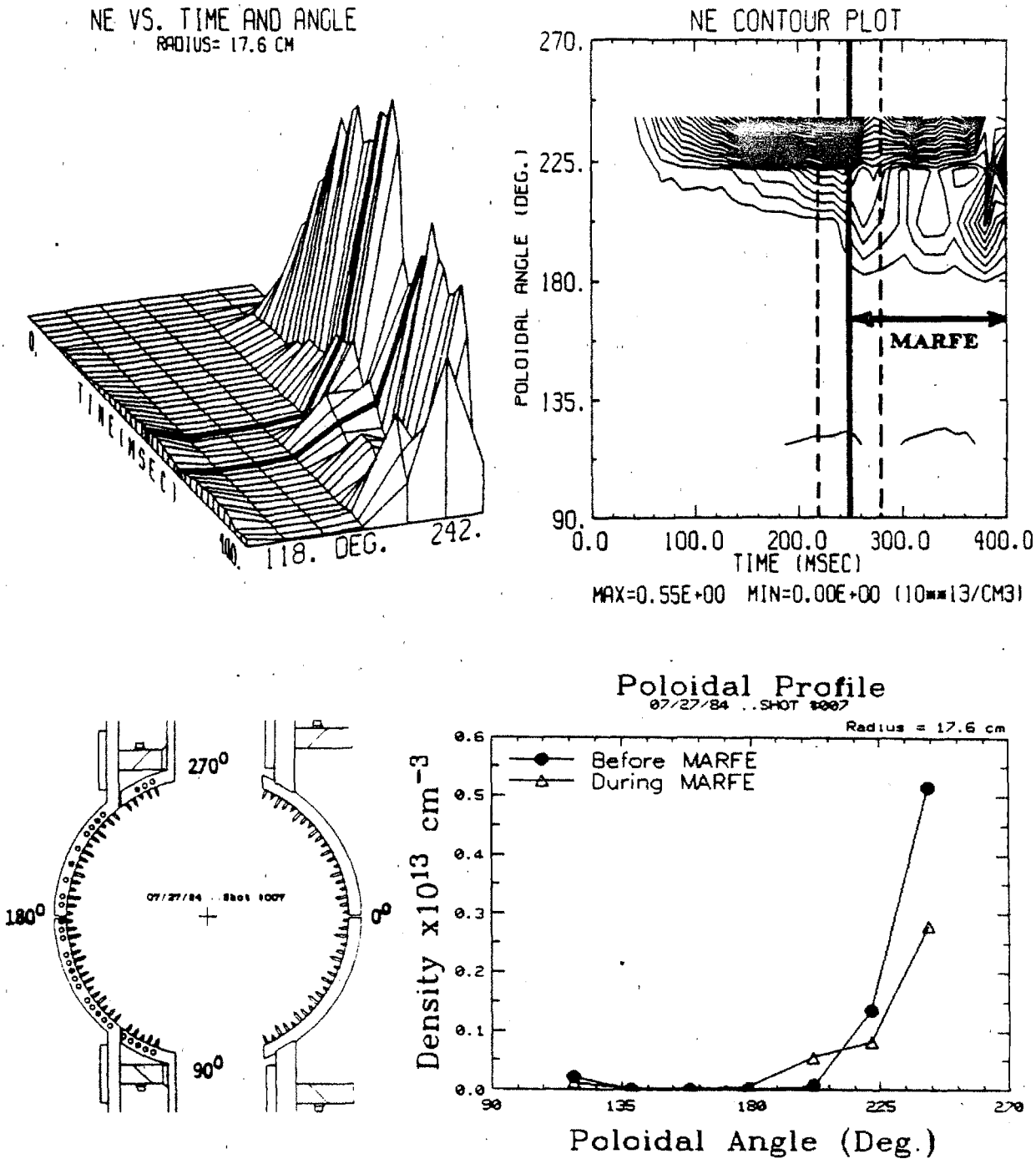

Figure 11.2 Inside Edge Density at r = 17.6 cm vs. Time and Angle During Pellet-Induced MARFE

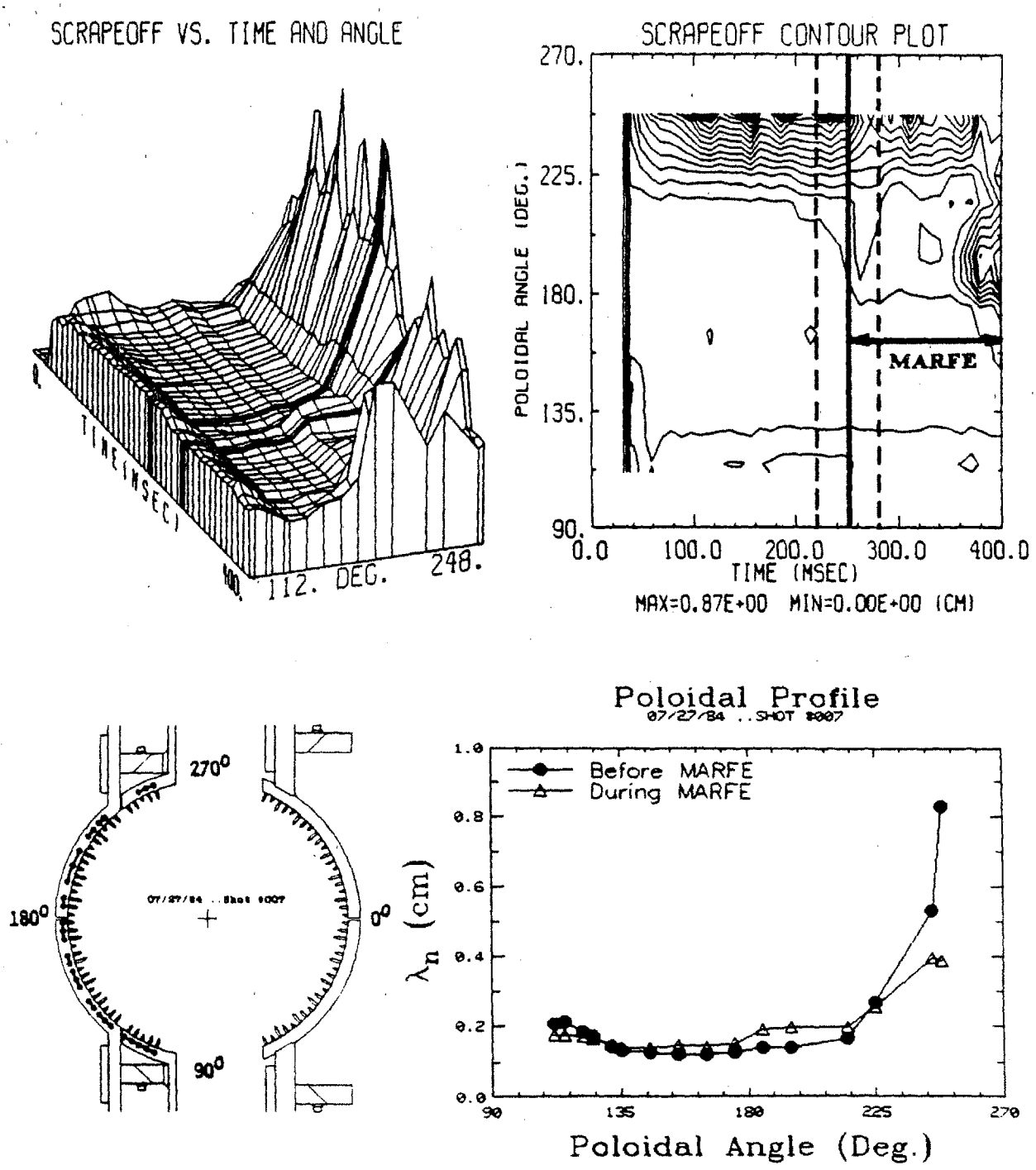

Figure 11.3 Inside Scrape-off Length vs. Time and Angle During Pellet-Induced MARFE

11.1.2 Comparison of DENSEPACK Data with Single Probe Data

These observations of density decreasing near the top of the poloidal cross section and increasing at large minor radii in the MARFE region is consistent with the early single Langmuir probe measurements of MARFEs in Alcator C.[2,72] At that time, probes at the top location detected a 'density depletion' during the MARFE while a probe in the MARFE region ('MARFE probe', section 4.4.3) detected a density increase.

The increase in density scrape-off length detected by DENSEPACK in the MARFE region is also consistent with the probe results reported in section 4.4.3. The MARFE probe measured an increase in λ_n from $\sim$ 0.25 cm to $\sim$ 0.41. In comparison, the inside probes on DENSEPACK measured an increase in λ_n from $\sim$ 0.15 cm to $\sim$ 0.20 cm for the MARFE displayed in Figs. 11.1–11.3 before the current ramp down. During current ramp down, λ_n exceeded $\sim$ 0.4 cm. Unfortunately, molybdenum limiters were used during the MARFE probe experiments while silicon carbide coated carbon limiters were used during the DENSEPACK probe experiments. Since edge impurities play a major role in power balance of a MARFE, it is not expected that the same edge conditions are accurately reproduced with such different limiter materials. Nevertheless, the general features of the MARFE detected by DENSEPACK were found to agree qualitatively with earlier probe measurements.

11.2 MARFE Oscillations

During a number of discharges with reversed toroidal field, the up-down position of the maximum H_α brightness associated with a MARFE was found to oscillate with poloidal displacement of approximately $\pm 30^0$ about the inside midplane. Figure 11.4 shows the time evolution of plasma current (a), central line-averaged density (b), inside line-averaged density (-12.0 cm vertical chord) (c), and total H_α brightness (spatially unresolved) (d) during a discharge which exhibited this 'MARFE oscillation'. The usual signature for the start of a MARFE occurs near $t = 120$ msec. The MARFE oscillation appears at $t = 220$ msec and is seen as a modulation of the total H_α emission (trace d). No MHD activity was correlated with this oscillation. Oscillations in loop voltage and plasma positioning circuits (from power supply regulation, typically 360 Hz) also did not correlate with the frequency of the MARFE oscillation, $f \approx 265$ Hz.

The central plasma parameters which lead to a MARFE oscillation are identical to those needed to form a stationary MARFE (section 4.4). The stationary MARFE formed first when $\bar{n}_e/I_p$ exceeded ≈ 0.6. As $\bar{n}_e/I_p$ was increased further, an oscillating MARFE region occurred. It is not clear why some discharges display this oscillation while other discharges do not. However, these oscillations are only observed during reversed toroidal field operation which indicates that subtle differences in outer flux surface shape may be an important factor. (Outer flux surfaces tend to be slightly 'D' shaped in reversed toroidal field operation.[77,118])

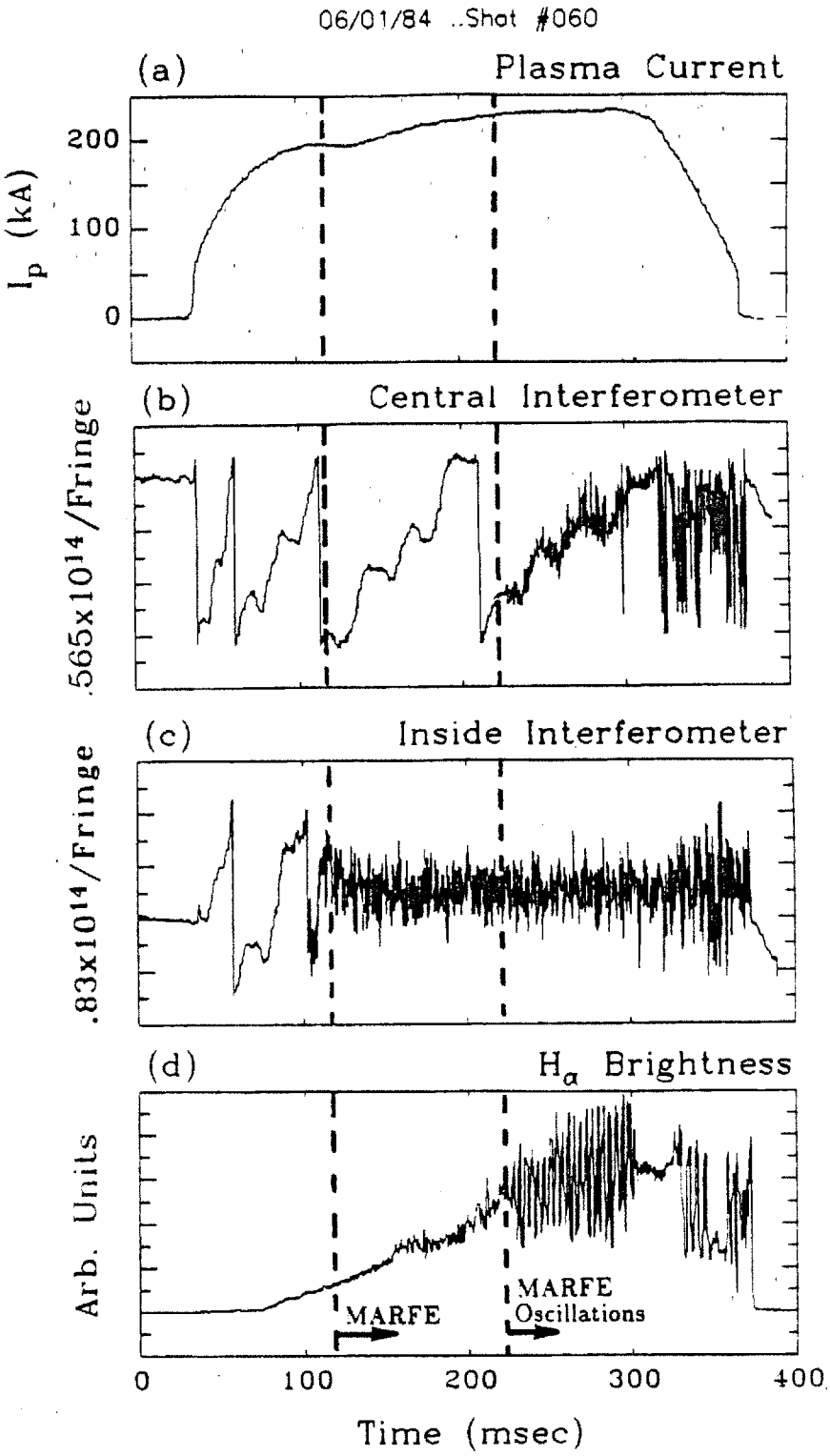

Figure 11.4 Time History of Central Plasma Density, Plasma Current, and H_α Brightness During a 'MARFE Oscillation' Discharge

11.2.1 Oscillation in Up-Down H_α Brightness Profile

The modulation in the total H_α emission in Fig. 11.4 (*d*) coincides with an up-down oscillation in the H_α brightness profile. Figure 11.5 shows the plasma volume viewed by the H_α camera system (*a*) and the corresponding H_α brightness profile (*b*) at two sample times during a MARFE oscillation. The H_α camera was positioned to view plasma along horizontal chords at the same toroidal location that the DENSEPACK array was installed. The view of channels 1 and 16 was slightly obstructed by the window geometry. Thus, the data points obtained by these channels are systematically lower and more sensitive to stray light.

Normally, a stationary MARFE is evident as a vertical H_α brightness profile similar to Fig. 4.6*b* for forward toroidal field operation and to the solid circle trace in Fig. 11.5*b* for reversed field. During a MARFE oscillation, the vertical H_α brightness profile oscillates between the solid and open circle traces in Fig. 11.5*b*. Thus, the enhanced H_α emission associated with the MARFE region moves in poloidal angle, past probes on the DENSEPACK array.

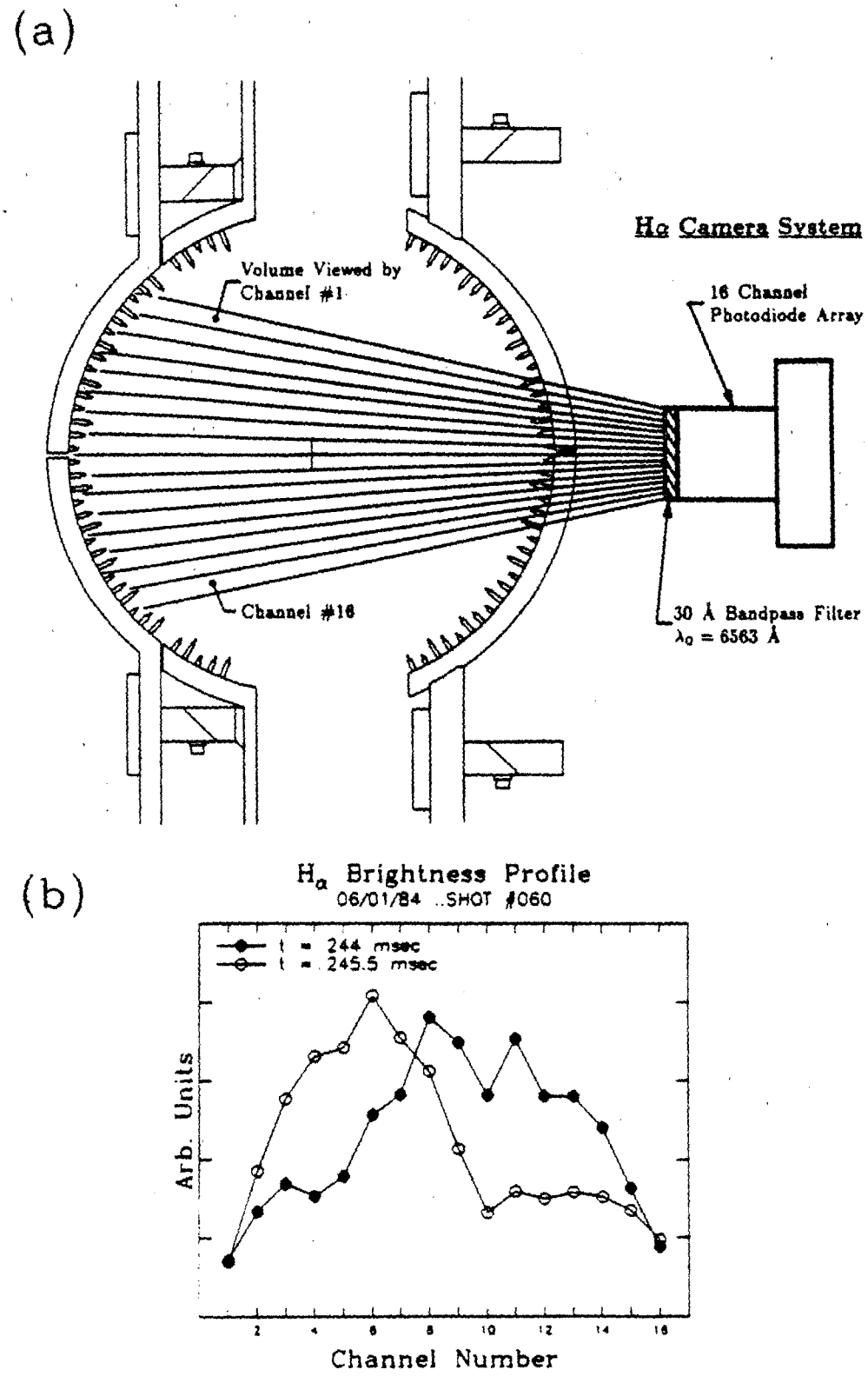

Figure 11.5 Plasma Volume Viewed by H_α Camera System and Typical Brightness Profiles During a MARFE Oscillation

11.2.2 Correlation of H_α Brightness with DENSEPACK Signals

With the DENSEPACK probe array and H_α camera system operating simultaneously, a correlation of changes in H_α light emission with changes in ion saturation currents can be made during the MARFE oscillation. To facilitate this comparison, the following quantities are computed from the spatial and temporal H_α brightness, $S(\theta,t)$, and DENSEPACK ion saturation currents, $J(\theta,t)$:

$$\frac{\Delta S}{\bar{S}} = \frac{S - \bar{S}}{\bar{S}} \tag{11.1}$$

$$\frac{\Delta J}{\bar{J}} = \frac{J - \bar{J}}{\bar{J}} \tag{11.2}$$

where $\bar{S}$ and $\bar{J}$ are the time average of S and J over some interval. Thus, $\Delta S/\bar{S}$ and $\Delta J/\bar{J}$ represent the relative change in H_α brightness and ion saturation current about their mean values. With the steady state background in S and J removed, $\Delta S/\bar{S}$ and $\Delta J/\bar{J}$ readily show perturbations about the time averaged, poloidally asymmetric equilibrium.

Figures 11.6 and 11.7 plot 3-D surfaces of $\Delta S/\bar{S}$ and $\Delta J/\bar{J}$ versus time and angle for a 10 msec portion of a MARFE oscillation. $\bar{S}$ and $\bar{J}$ are computed over this same 10 msec interval.

The diagram in the lower left corner of Fig. 11.6 indicates the plasma region over which the changes in H_α signal were detected (cross-hatched region). The contour plot in this figure shows an oscillation of H_α brightness in poloidal angle and time. Solid contours correspond to positive values of $\Delta S/\bar{S}$ and dashed contours correspond to negative values. Poloidal profiles of $\Delta S/\bar{S}$ are shown at $t = 243.5$ and $t = 245.5$ msec. The MARFE oscillation appears as a clear oscillation in $\Delta S/\bar{S}$ with a frequency of $f \approx 265$ Hz.

A similar picture is constructed for $\Delta J/\bar{J}$ in Fig. 11.7. Relative changes in ion saturation current show a pattern that is nearly identical to the relative

changes in H_α emission. Again the frequency of oscillation is ~ 265 Hz; however, maxima and minima in $\Delta J/\bar{J}$ do not exactly coincide with maxima and minima in $\Delta S/\bar{S}$.

A change in ion saturation current can arise from a change in local plasma density and/or a change in electron temperature. In order to unfold these two contributions, it was necessary to sweep the DENSEPACK probes at a frequency which was faster than the frequency of MARFE oscillation. For a limited number of discharges, the DENSEPACK array was driven with a 5 kHz triangle voltage waveform spanning +30 to −60 volts. A Langmuir probe characteristic was thereby obtained every 100 μsec and recorded for a total of 8 msec by the 1 MHz data loggers. Pairs of positive-ramping and negative-ramping characteristics were combined and fitted using the simple exponential model (section 6.3.4). In this manner, displacement currents due to any stray capacitances were effectively averaged out. The result was an estimate of plasma density and electron temperature every 200 μsec.

Figure 11.8 shows the time evolution of plasma density (*b*) and electron temperature (*c*) obtained in this manner for a single probe of the DENSEPACK array during a MARFE oscillation. H_α brightness on a horizontal chord that terminates near the probe is also displayed (*a*). This figure shows that the increase in H_α brightness corresponds to a local increase in plasma density and decrease in electron temperature. Thus, the radiation thermal instability model for MARFE formation is borne out in this analysis of the MARFE oscillations. A local increase in edge radiation is indeed coincident with an increase in density and decrease in temperature. This radiation can, in turn, locally cool the plasma. Inferred electron temperatures of 7–14 eV correspond to those values needed for the radiation thermal instability to develop.

The density and temperature data in Fig. 11.8 also indicates that the local electron pressure is not constant during the MARFE oscillation. At the maximum in H_α brightness, the electron pressure is $n_e T_e \approx 2.4\text{–}3.1\times10^{13}\text{eV/cm}^3$.

while during the minimum in H_α brightness, $n_e T_e \approx 2.0$–$2.2 \times 10^{13} \mathrm{eV/cm^3}$. This corresponds to an average electron pressure increase of $\sim 30\%$ during the H_α increase. Thus, the MARFE oscillation cannot be simply explained in terms of a radiatively cooling plasma with $n_e T_e \approx const.$ Other effects such as parallel and perpendicular transport must be considered. These processes may ultimately determine the oscillation frequency and spatial extent of the MARFE oscillation.

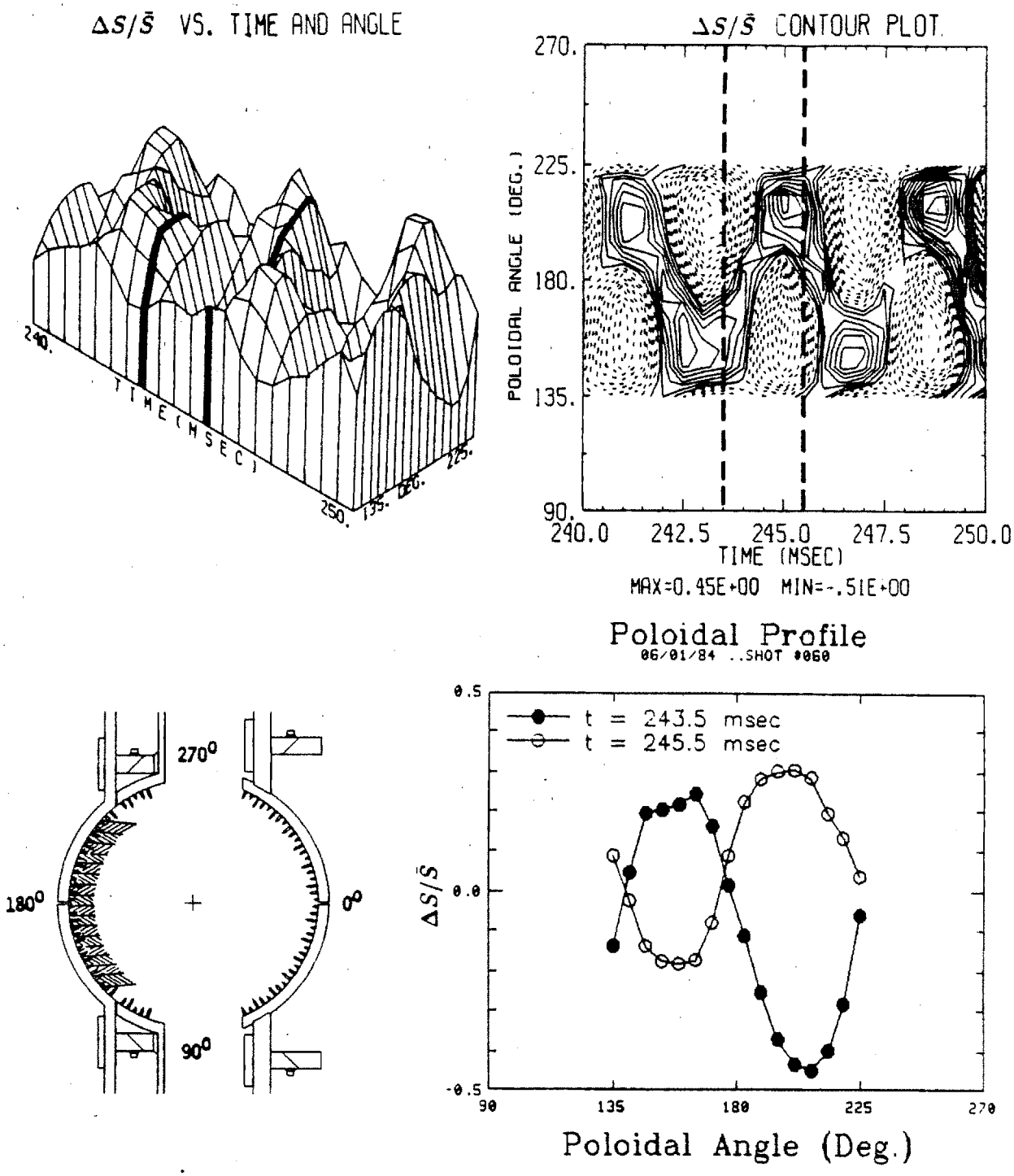

Figure 11.6 Normalized Deviation in H_α Brightness vs. Time and Angle During a MARFE Oscillation

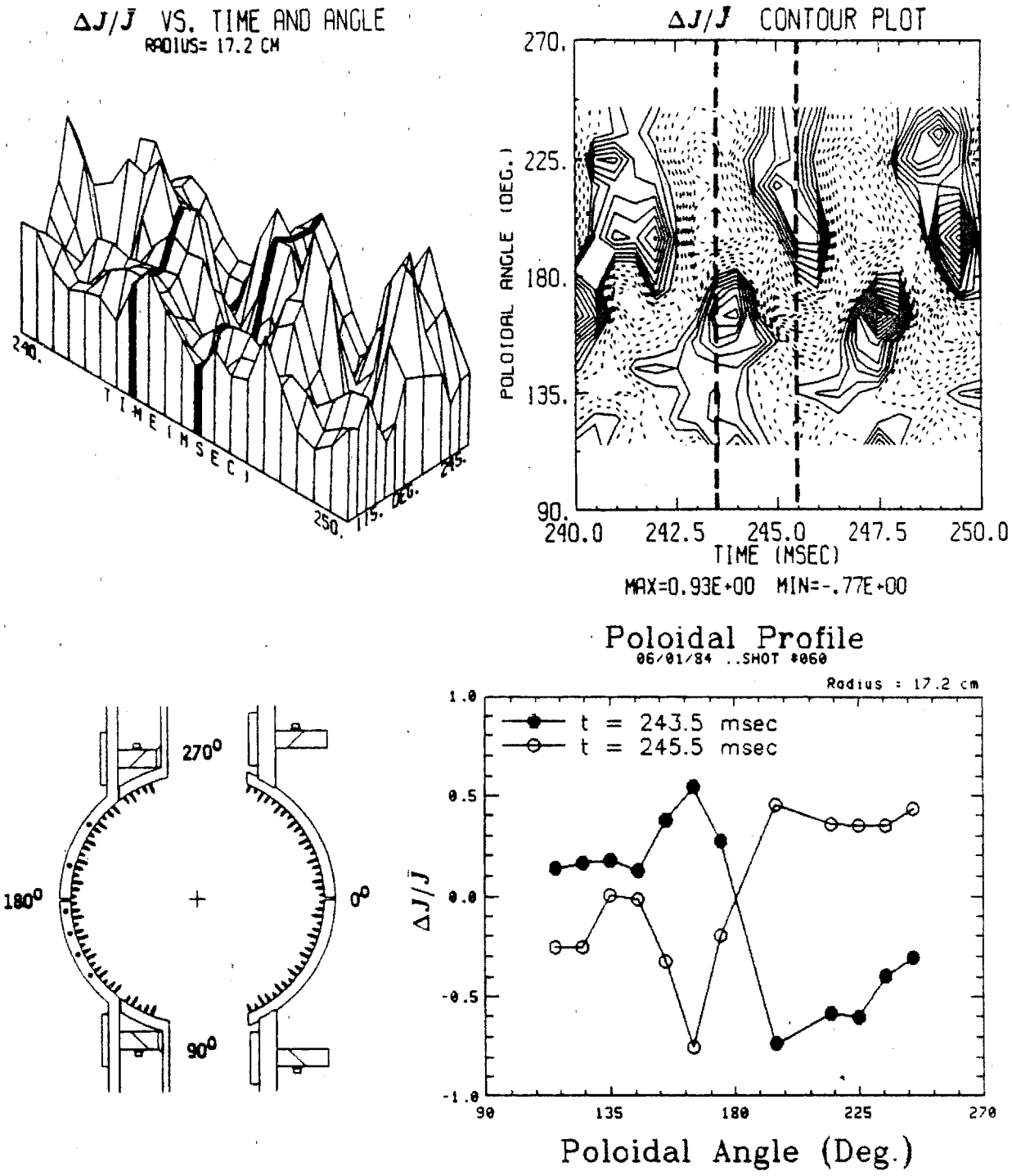

Figure 11.7 Normalized Deviation in Ion Saturation Current vs. Time and Angle During a MARFE Oscillation

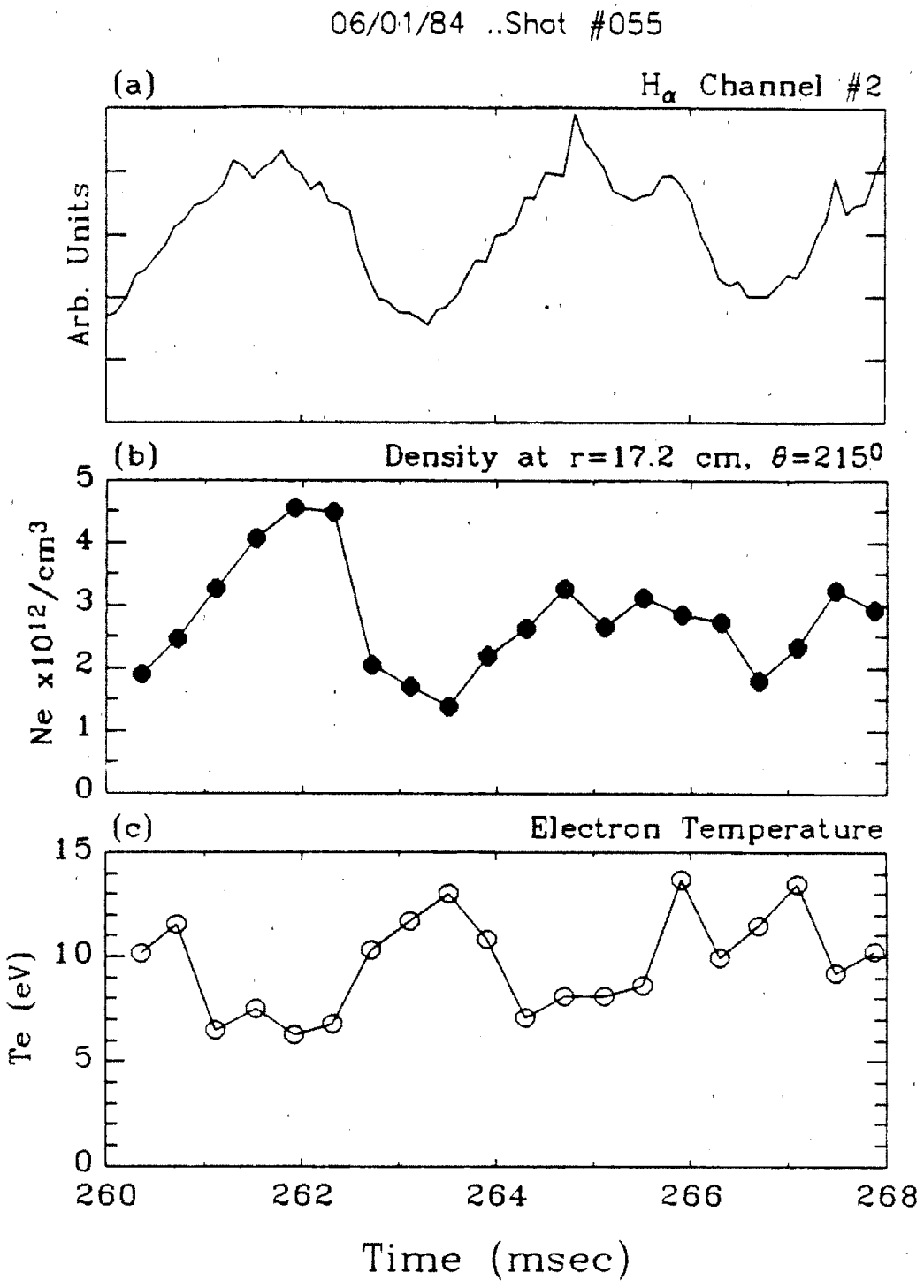

Figure 11.8 Time Evolution of Local H_α Brightness, Plasma Density, and Electron Temperature During a MARFE Oscillation

11.2.3 MARFE Oscillation and Edge Plasma Transport Times

During a MARFE oscillation, the MARFE region moves from the $\theta \approx 210^0$ to $\theta \approx 150^0$ location in $\tau \approx 2$ msec. This characteristic time can be compared to other transport times in the edge plasma of Alcator C.

One possibility is that the MARFE oscillation is made up of adjacent flux tubes that become successively unstable. For a given flux tube, the radiation thermal instability might develop at some point along its length. As the temperature suddenly drops, particles and energy would be convected along field lines, quenching the instability. At the time of recovery, an adjacent flux tube could begin its cycle. Thus, the radiating region might appear to propagate in poloidal angle but may actually be composed of many independently acting flux tubes.

The characteristic time for this relaxation process would be the transit time of sound speed flow along a flux tube or

$$\tau_{transit} \approx \frac{\Delta Z}{C_s} \tag{11.3}$$

where ΔZ is the parallel distance that particles must travel. However, even when $\Delta Z \approx 100$ cm, $\tau_{transit} \approx 25$ μsec. Thus, this relaxation process is much too fast to account for the observed oscillation.

Another possibility is that the boundaries of the MARFE region are defined by some spatially dependent perpendicular transport that changes in time. If the radial diffusion and/or convection flux of particles and energy depends on poloidal angle, then a preferred position for instability might develop. The position of this MARFE region would simply depend on the poloidal structure of this radial transport at a particular point in time. However, there is currently no data to support or refute this hypothesis.

Finally, poloidal convection could also affect the position of the MARFE boundary. As shown in section 7.2.4, poloidal $\underline{E} \times \underline{B}$ convection can be on the

order of $\underline{V}_\theta \approx 2 \times 10^4$ cm/sec in the limiter shadow plasma. A MARFE moving $\sim 60^0$ in 2 msec implies a poloidal velocity of

$$\underline{V}_\theta \approx \frac{\Delta\theta\ a}{\tau} \approx 9 \times 10^3 \quad \text{cm/sec} \tag{11.4}$$

at the limiter radius. Thus, the timescale of the MARFE oscillation is within the range of transport times expected from poloidal $\underline{E} \times \underline{B}$ fluxes.

11.3 Comments on MARFEs and Poloidal Asymmetries

When MARFE phenomena were first detected on Alcator C,[3] it was suspected that a low temperature, high density, radiating plasma region was forming as a result of a radiation thermal instability. A model of the MARFE was first proposed as a localized, low temperature plasma region satisfying $nT = const.$ on a flux surface.[2] In this way, the formation of a high density plasma which could refract the inside laser interferometer beam could be explained.

A picture for the MARFE presented at that time was a toroidal band of high density, low temperature plasma forming at the upper-inside position of the poloidal cross-section. The fact that the MARFE formed at this poloidal position was attributed to asymmetries in impurity concentrations and/or heat fluxes from the central plasma.[5] Thus, it was expected that in the absence of a MARFE, the edge plasma would exhibit poloidal symmetry in density and temperature. During a MARFE, a strong poloidal asymmetry was expected to develop.

The DENSEPACK probe experiment has since yielded much more information about the edge plasma in Alcator C and has led to a clearer picture of MARFEs and edge plasma poloidal asymmetries. The MARFE was found to be a result rather than a cause of asymmetries in the edge plasma. Perpendicular transport in the limiter shadow region was inferred by DENSEPACK to be higher at the larger major radius edge of the plasma and lower at the smaller minor radius edge. Thus, the hypothesis of a preferentially cooler, MARFE-prone plasma region existing at the upper-inside poloidal location is verified by this experiment. Futhermore, the density at the limiter radius was found to be strongly poloidally asymmetric, independent of a MARFE. In fact, a MARFE was detected as a relatively weak poloidal perturbation. Flux surface pressure asymmetries were found to be always present. This suggests that the toroidally symmetric character of the MARFE was due to an entire edge plasma that was poloidally asymmetric yet toroidally symmetric. The existence of such an edge

plasma requires that perpendicular transport fluxes dominate over parallel transport fluxes, a condition that can be satisfied in the edge plasma.

MARFE phenomena are now being reported on most current day tokamaks. As the plasma density is raised above some threshold, the edge plasma first 'lights up' somewhere on the smaller major radius edge of the plasma. Raising the density further causes a larger MARFE region until this radiating plasma completely engulfs the entire plasma, defining the tokamak density limit. Thus, it appears that strong poloidal asymmetries in perpendicular transport of the edge plasma exist universally in tokamaks.

IV. SUMMARY

CHAPTER 12

THESIS SUMMARY & SUGGESTIONS FOR FUTURE WORK

The primary focus of this thesis was on the measurement and analysis of poloidal asymmetries in the Alcator C limiter shadow plasma. An edge plasma diagnostic system consisting of a poloidal array of 80 closely spaced Langmuir probes (DENSEPACK) was developed to record spatial variations in plasma parameters over the entire poloidal extent (360^0) of the edge plasma in the Alcator C tokamak. However, during the course of this thesis, a number of other topics relevant to the study of edge plasma were investigated.

Section 12.1 summarizes the topics which were covered and the major results which were obtained during this study. This section is divided into three subsections: *Introduction & Background, Experimental Apparatus & Data Reduction*, and *Experimental Results*, corresponding to the major divisions under which this thesis was organized.

Section 12.2 points to some of the limitations that were encountered during this work. Possible avenues of approach for further studies are identified.

12.1 Thesis Summary

12.1.1 Summary: *Introduction & Background*

As an introduction to the physics of a tokamak edge plasma, the topics of electric sheath formation, plasma-surface interactions, perpendicular transport processes, and radiation processes were reviewed. The edge plasma conditions necessary for the onset of a radiation thermal instability (MARFE) were derived. A brief summary of typical edge plasma parameters measured in a number of tokamaks was presented.

Generally, the radial density profile in the limiter shadow region of tokamaks follows an exponential law. A simple radial diffusion model which predicts an exponential density profile in radius was therefore presented. A relationship between the radial density e-folding length (scrape-off length), neutral density, electron temperature, and perpendicular diffusion coefficient was obtained. It was shown that the perpendicular diffusion coefficient ($D_\perp$) can be simply related to the density scrape-off length (λ_n), the connection length to limiter surfaces (L), and the plasma sound speed (C_s) through the formula

$$D_\perp \approx \frac{\lambda_n^2 \, C_s}{L} \tag{12.1}$$

when the edge neutral density in Alcator C is below $\sim 3 \times 10^{12}/\mathrm{cm}^3$. A relationship for the global particle confinement time in terms of the edge density, density scrape-off length, electron temperature, and central line-averaged density was also obtained from this model with the same restriction on the edge neutral density.

This simple radial diffusion model is lacking in that it predicts a poloidally and toroidally uniform edge plasma. Observations of MARFE phenomena and direct measurements of edge plasma parameters made during the course of this thesis indicate that the edge plasma in Alcator C is poloidally asymmetric. It

is recognized that poloidally asymmetric diffusion and/or convection may cause the limiter shadow plasma to depart from poloidal symmetry. Consequently, a special case fluid model of the limiter shadow plasma which includes diffusion and neoclassical Pfirsch-Schlüter convection was developed. It was found that both the density and temperature profile can be significantly perturbed from poloidal symmetry under the conditions of high plasma density (n) and low plasma current (I). A correlation was made between this simple asymmetry scaling in n and I, and with the observation of a similar n and I scaling for the threshold of MARFE formation in Alcator C.

In order to more carefully investigate transport in the edge plasma, a system of reduced, fluid transport equations appropriate for Alcator C edge conditions was identified. These continuity, momentum, and energy equations retained explicit convection terms and provided a more formal basis for estimating edge plasma transport from experimental data presented in subsequent sections of this thesis.

Finally, the introduction and background section of this thesis reviewed previous experimental observations of edge plasma in Alcator C. Asymmetric limiter damage, first probe measurements on Alcator C, and MARFE phenomena were reviewed. All these earlier observations pointed to the existence of a highly asymmetric edge plasma and motivated the development of the primary diagnostic used in this thesis, the DENSEPACK probe array.

12.1.2 Summary: *Experimental Apparatus & Data Reduction*

The primary edge diagnostic developed to record poloidal variations in Alcator C edge plasma parameters was an array of 80 closely spaced Langmuir probes (DENSEPACK). DENSEPACK consisted of three different length molybdenum probes mounted with ~ 1 cm spacing on a rigid stainless steel support ring. Plasma was thereby sampled at minor radii in the limiter shadow region of 16.8, 17.2, and 17.6 cm over a poloidal angular extent of 360^0. Data acquisition electronics allowed 30 probes to be operated simultaneously. The goal was to map out any poloidal variations in plasma density and temperature, particularly during those discharges which exhibited a MARFE event. Through the use of fast data loggers, this system was also used to look for large spatial scale fluctuation correlations between probes.

In a typical plasma shot, DENSEPACK generated over 100 Langmuir probe characteristics for each of the 30 data channels. Consequently, much effort was spent on developing a series of data processing programs to facilitate the fitting of many probe characteristics in a fast, reliable way.

Two models for the Langmuir characteristic were used. The first and simplest model uses one dimensional, non-magnetized probe theory to approximate the current collected along field lines by the DENSEPACK probes. However, data points obtained near electron saturation voltage biases had to be ignored since this model does not properly account for perpendicular electron diffusion into the collecting flux tube. Nevertheless, values for local electron density and temperature were most readily obtained by this model.

The second, more complicated probe characteristic model was employed, based on the work of Stangeby.[19] Here the full probe characteristic is used, and the diffusion limited electron saturation flux is taken into account by the introduction of an additional parameter, the reduction factor (r). A fast numerical algorithm was developed to iteratively fit this model to probe data and arrive at values for electron density, temperature, and reduction factor.

Fits of the simple plane probe model and the more complicated Stangeby model to the same probe data showed a discrepancy in the inferred electron temperature. The Stangeby model was found to systematically predict lower electron temperatures ($\sim 30\%$) than the plane probe model. At the same time that this thesis work was progressing, simultaneous measurements of electron temperatures at the same location were made in Alcator C using a retarding field energy analyzer and a Langmuir probe.[73,97] These data showed that the electron temperatures inferred by the plane probe model more closely agreed with electron temperatures inferred from the retarding field energy analyzer. Thus, the accuracy of electron temperatures obtained by the Stangeby model was questioned. In any case, both models were used to analyze DENSEPACK probe data.

12.1.3 Summary: *Experimental Results*

A. Poloidal Structure of Edge Plasma

A major result of the DENSEPACK probe experiment was that the edge plasma in Alcator C was found to be highly asymmetric independent of the occurence of a MARFE. Relatively high density and temperature plasma was detected on the top and bottom of the poloidal cross-section. The density scrape-off length was measured to be short ($\sim$ 0.15 cm) on the inside major radius edge of the torus and long ($\sim$ 0.8 cm) on the outside. The electron pressure was found to vary by a factor of $\sim$ 20 or more over poloidal angle at a fixed minor radius.

The probe floating potential was found to systematically depend on poloidal angle (θ). A $-sin\theta$ variation was typically recorded, consistent in sign and magnitude with charge separation in the edge plasma due to $\underline{B} \times \nabla B$ particle drifts.

The ion saturation current fluctuation spectrum ($S(\omega)$) obtained at various poloidal angles was also investigated. No systematic variation in the spectral shape of $S(\omega)$ or total power in the fluctuations was found with respect to poloidal angle. The probe spacing on the DENSEPACK probe array ($\sim$ 1 cm) was large compared to typical spatial correlation lengths for fluctuations ($\sim 2\pi/k_\perp \approx 6\pi\rho_s \approx 0.1$ cm).[14] As a result, a cross-correlation of probe signals did not reveal any significant coherence.

B. Mechanisms to Support Poloidal Asymmetry

The question of why the edge plasma should exhibit such a strong poloidal asymmetry arose. Independent of a MARFE event, the edge plasma in Alcator C was found to maintain a highly asymmetric structure. Five possible explanations for the measured asymmetry were investigated: 1) systematic errors in measurement due to incorrect installation of DENSEPACK and/or DENSEPACK perturbing the edge plasma, 2) noncircular magnetic flux surfaces, 3) spatially

dependent diffusion, 4) spatially dependent perpendicular convection, and 5) parallel plasma flows.

The possibility of systematic errors in the data set from an incorrect installation of DENSEPACK or from DENSEPACK perturbing the edge plasma was checked and eliminated.

At first, it was thought that the outer magnetic flux surfaces were noncircular so that plasma was being scraped off nonuniformly on the circular poloidal ring limiters. However, magnetic flux surface measurements clearly showed that this was not the case. The outer flux surfaces in Alcator C were measured to be very nearly circular. In reviewing previous probe measurements in the Alcator C edge plasma, it was found that edge plasma asymmetries detected at that time also violated magnetic flux surfaces, supporting this result.

The possibility that spatially dependent diffusion played a role in supporting the asymmetry was examined. Measurements of ion saturation current fluctuations ($\tilde{J}/\bar{J}$) from DENSEPACK showed that the relative density fluctuation amplitude ($\tilde{n}/\bar{n}$) was nearly independent of space. Thus, in order to explain the poloidal asymmetry in terms of plasma fluctuations, it was required that the relative phase of density ($\tilde{n}$) and potential fluctuations ($\tilde{\Phi}$) be dependent on spatial position. Unfortunately, no such detailed measurements of $\tilde{n}$ and $\tilde{\Phi}$ versus poloidal position in Alcator C are available at this time.

Perpendicular convective transport in the edge plasma was considered as a mechanism to support asymmetries. Motivated by the Pfirsch-Schlüter convection plus diffusion model outlined in the introductory section, perpendicular $\underline{E} \times \underline{B}$ convection as inferred from DENSEPACK data was examined. It was found that although $\underline{E} \times \underline{B}$ particle transport could be significant compared to the particle loss rate to the limiter, it possessed neither the magnitude nor the structure to simply explain the observed density asymmetry in the limiter shadow plasma. $\underline{E} \times \underline{B}$ electron energy transport was found to be even less important compared to parallel power fluxes to the limiter. Thus, perpendicular transport

was found only to perturb the edge and did not, by itself, explain the asymmetric equilibrium that was established. However, it was pointed out that for minor radii less than the limiter radius ($r \lesssim a$), where the metallic limiter can no longer 'short out' poloidal potential variations and where there is no strong parallel transport to limiter surfaces, $\underline{E} \times \underline{B}$ fluxes may play a more dominant role.

Finally, parallel convection in the edge plasma was considered. Independent of the mechanism by which plasma pressure is maintained to be nonuniform on a flux surface, bulk plasma flows along $\underline{B}$ can be driven by such pressure asymmetries. It was suggested that the asymmetries detected by the thermocouple array previously operated on Alcator C could be explained in terms of such pressure asymmetries and/or parallel flows. More recently, data obtained using a two-sided energy analyzer/Langmuir probe/heat flux probe[73,97,98] supports this hypothesis. It was suggested that the asymmetric limiter damage can also be explained in terms of parallel plasma flows in the edge plasma. It was concluded that poloidally asymmetric plasma might exist not only in the shadow plasma but also just inside the limiter radius. Such a hypothesis is consistent with the very high edge densities recorded on some shots by the inside interferometer immediately prior to a MARFE.

C. Scaling of Edge versus Central Plasma Parameters

The DENSEPACK probe diagnostic recorded edge plasma parameters for a range of central plasma densities, currents, toroidal magnetic fields, and fill gasses. Consequently, a survey of edge versus central plasma parameters was performed.

An important finding of this survey was that the edge density varied as some function of the ratio of central line-averaged density to plasma current, $\bar{n}_e/I_p$. Multiple parameter, nonlinear regression analysis techniques were applied to density data in order to further investigate this trend. It was found that a critical value of $\bar{n}_e/I_p$ differentiated between two distinct scaling laws that the

edge density obeyed: 1) $n_{edge}/\bar{n}_e \propto a + b(\bar{n}_e/I_p)^{\alpha}$, α = 3–5, and 2) $n_{edge} \propto I_p^{\beta}$, β = 1.2–1.4. These two regimes were identified with non-MARFE and MARFE regimes, respectively.

Critical values of $\bar{n}_e$ and I_p computed independently from matching the transition between these two regimes were found to correspond to the MARFE threshold in $\bar{n}_e$ and I_p observed in Alcator C. A proposed interpretation was that the edge radiation power balance associated with a MARFE regime limits the achievable edge density. Conversely, the onset of the MARFE regime is tied to the edge density reaching a critical value for a given plasma current.

The central plasma quantity $\bar{n}_e/I_p$ appeared to be important for other edge parameters as well. Poloidally averaged density, electron temperature, floating potential, and ion saturation current fluctuation amplitude along with global particle confinement time were documented in plots versus $\bar{n}_e/I_p$.

In contrast to expectations, the degree of edge plasma density asymmetry was found to be relatively insensitive to central parameters. However, temperature and floating potential asymmetries were found to change, decreasing at high values of $\bar{n}_e/I_p$.

D. Edge Plasma During Lower Hybrid Heating and Pellet Injection

In addition to ohmic, gas fueled discharges, data was recorded by the DENSEPACK probe array during Lower Hybrid Radio Frequency (LHRF) heating and pellet fueling. During LHRF heating, edge densities and temperatures were found to increase uniformly with RF power by up to ~50% and ~25% respectively over the values measured during ohmic heating alone. This resulted in a relative reduction in the global particle confinement time (up to ~ 50% at the highest LHRF powers) and an increased power loading on limiter surfaces.

Following pellet injection, the edge plasma was found to achieve one of two states. For small increases in central line-averaged density, the change in edge plasma parameters for changing central parameters followed the ohmic, gas

fueled relationships. However, for large increases in central $\bar{n}_e$ resulting from pellet injection, the final edge plasma state was found to deviate from the gas fueled scaling laws. The edge plasma in this new regime was characterized by lower densities at all radii for the same central $\bar{n}_e$. The result was an increase in the global particle confinement time. It was found that a relative density increase due to pellet injection of $\Delta\bar{n}_e/\bar{n}_e \gtrsim 1$ was required to attain this high particle confinement regime.

E. MARFES

One goal of the DENSEPACK probe experiment was to study the temporal and spatial evolution of the MARFE phenomena in Alcator C edge plasma. However, strong poloidal asymmetries were detected by the DENSEPACK probe array which overshadowed any effects due to a MARFE. The MARFE was detected in the shadow plasma as only a relatively slight perturbation to this already poloidally asymmetric equilibrium.

Pellet injection provided a means of studying the difference in edge parameters with and without a MARFE in a single discharge because central plasma parameters could be suddenly changed from non-MARFE to MARFE conditions. Contrary to expectations, only a slight 'filling in' of the poloidal density asymmetry was found to occur during a MARFE. This led to an increase in plasma density and scrape-off length at the poloidal location where the MARFE was observed. Thus, the single Langmuir probe measurements first reported during a MARFE in Alcator C were reproduced by the DENSEPACK probe array. However, the conceptual picture of the MARFE changed from being the development of an asymmetric 'clump' of high density, low temperature plasma to being the result of a 'filling in' of a highly poloidally asymmetric edge plasma.

Finally, a new edge plasma phenomenon, a 'MARFE oscillation', was introduced. This 'moving' MARFE was simultaneously detected by the DENSEPACK probe array and a H_γ camera system. The 265 Hz MARFE oscillation provided

a unique opportunity to correlate changes in H_α emission with changes in density and temperature in this 'moving' MARFE region. It was found that a local density increase and temperature decrease corresponded to a local enhancement in H_α emission, consistent with a radiation thermal instability model for MARFE formation.

The fact that this radiating plasma region oscillated in spatial position implied that local particle and energy transport to the MARFE region changed as the MARFE evolved. The timescale for this relaxation process ($\sim$ 2 msec) and spatial amplitude of the oscillation ($\sim$ 17 cm) suggested that perpendicular transport is important in defining the MARFE boundary.

12.2 Suggestions for Future Work

A number of unanswered questions were identified during this edge plasma study and remain for further investigation. The most important issues are summarized below.

A. Correlated $\tilde{n}$, $\tilde{\Phi}$ Fluxes

Although the DENSEPACK probe system was configured to record ion saturation current fluctuations and floating potential fluctuations, it was not possible to record them simultaneously. This made it impossible to estimate the correlation between $\tilde{n}$ and $\tilde{\Phi}$ fluctuations. The importance of this limitation grew more apparent as it became clear that edge plasma asymmetries in density and temperature could not be simply explained in terms of other transport mechanisms. It was concluded that the poloidal asymmetry might be entirely explained in terms of particle and energy fluxes from correlated $\tilde{n}$,$\tilde{\Phi}$ fluctuations, yet there was no data from DENSEPACK to test this hypothesis.

In order to test this hypothesis, one would need to simultaneously measure $\tilde{n}$ and $\tilde{\Phi}$ over short radial and poloidal distances (~ 0.1 cm) at various poloidal angles. In this way, local $\nabla\tilde{n}$ and $\nabla\tilde{\Phi}$ could be inferred and the divergence of the resultant flux computed (section 8.3.2). Since the dominant component of this particle flux is expected to be in the radial direction, only $\nabla_r\tilde{n}$ and $\nabla_\theta\tilde{\Phi}$ would need to be estimated. Thus, a combination of four Langmuir probes, two sampling $\tilde{J}$ in the poloidal direction and two sampling $\tilde{\Phi}$ in the poloidal direction might be employed at various poloidal locations. Alternatively, $\nabla_r\tilde{n}$ might be inferred independently by a high spatial resolution optical system and spectroscopic techniques.

B. Non-Ambipolar Effects

The floating potential of DENSEPACK probes was found to vary systematically in poloidal angle. Both the sign and magnitude of this overall potential variation could be attributed to $\underline{B} \times \nabla|\underline{B}|$ particle drifts. However, the small spatial scale structure in floating potential could not be easily explained. This structure was attributed to both poloidal and toroidal variations in electron temperature and to 'non-ambipolar effects'. The issue of non-ambipolar transport other than $\underline{B} \times \nabla|\underline{B}|$ drifts was never addressed in a quantitative fashion in this thesis and remains an open topic.

C. Toroidal Symmetry

The DENSEPACK probe array sampled plasma at only one toroidal location. Hence, there was no direct measurement of possible toroidal variations. MARFE phenomena has been observed to be toroidally symmetric, not following field lines. On this basis, it was assumed throughout most of the discussion in this thesis that the edge plasma in Alcator C tends to be more toroidally symmetric than poloidally symmetric. The implication is that density and temperature varies along a magnetic field line.

This assumption has yet to be directly verified on Alcator C. A simple probe experiment at two toroidal locations could easily test the toroidal symmetry hypothesis. Alternatively or in addition, identical probes could be positioned on the same magnetic field line to look for a variation in density and/or temperature. In a more ambitious experiment, two or more probe arrays similar to DENSEPACK could be installed at different toroidal locations.

C. Parallel Flows

The detection of strong poloidal asymmetries in pressure on a flux surface implies that parallel flows may be important in the edge plasma. In a simple picture, one can imagine that plasma pressure is not constant but that the total kinetic plus flow energy is constant on a flux surface. As a result, parallel flows on the order of the local sound speed become possible. With such flows, the effects of parallel momentum transfer through viscosity and cross field particle transport become important. These processes determine the parallel flow pattern and possibly the asymmetric pressure profile as well.

At this time there is no direct measurement of parallel flows in Alcator C edge plasma. However, such flows could be easily detected by a small, two-sided Langmuir probe or by spectroscopic methods.

D. Probe Theory

The validity of probe theory in a magnetic field is always worrisome to the edge plasma experimentalist. No completely rigorous magnetized probe theory exists and in view of the difficulty of the problem, none is likely to arise in the near future.

The magnetized probe model proposed by Stangeby[19] was used in this thesis work. However, some problems were encountered. First, electron temperatures predicted by this model were found to be systematically low compared to retarding field energy analyzer results[94,106]. Second, the electron saturation current reduction factor (r) predicted by this theory was found to be a factor of ~ 10 too low even when a correction was made for the relatively close proximity of the limiter surfaces (section 7.2.5). Thus, an empirically verified magnetized probe theory has yet to be formulated. A lesson learned during this Langmuir probe work was not to worry about the entire probe characteristic but to use the simple plane probe model and to ignore the probe data points that depart from this model near electron saturation (section 6.3). This approach led to the

most reliable results and could be used to numerically fit probe data in $\sim 1/4$ the CPU time (appendix D).

Another area where probe theory is lacking is in dealing with a probe immersed in a flowing plasma. Again Stangeby[103] has formulated a simplified fluid model for probe current collected in the presence of plasma flow. However, at sonic speeds the theory breaks down. Furthermore, the analysis of data from large probes in which the current collecting electrode is recessed is not handled by this theory. Unfortunately, many edge plasma probes must be designed with a recessed electrode to satisfy other design constraints. Consequently, much effort is needed in both theoretical modelling and experimental verification of models which include such effects.

F. Plasma Parameters Inside $r = a$

One inherent limitation of probe measurements in high density tokamaks is the inability to sample the plasma region inside the limiter radius ($r \lesssim a$). Power fluxes become too high for the probe to withstand without serious damage. Unfortunately, perhaps the most interesting physics occurs just inside the limiter radius. At this location the radial density gradients are still large and determined by neutral ionization and radial transport. Parallel transport to limiter surfaces no longer occurs. MARFE phenomena reside at this minor radius location, and poloidal asymmetries detected in the limiter shadow plasma probably originate there. Thus, the next step in understanding and diagnosing the physics of the edge plasma is the development of diagnostic systems to probe this plasma region in detail.

References

[1] McCracken, G. M., Stott, P. E.,"Plasma Surface Interactions in Tokamaks," *Nucl. Fus.* **19** (1979).

[2] Pickrell, M. M., "The Role of Radiation on the Power Balance of the Alcator C Tokamak," M.I.T. Plasma Fusion Center Report No. PFC/RR-82-30 (1982).

[3] Terry, J. L., *et al.*, "Strongly Enhanced Low Energy Continuum and Hydrogen Line Emission in Some Alcator Discharges," *Bull. Amer. Phys, Soc.* **26** (Oct. 1981) 886, paper 2R7.

[4] Baker, D. R., Snider, R. T., General Atomic, Nagami, M., JAERI, "Observation of Cold, High-Density Plasma Near the Doublet III Limiter," General Atomic Report No. GA-A16337 (June 1981).

[5] Lipschultz, B., LaBombard, B., Marmar, E. S., Pickrell, M. M., Terry, J. L., Watterson, R., Wolfe, S. M., "MARFE: An Edge Plasma Phenomenon," *Nucl. Fus.* **24** (1984) 977.

[6] Alladio, F., *et al.*, "The Regime of Enhanced Particle Recycling in High Density Tokamak Discharges in the Frascati Torus," *Phys. Let.* **90A** (1982) 405.

[7] Wagner, F., Keilhacker, M., and the ASDEX and NI Teams, "Importance of the Divertor Configuration for Attaining the H-Regime in ASDEX," *J. Nucl. Mat.* **121** (1984) 103–113.

[8] Nagami, M., *et al.*, "Production of High Temperature and High Density Plasmas by Controlling Edge Particle Recycling in D-III Divertor Equilibria," *J. Nucl. Mat.* **121** (1984) 114.

[9] Kaye, S. M. *et al.*, "Attainment of High Confinement in Neutral Beam Heated Divertor Discharges in the PDX Tokamak," *J. Nucl. Mat.* **121** (1984) 115–125.

[10] LaBombard, B., Overskei, D. O., Lipschultz, B., "Limiter Power Loading During Operation of Alcator Tokamaks," *Bull. Amer. Phys. Soc.* **26** (Sept 1981) 886, paper 2R13.

[11] Starfire Design Team, "STARFIRE - A Commercial Tokamak Fusion Power Plant Study," Argonne National Lab. Report No. ANL/FFP-80-1 (1980).

[12] Ohyabu, N., DeBoo, J. C., Mahdavi, A., "Radiative Cooling in the Magnetically Expanded Boundary," General Atomic Report No. GA-A16434 (1982).

[13] Feneberg, W., Wolf, G., "A Helical Megnetic Limiter for Boundary Control in Large Tokamaks," *Nucl. Fusion* **21** (1981) 669.

[14] Liewer, P. C., "Measurements of Microturbulence in Tokamaks and Comparisons with Theories of Turbulence and Anomalous Transport," *Nucl. Fus.* **25** (1985) 543-621.

[15] Alcator Group, "Alcator C Status and Program Plan," M.I.T. Plasma Fusion Center Report No. PFC/IR-83-3.

[16] Greenwald, M., Gwinn, D., Milora, S., Parker, J., Parker, R., Wolfe, S., and Alcator Group, "Energy Confinement of High-Density Pellet-Fueled Plasmas in the Alcator C Tokamak," *Phys. Rev. Let.* **53** (1984) 352.

[17] Hayzen, A. J., Overskei, D. O., Moreno, J., "Probe Measurements of the Boundary Plasma in Alcator C," M.I.T. Plasma Fusion Center Report No. PFC/JA-81-10 (April 1981).

[18] Tonks, L., Langmuir, I., *Phys. Rev.* **33** (1929) 1070, Phys. Rev. **34** (1929) 876.

[19] Stangeby, P. C.,"Effect of Bias on Trapping Probes and Bolometers for Tokamak Edge Diagnosis," *J. Phys. D: Appl. Phys.* **15** (1982) 1007-1029.

[20] Bohm, D., Burhop, E. H. S., Massey, H. S. W., The Characteristics of Electrical Discharges in Magnetic Fields, Editors: Guthrie, A., Wakerling, K. R., McGraw Hill, New York (1949).

[21] Stangeby, P. C., "Plasma Sheath Transmission Factors for Tokamak Edge Plasmas," *Phys. Fluids* **27** (1984) 682.

[22] Motley, R. W., "Electrical Characteristics of an Ideal Tokamak Limiter," *Nucl. Fus.* **21** (1981) 1541.

[23] Daybelge, U., Bein, B., "Electric Sheath Between a Metal Surface and Magnetized Plasma," *Phys. Fluids* **24** (1981) 1190.

[24] Chodura, R.,"Plasma-Wall Transition in an Oblique Magnetic Field," *Phys. Fluids* **25** (1982) 1628.

[25] Chodura, R.,"Numerical Analysis of Plasma-Wall Interaction for an Oblique Magnetic Field," *J. Nucl. Mat.* **111 & 112** (1982) 420.

[26] Gierszewski, P. J., "Plasma/Neutral Gas Transport in Divertors and Limiters," M.I.T. Plasma Fusion Center Report No. PFC/RR-83-28 (Sept 1983).

[27] Bailey, A. W., Emmert, G. A., "A Theoretical Model for Hot Plasma Flowing to a Wall with Recycling," Univerisity of Wisconsin Report No. UWFDM-473 (May 1982).

[28] Chen, F. F., "Electric Probes," Chapter 3 in Plasma Diagnostic Techniques, Editors: Huddlestone, R. H., and Leonard, S. L., Academic Press, New York (1965).

[29] Dnestrovskii, Yu. N., Kostomarov, D. P., Paviova, N. L., "Energy Balance in Devices of the Tokamak Type Considering Charge Exchange," Moscow University Press, 1971, Princeton Plasma Physics Laboratory Report No. Matt-Trans-107 (Dec. 1971).

[30] Heifetz, D., *et al.*, "A Monte carlo Model of Neutral Particle Transport in Diverted Plasmas," Princton Plasma Physics Lab. Report No. PPPL-1843. *J. Comp. Phys.* **46** (1982) 309.

[31] Audenaerde, K., Emmert, G. A., Gordinier, M., "SPUDNUT: A Transport Code for Neutral Atoms in Plasmas," *J. Comp. Phys.* **34** (1980) 268– 284.

[32] Uehara, K., Gomay, Y., Yamamoto, T., Suzuki, N., Maeno, M., Hirayama, T., Shimada, M., Konoshima, S., Fujisawa, N., "Gross Particle Confinement Characteristics by the Boundary Plasma in the JFT-2 Tokamak," *Plasma Physics* **21** (1979) 89–99.

[33] Ohyabu, N., "Density Limit in Tokamaks," *Nucl. Fusion* **19** (1979) 1491.

[34] Chen, F. C., Introduction to Plasma Physics, Plenum Press, New York (1974).

[35] Brower, D. L., "Spatial and Spectral Asymmetries in the Distribution of Microturbulence on TEXT," *Bull. Amer. Phys. Soc.* **29** (1984) 1259, paper 4A5.

[36] Slusher, R. E., Surko, C. M., "Study of Plasma Density Fluctuations by the Correlation of Crossed CO_2 Laser Beams," *Phys. Fluids* **23** (1980) 2425–2439.

[37] Watterson, R. L., Slusher, R. E., Surko, C. M., "Low Frequency Density Fluctuations in the Alcator C Tokamak," M.I.T. Plasma Fusion center Report No. PFC/JA-85-7 (Feb. 1985).

[38] Zweben, S. J.,Gould, R. W., "Scaling of Edge-Plasma Turbulence in the CalTech Tokamak," *Nucl. Fusion* **23** (1983) 1625.

[39] Levinston, S. J., Beall, J. M., Powers, E. J., Bengtson, R. D., "Space-Time Statistics of the Turbulence in a Tokamak Edge Plasma," University of Texas Report No. FRCR#259 (Oct. 1983).

[40] Zweben, S. J., McChesney, J., Gould, R. W., "Optical Imaging of Edge Turbulence in the CalTech Tokamak," *Nucl. Fus.* **23** (1983) 825–830.

[41] Zweben, S. J., Taylor, R. J., "Phenomenological Comparison of Magnetic and Electrostatic Fluctuations in the Macrotor Tokamak," *Nucl. Fusion* **21** (1981) 193.

[42] Zweben, S. J., Liewer, P. C., Gould, R. W., "Edge Plasma Transport Experiments in the CalTech Tokamak," *J. Nucl. Mat.* **111 & 112** (1982) 39–43.

[43] Bateman, G., MHD Instabilities, M.I.T. Press, Cambridge, Ma. (1980).

[44] Miyamoto, K., Plasma Physics for Nuclear Fusion, M.I.T. Press Cambridge Ma. (1980).

[45] LaBombard, B., "Comments on Equilibrium Plasma Flows in the Limiter Shadow Region of Alcator C," M.I.T. Plasma Fusion Center Report PFC/RR-83-26 (Nov. 1983).

[46] Motley, R. W., Hooke W. M., Anania, G., "Formation of Thermal Eddies During RF Heating of Plasma," *Phys. Rev. Lett.* **43** (1979) 1799.

[47] Greene, J. M., Winsor, N. K., "Stationary Shocks and Toroidal Diffusion," Princeton Plasma Physics Lab. Report No. MATT-908 (July 1972).

[48] Perkins, F. W., Jassby, D. L., "Velocity Shear and Low-Frequency Plasma Instabilities," *Phys. Fluids* **14** (1971) 102.

[49] Hickok, R. L., "Space Potential Measurements in Tokamaks," *Bull. Amer. Phys. Soc.* **29** (Oct 1984) 1259, paper 4A4.

[50] Ivanov, R. S., Stotskii, G. I., Fidel'man, G. N., "Nonambipolar Plasma Transport in the Shadow of the Limiter in a Tokamak," *Sov. J. Plasma Phys.* **10** (1984) 256.

[51] Bengtson, R. D., Ritz, CH. P., Levinson, S. J., Powers, E. J., "Turbulent Transport in the Edge Plasma of the TEXT Tokamak," *Bull. Amer. Phys. Soc.* **29** (Oct 1984) 1396, paper 8T16.

[52] Rhodes, T. L., Bengtson, R. D., Powers, E. J., Ritz, CH. P.,"Two-Dimensional Structure of the Turbulence in the Edge Plasma of TEXT," *Bull. Amer. Phys. Soc.* **29** (Oct 1984) 1396, paper 8T18.

[53] Griem, H. R., Plasma Spectroscopy, McGraw-Hill, New York (1964).

[54] Niedermeyer, H., *et al.*, "Change in Plasma Properties Prior to High Density Disruptions in ASDEX," Max-Planck-Institute Für Plasmaphysik Report No.. IPP III/90 (Oct. 1983).

[55] Lipschultz, B., LaBombard, B., Pickrell, M. M., Terry, J. L., "MARFES: Poloidally Asymmetric Edge Conditions in Alcator C," *Bull. Amer. Phys. Soc.* **27** (Nov. 1982) 937, paper 2E4.

[56] Glasstone, S., Lovberg, R. H., Controlled Thermonuclear Reactions, Robert E. Krieger Publishing Company, Huntington, New York (1960).

[57] Post, D. E., Jensen, R. U., Tarter, C. B., Grasberger, W. H., Lokke, W. A., "Steady State Radiative Cooling Rates for Low-Density, High-Temperature Plasma," *Atomic Data and Nuclear Tables* **20** (1977) 397.

[58] Carolan, P. G., Piotrowicz, V. A., "The Behavior of Impurities Out of Coronal Equilibrium," *Plasma Physics* **25** (1983) 1065–1086.

[59] Braginskii, S. I., "Transport Processes in a Plasma," *Reviews of Plasma Physics* **1** (1965) 205–311.

[60] Staib, P., "Probe Measurements in the Plasma Boundary Layer," *J. Nucl. Matt.* **111 & 112** (1982) 109–122.

[61] Zweben, S. J., Taylor, R. J., "Edge-Plasma Properties of the UCLA Tokamaks," *Nucl. Fusion* **23** (1983) 513.

[62] Harbour, P. J., Morgan, J. G., "Models and Codes for the Plasma Edge Region," Culham Laboratory Report No. CLM-R234 (Dec. 1982).

[63] Braams, B. J., Harbour, P. J., Harrison, M. F. A., Hotston, E. S., Morgan, J. G., "Modelling of the Boundary Plasma of Large Tokamaks," *J. Nucl. Matt.* **121** (1984) 75–81.

[64] Schneider, W., Heifetz, D. B., Lackner, K., Neuhauser, J., Post, D. E., Rauh, K. G., "Modelling of the ASDEX Scrape-off and Divertor," *J. Nucl. Matt.* **121** (1984) 178–183.

[65] Mense, A. T., Emmert, G. A., "Simulation of Poloidal Divertors in One-Dimensional Tokamak Transport Codes," *Nucl. Fusion* **19** (1979) 361.

[66] Ogden, J. M., Singer, C. E., Post, D. E., Jensen, R. V., Seidel, F. G. P., "One-Dimensional Transport Code Modeling of the Divertor-Limiter Region in Tokamaks," IEEE Transactions on Plasma Science **PS-9** (Dec. 1981) 274.

[67] LaBombard, B., Lipschultz, B., "An Edge Plasma MHD Equilibrium Model for Alcator C," *Bull. Amer. Phys. Soc.* **28** (Oct. 1983) 1250, paper 9S13.

[68] LaBombard, B., "Reduced Transport Equations for the Edge Plasma in Alcator C," M.I.T. Plasma Fusion Center Report No. PFC/RR-86-9 (1986).

[69] Stangeby, P. C., McCracken, G. M., Erents, S. K., Matthews, G., "DITE Langmuir Probe Results Showing Probe-Size and Limiter-Shadow Effects," *J. Vac. Sci. Technol. A* **2** (1984) 72.

[70] Stangeby, P. C., "The Disturbing Effect of Probes Inserted into Edge Plasmas of Fusion Devices," *J. Nucl. Matt.* **121** (1984) 36–40.

[71] Singer, C. E., Langer, W. D., "Axisymmetric Tokamak Scrapeoff Transport," Princeton Plasma Physics Lab. Report No. PPPL-1920 (August 1982).

[72] LaBombard, B., Lipschultz, B., Pickrell, M. M., Takase, Y., "Langmuir Probe Measurements of the Edge Plasma in Alcator C," *Bull. Amer. Phys. Soc.* **27** (Nov. 1982) 1036, paper 5W4.

[73] Wan, A. S., Yang, T. F., Parker, R. R., "A Localized Directional Edge Plasma Diagnostic on Alcator C," *Bull. Amer. Phys. Soc.* **29** (Oct. 1984) 1223, paper 2V7.

[74] Pfeifer, L., LaBombard, B., Lipschultz, B., Hutchinson, I. A., "DENSEP-ACK: A Poloidal Array of Langmuir Probes in the Limiter Shadow Region of Alcator C," *Bull. Amer. Phys. Soc.* **29** (Oct. 1984) 1223, paper 2V6.

[75] LaBombard, B., Lipschultz, B., Pribyl, P., "Poloidal Asymmetries in the Limiter Shadow Region of Alcator C," *Bull. Amer. Phys. Soc.* **29** (Oct 1984) 1320, paper 6F6.

[76] Lipschultz, B., LaBombard, B., "The Effects of Pellet Injection, RF Heating and Current Drive on the Alcator C Edge Plasma," *Bull. Amer. Phys. Soc.* **29** (Oct 1984) 1320, paper 6F7.

[77] Pribyl, P., "Measurements of MHD Equilibrium in Alcator C," M.I.T doctoral thesis.

[78] Data provided by H. Manning.

[79] A. Pachtman, M.I.T. doctoral thesis in progress.

[80] B. Lipschultz, private communication.

[81] Emmert, G. A., Wieland, R. M., Mense, T. A., Davidson, J. N., "Electric Sheath and Presheath in a Collisionless, Finite Ion Temperature Plasma," *Phys. Fluids* **24** (1980) 803.

[82] Liewer, P.C, McChesney, J.M., Zweben, S.J., Gould, R.W., "Temperature Fluctuations and Heat Transport in the Edge Regions of a Tokamak," *Phys. Fluids* **29** (1986) 309–317.

[83] Rosen, M. D., Greene, J. M., "Radial Boundary Layers in Diffusing Torodial Equilibria," Princeton Plasma Physics Lab. Report No. PPPL-1315 (Jan 1977).

[84] Marmar, E. S., "Recycling Processes in Tokamaks," *J. Nucl. Matt.* **76 & 77** (1978) 59–67.

[85] Lipschultz, B., LaBombard, B., Marmar, E. S., Pickrell, M. M., Rice, J., "Calculation of Molybdenum Sputtering from the Limiter in Alcator C," *J. Nucl. Matt.* **128 & 129** (1984) 555–558.

[86] Ritz, Ch. P., Bengston, R. D., Levinson, S. J., Powers, E. J., "Turbulent Structure in the Edge Plasma of the TEXT Tokamak," *Phys. Fluids* **27** (1984) 2956–2959.

[87] Parker, J. K., "Density Fluctuations Following Fuel Pellet Injection on the Alcator C Tokamak," M.I.T. Plasma Fusion center Report No. PFC/RR-85-8 (May 1985).

[88] Foord, M. E., Marmar, E. S., Terry, J. L., "Multichannel Light Detector System for Visible Continuum Measurements on Alcator C," *Rev. Sci. Instrum.* **53** (Sept. 1982) 1407–1409.

[89] McArther, G.R., "The SCD Graphics Utilities," National Center for Atmospheric Research, Technical Note No. NCAR-TN/166+IA (May 1983).

[90] special graphics programs developed by S. McCool at the M.I.T. Plasma Fusion Center.

[91] Hooper, E. B., "Correlation Techniques in Experimental Plasma Physics," Plasma Physics Vol. 13, pp. 1–18, Pergamon Press 1971.

[92] Beall, J. M., Kim, Y. C., Powers, E. J., "Estimation of Wavenumber and Frequency Spectra using Fixed Probe Pairs," *J. Appl. Physics* **53** (1982) 3933–3940.

[93] Bevington, P. R., Data Reduction and Error Estimation for the Physical Sciences, McGraw-Hill (1969).

[94] A. Wan, private communication.

[95] Hildebrand, F. B., Advanced Calculus for Applications, 2nd Ed., Prentice-Hall Inc., Englewood Cliffs, N. J., 1976.

[96] Brigham, E.O., The Fast Fourier Transform, Pretince-Hall, Inc., Englewood Cliffs, N.J., 1974.

[97] Wan, A. S., Yang, T. F., Lipschultz, B., LaBombard, B., "JANUS: a Bi-Directional, Multi-Functional Plasma Diagnostic," M.I.T. Plasma Fusion center Report No. PFC/JA-85-44 (Dec. 1985).

[98] Wan, A., Lipschultz, B., Yang, T., LaBombard, B., "Directional Measurement of Edge Electron and Ion Parameters on Alcator C," *Bull. Amer. Phys. Soc.* **30** (Nov 1985).

[99] LaBombard, B., Lipschultz, B., Hutchinson, I.A., Wan, A., "Pressure Asymmetries and Sound Speed Flows in the Alcator C Limiter Shadow Plasma," *Bull. Amer. Phys. Soc.* **30** (Nov 1985).

[100] Lipschultz, B., LaBombard, B., Manning, H.L., Rice, J., Terry, J.L., "Determination of Impurity Generation Processes During Lower Hybrid Heating on Alcator C," *Bull. Amer. Phys. Soc.* **30** (Nov 1985).

[101] Fussmann, *et al.*, "Impurity Retainment in the Divertor of ASDEX," in Proceedings of the Eleventh European Conference on Controlled Fusion and Plasma Physics (Aachen, Germany, 1983) European Physical Society (1983), Vol. 70, Part II, p. 373.

[102] Nedospasov, A.V., Petrov, V.G., Fidel'man, G.N., "Plasma Convection in the Poloidal Limiter Shadow of a Tokamak," *Nucl. Fus.* **25** (1985) 21.

[103] Stangeby, P.C., "Measuring Plasma Drift Velocities in Tokamak Edge Plasmas using Probes," *Phys. Fluids* **27** (1984) 2699–2704.

[104] Harbor, P.J., Proudfoot, G., "Mach Number Deduced from Probe Measurements in the Divertor and Boundary Layer of DITE," *J. Nucl. Mat.* **121** (1984) 222–228.

[105] Zawaideh, E., Najmabadi, F., Conn, R.W., "Generalized Fluid Equations for Parallel Transport in Collisional to Weakly Collisional Plasmas," Center

for Plasma Physics and Fusion Engineering, UCLA report no. PPG-843 (October 1984).

[106] A. Wan, M.I.T doctoral thesis in progress.

[107] Stangeby, P.C., "Large Probes in Tokamak Scrape-off Plasmas. The Collisionless Scrape-off Layer: Operation in the Shadow of Limiters or Divertor Plates," *J. Phys. D: Appl. Phys.* **18** (1985) 1547–1559.

[108] Stangeby, P.C., "Large Probes in Tokamak Scrape-off Plasmas. Analytic Model for the Collisionless Scrape-off Plasma.," *Phys. Fluids* **28** (1985) 644.

[109] Owens, D.K., *et al.*, "Global Particle Balance Study in the TFTR Tokamak," *Bull. Amer. Phy. Soc.* **30** (1985), 1520.

[110] Pericoli-Ridoleni, V., "The Scrape-off Layer Characteristics as a Function of the Plasma Current and Density in the FT Tokamak Discharges," *Plasma Phys. and Controlled Fusion* **27** (1985) 493–499.

[111] Martin Greenwald, private communication.

[112] Keilhacker *el al.*, "The ASDEX Divertor Tokamak," *Nucl. Fus.* **25** (1985) 1045–1054.

[113] Yuiche Takase, private communication.

[114] Lipschultz, B., *et al.*, "Impurity Sources During Lower-Hybrid Heating on Alcator C," M.I.T. Plasma Fusion center Report No. PFC/JA-85-45 (December 1985).

[115] Greenwald, M., Alcator Group, "Pellet Fueling Experiments on Alcator C," *Bull. Amer. Phys. Soc.* **30** (1985), 1412.

[116] Foord, M. E., Marmar, E. S., Greenwald, M. J., "Particle Transport in Pellet Fueled Alcator C Discharges from Analysis of Visible Continuum Profiles," *Bull. Amer. Phys. Soc.* **30** (1985), 1412.

[117] Terry, J. L., *et al.*, "Observation of an Increase in Impurity Paricle Confinement After Injection of Large Pellets," *Bull. Amer. Phys. Soc.* **30** (1985), 1412.

[118] P. Pribyl, private communication.

[119] Blackwell, B., *et al.*, "Energy and Impurity Transport in the Alcator C Tokamak," in Proceedings of the Nineth International Conference on Plasma Physics and Controlled Nuclear Fusion Research (Baltimore, 1982), Vol. *I*, p. 27.

[120] Boody, F.P., *et al.*, "Macroscopic Edge Phenomena in TFTR: MARFEs, Moving MARFEs, and Detached Plasmas," *Bull. Amer. Phys. Soc.* **30** (1985), 1518.

[121] Terry, J.L., Marmar, E.S., Chen. K.I., "Observation of Poloidal Asymmetry in Impurity-Ion Emission Due to ∇B Drifts," *Phys. Rev. Lett.* **39** (1977) 1615–1618.

[122] Brau, K., Suckewer, S., Wong, S.K., "Vertical Poloidal Asymmetries of Low-Z Element Radiation in the PDX Tokamak," *Nucl. Fus.* **23** (1983) 1657–1668.

[123] Fussmann, G., *et al.*, "Studies on Impurity Retainment in the ASDEX Divertor", *J. Nucl. Mat.* **121** (1984), 164–170.

[124] O'Rourke, J., *et al.*, "Poloidally Asymmetric Edge Phenomena in JET," in Proceedings of the Twelveth European Conference on Controlled Fusion and Plasma Physics (Budapest, 1985) European Physical Society (1985), Vol. 9F, Part I, p. 155.

APPENDIX A: Toroidal Coordinate System and Operators

The right hand coordinate system $(\hat{r}, \hat{\theta}, \hat{\phi})$ describing the toroidal geometry referenced in this thesis is illustrated in Fig. A.1. $r = 0$ defines the central axis of the torus and the poloidal angle, θ, is measured from the outside midplane. A differential arc length in this coordinate system is defined as

$$\partial \underline{s} \;=\; \partial r\ \hat{r} \;+\; r\partial\theta\ \hat{\theta} \;+\; (R_0 + r cos\theta)\partial\phi\ \hat{\phi}\ .$$

With the definition, $\epsilon = r/R_0$, the following operators are thus defined:

$$\nabla f \;=\; \hat{r}\frac{\partial f}{\partial r} \;+\; \frac{\hat{\theta}}{r}\frac{\partial f}{\partial \theta} \;+\; \frac{\hat{\phi}}{(R_0 + r\ cos\theta)}\frac{\partial f}{\partial \phi}$$

$$\nabla \cdot \underline{V} \;=\; \frac{1}{r(1+\epsilon\ cos\theta)}\left\{\frac{\partial}{\partial r}\left[r(1+\epsilon\ cos\theta)\ V_r\right] + \frac{\partial}{\partial\theta}\left[(1+\epsilon\ cos\theta)\ V_\theta\right] + \frac{\partial}{\partial\phi}\left[\epsilon\ V_\phi\right]\right\}$$

$$\nabla \times \underline{V} \;=\; \frac{1}{r(1+\epsilon\ cos\theta)}\left\{\ \hat{r}\ \left[\frac{\partial}{\partial\theta}(1+\epsilon\ cos\theta)\ V_\theta - \frac{\partial}{\partial\phi}\epsilon\ V_\theta\right]\right.$$

$$-\ \hat{\theta}\ \epsilon\ \left[\frac{\partial}{\partial r}(R_0 + r\ cos\theta)\ V_\phi - \frac{\partial}{\partial\phi}V_r\right]$$

$$\left.-\ \hat{\phi}\ (1+\epsilon\ cos\theta)\ \left[\frac{\partial}{\partial r}rV_\theta - \frac{\partial}{\partial\theta}V_r\right]\right\}$$

$$\nabla^2 f = \frac{1}{r(1+\epsilon\ cos\theta)}\left\{ \frac{\partial}{\partial r}\left[r(1+\epsilon\ cos\theta)\frac{\partial f}{\partial r}\right] + \frac{\partial}{\partial \theta}\left[\frac{(1+\epsilon\ cos\theta)}{r}\frac{\partial f}{\partial \theta}\right] \right.$$

$$\left. + \frac{\partial}{\partial \phi}\left[\frac{\epsilon}{(R_0 + r\ cos\theta)}\frac{\partial f}{\partial \phi}\right]\right\}$$

$$(\underline{V}\cdot\nabla)\underline{A} = \hat{r}\left[V_r\frac{\partial A_r}{\partial r} + \frac{V_\theta}{r}\left(\frac{\partial A_r}{\partial \theta} - A_\theta\right) + \frac{V_\phi}{(R_0 + r cos\theta)}\left(\frac{\partial A_r}{\partial \phi} - cos\theta A_\phi\right)\right]$$

$$+ \hat{\theta}\left[V_r\frac{\partial A_\theta}{\partial r} + \frac{V_\theta}{r}\left(\frac{\partial A_\theta}{\partial \theta} + A_r\right) + \frac{V_\phi}{(R_0 + r cos\theta)}\left(\frac{\partial A_\theta}{\partial \phi} + sin\theta A_\phi\right)\right]$$

$$+ \hat{\phi}\left[V_r\frac{\partial A_\phi}{\partial r} + \frac{V_\theta}{r}\frac{\partial A_\phi}{\partial \theta} + \frac{V_\phi}{(R_0 + r cos\theta)}\left(\frac{\partial A_\phi}{\partial \phi} + cos\theta A_r - sin\theta A_\theta\right)\right]$$

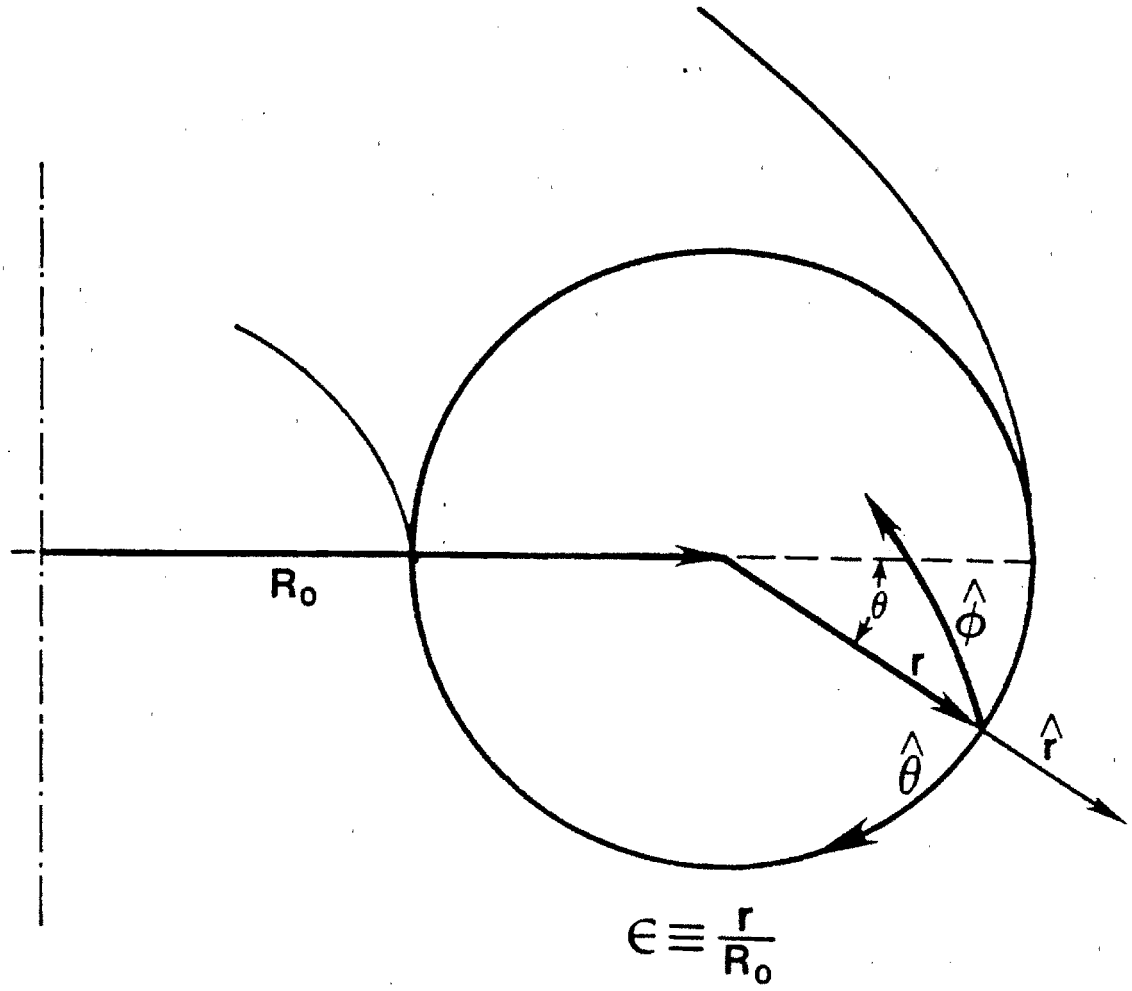

Figure A.1 Toroidal Coordinate System

APPENDIX B: Relationship Between $(\hat{\theta}, \hat{\phi})$ Coordinate System and Parallel and Perpendicular Directions

The rotational transform in a tokamak relates the $(\hat{\theta}, \hat{\phi})$ coordinate system (subset of $(\hat{r}, \hat{\theta}, \hat{\phi})$ coordinate system discussed in Appendix A) to the coordinates parallel and perpendicular to the magnetic field. From construction in Fig. $B.1$, the following vector component relationships hold:

$$\frac{E_{\perp\phi}}{E_{\perp\theta}} = \frac{-B_\theta}{B_\phi}$$

$$\frac{E_{\parallel\theta}}{E_{\parallel\phi}} = \frac{B_\theta}{B_\phi}$$

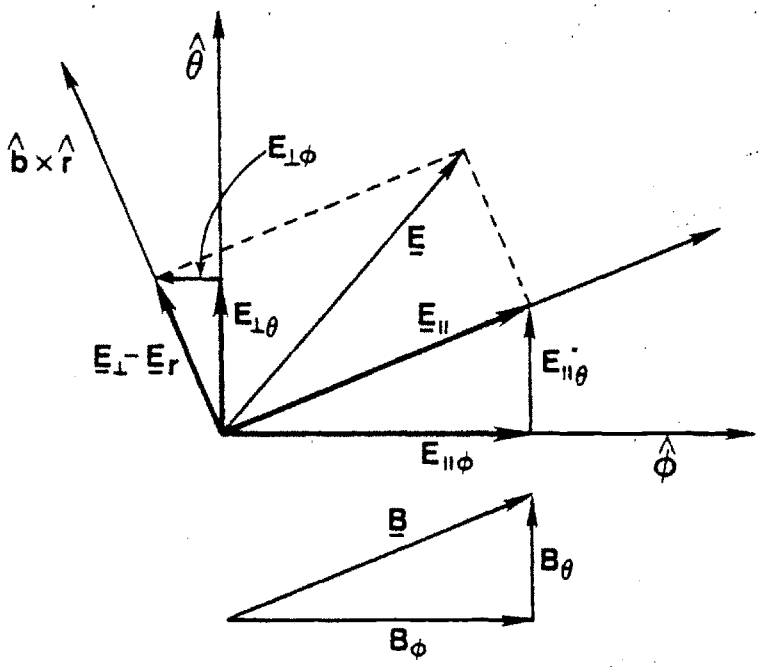

Figure B.1 Relationship Between $(\hat{\theta}, \hat{\phi})$ Coordinate System and Parallel and Perpendicular Directions

APPENDIX C: DENSEPACK Probe Current & Bias Monitor Circuits

C.1 DENSEPACK Probe Current Monitor Circuit

Two versions of probe current monitor circuits were used in DENSEPACK's probe drive system. The first version is shown in Fig. *C*.1. One of two drive voltages from programmed power supplies could be selected for any probe using switch S3. The probe drew current from this source through a load resistor determined by the position of S1. A 1–2 amp fuse in series with the probe protected the system in the event of a short circuit or when the probe drew too much current. The voltage drop across the load resistor was differentially stepped down and amplified through resistor dividers and four LF357 operational amplifiers. This arrangement of LF357s provided a common mode voltage rejection of 100 volts with optimum common mode frequency rejection up to 1 MHz. Switch S2 allowed a selection of simple RC filtering at $\sim$ 1 MHz, 100 kHz, and 10 kHz. The output voltage was calibrated and balanced using trim pots so that it was equal to the voltage drop across the load resistor. When switch S1 was in position 1, only the positive leg of the differential amplifier system was used. The output of this circuit then corresponded to the floating potential of the probe.

DENSEPACK PROBE CURRENT MONITOR CIRCUIT (First Version)

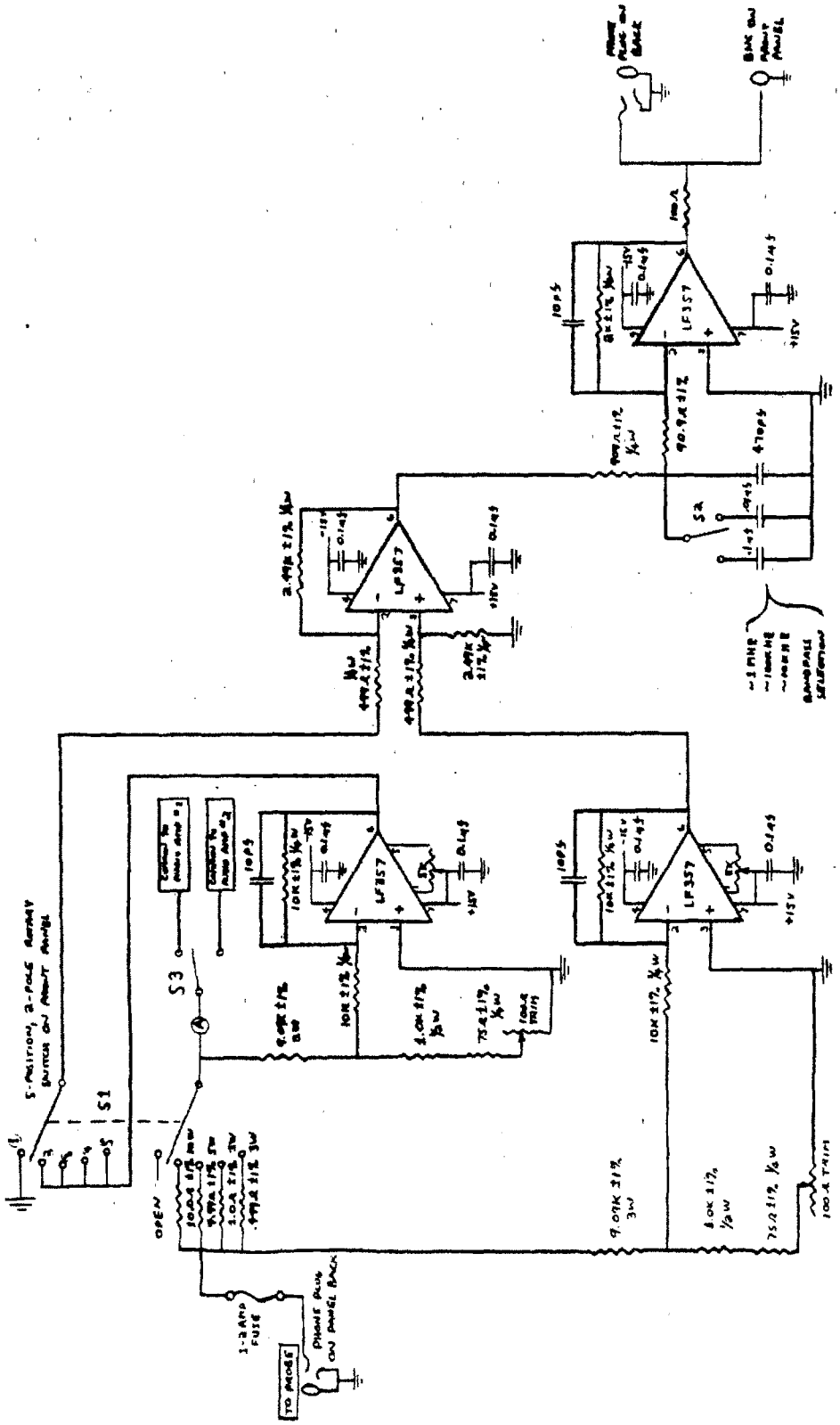

Figure C.1 Current Monitor Circuit Diagram

(First Version)

The second version probe current monitor circuit is shown in Fig. *C*.2. The option of monitoring the floating potential was eliminated in favor of another load resistor and a trim pot for each position of switch S1. DENSEPACK Langmuir probes on the inside wall location in Alcator C measured very low plasma densities. This circuit modification was performed to improve low current sensitivity. In order to balance the resistor dividers at high load resistor values, individual trim pots for each load resistor were necessary.

Each circuit combined with a CAMAC logger channel was capable of cleanly recording from $\sim$ 2 amps to $\sim$ 1 milliamp of probe current for triangle bias waveforms of $\pm$60 volts at 100 Hz - 5 kHz. The bandwidth of the amplifier system was designed to be $\approx$ 1 MHz, which was needed for recording high frequency fluctuations.

DENSEPACK PROBE CURRENT MONITOR CIRCUIT (Second Version)

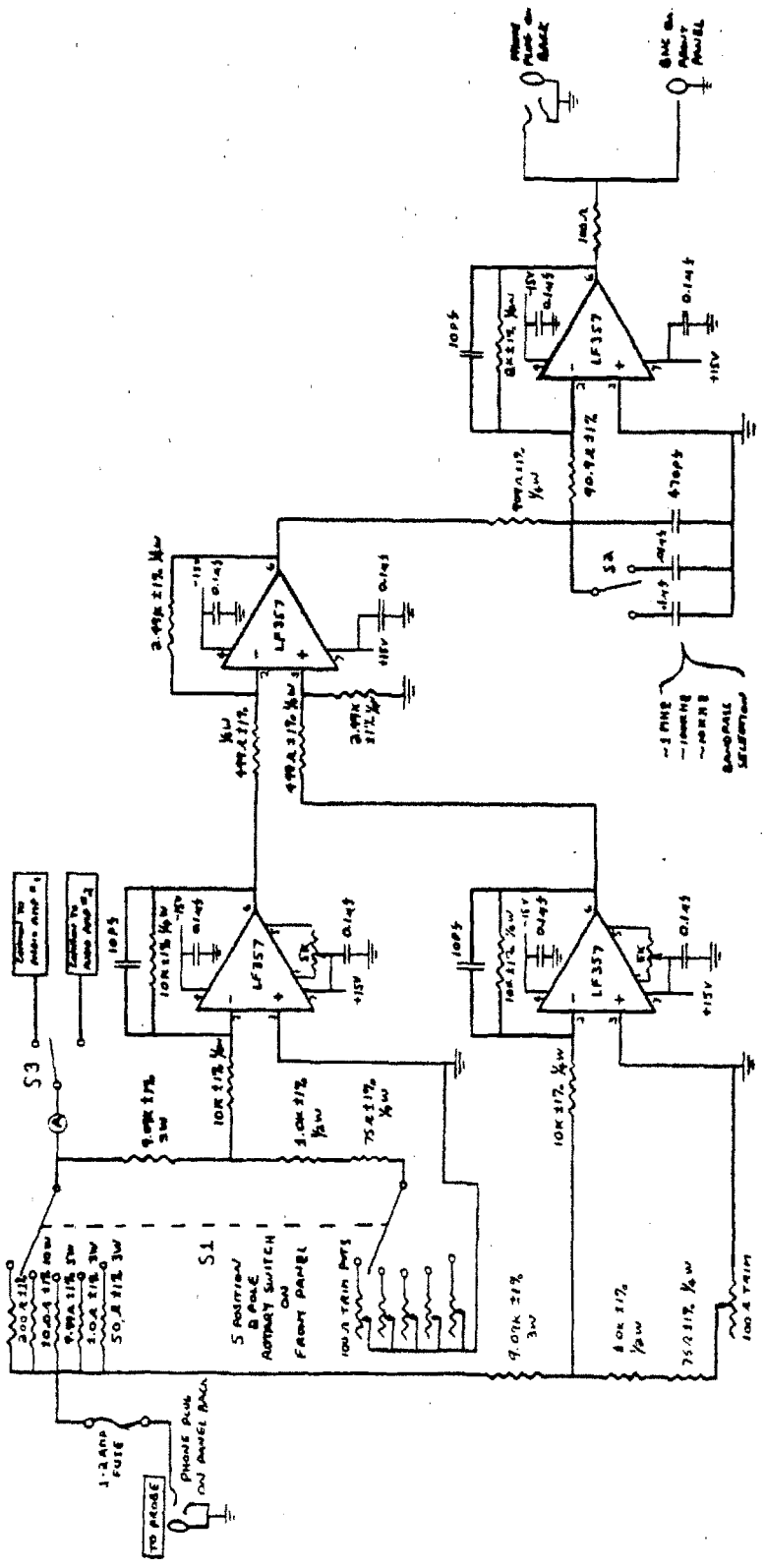

Figure C.2 Current Monitor Circuit Diagram

(Second Version)

C.2 DENSEPACK Bias Voltage Monitor Circuit

The voltage output of each probe bias power supply was monitored by the circuit shown in Fig. *C*.3. The circuit divides the input voltage by 20, inverts it, and sends it to a CAMAC logger channel. The operational amplifier and filter arrangement that was used matched the probe current monitor circuit.

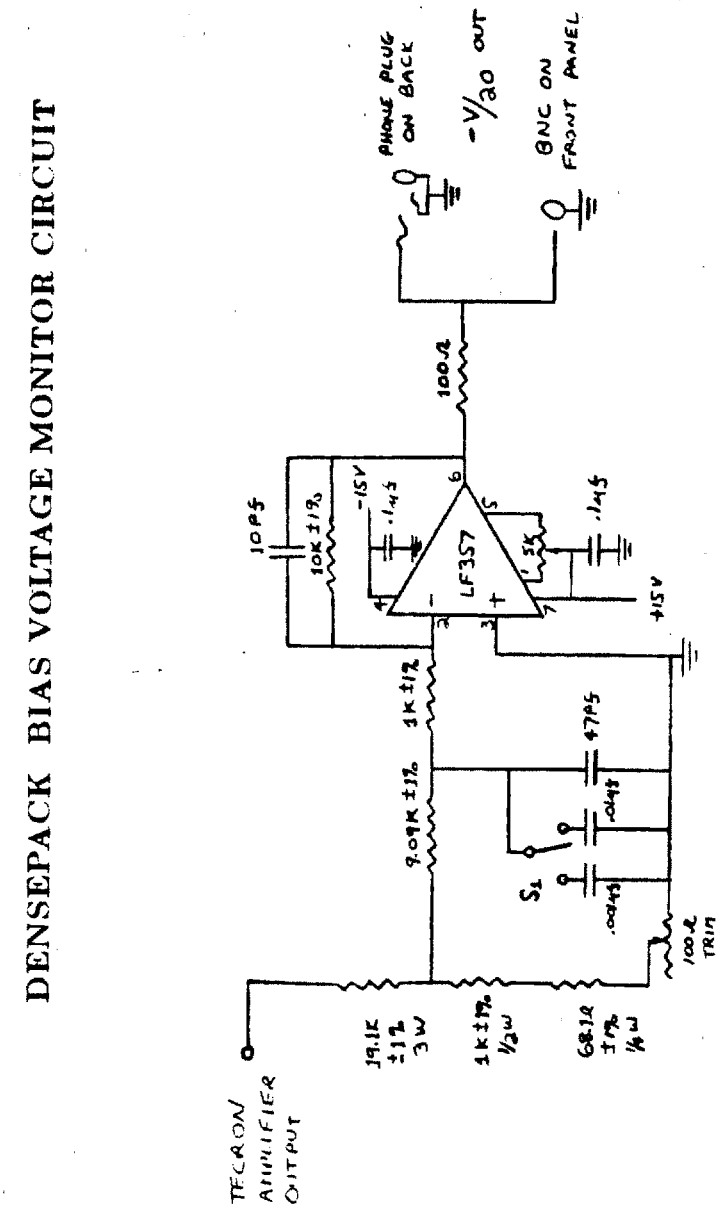

Figure C.3 Voltage Monitor Circuit Diagram

APPENDIX D: DENSEPACK Probe Fitting Algorithm

D.1 Outline of Fitting Algorithm

The procedure which was used to estimate n_0, T_e, V_f, r, and $\tilde{n}_0/n_0$ for DENSEPACK probe data in program 'DPACK' is diagrammed in Fig. $D.1$. The computer code was written to be general enough to handle a wide range of bias waveform shapes and frequencies (10 Hz – 10 kHz) at various digitization rates. Langmuir probe data recorded by both the 10 kHz data loggers (8212 units) and 1 MHz data loggers (8210 units) could be processed using this algorithm.

First a menu file containing program control information and default first guess parameters is read. The raw probe bias voltage data is then read and processed by the subroutine 'SETSW'.

D.1.1 Subroutine 'SETSW'

The subroutine 'SETSW' scans a probe bias voltage array, generating the starting and ending array subscript locations plus sweep direction for positive-going and negative-going sweeps. The voltage data set can have from one complete sweep period to many. The only limitation is that the voltage be monotonically changing between periodic absolute minima and maxima. SETSW first takes the fast fourier transform of the voltage data to arrive at the fundamental sweep period. Then an absolute maxima and minima search is performed about the location estimated from the period. Array locations of these maxima and minima and the sign of the sweep are outputted.

Once the bias voltages are divided into discrete sweeps, current data from each probe is read and analyzed. Before data fitting is performed, any D.C. offset and coupling of the measured current data with the bias voltage is removed using the subroutine 'DECOUPLE'.

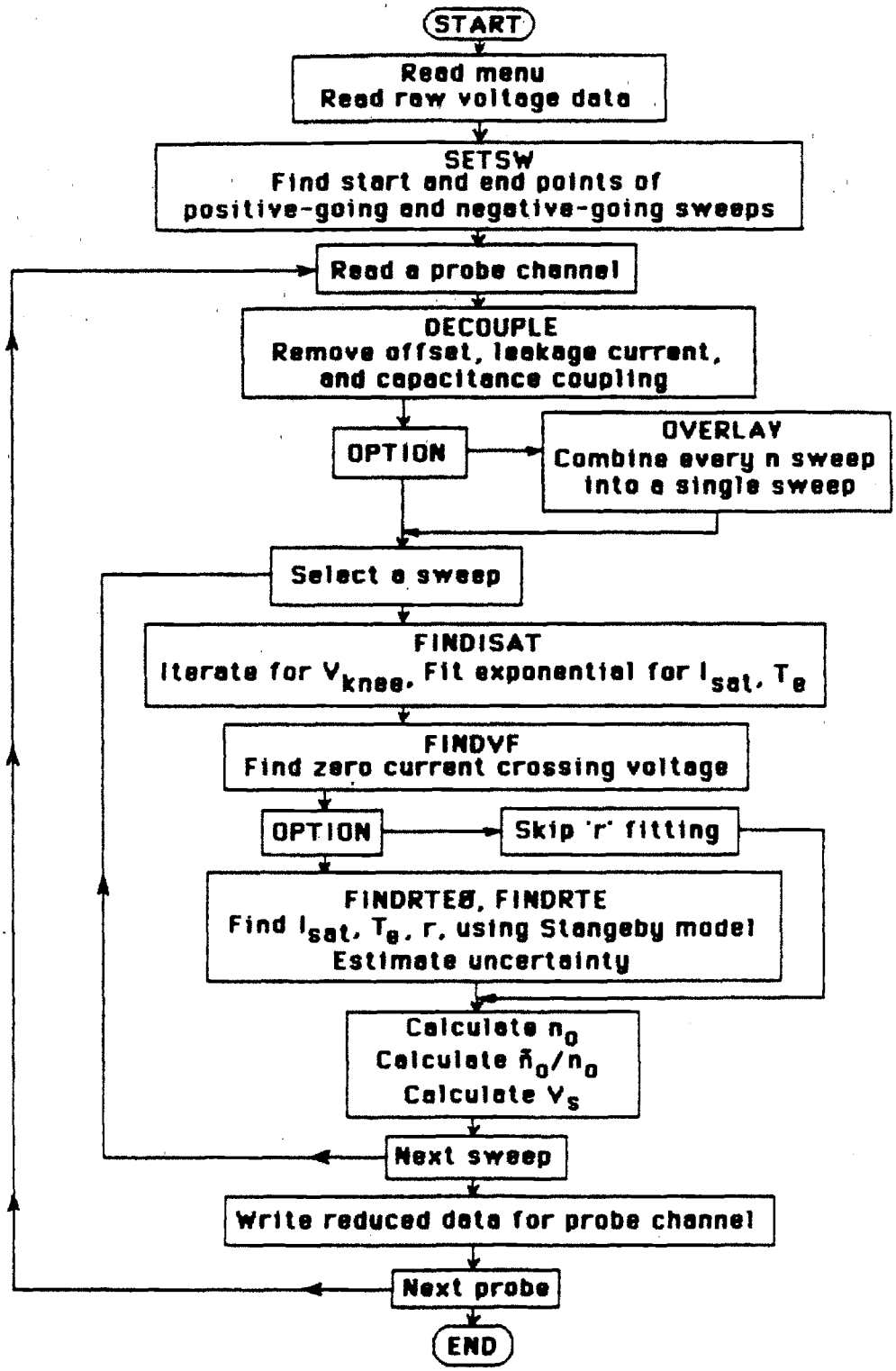

Figure D.1 Flowchart of Langmuir Probe Fitting Algorithm (Program 'DPACK')

D.1.2 Subroutine 'DECOUPLE'

Subroutine 'DECOUPLE' assumes that the probe current signal results from four possible sources: 1) current collected by the probe, 2) leakage current from the probe to ground or voltage on an unbalanced resistor bridge, 3) displacement current due to capacitive coupling, and 4) an offset voltage from the instrumentation electronics. To account for these effects, the measured current (I^{meas}) is assumed to be related to the current collected by the probe (I^{coll}) and the probe voltage (V_p) through

$$I_i^{meas} = I_i^{coll} + Y\ V_{pi} + C\left(\frac{\partial V_p}{\partial t}\right)_i + I_{offset} \qquad (D.1)$$

where Y and C are conductance and capacitance coefficients and I_{offset} is an offset current. Before a plasma shot when I_i^{coll} is zero, the three coupling coefficients are determined through a least squares fitting method by requiring that the error,

$$\epsilon = \sum_{i=1}^{n}\left[I_i^{meas} - Y\ V_{pi} - C\left(\frac{\partial V_p}{\partial t}\right)_i + I_{offset}\right]^2, \qquad (D.2)$$

be a minimum. A numerical differentiation subroutine is used to compute $\frac{\partial V_i}{\partial t}$ at each data sample time, i. The actual collected current is then computed for all data points using these coefficients and Eq. $D.1$. It is found that a total of about six sweeps before the discharge is sufficient to obtain a good estimate of Y, C, and I_{offset}.

Figure $D.2$ demonstrates the action of the subroutine DECOUPLE. Raw data is displayed for 30 msec before a discharge in Alcator C, (a). The data exhibits a D.C. offset and a component proportional to the sweep voltage. At this sweep rate, no appreciable current due to capacitance coupling is evident. From the coupling coefficients obtained by DECOUPLE, the actual collected

current is estimated for all data points. The first 30 msec of the processed data is shown in Fig. *D.1b*. Here, the uncertainty of the zero current level is reduced from ~ 10 milliamps to ~ 0.5 milliamps.

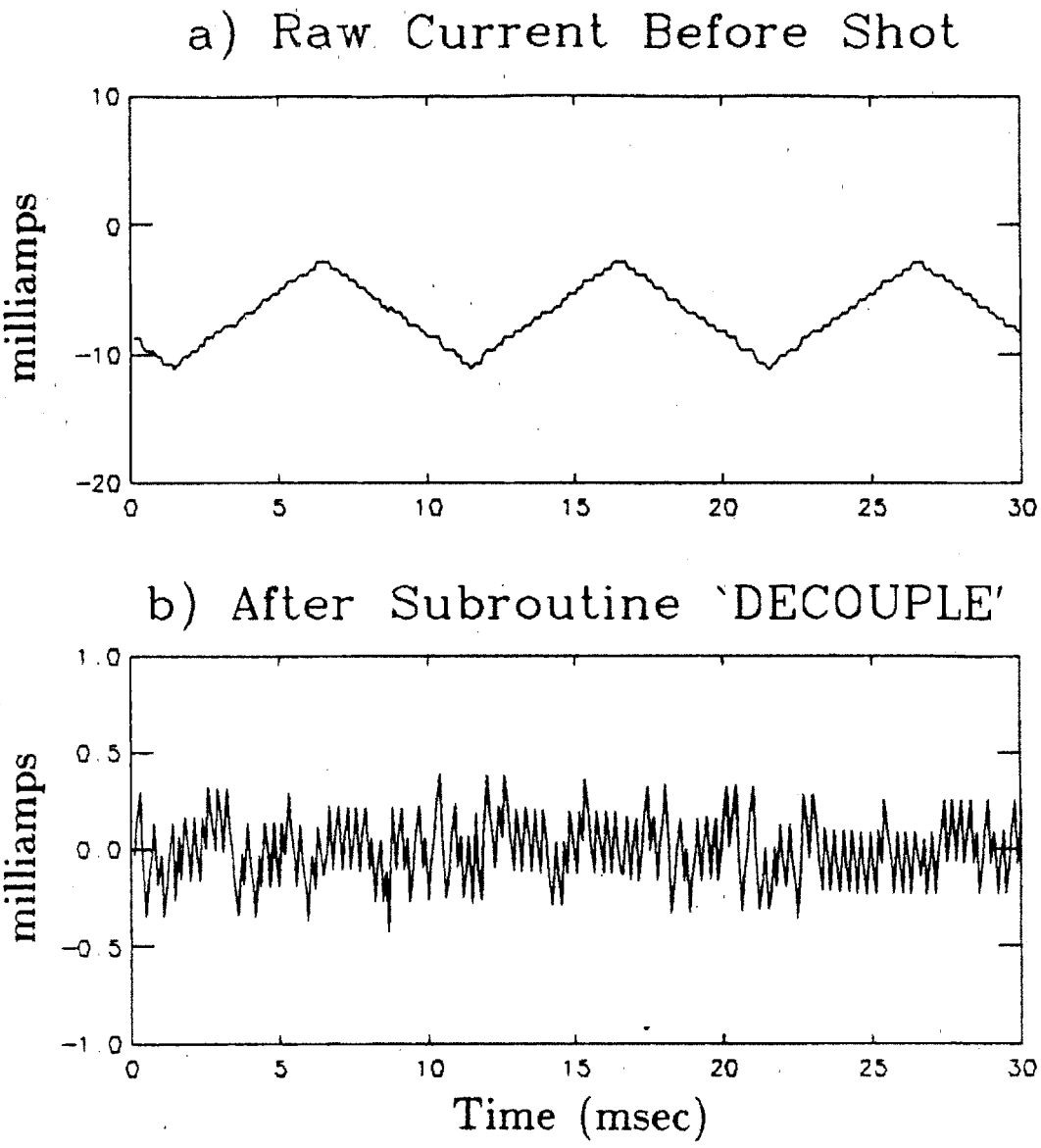

Figure D.2 Demonstration of Subroutine 'DECOUPLE'

D.1.3 Subroutine 'OVERLAY'

In some cases, it is more desirable to combine a number of probe sweeps into one sweep for fitting purposes. Because of the structure of the algorithm in subroutine 'FINDISAT', it is necessary that a combined set of current-voltage data points, $\{I_i, V_{pi}\}$, be ordered by voltage. Subroutine 'OVERLAY' performs this task for an arbitrary number of combined sweeps. Since this subroutine can take a significant fraction of the CPU time, often it is skipped and no combining of sweep data is done.

At this point in the probe data reduction algorithm, the sweep data sets, $\{I_i, V_{pi}\}$, are identified and ready for processing. Now for each sweep of each probe signal, the series of subroutines, 'FINDISAT', 'FINDVF', 'FINDRTE0', and 'FINDRTE' act in succession to arrive at reduced data quantities such as I_{sat}, T_e, and r.

D.1.4 Subroutine 'FINDISAT'

This first step in fitting the Langmuir characteristic utilizes the exponential fitting technique discussed in section 6.3.4. The transition voltage, V_{knee}, is first determined. Then an exponential fit is made to the data for all data points with $V_{pi} < V_{knee}$. In this way an accurate estimate of I_{sat} and a first guess estimate of T_e is obtained. A typical exponential fit to DENSEPACK data is shown in Fig. 6.11.

D.1.5 Subroutine 'FINDVF'

The floating potential, V_f, is simply defined as the bias voltage at which no net current is drawn. V_f is first calculated from the exponential fit obtained previously by FINDISAT. A more accurate estimate for V_f is then performed in subroutine 'FINDVF' by looking at data points about V_f and fitting a straight

line through these points. The zero current crossing point then becomes the new and more accurate estimate for V_f.

Program 'DPACK' has the option of exiting the fitting algorithm at this point. At this time, I_{sat} and T_e, have been estimated. If the exponential fit is found to be sufficient (see section 6.3.6) or the CPU time becomes limiting, the following estimate of r and T_e based on Stangeby's model can be skipped.

D.1.6 Subroutines 'FINDRTE0' and 'FINDRTE'

Subroutines 'FINDRTE0' and 'FINDRTE' fit r and T_e to the $\{I_i, V_{pi}\}$ data set based on Stangeby's model described in section 6.3.5 with I_{sat} already determined. Equations 6.31–6.35 are highly nonlinear in T_e and r. In addition, the normalized hill potential, η_h, must satisfy the transcendental relationship of Eq. 6.35. The task of fitting r and T_e is therefore divided into two steps. First, r and T_e are estimated for a simpler version of Eqs. 6.31–6.35 in which $\eta_h = 0$ for all biases. This is performed by subroutine 'FINDRTE0'. Then using this initial guess for r and T_e, η_h is allowed to satisfy Eq. 6.35. 'FINDRTE' performs this more general iteration for the final values of r and T_e. By this two step process, the time consuming intermediate iteration for η_h at each η_{pi} and r is delayed until the final r and T_e values are approached. In addition, the algorithm is found to converge more reliably by introducing this nonlinear correction at the end.

A number of iteration schemes were tried for subroutines FINDRTE0 and FINDRTE, ranging from generalized packaged library routines to hand written routines. Generalized nonlinear fitting library routines were found to be very slow, possibly because they are too general. The fastest and most reliable iteration method which was found for FINDRTE0 and FINDRTE is a custom written scheme. The scheme is based on a least squares method that approximates the fitting function as a Taylor expansion near the final solution.

Let the ideal probe characteristic given by Eqs. 6.31–6.35 be represented by

$$I_i^{model} = f(r, T_e, V_{pi}) \ . \qquad (D.3)$$

The best combination of r and T_e can be found by minimizing the error, ϵ, given by

$$\epsilon = \sum_{i=1}^{n} \Big[I^{meas} - f(r, T_e, V_{pi}) \Big]^2 \ . \qquad (D.4)$$

Near the optimum solution, $f(r, T_e, V_{pi})$ can be expanded as

$$f(r, T_e, V_{pi}) \approx f(r_0, T_{e0}, V_{pi}) + (r - r_0) \frac{\partial f}{\partial r}\Big|_{r_0, T_{e0}, V_{pi}}$$

$$+ (T_e - T_{e0}) \frac{\partial f}{\partial T_e}\Big|_{r_0, T_{e0}, V_{pi}} \ . \qquad (D.5)$$

Since $f(r, T_e, V_{pi})$ is an analytic function, $\frac{\partial f}{\partial r}$ and $\frac{\partial f}{\partial T_e}$ are also analytic and readily evaluated. Thus given an initial guess of r_0 and T_{e0}, a new r and T_e pair can be found by using a linear least squares method of solution. This technique is used repeatedly in FINDRTE0 and FINDRTE to arrive at a final estimate of r and T_e. A check is made at various points to insure that the stepsize change in r or T_e is sufficiently small that Eq. $D.5$ is valid and that ϵ is indeed becoming smaller.

The algorithm is fast since new guesses of both r and T_e are obtained each iteration. This method has the additional benefit in that an estimate of the uncertainty in T_e and r can be made using techniques such as those described

in Ref. [93]. A DENSEPACK Langmuir probe current data set of 100 sweeps spanning a total of 5,000 data points is typically processed in ≈ 15 CPU seconds on a VAX with floating point accelerator. Skipping subroutines FINDRTE0 and FINDRTE, the probe data can be processed based on just the exponential fitting algorithm in ≈ 4 CPU seconds.

D.1.7 Calculating n_0, and $\tilde{n}_0/n_0$

Once I_{sat}, T_e, and r are known, n_0 is estimated using Eq. 6.36. $\tilde{n}_0/n_0$ is computed as the RMS deviation of I_i about I_{sat} divided by I_{sat} for data points in ion saturation. A cut-off upper voltage defining the ion saturation region is inputted via the program menu.

When all sweeps are processed for a given probe, the reduced data is written as a data record in a data file. The algorithm is repeated until all probe data is processed. Reduced data is reviewed or combined into a data base by programs described in section 6.1. Extensive diagnostic outputs can be switched on at multiple points in program DPACK to check the fitting algorithm and examine the accuracy of the fit.

APPENDIX E: Electron Saturation Flux to a Probe when $\lambda_{ei} \gg L$

E.1 Statement of Problem: Bounded Flux Tube

The rate of electron collection by a Langmuir probe biased at the plasma space potential was first considered in a magnetized plasma by Bohm.[20] This treatment, which leads to a reduction parameter (r) as in Eq. 6.17, considers perpendicular and parallel electron diffusion into a long, thin 'flux tube' depleted of electrons by the probe as shown in Fig. *E.1a*. For DENSEPACK probes, the parallel electron mean free path and/or parallel disturbance length (see section 6.2.2) can be large compared to the distance to a limiter surface. The collection tube can therefore be cut-off as shown in Fig. *E.1b*. In this case, the usual analysis of electrons diffusing both parallel and perpendicular to $\underline{B}$ into an unbounded flux tube must be replaced by perpendicular diffusion alone into a flux tube bounded by the limiter. This appendix estimates the saturated rate of electron collection in this limit when $\lambda_{ei} \gg L$ (L = distance to limiter surface).

E.2 1-D Model: Perpendicular Diffusion, Collisionless Parallel Flow

The geometry for this problem is shown in Fig. *E.1b*. It is assumed that the probe is immersed in a uniform maxwellian plasma with electron and ion temperatures, T_e and T_i. Electrons diffuse perpendicular to $\underline{B}$ and travel along field lines to be collected by the probe surface which is biased above the plasma space potential. Ions also diffuse perpendicular to $\underline{B}$ and travel along field lines but are reflected by the positive probe potential and collected at the sound speed rate by the limiter surface which is assumed to be biased at the local floating potential. The presence of this floating potential sheath at the limiter causes most of the electrons that were initially heading towards the limiter to be reflected back towards the probe. Thus, the probe does mostly all of the

electron collecting in this flux tube region. In terms of electron collection, the limiter surface behaves as a reflecting plane of symmetry. For the rest of this analysis, the limiter will be treated as such. One could just as well change the geometry to include mirror image probes a distance $2 \times L$ to the right and left of the probe in Fig. $E.1b$.

As stated, the electron-ion mean free path is long compared to the flux tube length, L, so that the electrons and ions can be considered collisionless in this region. Still, electrons and ions can undergo a collisionless random walk perpendicular to $\underline{B}$ driven by classical diffusion and/or electrostatic turbulence. The perpendicular diffusion and mobility of the electrons is therefore modelled by the transport equation,

$$\underline{\Gamma}_{\perp e} \;=\; -D_{\perp e}\,\nabla_{\perp} n \;-\; n\,\mu_{\perp e}\,\nabla_{\perp}\Phi\;, \qquad (E.1)$$

where the Einstein relationship, $D_{\perp} = -T_e\,\mu_{\perp}$, is assumed to apply (to be consistent with Bohm's analysis) and Φ is the electrostatic potential (time averaged in the case of electrostatic fluctuations). The ions, on the other hand, are assumed to follow a Boltzmann relationship and with $n_e = n_i$ in the collection tube region,

$$n \;=\; e^{-\Phi/T_i}\;. \qquad (E.2)$$

Combining Eqs. $E.1$ and $E.2$, the perpendicular electron flux filling the collection tube becomes

$$\underline{\Gamma}_{\perp e} \;=\; -D_{\perp e}\,(1+\tau)\,\nabla_{\perp} n\;. \qquad (E.3)$$

Here, the usual definition of $\tau = T_i/T_e$ applies.

The rate at which electrons are removed along a field line by the probe can be related to their average random thermal velocity, $\overline{C}_e$, and the field line length. If the probe potential is equal to the space potential, the parallel electron velocity is unchanged as it moves about the flux tube region. On the average, the electron must traverse a parallel distance L before reaching the probe. This includes electrons reflected at the limiter sheath. The average velocity component in a direction along $\underline{B}$, $\overline{|V_z|}$, is simply related to $\overline{C}_e$ by $\overline{|V_z|} = \overline{C}_e/2$. Therefore, the average residence time of an electron on a field line in the flux tube region is approximately

$$\tau_{res} \approx \frac{2\,L}{\overline{C}_e} \,. \qquad (E.4)$$

The electron distribution function will depend on the parallel distance from the probe. At the probe surface, most of the electrons are moving toward the probe while at the limiter sheath, an equal number of electrons are moving in both directions. The details of the distribution need not be considered in this analysis. Only an estimate of the electron density on a field line in the flux tube region is required. Here, it is assumed that although the distribution function varies along $\underline{B}$, the spatial density is constant along a field line. The electron density therefore only depends on the perpendicular coordinate. In this case, the density profile must be such that perpendicular continuity is satisfied,

$$\nabla_\perp \cdot \underline{\Gamma}_{\perp e} = -\frac{n}{\tau_{res}} \,. \qquad (E.5)$$

The average residence time of an electron on a field line in the flux tube region has been used in writing an effective perpendicular particle sink term. Using an (r, z) cylindrical coordinate system centered at the probe and assuming that $D_\perp$ and τ are independent of space, Eqs. $E.3$–$E.5$ become

$$D_\perp \ (1+\tau) \ \frac{1}{r}\frac{\partial}{\partial r}\left(r\frac{\partial n}{\partial r}\right) \ = \ \frac{\overline{C}_e \ n}{2 \ L} \ . \qquad (E.6)$$

Letting the probe collection area become a disk with radius ρ, the boundary conditions on Eq. $E.6$ are that $n(r = \rho) = n_0$, the unperturbed density, and that $n(r \rightarrow 0)$ is bounded. These conditions lead to a modified Bessel function solution[95] for the density,

$$n(r) \ = \ n_0 \ \frac{I_0(\alpha r)}{I_0(\alpha \rho)} \ , \qquad (E.7)$$

with

$$\alpha \ = \ \sqrt{\frac{\overline{C}_e}{2 \ L \ D_\perp \ (1+\tau)}} \ . \qquad (E.8)$$

The resultant radial density profile across the probe surface as given by Eqs. $E.7$ and $E.8$ is shown in Fig. $E.2a$.

The total electron current collected by the probe at a given radius can be obtained by recognizing that the local electron flux on the probe surface is simply

$$\Gamma_{\|e} \ = \ \frac{1}{4} \ n(r) \ \overline{C}_e \ . \qquad (E.9)$$

Integrating $\Gamma_{\|e}$ over a single side of the probe, the electron current becomes

$$I_e \ = \ -q \ n_0 \ \overline{C}_e \ \frac{\pi}{2} \ \frac{\rho \ I_1(\alpha\rho)}{\alpha \ I_0(\alpha\rho)} \ . \qquad (E.10)$$

This can be compared to the electron current that would be collected if the flux tube did not cause a density depression,

$$I_e^{max} = -q\, n_0\, \overline{C}_e\, \pi\, \frac{\rho^2}{4} . \qquad (E.11)$$

Figure $E.2b$ illustrates the reduction in electron current collected by a probe because of this density depletion effect.

It is now possible to estimate a reduction parameter, r, based on this model by requiring that

$$\frac{r}{1+r} = \frac{I_e}{I_e^{max}} . \qquad (E.12)$$

This results in

$$\frac{r}{1+r} = \frac{2}{\alpha\rho}\,\frac{I_1(\alpha\rho)}{I_0(\alpha\rho)} . \qquad (E.13)$$

When $\alpha\rho \ll 1$, the right hand side of Eq. $E.13$ reduces to unity, implying that $r \rightarrow \infty$. This model then predicts that the electron saturation current is not reduced in this case. However, the approximation that n is constant along a field line also breaks down. Cross-field diffusion is then strong enough relative to parallel transport to cause the density to vary significantly along a field line. This analysis therefore also requires that $\alpha\rho \gtrsim 1$, which is similar to the parallel density disturbance length in electron saturation, d_e, (section 6.2.2) being large compared to the distance to the limiter. In the other limit when $\alpha\rho \gg 1$, which validates this one-dimensional model, Eq. $E.13$ reduces to

$$\frac{r}{1+r} \approx \frac{2}{\alpha\rho} \qquad (E.14)$$

or

$$r \approx \frac{2}{\alpha\rho} \qquad (E.15)$$

so that the reduction parameter can be simply estimated when it is expected to be small. For DENSEPACK probes, the reduction parameter was found to be 0.1–0.4, making Eq. $E.15$ of interest. Including the definition of α, Eq. $E.15$ becomes

$$r \approx \frac{(1+\tau)^{1/2}}{\rho} \sqrt{\frac{8\ L\ D_\perp}{\overline{C}_e}} \qquad (E.16)$$

and for a square probe with area s^2,

$$r \approx \frac{(1+\tau)^{1/2}}{s} \sqrt{\frac{8\ \pi\ L\ D_\perp}{\overline{C}_e}} \ . \qquad (E.17)$$

Comparing these equations to Bohm's original result restated in Eq. 7.5, one can see that the form is very similar. The important difference is that in this case of a bounded flux tube ($\lambda_{ei} \gg L$, $\alpha\rho \gtrsim 1$), the electron-ion mean free path is replaced by the distance to the limiter surface. It is also interesting to note that Eq. 7.5, with λ_{ei} replaced by $L/4$, agrees with Eq. $E.17$ within a factor of 1–2 depending on the value of τ. For $\alpha\rho \lesssim 8$, Eq. $E.10$, which retains the hyperbolic Bessel functions explicitly, must be used in estimating r.

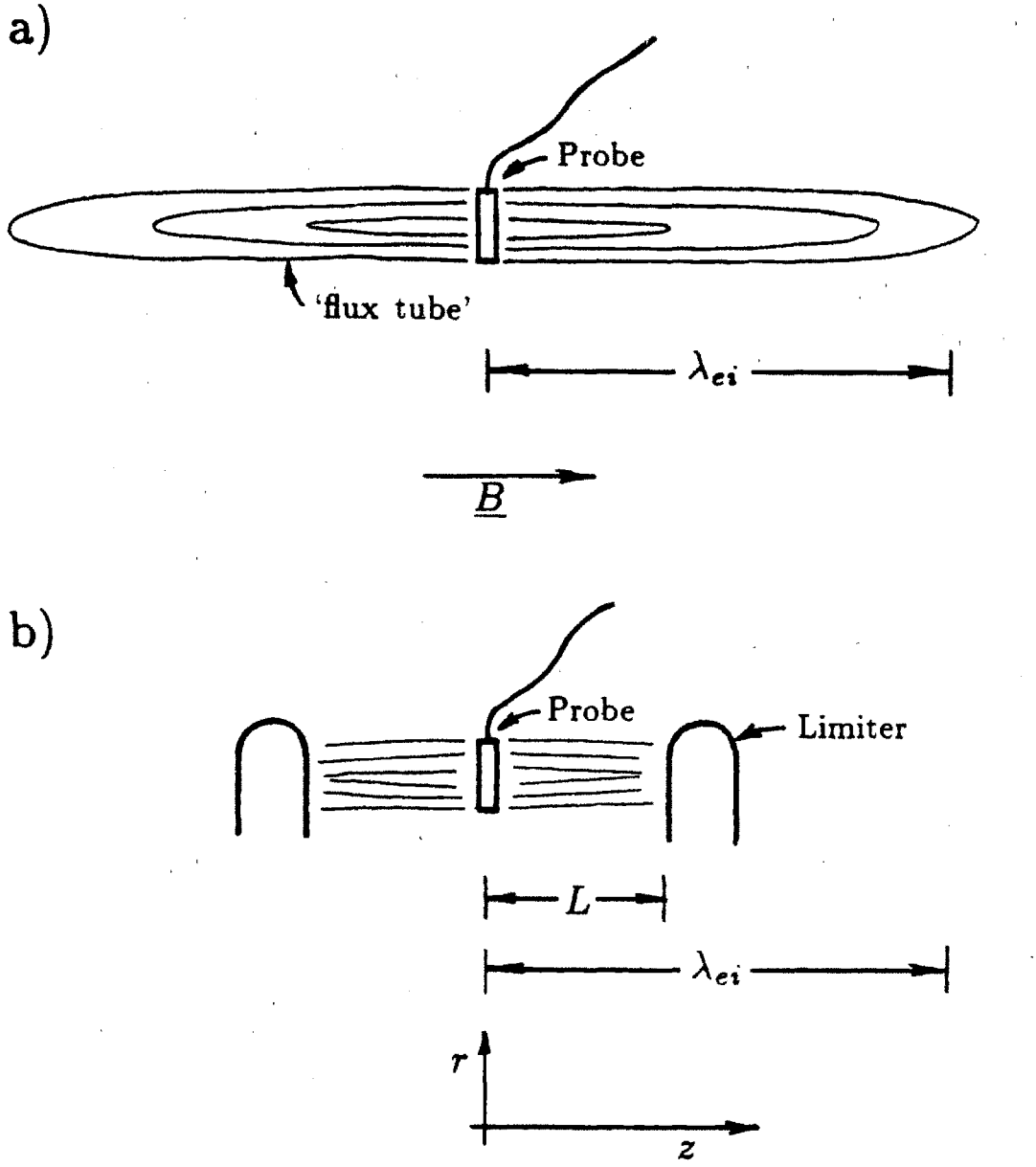

Figure E.1 Unbounded and Bounded Electron Collection Flux Tubes

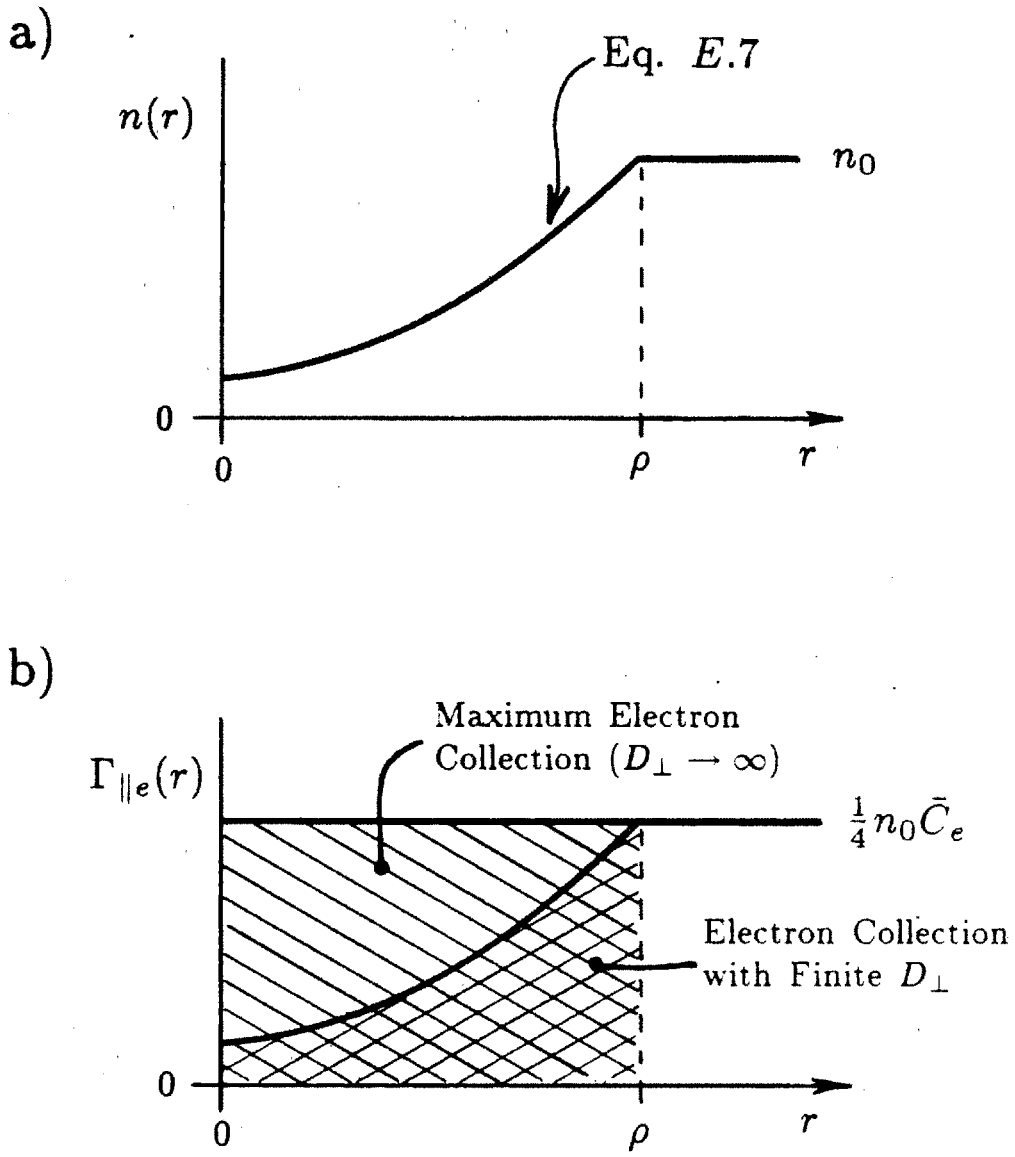

Figure E.2 Electron Density and Flux Depletion Across Probe Disk